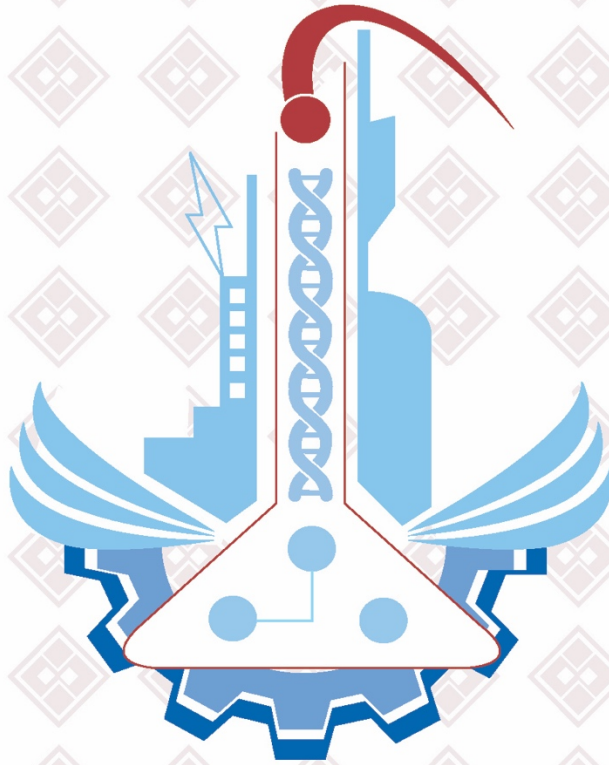


PRINTED ISSN: 1308-9080 / OLINE ISSN: 1308-9099

Volume: 18 / Number: 2 / Year: 2023

TURKISH JOURNAL OF SCIENCE & TECHNOLOGY



TURKISH JOURNAL OF SCIENCE AND TECHNOLOGY (TJST)

Year: 2023 Vol: 18 Number: 2

Address:

Fırat Universitesi
Fen Bilimleri Enstitüsü
23119, Elazig - TURKEY

Tel: 0 424 212 27 07
Fax: 0 424 236 99 55
e-mail: fenbilim@firat.edu.tr

New ISSN

Online: 1308-9099
Printed: 1308-9080

Old ISSN

Online: 1306 – 8555
Printed: 1306 – 8547

Refereed journal. Published twice a year

<https://dergipark.org.tr/tr/pub/tjst>

TURKISH JOURNAL OF SCIENCE & TECHNOLOGY (TJST)
Published by Firat University

Owner

Prof. Dr. Fahrettin GÖKTAŞ
Rector of Firat University

Editor in Chef

Assist. Prof. Dr. Ferhat UÇAR
Firat University, Faculty of Technology
Department of Software Engineering

Responsible Director

Prof. Dr. Burhan ERGEN
Firat University, Faculty of Engineering
Department of Computer Engineering

Editor

Assoc. Prof. Dr. Nida KATI
Firat University, Faculty of Technology
Department of Metallurgical and Materials Engineering

ADVISORY BOARD

Eyüp BAĞCI

Firat University, Department of Biology,
Elazig-Turkey

Eres SOYLEMEZ

Middle East Technical University,
Department of Engineering Science,
Ankara-Turkey

Coskun BAYRAK

UALR Donaghey Collage of Eng. and
Information Tech. Dept. of Computer
Science, Little Rock, AR, USA

Hikmet GECKIL

Inonu University, Department of Biology,
Malatya-Turkey

Metin CALTA

Firat University, Fisheries Faculty,
Elazig-Turkey

Ertan GOKALP

Karadeniz Technical University,
Department of Geodesy and
Photogrametry Engineering, Trabzon-
Turkey

Abdulkadir ŞENGÜR

Firat University, Department of
Electronics and Computer Education,
Elazig-Turkey

Hasan EFEOGLU

Ataturk University, Department of
Electrical-Electronics Engineering,
Erzurum-Turkey

Yanhui GUO

St. Thomas University, School of Science
and Technology, Miami, FL, USA

İbrahim TURKMEN

Balıkesir University, Department of
Geology Engineering, Balıkesir-Turkey

Deniz UNER

Middle East Technical University,
Department of Chemical Engineering,
Ankara-Turkey

M.Polat SAKA

Bahreyn University, Department of Civil
Engineering, Bahrain

Siqing XIA

Tongji Univ, State Key Lab Pollut Control
& Resource Reuse, Coll Environm Sci &
Engn, Shanghai 200092, R China

Zihni DEMIRBAG

Karadeniz Technical University,
Department of Biology, Trabzon-Turkey

Hanifi GULDEMİR

Firat University, Department of Electronics
and Computer Education, Elazig-Turkey

Nilgun GULEC

Middle East Technical University,
Department of Geology Engineering,
Ankara-Turkey

Erdogan GUNEL

West Virginia University, Department of
Statistics, Morgontown, USA

Sedigheh GHOFRANI

Islamic Azad University, Electrical
Engineering Department, Tehran South
Branch, Iran

Wang XIBAO

Tianjin University, The School of
Materials Science and Engineering, China

Brain WOERNER

West Virginia University, Department of
Computer Sciences & Electrical
Engineering, Morgontown, WV, USA

A. Kadri CETIN

Firat University, Department of Biology,
Elazig-Turkey

Yusuf Kağan KADIOĞLU

Ankara University, Department of Geology
Engineering, Ankara-Turkey

Sezgin BAKIRDERE

Yıldız Technical University, Department of
Chemistry, Ankara-Turkey.

Tuncay OREN

Ottawa Univ, Fac Eng, Inform Technol.
McLeod Inst Sim.t Sci, Ottawa, ON KIN
6N5 Canada

Halil ONDER

Middle East Technical University,
Department of Civil Engineering, Ankara-
Turkey

Nazmi POLAT

Ondokuz Mayıs University, Department of
Biology, Samsun-Turkey

Mustafa DORUCU

Firat University, Fisheries Faculty,
Elazig-Turkey

Binod Chandra TRIPATHY

Mathematical Sciences Division, Institute
of Advanced Study Science and Tech.
Paschim Boragaon; Guwahati, India

Eoin CASEY

University College Dublin, Chemical and
Bioprocess Engineering, Dublin, Ireland

Farid El-TANTAWY

Suez Canal University, Faculty of
Science, Department of Physics, Ismailia,
Egypt

Saleem HASHMI

International College of Technology,
Dublin, Ireland

Sakir ERDOĞDU

Karadeniz Technical University,
Department of Civil Engineering, Trabzon-
Turkey

Serdar SALMAN

Marmara University, Metallurgical and
Materials Engineering, İstanbul-Turkey

Firat University Turkish Journal of Science & Technology (TJST)
18-2, 2023

CONTENTS / İÇİNDEKİLER

- 1. Deep Learning for Physical Damage Detection in Buildings: A Comparison of Transfer Learning Methods**
Binalarda Fiziksel Hasar Tespiti için Derin Öğrenme: Transfer Öğrenme Yöntemlerinin Karşılaştırılması
Saltuk Taha USTAOĞLU, Betül BEKTAŞ EKİCİ 291-299
- 2. Some Approaches for Solving Multiplicative Second-Order Linear Differential Equations with Variable Exponentials and Multiplicative Airy's Equation**
İkinci Mertebeden Değişken Üslü Çarpımsal Lineer Diferansiyel Denklemlerin ve Çarpımsal Airy Denkleminin Çözümleri için Bazı Yaklaşımlar
Tuba GÜLŞEN 301-309
- 3. Evaluation of GPT-3 AI Language Model in Research Paper Writing**
Araştırma Makalesi Yazımında GPT-3 Yapay Zeka Dil Modeli Değerlendirmesi
Oğuzhan KATAR, Dilek ÖZKAN, GPT-3, Özal YILDIRIM, U. Rajendra Acharya..... 311-318
- 4. The Effect of the Second Stage Estimator on Model Performance in Post-LASSO Method**
Post-LASSO Yönteminde İkinci Aşama Tahmin Edicisinin Model Performansına Etkisi
Murat GENÇ, Ömer ÖZBİLEN..... 319-330
- 5. The Effect of Super Resolution Method on Classification Performance of Satellite Images**
Süper Çözünürlük Yönteminin Uydu İmgelerinin Sınıflandırma Performansına Etkisi
Ayşe CENGİZ, Derya AVCI..... 331-344
- 6. Antimicrobial and Antioxidant Activities of Different Extracts of Helichrysum arenarium subsp. (L.) Moench aucheri**
Helichrysum arenarium subsp. (L.) Moench aucheri'nin Farklı Ekstraktlarının Antimikrobiyal ve Antioksidan Aktivitesi
Ayşe EREN, Şule İNCİ, Kochar Khasro SALEH, Sevda KIRBAĞ, Kemal GÜVEN..... 345-351
- 7. Using MATLAB Statistics Toolbox for Data Analysis in Social Sciences with Chat GPT-3 prompts**
ChatGPT-3 Sorguları ile Sosyal Bilimlerde Veri Analizi için MATLAB İstatistik Araç Kutusu Kullanımı
Dönüş ŞENGÜR 353-361
- 8. Numerical Investigation of Heat Transfer on Hot and Cold Sides of a Thermoelectric Generator Using Heat Sinks**
Isı Kuyuları Kullanılarak Bir Termoelektrik Jeneratörün Sıcak ve Soğuk Yüzeyindeki Isı Transferinin Sayısal Olarak İncelenmesi
Enes KILINÇ 363-378
- 9. Measurement of Ultraviolet Light Transmittance of Different Contact Lens Types**
Farklı Türden Kontak Lenslerin Ultraviyole Işık Geçirgenliğinin Ölçülmesi
Ahmet BARLIK, Gonca ATEŞ..... 379-385

10. An Analysis Tool for Cryptographic Designs Based on Chaotic Systems <i>Kaotik Sistemler Tabanlı Kriptografik Tasarımlar için Bir Analiz Aracı</i> Yılmaz AYDIN, Fatih ÖZKAYNAK.....	387-395
11. The Effect of TiO₂ Thin Films Produced in Different Thicknesses on Dye-Sensitized Solar Cell Performance <i>Farklı Kalınlıklarda Üretilen TiO₂ İnce Filmlerinin Boya Duyarlı Güneş Pili Performansına Etkisi</i> Fehmi ASLAN.....	397-403
12. Second Generation Current Controlled Current Conveyor Based Low Pass Filter Design For The Processing of EEG Signals <i>EEG Sinyallerinin İşlenmesi için İkinci Nesil Akım Kontrollü Akım Taşıyıcı Tabanlı Alçak Geçiren Filtre Tasarımı</i> Kübra TEKİN, Hasan GÜLER.....	405-413
13. The Effect of Using Molybdenum Profile in Columns of Steel Building Models on The Modal Parameters <i>Çelik Bina Modellerinin Kolonlarında Molibden Profil Kullanımının Modal Parametrelere Etkisi</i> Furkan GÜNDAY.....	415-424
14. Computer Vision Based AutoML Platform <i>Bilgisayarlı Görü Tabanlı AutoML Platformu</i> Burak ŞAHİN, Aytuğ BOYACI.....	425-433
15. Investigation of Flight Performance of Notched Delta Wing Rockets on Different Types of Nose Cones <i>Farklı Tip Burun Konilerinde Çentikli Delta Kanat Roketlerin Uçuş Performansının İncelenmesi</i> Cihan OZEL, Cevher Kursat MACIT, Meral OZEL.....	435-447
16. Development of Unmanned Aerial Vehicle for Detecting the Forest Fires <i>Orman Yangınlarının Tespiti İçin İnsansız Hava Aracı Geliştirilmesi</i> Baris Mert KADIOGLU, Secil KARATAY, Yucel CETINCEVİZ, Faruk ERKEN.....	449-459
17. A Hybrid Classification Approach for Fasteners Based on Transfer Learning with Fine-Tuning and Deep Featurest <i>Derin Öznitelik ve İnce-Ayar ile Aktarım Öğrenme Tabanlı Bağlantı Elemanlarının Hibrit Sınıflandırma Yaklaşımı</i> Canan TASTIMUR, Erhan AKIN.....	461-475
18. The Solvent Effect on Nanomaterials Composed of Liquid Crystals and Nanoparticles: uv-vis Absorbance and Fluorescence Spectra <i>Sıvı Kristaller ve Nanoyapılardan Oluşan Nanomalzemeler Üzerine Çözücü Etkisi: uv-vis Absorbans ve Floresans Spektrumları</i> Yunus Emre KARA, Yadigar GÜLSEVEN SIDIR, Sabit HOROZ.....	477-486
19. R&D and Innovation Map of Turkey: Hybrid Model Approach <i>Türkiye Ar-Ge ve İnovasyon Haritası: Hibrit Model Yaklaşımı</i> Muhammed ÇUBUK.....	487-502
20. Development of a Nanocomposite-Based Electrochemical Sensing of Arsenic in Aqueous Solution <i>Sulu Çözeltide Arseniğin Nanokompozit Tabanlı Elektrokimyasal Algılanmasının Geliştirilmesi</i> Omer Sadak.....	503-510

21. **Pretrained Models and the Role of Feature Selection: An Artificial Intelligence-Based Approach in the Diagnosis of Diabetic Retinopathy**
Ön Eğitimli Modeller ve Özellik Seçiminin Rolü: Diyabetik Retinopati Tanısında Yapay Zeka Tabanlı Yaklaşım
Mehmet Kaan KAYA, Burak TAŞCI..... 511-517
22. **Enhancing Strawberry Harvesting Efficiency through Yolo-v7 Object Detection Assessment**
Yolo-v7 Nesne Tespiti ile Çilek Hasat Verimliliğinin Artırılması
Mehmet NERGİZ..... 519-533
23. **Statistical Evaluation of Treatment Compliance In Children With Attention Deficit Hyperactivity Disorder**
Dikkat Eksikliği Hiperaktivite Bozukluğu Olan Çocuklarda Tedavi Uyumunun İstatistiksel Değerlendirilmesi
Duygu MURAT, Uğur TEKİN..... 535-542
24. **MVSR Normalization Algorithm Method for Improving Vehicle License Plate Recognition**
Araç Plaka Tespitinin İyileştirilmesine Yönelik MVSR Normalleştirme Algoritması Yöntemi
Sertaç YAMAN, Yavuz EROL..... 543-552

Deep Learning for Physical Damage Detection in Buildings: A Comparison of Transfer Learning Methods

Saltuk Taha USTAOĞLU¹, Betül BEKTAŞ EKİCİ^{2*}

¹ Master Student, Department of Architecture, Fırat University, Elazığ, Türkiye

² Department of Architecture, Faculty of Architecture, Fırat University, Elazığ, Türkiye

¹ saltukustaoglu@gmail.com, ² bbektas@firat.edu.tr

(Geliş/Received: 04/05/2023;

Kabul/Accepted: 23/05/2025)

Abstract: The detection of physical damage in buildings is a critical task in ensuring the safety and integrity of structures. In this study, the effectiveness of deep learning methods for detecting physical damage in buildings, specifically focusing on cracks, defects, moisture, and undamaged classes was investigated. Transfer learning methods, including VGG16, GoogLeNet, and ResNet50, were used to classify a dataset of 7200 images. The dataset was split into training, validation, and testing sets, and the performance of the models was evaluated by using metrics such as accuracy, precision, recall, and F1-score. Results show that all three models achieved high accuracy on the test set, with VGG16 and ResNet50 outperforming GoogLeNet. Additionally, precision, recall, and F1-score metrics indicate strong performance across all classes, with VGG16 and ResNet50 achieving particularly high scores. It is demonstrated the effectiveness of deep learning methods for physical damage detection in buildings and provides insights into the comparative performance of transfer learning methods.

Key words: Structural damage classification, deep learning, convolutional neural networks, transfer learning.

Binalarda Fiziksel Hasar Tespiti için Derin Öğrenme: Transfer Öğrenme Yöntemlerinin Karşılaştırılması

Öz: Binalardaki fiziksel hasarın tespiti, yapıların güvenliğini ve bütünlüğünü sağlamada kritik bir görevdir. Bu çalışmada, özellikle çatlaklar, kusurlar, nem ve hasarsız sınıflara odaklanarak binalardaki fiziksel hasarı tespit etmek için derin öğrenme yöntemlerinin etkinliği araştırılmıştır. VGG16, GoogLeNet ve ResNet50 dahil olmak üzere transfer öğrenme yöntemleri, 7200 görüntüden oluşan bir veri kümesini sınıflandırmak için kullanılmıştır. Veri kümesi eğitim, doğrulama ve test kümelerine ayrılmış ve modellerin performansı doğruluk, kesinlik, geri çağırma ve F1-skoru gibi ölçütler kullanılarak değerlendirilmiştir. Sonuçlar, üç modelin de test setinde yüksek doğruluk elde ettiğini, VGG16 ve ResNet50'nin GoogLeNet'ten daha iyi performans gösterdiğini ortaya koymuştur. Ayrıca, hassasiyet, geri çağırma ve F1-skoru ölçümleri tüm sınıflarda güçlü performans gösterirken, VGG16 ve ResNet50 özellikle yüksek puanlar elde etmiştir. Binalarda fiziksel hasar tespiti için derin öğrenme yöntemlerinin etkinliği gösterilmiş ve transfer öğrenme yöntemlerinin karşılaştırmalı performansına ilişkin içgörüler sağlanmıştır.

Anahtar kelimeler: Yapısal hasar sınıflandırması, derin öğrenme, evrişimli sinir ağları, transfer öğrenme.

1. Introduction

The detection of physical damage in buildings is a critical task for ensuring their safety and longevity. Physical damage can take various forms, including cracks, deformation, and moisture, and can be caused by factors such as natural disasters, structural weaknesses, or aging. Detecting and assessing physical damage is typically performed by human inspectors, who visually inspect buildings for signs of damage. However, this process can be time-consuming, costly, and subject to human error [1].

Recent advances in machine learning, particularly deep learning, have opened up new possibilities for automated physical damage detection in buildings. Deep learning is a subset of machine learning that uses neural networks to learn patterns and features from large datasets and has been successfully applied to various image classification tasks, including medical diagnosis, object recognition, and natural language processing [2].

This study investigates the effectiveness of deep learning methods for detecting physical damage in buildings. Four classes of physical damage: crack, defect, moisture, and undamaged are taken into consideration. We use a dataset of 7200 images, with 1800 images in each class, and employ transfer learning methods to classify the images. Transfer learning is a popular approach in deep learning that leverages pre-trained models on large datasets to improve the performance of smaller, task-specific datasets [3], [4].

* Corresponding author: bbektas@firat.edu.tr. ORCID Number of authors: ¹ 0000-0001-7378-3374, ² 0000-0003-0142-0587.

Specifically, we compare the performance of three transfer learning methods: VGG16, GoogLeNet, and ResNet50. VGG16Net is a deep convolutional neural network architecture used for image recognition and classification. It was developed by the Visual Geometry Group (VGG) at the University of Oxford in 2014 and consists of 16 layers of convolutional and fully connected neural network layers. VGG16Net achieved state-of-the-art performance in several image recognition and classification tasks and has been widely used as a pre-trained model in transfer learning for various computer vision applications [5]. GoogLeNet, also known as Inception V1, is another CNN that won the ImageNet competition in 2014 and is known for its efficient use of computational resources [6]. ResNet50 is a more recent CNN architecture that uses residual connections to improve the training of deep neural networks [7].

We split our dataset into training, validation, and testing sets, and evaluate the performance of the models using metrics such as accuracy, precision, recall, and F1-score. Our study contributes to the growing body of literature on using deep learning for physical damage detection in buildings and provides insights into the comparative performance of transfer learning methods. The results of our study have important implications for the development of automated systems for building inspection and maintenance, which can improve the safety and longevity of buildings while reducing costs and human error.

2. Literature Review

Deep learning-based approaches have shown remarkable results in the field of computer vision, particularly in object detection and classification tasks. In recent years, these methods have also been applied to building damage detection tasks, with promising results. The detection of physical damage in buildings is a critical task for ensuring their safety and structural integrity. Traditional methods for damage detection require expert knowledge and are often time-consuming and expensive. The use of machine learning methods for physical damage detection in buildings has gained significant attention in recent years. Deep learning, in particular, has shown promise for automated building inspection and maintenance, which can improve safety, reduce costs, and increase efficiency.

Several studies have investigated the application of deep learning methods for building damage detection. For example, Kung et al. [8] proposed a method that combined UAV with a deep learning model to detect external wall tile deterioration of buildings, using images taken by the UAV. The authors made modifications to improve the efficiency of their method and tested the model's accuracy for efflorescence (Accuracy 91%, Recall 80%), spalling (Accuracy 76%, Recall 100%), cracking (Accuracy 86%, Recall 86%), and defacement (Accuracy 98%, Recall 78%). The model achieved high accuracy and recall rates for efflorescence, cracking, and defacement, but slightly lower rates for spalling. Similarly, Flah [9] has introduced an automated inspection model that employs image processing and deep learning techniques to identify defects in concrete structures that are not easily accessible. This model has demonstrated a remarkable classification accuracy of 97.63%, 96.5%, and 96.17% for the training, validation, and testing datasets, respectively. Additionally, it has achieved low quantification error in determining crack length, width, and angle of orientation.

In another study, Wang et al. [10] Wang et al. [10] have presented a two-tier approach for detecting and segmenting objects using Faster R-CNN and Mask R-CNN, respectively. This approach is specifically designed to identify and quantify the damage on historic glazed tiles. The method achieved an average precision of 0.910 and 0.890 for roll roofing and pan tiles, respectively, and an average precision of 0.975 for damage segmentation. A hierarchical CNN and gated recurrent unit framework were suggested by Yang et al. [11] for detecting structural damage, incorporating both spatial and temporal relationships. This framework was assessed using two datasets: the IASC-ASCE structural health monitoring benchmark and a scale model of a three-span continuous rigid frame bridge structure. The results of the evaluation showed that the proposed method outperformed other existing approaches with a detection rate of 84.3%. A new approach for rapid investigation and damage detection of the Great Wall was presented by Wang et al. [12], which combined mobile crowd sensing with deep learning techniques. The proposed Great Watcher system demonstrated an accuracy of 78.2% in classifying damage to the Great Wall. Furthermore, a surface damage identification and location technique based on Faster R-CNN was introduced, which quickly identified and located damage to masonry structures on the Great Wall. Nex et al. [13] proposed a CNN model for visible structural damage detection using heterogeneous and large datasets covering different locations, spatial resolutions, and platforms. The results showed that quality metrics are influenced by the composition of training samples used in the network and pre-trained networks optimized for different spatial resolutions.

In another study, Jiang et al. [14] proposed a method based on deep learning called DDSNet, combines optimized YOLOv4 and deeplabv3+ models for two-stage pavement crack detection and segmentation. They stated that the accuracy is improved by 2.23% and 7.47%, respectively, and the inference speed is increased by

35.3% and 50.3%, respectively. Lin et al. [15] proposed a structural damage detection approach using deep convolutional neural networks that can automatically extract features from low-level waveform signals. Their results show that the CNN approach achieves high accuracy, even with noisy data, and can identify multiple damages while also providing insights into the learned hierarchical features.

Transfer learning has also been widely used in deep learning-based building damage detection. For example, Dais et al. [16] used deep learning technique, including transfer learning, for crack detection on images of masonry walls, achieving 95.3% accuracy at patch level and 79.6% F1-score on pixel level. Similarly, Perez et al. [17] developed a deep learning-based method using fine-tuning transfer learning to classify images of building defects caused by dampness into four categories and achieved an overall accuracy of 87.50% on a separate evaluation set of 732 images with high precision in defect localization using the class activation mapping technique. In their study, Teng et al. [18] put forward a structural damage detection approach that relies on digital twin (DT) and transfer learning. DT technology was utilized to obtain a vast number of damage samples of numerical models, which were then used to train a convolutional neural network (CNN) as a pre-trained network. The pre-trained CNN was subsequently transferred to experimentally tested structures and a real bridge structure using transfer learning technology. The proposed method achieved a remarkable detection accuracy of up to 97.3% for the real bridge structure. Elghaish et al. [19] tested four pre-trained CNN models and developed a new CNN model to detect and classify types of highway cracks. The accuracies of the pre-trained models were above average, with GoogleNet achieving the highest accuracy of 89.08%. The newly developed CNN model outperformed all pre-trained models with an accuracy of 97.62% using Adam's optimization algorithm at a learning rate of 0.001. Feng et al. [20] processed the image data collected by high-resolution cameras from the hydro-junction infrastructure and used it for damage detection. They emphasized that the network they created by changing the structure of Inception-v3 has an accuracy value of 96.8% in damage detection. Gulgec et al. [21] used the CNN method to classify damaged and undamaged samples modeled by finite element simulations to detect deficiencies that affect the performance of the building. Based on the findings, they stated that their application has high accuracy, robustness and computational efficiency.

In addition to deep learning, other machine learning methods have been used for building damage detection. For instance, Eltouny et al. [22] presented a density-based unsupervised learning technique for detecting and localizing structural damage, which employs cumulative intensity measures for feature extraction and a statistical model construction process based on kernel density maximum entropy and Bayesian optimization. The efficacy of this framework was tested using three case studies, and the outcomes indicated an average accuracy of 92% in detecting and localizing damage in both numerical and experimental structures.

Although there have been several studies on the detection of building defects using deep learning techniques, most of them have focused on a specific type of defect or have used a relatively small dataset. In this study, we aim to develop a deep learning model that can detect and classify four types of building defects, including crack, deformation, moisture, and undamaged areas, using a larger dataset of 7200 images. We evaluate the performance of three popular deep learning models, VGG16, GoogLeNet, and ResNet50, on this dataset and compare their results. The findings of this study could potentially aid in the efficient and accurate detection of building defects, thereby reducing the costs and time associated with manual inspection and maintenance.

3. Materials and Methods

The visual data in the dataset include images of building elements made of building materials such as brick, stone, reinforced concrete, plaster and wood. In addition to these, deterioration and building damage on walls and decorations are also included. Most of the images were obtained from the authors' own archives and not used by other researchers in any previous study. A dataset of 7200 images was collected for this study, which included four categories of physical damage in buildings: crack, deformation, moisture, and undamaged [23]. The dataset was divided into four equal parts, with each category containing 1800 images. The dimensions of the images were 227x227x3. Three popular transfer learning models, VGG16, GoogLeNet, and ResNet50, were used for this study. The structure of transfer learning applied in this study is depicted in Figure 1. The collected data were preprocessed before training the models. The images were resized to fit the input size of the models. The data were also normalized to have a mean of 0 and a standard deviation of 1. The randomly selected images from each class, including cracked walls, deformed structures, moisture damage, and undamaged buildings can be seen in Figure 2.

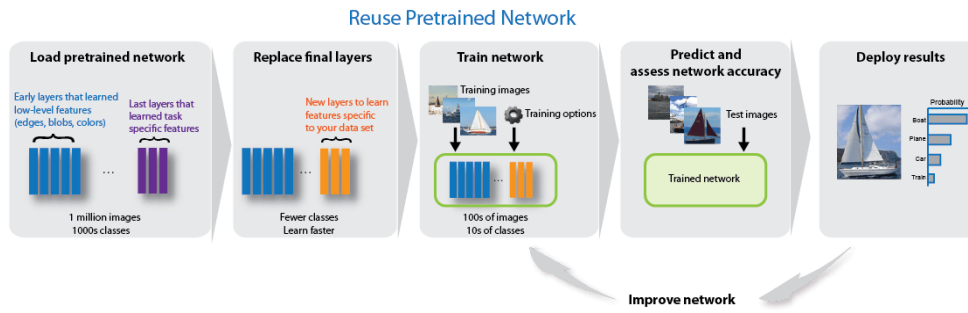


Figure 1. Structure of pre-trained neural network [24].



Figure 2. Randomly selected images from each class.

In the fine-tuning process, the pre-trained models were first loaded with their pre-trained weights, and the output layers were removed. A new output layer was added with the appropriate number of units for the 4-class classification task. The output layer was then trained with the dataset while keeping the weights of the pre-trained layers frozen. Finally, the weights of all layers were fine-tuned with the dataset. The models were trained using both MATLAB Deep Learning Designer and Python software. The training process was performed with a mini-batch size of 20 in MATLAB and 32 in Python. The number of epochs for training was 150 in MATLAB and 50 in Python, with a learning rate of 0.00001 in MATLAB and 0.0001 in Python. The validation dataset, which consisted of 20% of the training dataset, was used to optimize the hyperparameters. To visually represent the training and validation accuracy and loss over epochs, line plots were created for each of the models. Confusion matrices were also generated to visualize the number of correct and incorrect predictions for each class.

The models' performance was evaluated using several metrics, including accuracy, precision, recall, and F1-score. The accuracy of the models was calculated as the percentage of correctly classified images in the test dataset. The precision, recall, and F1-score were calculated for each class based on their scores.

The models were trained on a computer equipped with an Nvidia GeForce RTX 2070 Super graphics card. MATLAB Deep Learning Designer and Python 3.10.11 with TensorFlow 2.10.0, CUDA 11.2, and cuDNN 8.1 were used for implementing the transfer learning methods. The training parameters used in the MATLAB deep learning models are shown in Figure 3.

SOLVER	
Solver	sgdm
InitialLearnRate	0.0001
BASIC	
ValidationFrequency	50
MaxEpochs	150
MiniBatchSize	20
ExecutionEnvironment	gpu
SEQUENCE	
SequenceLength	longest
SequencePaddingValue	0
SequencePaddingDirection	right
ADVANCED	
L2Regularization	0.0001
GradientThresholdMethod	l2norm
GradientThreshold	Inf
ValidationPatience	Inf
Shuffle	every-ep...
CheckpointPath	
LearnRateSchedule	none
LearnRateDropFactor	0.1
LearnRateDropPeriod	10

Figure 3. Training parameters for Matlab deep learning designer.

The model was trained using a solver of SGDM, a mini-batch size of 20, a max epoch of 150, an initial learning rate of 0.00001, and a learning rate drop factor of 0.1 (see Figure 2).

4. Results and Analysis

Three different deep learning models, VGG16, GoogLeNet, and ResNet50, were trained and tested on a dataset of 7200 images that were divided into four classes: crack, defect, moisture, and undamaged. The models were evaluated based on their accuracy, loss, and confusion matrices. The precision, recall, and F1-score metrics were also calculated for each class.

The accuracy and loss graphs obtained from Python experiments for the three models are shown in Figure 4-6 respectively. As can be seen from the graphs, all three models show a similar trend, with a gradual increase in accuracy and a decrease in loss over the epochs.

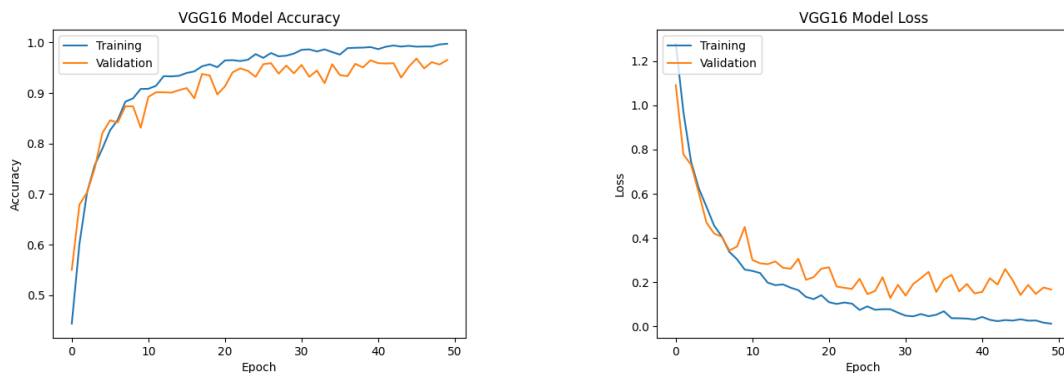


Figure 4. Accuracy and loss for VGG16 model.

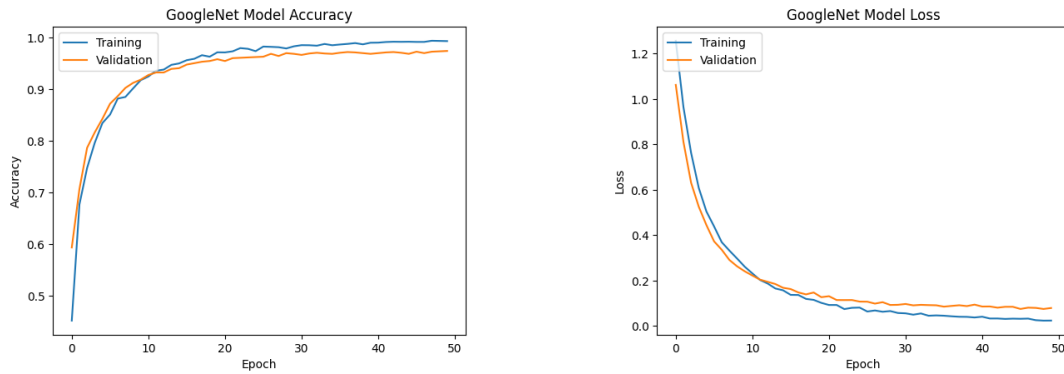


Figure 5. Accuracy and loss for GoogleNet model.

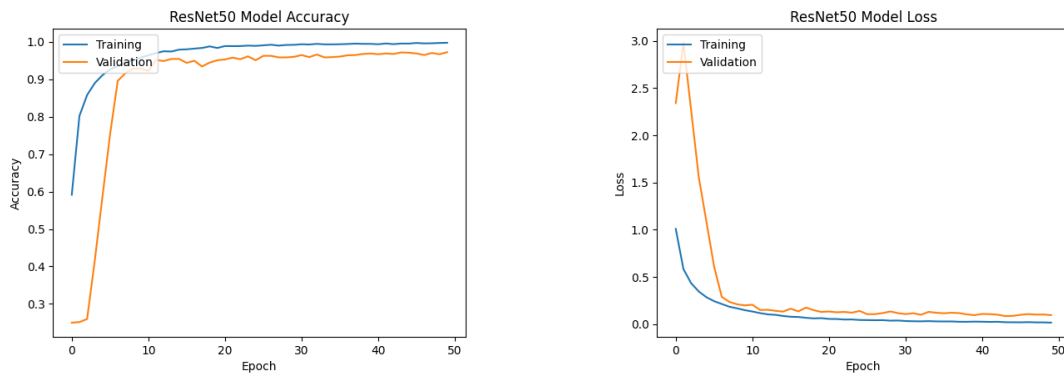


Figure 6. Accuracy and loss for ResNet50 model.

The confusion matrices for the three models are shown in Figure 7-9 respectively. As can be seen from the matrices, all three models perform well in detecting the different types of physical damage in buildings, with high accuracy rates for each class. However, the VGG16 and ResNet50 models outperform the GoogLeNet model in terms of overall accuracy. ResNet50 model has the best model according to confusion matrix results.

	crack	deterioration	moisture	undamaged
True Class	crack	deterioration	moisture	undamaged
	360	4	3	
		356	357	360
	crack	deterioration	moisture	undamaged
	Predicted Class			

Figure 7. Confusion matrix for VGG16 model.

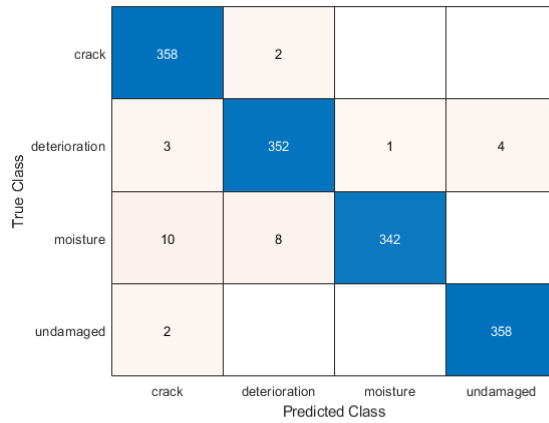


Figure 8. Confusion matrix for GoogleNet model.

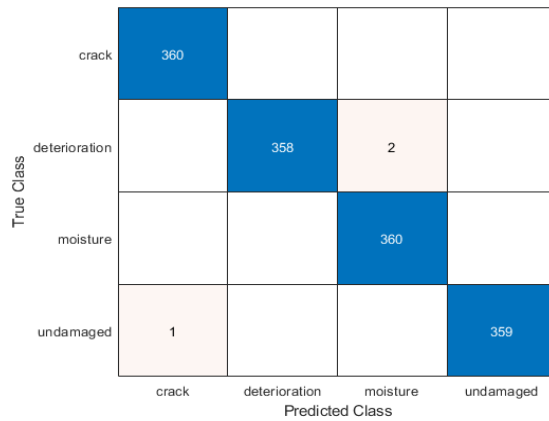


Figure 9. Confusion matrix for ResNet50 model.

The validation and testing accuracy values for the three models are shown in Table 1. The results indicate that all three models perform well, with high accuracy rates for both validation and testing datasets. The VGG16 and ResNet50 models show the highest accuracy rates, with both models achieving over 99% accuracy in the validation dataset.

Table 1. Validation and testing accuracy for three models

Model	Matlab Validation Accuracy (%)	Matlab Testing Accuracy (%)	Python Testing Accuracy (%)
VGG16	99.83	99.51	96.53
GoogLeNet	99.22	97.92	97.71
ResNet50	99.83	99.79	97.22

The precision, recall, and F1-score metrics for the three models are shown in Table 2. The results indicate that all three models perform well in detecting physical damage in buildings, with high precision, recall, and F1-score values for each class. However, the VGG16 and ResNet50 models show higher values than the GoogLeNet model for most of the classes.

Table 2. Precision, recall, and f1-score metrics for three models

Model	Class	Precision (%)	Recall (%)	F1-score (%)
VGG16	Crack	98.09	100.00	99.04
	Deformation	100.00	98.89	99.44
	Moisture	100.00	99.17	99.58
	Undamaged	100.00	100.00	100.00
GoogLeNet	Crack	95.98	99.44	97.68
	Deformation	97.24	97.78	97.51
	Moisture	99.71	95.00	97.30
	Undamaged	98.90	99.44	99.17
ResNet50	Crack	99.72	100.00	99.86
	Deformation	100.00	99.44	99.72
	Moisture	99.45	100.00	99.72
	Undamaged	100.00	99.72	99.86

Overall, the results of this study suggest that deep learning models can be effective in detecting physical damage in buildings using image data. The VGG16 and ResNet50 models show higher accuracy rates and better performance metrics than the GoogLeNet model.

5. Discussion

The results of this study demonstrate that deep learning models can be successfully applied to detect physical damage in buildings using image analysis techniques. The use of transfer learning with VGG16, GoogLeNet, and ResNet50 allowed for the accurate classification of images into four different classes of crack, deformation, moisture, and undamaged, with overall test accuracy scores ranging from 96.53% to 99.79%. The high accuracy and precision of the models suggest that deep learning could be a useful tool for identifying building damage in a variety of real-world scenarios.

In terms of model performance, VGG16 and ResNet50 achieved the highest accuracy scores in the experiments. This could be due to the deeper architecture of these models, which allowed for more complex features to be learned and extracted from the input images. GoogLeNet, although achieving high accuracy scores, was slightly less accurate than the other two models. This could be attributed to the use of "inception modules" in its architecture. GoogLeNet stacks multiple inception modules together to form a deep neural network. The main idea of the Inception module is that of running multiple operations (pooling, convolution). So, this may not have been as effective at capturing the features relevant to building damage in this particular dataset.

The results also indicate that the model performance was not significantly impacted by the choice of software or hardware used for training. Both Matlab and Python experiments using GPU achieved high accuracy scores, and the differences in accuracy scores between the two software were relatively small.

Finally, it should be noted that this study has several limitations. The dataset used in this study was limited to only four classes of building damage and did not include other types of damage such as fire or structural damage. Additionally, the dataset was generated artificially and may not fully represent the complexities and variations in real-world building damage scenarios. Nevertheless, this study provides a foundation for future research in the use of deep learning for building damage detection.

6. Conclusion

In conclusion, this study demonstrates the potential of deep learning models for detecting physical damage in buildings using image analysis techniques. The use of transfer learning with VGG16, GoogLeNet, and ResNet50 resulted in the accurate classification of images into four different classes of crack, deformation, moisture, and undamaged. The high accuracy and precision of the models suggest that deep learning could be a useful tool for identifying building damage in a variety of real-world scenarios.

Future research could expand on this study by incorporating more diverse and complex datasets and exploring other deep-learning architectures. Additionally, this study provides a foundation for the development of automated building damage detection systems that could help prevent further damage and ensure the safety of occupants in affected buildings.

Acknowledgement

The data set used in this study was obtained from the master's thesis prepared by S.T.U, entitled "Detection of Building Physics Problems with Convolutional Neural Networks". B.B.E., the idea owner and thesis advisor, played an active role in the implementation of the applications and the writing of the article. S.T.U., prepared the data set, took part in the literature review and implementation of the applications.

References

- [1] Ekici BB. Detecting damaged buildings from satellite imagery. *J. Appl. Remote Sens* 2021; 15(3): 032004.
- [2] Sharma N, Sharma R, Jindal N. Machine learning and deep learning applications-a vision. *Glob. Transitions Proc* 2021; 2(1): 24–28.
- [3] Iman M, Arabnia HR, Rasheed K. A review of deep transfer learning and recent advancements. *Technol* 2023; 11(2): 40.
- [4] Zhuang F, Qi Z, Duan K, Xi D, Zhu Y, Zhu H, Xiong H, He Q. A comprehensive survey on transfer learning. *Proc. IEEE* 2021; 109(1): 43–76.
- [5] “Visual Geometry Group - University of Oxford.” <https://www.robots.ox.ac.uk/~vgg/> (accessed May 02, 2023).
- [6] “ILSVRC2014 Results.” <https://image-net.org/challenges/LSVRC/2014/results> (accessed May 02, 2023).
- [7] “Deep Residual Networks (ResNet, ResNet50) 2023 Guide - viso.ai.” <https://viso.ai/deep-learning/resnet-residual-neural-network/> (accessed May 02, 2023).
- [8] Kung RY, Pan NH, Wang CCN, Lee PC. Application of deep learning and unmanned aerial vehicle on building maintenance. *Adv. Civ. Eng* 2021; 2021: 5598690.
- [9] Flah M, Suleiman AR, Nehdi ML. Classification and quantification of cracks in concrete structures using deep learning image-based techniques. *Cem Concr Compos* 2020; 114: 103781.
- [10] Wang N, Zhao X, Zou Z, Zhao P, Qi F. Autonomous damage segmentation and measurement of glazed tiles in historic buildings via deep learning. *Comput Civ Infrastruct Eng* 2020; 35(3): 277–291.
- [11] Yang J, Zhang L, Chan C, Li Y, Li R, Wang G, Jiang S, Zeng Z. A hierarchical deep convolutional neural network and gated recurrent unit framework for structural damage detection. *Inf Sci* 2020; 540: 117–130.
- [12] Wang N, Zhao X, Wang L, Zou Z. Novel system for rapid investigation and damage detection in cultural heritage conservation based on deep learning. *J Infrastruct Syst* 2019; 25(3):04019020.
- [13] Nex F, Duarte D, Tonolo FG, Kerle N. Structural building damage detection with deep learning: assessment of a state-of-the-art cnn in operational conditions. *Remote Sens* 2019; 11(23): 2765.
- [14] Jiang Y, Pang D, Li C, Yu Y, Cao Y. Two-step deep learning approach for pavement crack damage detection and segmentation. *Int. J. Pavement Eng* 2022:1-14. doi: 10.1080/10298436.2022.2065488.
- [15] Lin YZ, Nie ZH, Ma HW. Structural damage detection with automatic feature-extraction through deep learning. *Comput Civ Infrastruct Eng* 2017; 32(12): 1025–1046.
- [16] Dais D, Bal İE, Smyrou E, Sarhosis V. Automatic crack classification and segmentation on masonry surfaces using convolutional neural networks and transfer learning. *Autom Constr*; 125: 103606.
- [17] Perez H, Tah JHM, Mosavi A. Deep learning for detecting building defects using convolutional neural networks. *Sensors* 2019; 19 (16): 3556.
- [18] Teng S, Chen X, Chen G, Cheng L. Structural damage detection based on transfer learning strategy using digital twins of bridges. *Mech Syst Signal Process* 2023; 191:110160.
- [19] Elghaish F, Talebi S, Abdellatef E, Matarneh ST, Reza Hosseini M, Wu S, Mayouf M, Hajirasouli A, Nguyen TQ. Developing a new deep learning cnn model to detect and classify highway cracks. *J Eng Des Technol* 2022; 20 (4): 993–1014.
- [20] Feng C, Zhang H, Wang S, Li Y, Haoran W, Yan F. Structural Damage Detection using deep convolutional neural network and transfer Learning. *KSCE J Civ Eng* 2019; 23(1); 1-10.
- [21] Gulgec, NS, Takáč M, Pakzad, SN. Structural Damage Detection Using Convolutional Neural Networks. In: 35th IMAC, A conference and exposition on structural dynamics; Ja 30-Feb 2 2016; CA, USA: Cham, Germany: Springer. pp. 331-337.
- [22] Eltouny KA, Liang X. Bayesian-optimized unsupervised learning approach for structural damage detection. *Comput Civ Infrastruct Eng* 2021; 36 (10): 1249–1269.
- [23] S. T. Ustaoğlu, “Detection of Building Physics Problems With Convolutional Neural Networks. MSc, Firat University, Elazığ, Türkiye, 2023.
- [24] “Transfer Learning Using Pretrained Network - MATLAB & Simulink.” <https://www.mathworks.com/help/deeplearning/ug/transfer-learning-using-pretrained-network.html> (accessed May 02, 2023).

Some Approaches for Solving Multiplicative Second-Order Linear Differential Equations with Variable Exponentials and Multiplicative Airy's Equation

Tuba GÜLŞEN^{1*}

¹ Department of Mathematics, Faculty of Science, Fırat University, Elazığ, Türkiye
*¹ tyalcin@firat.edu.tr

(Geliş/Received: 12/04/2023;

Kabul/Accepted: 29/05/2023)

Abstract: This paper offers several approaches for solving multiplicative second-order linear differential equations with variable exponentials, such as normalization and reduction to Riccati equations. In addition, in this paper, the multiplicative version of the Airy equation, which emerges in fluid mechanics, geophysics, and atomic physics, is solved using the multiplicative power series solution method.

Key words: Multiplicative calculus, transform, multiplicative Airy's equation.

İkinci Mertebeden Değişken Üslü Çarpımsal Lineer Diferansiyel Denklemlerin ve Çarpımsal Airy Denkleminin Çözümleri için Bazı Yaklaşımlar

Öz: Bu makale, normalleşme ve Riccati denklemlerine indirgenme gibi ikinci mertebeden değişken katsayılı çarpımsal lineer diferansiyel denklemleri çözmek için çeşitli yaklaşımlar sunmaktadır. Ayrıca bu makalede akışkan mekaniği, jeofizik ve atom fiziğinde ortaya çıkan Airy denkleminin çarpımsal versiyonu çarpımsal kuvvet serisi çözüm yöntemi kullanılarak çözülmüştür.

Anahtar kelimeler: Çarpımsal hesap, dönüşüm, çarpımsal Airy denklemleri.

1. Introduction

As a substitute for traditional calculus, Grossman and Katz [1-2] invented multiplicative calculus in 1967. Because it differs from the traditional calculus of Newton and Leibniz, this sort of calculus is often referred to as "non-Newtonian calculus". Multiplicative calculus is a valuable addition to standard calculus since it is designed to be similar to how standard calculus is suited to cases involving linear functions and scenarios involving exponential functions. In multiplicative calculus, the functions of addition and subtraction are moved to multiplication and division. There are a lot of benefits to studying the calculation of multiplicative. It enhances the effectiveness of additive computations indirectly. Problems that are challenging to tackle in a traditional situation are solved here with amazing simplicity. Within the confines of specific constraints, multiplicative analysis may specify any attribute in the Newtonian situation.

Natural phenomena frequently change exponentially. Events that act in this way include the populations of nations and the magnitude of earthquakes, to quote Benford [3] as an example. Multiplicative analysis, as opposed to classical analysis, enables a better physical assessment of these types of occurrences. In several disciplines, including finance, economics, biology, and demography, this calculus also yields better findings than typical. Up until the beginning of the 2000s, relatively little research had been done on this analysis. Numerous studies have recently been conducted on it, and the results are of high quality and effectiveness (see [3-17]). Using the fundamental ideas of multiplicative analysis, various investigations on multiplicative ordinary differential equations have been conducted in recent years [18-22].

The Airy's equation, a classical equation in mathematical physics, has recently gained popularity among scientists because it is used to model light deflection and some optics problems. It is possible to see Airy's equation that in several solutions in the fields fluid mechanics, geophysics and atomic physics etc. Because of the need to effectively and necessity to express a physical phenomenon and Airy's equation resulting from the need to express it in comprehensive analytical form, many equations in mathematical physics can be written in the Airy's equation format by making appropriate transforms [23,24]. Given that the Airy's equation is linear, the analytical solution at the origin may be discovered using the power series solution approach. Their use in the approximate solution of differential equations with a simple turning point, the approximate solution of integrals with converging saddle points, and the mathematical modeling of physical processes is becoming more and more common [25-32]. However, this equation has not been examined in the multiplicative analysis.

* Corresponding author: tyalcin@firat.edu.tr. ORCID Number of authors: ¹ 0000-0002-2288-8050

2. Preliminaries

This section will provide some fundamental definitions and characteristics of multiplicative calculus theories.

Definition 2.1. [33] Assume that $\varphi: A \subset \mathbb{R} \rightarrow \mathbb{R}$ is positive, differentiable in the usual case, and that $\varphi > 0$ for every t . $\varphi^*(t)$ is known as the multiplicative derivative of φ at t if the limit:

$$\varphi^*(t) = \lim_{h \rightarrow 0} \left[\frac{\varphi(t+h)}{\varphi(t)} \right]^{\frac{1}{h}}, \quad (2.1)$$

is positive and exists.

Definition 2.2. [33] Assume that $\varphi: A \rightarrow \mathbb{R}$ is positive, usual differentiable at t . The following is the relationship between classical and multiplicative derivatives:

$$\varphi^*(t) = e^{(\ln \circ \varphi)'(t)}.$$

Theorem 2.1. [33] Assume that φ, ψ are multiplicative differentiable and that κ is usual differentiable at t . The phrases listed below are offered for multiplicative derivative.

- i) $(\vartheta\varphi)^*(t) = \varphi^*(t), \quad \vartheta \in \mathbb{R}^+,$
- ii) $(\varphi\psi)^*(t) = \varphi^*(t)\psi^*(t),$
- iii) $(\varphi/\psi)^*(t) = \varphi^*(t)/\psi^*(t),$
- iv) $(\varphi^\kappa)^*(t) = \varphi^*(t)^{\kappa(t)} \varphi(t)^{\kappa'(t)},$
- v) $(\varphi + \psi)^*(t) = \varphi^*(t)^{\frac{\varphi(t)}{\varphi(t)+\psi(t)}} \psi^*(t)^{\frac{\psi(t)}{\varphi(t)+\psi(t)}}.$

Definition 2.3. [33] Assume that φ is positive, bounded function on finite interval $[a, b]$. The symbol $\int_a^b \varphi(t) dt$ is then known as multiplicative integral of φ on $[a, b]$. According to this definition, if φ is positive and Riemann integrable on $[a, b]$, then it is multiplicative integrable on $[a, b]$ and

$$\int_a^b \varphi(t) dt = e^{\int_a^b (\ln \circ \varphi)(t) dt}.$$

On the other hand, if φ is Riemann integrable on $[a, b]$, one may demonstrate that:

$$\int_a^b \varphi(t) dt = \ln \int_a^b (e^{\varphi(t)}) dt.$$

Theorem 2.2. [33] Assume that φ, ψ are positive, bounded function on $[a, b]$. The multiplicative derivative is provided with the following expressions.

- i) $\int_a^b (\varphi(t)^\vartheta) dt = \left(\int_a^b \varphi(t) dt \right)^\vartheta, \quad \vartheta \in \mathbb{R},$
- ii) $\int_a^b \varphi(t)\psi(t) dt = \int_a^b \varphi(t) dt \int_a^b \psi(t) dt,$
- iii) $\int_a^b \left(\frac{\varphi(t)}{\psi(t)} \right) dt = \frac{\int_a^b \varphi(t) dt}{\int_a^b \psi(t) dt},$

$$\text{iv) } \int_a^b \varphi(t) dt = \int_a^c \varphi(t) dt + \int_c^b \varphi(t) dt, \quad c \in [a, b].$$

3. Some Methods for General Solution of Multiplicative Second-Order Linear Differential Equations with Variable Exponentials and Multiplicative Airy's Equation

In this section, firstly, multiplicative second-order differential equations will be considered and solved by using some transforms. Then, using the multiplicative power series method [20, 22] multiplicative Airy's equation will be solved.

The definition of multiplicative linear differential equations is given in [21, 34] by

$$(y^{*(n)}(\chi))^{a_n(\chi)} (y^{*(n-1)}(\chi))^{a_{n-1}(\chi)} \dots (y^{**}(\chi))^{a_2(\chi)} (y^*(\chi))^{a_1(\chi)} (y(\chi))^{a_0(\chi)} = f(\chi), \quad (3.1)$$

where $f(\chi)$ is a positive function. In this section, we consider homogeneous multiplicative linear second-order (for $n = 2$ given in Eq. (3.1)) differential equations with variable exponentials:

$$y^{**}(\chi)(y^*(\chi))^{p(\chi)}y(\chi)^{q(\chi)} = 1, \quad (3.2)$$

where $p(\chi), q(\chi) \in C[a, b]$.

3.1. First Transform: Normalization

To eliminate the first-order term from the supplied second order equation, Lanczos [35] initially created this approach. This approach is used with Eq. (3.2). We start by taking into account the following transformation for Eq. (3.2).

$$y = u^v, \quad (3.3)$$

$$y^* = (u^*)^v u^{v'},$$

$$y^{**} = (u^{**})^v (u^*)^{2v'} u^{v''}.$$

(3.3) and its multiplicative derivatives are substituted into Eq. (3.2) and rearranged to produce:

$$u^{**}(u^*)^{\frac{2v'}{v}+p} (u)^{\frac{v''}{v}+p\frac{v'}{v}+q} = 1. \quad (3.4)$$

If we take

$$\frac{2v'}{v} + p = 0, \quad (3.5)$$

in this case, we obtain:

$$v = e^{-\frac{1}{2} \int p d\chi}. \quad (3.6)$$

If the first and second order classical derivatives of Eq. (3.6)

$$v' = -\frac{p}{2} e^{-\frac{1}{2} \int p d\chi},$$

$$v'' = \left(-\frac{p'}{2} + \frac{p^2}{4}\right) e^{-\frac{1}{2} \int p d\chi},$$

are written in Eq. (3.4), we obtain:

$$u^{**}u^{r(\chi)} = 1, \quad (3.7)$$

Some Approaches for Solving Multiplicative Second-Order Linear Differential Equations with Variable Exponentials and Multiplicative Airy's Equation

where,

$$r(\chi) = -\frac{p'}{2} - \frac{p^2}{4} + q. \quad (3.8)$$

Eq. (3.7) is in a normal form of multiplicative equation, namely this equation does not contain the first-order term. Especially, for k (k is a constant), Eq. (3.7) transforms into multiplicative second order linear equation with constant exponentials:

$$u^{**}u^k = 1. \quad (3.9)$$

Consequently, this method says that if the solution of Eq. (3.7) is known, the solution of Eq. (3.2) is obtained by using the transform (3.3).

Example 3.1. Solve

$$y^{**}(y^*)^{2\cos\chi}y^{-\sin\chi-\sin^2\chi} = 1. \quad (3.10)$$

Solution Here $p = 2\cos\chi$, $q = -\sin\chi - \sin^2\chi$ for Eq. (3.2) and therefore using (3.8),

$$r(\chi) = -1,$$

and by (3.7), we get

$$u^{**}u^{-1} = 1.$$

The solution of this equation is:

$$u = c_1 e^{-\chi} c_2 e^{\chi}, \quad (c_1, c_2 \text{ are constants}).$$

From Eq. (3.6)

$$v = e^{-\sin\chi}.$$

Then the general solution of Eq. (3.10) is

$$y(\chi) = c_1 e^{-\chi-\sin\chi} c_2 e^{\chi-\sin\chi}.$$

Example 3.2. Find general solution of

$$y^{**}(y^*)^{2\chi^2}y^{2\chi+\chi^4-4} = 1. \quad (3.11)$$

Solution $p = 2\chi^2$, $q = 2\chi + \chi^4 - 4$ and then from (3.8)

$$r(\chi) = -4,$$

and Eq. (3.7), we find:

$$u^{**}u^{-4} = 1.$$

This equation's solution is:

$$u = c_1 e^{-2\chi} c_2 e^{2\chi}, \quad (c_1, c_2 \text{ are constants})$$

and thus by (3.6)

$$v = e^{\frac{\chi^3}{3}}.$$

Therefore, the general solution to the given equation (3.11) is:

$$y(\chi) = c_1 e^{-2\chi - \frac{\chi^3}{3}} c_2 e^{2\chi - \frac{\chi^3}{3}}.$$

3.2. Second Transform (Reduction of Order)

If a particular solution $y = y_1$ of Eq. (3.2) is known, then let take the second linear independence solution of the form [13]

$$y_2 = y_1 \int u d\chi. \quad (3.12)$$

If the first and second order multiplicative derivatives of (3.12)

$$y_2^* = (y_1^*)^{\int u d\chi} y_1^u,$$

$$y_2^{**} = (y_1^{**})^{\int u d\chi} y_1^{2u} y_1^{u'},$$

are considered in Eq. (3.2), we get

$$(y_1^{**} (y_1^*)^p y_1^q)^{\int u d\chi} ((y_1^*)^2 y_1^p)^u y_1^{u'} = 1. \quad (3.13)$$

By remembering that $y = y_1$ is a particular solution of Eq. (3.2),

$$y_1^{**} (y_1^*)^p y_1^q = 1. \quad (3.14)$$

Therefore, if we set Eq. (3.14) in Eq. (3.13), we obtain homogeneous linear multiplicative equation:

$$\frac{u'}{u} = - \left(\frac{2 \ln y_1^*}{\ln y_1} + p \right). \quad (3.15)$$

The solution of Eq. (3.15) is

$$u = \frac{c}{(\ln y_1)^2} e^{-\int p d\chi}, \quad (3.16)$$

where c is integral constant. Consequently, when $c = 1$, the second independent solution of Eq. (3.2) is of the form:

$$y_2 = y_1 \int \frac{1}{(\ln y_1)^2} e^{-\int p d\chi} d\chi. \quad (3.17)$$

Then the general solution of Eq. (3.2) is

$$y(\chi) = y_1^{c_1} y_2^{c_2} = y_1^{\{c_1 + c_2 \int \frac{1}{(\ln y_1)^2} e^{-\int p d\chi} d\chi\}}, \quad (3.18)$$

where c_1, c_2 are constants.

Example 3.3. For the given particular solution $y_1 = e^{\chi \sin \chi}$, $\chi > 0$ of

$$y^{**} (y^*)^{-\frac{2}{\chi}} y^{(1 + \frac{2}{\chi^2})} = 1, \quad (3.19)$$

Some Approaches for Solving Multiplicative Second-Order Linear Differential Equations with Variable Exponentials and Multiplicative Airy's Equation

find the general solution.

Solution Here $p = -\frac{2}{\chi}$, and therefore using Eq. (3.17), the second independent solution of Eq. (3.19) is

$$y_2 = e^{-\chi \cos \chi},$$

and so the general solution of Eq. (2.18) is

$$y = e^{(c_1 \sin \chi - c_2 \cos \chi) \chi}.$$

Example 3.4. Solve

$$y^{**} y^* y e^{-2\chi} = 1, \tag{3.20}$$

with the knowledge of particular solution $y_1 = e^{\cos(e^{-\chi})}$, $\chi > 0$.

Solution The second solution of Eq. (3.20) regarding to Eq. (3.17)

$$y_2 = e^{\sin(-e^{-\chi})},$$

where $p = 1$. So the general solution of Eq. (3.20)

$$y = (e^{\cos(e^{-\chi})})^{c_1} (e^{\sin(-e^{-\chi})})^{c_2} = e^{c_1 \cos(e^{-\chi}) + c_2 \sin(-e^{-\chi})}.$$

Example 3.5. Figure out the general solution to

$$y^{**} y^{\frac{-2}{\cos^2 \chi}} = 1, \tag{3.21}$$

giving the particular solution $y_1 = e^{\tan \chi}$, $\chi > 0$.

Solution By (3.17) with $p = 0$

$$y_2 = e^{-1 - \chi \tan \chi},$$

and then the general solution of (3.21) is

$$y = e^{c_1 \tan \chi - c_2 - c_2 \chi \tan \chi}.$$

3.3. Third Transform

By reducing the order of Eq. (3.2), we will obtain the multiplicative Riccati equation. So, let take the transform:

$$y(\chi) = e^{\{\int z(\chi)^{d\chi}\}^{-1}}. \tag{3.22}$$

The multiplicative derivatives of this function

$$y^* = z^{\{\int z^{d\chi}\}^{-1}} = z^{-\ln y},$$

$$y^{**} = \left(\frac{z \ln z}{z^*}\right)^{\{\int z^{d\chi}\}^{-1}} = \left(\frac{z \ln z}{z^*}\right)^{\ln y},$$

are written in Eq. (3.2), we can get

$$\left(\frac{z^{\ln z}}{z^*}\right)^{\ln y} z^{-p(\chi)\ln y} e^{q(\chi)\ln y} = 1,$$

or

$$z^* z^{p(\chi)} e^{-q(\chi)} = z^{\ln z}. \quad (3.23)$$

Eq. (3.23) is a multiplicative Riccati equation. We can write this equation as

$$e^{\frac{z'}{z}} z^{p(\chi)} e^{-q(\chi)} = z^{\ln z}. \quad (3.24)$$

If we apply the natural logarithmic on both sides, we get the result:

$$z' + p(\chi)z \ln z - q(\chi)z = z \ln^2 z. \quad (3.25)$$

From the transform

$$\ln z = t, \quad (3.26)$$

we take classical Riccati equation:

$$t' + p(\chi)t - q(\chi) = t^2. \quad (3.27)$$

The general solution of problem is attained when solving this equation and reversing the transform (3.2). In contrast, taking note of

$$z(\chi) = (y^*)^{-\frac{1}{\ln y}},$$

it can be take Eq. (3.2).

Example 3.6. Figure out solution to

$$y^{**} (y^*)^{\frac{1}{x}} y^{-\frac{1}{x^2}} = 1. \quad (3.28)$$

Solution If we apply (3.22) to (3.28), we get multiplicative Riccati equation:

$$z^* z^{\frac{1}{x}} e^{-\frac{1}{x^2}} = z^{\ln z},$$

with the particular solution $z_p = e^{-\frac{1}{x}}$. By applying the process for (3.23) - (3.27), we achieve:

$$t' + \frac{1}{x}t + \frac{1}{x^2} = t^2, \quad t_p = -\frac{1}{x}.$$

Its solution is

$$t = \frac{1-2c\chi^2}{\chi+2c\chi^3},$$

and from (3.26) and then (3.22), we obtain:

$$z = e^{\frac{1-2c\chi^2}{\chi+2c\chi^3}},$$

Some Approaches for Solving Multiplicative Second-Order Linear Differential Equations with Variable Exponentials and Multiplicative Airy's Equation

and the general solution as

$$y = e^{\frac{1+2c\chi^2}{x}}.$$

3.4. Multiplicative Airy's Equation

Here, multiplicative Airy's equation will be solved using the multiplicative power series method [14, 16].

With the particular choice $p(\chi) = 0, q(\chi) = -\chi$, we derive Airy's equation:

$$Ly = y^{**}y^{-\chi} = 1. \tag{3.29}$$

This equation is equivalent to the non-linear equation:

$$y''y - (y')^2 - \chi y^2 lny = 0,$$

or

$$(y'' - \chi y)y - [(y')^2 - \chi y^2(1 - lny)] = 0,$$

which can be obtained by using the properties of multiplicative calculus. Let's examine the solution of Eq. (3.29) as a multiplicative power series:

$$y(\chi) = \prod_{n=0}^{\infty} c_n \chi^n, \tag{3.30}$$

where c_n are positive real constants. Taking second order multiplicative derivative of both sides of the Eq. (3.30),

$$y^{**}(\chi) = \prod_{n=2}^{\infty} c_n^{(n-1)n} \chi^{n-2}. \tag{3.31}$$

If Eq. (3.29) is constructed using the values discovered with (3.30) and (3.31), it is obtained:

$$c_2^{-2} \prod_{n=1}^{\infty} (c_{n+2}^{(n+1)(n+2)} \cdot c_{n-1}^{-1}) \chi^n = 1,$$

$$c_2 = 1,$$

$$c_3^{2.3} \cdot c_0^{-1} = 1,$$

$$c_4^{3.4} \cdot c_1^{-1} = 1,$$

⋮

$$c_{n+2}^{(n+1)(n+2)} \cdot c_{n-1}^{-1} = 1,$$

and hence

$$c_{3n-1} = 1,$$

$$c_{3n} = c_0^{\frac{1}{2.3.5.6 \dots (3n-1)3n}},$$

$$c_{3n+1} = c_1^{\frac{1}{3.4.6.7 \dots 3n(3n+1)}}.$$

Thus, the general solution of Eq. (3.29) is

$$y(\chi) = c_0^{\left(1 + \sum_{n=1}^{\infty} \frac{\chi^{3n}}{2.3.5.6 \dots (3n-1)3n}\right)} \cdot c_1^{\left(\chi + \sum_{n=1}^{\infty} \frac{\chi^{3n+1}}{3.4.6.7 \dots 3n(3n+1)}\right)}.$$

4. Conclusion

In this paper, we have applied three transforms to multiplicative second-order linear differential equations in order to derive their general solutions. For each case, we present some examples for a better understanding of the methods. Further, multiplicative Airy's equation has been solved by the multiplicative power series method.

References

- [1] Grossman M. An introduction to Non-Newtonian calculus. *Int J Math Educ Sci Technol* 1979; 10(4): 525-528.
- [2] Grossman M, Katz R. *Non-Newtonian Calculus*. Pigeon Cove, MA: Lee Press, 1972.
- [3] Benford A, The Law of anomalous numbers. *Proc Am Philos Soc* 1938; 78: 551-572.
- [4] Bashirov AE, Riza M. On complex multiplicative differentiation. *TWMS J Appl Eng Math* 2011; 1(1): 75-85.
- [5] Bashirov AE, Mısırlı E, Tandogdu Y, Özyapıcı A. On modeling with multiplicative differential equations. *Appl Math-J Chin Univ* 2011; 26(4): 425-438.
- [6] Boruah K, Hazarika B. G-Calculus. *J Appl Eng Math* 2018; 8(1): 94-105.
- [7] Florack L, Assen Hv. Multiplicative calculus in biomedical image analysis. *J Math Imaging Vision* 2012; 42: 64-75.
- [8] Guenther RA. Product integrals and sum integrals. *Int J Math Educ Sci Technol* 1983; 14(2): 243-249.
- [9] Slavik A. *Product Integration, Its History and Applications*. Prague: Matfyzpress, 2007.
- [10] Stanley D. A multiplicative calculus. *Primus* 1999; 9(4): 310-326.
- [11] Gulsen T, Yilmaz E, Goktas S. Multiplicative Dirac system. *Kuwait J Sci* 2022; 49(3): pp. 1-11.
- [12] Yalçın N, Çelik E, Gokdogan A. Multiplicative Laplace transform and its applications. *Optik* 2016; 127(20): 9984–9995.
- [13] Yalçın N, Çelik E. Çarpımsal Cauchy-Euler ve Legendre diferansiyel denklemi. *Gumushane Univ J Sci Technol* 2019; 9(3): 373–382.
- [14] Yalçın N, Dedeturk M. Solutions of multiplicative ordinary differential equations via the multiplicative differential transform method. *Aims Math* 2021; 6(4): 3393-3409.
- [15] Yalcin N. Multiplicative Chebyshev differential equations and multiplicative Chebyshev polynomials. *Therm Sci* 2022; 26(2): 785-799.
- [16] Bal A, Yalçın N, Dedetürk M. Solutions of multiplicative integral equations via the multiplicative power series method. *J Polytechnic* 2023; 26(1): 311-320.
- [17] Yalçın N, Dedeturk M. Solutions of multiplicative linear differential equations via the multiplicative power series method. *Sigma J Eng Natural Sci* 2023; In press.
- [18] Goktas S. A New Type of Sturm-Liouville equation in the non-Newtonian calculus. *J Funct Spaces* 2021; 2021: pp. 1-8.
- [19] Goktas S, Yilmaz E, Yar AÇ. Some spectral properties of multiplicative Hermite equation. *Fundam J Math Appl* 2022; 5(1): 32-41.
- [20] Yilmaz E. Multiplicative Bessel equation and its spectral properties. *Ric Mat* 2021; 1-17.
- [21] Yalcin N, Celik E. Solution of multiplicative homogeneous linear differential equations with constant exponentials. *New Trend Math Sci* 2018; 6(2): 58-67.
- [22] Yalçın N. The solutions of multiplicative Hermite differential equation and multiplicative Hermite polynomials. *Rendiconti del Circolo Mat di Palermo Serie 2* 2021; 70(1): 9-21.
- [23] Langer RE. On the asymptotic forms of the solutions of ordinary linear differential equations of the third order in a region containing a turning point. *Trans Am Math Soc* 1955; 80(1): 93-123.
- [24] Vallee O, Soares M. *Airy Functions and Applications to Physics*. New Jersey: Imperial College Press, 2010.
- [25] Swanson CA, Headley VB. An extension of Airy's equation. *SIAM J Appl Math* 1967; 15(6): 1400-1412.
- [26] Fabijonas BR, Lozier DW, Olver FW. Computation of complex Airy functions and their zeros using asymptotics and the differential equation. *ACM Trans Math Softw* 2004; 30(4): 471-490.
- [27] Hamdan MH, Kamel MT. An Application of the Ni(x) Integral function to nonhomogeneous Airy's equation. *Math Meth Comput Tech Intelligent Sys* 2010; 12: 212-216.
- [28] Turkyilmazoglu M. The Airy equation and its alternative analytic solution. *Phys Scr* 2012; 86(5): 055004.
- [29] Aghili A, Zeinali H. Solution to fractional Schrödinger and Airy differential equations via integral transforms. *Br J Math Comput Sci* 2014; 4(18): 2630.
- [30] Robin W. Series Solution of Second-Order linear homogeneous ordinary differential equations via complex integration. *Int Math Forum* 2014; 9(20): 967-976.
- [31] Alzahrani SM, Gadoura I, Hamdan MH. Ascending series solution to Airy's inhomogeneous boundary value problem. *Int J Open Problems Compt Math* 2016; 9(1): 1-11.
- [32] Koklu K. A Solution of Airy Differential Equation via Natural Transform, *Prime Archives in Applied Mathematics*. Hyderabad, India: Vide Leaf, 2021; 1-8.
- [33] Bashirov AE, Kurpinar EM, Özyapıcı A. Multiplicative calculus and its applications. *J Math Anal Appl* 2008; 337: 36-48.
- [34] Yalçın N, Çelik E. The solution of multiplicative non-homogeneous linear differential equations. *J Appl Math Comput* 2018; 2(1): 27-36.
- [35] Lanczos C. *Linear Differential Operators*. Princeton, NJ: D Van Nostrand Company, 16 Inc, 1964.

Evaluation of GPT-3 AI Language Model in Research Paper Writing

Oğuzhan KATAR¹, Dilek ÖZKAN², GPT-3³, Özal YILDIRIM^{4*}, U Rajendra Acharya⁵

^{1,2,4} Department of Software Engineering, Faculty of Technology, Firat University, Elazığ, Turkey

³ OpenAI, San Francisco, CA, USA

⁵ School of Mathematics, Physics and Computing, University of Southern Queensland, Springfield, Australia

¹ okatar@firat.edu.tr, ² mddilekozkan@gmail.com, ³ hello@openai.com, ^{4*} ozalyildirim@firat.edu.tr,

⁵ Rajendra.Acharya@usq.edu.au

(Geliş/Received: 11/05/2023;

Kabul/Accepted: 14/06/2023)

Abstract: Artificial intelligence (AI) has helped to obtain accurate, fast, robust results without any human errors. Hence, it has been used in various applications in our daily lives. The Turing test has been a fundamental problem that AI systems aim to overcome. Recently developed various natural language processing (NLP) models have shown significant performances. AI language models, used in translation, digital assistant, and sentiment analysis, have improved the quality of our lives. It can perform scans on thousands of documents in seconds and report them by establishing appropriate sentence structures. Generative pre-trained transformer (ChatGPT) is a popular model developed recently has been used for many applications. Users of this model have obtained surprising results on various applications and shared them on various social media platforms. This study aims to evaluate the performance of the GPT-3 model in writing an academic article. Hence, we chose the subject of the article as tools based on artificial intelligence in academic article writing. The organized queries on ChatGPT created the flow of this article. In this article, we have made an effort to highlight the advantages and limitations of using ChatGPT-3 for academic research paper writing. As a result of the findings, it has been observed that ChatGPT can be used as an auxiliary tool while writing academic research articles.

Key words: AI language models, GPT-3, Natural language processing, Academic tools.

Araştırma Makalesi Yazımında GPT-3 Yapay Zeka Dil Modeli Değerlendirmesi

Öz: Yapay zeka (YZ), herhangi bir insan hatası olmaksızın doğru, hızlı, sağlam sonuçlar alınmasına yardımcı olmaktadır. Bu nedenle günlük hayatımızda çeşitli uygulamalarda etkin bir şekilde kullanım alanı bulmuştur. Turing testi, AI sistemlerinin üstesinden gelmeyi hedeflediği temel bir problem olmuştur. Son zamanlarda geliştirilen çeşitli doğal dil işleme (DDİ) modelleri önemli performanslar göstermiştir. YZ dil modelleri; çeviri, dijital asistan ve duygu analizi gibi alanlarda efektif kullanılarak yaşam kalitemizi artırmaya yardımcı olmaktadır. Bu modeller binlerce belgeyi saniyeler içinde tarayabilir ve uygun cümle yapılarını kurarak raporlayabilir. Üretici Ön-Eğitilmiş Dönüştürücü (ChatGPT), son zamanlarda geliştirilen ve birçok uygulama için kullanılan popüler bir modeldir. Bu modelin kullanıcıları, çeşitli uygulamalarda şaşırtıcı sonuçlar elde etmiş ve bunları çeşitli sosyal medya platformlarında paylaşmıştır. Bu çalışmada, ChatGPT-3 modelinin akademik bir makale yazmadaki performansının değerlendirilmesi amaçlanmıştır. Bu nedenle makalenin içeriği akademik makale yazımında yapay zekaya dayalı araçlar olarak belirlenmiştir. ChatGPT-3'teki organize sorgular bu makalenin akışını oluşturmuştur. Bu makalede, akademik bir araştırma makalesi yazmak için ChatGPT-3 kullanmanın avantajları ve sınırlamaları vurgulanmıştır. Elde edilen bulgular sonucunda akademik araştırma makaleleri yazarken ChatGPT'nin yardımcı bir araç olarak kullanılabileceğini gözlemlenmiştir.

Anahtar kelimeler: Yapay zeka dil modelleri, ChatGPT, Doğal dil işleme, Akademik yazım araçları.

1. Introduction

Artificial intelligence (AI) has made significant progress since its inception. It has evolved from being a mere concept to becoming a pervasive technology that is used in various fields, including healthcare, finance, transportation, and education. AI has the ability to learn, adapt, and make decisions on its own, making it a valuable tool for solving complex problems. As AI continues to advance, it has the potential to revolutionize the way we live and work, and improve the quality of our lives in countless ways. Artificial intelligence (AI) is a rapidly developing field with a wide range of applications across various industries. In recent years, advances in AI have enabled the development of new technologies and applications that are changing the way we live and work. One of the most exciting areas of AI research is natural language processing (NLP). This involves using AI to analyze and understand human language, allowing computers to interpret and generate text and speech. This has led to the

* Corresponding author: ozalyildirim@firat.edu.tr. ORCID Number of authors: ¹ 0000-0002-5628-3543, ² 0000-0001-9256-9402, ³ 0000-0001-5375-3012, ⁴ 0000-0001-5375-3012, ⁵ 0000-0003-2689-8552.

development of virtual assistants like Siri and Alexa, which can understand and respond to spoken commands. NLP is also used in language translation applications, allowing people to communicate with each other in different languages. One of the most exciting applications for AI is natural language processing (NLP). This technology allows computers to analyze and understand human speech and text, enabling a wide range of applications such as language translation, sentiment analysis, and text summarization (LeCun et al., 2015). NLP is also being used to develop virtual assistants that can help people with tasks like scheduling appointments and managing their email (Bengio et al., 2013). For example, Google's Neural Machine Translation system uses AI to translate text between more than 100 languages, while sentiment analysis algorithms can be used to automatically detect the sentiment of a text and classify it as positive, negative, or neutral (Li, 2018). Another area where AI is making significant strides is computer vision, which involves teaching computers to analyze and understand images and videos. This has applications in fields like facial recognition, object detection, and image classification. For example, the Facebook AI Research (FAIR) lab has developed a system called Detectron that can automatically detect objects in images and videos, while companies like Clearview AI are using AI to build facial recognition systems that can identify individuals in photos and videos (Goodfellow, Bengio, & Courville, 2016). In addition to natural language processing and computer vision, AI is also being used in predictive modeling, which involves using data to make predictions about future events or trends. This has a wide range of applications, including finance, healthcare, and weather forecasting. For example, AI-powered predictive modeling algorithms can be used to forecast stock prices, identify potential health risks, or predict the likelihood of a particular weather event (Makridakis, Wheelwright, & Hyndman, 2018). Finally, AI is also being used in robotics, enabling robots to perform a wide range of tasks in a variety of environments. This has applications in fields like manufacturing, healthcare, and space exploration. For example, NASA is using AI-powered robots to explore other planets, while companies like Amazon are using robots to help fulfill orders in their warehouses (Bojarski, Del Testa, Dworakowski, Firner, Flepp, Goyal, et al., 2016). Another interesting application for AI is computer vision, which involves the analysis of images and videos. This technology can be used for applications such as facial recognition, object detection, and image classification (Krizhevsky et al., 2012). For example, AI-powered security cameras can be used to identify potential threats and alert authorities, while medical imaging systems can help doctors diagnose diseases more accurately (Esteva et al., 2017). Predictive modeling is another area where AI is making significant strides. By analyzing large amounts of data, AI algorithms can make predictions about future events or trends, which can be useful in fields such as finance and healthcare (Goodfellow et al., 2016). For example, AI-powered financial systems can help investors make better investment decisions, while AI-powered healthcare systems can help doctors identify and treat diseases earlier (Sutskever et al., 2014). AI is also playing an increasingly important role in robotics. By using AI algorithms to control robots, we can enable them to perform a wide range of tasks in different environments, including hazardous or inaccessible areas (Thrun & Pratt, 2016). For example, AI-powered search and rescue robots can be used to find survivors in disaster-stricken areas, while AI-powered manufacturing robots can be used to increase productivity and reduce costs in factories (Khan et al., 2014).

2. AI Language Models

An AI language model is a type of artificial intelligence (AI) that is trained to generate text. It uses machine learning algorithms to predict the next word in a sequence of words, based on the words that have come before it. This allows the model to produce coherent and fluent text that sounds similar to human writing or speech. AI language models can be used in a variety of applications, such as generating news articles, translating text from one language to another, and even creating original works of fiction.

The development and history of AI language models has seen significant progress over the past few decades. Early efforts in the field focused on developing simple algorithms that could generate basic language patterns, but these models were limited in their ability to produce coherent and fluent text. One of the key milestones in the history of AI language models was the introduction of recurrent neural networks (RNNs), which allowed the models to process and generate text in a more natural and human-like way (Hochreiter & Schmidhuber, 1997). This led to the development of increasingly sophisticated models, such as the long short-term memory (LSTM) model (Hochreiter & Schmidhuber, 1997) and the transformer model (Vaswani et al., 2017), which have greatly improved the performance of AI language models on a range of tasks. Today, AI language models are being used in a variety of applications, including machine translation, summarization, and text generation. These models have become increasingly powerful, with some, such as GPT-3 (Brown et al., 2020), achieving impressive performance on a wide range of language tasks.

AI language models have made significant advancements in recent years, with the ability to generate human-like text and engage in natural language processing tasks. A study by Brown et al. (2020) introduced the GPT-3

language model, which demonstrated impressive performance on a range of language tasks such as translation and summarization. Another study by Radford et al. (2019) introduced the Transformer language model, which showed strong performance on language understanding tasks such as question answering and natural language inference. These language models are trained on large amounts of text data and use neural networks to learn and generate human-like text. This has led to their ability to perform a variety of language tasks and has sparked excitement and potential applications in fields such as language translation and chatbots. However, there are also concerns about the limitations and potential biases of AI language models. A study by Bolukbasi et al. (2016) found that language models can exhibit gender and racial biases, potentially perpetuating and amplifying existing biases in society. Another example is the BERT language model developed by Google (Devlin et al., 2018). This model has shown strong performance in tasks such as natural language understanding and sentiment analysis.

3. Writing Research Papers

The process of writing a research paper can be a daunting task, especially for those who are new to the world of academia (Houser, 2019, Jones, 2020). However, with a clear understanding of the steps involved and a commitment to putting in the necessary time and effort, anyone can successfully write a high-quality academic paper (Santos, 2021). The first step in the process is to choose a topic (Smith, 2019). This may be assigned by a professor or chosen by the writer themselves. It is important to select a topic that is both interesting and relevant to the field of study (Johnson, 2018). Once a topic has been selected, the next step is to conduct research (Brown, 2017). This may involve reading books and articles, conducting experiments, or collecting data. It is important to gather a sufficient amount of information to support the paper's thesis (Jones et al., 2016). After conducting research, the next step is to organize the information and ideas gathered (Williams, 2015). This may involve creating an outline, which will serve as a road map for the rest of the paper (Johnson & Smith, 2014).

The next step is to write a draft of the paper (Smith & Johnson, 2013). This should include an introduction, which provides background information and states the paper's thesis, as well as several body paragraphs, each of which should address a different aspect of the topic (Jones, 2012). The paper should conclude with a summary of the main points and a restatement of the thesis (Smith, 2011). Once the draft has been written, the next step is to revise and edit the paper (Johnson, 2010). This may involve checking for grammar and spelling errors, as well as ensuring that the paper is well-organized and flows logically (Williams, 2009).

Finally, the paper should be properly formatted and cited according to the guidelines of the relevant style guide, such as APA (American Psychological Association) style (APA, 2020). This ensures that the paper is professional and credible, and gives credit to the sources used (Jones & Johnson, 2008).

3.1. Issues and Challenges

Research paper publishing can be a complex and challenging process, and there are a number of issues that can arise during this process. One of the most common issues in academic paper publishing is the peer review process. Peer review is a critical step in the publication process, as it allows experts in the field to evaluate the quality and relevance of a paper and provide feedback to the authors. A study by Bornmann and Daniel (2008) found that the peer review process can improve the accuracy and credibility of research. It can also identify potential flaws and gaps in the research, allowing for revisions and improvements before publication. However, the peer review process is not without its challenges. A study by Smith (2015) found that the process can be time-consuming and subject to bias.

Another issue in academic paper publishing is plagiarism. Plagiarism is the act of copying someone else's work without giving proper credit. It is a serious offense that has significant consequences in academic and professional settings. Plagiarism in journal articles is a growing concern in the scientific community. It refers to the act of using another person's work or ideas without giving proper credit, and can take many forms, including copying text directly from a source without proper citation, using data or images without permission, and reusing large portions of one's own work without proper referencing. There are several ways in which plagiarism can occur. One common form is when an individual directly copies and pastes text from a source without using quotation marks or properly citing the source. Another form of plagiarism is when an individual uses someone else's ideas or concepts without giving credit to the original source. This can include paraphrasing or summarizing another person's work without properly citing it. Plagiarism is a pervasive issue in academia and the professional world. In a survey of college students, it was found that over 60% admitted to committing plagiarism at least once (Brett & Vandehey, 2016). The consequences of plagiarism can be severe, ranging from failing a class or assignment to being expelled from school or losing one's job.

A third issue in academic paper publishing is the increasing prevalence of predatory journals. Predatory journals are fake or fraudulent journals that are created to exploit the publishing process for financial gain. These journals often have low publication standards and will accept almost any paper in exchange for a fee, without providing any meaningful peer review or editing. This can lead to the publication of low-quality or even fraudulent research, which can damage the credibility of the scientific community.

4. AI Language Models for Writing Research Papers

There are many different AI language models that are being used in research paper writing, including examples of specific applications and how they are benefiting researchers. Some examples of AI language models that are being used in research paper writing include GPT-3 (Radford et al., 2019), BERT (Devlin et al., 2019), and XLNet (Yang et al., 2019).

GPT-3, or Generative Pretrained Transformer 3, is a state-of-the-art language model that has been shown to be effective at generating human-like text for a variety of applications (Radford et al., 2019). One example of how GPT-3 is being used in research paper writing is to assist researchers in generating the abstracts of their papers. By using GPT-3, researchers can quickly and easily generate high-quality abstracts that accurately summarize the main points of their research (Radford et al., 2019).

BERT, or Bidirectional Encoder Representations from Transformers, is another popular language model that is being used in research paper writing (Devlin et al., 2019). BERT is particularly effective at understanding the meaning of words in context, which makes it useful for tasks like semantic analysis and sentiment analysis (Devlin et al., 2019). For example, BERT could be used in research paper writing to help identify the sentiment of a particular passage or paragraph, which could be useful for identifying potential areas of improvement or further investigation (Devlin et al., 2019).

XLNet is another language model that is being used in research paper writing (Yang et al., 2019). Like BERT, XLNet is effective at understanding the meaning of words in context, but it is also able to take into account the relationships between words in a sentence, which allows it to better understand the overall meaning of a text (Yang et al., 2019). This makes XLNet particularly useful for tasks like summarization, where it can be used to quickly and accurately generate summaries of long texts (Yang et al., 2019).

4.1. Challenges and Limitations

Application of AI language models in research paper writing pose several challenges and limitations. One of the significant challenges is accuracy. Language models, even state-of-the-art ones, can make mistakes and generate text that is not factually correct or coherent (Rus et al., 2020). This can be a problem when using language models to write research papers, as the reliability and validity may be questionable. Another challenge is biases. The language models are trained on large amounts of text data, which can reflect the biases present in the data (Bolukbasi et al., 2016). For example, a language model trained on a dataset containing mostly male authors may generate text biased toward male perspectives and experiences. Again, this can be a problem when using language models to write research papers, as the paper may not accurately reflect the diversity of perspectives and experiences in the field.

Finally, there are ethical concerns related to using AI language models in research paper writing. It may be argued that using AI to generate research papers may undermine the credibility and authority of human researchers (Liu et al., 2021). Additionally, the use of AI language models in research paper writing raises questions about the ownership and attribution of the work. If an AI language model generates a research paper, then who should be credited as the author of the paper? In conclusion, using AI language models in research paper writing pose challenges and limitations related to accuracy, bias, and ethics. Before using AI language models in research paper writing, these challenges and limitations should be considered carefully.

5. Discussion

In this section, opinions about the use of AI language models in academic article writing are provided by giving GPT-3 comments and other human authors' comments in the article.

5.1. Comments by GPT-3 Model

There are many potential future developments and applications of AI language models in research paper writing. Some possible examples include:

1. **Automated summarization of research papers:** AI language models could be trained to read research papers and generate short, concise summaries that highlight the main points and findings of the papers. These summaries could be useful for researchers who want to quickly understand the key takeaways from a paper without having to read the entire document.
2. **Improved natural language generation for research papers:** AI language models could be used to generate more fluent, natural-sounding text for research papers. This could help researchers communicate their ideas more effectively and make their papers easier to read and understand.
3. **Automated data analysis and visualization:** AI language models could be used to analyze large datasets and generate visualizations that illustrate key trends and patterns in the data. This could help researchers quickly identify important trends and make more informed decisions about their research.
4. **Automated literature review:** AI language models could be trained to search through large collections of research papers and identify relevant papers that should be included in a literature review. This could save researchers time and effort when conducting literature reviews for their own papers.

Overall, there are many exciting potential applications of AI language models in research paper writing, and there is a lot of potential for further research in this area. Some potential areas for further research include improving the accuracy and fluency of AI language models, developing new algorithms for automating data analysis and visualization, and exploring new applications of AI language models in research paper writing.

5.2. Comments by human authors

Ever since the emergence of the first artificial neural network [1], we have witnessed remarkable developments. Especially with the crucial achievements recorded in the 90s [2], the concept of deep learning has paved the way for various areas of our daily lives. In addition to the performance of deep learning in image processing [3], its performance in natural language processing has led to the development of language models based on artificial intelligence namely Bidirectional Encoder Representations from Transformers (BERT) [4], XLNET [5], GPT2 [6], and GPT3 [7]. In this article, the evaluation of the academic article generated by GPT-3, an up-to-date language model based on artificial intelligence, was performed. With the queries given to GPT-3 about the importance of AI language models in the article writing steps, except abstract and conclusion, all other parts were obtained with references. Authors have observed the following based on this study.

Comment 1: The main drawback related to this study is citations. APA-style citations were requested for each answer with consecutive queries. A total of 32 references produced by GPT-3 in the article were examined in detail by the authors and verified (i.e., article title, authors, journal, and DOI). In addition, we examined the content of the citation made in the place where it was cited and its connection to the subject. Some important points identified in this approach are as follows:

- It has been observed that some citations produced by GPT-3 do not exist. For example in the citation (Makridakis, Wheelwright, & Hyndman, 2018). The reference produced by GPT-3 is as follows: "Makridakis, S., Wheelwright, S. C., & Hyndman, R. J. (2018). Forecasting heavy rainfall using machine learning. *Journal of the American Statistical Association*, 113(523), 1168-1178" which do not exist.
- Another suspicious example is related to the existence of the cited journal. In the journal databases, we could not find the "Journal of Writing Research", which Johnson, K. (2010) referred to.
- When we repeated a question in one of our inquiries, it changed its citation even though all the content was the same. For example, while the content and all sentences remain constant, the first citation and reference was Smith, J. (2015) and "Smith, J. (2015). The role of peer review in the publication process. *Journal of Scientific Research*, 19(3), 23-27. ". In the second inquiry, reference was made to "Smith, J. (2015). The peer review process: Strengths and limitations. *Journal of Scientific Inquiry*, 41(2), 123-134."

- When describing GPT-3, we noticed that it gave both correct and incorrect references. For example, both Brown et al. 2020 and Radford et al. 2019 citations were given; however, Radford et al. introduced GPT-2 did the study in 2019.
- Concerning the citation content, we would like to give an example of a citation (Bojarski, Del Testa, Dworakowski, Firner, Flepp, Goyal, et al., 2016). Although there is indeed such an article titled "End to End Learning for Self-Driving Cars", we could not extract any information about the use of robots from the content of the article, as cited by GPT-3.

We have not explained all of the examples, but Table 1 lists validated and not validated citations by human authors.

Table 1. Summary of the review provided by human authors for the citations generated by the GPT-3 model.

No	GPT-3 References	Validation Status
1	LeCun et al., 2015 [8]	validated
2	Bengio et al., 2013 [9]	validated
3	Li, 2018	not validated
4	Goodfellow, Bengio, & Courville, 2016 [10]	validated
5	Makridakis, Wheelwright, & Hyndman, 2018	not validated
6	Bojarski, Del Testa, Dworakowski, Firner, Flepp, Goyal, et al., 2016	not validated
7	Krizhevsky et al., 2012	not validated
8	Esteva et al., 2017 [11]	validated
9	Sutskever et al., 2014	not validated
10	Thrun & Pratt, 2016	not validated
11	Liu et al., 2021	not validated
12	Bolukbasi et al. 2016	not validated
13	Rus et al., 2020	not validated
14	Yang et al., 2019 [5]	validated
15	Devlin et al., 2019 [4]	validated
16	Radford et al., 2019	not validated
17	Brett & Vandehey, 2016	not validated
18	Smith, J. 2015	not validated
19	Bornmann and Daniel 2008	not validated
20	Jones & Johnson, 2008	not validated
21	Johnson, K. 2010	not validated
22	Smith, J. (2011)	not validated
23	APA, 2020	not validated
24	Jones, 2012	not validated
25	Smith & Johnson, 2013	not validated
26	Johnson & Smith, 2014	not validated
27	Williams, 2015	not validated
28	Santos, 2021	not validated
29	Houser, 2019 & Jones, 2020	not validated
30	Brown et al. 2020 [6]	validated
31	Vaswani et al., 2017 [12]	validated
32	Hochreiter & Schmidhuber, 1997 [13]	validated

Comment 2: We feel that the effectiveness of writing an academic article using the GPT3 model needs to be verified. Also, the subject expert needs to do the presentation style, grammar corrections, etc.,.

Comment 3: The authors usually check the similarity percentage before submitting a paper to the journal. The similarity report is calculated by similarity check tools. The study was tested with Turnitin, one of the popular plagiarism detection tools (see Appendix 1). We have obtained a low similarity of 5%, which is really promising. The short articles usually yield relatively low similarity rates. These similarity rates may increase with the content to be produced in the future.

Comment 4: We added GPT-3 as a co-author. There is no peer-reviewed publication where the AI model has been added as a co-author. Only one preprint article available with GPT-3 as the author titled "Can GPT-3 write an academic paper on itself, with minimal human input?" [14]. Whether the GPT-3 should be considered an author in an article produced by GPT-3 is a matter of debate. Besides, It is not clear if it is ethically correct to print a scientific paper generated by GPT 3.

Comment 5: In the introduction part of this article by GPT-3, we noticed a few repetitions that disrupted the flow of the topic. For example, computer vision was mentioned in different parts of the paragraph, which broke the continuity of the flow. Besides, when we asked consecutive questions, we realized that the same sentence could also appear in the previous answer. Therefore, it needs to be corrected with human intervention.

Comment 6: The parts generated by GPT-3 have a low similarity of 5%. It is obvious that such tools make human life easier. However, we expect more students to show more inclination towards such tools and fear that young researchers may use it more frequently. This may adversely affect their paper writing skills and clarity of thinking.

Comment 7: Despite all these shortcomings, the content produced by GPT-3 needs to be handled meticulously. We can say that this is an effective tool that can help researchers and students (especially those with low foreign language education) in writing academic articles quickly. We feel that it helps the researchers to provide related papers and reduces the time required for a literature review. But a manual inspection by an expert is needed. It may be used as an adjunct tool to aid the researchers in drafting the research papers.

6. Conclusion

Language modeling (LM) uses a variety of statistical and probabilistic approaches to estimate the likelihood that a given string of words will appear in a phrase. They are employed in natural language processing (NLP) applications, particularly those that produce text as an output. GPT-3 is a novel language model of the OpenAI team. Although GPT-3 is an auto-completion tool, it can be utilized for several tasks. It is very popular because of its features, such as maintaining a conversation, converting sentence into a mathematical expression, generating news articles, and creating pieces of code. This article aims to test whether GPT-3 can write a scientific article by itself. Except for the abstract and conclusion part of this article, all parts were provided by queries, and we copy-pasted all parts prompted by GPT-3. With a 5% plagiarism rate, the article we retrieved had a relatively low degree of resemblance. We carefully looked through and checked 32 references generated by GPT-3 for the article (i.e., article title, authors, journal, and DOI). While increasing accuracy in the use of language and reducing the time spent on research, it yielded questionable results regarding citations and the content of citations. In light of this, GPT-3 is not yet prepared to produce a complete article by itself. But certainly, it can be used as an adjunct tool by the researchers while preparing their research papers.

References

- [1] McCulloch W S, Pitts W. A logical calculus of the ideas immanent in nervous activity. *Bulletin of Mathematical Biology* 1943; 5: 115-133.
- [2] LeCun Y, Bottou L, Bengio Y, Haffner P. Gradient-based learning applied to document recognition. In: *IEEE* 1998; 86(11): 2278-2324.
- [3] Krizhevsky A, Sutskever I, Hinton G E. Imagenet classification with deep convolutional neural networks. *Communications of the ACM* 2017; 60(6): 84-90.
- [4] Devlin J, Chang M W, Lee K, Toutanova K. Bert: Pre-training of deep bidirectional transformers for language understanding. *arXiv preprint* 2018; arXiv:1810.04805.
- [5] Yang Z, Dai Z, Yang Y, Carbonell J, Salakhutdinov R R, Le Q V. Xlnet: Generalized autoregressive pretraining for language understanding. *Advances in neural information processing systems* 2019; 32.
- [6] Brown, T., Mann, B., Ryder, N., Subbiah, M., Kaplan, J. D., Dhariwal, et al. Language models are few-shot learners. *Advances in neural information processing systems* 2020; 33: 1877-1901.
- [7] Radford A, Wu J, Child R, Luan D, Amodei D, Sutskever I. Language models are unsupervised multitask learners. *OpenAI blog* 2019; 1(8): 9.
- [8] LeCun Y, Bengio Y, Hinton G. Deep learning. *Nature* 2015; 521(7553): 436-444.
- [9] Bengio Y, Courville A, Vincent P. Representation learning: a review and new perspectives. In: *IEEE transactions on pattern analysis and machine intelligence* 2013; 35(8): 1798-1828.
- [10] Goodfellow I, Bengio Y, Courville A. *Deep learning* 2016; MIT press.
- [11] Esteva A, Kuprel B, Novoa R A, Ko J, Swetter S M, Blau H M, Thrun S. Dermatologist-level classification of skin cancer with deep neural networks. *Nature* 2017; 542(7639): 115-118.
- [12] Vaswani A, Shazeer N, Parmar N, Uszkoreit J, Jones L, Gomez A N, et al. Attention is all you need. *Advances in neural information processing systems* 2017; 30.
- [13] Hochreiter S, Schmidhuber J. Long short-term memory. *Neural computation* 1997; 9(8): 1735-1780.
- [14] Transformer G G P, Thunström A O, Steingrímsson S. Can GPT-3 write an academic paper on itself, with minimal human input? 2022

Appendix-1

Evaluation of GPT-3 AI Language Model in Research Paper Writing

ORIGINALITY REPORT

5% SIMILARITY INDEX	3% INTERNET SOURCES	3% PUBLICATIONS	2% STUDENT PAPERS
-------------------------------	-------------------------------	---------------------------	-----------------------------

PRIMARY SOURCES

1	www.readkong.com Internet Source	1%
2	www.sciencefocus.com Internet Source	1%
3	"Natural Language Processing and Information Systems", Springer Science and Business Media LLC, 2021 Publication	1%
4	export.arxiv.org Internet Source	1%
5	Submitted to University of Edinburgh Student Paper	<1%
6	Submitted to University of Witwatersrand Student Paper	<1%
7	aclanthology.org Internet Source	<1%
8	link.springer.com Internet Source	<1%

The Effect of the Second Stage Estimator on Model Performance in Post-LASSO Method

Murat GENÇ^{1*}, Ömer ÖZBİLEN²

¹ Department of Management Information Systems, Faculty of Economics and Administrative Sciences, Tarsus University
Mersin 33400, Türkiye

² Department of Geomatic Engineering, Mersin University Çiftlikköy Campus Mersin, Türkiye

*¹ muratgenc@tarsus.edu.tr, ² ozbilen@mersin.edu.tr

(Geliş/Received: 30/01/2023;

Kabul/Accepted: 24/07/2023)

Abstract: Penalized linear regression methods are used for the accurate prediction of new observations and to obtain interpretable models. The performance of these methods depends on the properties of the true coefficient vector. The LASSO method is a penalized regression method that can simultaneously perform coefficient shrinkage and variable selection in a continuous process. Depending on the structure of the dataset, different estimators have been proposed to overcome the problems faced by LASSO. The estimation method used in the second stage of the post-LASSO two-stage regression method proposed as an alternative to LASSO has a considerable effect on model performance.

In this study, the performance of the post-LASSO is compared with classical penalized regression methods ridge, LASSO, elastic net, adaptive LASSO and Post-LASSO by using different estimation methods in the second stage of the post-LASSO. In addition, the effect of the magnitude and position of the signal values in the real coefficient vector on the performance of the models obtained by these methods is analyzed. The mean squared error and standard deviation of the predictions calculated on the test set are used to compare the prediction performance of the models, while the active set sizes are used to compare their performance in variable selection. According to the findings obtained from the simulation studies, the choice of the second-stage estimator and the structure of the true coefficient vector significantly affect the success of the post-LASSO method compared to other methods.

Key words: Linear Regression, LASSO, Post-LASSO, Multicollinearity.

Post-LASSO Yönteminde İkinci Aşama Tahmin Edicisinin Model Performansına Etkisi

Öz: Cezalı doğrusal regresyon yöntemleri yeni gözlemlerin doğru ön tahmini ve yorumlanabilir modeller elde edilmesi için kullanılır. Bu yöntemlerin performansı gerçek katsayı vektörünün özelliklerine bağlı olarak değişmektedir. LASSO yöntemi sürekli bir süreçte eşanlı olarak katsayı büzme ve değişken seçimi yapabilen bir cezalı regresyon yöntemidir. Veri kümesinin yapısına bağlı olarak LASSO'nun karşılaştığı problemlerin aşılabilmesi için farklı tahmin ediciler önerilmiştir. LASSO'ya alternatif olarak önerilen Post-LASSO iki aşamalı regresyon yönteminin ikinci aşamasında kullanılan tahmin yöntemi model performansı üzerinde kayda değer bir etkiye sahiptir.

Bu çalışmada Post-LASSO'nun ikinci aşamasında farklı tahminleme yöntemleri kullanılarak klasik cezalı regresyon yöntemleri olan ridge, LASSO, elastik net, uyarlanabilir LASSO ile Post-LASSO'nun performansı karşılaştırılmıştır. Ayrıca gerçek katsayı vektöründeki sinyal değerlerinin büyüklük ve konumunun söz konusu yöntemlerle elde edilen modellerin performansı üzerindeki etkisi incelenmiştir. Modellerin ön tahmin performansının karşılaştırılması için test kümesi üzerinde hesaplanan hata kareler ortalaması ve tahminlerin standart sapması; değişken seçimindeki performanslarının karşılaştırılması için aktif küme büyüklükleri kullanılmıştır. Simülasyon çalışmalarından elde edilen bulgulara göre ikinci aşama tahmin edicinin seçimi ile gerçek katsayı vektörünün yapısı Post-LASSO yönteminin diğer yöntemlere göre başarısını önemli ölçüde etkilemektedir.

Anahtar kelimeler: Doğrusal regresyon, LASSO, Post-LASSO, Çoklu İç İlişki.

1. Introduction

In statistical modeling, linear regression analysis is a technique used to estimate the relationship between a continuous response variable and explanatory variables. The regression analysis has many applications in different disciplines 1, 2, 3. The first step in forming a linear regression model is the estimation of regression coefficients.

A linear regression model is defined as

$$\mathbf{y} = \mathbf{X}\boldsymbol{\beta} + \boldsymbol{\varepsilon} \quad (1)$$

* Corresponding author: muratgenc@tarsus.edu.tr. ORCID Number of authors: ¹ 0000-0002-6335-3044, ² 0000-0001-6110-1911

where \mathbf{y} is an $n \times 1$ vector of response variables, \mathbf{X} is an $n \times p$ matrix of explanatory variables, $\boldsymbol{\beta}$ is an $p \times 1$ vector of unknown coefficients, and $\boldsymbol{\varepsilon}$ is an $n \times 1$ vector of error terms with mean $\mathbf{0}$ and covariance matrix $\sigma^2\mathbf{I}$. The most used method for coefficient estimation in linear regression is the ordinary least squares (OLS) method. The OLS estimator of the coefficients for the regression model in Equation (1) is

$$\hat{\boldsymbol{\beta}}_{\text{ols}} = (\mathbf{X}^T\mathbf{X})^{-1}\mathbf{X}^T\mathbf{y}. \quad (2)$$

A dataset becomes ill-conditioned if there is multicollinearity, which is defined as a high degree of the linear relationship between explanatory variables. Although the OLS is often used to estimate regression coefficients, the OLS estimator yields unsatisfactory estimates due to inflation of the variance of the coefficients when the matrix of explanatory variables is ill-conditioned. Moreover, by its nature, the OLS estimator cannot estimate any coefficient as zero. Therefore, it cannot perform automatic variable selection. New estimators have been proposed to overcome these drawbacks of the OLS estimator. The ridge 4, Liu 5 restricted least squares 6 and restricted ridge estimator 7 are the methods that can produce more accurate prediction accuracy than the OLS by using some constraints on the coefficients. In contrast, the non-negative garrote 8, bridge regression 9, LASSO (least absolute shrinkage and selection operator) 10, elastic net 11 and adaptive LASSO 12 are methods that provide automatic variable selection as well as shrinkage of regression coefficients. The Bridge regression is a penalized regression method with $\|\boldsymbol{\beta}\|_1^\gamma$, $\gamma > 0$ penalty function. The $\gamma = 1$ case of the penalty function of the Bridge regression corresponds to the LASSO method. The elastic net is obtained by adding the ℓ_2 norm term to the penalty function of the LASSO and is more flexible than the LASSO. The adaptive LASSO is a method based on the calculation of LASSO estimates using adaptive weights.

The Post-LASSO estimator is a two-stage regression analysis method. In the first stage of the post-LASSO, the coefficient estimates are calculated. The variables with the non-zero coefficients (signals) among these estimates are selected. In the second stage, the regression coefficients of the explanatory variables selected at the end of the first stage on the original response variable are calculated by using a certain estimator. There are various studies in the literature on such two-stage methods. 13 proposed a post-LASSO estimator based on the implementation of the LASSO in the first stage and the OLS in the second stage and showed that this estimator is at least as good as LASSO in terms of convergence speed while being less biased than LASSO. 14 takes into consideration a two-step estimation technique for estimating the interaction effects in a spatial autoregressive panel model with a potentially large spatial dimension. 15 used the post-LASSO estimator with the ridge in the second stage for selecting the nested groups of the relevant genes from microarray data. 16 proposed the double LASSO and compared its performance with some estimators performing variable selection via simulation studies and applied it to Parents' Life Satisfaction data.

In the literature, there are various studies conducted to compare different linear regression methods through simulation studies. 17 conducted a simulation study for variable selection using the bootstrap method in principal component regression for high-dimensional data analysis. 18 conducted a study on the performance of penalized regression methods on high-dimensional datasets. 19 conducted a study on the comparison of convex penalized regression methods depending on the structure of the true coefficient vector in classical datasets.

This study investigates the performance of the post-LASSO two-stage method depending on the second-stage estimator, the characteristics of the true coefficient vector and the amount and location of the signals. The classical penalized regression methods the ridge, LASSO, elastic net, adaptive LASSO, and the post-LASSO methods are used for comparison. In the second stage of the post-LASSO, the OLS, ridge and LASSO methods are used respectively and the effect of the selected method in the second stage on the performance of post-LASSO is analyzed.

In Section 2 of the study, the penalized regression methods compared are summarized and the comparison criteria are given. The characteristics of the simulation studies used in the comparison are also mentioned. In Section 3 of the study, the findings obtained from the simulation studies are presented and the results are discussed in detail. In section 4 of the study, conclusions are given, and the study is completed.

2. Material and Method

2.1. Penalized Regression Methods

Since the OLS fails to predict new observations accurately depending on the structure of the dataset and fails to select variables, various methods based on the calculation of model coefficients under certain constraints have

been proposed as an alternative to the OLS. These methods are known as penalized regression methods and are widely used 20. These methods are used to obtain stable regression coefficient estimates by dealing with the problem of inflation of the variance of the coefficients. Some of the penalized regression methods can also perform automatic variable selection.

Let $(\mathbf{x}_1, y_1), (\mathbf{x}_2, y_2), \dots, (\mathbf{x}_n, y_n)$ be an independent and identically distributed dataset, where \mathbf{x}_i is the i -th observation vector of size $p \times 1$ and y_i is the response of i -th observation. The objective function of the linear regression model given in Equation (1) is

$$Q(\boldsymbol{\beta}) = \|\mathbf{y} - \mathbf{X}\boldsymbol{\beta}\|_2^2/2n + p_\lambda(\boldsymbol{\beta}) \quad (3)$$

where $\boldsymbol{\beta}$ is the vector of unknown coefficients, $p_\lambda(\cdot)$ is the penalty function and λ is the tuning parameter. In these methods, coefficient estimates are obtained by minimizing the objective function given in Equation (3).

The OLS estimator in Equation (2) has the smallest variance in the class of unbiased estimators. However, in the case of multicollinearity in the dataset, The OLS estimates are far from being satisfactory. To overcome this problem, penalty functions that affect the coefficient estimates in different ways have been proposed in the literature.

Among penalized regression methods, there are one-stage methods where coefficient estimates are obtained directly or two-stage methods where coefficient estimates are obtained after two stages. One-stage and two-stage penalized regression methods have been proposed whose performance varies depending on the characteristics of the datasets.

In the literature, there are various penalized regression methods that shrink the regression coefficients to achieve higher prediction accuracy than the OLS. 4 proposed ridge regression as a method based on the trade-off between the bias and variance of regression coefficients. Ridge regression aims to overcome the problem of over-inflation of variance by compromising the unbiasedness of the model coefficients. In ridge regression, coefficient estimates are obtained by solving the problem

$$\widehat{\boldsymbol{\beta}}_R = \underset{\boldsymbol{\beta}}{\operatorname{argmin}}\{\|\mathbf{y} - \mathbf{X}\boldsymbol{\beta}\|_2^2/2n + \lambda\|\boldsymbol{\beta}\|_2^2\} \quad (4)$$

where $\lambda > 0$ is the tuning parameter. The larger λ , the greater the shrinkage of the coefficients. The ridge regression coefficient estimates are found as

$$\widehat{\boldsymbol{\beta}}_R = (\mathbf{X}^T\mathbf{X} + \lambda n\mathbf{I}_p)^{-1}\mathbf{X}^T\mathbf{y} \quad (5)$$

by solving the problem given in Equation (4) where \mathbf{I}_p is the $p \times p$ identity matrix. If the dataset is ill-conditioned, ridge regression gives more accurate preliminary prediction values than EKK. Despite its prediction success, ridge regression cannot perform automatic variable selection. Therefore, estimators that can perform variable selection have been proposed as an alternative to ridge regression.

Considering the deficiency of ridge regression in variable selection, 10 proposed the LASSO method. In the LASSO method, coefficient estimates are obtained by solving the problem.

$$\widehat{\boldsymbol{\beta}}_L = \underset{\boldsymbol{\beta}}{\operatorname{argmin}}\{\|\mathbf{y} - \mathbf{X}\boldsymbol{\beta}\|_2^2/2n + \lambda\|\boldsymbol{\beta}\|_1\}. \quad (6)$$

Due to the ℓ_1 norm term in Equation (6), some of the LASSO coefficient estimates become zero for sufficiently large tuning parameter values. Therefore, the LASSO is not only a coefficient shrinkage method but also an automatic variable selection method. The problem in Equation (6) does not have a closed-form solution. Therefore, various algorithms have been proposed to obtain the LASSO estimates. The least angle regression 21, alternating direction method of multipliers 22, and coordinate descent 23 are some of the algorithms that can be used to obtain the LASSO estimates.

As the correlation between explanatory variables increases, the prediction success of LASSO regression reduces 10. In this case, an alternative to the LASSO is the elastic net (ENET) 11 method. ENET is obtained by adding an ℓ_2 norm term to the penalty function of the LASSO. The ENET estimator is obtained by solving the problem

$$\hat{\boldsymbol{\beta}}_E = \underset{\boldsymbol{\beta}}{\operatorname{argmin}} \{ \|\mathbf{y} - \mathbf{X}\boldsymbol{\beta}\|_2^2 / 2n + \lambda(\alpha \|\boldsymbol{\beta}\|_1 + (1 - \alpha) \|\boldsymbol{\beta}\|_2^2) \} \quad (7)$$

where $0 \leq \alpha \leq 1$ is the second tuning parameter. The ridge and LASSO correspond to $\alpha = 1$ and $\alpha = 0$ respectively in the ENET. In addition, due to the ridge-type penalization term, the ENET has the ability to group highly correlated variables. Therefore, the ENET is expected to perform better than the LASSO when there are highly correlated variables in the dataset.

In cases where the LASSO is not consistent in variable selection, the adaptive LASSO (A-LASSO) proposed by 12 can be used to estimate the model coefficients. The A-LASSO is consistent in variable selection and is approximately minimax optimal 12. The A-LASSO is based on the principle of using adaptive weights in the penalty function of the LASSO. The coefficient estimates of the A-LASSO are obtained by solving the problem

$$\hat{\boldsymbol{\beta}}_{A-LASSO} = \underset{\boldsymbol{\beta}}{\operatorname{argmin}} \left\{ \|\mathbf{y} - \mathbf{X}\boldsymbol{\beta}\|_2^2 / 2n + \sum_{j=1}^p w_j |\beta_j| \right\} \quad (8)$$

where w_j , $i = 1, 2, \dots, p$ are adaptive weights. 12, selected the vector of adaptive weights as $\hat{\mathbf{w}} = 1/|\hat{\boldsymbol{\beta}}_{EKK}|$. Accordingly, there are two stages for the calculation of A-LASSO:

1. Calculation of the EKK coefficient estimates and the vector of adaptive weights using these estimates.
2. Solving the problem in Equation (8) by reweighting the LASSO penalty function with the weights from stage 1.

The Post-LASSO estimator is a two-stage method like the A-LASSO. However, its stages are quite different from the stages of the A-LASSO. The stages of the Post-LASSO are

1. Finding LASSO coefficient estimates and detecting the signals by solving the minimization problem given in Equation (6),
2. Regression modeling of the response variable on the subset of the original dataset corresponding to the signals.

In this study, the OLS estimator given in Equation (2) (post-LO, 13), the ridge estimator given in Equation (5) (post-LR, 15) and the LASSO estimator given in Equation (6) (post-LL, 16) are used in the second stage of post-LASSO.

2.2. Simulation Studies and Comparison Criteria

In this study, classical penalized regression methods ridge, LASSO, ENET and A-LASSO, and two-stage post-LASSO type methods post-LO, post-LR and post-LL are compared through simulation studies. In the simulation studies, datasets are generated according to the model given in Equation (1) based on the method described in 10. In each simulation study, 100 datasets consisting of 50 explanatory variables are generated. In the simulation studies, the correlation between i . and j . explanatory variables is $\rho^{|i-j|}$ and the values of ρ are chosen as 0.5 and 0.7, which are commonly used in the literature 10, 24, 25. coefficients vector on the performance of the methods, simulation studies are classified into two groups.

- S1. In the first group of simulation studies, the signals of the true coefficients vector precede the noise (represented by a zero-valued coefficient). In this group, the true coefficient vector has the form $\boldsymbol{\beta} =$

$$\left[\underbrace{1.5 \dots 1.5}_{s/2}, \underbrace{0.5 \dots 0.5}_{s/2}, \underbrace{0, 0, \dots, 0}_{50-s} \right].$$

The number of signals, s , is taken as $s = 5, 10, 25, 50$ to represent different sparsity levels. As the value of s increases, the sparsity level reduces.

- S2. In the second group of simulation studies, the magnitude of the signals is taken equal, and the number and position of the noises are changed to examine the effect of sparsity and position. In the simulation studies in this group, the real coefficient vector has the form $\boldsymbol{\beta} = [a, \mathbf{0}_k, a, \mathbf{0}_k, \dots, a, \mathbf{0}_k]$. Here a is the signal value and k is the dimension of the zero vector. The value of k represents the sparsity level of the true coefficient vector. In this study, $a = 0.5, 1.5$ and $k = 1, 4, 9$.

For tuning parameter selection and calculation of performance criteria, it is common to decompose the dataset into training, validation and test sets 11, 26. First, the penalized regression methods to be compared are trained on the selected tuning parameter values. The mean squared error for these models is calculated using the validation set. The model with the smallest mean squared error in the validation set is determined as the best model. The performance of the models is compared with the mean squared error on the test set.

Table 1. Quality measures of methods for S1 group simulation studies.

ρ	s	Comparison Criterion	Ridge	LASSO	ENET	A-LASSO	Post-LO	Post-LR	Post-LL
0.5	5	Median of	2.2937	0.8678	1.1947	0.9517	2.1560	1.4641	0.7039
		TMSE							
		Standard Deviation	0.08	0.10	0.07	0.06	0.08	0.10	0.05
		Active Set Size	50	9	17	6	9	9	9
0.5	10	Median of	3.1850	1.8068	2.0322	2.2592	3.1778	2.0364	1.4044
		TMSE							
		Standard Deviation	0.12	0.07	0.08	0.08	0.13	0.08	0.10
		Active Set Size	50	18	26	12.5	18	18	18
0.5	25	Median of	3.9187	4.0861	3.4786	5.7695	5.4639	3.2915	3.3642
		TMSE							
		Standard Deviation	0.15	0.13	0.14	0.26	0.22	0.13	0.11
		Active Set Size	50	30	36	26	30	30	30
0.5	50	Median of	4.8628	6.9273	5.4853	9.5477	7.5741	4.3638	6.4777
		TMSE							
		Standard Deviation	0.14	0.24	0.11	0.37	0.23	0.15	0.15
		Active Set Size	50	46	47	43	46	46	46
0.7	5	Median of	1.9134	0.7022	0.9238	1.0306	1.7544	0.9893	0.4967
		TMSE							
		Standard Deviation	0.08	0.05	0.06	0.06	0.12	0.09	0.04
		Active Set Size	50	8	15.5	6	8	8	8
0.7	10	Median of	2.4281	1.5319	1.5066	2.5802	2.8661	1.6802	1.1579
		TMSE							
		Standard Deviation	0.07	0.06	0.05	0.13	0.14	0.08	0.08
		Active Set Size	50	16	24	13	16	16	15
0.7	25	Median of	2.7236	3.4224	2.4956	5.4789	5.3446	2.6762	3.1084
		TMSE							
		Standard Deviation	0.09	0.17	0.09	0.32	0.25	0.14	0.16
		Active Set Size	50	27	34.5	25	27	27	27
0.7	50	Median of	3.4368	6.3575	4.3326	9.3805	8.7705	4.4902	7.1900
		TMSE							
		Standard Deviation	0.15	0.29	0.18	0.30	0.35	0.16	0.25
		Active Set Size	50	44	47	40	44	44	44

In this study, independent training sets of 100 observations, validation sets of 100 observations and test sets of 400 observations are formed for each simulation run. The standard deviation of the errors in Equation (1) is taken $\sigma = 3$ as in 10. $\alpha = 0.5$ is chosen in order to observe the level of difference between the ridge, LASSO and ENET methods.

Various criteria are used to compare the performance of the models produced by the methods. Let Σ , the covariance matrix of the explanatory variables and $\tilde{\beta}$, the coefficients vector of the related penalized regression method. The mean squared error on the test set

$$TMSE = (\boldsymbol{\beta} - \tilde{\boldsymbol{\beta}})^T \boldsymbol{\Sigma} (\boldsymbol{\beta} - \tilde{\boldsymbol{\beta}})$$

is used to compare the performance of the models in the prediction. The standard deviations of the TMSE values are also given. Finally, the active set sizes obtained based on each method are reported as an estimate of the number of signals in the true model.

3. Findings and Discussion

The results of the S1 group simulation studies are summarized in Table 1. According to Table 1, when the correlation level between variables is low and the sparsity level is high, the methods that can select variables give a better TMSE value than ridge regression. As the sparsity level reduces, the performance of these methods decreases compared to ridge regression. The ENET is the least affected method by the ridge-type penalty term and is always better than ridge except when the sparsity level is zero. At fixed correlation values, the TMSE value of all methods increases as the sparsity level reduces. When the correlation level is low, at least one post-LASSO type method gave a superior TMSE value compared to the other methods. The post-LL is better than the other methods when the sparsity level is high while the post-LR is better when it is low. The post-LO improved over the ridge at high sparsity, however, is dominated by the ridge as the sparsity level is reduced. As the correlation level increases, the sparsity level determines the performance of the post-LASSO methods. More precisely, in terms of TMSE, the post-LASSO type methods are superior in sparse models, while in other cases the ENET is superior to other methods.

In terms of active set size, A-LASSO always yielded the sparsest models. In most cases, the post-LASSO type methods have the same sparsity level as the LASSO while the ENET produced the densest models.

The line plots of the TMSE values obtained with the ridge, LASSO, ENET, A-LASSO, Post-LO, Post-LO, Post-LR and Post-LL penalized regression methods in the simulation studies in the S1 group are shown in Figure 1. The line plots support the inferences given in Table 1.

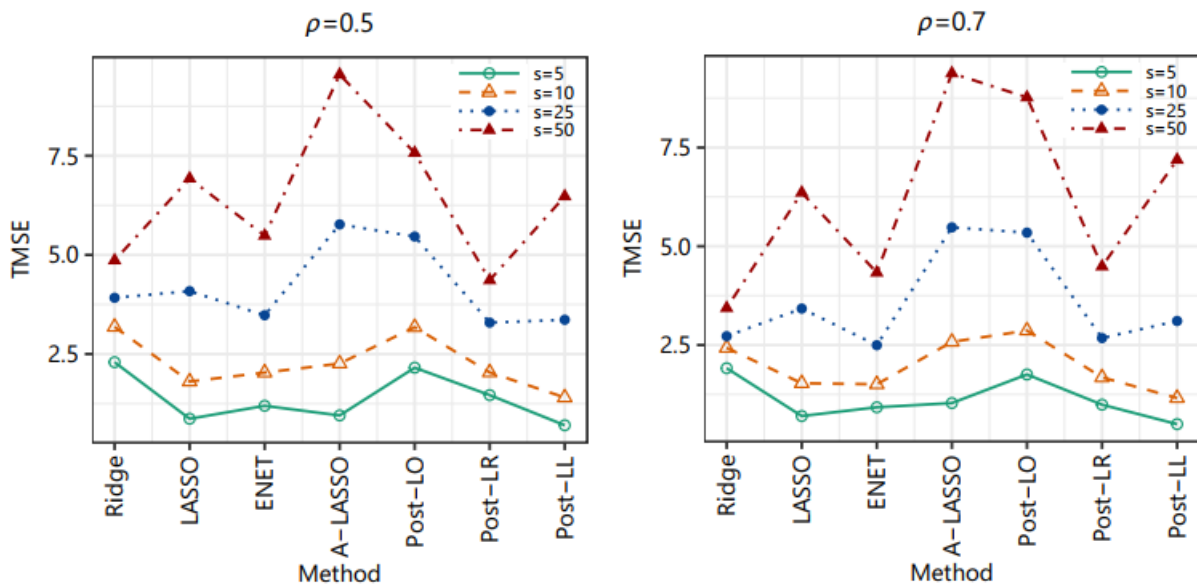


Figure 1. Line plots of TMSE values of the methods in S1 group simulation studies.

The results obtained from the S2 group simulation studies are given in Table 2,3,4. According to Table 2,3,4, when the correlation level is low and the signal value is small, at least one post-LASSO type method dominates the other methods in terms of TMSE. When the signal value is large, the A-LASSO method is more successful than the other methods at both correlation levels. As the correlation level increases, the post-LASSO type methods are superior in the case of a sparse model, while the ridge gives a better result when the model is dense. In sparse

model cases where the signal value is not small, the post-LL is superior to the post-LR, while the post-LR dominates the post-LL as the sparsity level decreases.

In terms of active set sizes, the models produced by the A-LASSO are sparser than those of the other methods. The LASSO and post-LASSO type methods mostly produced models with the same sparsity level.

Table 2. Quality measures of methods for S2 group simulation studies ($k = 1$).

ρ	a	Comparison Criterion	Ridge	LASSO	ENET	A-LASSO	Post-LO	Post-LR	Post-LL
0.5	0.5	Median of	2.5747	3.5612	3.0367	4.8732	4.7599	1.4948	2.2906
		TMSE							
		Standard Deviation	0.09	0.09	0.08	0.09	0.18	0.08	0.11
		Active Set Size	50	29	35	22	29	29	29
0.5	1	Median of	4.7383	5.5140	4.9097	7.3843	6.7050	4.1501	4.9141
		TMSE							
		Standard Deviation	0.12	0.18	0.13	0.31	0.26	0.14	0.22
		Active Set Size	50	39	43	34	39	39	39
0.5	5	Median of	11.2373	5.8086	8.7083	3.4424	7.3974	9.6831	5.8456
		TMSE							
		Standard Deviation	0.47	0.20	0.35	0.11	0.26	0.44	0.21
		Active Set Size	50	41	49	27	41	41	41
0.7	0.5	Median of	1.8008	2.9484	2.3976	4.2599	6.0278	2.2575	3.3732
		TMSE							
		Standard Deviation	0.05	0.10	0.05	0.17	0.20	0.14	0.14
		Active Set Size	50	29	35	20	29	29	29
0.7	1	Median of	3.6069	4.8343	3.9805	7.0343	7.0497	3.8334	4.9598
		TMSE							
		Standard Deviation	0.09	0.15	0.15	0.29	0.55	0.19	0.21
		Active Set Size	50	37	43	32	37	37	37
0.7	5	Median of	11.3546	5.7803	8.7258	3.5676	7.2909	9.6696	5.7679
		TMSE							
		Standard Deviation	0.35	0.16	0.41	0.16	0.28	0.37	0.18
		Active Set Size	50	40	48	27	40	40	40

Table 3. Quality measures of methods for S2 group simulation studies ($k = 4$).

ρ	a	Comparison Criterion	Ridge	LASSO	ENET	A-LASSO	Post-LO	Post-LR	Post-LL
0.5	0.5	Median of	1.5915	1.8618	1.7361	2.2162	2.6404	0.8594	0.9044
		TMSE							
		Standard Deviation	0.07	0.05	0.04	0.08	0.18	0.07	0.09
		Active Set Size	50	15	19	7.5	16	16	15
0.5	1	Median of	3.3773	3.0304	2.8857	3.3551	4.2139	2.7540	2.3923
		TMSE							
		Standard Deviation	0.07	0.17	0.14	0.16	0.26	0.12	0.10
		Active Set Size	50	24	32	17	24	24	24
0.5	5	Median of	8.8303	3.0302	6.7399	1.3167	4.7968	5.3831	2.8519
		TMSE							
		Standard Deviation	0.35	0.15	0.26	0.07	0.28	0.29	0.17
		Active Set Size	50	25	46	12	25	25	25
0.7	0.5	Median of	1.2716	1.7106	1.5406	2.0603	3.0647	0.9003	1.1739
		TMSE							
		Standard Deviation	0.03	0.03	0.03	0.06	0.25	0.07	0.07
		Active Set Size	50	16	22.5	11	16	16	16
0.7	1	Median of	2.7524	2.7390	2.6709	3.5810	4.4794	2.4284	2.4504
		TMSE							
		Standard Deviation	0.08	0.07	0.08	0.11	0.26	0.08	0.13
		Active Set Size	50	24	31.5	19	24	24	24
0.7	5	Median of	8.4963	3.0106	6.7301	1.3705	4.5300	5.5549	2.9878
		TMSE							
		Standard Deviation	0.20	0.10	0.33	0.07	0.16	0.21	0.13
		Active Set Size	50	26.5	45	12	26.5	26.5	25.5

Table 4. Quality measures of methods for S2 group simulation studies ($k = 9$).

ρ	a	Comparison Criterion	Ridge	LASSO	ENET	A-LASSO	Post-LO	Post-LR	Post-LL
0.5	0.5	Median of	0.9863	1.0334	1.0083	1.1286	2.1345	0.4742	0.5186
		TMSE							
		Standard Deviation	0.03	0.06	0.05	0.04	0.20	0.06	0.08
		Active Set Size	50	7	10.5	4	10	10	7
0.5	1	Median of	2.3335	1.6554	1.7667	1.8022	3.086	1.8000	1.3230
		TMSE							
		Standard Deviation	0.07	0.12	0.10	0.11	0.19	0.11	0.08
		Active Set Size	50	16	22	11	16	16	16
0.5	5	Median of	7.3924	1.6618	4.8912	0.6125	3.3622	3.5476	1.5437
		TMSE							
		Standard Deviation	0.26	0.13	0.29	0.05	0.16	0.18	0.1
		Active Set Size	50	17	42	6	17	17	17
0.7	0.5	Median of	0.8695	1.0740	1.0122	1.1994	2.2889	0.5482	0.6073
		TMSE							
		Standard Deviation	0.02	0.05	0.04	0.02	0.2	0.06	0.06
		Active Set Size	50	8	13	4	11	11	8
0.7	1	Median of	1.9657	1.6302	1.6825	2.1701	2.7410	1.6528	1.4061
		TMSE							
		Standard Deviation	0.04	0.10	0.08	0.12	0.24	0.06	0.08
		Active Set Size	50	15.5	22.5	11	15.5	15.5	15
0.7	5	Median of	6.8640	1.6598	4.6428	0.6262	2.7658	3.2971	1.5978
		TMSE							
		Standard Deviation	0.27	0.10	0.14	0.05	0.28	0.19	0.09
		Active Set Size	50	16	40	6	16	16	16

The line plots of the TMSE values obtained with the ridge, LASSO, ENET, A-LASSO, Post-LO, Post-LR and Post-LL in the S2 group simulation studies are given in Figures 2,3,4. The line plots are consistent with the analysis results given in Table 2,3,4.

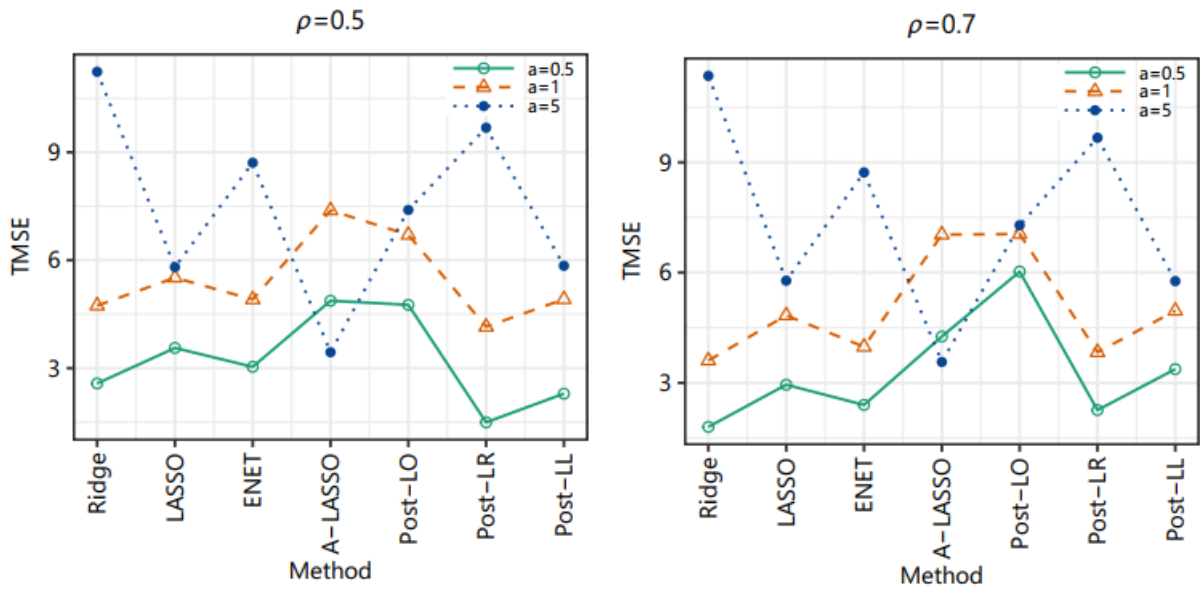


Figure 2. Line plots of TMSE values of the methods in S1 group simulation studies ($k = 1$).

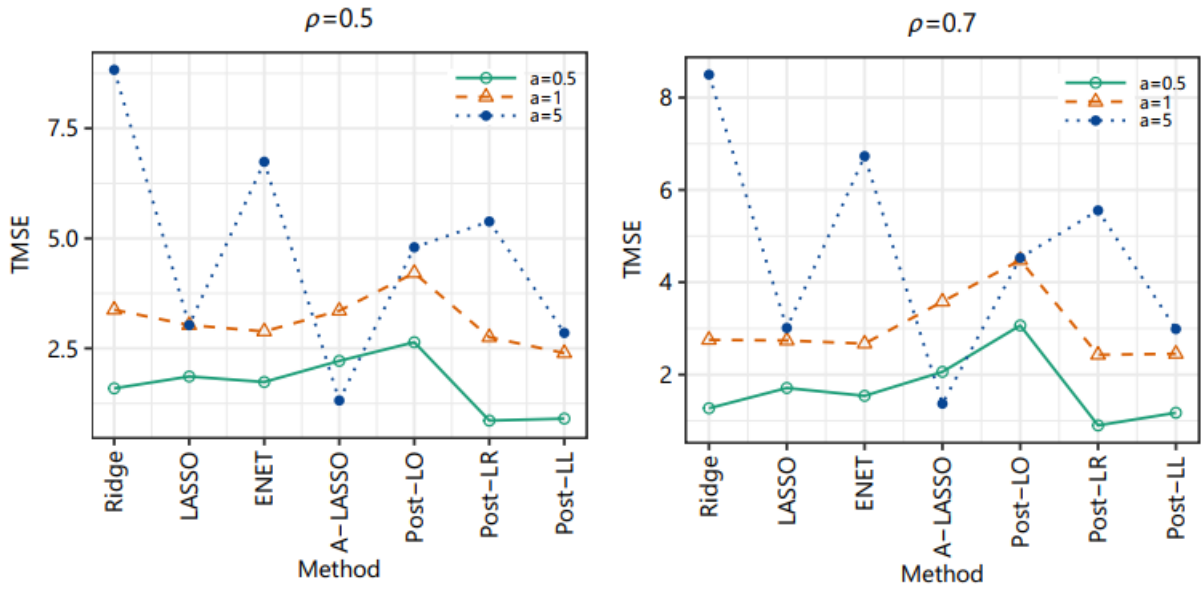


Figure 3. Line plots of TMSE values of the methods in S1 group simulation studies ($k = 4$).

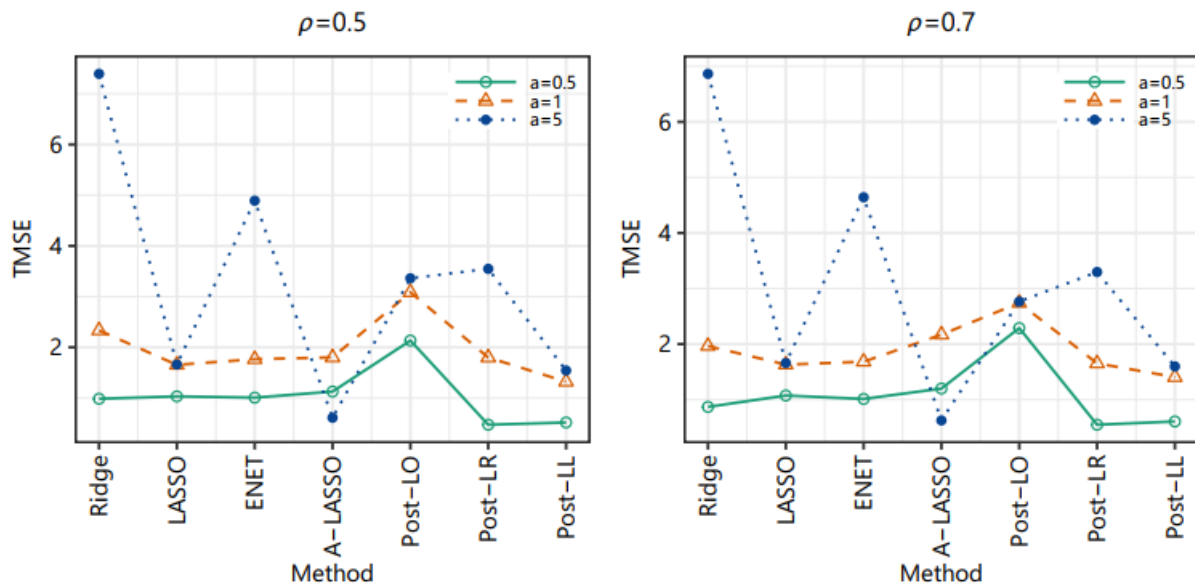


Figure 4. Line plots of TMSE values of the methods in S1 group simulation studies ($k = 9$).

4. Conclusions

In this study, the effect of the properties of the true coefficient vector on the performance of classical penalized regression methods and two-stage post-LASSO type methods is investigated. A detailed comparison of the ridge, LASSO, ENET and A-LASSO classical penalized regression methods with the post-LASSO type penalized regression methods, post-LO, post-LR, post-LR and post-LL are performed by considering the size and position of the signals.

According to the results obtained from the comparison criterion, the estimator in the second stage of the post-LASSO type methods is quite effective in the performance of these methods. In addition, the structure of the true coefficient vector of the model is very effective in the performance of classical and post-LASSO type methods. According to the active set sizes obtained by the post-LASSO type methods, the true coefficient vector and the properties of the dataset have an impact on the success of post-LASSO type methods in variable selection. With the simulation studies, the strengths and weaknesses of post-LASSO methods in terms of estimation and variable selection in models with different structures in terms of sparsity and signal magnitude are revealed.

References

- [1] Montgomery DC, Runger GC, Hubele NF. Engineering Statistics. New York: John Wiley & Sons; 2009.
- [2] Bzovsky S, Phillips MR, Guymer RH, Wykoff CC, Thabane L, Bhandari M, Chaudhary V. The clinician's guide to interpreting a regression analysis. *Eye* 2022; 36(9):1715-1717.
- [3] Venkateshan SP. Mechanical Measurements. New York: John Wiley & Sons; 2015.
- [4] Hoerl AE, Kennard RW. Ridge regression: Biased estimation for nonorthogonal problems. *Technometrics* 1970; 12(1):55-67.
- [5] Liu K. Using Liu-type estimator to combat collinearity. *Commun Stat - Theory Methods* 2003; 32(5):1009-1020.
- [6] Rao CR, Toutenburg H. Linear Models: Springer; 1995.
- [7] Sarkar N. A new estimator combining the ridge regression and the restricted least squares methods of estimation. *Commun Stat - Theory Methods* 1992; 21(7):1987-2000.
- [8] Breiman L. Better subset regression using the nonnegative garrote. *Technometrics* 1995; 37(4):373-384.
- [9] Frank LE, Friedman JH. A statistical view of some chemometrics regression tools. *Technometrics* 1993; 35(2):109-135.
- [10] Tibshirani R. Regression shrinkage and selection via the lasso. *J R Stat Soc Ser B Methodol* 1996; 58(1):267-288.
- [11] Zou H, Hastie T. Regularization and variable selection via the elastic net. *J R Stat Soc Ser B Methodol* 2005; 67(2):301-320.

- [12] Zou H. The adaptive lasso and its oracle properties. *J Am Stat Assoc* 2006; 101(476):1418-1429.
- [13] Belloni A, Chernozhukov V. Least squares after model selection in high-dimensional sparse models. *Bernoulli* 2013; 19(2):521-547.
- [14] Ahrens A, Bhattacharjee A. Two-step lasso estimation of the spatial weights matrix. *Econometrics* 2015; 3(1):128-155.
- [15] De Mol C, Mosci S, Traskine M, Verri A. A regularized method for selecting nested groups of relevant genes from microarray data. *J Comput Biol* 2009; 16(5):677-690.
- [16] Urminsky O, Hansen C, Chernozhukov V. Using double-lasso regression for principled variable selection. SSRN Working Paper No. 273374. 2016.
- [17] Shahriari S, Faria S, Gonçalves AM. Variable selection methods in high-dimensional regression-A simulation study. *Commun Stat - Simul Comput* 2015; 44(10):2548-2561.
- [18] Ahmed SE, Kim H, Yıldırım G, Yüzbaşı B. High-Dimensional Regression Under Correlated Design: An Extensive Simulation Study. *International Workshop on Matrices and Statistics*, Springer. 2016:145-175.
- [19] Genç M. Bir Simülasyon Çalışması ile Cezalı Regresyon Yöntemlerinin Karşılaştırılması. *Bilecik Şeyh Edebali Üniv Fen Bilim Derg* 2022; 9(1):80-91.
- [20] Hastie T, Tibshirani R, Friedman J. *The Elements of Statistical Learning*. New York: Springer series in statistics; 2001.
- [21] Efron B, Hastie T, Johnstone I, Tibshirani R. Least angle regression. *Ann Stat* 2004; 32(2):407-499.
- [22] Boyd S, Parikh N, Chu E, Peleato B, Eckstein J. Distributed optimization and statistical learning via the alternating direction method of multipliers. *Found Trends Mach Learn* 2011; 3(1):1-122.
- [23] Friedman J, Hastie T, Tibshirani R. Regularization paths for generalized linear models via coordinate descent. *J Stat Softw* 2010; 33(1):1-22.
- [24] Chang L, Roberts S, Welsh A. Robust lasso regression using Tukey's biweight criterion. *Technometrics* 2018; 30(1):36-47.
- [25] Chong IG, Jun CH. Performance of some variable selection methods when multicollinearity is present. *Chemom Intell Lab Syst* 2005; 78(1-2):103-112.
- [26] Hussami N, Tibshirani RJ. A component lasso. *Can J Stat* 2015; 43(4):624-646.

The Effect of Super Resolution Method on Classification Performance of Satellite Images

Ayşe CENGİZ¹, Derya AVCI^{2*}

¹ Institute of Science and Technology, Fırat University, Elazığ, Turkey

² Technical Sciences Department of Computer Technology, Fırat University, Elazığ, Turkey

¹ aayscengiz@gmail.com , ² davci@firat.edu.tr

(Geliş/Received: 17/02/2023;

Kabul/Accepted: 27/07/2023)

Abstract: The high resolution of the image is very important for applications. Publicly available satellite images generally have low resolutions. Since low resolution causes loss of information, the desired performance cannot be achieved depending on the type of problem studied in the field of remote sensing. In such a case, super resolution algorithms are used to render low resolution images high resolution. Super resolution algorithms are used to obtain high resolution images from low resolution images. In studies with satellite images, the use of images enhanced with super resolution is important. Since the resolution of satellite images is low, the success rate in the classification process is low. In this study, super resolution method is proposed to increase the classification performance of satellite images. The attributes of satellite images were extracted using AlexNet, ResNet50, Vgg19 from deep learning architecture. Then the extracted features were then classified into 6 classes by giving input to AlexNet-Softmax, ResNet50-Softmax, Vgg19-Softmax, Support Vector Machine, K-Nearest Neighbor, decision trees and Naive Bayes classification algorithms. Without super resolution and with super resolution feature extraction and classification processes were performed separately. Classification results without super resolution and with super resolution were compared. Improvement in classification performance was observed using super resolution.

Key words: Super Resolution, Convolutional Neural Networks, Deep Learning, Classification.

Süper Çözünürlük Yönteminin Uydu İmgelerinin Sınıflandırma Performansına Etkisi

Öz: Görüntünün yüksek çözünürlüğü uygulamalar için çok önemlidir. Halka açık sunulan uydu görüntülerinin çözünürlükleri genellikle düşüktür. Düşük çözünürlük bilgi kaybına yol açtığından uzaktan algılama alanında çalışılan problemin türüne bağlı olarak istenilen başarımlar sağlanamamaktadır. Böyle bir durumda düşük çözünürlüklü görüntülerden yüksek çözünürlüklü görüntü elde etmek için süper-çözünürlük algoritmaları kullanılmaktadır. Uydu görüntüleri ile yapılan çalışmalarda süper çözünürlükle zenginleştirilmiş görüntülerin kullanılması önemlidir. Uydu görüntülerinin çözünürlükleri düşük olduğundan dolayı sınıflandırma işleminde başarımlar düşük çıkmaktadır. Bu çalışmada, uydu görüntülerinin sınıflandırma başarımlarını artırmak için süper çözünürlük yöntemi önerilmiştir. Derin öğrenme mimarisinden AlexNet, ResNet50, Vgg19 kullanılarak uydu imgelerinin özellikleri çıkarılmıştır. Ardından çıkarılan özellikler, AlexNet-Softmax, ResNet50-Softmax, Vgg19-Softmax, Destek Vektör Makinesi, K- En Yakın Komşu ve Naive Bayes sınıflandırma algoritmalarının girişine verilerek 6 sınıfa ayrılmıştır. Süper çözünürlük öncesi ve süper çözünürlük sonrası özellik çıkarma ve sınıflandırma işlemleri ayrı ayrı yapılmıştır. Süper çözünürlükten önce ve sonra sınıflandırma sonuçları karşılaştırılmıştır. Süper çözünürlük kullanılarak sınıflandırma performansında iyileşme gözlemlenmiştir.

Anahtar kelimeler: Süper Çözünürlük, Evrimsel Sinir Ağları, Derin Öğrenme, Sınıflandırma

1. Introduction

Today, satellite images are actively used in many fields such as address inquiry, field investigation, city planning, agriculture. A large amount of high-resolution (HR) satellite images that enable topographic measurements of the Earth have been obtained by satellites. However, high spatial resolution satellite images present many problems in image classification. With the increase in spatial resolution, more and more details found on the earth's surface appear in satellite images. Objects in the same type of scenes can be seen at different scales and orientations between HR images. When zooming in on satellite images, it is difficult to obtain a clear image because the resolution decreases, and good performance cannot be obtained when classification is made, since the image quality is reduced at low resolution (LR). Super resolution (SR) is a method of obtaining HR images from one or more LR versions of the same image SR has high pixel density. The rate of correct classification of images with increasing resolution increases [1].

In recent years, many new algorithms based on HR image reconstruction [2-5], instance-based [6-8], regression-based [9-11] and deep learning [12-15] have been proposed. One of the main approaches for single

* Corresponding author: davci@firat.edu.tr. ORCID Number of authors: ¹ 0000-0003-3829-3243, ² 0000-0002-5204-0501

frame SR of the image is the interpolation of the image, in which the high frequency information is extracted from the low frequency image and the estimation is made for the detailed information in the first image [16].

There are many methods based on standard interpolation techniques (pixel replication, bilinear, bi-cubic, linear interpolation) that increase the number of pixels without adding details for SR [17-21]. According to image priorities, single image SR algorithms can be categorized into four types. These are prediction models, edge-based methods, image statistical methods and sample-based methods [22-24]. Among them, instance-based methods [25-27] achieve improved performance. Internal instance-based methods take advantage of self-similarity and generate sample patches from the input image. Firstly, Glasner et al. in the study [28], some improved variants are suggested to speed up the implementation. External instance-based methods [29-32] learn from external datasets between low/high resolution patches. SR is applied using multiple images or single images in the frequency domain or spatial domain [33].

SR studies started before deep learning [34]. Advances in deep learning have affected SR studies and successful results have been observed [35-38]. Deep learning-based methods can be grouped according to the type of network architecture, the type of error function used, and different learning principles [39]. Deep learning-based SR is a class of techniques that use deep neural networks to learn the mapping between LR images and their corresponding HR images. The basic idea is to train a deep neural network using a large set of HR and LR image pairs. The network is then used to predict the HR image from the LR input image. Deep learning-based SR methods use convolutional neural networks (CNNs) to learn the mapping between LR and HR images. These methods can improve the accuracy and efficiency of SR, and they have become the state-of-the-art for SR tasks [40,41]. Recurrent Neural Network (RNN), Long Short Term Memory (LSTM), Convolutional Neural Networks (CNN), Generative Adversarial Networks (GAN), Gated Recurrent Unit (GRU) are frequently used deep learning models [42]. In the literature, there are studies in which RNN [43], LSTM [44], CNN [45], GAN [46] network architectures and SR method are used together.

Deep learning-based SR has several applications in computer vision. One of the most popular applications is in the field of image and video processing [47]. SR techniques can be used to improve the resolution of LR images and videos, making them more suitable for various applications such as surveillance [48], medical imaging [49], and remote sensing [50].

Single Image Super-Resolution (SISR) is a technique used in computer vision and image processing to enhance the resolution and quality of a single LR image. The goal of SISR is to generate a HR image from its LR counterpart by inferring the missing high-frequency information [51]. SISR techniques primarily rely on deep learning methods, with convolutional neural networks (CNNs) being widely employed for this task. CNN models are trained on large datasets consisting of paired LR and HR images. The LR images are used as input, while the corresponding HR images serve as ground truth. During the training phase, the CNN model learns to extract relevant features from LR images and generate HR outputs. The optimization objective is to minimize the difference between the generated HR image and the ground truth. This training process enables the model to learn the mapping between LR and HR images, capturing fine details and structures [52]. SISR techniques have significant applications in enhancing the quality of LR images captured from digital cameras or video footage. By upscaling these images, details and textures can be enhanced, resulting in visually improved images [53]. In the medical field, SISR plays a vital role in improving the resolution of medical images, such as MRI or CT scans. HR images facilitate better diagnosis, analysis, and treatment planning, leading to improved patient care [54]. SISR is crucial for improving the resolution of satellite or aerial imagery used in various applications, including surveillance, mapping, and urban planning. HR imagery aids in better understanding and decision-making processes [55].

The classification of satellite imagery has been investigated in the literature. Many studies have focused on the accuracy of classification. Kadhim et al. [56] proposed CNN architectures, namely AlexNet, VGG19, GoogLeNet and Resnet50, to improve the performance of satellite image classification. They compared all the results of the models on three datasets, SAT 4, SAT6 and UCMD. Basu et al. [57] proposed the "DeepSat" method for classification of satellite images. They achieved an accuracy of 97.946 by classifying based on deep unsupervised learning with Convolutional Neural Networks. Albert et al. [58] analyzed land use patterns in urban neighborhoods with state-of-the-art computer vision techniques based on deep convolutional neural networks using satellite images. Robinson et al. [59] proposed a deep learning convolutional neural network model for generating HR population estimates from satellite images. The proposed model demonstrated how machine learning techniques can be an effective tool for extracting information from remotely sensed data. Unnikrishnan et al. [60] proposed three different network architectures (AlexNet, ConvNet, VGG) for the classification of SAT-4 and SAT-6 datasets of satellite images. The proposed models demonstrated the performance of comparative deep learning architectures for high accuracy satellite image classification with fewer trainable parameters. Özbay et al.

[61] analyzed the classification performance of deep learning models in satellite image analysis. They used MobileNetV2, DenseNet201 and ResNet50 architectures as feature extractors. They used convolutional neural network (CNN) models and neighborhood component analysis (NCA) together to manage the classification process more efficiently. The success rate of satellite image classification was 96.46%.

In this study, SR method was proposed to increase the resolution of satellite images and with SR enhanced images were analyzed. Deep learning-based convolutional neural networks are used to make applications such as building detection over enhanced images. Satellite images usually have LR. Therefore, the success rate in the classification process is low. An increase in classification performance was observed with SR.

The organization of this article is as follows: In Chapter 2, information about SR is presented. In Chapter 3, Material and Method is presented. Experimental Results and Discussion is described in Chapter 4. In Chapter 5, Conclusion is presented.

2. Super Resolution

There are two key elements that need to be resolved in SR rendering algorithm. First, all images must be aligned correctly and on top of each other on a common base. The second is to create a new image with higher resolution from these images. If any of these two steps is done incorrectly, no resolution gain can be obtained and the resulting image will not be of the desired quality.

SR in image is the process of recovering HR images from LR images. SR is an important technique used in image processing. SR is used in many fields such as medical imaging [62], satellite imaging [63-65], surveillance and security [66-68], astronomical imaging [69], military imaging [70]. It can be observed that there are some minor differences when using LR images. However, the same LR image cannot be reused when obtaining LR images.

The most common Mean Square Error (MSE), Peak Signal to Noise Ratio(PSNR), Structural Similarity Index Measure (SSIM) metrics are used to measure the performance of models. MSE is the mean squared error. It has been the basis of image quality measurement. Generally, the original image is assumed to be free of any distortion, while the other image is assumed to be contaminated with noise or some other type of error. The difference between them is called the error signal [71].

MSE is a measure of the average squared difference between the pixel values of two images. It is commonly used as a metric to quantify the dissimilarity between an original image and a reconstructed image. The formula to calculate MSE is as follows:

$$MSE = \frac{1}{M \times N} \sum_{i=1}^M \sum_{j=1}^N (X_{ij} - Y_{ij})^2 \quad (1)$$

In the formula, M and N are the dimensions of the images (typically width and height), $X(i,j)$ is the pixel value of the original image at position (i, j), $Y(i,j)$ is the pixel value of the reconstructed image at position (i, j), Σ denotes the sum over all pixels in the image. $(X(i,j) - Y(i,j))^2$ represents the squared difference between the pixel values at corresponding positions (i, j) in the original and reconstructed images.

PSNR is the peak signal to noise ratio. Generally, PSNR is used in image processing. PSNR is more useful than MSE only when comparing images in different dynamic ranges, otherwise equivalent to MSE. The correct range of values for PSNR is typically from 0 to infinity [71]. PSNR is expressed in decibels (dB), and higher PSNR values indicate better quality or higher similarity between two signals or images. The PSNR value is calculated based on the MSE between two signals or images. The MSE is first computed, and then it is used in the PSNR formula to derive the value. C is the maximum possible pixel value of the image data.

$$PSNR = 10 * \log_{10} \frac{C_{max}^2}{MSE} \quad (2)$$

Structural Similarity (SSIM) is used to compare the perceptual quality of two images with the mean.

$$SSIM(x, y) = \frac{(2\mu_x\mu_y + c_1)(2\sigma_{xy} + c_2)}{(\mu_x^2 + \mu_y^2 + c_1)(\sigma_x + \sigma_y + c_2)} \quad (3)$$

In equality, μ_x : mean of X, μ_y : mean of Y, σ_x : variance of X, $2\sigma_y$: variance of Y, σ_{xy} : covariance of X and Y [72].

SR algorithms are techniques used to enhance the resolution and level of detail in digital images or videos. They aim to generate HR versions of LR images by utilizing various computational methods and statistical models. These algorithms have found applications in several domains, including computer vision, image processing, medical imaging, surveillance, and remote sensing.

Single-Image Super-Resolution (SISR) algorithm is used in this study. SISR refers to the task of enhancing the resolution of a single LR image to obtain a HR version. This branch of SR focuses on improving the level of detail, sharpness, and overall visual quality of an image without relying on additional images or frames. SISR algorithms utilize various techniques to infer the missing high-frequency details in a LR image. SISR algorithms find applications in various fields, including digital photography, surveillance systems, medical imaging, satellite imaging, and more. They are used to enhance image quality, support image analysis tasks, improve visualization, and facilitate better decision-making based on HR information.

Algorithm showing the basic steps of SISR algorithm is shown below. Input: The LR image is provided as the input to the algorithm.

1. Preprocessing: Optional preprocessing steps may be applied, such as noise reduction, contrast adjustment, or color space conversion, to improve the quality of the input image.
2. Feature Extraction: Extract relevant features from the LR image. This step involves capturing low-level and high-level features that will help in understanding the image content and structure.
3. SR Network: Train the network using a dataset of LR and corresponding HR image pairs. The network learns the mapping between LR and HR images.
4. Image Reconstruction: Feed the LR image through the trained SR network to generate an initial HR image. The network's architecture and parameters determine how the upsampling and detail enhancement are performed.
5. Post-processing: Apply post-processing techniques to refine the initial HR image. Common post-processing steps include denoising, sharpening, texture enhancement, and artifact reduction.
6. Output: The final output of the SISR algorithm is the enhanced HR image.

3. Material and Method

Since the resolution of satellite images is low, the success rate in the classification process is low. The SR method is proposed to improve the classification performance of satellite images. The main objective of this study is to improve the classification performance of satellite images by using deep learning based SR method to classify satellite images. While determining the main classes, satellite images were used and a total of 6 classes were determined, including mosque, home, hospital, school, park and stadium, which have distinctive features. In order to see the effects of classification performance, the data set was collected manually using Google Earth [73], which has 150 images for each class, belonging to each classes from various provinces in Turkey. In total, deep learning-based classification and SR algorithms were applied on 900 images. In Figure 1, some of the satellite images of the data set used in this study are given. Matlab 2020a software was used to process the data divided into two main parts, training and testing for convolutional neural networks. For deep machine learning applications, MacBook Pro with an Intel i7 3.1 Ghz processor with 16 GB of RAM was used.



Figure 1. Satellite images of the data set.

The details of the SISR implementation phase used in this study are as follows.

Preparation of LR and HR Images: LR images are obtained from HR images by reducing their resolution. This reduction is typically achieved using a sub-sampling operator. Sub-sampling operators combine pixels in a known factor (e.g., 2x, 3x) to create LR images. This sub-sampling reduces the resolution of pixels based on the subsampling factor.

Image Sizes: The sizes of LR and HR images depend on the requirements of the application. Input images to have dimensions that are multiples of 2. LR image with a size of 128x128 pixels correspond to an HR image with a size of 256x256 pixels. These dimensions are important for model training and obtaining the SR output.

Data Preparation and Normalization: Data Preparation and Normalization: Images enhanced through pre-processing steps such as denoising, contrast adjustment, color space conversion, respectively. Then data normalization applied. For example, techniques like scaling pixel values to the [0, 1] range, zero-centering the mean, or unitizing the standard deviation used.

Image Feeding and Classifier Sizes: The SISR model takes LR images as input and attempts to predict HR images. In some cases, classifiers used to evaluate the quality of the SR images. The size of the images fed to classifiers depended on their specific requirements and input size constraints.

Overall, the implementation phase involves preparing LR and HR image pairs, ensuring appropriate dimensions, applying pre-processing and normalization techniques, and adapting to any specific requirements or constraints of the SISR model or associated classifiers. These steps help create an effective pipeline for generating HR images from LR inputs.

In this study, feature extraction is performed using AlexNet, ResNet50 and VGG19 pre-trained models. These models have been trained on large-scale image datasets and have learned feature representations. This typically involves resizing the image to the expected input size of the model and performing any necessary normalization or preprocessing steps. Images are given as input to the pre-trained model. Depending on the model, it extracted features from different layers. Each layer captures different levels of abstraction and represents different types of features. The features are extracted from the last convolutional layers of the algorithms. 1000 attributes were extracted from 3 architectures. The feature extraction process was applied to the images separately for without SR and with SR.

As a general approach, the available data is divided into clusters of 70% for training and 30% for testing. The training and result data of the Softmax classifier layers were extracted with Matlab software, then all images were improved over the Matlab software again for the SR method, depending on the classes. In order to prove a better classification performance by improving the satellite images of the SR algorithm, the improved images were classified with the help of convolutional neural networks after the SR step. The graphs, test times, accuracy values, complexity matrices and analysis information required for classification performance control are explained in the findings and discussion section.

First, a total of 900 image features were extracted with AlexNet, ResNet50 and VGG19 convolutional neural network architectures. Then these features are classified with classifiers such as AlexNet Softmax, ResNet50

Softmax, VGG19 Softmax, Support Vector Machine (SVM), K-Nearest Neighbor (KNN), decision trees and Naive Bayes. Resolution of the images has been increased by using SR method which has proven to perform well, which does not need the matconvnet library. SR-applied images are feature extracted with AlexNet, ResNet50 and VGG19 convolutional neural network architectures. Then these features are classified with classifiers such as AlexNet Softmax, ResNet50 Softmax, VGG19 Softmax, Support Vector Machine (SVM), K-Nearest Neighbor (KNN), decision trees and Naive Bayes. Classification performance without SR and with SR was compared. The results are explained in the findings and discussion section.

4. Experimental Results and Discussion

In this study, which aims to improve satellite images with SR, first of all, SR algorithm is applied by using satellite images. The satellite image used in the study is given in Figure 2, and the image with SR applied to the satellite image is given in Figure 3.

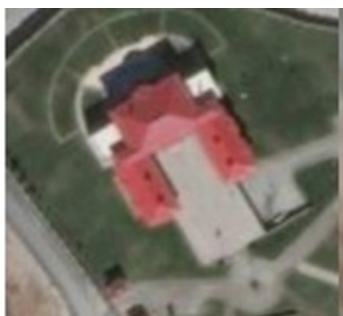


Figure 2. Satellite image.

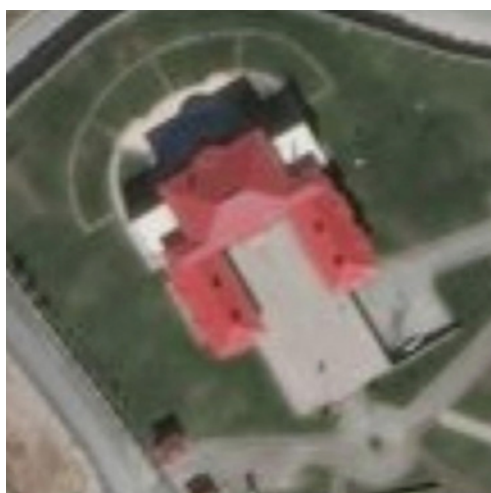


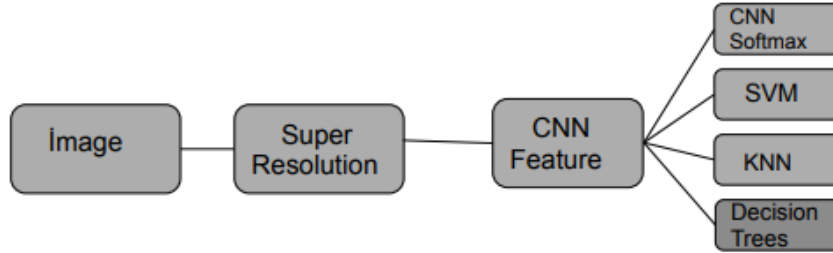
Figure 3. Image with SR applied to satellite image.

In Table 1, the peak signal-to-noise ratio (PSNR) and structural similarity index metrics (SSIM) for an image for each class of mosque, house, hospital, school, park and stadium classes used in the data set are given under the scale factor X2.

Table 1. Display Metrics.

Dataset classes	PSNR	SSIM
Data set 1	38.04	0.96
Data set 2	34.48	0.92
Data set 3	38.07	0.96
Data set 4	38.12	0.95
Data set 5	38.32	0.94
Data set 6	38.17	0.96

The satellite images were classified with deep convolutional neural networks, SVM, KNN and decision trees without SR and with SR and the results were compared. A diagram of the methods applied to satellite images is given in Figure 4.

**Figure 4.** The diagram of the applied methods.

In another application, an accuracy of 95.6% was achieved with the softmax structure of the AlexNet convolutional neural network architecture. SR was applied to the images in order to increase the correct recognition rate. The new images obtained as a result of the SR algorithm were reclassified. Increasing the resolution of the images increased the correct recognition rate and a 97.2% success rate was achieved. Afterwards, 1000 features were extracted with AlexNet. Extracted features were given to classifiers such as SVM, KNN, Naive Bayes and Bagged Trees, and the success rates without SR and with SR were observed. All obtained results are given in Table 2 in the form of without SR and with SR. The most successful result was obtained with AlexNet-Quadratic SVM with a rate of 97.3%. 1.8% increase in performance was achieved by using SR.

Table 2. AlexNet Results.

Method	Without SR Accuracy Rates	With SR Accuracy Rates
AlexNet Softmax	95.6%	97.2%
AlexNet-Cubic SVM	94.9%	97.1%
AlexNet-Quadratic SVM	95.5%	97.3%
AlexNet-Linear SVM	93.5%	94.3%
AlexNet-Medium Guassian SVM	94.4%	95.8%
AlexNet-Coarse Guassian SVM	85.9%	89.3%
AlexNet-Fine KNN	90.6%	95.8%
AlexNet-Medium KNN	87.1%	88.2%
AlexNet-Coarse KNN	78.9%	81.3%
AlexNet-Cosine KNN	86.8%	87.0%
AlexNet-Cubic KNN	86.7%	88.4%
AlexNet-Weighted KNN	90.5%	93.4%
AlexNet-Subspace KNN	91.1%	95.9%
AlexNet-Bagged Trees	92.5%	89.7%
AlexNet-Kernel Naive Bayes	83.3%	85.3%

Confusion matrix of the AlexNet-Quadratic SVM method with the best classification success was created. Confusion matrix created as a result of the classification without the SR is shown in Figure 5(a) and confusion matrix created as a result of the classification with the SR is shown in Figure 5(b).

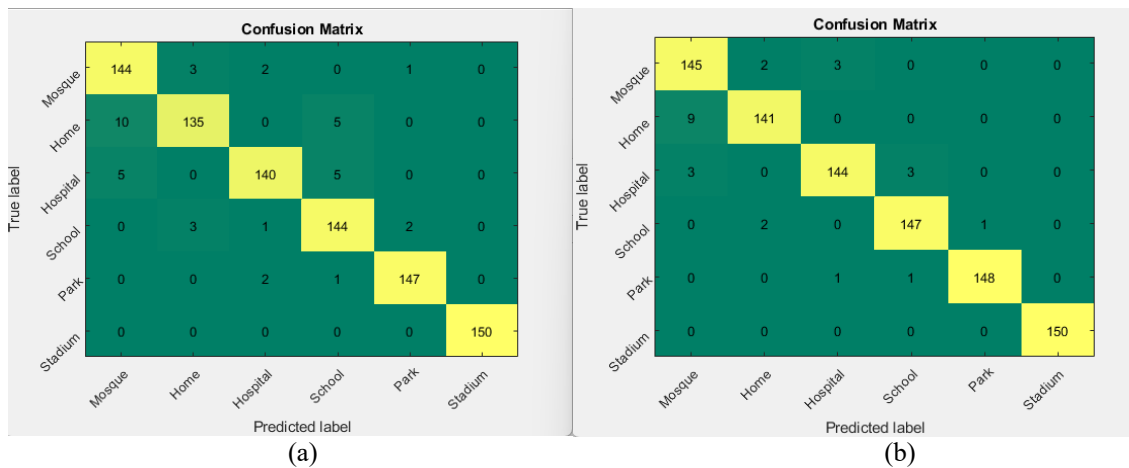


Figure 5. (a) AlexNet-Quadratic SVM confusion matrix without SR (b) AlexNet-Quadratic SVM confusion matrix with SR.

In another application, an accuracy of 92.2% was achieved with the softmax structure of the ResNet50 convolutional neural network architecture. SR was applied to the images in order to increase the correct recognition rate. The new images obtained as a result of the SR algorithm were reclassified. Increasing the resolution of the images increased the correct recognition rate and a 94.1% success rate was achieved. Afterwards, 1000 features

were extracted with ResNet50. Extracted features were given to classifiers such as SVM, KNN, Naive Bayes and Bagged Trees, and the success rates without SR and with SR were observed. All obtained results are given in Table 3 in the form of without SR and with SR. The most successful result was obtained with ResNet50-Cubic SVM a rate of 98.5%. 2.2% increase in performance was achieved by using SR.

Table 3. ResNet50 Results.

Method	Without SR Accuracy Rates	With SR Accuracy Rates
ResNet Softmax	92.2%	94.1%
ResNet-Cubic SVM	96.3%	98.5%
ResNet-Quadratic SVM	96.3%	98.2%
ResNet-Linear SVM	94.4%	96.8%
ResNet-Medium Guassian SVM	95.6%	96.9%
ResNet-Coarse Guassian SVM	85.9%	87.9%
ResNet-Fine KNN	92.2%	96.6%
ResNet-Medium KNN	84.9%	85.0%
ResNet-Coarse KNN	69.8%	72.4%
ResNet-Cosine KNN	85.2%	86.8%
ResNet-Cubic KNN	85.2%	84.6%
ResNet-Weighted KNN	88.6%	89.3%
ResNet-Subspace KNN	92.2%	96.6%
ResNet-Bagged Trees	90.6%	94.7%
ResNet-Kernel Naive Bayes	85.1%	86.7%

Confusion matrix of the ResNet-Cubic SVM method with the best classification success was created. Confusion matrix created as a result of the classification without SR is shown in Figure 6(a) and confusion matrix created as a result of the classification with SR is shown in Figure 6(b).

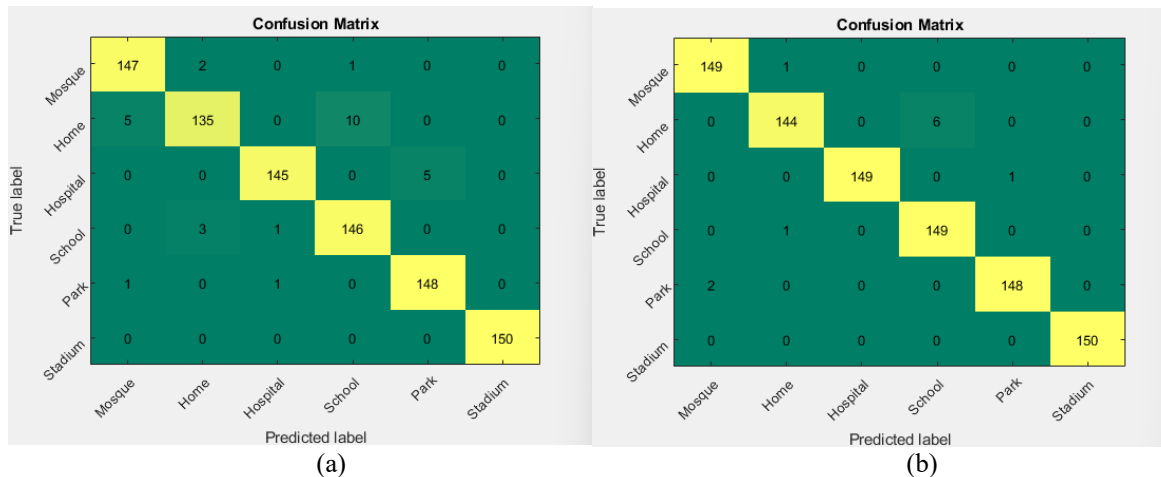


Figure 6. (a) ResNet50- Cubic SVM confusion matrix without SR, (b) ResNet50- Cubic SVM confusion matrix with SR.

In another application, an accuracy of 92.2% was achieved with the softmax structure of the VGG19 convolutional neural network architecture. SR was applied to the images to increase the correct recognition rate. The new images obtained as a result of the SR algorithm were reclassified. Increasing the resolution of the images increased the correct recognition rate and a 95.2% success rate was obtained. Afterwards, 1000 features were extracted with VGG19. Extracted features were given to classifiers such as SVM, KNN, Naive Bayes and Bagged Trees, and the success rates without SR and with SR were observed. All obtained results are given in Table 4 in the form of without SR and with SR. The most successful result was obtained with VGG19-Softmax a rate of 95.2%. 3% increase in performance was achieved by using SR.

Table 4. VGG19 Results.

Method	Without SR Accuracy Rates	With SR Accuracy Rates
VGG19-Softmax	92.2%	95.2%
VGG19-Cubic SVM	91.7%	94.4%
VGG19-Quadratic SVM	91.7%	94.6%
VGG19-Linear SVM	89.4%	91.4%
VGG19-Medium Guassian SVM	90.8%	93.4%
VGG19-Coarse Guassian SVM	80.5%	82.2%
VGG19-Fine KNN	87.6%	91.9%
VGG19-Medium KNN	79.4%	80.9%
VGG19-Coarse KNN	65.4%	68.0%
VGG19-Cosine KNN	78.4%	81.6%
VGG19-Cubic KNN	79.8%	80.4%
VGG19-Weighted KNN	83.5%	87.9%
VGG19-Subspace KNN	87.3%	91.6%
VGG19-Bagged Trees	89.4%	92.2%
VGG19-Kernel Naive Bayes	79.4%	79.2%

Confusion matrix of the VGG19-Softmax method with the best classification success was created. Confusion matrix created as a result of the classification without SR is shown in Figure 7(a) and confusion matrix created as a result of the classification with SR is shown in Figure 7(b).

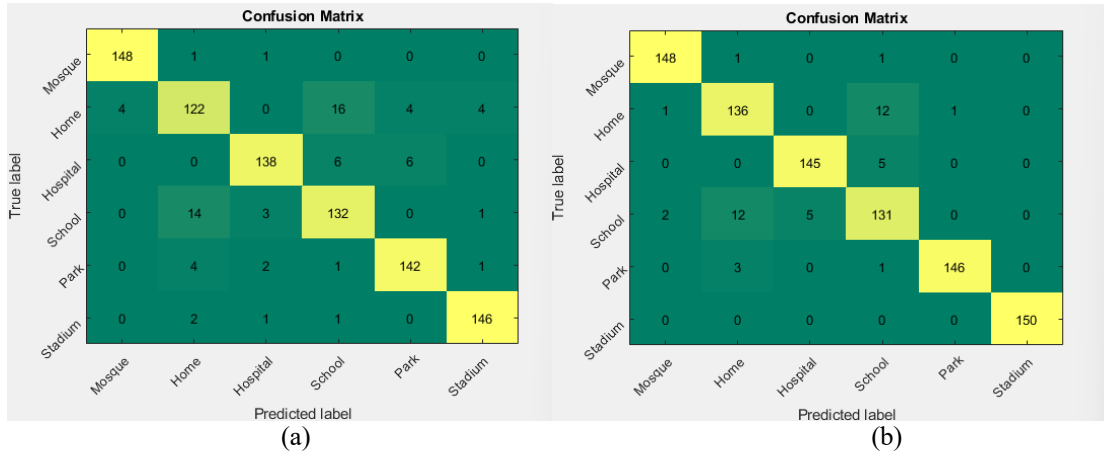


Figure 7. (a) VGG19 confusion matrix without SR, (b) VGG19 confusion matrix with SR.

Table 5 shows the best results of the 3 architectures with and without SR. As a result of the applications, it has been proven that the classification success has been increased for 3 architectures. Classification performance of convolutional neural networks has increased on satellite images with SR algorithm.

Table 5. Comparison of the most successful methods.

Method	Accuracy(%)	Precision(%)	Recall(%)	F1 Score (%)	Test Time (ms)
ResNet50- Cubic SVM without SR	96.34	96.42	96.34	96.38	0.78684
ResNet50- Cubic SVM with SR	98.50	98.48	98.50	98.49	0.82138
AlexNet-Quadratic SVM without SR	95.54	95.57	95.53	95.55	0.50285
AlexNet-Quadratic SVM with SR	97.33	97.35	97.33	97.34	0.42922
VGG19-Softmax without SR	92.23	92.32	92.24	92.28	0.91659
VGG19-Softmax with SR	95.17	95.15	95.17	95.16	0.88269

5. Conclusion

Since the resolution of satellite images is low, the success rate in the classification process is low. In this study, SR method is proposed to increase the classification performance of satellite images. The attributes of satellite images were extracted using ResNet50, Vgg19 from deep learning architecture. Then, extracted features are divided into 6 classes by giving input to AlexNet-Softmax, ResNet50-Softmax, Vgg19-Softmax, SVM, KNN and Naive Bayes classification algorithms. without SR and with SR feature extraction and classification processes were performed separately. Classification results without SR and with SR were compared. Improvement in classification performance was observed using SR.

In this study, it is aimed to apply SR algorithms to satellite images and to increase classification accuracy by classifying images with convolutional neural network architectures. With the comparison of the applications in the study, while the success rate for ResNet50 architecture was 96.3%, it was 98.5% with SR. While the success rate for AlexNet architecture was 95.5%, it was 97.3% with SR. While the success rate for the VGG19 architecture was 92.2%, it was 95.2% with SR. In Table 5, the accuracy rates and test times of the best classifications among the classification architectures applied to the images, and the SR accuracy rates, and SR test times obtained after applying SR to the images are given. The highest accuracy rate was calculated as 97.3% for ResNet50- Cubic SVM. As seen in the applied convolutional neural networks, the accuracy values increased with the SR process. As a result of the applications, it has been proven that the classification success has been increased for 3 architectures. Classification performance of convolutional neural networks has increased on satellite images with SR algorithm.

References

- [1] Dong C, Loy C, He K, Tang X. Image super-resolution using deep convolutional networks. *IEEE Trans Pattern Anal Mach Intell.* 2015; 38(2): 295-307.
- [2] Chen H, He X, Qing L, & Teng Q. Single image super-resolution via adaptive transform-based nonlocal self-similarity modeling and learning-based gradient regularization. *IEEE Trans Multimedia* 2017; 19(8): 1702-1717.
- [3] Chang K, Zhang X, Ding P. L. K, Li B. Data-adaptive low-rank modeling and external gradient prior for single image super-resolution. *J Signal Process Syst* 2019; 161: 36-49.
- [4] Li T, Dong X, Chen H. Single image super-resolution incorporating example-based gradient profile estimation and weighted adaptive p-norm. *Neurocomputing* 2019; 355: 105-120.
- [5] Li J, Guan W. Adaptive lq-norm constrained general nonlocal self-similarity regularizer based sparse representation for single image super-resolution. *Inf Fusion* 2020; 53: 88-102.
- [6] Huang J. J, Liu T, Luigi Dragotti P, Stathaki T. SRHRF+: Self-example enhanced single image super-resolution using hierarchical random forests. In *Proceedings of the IEEE Conference on Computer Vision and Pattern Recognition Workshops; 2017; London.* (pp. 71-79).
- [7] Huang J. B, Singh A, Ahuja N. Single image super-resolution from transformed self-exemplars. In *Proceedings of the IEEE conference on computer vision and pattern recognition; 2015; (pp. 5197-5206).*
- [8] Xiong Z, Xu D, Sun X, Wu F. Example-based super-resolution with soft information and decision. *IEEE Trans Multimedia* 2013; 15(6): 1458-1465.
- [9] Huang J. B, Singh A, Ahuja N. Single image super-resolution from transformed self-exemplars. In *Proceedings of the IEEE conference on computer vision and pattern recognition; 2015; (pp. 5197-5206).*
- [10] Luo J, Sun X, Yiu M. L, Jin L, Peng X. Piecewise linear regression-based single image super-resolution via Hadamard transform. *Inf Sci* 2018; 462: 315-330.
- [11] Zhang Y, Du Y, Ling F, Li X. Improvement of the example-regression-based super-resolution land cover mapping algorithm. *IEEE Geosci Remote Sens Lett* 2015; 12(8): 1740-1744.
- [12] Liu T, De Haan K, Rivenson Y, Wei Z, Zeng X, Zhang Y, Ozcan A. Deep learning-based super-resolution in coherent imaging systems. *Sci Rep* 2019; 9(1): 1-13.
- [13] Jiang J, Wang C, Liu X, Ma J. Deep learning-based face super-resolution: A survey. *ACM Comput Surv* 2021; 55(1): 1-36.
- [14] Lim B, Son S, Kim H, Nah S, Mu Lee K. Enhanced deep residual networks for single image super-resolution. In *Proceedings of the IEEE conference on computer vision and pattern recognition workshops; 2017; (pp. 136-144).*
- [15] Hatvani J, Horváth A, Michetti J, Basarab A, Kouamé D, Gyöngy M. Deep learning-based super-resolution applied to dental computed tomography. *IEEE Trans Radiat Plasma Med Sci* 2018; 3(2): 120-128.
- [16] Singh A, Singh J. Content adaptive single image interpolation based Super Resolution of compressed images. *Int J Electr Comput Syst Eng* 2020; 10(3): 3014-3021.
- [17] Zhou F, Yang W, Liao Q. Interpolation-based image super-resolution using multisurface fitting. *IEEE Trans Image Process* 2012; 21(7): 3312-3318.
- [18] Mahmoudzadeh A. P, Kashou N. H. Interpolation-based super-resolution reconstruction: effects of slice thickness. *J Med Imaging Health Inf* 2014; 1(3): 034007-034007.
- [19] Zhang L, Zhang W, Lu G, Yang P, Rao Z. Feature-level interpolation-based GAN for image super-resolution. *Pers Ubiquitous Comput* 2022; 26(4): 995-1010.
- [20] Gulzar S, Arora S. Optical Flow Video Frame Interpolation Based MRI Super-Resolution. In *Machine Intelligence and Smart Systems; 2022; Springer, Singapore.* (pp. 451-462).
- [21] Alao H, Kim J. S, Kim T. S, Oh J, Lee K. Interpolation based Single-path Sub-pixel Convolution for Super-Resolution Multi-Scale Networks. *Multimedia Syst* 2021; 8(4): 203-210.
- [22] Nazeri K, Thasarathan H, Ebrahimi M. Edge-informed single image super-resolution. In *Proceedings of the IEEE/CVF International Conference on Computer Vision Workshops ; 2019; (pp. 1-10).*
- [23] Zope A, Inamdar V. Edge Enhancement for Image Super-Resolution using Deep Learning Approach. *2nd Global Conference for Advancement in Technology (GCAT); 2021; Bangalore, India.* (pp. 1-4).
- [24] Zhou W, Wang Z, Chen Z. Image super-resolution quality assessment: Structural fidelity versus statistical naturalness. *13th International Conference on Quality of Multimedia Experience (QoMEX); 2021; (pp. 61-64).*
- [25] Jia S, Han B, Kutz J. N. Example-based super-resolution fluorescence microscopy. *Sci Rep* 2018; 8(1): 1-8.
- [26] Robey A, Ganapati V. Optimal physical preprocessing for example-based super-resolution. *Opt Express* 2018; 26(24): 31333-31350.
- [27] Yang Q, Zhang Y, Zhao T. Example-based image super-resolution via blur kernel estimation and variational reconstruction. *Pattern Recognit Lett* 2019; 117: 83-89.
- [28] Glasner D, Bagon S, Irani M. Super-resolution from a single image. *12th international conference on computer vision; 2009; Kyoto.* (pp. 349-356).
- [29] Timofte R, De Smet V, Van Gool L. Anchored neighborhood regression for fast example-based super-resolution. In *Proceedings of the IEEE international conference on computer vision; 2013; Sydney, Australia.* (pp. 1920-1927).
- [30] Gao X, Zhang K, Tao D, Li X. Joint learning for single-image super-resolution via a coupled constraint. *IEEE Trans Image Process* 2011; 21(2): 469-480.

- [31] Cheong J. Y., Park I. K. Deep CNN-based super-resolution using external and internal examples. *IEEE Signal Process Lett* 2017; 24(8): 1252-1256.
- [32] Wang Z, Wang Z, Chang S, Yang J, Huang T. A joint perspective towards image super-resolution: Unifying external-and self-examples. In *IEEE Winter Conference on Applications of Computer Vision* ; 2014; USA. (pp. 596-603).
- [33] Nasrollahi K, Moeslund T. B, Super-resolution: a comprehensive survey. *Mach Vision Appl* 2014; 25(6) :1423-1468.
- [34] Chaudhuri S. Super-resolution imaging. London: Kluwer Academics Publishers, 2001.
- [35] Yang W, Zhang X, Tian Y, Wang W, Xue J. H, Liao Q. Deep learning for single image super-resolution: A brief review. *IEEE Trans Multimedia* 2019; 21(12): 3106-3121.
- [36] Wang Z, Chen J, Hoi S. C. Deep learning for image super-resolution: A survey. *IEEE Trans Pattern Anal Mach Intell* 2020; 43(10): 3365-3387.
- [37] Jiang J, Wang C, Liu X, Ma J. Deep learning-based face super-resolution: A survey. *ACM Comput Surv* 2021; 55(1): 1-36.
- [38] Li Y, Sixou B, Peyrin F. A review of the deep learning methods for medical images super resolution problems. *IRBM* 2021; 42(2): 120-133.
- [39] Coşkun M, Yıldırım Ö, Uçar A, Demir, Y. An overview of popular deep learning methods. *European Journal of Technique* 2017; 7(2): 165-176.
- [40] Dong C, Loy C. C, He K, Tang X. Learning a deep convolutional network for image super-resolution. In *Computer Vision–ECCV 2014: 13th European Conference*; 2014; Zurich. (pp. 184-199).
- [41] Kim J, Lee J. K, Lee K. M. Accurate image super-resolution using very deep convolutional networks. In *Proceedings of the IEEE conference on computer vision and pattern recognition*; 2016; (pp. 1646-1654).
- [42] Goodfellow I, Bengio Y, Courville A. *Deep learning*. London: MIT press, 2016.
- [43] Fu Y, Liang Z, You S. Bidirectional 3d quasi-recurrent neural network for hyperspectral image super-resolution. *IEEE J Sel Top Appl Earth Obs Remote Sens* 2021;14: 2674-2688.
- [44] Chang Y, Luo B. Bidirectional convolutional LSTM neural network for remote sensing image super-resolution. *J Remote Sens* 2019; 11(20): 2333.
- [45] Zhu H, Xie C, Fei Y, Tao H. Attention mechanisms in CNN-based single image super-resolution: A brief review and a new perspective. *Electronics* 2021; 10(10): 1187.
- [46] Fu K, Peng J, Zhang H, Wang X, Jiang F. Image super-resolution based on generative adversarial networks: a brief review. *Comput Mater Continua CMC* 2020; 64(3): 1977-1997.
- [47] Shi W, Caballero J, Huszár F, Totz J, Aitken A. P, Bishop R, Wang Z. Real-time single image and video super-resolution using an efficient sub-pixel convolutional neural network. In *Proceedings of the IEEE conference on computer vision and pattern recognition*; 2016; (pp. 1874-1883).
- [48] Yue Y, Cheng X, Zhang D, Wu Y, Zhao Y, Chen Y, Zhang Y. Deep recursive super resolution network with Laplacian Pyramid for better agricultural pest surveillance and detection. *Comput Electron Agric* 2018;150: 26-32.
- [49] Goyal B, Lepcha D. C, Dogra A, Wang S. H. A weighted least squares optimisation strategy for medical image super resolution via multiscale convolutional neural networks for healthcare applications. *Complex Intell Syst* 2022; 8:3089-3104.
- [50] Zhang H, Wang P, Jiang Z. Nonpairwise-trained cycle convolutional neural network for single remote sensing image super-resolution. *IEEE Trans Geosci Remote Sens* 2020; 59(5): 4250-4261.
- [51] Yang C. Y, Ma C, Yang M. H. Single-image super-resolution: A benchmark. In *Computer Vision–ECCV 2014 13th European Conference*; 2014; Zurich. (pp. 372-386).
- [52] Chen H, He X, Qing L, Wu Y, Re C, Sheriff R. E, Zhu C. Real-world single image super-resolution: A brief review. *Inf Fusion* 2022; 79:124-145.
- [53] Deng X. Enhancing image quality via style transfer for single image super-resolution. *IEEE Signal Process Lett* 2018; 25(4): 571-575.
- [54] Zamzmi G, Rajaraman S, Antani S. Accelerating super-resolution and visual task analysis in medical images. *Adv Nat Appl Sci* 2020; 10(12): 1-16.
- [55] Wagner L, Liebel L, Körner M. Deep Residual Learning For Single-Image Super-Resolution Of Multi-Spectral Satellite Imagery. *SPRS Ann Photogramm Remote Sens Spatial Inf Sci* 2019;4:189-196.
- [56] Kadhim M. A, Abed M. H. Convolutional neural network for satellite image classification. *Int J Intell Inf Database Syst* 2020; 11: 165-178.
- [57] Basu S, Ganguly S, Mukhopadhyay S, DiBiano R, Karki M, Nemani R. DeepSat: a learning framework for satellite imagery. In *Proceedings of the 23rd SIGSPATIAL international conference on advances in geographic information systems*; 2015; USA. (pp. 1-10).
- [58] Albert A, Kaur J, Gonzalez M. C. Using convolutional networks and satellite imagery to identify patterns in urban environments at a large scale. In *Proceedings of the 23rd ACM SIGKDD international conference on knowledge discovery and data mining*; 2017; Canada. (pp. 1357-1366).
- [59] Robinson C, Hohman F, Dilkina B. A deep learning approach for population estimation from satellite imagery. In *Proceedings of the 1st ACM SIGSPATIAL Workshop on Geospatial Humanities*; 2017; USA. (pp. 47-54).
- [60] Unnikrishnan A, Sowmya V, Soman K. P. Deep learning architectures for land cover classification using red and near-infrared satellite images. *Multimedia Tools Appl* 2019; 78: 18379-18394.

- [61] Özbay E, Yıldırım M. Classification of satellite images for ecology management using deep features obtained from convolutional neural network models. *Iran J Comput Sci* 2023; 1-9.
- [62] Chen Z, Guo X, Woo P. Y, Yuan Y. Super-resolution enhanced medical image diagnosis with sample affinity interaction. *IEEE Trans Med Imaging* 2021; 40(5): 1377-1389.
- [63] Wang P, Bayram B, Sertel E. A comprehensive review on deep learning based remote sensing image super-resolution methods. *Earth Sci Rev* 2022; 232:1-25.
- [64] Nguyen N. L, Anger J, Davy A, Arias P, Facciolo G. Self-supervised multi-image super-resolution for push-frame satellite images. In *Proceedings of the IEEE/CVF Conference on Computer Vision and Pattern Recognition*; 2021; USA.(pp. 1121-1131).
- [65] He Z, Li J, Liu L, He D, Xiao M. Multiframe video satellite image super-resolution via attention-based residual learning. *IEEE Trans Geosci Remote Sens* 2021; 60: 1-15.
- [66] Agarwal A, Ratha N, Vatsa M, Singh R. Impact of Super-Resolution and Human Identification in Drone Surveillance. In *2021 IEEE International Workshop on Information Forensics and Security (WIFS)*; 2021; France. (pp. 1-6).
- [67] Toan N. Q. Super-Resolution Method for Reconstructing Street Images from Surveillance System based on Real-ESRGAN. *8th Student Computing Research Symposium*; 2022; Slovenia. (pp.13-16).
- [68] Farooq M, Dailey M. N, Mahmood A, Moonrinta J, Ekpanyapong M. Human face super-resolution on poor quality surveillance video footage. *Neural Comput Appl* 2021; 33(20): 13505-13523.
- [69] Dabbech A, Terris M, Jackson A, Ramatsoku M, Smirnov O. M, Wiaux Y. First AI for deep super-resolution wide-field imaging in radio astronomy: unveiling structure in ESO 137-006. *Astrophys J Lett* 2022; 939(1): 1-22.
- [70] Karwowska K, Wierzbicki D. Using Super-Resolution Algorithms for Small Satellite Imagery: A Systematic Review. *IEEE J Sel Top Appl Earth Obs Remote Sens* 2022; 15: 3292-3312.
- [71] Ndajah P, Kikuchi H, Yukawa M, Watanabe H, Muramatsu S. SSIM image quality metric for denoised images. In *Proc. 3rd WSEAS Int. Conf. on Visualization, Imaging and Simulation*; 2010; (pp. 53-58).
- [72] http://en.wikipedia.org/wiki/Structural_similarity, (Access date: 23.11.2022).
- [73] <http://www.google.com/int/tr/earth>, (Access date: 16.05.2022)

Antimicrobial and Antioxidant Activities of Different Extracts of *Helichrysum arenarium* subsp. (L.) Moench *aucheri*

Ayşe EREN^{1*}, Şule İNCİ², Kochar Khasro SALEH³, Sevda KIRBAĞ⁴, Kemal GÜVEN⁵

^{1,5} Molecular Biology and Genetics Department, Faculty of Science, Dicle University, 21280 Diyarbakır, Turkey

^{2,4} Firat University, Science Faculty, Department of Biology, 23270, Elazığ, Turkey

³ Erbil Polytechnic University, Koya Technical Institute, Department of Community Health, Erbil, Iraq

*¹flow.eren@hotmail.com, ²sule.inci@hotmail.com, ³Kochar.Saleh@epu.edu.iq, ⁴skirbag@firat.edu.tr, ⁵kemalg@dicle.edu.tr

(Geliş/Received: 04/03/2023;

Kabul/Accepted: 10/07/2023)

Abstract: *Helichrysum arenarium* (L.) Moench subsp. *aucheri* is a herbaceous perennial herb belonging to the Asteraceae. This plant has biological activities such as antibacterial, antiviral, anti-inflammatory, antifungal, antiproliferative, antioxidant, and antiradical. In this study, antimicrobial and antioxidant activities of methanol and ethanol extracts of aerial parts of *H. arenarium* subsp. *aucheri* were investigated. To determine the antimicrobial activity pathogenic microorganisms *Escherichia coli*, *Pseudomonas aeruginosa*, *Klebsiella pneumoniae*, *Staphylococcus aureus*, *Bacillus megaterium*, *Candida glabrata*, *Candida albicans* and *Trichophyton* sp. Antioxidant activity was determined with total antioxidant value (TAS), total oxidant value (TOS) and 2,2-diphenyl-1-picrylhydrazil (DPPH) radical scavenging capacity. In the results obtained, it was determined that the methanol extract had an antimicrobial effect (9.3 mm) only against *C. albicans*. It was found that the ethanol extract showed antimicrobial activity at different rates (8.8-20.4 mm) against *S. aureus*, *B. megaterium*, *C. glabrata*, *C. albicans* and *Trichophyton* sp. The TAS value of the methanol extract was 3.00 mmol, and the TAS value of the ethanol extract was 3.15 mmol. The TOS value of the methanol extract of the same species was calculated as 6.81 µmol, and the TOS value of the ethanol extract was calculated as 12.64 µmol. The DPPH radical scavenging effects of extracts of goldengrass was found to increase depend on concentrations.

Key words: *Helichrysum arenarium* subsp. *aucheri*, goldengrass, antimicrobial, antioxidant.

Helichrysum arenarium subsp. (L.) Moench *aucheri*'nin Farklı Ekstraktlarının Antimikrobiyal ve Antioksidan Aktivitesi

Öz: *Helichrysum arenarium* (L.) Moench subsp. *aucheri*, Asteraceae ait otsu çok yıllık bir bitkidir. Bu bitki, antibakteriyel, antiviral, antiinflamatuvar, antifungal, antiproliferatif, antioksidan, antiradikal gibi biyolojik aktivitelere sahiptir. Bu çalışmada, *H. arenarium* subsp. *aucheri*'nin toprak üstü kısımlarının metanol ve etanol ekstraktlarının antimikrobiyal ve antioksidan aktiviteleri araştırılmıştır. Antimikrobiyal aktivitenin belirlenebilmesi için *Escherichia coli*, *Pseudomonas aeruginosa*, *Klebsiella pneumoniae*, *Staphylococcus aureus*, *Bacillus megaterium*, *Candida glabrata*, *Candida albicans*, *Trichophyton* sp. patojenik mikroorganizmalar kullanılmıştır. Antioksidan aktivite toplam antioksidan değeri (TAS), toplam oksidan değeri (TOS) ve 2,2-diphenyl-1-picrilhidrazil (DPPH) radikal süpürme kapasitesi ile belirlenmiştir. Elde edilen sonuçlarda metanol ekstresinin sadece *C. albicans*'a karşı antimikrobiyal etkisinin (9.3 mm) olduğu tespit edilmiştir. Etanol ekstresinin ise *S. aureus*, *B. megaterium*, *C. glabrata*, *C. albicans*, ve *Trichophyton* sp.'ye karşı farklı oranlarda antimikrobiyal etki (8.8-20.4 mm) gösterdiği bulunmuştur. Metanol ekstresinin TAS değeri 3.00 mmol, etanol ekstresinin TAS değeri 3.15 mmol olarak tespit edilmiştir. Aynı türün metanol ekstresinin TOS değeri 6.81 µmol, etanol ekstresinin TOS değeri 12.64 µmol olarak hesaplanmıştır. Altın otun'un ekstrelerinin DPPH radikalini süpürücü etkilerinin artan konsantrasyonlara bağlı olarak arttığı belirlenmiştir.

Anahtar kelimeler: *Helichrysum arenarium* subsp. *aucheri*, Altın otu, antimikrobiyal, antioksidan.

1. Introduction

There are around 600 species of *Helichrysum* in the Asteraceae family. The members of this genus are native to Africa (South Africa has 244 species), Madagascar, Australasia, and Eurasia. The inflorescences of plant species belonging to this genus are usually bright yellow [1,2]. Researchers have reported that some *Helichrysum* species are used in traditional medicine to treat various ailments such as skin infections, gallbladder, respiratory and digestive system disorders, and kidney stones [3-6]. It has also been used in folk medicine for the treatment

* Corresponding author: flow.eren@hotmail.com. ORCID: ¹0000-0002-5601-6808, ²0000-0002-4022-5269, ³0000-0002-5175-8431, ⁴0000-0002-4337-8236, ⁵0000-0002-0181-3746

of urogenital disorders, asthma, jaundice, stomach ailments and various ailments such as diarrhea, gallbladder, arthritis and cystitis [7-9]. It has been used for many years in the cosmetic industry for its fragrance [10]. In Central Europe, this strain is used to make antiseptic medications, while in South Africa, it is used to cure tuberculosis and its symptoms [11-15]. This plant, which grows wild in Anatolia, is used in herbal tea [7]. Recent years, some species have been reported to have antimicrobial and antioxidant effects [16]. The best known and studied species of this genus are *Helichrysum italicum*, *Helichrysum stoechas* and *Helichrysum arenarium* [2]. *Helichrysum arenarium* (L.) Moench subsp. *aucheri* is a species of Asteraceae family, commonly known as 'immortal flower, golden herb or mantuvar' in Turkey [17]. Essential oils, polyphenols, fatty acids, carotenoids, bitter substances, mineral salts, vitamins, steroids, polysaccharides, glycosides, coumarins, and other compounds may be found in *H. arenarium* flowers. It has been approved to contain a high concentration of phenolic compounds [7,10,15,18-20]. It is also known that this species has different medicinal effects antioxidant, hepatoprotective, antibacterial, antiviral, antifungal, anti-inflammatory and antiproliferative [2,21-22]. In particular, it is known that the most important group of compounds responsible for biological effects are phenolics [23]. Recent studies have focused on the essential oils of this species. Because the essential oils obtained are known to have antimicrobial and antioxidant effects. Especially the height at which the plant is collected and which parts of the plant are used are important in terms of evaluating these results [20,24-25]. Volatile compounds such as trans-caryophyllene, α -humulene, α -pinene, dl-limonene, trans-caryophyllene, β -pinene, limonene were detected in *H. arenarium* subsp. *aucheri* [17].

Due to the fact that this species grows naturally in our country, its bioactive components and the fact that it has been little studied in the literature, in this study, it was aimed to evaluate the antimicrobial and antioxidant properties of methanol and ethanol extracts of aerial parts of *H. arenarium* subsp. *aucheri*.

2. Material and Methods

2.1. Obtaining of Plant Material

H. arenarium subsp. *aucheri* samples were collected around the Nemrut crater lake of Bitlis (north-38°37'10"; east-42°14'28"; 2628 m) in August 2020 (Figure 1). Taxonomic description of plant material was carried out by the systematics-botany expert Prof. Dr. Şemsettin Civelek of Firat University using the book Flora of Turkey [26]. The powdered plant material weighed 0.5 g. 100 mL of solvent 96% methanol (MetOH) and ethanol (EtOH) was added to the weighed plant. It was then mixed on a rotary shaker and filtered using Whatman filter paper (pore size 11 μ).



Figure 1. Golden Grass (*H. arenarium* subsp. *aucheri*).

2.2. Extraction Process

The drying process of the plant was carried out in a dark and moisture-free environment. Then 0.5 g of the powdered aerial parts was weighed. 100 mL of 96% methanol (MetOH) and ethanol (EtOH) were added to the weighed plant. It was then stirred on a rotary shaker (Gerhardt RO500/Germany) in a dark environment at room temperature for 72 hours (Shaker speed 60) and filtered using Whatman filter paper. The prepared extracts were stored at +4 °C.

2.3. Analysis Method

In this study; *Escherichia coli* ATCC25922, *Pseudomonas aeruginosa* DMS 50071, *Klebsiella pneumoniae* ATCC700603, *Bacillus megaterium* DSM32, *Staphylococcus aureus* COWAN1, *Candida glabrata* ATCC66032, *Candida albicans* FMC17, *Trichophyton* sp. microorganisms were used. Antimicrobial activities of the extracts of aerial parts of *H. arenarium* subsp. *aucheri* were determined according to the disk diffusion method [27]. Prepared broth cultures yeast (*C. glabrata* and *C. albicans*), dermatophyte fungi (*Trichophyton* sp.) and bacterial (*E. coli*, *P. aeruginosa*, *K. pneumoniae*, *B. megaterium*, *S. aureus*) were cultured on Sabouraud Dextrose Agar, Glucose Sabouraud Buyyon (Difco) and Müller Hinton Agar, respectively inoculated at 1% (10^4 yeast/ml, 10^4 yeast/ml and 10^6 bacteria/ml) and placed in sterile petri dishes. Antimicrobial discs (6 mm diameter), each impregnated with 100 µl (500 µg) of different extracts, were gently transferred on agar medium. Following incubation for 1.5-2 hours at 4°C, the yeast, dermatophyte fungi and bacteria were transferred onto plates and incubated for 72 hours at $25 \pm 0.1^\circ\text{C}$, for 72 hours at $25 \pm 0.1^\circ\text{C}$ and 24 hours at $37 \pm 0.1^\circ\text{C}$, respectively. Nystatin (30 µg/disc) (for yeast) and Streptomycin sulfate (10 µg/disc) (for bacteria) were used as standard disc. The zones (mm) were then measured. Total oxidant and total antioxidant effects of methanol and ethanol extracts of were determined using Rel Assay kits (Rel Assay Kit Diagnostics, Turkey). TOS and TAS values were expressed as µmol H₂O₂ equivalent/L and mmol Trolox equivalent/L, respectively [28-29]. The antioxidant activity was carried out by the 2,2-diphenyl-1-picrylhydrazyl (DPPH) (the absorbances of each mixture were read at 570 nm in the Elisa reader) radical scavenging capacity method [30-31].

2.4. Statistical Analysis

SPSS Statistics (version 22) was used to perform the statistical analysis and generate the figures. Analysis of variance (ANOVA) and Student's t-test were performed, and $p < 0.01$ was considered significant.

3. Result and Discussion

3.1. Antimicrobial Effect

The antimicrobial effect of the methanol and ethanol extracts of the plant is as seen in Table 1.

Table 1. Results of the disk diffusion method of plant extracts against the tested microorganisms (Inhibition zones measured in mm).

Microorganisms	Methanol	Ethanol	Standard antibiotics
<i>S. aureus</i>	-	9.6± 0.7	19.5± 0.11
<i>E. coli</i>	-	-	19.8± 0.15
<i>K. pneumoniae</i>	-	-	17.5± 0.13
<i>B. megaterium</i>	-	20.4 ± 0.2	21.6± 0.13
<i>P. aeruginosa</i>	-	-	20.5± 0.19
<i>C. glabrata</i>	-	9.5± 0.9	21.5± 0.16
<i>C. albicans</i>	9.3± 0.13	8.8± 0.15	23.7± 0.17
<i>Trichophyton</i> sp.	-	13.8± 0.8	22.8± 0.18

No significant differences were found in the means with the '-' symbol in the same column ($p > 0.01$)

MetOH extract of plant created 9.3 mm zone of inhibition against *C. albicans*. EtOH extract of *H. arenarium* subsp. *aucheri* showed inhibition zone on *B. megaterium*, *S. aureus*, *C. glabrata*, *C. albicans*, *Trichophyton* sp. (8.8-20.4 mm), but it did not show inhibition zone against *K. pneumoniae*, *E. coli*, *P. aeruginosa* (Table 1). The comparison of the ethanol and methanol extracts of *H. arenarium* subsp. *aucheri* in terms of antimicrobial activity against *B. megaterium* showed that the ethanol extract was the most effective (20.4 mm) (Table 1). Lourens et al. [32] showed that the antibacterial antimicrobial effects of *Helichrysum excisum* and *Helichrysum dasyanthum* acetone extracts against *S. aureus* were 312.5 and 15.63 µg/mL, respectively. Furthermore, minimum inhibitory concentration (MIC) results on tested bacteria treated with *Helichrysum* extract revealed that *S. aureus* was more susceptible than *Streptococcus pneumoniae* as 0.62 and 1.25 mg/mL, respectively [11]. The antimicrobial effects of *H. arenarium* L. essential oil against *S. aureus*, *E. coli*, *Bacillus subtilis*, *Saccharomyces cerevisiae*, *C. albicans*, *Aspergillus parasiticus* and *Aspergillus flavus* were investigated. As a result, *B. subtilis* was found to be more

resistant than the other two bacterial species (MIC=781.25 and MBC=6250 µg/ml). Among the tested yeasts the sensitive of *S. cerevisiae* (MIC=97.65 and MFC=781.25 µg/ml) was more sensitive than *C. albicans* [12].

Bigović et al. [33] reported that the antimicrobial effects of *H. plicatum* ethanol extracts against various microorganisms including *B. subtilis*, *E. coli*, *Listeria monocytogenes*, *Micrococcus flavus*, *Micrococcus luteus*, *Proteus mirabilis*, *P. aeruginosa*, *Salmonella typhimurium*, *Salmonella enteritidis* and *S. aureus* were between (0.01 and 0.055 mg/mL). In a previous study, by using the methanol and water extracts of *H. foetidum*, the MIC values were higher than 4 mg/ml against the test bacteria such as *E. coli*, *P. aeruginosa*, *S. aureus* and *Streptococcus pyogenes* [34]. There have been more studies using different *Helichrysum* species for their antimicrobial effects, particularly of methanol extracts against a wide variety of test microorganisms (*Bacillus brevis*, *Aeromonas hydrophila*, *B. cereus*, *P. aeruginosa*, *E. coli*, *K. pneumoniae*, *C. albicans* and *S. aureus*). Inhibition zones ranged from 6.5 mm to 28 mm, but no activity was detected against *E. coli* [35]. A recent study by Babotă et al. [16] showed that both *S. aureus* and *E. coli* were similarly affected by ethanolic extracts of *H. arenarium*, with a MIC value of 7.81 mg/mL. On the other hand, *H. arenarium* ethanol extract at concentrations of 20 and 50 mg/mL caused an inhibitory effect on *S. aureus* as zones of 25 mm and 28 mm, respectively [14].

Bozyel et al. [36] Most recently reported that *H. arenarium* spp. *aucheri* ethanol extract as 50 µL presented an antimicrobial activity with inhibition against *C. albicans* (10 mm), *K. pneumoniae* (7 mm), *S. aureus* (15 mm), while antimicrobial activity by 100 µL of ethanol extract of the same species was against *P. aeruginosa* was found to be $12 \pm 0,71$ mm. Noori et al. [37] A chemical analysis of the essential oil of *H. arenarium* L. found a total of 38 components. A-pinene, 1,8-cineole, α -humulene, and α -caryophyllene were the main components of essential oil. Less than 29% of the oil was made up of the other separated components. The antimicrobial effect of *Helichrysum arenarium* L. essential oil was found against *Streptococcus agalactiae*, *S. aureus* and *Serratiamarcescens* with MIC rate of ml respectively (812 ,812 and 406 µg). Djihane et al. [38] The essential oil of *H. italicum* (Roth) G. Don has been found to have antimicrobial activity against various microorganisms (*S. aureus*, *E. coli*, *Micrococcus luteus*, *Enterococcus cereus*, *K. pneumonia*, *Bacillus cereus*, *B. subtilis*, *Staphylococcus epidermidis*, *Enterococcus faecalis*, *P. aeruginosa*, *Proteus mirabilis*, *Listeria monocytogenes* and yeasts *C. albicans*, *Saccharomyces cerevisiae*, *Fusarium solani* var. *coeruleum*, *Alternaria alternata*, *Aspergillus niger*, *Ascochyta rabi*). *H. italicum* inhibited the growth of all microorganisms tested except *E. coli*, *K. pneumonia* and *L.monocytogenes*. The most sensitive bacterium is *E. cereus* with bactericidal (MBC) and minimal inhibitory (MIC) value of $0.79 \mu\text{g ml}^{-1}$. Vujic et al. [39], reported that different (ethanol, dichloromethane and acetonitrile oil) extracts of *H. plicatum* have antimicrobial effects against three Gram-positive bacteria (*B. subtilis*, *S. aureus*, *Clostridium sporogenes*) and five Gram-negative bacteria (*P. aeruginosa*, *E. coli*, *K. pneumoniae*, *Salmonella enterica* subsp. *enterica*, *Proteus hauseri*) two yeasts (*S. cerevisiae*, *C. albicans*), and *Aspergillus brasiliensis*. All extracts (ethanol, dichloromethane and acetonitrile oil) were found to have significant antibacterial activity at concentrations of 0.157-2.5 mg/mL. Zheljzkov et al. [24] It was determined the antimicrobial effect of *H. italicum* EO against nine microorganisms by using the disk diffusion method. Microorganisms antimicrobial activity was found to range of 2.33-14.67 mm. The EO of *H. italicum* against *S. aureus* was found to be 9.33 to 14.67 mm. Duran et al. [40] The antimicrobial effect results showed that *H. plicatum* extracts had stronger antibacterial activity against *Salmonella enteritidis* (24.13 ± 1.15 and $156 \mu\text{g/mL}$) among gram-negative bacteria. Additionally, it was found to have inhibitory activities for *B. cereus* (16.66 ± 1.52 and $312 \mu\text{g/mL}$).

The comparisons of results obtained from different studies in the literature clearly show the differences depending on the species and microorganisms tested. The reason for that is most likely to be due to the bioactive contents of the plants, the place of collection, the solvent used and the extraction methods used.

3.2. Antioxidant Effect

The TAS value of the MeOH extract of the plant at 1mg/mL concentration was calculated as 3.00 mmol, and TAS value of the EtOH extract was calculated as 3.15 mmol. The TOS value of the MeOH extract of the same species was calculated as 6.81 µmol, and the TOS value of the EtOH extract was calculated as 12.64 µmol (Table 2).

Table 2. TAS and TOS values of *H. arenarium* subsp. *aucheri*.

	TAS (mmol Trolox equiv./L)	TOS (µmol H ₂ O ₂ equiv./L)
<i>H. arenarium</i> subsp. <i>aucheri</i> -MetOH	3.00± 0.11	6.81± 0.9
<i>H. arenarium</i> subsp. <i>aucheri</i> -EtOH	3.15± 0.17	12.64± 0.16

Table 3. Percent inhibition of the DPPH radical of *H. arenarium* subsp. *aucheri*.

Concentrations	<i>H.arenarium</i> subsp. <i>aucheri</i> -MetOH	<i>H.arenarium</i> subsp. <i>aucheri</i> -EtOH
1000 µg/mL	34.55± 0.17	34.45± 0.19
500 µg/mL	29.48± 0.21	26.22± 0.23
250 µg/mL	17.58± 0.27	17.32± 0.32
125 µg/mL	10.05± 0.11	12.35± 0.14

It has been determined that the scavenging effects of DPPH radicals of MetOH and EtOH extracts of *plant* increased with increasing concentrations (Table 3). The antioxidant levels of various plant members have been studied extensively in the literature. Antioxidant level of *H. chasmolyticum* aerial parts followed by methanol extract was measured as IC₅₀ 0.92 mg/mL by using DPPH method [5]. Moreover, Albayrak et al. [35], investigated antioxidant properties of four different subspecies belong to *H. arenarium* which were subsp. *erzincanicum*, *rubicundum*, *araxinum* and *pseudoplicatum* evaluated by DPPH IC₅₀ (µg/mL) values as 23.03 µg/mL, 47.64 µg/mL, 27.32 µg/mL and 38.82 µg/mL, respectively. The antioxidant activities of the extracts of *Helichrysum* species including *H. chionophilum*, *H. chasmolyticum*, *H. arenarium* subsp. *aucheri* and *H. plicatum* subsp. *plicatum* were also reported where the IC₅₀ values were found as 40.5 µg/mL, 246.83 ± 1.23 mg AAE/g, 47.6 and 48.0 µg/mL, respectively [41,42]. The DPPH radical scavenging effects of *H. arenarium* methanol and ethanol extracts were 4.91 ± 1.90 and 7.21 ± 2.81 mg TE/mL, respectively. In the same study, it is emphasized that the antioxidant effect of *H. arenarium* may be related to the phenolic compounds it contains [16]. Further research has also shown that aqueous alcoholic extracts of *H. italicum* have high antioxidant properties, so that different extracts (MeOH, EtOH, 60% EtOH and 70% MeOH) of *H. italicum* led to the TEAC values of 73.18 ± 3.51, 58.35 ± 5.25, 132.38 ± 1.15 and 144.36 ± 7.01 mM TE/g DW, respectively. On the other hand, the ethyl acetate extract caused low antioxidant activity of 24.58 ± 2.00 mM TE/g DW [43]. More recently, antioxidant properties of various species including *Helichrysum pandurifolium*, *Helichrysum foetidum*, *Helichrysum petiolare* and *Helichrysum cymocum* have been studied. The IC₅₀ values of the radical scavenging activity for all plants studied ranged from 20.81-36.19 µg/mL (NO), 11.85-41.13 µg/mL (DPPH) and 0.505-0.636 µg/mL (FRAP). Among all these, *H. petiolare* had highest total phenolic content (54.69 ± 0.23 mg/g), highest total flavonoid content (56.19 ± 1.01 mg/g) and thus the highest total antioxidant capacity (48.50 ± 1.55 mg/g), in comparison to other species studied [44]. Kherbache et al. [45] found that the radical scavenging activity of the ethyl acetate extract (IC₅₀ = 54.82 ± 1.50 µg/mL) of *Helichrysum stoechas* was significantly higher than that of the butanolic extract (IC₅₀ = 83.66 ± 1.02 µg/mL). Stankov et al. [46] determined that the total polyphenol and flavonoid contents in the ethanol extract of *Helichrysum arenarium* varied. They reported that the antioxidant effect of ethanol extract is related to these components. A more recent study on Sandy everlasting extracts of *H. italicum* (Roth) and *H. arenarium* (L.) Moench showed that these plants possessed significantly higher radical scavenging activities (for inflorescences from 1.96 to 6.13 mmol/L and for leaves ranged from 11.18 to 19.13 TROLOX equivalent) revealed by comparison to those of all tested EOs (0.25 to 0.46 mmol/L TROLOX equivalent) [20].

The results of the present study compared with those obtained in the literature in terms of antioxidant properties of different plant extracts clearly showed that, there is a large variability, depending on the plant collection site, the plant species, plant parts, its biochemical contents, methods, solvents and concentrations used.

4. Conclusion

In this study, antimicrobial and antioxidant effects of aerial parts of *H.arenarium* subsp. *aucheri* extracts on some tested microorganisms were investigated. The EtOH extract of *H. arenarium* subsp. *aucheri* showed the best antimicrobial effect against *B. megaterium*. Moreover, the total antioxidant level of the ethanol extract of the same species was also high, but differently the total oxidant level of the ethanol extract was interestingly found high. These differences might be due to the presence or absence of oxidant/antioxidant compounds produced by the plant in sufficient amounts depending on the solvent. It is clear that the biological effects of *H. arenarium* subsp. *aucheri* determined in this study may well be important and thus need further study.

References

- [1] Perrini R, Morone-Fortunato I, Lorusso E, Avato P. Essential oils and in vitro establishment of *Helichrysum italicum* (Roth) G. Don ssp. *Microphyllum* (Willd.). Nyman. *Ind Crops Prod* 2009; 29: 395-403.
- [2] Akaberi M, Sahebkar A, Azizi N, Emami SA. Everlasting flowers: Phytochemistry and pharmacology of the genus *Helichrysum*. *Ind Crops Prod* 2019; 138, 111471.
- [3] Lourens ACU, Viljoen AM, Van Heerden FR. South African *Helichrysum* species: a review of the traditional uses, biological activity and phytochemistry. *J Ethnopharmacol* 2008; 119(3): 630-652.
- [4] Lourens ACU, Van Vuuren SF, Viljoen AM, Davids H, Van Heerden FR. Antimicrobial activity and in vitro cytotoxicity of selected South African *Helichrysum* species. *S Afr J Bot* 2011; 77(1): 229-235.
- [5] Süzgeç-Selçuk S, Birteksöz AS. Flavonoids of *Helichrysum chasmolyticum* and its antioxidant and antimicrobial activities. *S Afr J Bot* 2011; 77(1): 170-174.
- [6] Tirillini B, Menghini L, Leporini L, Scanu N, Marino S, Pintore G. Antioxidant activity of methanol extract of *Helichrysum foetidum* Moench. *Nat Prod Res* 2013; 27(16): 1484-1487.
- [7] Eroglu HE, Hamzaoglu E, Aksoy A, Budak U, Albayrak S. Cytogenetic effects of *Helichrysum arenarium* in human lymphocytes cultures. *Turk J Biol* 2010; 34: 253-259.
- [8] Radušienė J and Judžentienė A. Volatile composition of *Helichrysum arenarium* field accessions with differently coloured inflorescences. *Biologija* 2008; 54(2): 116-120.
- [9] Sani AM. Inhibitory Effect of *Helichrysum arenarium* essential oil on the growth of food contaminated microorganisms. *Int J Agric Biol Eng* 2014; 8(8): 839-843.
- [10] Liu X, Jing X. and Li GA. process to acquire essential oil by distillation concatenated Liquid-liquid extraction and flavonoids by solid-liquid extraction simultaneously from *Helichrysum arenarium* (L.) Moench inflorescences under ionic liquid-microwave mediated. *Sep Purif Technol* 2019; 209: 164-174.
- [11] Gradinaru AC, Silio, M, Trifan A, Miron A, Aprotosoae AC. *Helichrysum arenarium* subsp. *arenarium*: phenolic composition and antibacterial activity against lower respiratory tract pathogens. *Nat Prod Res* 2014; 28(22): 2076-2080.
- [12] Moghadam HD, Sani AM, Sangatash MM. Inhibitory effect of *Helichrysum arenarium* essential oil on the growth of food contaminated microorganisms. *J Essent Oil Bear Pl* 2014; 17(5): 911-921.
- [13] Reidel RVB, Cioni PL, Ruffoni B, Cervelli C, Pistelli L. Aroma profile and essential oil composition of *Helichrysum* Species. *Nat Prod Commun* 2017; 12(9): 1507-1512.
- [14] Akin M and Saki N. Antimicrobial, DPPH Scavenging and Tyrosinase Inhibitory activities of *Thymus vulgaris*, *Helichrysum arenarium* and *Rosa damascena* Mill. Ethanol Extracts by using TLC Bioautography and Chemical Screening Methods. *J Liq Chromatogr Relat Technol* 2019; 42: 204-216.
- [15] Umaz A and Umaz K. Determination and comparison of volatile compounds of gold grass (*Helichrysum arenarium*) from two different locations. *GUFBD* 2020; 10(3): 592-600.
- [16] Babotă M, Mocan A, Vlase L, Crișan O, Ielciu I, Gheldiu AM, Păltinean R. Phytochemical analysis, antioxidant and antimicrobial activities of *Helichrysum arenarium* (L.) Moench. and *Antennaria dioica* (L.) Gaertn. flowers. *Molecules* 2018; 23(2): 409.
- [17] Tıǧlı Kaytanlıoǧlu EHT, Özderin S, Fakir H, Gümüșay E. Determination of volatile components of *Helichrysum arenarium* subsp. *aucheri* naturally distributed in two different regions. *EJOSAT* 2021; (25): 152-158.
- [18] Rančić A, Soković M, Vukojević J, Simić A, Marin P, Duletić-Laušević S, et al. Chemical composition and antimicrobial activities of essential oils of *Myrrhis odorata* (L.) scop, *Hypericum perforatum* L and *Helichrysum arenarium* (L.) Moench. *J Essent Oil Res* 2005; 17(3): 341-345.
- [19] Jarzycka A, Lewińska A, Gancarz R, Wilk KA. Assessment of extracts of *Helichrysum arenarium*, *crataegus monogyna*, *sambucus nigra* in photoprotective uva and uvb; photostability in cosmetic emulsions. *J Photochem Photobiol B* 2013; 128: 50-57.
- [20] Judzentiene A, Budiene J, Nedveckyte I, Garjonyte R. Antioxidant and toxic activity of *Helichrysum arenarium* (L.) Moench and *Helichrysum italicum* (Roth) G. Don essential oils and extracts. *Molecules* 2022; 27(4): 1311.
- [21] Tagliatalata-Scafati O, Pollastro F, Chianese G, Minassi A, Gibbons S, Arunotayanun W, et al. Antimicrobial phenolics and unusual glycerides from *Helichrysum italicum* subsp. *Microphyllum*. *J Nat Prod* 2013; 76: 346-353.

- [22] Mao Z, Gan C, Zhu J, Ma N, Wu L, Wang L, et al. Anti-atherosclerotic activities of flavonoids from the flowers of *Helichrysum arenarium* L. Moench through the pathway of anti-inflammation. *Bioorg Med Chem Lett* 2017; 27: 2812-2817.
- [23] Pljevljakušić D, Bigović D, Janković T, Jelačić S, Šavikin K. Sandy everlasting (*Helichrysum arenarium* (L.) Moench): botanical, chemical and biological properties. *Front. Plant Sci* 2018; 9: 1123.
- [24] Zheljzakov VD, Semerdjieva I, Yankova-Tsvetkova E, Astatkie T, Stanev S, Dincheva I, et al. Chemical profile and antimicrobial activity of the essential oils of *Helichrysum arenarium* (L.) Moench. and *Helichrysum italicum* (Roth.) G. Don. *Plants* 2022; 11(7): 951.
- [25] Węglarz Z, Kosakowska O, Pióro-Jabrucka E, Przybył JL, Gniewosz M, Kraśniewska K, et al. Antioxidant and antibacterial activity of *Helichrysum italicum* (Roth.) G. Don. from central Europe. *Pharmaceutics* 2022; 15(6): 735.
- [26] Davis PH. *Flora of Turkey and the Aegean Islands*. V: 7, 8, 9 Edinburgh Univ. Press. 1970-1984-1985; England.
- [27] Collins CH, Lyne P M. *Microbiological methods butter worths & Co. (Publishers) Ltd*. pp. 410, 1989; London.
- [28] Erel OA. new automated colorimetric method for measuring total oxidant status. *Clin Biochem* 2005; 38:1103-1111.
- [29] Erel O. A novel automated direct measurement method for total antioxidant capacity using a new generation, more stable ABTS radical cation. *Clin Biochem* 2004; 37: 277-285.
- [30] Cuendet M, Hostettmann K, Potterat O, Dyatmiko W. Iridoid glucosides with free radical scavenging properties from *Fagraea blumei*. *Helv Chim Acta* 1997; 80(4): 1144-1152.
- [31] Kirby, AJ and Schmidt, RJ. The antioxidant activity of Chinese herbs for eczema and of placebo herbs. I. *J Ethnopharmacol* 1997; 56(2): 103-8.
- [32] Lourens ACU, Reddy D, Baser KHC, Viljoen AM, Van Vuuren SF. In vitro Biological activity and essential oil composition of four indigenous South African *Helichrysum* species. *J Ethnopharmacol* 2004; 95:253-258.
- [33] Bigović DJ, Stević TR, Janković TR, Noveski NB, Radanović DS, Pljevljakušić, DS. and Djurić ZR. Antimicrobial activity of *Helichrysum plicatum* DC. *Hemijska industrija* 2017; 71(4): 337-342.
- [34] Steenkamp V, Mathivha E, Gouws MC and van Rensburg CEJ. Studies on antibacterial, antioxidant and fibroblast growth stimulation of wound healing remedies from South Africa. *J Ethnopharmacol* 2004; 95: 353-357.
- [35] Albayrak S, Aksoy A, Sagdic O, Budak U. Phenolic compounds and antioxidant and antimicrobial properties of *Helichrysum* species collected from eastern Anatolia, Turkey. *Turk J Biol* 2010; 34: 463-473.
- [36] Bozyel ME, Canli K, Benek A, Yetgin A, Altuner EM. Biochemical composition and in vitro antimicrobial activity of endemic *Helichrysum arenarium* ssp. *aucheri* ethanol extract. *Fresenius Environ Bull* 2021; 869.
- [37] Noori M, Poodineh M, Hakimzadeh V. Composition of *Helichrysum arenarium* essential oil and antimicrobial activity against some food-born pathogens. *Biotechnol Ind J* 2015; 11: 121-125.
- [38] Djilane B, Wafa N, Elkhamssa S, Pedro HJ, Maria AE, Mohamed Mihoub Z. Chemical constituents of *Helichrysum italicum* (Roth) G. Don essential oil and their antimicrobial activity against Gram-positive and Gram-negative bacteria, filamentous fungi and *Candida albicans*. *Saudi Pharm J* 2017; 25: 780-787.
- [39] Vujčić B, Vidaković V, Jadranić M, Novaković I, Trifunović S, Tešević V, et al. Composition, antioxidant potential, and antimicrobial activity of *Helichrysum plicatum* DC. various extracts. *Plants* 2020; 9(3): 337.
- [40] Duran F, Kılıç DD, Tanrikulu Gİ, Keskiner AA, Baskan C, Siriken B. In vitro study on antimicrobial and cytotoxic activity of methanol extract of *Helichrysum plicatum* subsp. *polyphyllum* (Asteraceae). *SSHS* 2023; 5(1): 22-33.
- [41] Özkan G, Sağdıç O, Özçelik H. Some Turkish endemic herb extracts as antimicrobial and antioxidant agents. 4th International Congress on Environmental Micropaleontology, Microbiology and Meiobenthology, 2004; 13-18 September, İsparta, Turkey, 151-154.
- [42] Tepe B, Sokmen M, Akpulat HA. In vitro antioxidant activities of the methanol extracts of four *Helichrysum* species from Turkey. *Food Chem* 2005; 90: 685-689.
- [43] Bojilov DG, Manolov SP, Ivanov II and Mollova SL. Investigation of antioxidant activity of different extracts of antioxidant activity of different extracts of *Helichrysum italicum* from Bulgaria. *Materials, Methods & Technologies* 2019; (13): 241-249.
- [44] Akinyede KA, Hughes GD, Ekpo OE, Oguntibeju OO. Comparative study of the antioxidant constituents, activities and the gc-ms quantification and identification of fatty acids of four selected *Helichrysum* Species. *Plants* 2022; 11(8): 998.
- [45] Kherbache A, Senator A, Laouicha S, Al-Zoubi RM, Bouriche H. Phytochemical analysis, antioxidant and anti-inflammatory activities of *Helichrysum stoechas* (L.) Moench extracts. *Biocatal Agric Biotechnol* 2020; 29: 101826.
- [46] Stankov S, Fidan H, Petkova N, Stoyanova A, Dincheva I, Doğan H, et al. Phytochemical composition of *Helichrysum arenarium* (L.) Moench essential oil (aerial parts) from Turkey. *Ukrainian Food Journal* 2020; 9(3).

Using MATLAB Statistics Toolbox for Data Analysis in Social Sciences with Chat GPT-3 prompts

Dönüş ŞENGÜR*

Measurements and Evaluation Department, Education Faculty, Firat University, Elazig, Turkey

* dsengur@firat.edu.tr

(Geliş/Received: 24/05/2023;

Kabul/Accepted: 15/08/2023)

Abstract: This paper explores the potential usage of ChatGPT-3, a powerful language model developed by OpenAI, within the MATLAB Statistical Toolbox (ST) for social science research. ChatGPT-3 is a highly advanced model that has shown remarkable performance in a wide range of natural language processing tasks. However, its usage in social science research is still relatively new and has not been widely explored. The main advantage of using ChatGPT-3 in social science research is its ability to process large amounts of unstructured text data, which is becoming increasingly prevalent in social science research. However, there are also some potential disadvantages to using ChatGPT-3, such as its complexity, lack of interpretability, and proprietary nature. This paper aims to provide an overview of the current state of ChatGPT-3 usage in social science research and to discuss the potential advantages and disadvantages of using this model within MATLAB ST. This paper, it is aimed to show how ChatGPT-3 can assist social science researchers in MATLAB ST in the processing of their datasets. Because data analysis can be challenging for social science researchers for several reasons as social science data can often be complex, with multiple variables and multiple levels of analysis. This can make it difficult to analyze and interpret the data in a meaningful way. Therefore, some sample hints, where ChatGPT-3 prompts are used to handle such statistical operations in MATLAB ST, are provided. The comments that ChatGPT-3 gives out are analyzed. It is believed that ChatGPT-3 will be a good assistant for social science researchers in MATLAB ST.

Keywords: ChatGPT-3, MATLAB ST in social science, data analysis, Artificial intelligence.

ChatGPT-3 Sorguları ile Sosyal Bilimlerde Veri Analizi için MATLAB İstatistik Araç Kutusu Kullanımı

Öz: Bu makale, OpenAI tarafından geliştirilen güçlü bir dil modeli olan ChatGPT-3'ün sosyal bilim araştırmaları için MATLAB İstatistik Araç Kutusu (İAK) içindeki potansiyel kullanımını araştırmaktadır. ChatGPT-3, çok çeşitli doğal dil işleme görevlerinde dikkate değer performans gösteren oldukça gelişmiş bir modeldir. Bununla birlikte, sosyal bilim araştırmalarında kullanımı hala nispeten yenidir ve geniş çapta araştırılmamıştır. ChatGPT-3'ü sosyal bilim araştırmalarında kullanmanın temel avantajı, sosyal bilim araştırmalarında giderek yaygınlaşan büyük miktarlarda yapılandırılmamış metin verilerini işleyebilmesidir. Ancak, ChatGPT-3'ü kullanmanın karmaşıklığı, yorumlanamazlığı ve tescilli doğası gibi bazı potansiyel dezavantajları da vardır. Bu makale, sosyal bilim araştırmalarında ChatGPT-3 kullanımının mevcut durumuna genel bir bakış sunmayı ve bu modeli MATLAB İAK içinde kullanmanın potansiyel avantajlarını ve dezavantajlarını tartışmayı amaçlamaktadır. Bu yazıda, ChatGPT-3'ün sosyal bilim araştırmacılarına MATLAB İAK 'da veri kümelerini işlemelerinde nasıl yardımcı olabileceğinin gösterilmesi amaçlanmaktadır. Çünkü veri analizi, sosyal bilim araştırmacıları için, sosyal bilim verilerinin çoğu zaman birden çok değişken ve birden çok analiz düzeyi ile karmaşık olabilmesi gibi çeşitli nedenlerle zorlayıcı olabilir. Bu, verilerin anlamlı bir şekilde analiz edilmesini ve yorumlanmasını zorlaştırabilir. Bu nedenle, MATLAB İAK 'da bu tür istatistiksel işlemleri işlemek için ChatGPT-3 istemlerinin kullanıldığı bazı örnek ipuçları sağlanmaktadır. ChatGPT-3'ün verdiği yorumlar analiz edilir. ChatGPT-3'ün MATLAB İAK 'da sosyal bilim araştırmacıları için iyi bir yardımcı olacağına inanılmaktadır.

Anahtar kelimeler: ChatGPT-3, sosyal bilimlerde MATLAB İAK, veri analizi, Yapay zeka.

1. Introduction

Statistical Package for the Social Sciences (SPSS) is a popular software for data analysis in the social sciences. SPSS provides a wide range of statistical tools and techniques for analyzing and interpreting data. SPSS performs complex statistical analyses, including regression, factor analysis, and analysis of variance (ANOVA). It also has a range of visualization tools, including histograms, scatterplots, and box plots, which can be used to display and interpret data. However, it is worth noting that SPSS is not the only software available for data analysis in the social sciences. Other popular options include MATLAB, SAS, Stata, and R, each of which has its unique features and capabilities.

* Corresponding author: dsengur@firat.edu.tr. ORCID Number of authors: 0000-0002-8786-6557

The statistical toolbox (ST) in MATLAB is a powerful tool for analyzing and interpreting data in the social sciences. This toolbox contains a wide range of functions for statistical analysis, including regression, hypothesis testing, and ANOVA. One of the primary benefits of using the statistical toolbox in MATLAB for social science research is its ability to handle large datasets. This is particularly important in the social sciences, where data sets can often be quite large and complex. The statistical toolbox in MATLAB allows users to quickly and easily analyze large datasets, making it an efficient and effective tool for data analysis in the social sciences [1]. In addition to its ability to handle large datasets, the statistical toolbox in MATLAB also has several advanced features that make it well-suited for use in the social sciences. For example, it has functions for modeling complex relationships between variables, such as nonlinear regression and multivariate analysis. It also has functions for analyzing categorical data, such as chi-square tests and logistic regression. One of the most widely used functions in the ST in MATLAB is the regression function. This function allows users to fit a model to their data, allowing them to make predictions about future outcomes based on the relationships between variables. This is an important tool for social scientists, as it allows them to test hypotheses about the relationships between variables and to understand how different variables are related to one another.

Up to now, MATLAB ST was widely used in the social sciences and has been applied in a variety of research studies. For example, a study by [2] used the toolbox to analyze data from a survey of attitudes toward climate change. They found that the toolbox was able to handle the large data set and that the results of the analysis were meaningful. Similarly, a study by [3] used the toolbox to analyze data from an observational study of child development. They found that the toolbox was able to handle the complex data structure and that the results of the analysis were meaningful. MATLAB was used in advanced statistical analyses such as Bayesian statistics, hidden Markov models, and Monte Carlo simulations [4]. These advanced statistical techniques are not easily available in other statistical software packages, making MATLAB a powerful tool for researchers who require these specific capabilities. MATLAB was used to provide a wide range of visualization tools, including 2D and 3D plots, histograms, and heat maps, which enable researchers to easily explore and understand their data. Furthermore, the ability to create custom plots and visualizations using MATLAB's programming language allows for a high degree of flexibility in data visualization [4]. In the field of survey research, MATLAB can be used to analyze survey data and to conduct statistical analyses such as factor analysis, cluster analysis, and structural equation modeling (SEM) [1,10]. In the field of psychology, MATLAB can be used to analyze behavioral data and to conduct statistical analyses such as mixed-design ANOVA, multiple regression, and logistic regression [5]. In the field of economics, MATLAB can be used to analyze financial data and to conduct statistical analyses such as time series analysis, portfolio optimization, and econometric model building [4]. In the field of sociology, MATLAB can be used to analyze social network data and to conduct statistical analyses such as social network analysis, community detection, and diffusion analysis [6]. ChatGPT-3, which is defined as a language model developed by OpenAI that can generate human-like text, can be used to assist social science researchers in using MATLAB ST by providing explanations and examples of how to use the software. One way that ChatGPT-3 can assist beginners in learning MATLAB ST is by providing a general overview of the software and its capabilities. This could include information on the different features and tools available in MATLAB ST, as well as the types of data that can be analyzed using the software. Another way that ChatGPT-3 could assist social science researchers in using MATLAB ST is by providing the codes for using the software. This could include information on how to enter and process data, perform statistical analyses, and create graphs and charts to illustrate findings. ChatGPT-3 could also provide explanations of statistical concepts and techniques that are relevant to using MATLAB ST, such as t-tests, ANOVA, and regression.

Recently, several new works related to the usage of the ChatGPT-3 has been proposed [7, 8]. Frieder et al. [7] investigated the mathematical abilities of two versions of ChatGPT and GPT-4 using various datasets, including newly released datasets named GHOSTS and miniGHOSTS. The authors aimed to determine if these language models can serve as useful assistants to professional mathematicians and evaluates their performance using fine-grained metrics. Authors reported that ChatGPT is effective for querying mathematical facts and serving as a knowledge base, while GPT-4 performs adequately in undergraduate-level mathematics but struggles with more advanced material. In [8], a thorough investigation of the field of complex systems is offered, with ChatGPT serving as a vehicle for displaying the community's collective knowledge. In order to provide responses that reflect the dominant opinions, concepts, and linguistic expressions present within the community, ChatGPT has been trained to absorb linguistic structures and conventions from a sizable collection of internet texts.

In this paper, we propose to use of ChatGPT-3 prompts for using MATLAB ST for social science researchers. There are several reasons why using ChatGPT-3 may be preferable to using YouTube videos or online courses for using MATLAB ST. First of all, one advantage of using ChatGPT-3 for using MATLAB ST is the ability to customize the learning experience to individual needs and goals. With ChatGPT-3, users can input specific

questions or areas of focus, and the system can provide tailored responses and resources. This can be especially useful for those who have specific learning objectives or need to learn at their own pace. Besides, coding with MATLAB ST for data analysis may not be an easy task for social science researchers and it may also take a quite long time to settle a coding sense in a MATLAB environment. Thus, in this paper, we show that the ChatGPT-3 prompts make it quite easy to write the MATLAB segments for data analysis with ST.

In the next sections, the MATLAB ST and ChatGPT-3 terms are introduced briefly. Then, the data analysis with ChatGPT3 prompts for coding with MATLAB ST is introduced. Finally, several discussions and concluding remarks are given.

2. MATLAB Statistical Toolbox

The MATLAB statistical toolbox is a powerful tool for data analysis in the social sciences [9]. It offers a wide range of statistical functions and tools that can be used to analyze data from surveys, experiments, and observational studies. The toolbox includes functions for descriptive statistics, inferential statistics, and linear and nonlinear modeling. In addition, it offers a wide range of visualization tools that can be used to display and interpret data. The toolbox also offers a wide range of statistical models that can be used to analyze data in the social sciences. These models include linear and nonlinear models, mixed-effects models, and survival models. These models can be used to analyze a wide range of research questions, such as the effects of a particular treatment or intervention, the relationship between two or more variables, and the predictors of a particular outcome. One of the strengths of the MATLAB statistical toolbox is its visualization capabilities. The toolbox offers a wide range of visualization tools that can be used to display and interpret data. These tools include histograms, scatter plots, box plots, and 3D plots. These tools can be used to explore the data, identify patterns, and communicate the results of the analysis to others.

3. ChatGPT-3

ChatGPT-3 is a language model developed by OpenAI. It is one of the largest and most advanced language models to date, with a capacity of 175 billion parameters, and is capable of generating coherent and coherent text on a wide range of topics [10]. ChatGPT-3 works by processing large amounts of text data and learning patterns and relationships between words and sentences. It uses a machine learning technique called pre-training to build a large neural network model that can predict the next word in a sequence of words based on the words that come before it. Once the model has been pre-trained, it can then be fine-tuned for specific tasks, such as translation, summarization, or text generation. This is achieved through the use of "transformer" architecture, which allows the model to process the input text sequentially and capture long-range dependencies between words and sentences [11]. ChatGPT-3 has a wide range of applications, including language translation, text summarization, question answering, and text generation. It has been used to generate news articles, write code, and even generate poetry and music. In addition to its ability to generate text, ChatGPT-3 can also be used to perform natural language processing tasks, such as named entity recognition and part-of-speech tagging.

4. ChatGPT-3 Prompts for MATLAB ST Analysis

This section introduces several subsections where the ChatGPT-3 prompts are used to help to write the MATLAB ST codes for social science researchers for statistical data analyses. For each section, a brief introduction about the statistical analysis is given and the related ChatGPT-3 prompts and its answer are given, respectively.

4.1. Correlation analysis in MATLAB ST

A statistical technique called correlation analysis is used to check the relationship between two continuous variables [13]. It is possible to quantify the strength and direction of a linear link between two variables using a correlation coefficient. The range of the correlation coefficient is from -1 to 1, with -1 denoting a strong inverse association, or the idea that as one variable rises, the other falls. No association between the variables is shown by a value of 0, while a strong positive relationship is indicated by a value of 1, which means that as one variable rises, the other rises as well. The Pearson correlation coefficient, Spearman's rank correlation coefficient, and Kendall's tau are just a few examples of the different correlation coefficients that can be used [14]. When we ask

the ChatGPT-3 “How can I perform correlation analysis with MATLAB Statistical Toolbox?”, its responses as given in Fig. 1.

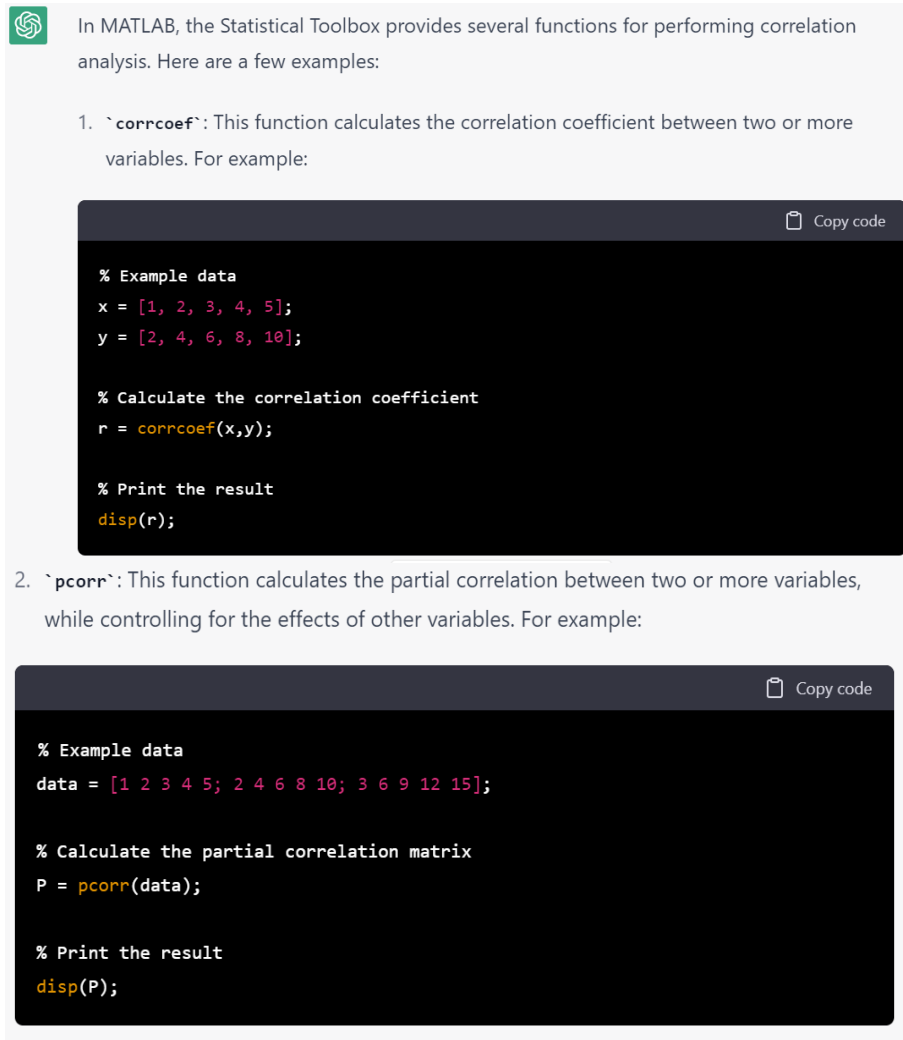
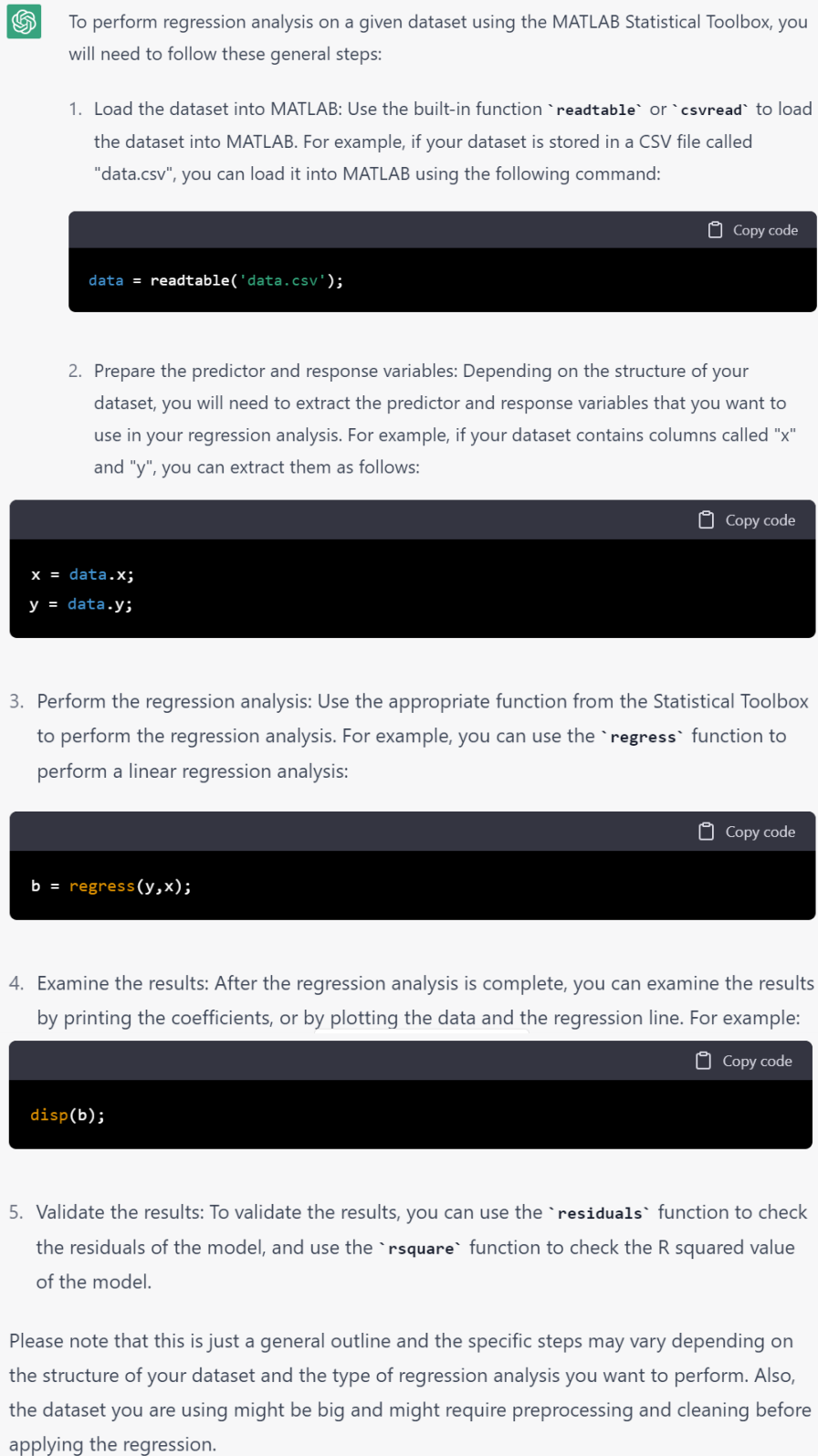


Figure 1. The response of the ChatGPT-3 for the prompt of “How can I perform correlation analysis with MATLAB Statistical Toolbox?”

As seen in Fig. 1, the ChatGPT-3 gives two correlation code examples for two different input datasets. The written codes include explanations for the coders. And the results are shown on the MATLAB screen.

4.2. Regression analysis on MATLAB ST

Regression analysis is a statistical method used to study the relationship between a dependent variable and one or more independent variables [15]. In the social sciences, it is often used to analyze the relationship between a dependent variable such as attitudes, behaviors, or outcomes, and one or more independent variables such as demographic characteristics, socioeconomic status, or other variables that might affect the dependent variable. In addition to predicting the value of the dependent variable based on the values of the independent variables, regression analysis may be used to determine the strength and direction of the link between the dependent and independent variables. It is a method that is frequently used in the social sciences to test hypotheses and comprehend the variables that could affect diverse social phenomena. When a ChatGPT-3 prompt such as “How can I perform regression analysis with MATLAB Statistical Toolbox on a given dataset?”, the following answer is given by it.



The image shows a screenshot of a ChatGPT-3 response. It begins with a green OpenAI logo icon. The text explains that to perform regression analysis using the MATLAB Statistical Toolbox, one must follow five general steps. Each step is followed by a code block containing MATLAB commands. The code blocks are dark-themed with light-colored text. Each code block has a 'Copy code' button in the top right corner. The steps are: 1. Load the dataset using `readtable` or `csvread`. 2. Prepare predictor and response variables by extracting columns 'x' and 'y'. 3. Perform regression analysis using the `regress` function. 4. Examine results by displaying coefficients with `disp`. 5. Validate results using `residuals` and `rsquare` functions. A concluding paragraph notes that these are general steps and may vary based on the dataset and analysis type.

To perform regression analysis on a given dataset using the MATLAB Statistical Toolbox, you will need to follow these general steps:

1. Load the dataset into MATLAB: Use the built-in function `readtable` or `csvread` to load the dataset into MATLAB. For example, if your dataset is stored in a CSV file called "data.csv", you can load it into MATLAB using the following command:

```
data = readtable('data.csv');
```
2. Prepare the predictor and response variables: Depending on the structure of your dataset, you will need to extract the predictor and response variables that you want to use in your regression analysis. For example, if your dataset contains columns called "x" and "y", you can extract them as follows:

```
x = data.x;  
y = data.y;
```
3. Perform the regression analysis: Use the appropriate function from the Statistical Toolbox to perform the regression analysis. For example, you can use the `regress` function to perform a linear regression analysis:

```
b = regress(y,x);
```
4. Examine the results: After the regression analysis is complete, you can examine the results by printing the coefficients, or by plotting the data and the regression line. For example:

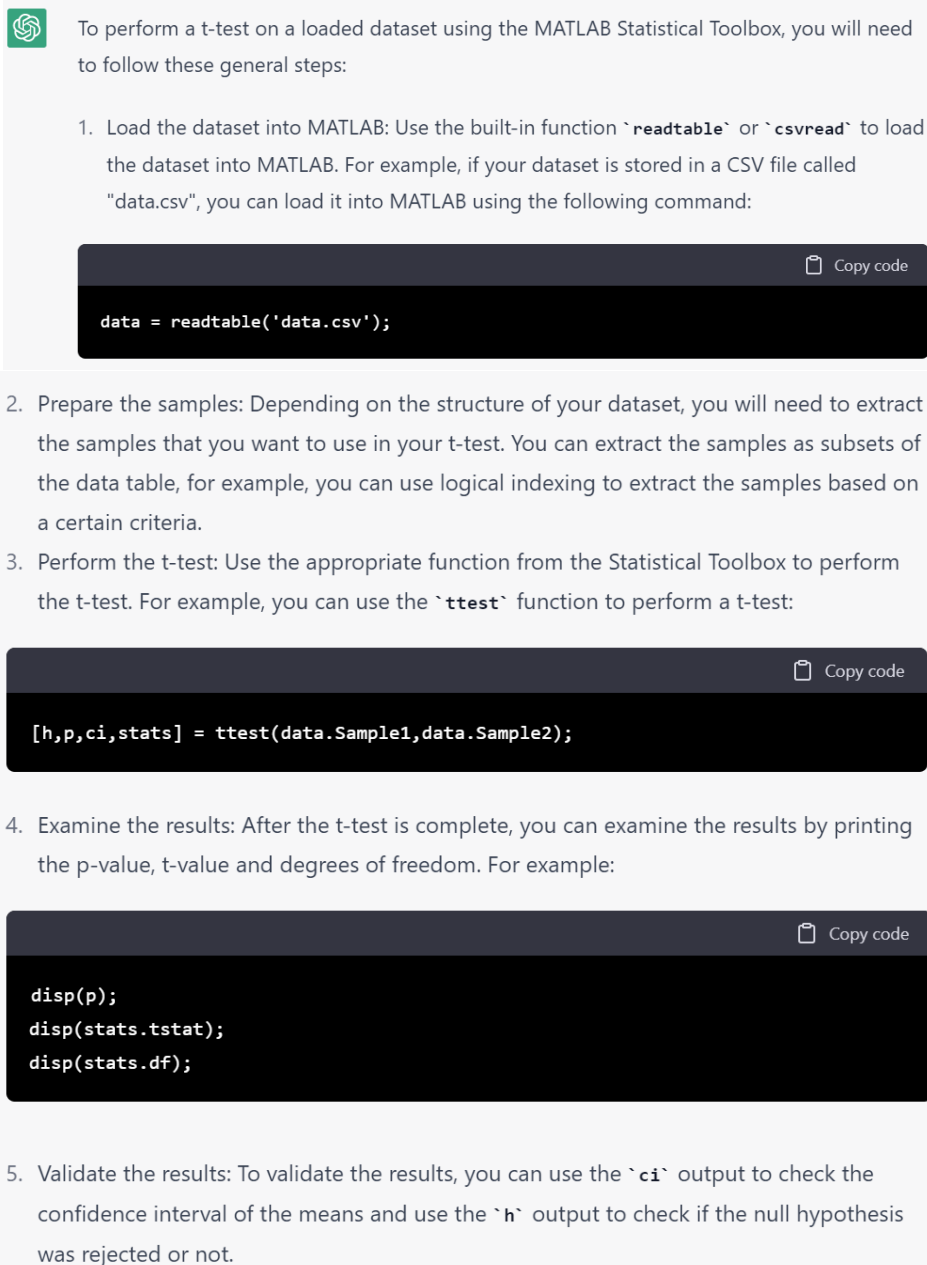
```
disp(b);
```
5. Validate the results: To validate the results, you can use the `residuals` function to check the residuals of the model, and use the `rsquare` function to check the R squared value of the model.

Please note that this is just a general outline and the specific steps may vary depending on the structure of your dataset and the type of regression analysis you want to perform. Also, the dataset you are using might be big and might require preprocessing and cleaning before applying the regression.

Figure 2. The response of the ChatGPT-3 for the prompt of “How can I perform regression analysis with MATLAB Statistical Toolbox on a given dataset?”

4.3. t-test with MATLAB ST

To evaluate whether there is a significant difference between the means of the two groups, a t-test is a statistical test that is employed [16]. The means of two groups on a certain variable are frequently compared in the social sciences. When the population variance is unknown, the t-test uses the t-distribution, a probability distribution, to describe the distribution of sample mean values. The t-test provides a test statistic that can be used to assess the likelihood that the difference between the means of the two groups is the result of chance when the sample size is small and the population variance is unknown.



The screenshot shows a chat interface with a green OpenAI logo icon. The text reads: "To perform a t-test on a loaded dataset using the MATLAB Statistical Toolbox, you will need to follow these general steps:"

1. Load the dataset into MATLAB: Use the built-in function `readtable` or `csvread` to load the dataset into MATLAB. For example, if your dataset is stored in a CSV file called "data.csv", you can load it into MATLAB using the following command:


```
data = readtable('data.csv');
```
2. Prepare the samples: Depending on the structure of your dataset, you will need to extract the samples that you want to use in your t-test. You can extract the samples as subsets of the data table, for example, you can use logical indexing to extract the samples based on a certain criteria.
3. Perform the t-test: Use the appropriate function from the Statistical Toolbox to perform the t-test. For example, you can use the `ttest` function to perform a t-test:


```
[h,p,ci,stats] = ttest(data.Sample1,data.Sample2);
```
4. Examine the results: After the t-test is complete, you can examine the results by printing the p-value, t-value and degrees of freedom. For example:


```
disp(p);
disp(stats.tstat);
disp(stats.df);
```
5. Validate the results: To validate the results, you can use the `ci` output to check the confidence interval of the means and use the `h` output to check if the null hypothesis was rejected or not.

Figure 3. The response of the ChatGPT-3 for the prompt “How can I perform a t-test with MATLAB Statistical Toolbox on a loaded dataset?”

There are several different types of t-tests, including the one-sample t-test, the independent samples t-test, and the paired samples t-test. The specific type of t-test that is used will depend on the research question and the characteristics of the data. Fig. 3 shows the response of the ChatGPT-3 when we ask “How can I perform a t-test with MATLAB Statistical Toolbox on a loaded dataset?”. As seen in Fig. 3, the ChatGPT-3 produces a series of steps for performing the t-test on MATLAB. It also gives a paragraph where some important related notes about the t-test are described.

4.4. ANOVA with MATLAB ST

ANOVA is a statistical technique used to compare the means of two or more groups [17]. It is used to determine whether there are significant differences between the means of the groups, and if so, where those differences lie. There are several types of ANOVA, namely one-way ANOVA, two-way ANOVA, and repeated-measures ANOVA, respectively. While the one-way ANOVA is used to compare the means of two or more groups on a single continuous dependent variable, the two-way ANOVA is used to compare the means of two or more groups on two different independent variables. The repeated-measures ANOVA is also used to compare the means of two or more groups on a single dependent variable, where each subject is measured multiple times. ANOVA is based on the assumption that the data are normally distributed and that the variances of the groups are equal. In Fig. 4, the response of the ChatGPT-3 is given where we asked “How can I perform ANOVA analysis on MATLAB Statistical Toolbox on a loaded dataset?”.



To perform ANOVA analysis on a loaded dataset in MATLAB's Statistical Toolbox, you can use the `anova1` function. The syntax for this function is as follows:

```
[p,tbl,stats] = anova1(y,group)
```

Where:

- `y` is the data vector or matrix to be analyzed,
- `group` is a vector or cell array of grouping variables.

For example, if your data is stored in a matrix called "data" and the grouping variable is stored in a vector called "groups", you would use the following command:

```
[p,tbl,stats] = anova1(data, groups)
```

This will perform an ANOVA analysis on the data, using the groups variable to divide the data into different groups for comparison. The p-value, ANOVA table and statistics will be returned in the variables `p`, `tbl` and `stats` respectively.

Figure 4. The response of the ChatGPT-3 for the prompt of “How can I perform ANOVA analysis on MATLAB Statistical Toolbox on a loaded dataset?”

5. Discussions

ChatGPT-3, as a language model, can be used in various ways to support the use of MATLAB's Statistical Toolbox for social science research [18]. ChatGPT-3 can be used to generate code snippets for various statistical

analyses that are commonly used in social science research, such as ANOVA, linear regression, and factor analysis. This can help researchers who are not familiar with MATLAB's syntax to quickly and easily perform the analyses they need. ChatGPT-3 can be used to generate explanations of statistical concepts and techniques that are used in social science research. This can be helpful for researchers who are new to a particular technique or concept and need a quick introduction to it. ChatGPT-3 can be used to generate reports that summarize the results of statistical analyses. This can be helpful for researchers who need to quickly create a report for a grant application or conference presentation. ChatGPT-3 can be used to generate code snippets for creating various types of data visualizations, such as histograms, box plots, and scatter plots, to help researchers explore and understand their data. ChatGPT-3 can be used to guide troubleshooting common issues that researchers may encounter when using MATLAB's Statistical Toolbox, such as how to handle missing data or how to interpret output from a particular function. ChatGPT-3 can be a valuable tool for social science researchers who use MATLAB's Statistical Toolbox by making it easier to perform complex analyses, understand statistical concepts, and communicate results.

Besides, there are a few potential disadvantages of using ChatGPT-3 within MATLAB ST for social science researchers. One disadvantage is that ChatGPT-3 is a highly complex model that may require significant computational resources and expertise to implement and use effectively. Additionally, ChatGPT-3 is a black box model, which means that it is difficult to understand how it is making its predictions and it can lead to a lack of interpretability. Furthermore, ChatGPT-3 is not specifically designed for social science research and may not be well-suited to certain types of data or research questions. Finally, ChatGPT-3 has some difficulties [19]. These difficulties include the model's sporadic difficulties in understanding intricately nuanced contextual nuances, the potential propensity for producing content that is sensitive or inappropriate, obstacles to the seamless maintenance of a coherent conversational trajectory, and the pressing need for meticulous verification of the information it disseminates. The model may also exhibit inclinations toward repetition or prolixity in its responses, and its creative output is prone to following established patterns. The process of clarifying ambiguities, dependent on the wording of input inquiries, coupled with the lack of emotional intelligence, add to the complex interrelationships that underlie the successful application of ChatGPT-3.

6. Conclusions

In conclusion, MATLAB is a powerful tool for analyzing data in the social sciences. Its ability to handle large and complex data sets, integrate with other software packages, and provide a wide range of statistical and data analysis functions make it a valuable tool for researchers in the social sciences. Furthermore, the advanced statistical techniques, visualization tools, and flexibility in data visualization available in MATLAB make it a powerful tool for researchers who require specific capabilities. However, its steep learning curve, the difficulty of use for those without a programming background, and high costs are limitations that should be considered when deciding to use MATLAB in a research project. Despite these limitations, the advantages that MATLAB provides in terms of data manipulation, visualization, advanced statistical techniques, and integration with other software packages make it a valuable tool for researchers in the social sciences.

References

- [1] Creswell JW, Creswell JD. *Research design: Qualitative, quantitative, and mixed methods approaches*. Sage publications, 2017.
- [2] Smith J, Brown T, Wilson K. Using the MATLAB statistical toolbox to analyze data from a survey of attitudes towards climate change. *J. Clim. Res.*, 2019; 12(3): 123-135.
- [3] Jones B, Smith J, Davis K. Using the MATLAB statistical toolbox to analyze data from an observational study of child development. *J. Child Dev.*, 2020; 32(4): 345-357.
- [4] Rao R. *Engineering optimization: theory and practice*. John Wiley & Sons, 2015.
- [5] Field A. *Discovering statistics using IBM SPSS statistics*. Sage, 2013.
- [6] Wasserman S, Faust K. *Social network analysis: methods and applications*. Cambridge university press.
- [7] Frieder S, Pinchetti L, Griffiths RR, Salvatori T, Lukasiewicz T, Petersen PC, Berner J. *Mathematical capabilities of chatgpt*. 2023; arXiv preprint arXiv:2301.13867.
- [8] Crokidakis N, Marcio AM, Daniel OC. *Questions of science: chatting with ChatGPT about complex systems*. 2023; arXiv preprint arXiv:2303.16870.
- [9] *MATLAB Statistical Toolbox documentation*. (n.d.), 1994.
- [10] Brockman J, Conley K, Wang S. *The GPT-3 model: Overview and content*. OpenAI, 2021. Retrieved from <https://beta.openai.com/docs/models/gpt3>
- [11] Radford A, Wu J, Child R, Luan D, Amodei D, Sutskever I. *Language models are unsupervised multitask learners*. OpenAI, 2019. Retrieved from <https://openai.com/blog/language-models-are-unsupervised-multitask-learners/>

- [12] Kline RB. Principles and practice of structural equation modeling. New York, NY: Guilford Press, 2015.
- [13] Senthilnathan S. Usefulness of correlation analysis. Available at SSRN 3416918, 2019.
- [14] Mukaka MM. A guide to appropriate use of correlation coefficient in medical research. *Malawi Med. J.*, 2012; 24(3): 69-71.
- [15] Freund RJ, Wilson WJ, Sa P. Regression analysis. Elsevier, 2006.
- [16] Kim TK. T test as a parametric statistic. *Korean J. Anesthesiol.*, 2015; 68(6): 540-546.
- [17] Lars ST, Wold S. Analysis of variance (ANOVA). *Chemom. Intell. Lab. Syst.*, 1989; 6(4): 259-272.
- [18] Johnson MA, Price KN. The use of MATLAB in teaching statistical process control. *J. Qual. Maint. Eng.*, 2007; 13(2): 208-223.
- [19] Abdullah M, Alia M, Yaser J. ChatGPT: Fundamentals, applications and social impacts. 2022 IEEE Ninth International Conference on Social Networks Analysis, Management and Security (SNAMS); 29 November- 1December 2022; Milan, Italy. pp. 1-8.

Numerical Investigation of Heat Transfer on Hot and Cold Sides of a Thermoelectric Generator Using Heat Sinks

Enes KILINÇ^{1*}

¹ Department of Mechanical Engineering, Faculty of Engineering, Karabük University, Karabük, Türkiye

*¹ eneskilinc@karabuk.edu.tr

(Geliş/Received: 05/04/2023;

Kabul/Accepted: 16/08/2023)

Abstract: This study represents Computational Fluid Dynamics (CFD) analyses to improve the heat transfer on the two sides of a thermoelectric generator (TEG) by utilizing heat sinks to recover the waste heat of hot air. In this respect, the temperature difference between the hot and cold sides of the TEG, the heat transfer rate on the hot and cold sides and the pressure drop between the inlet and outlet of the hot and cold air are investigated for varying hot air inlet temperature and Re number in terms of improving the heat transfer and accordingly the output power of the TEG. According to the numerical results, the maximum temperature difference between the hot and cold sides of the TEG concerning hot air inlet temperature of 600 °C and Re number of 16800 is specified as 418.9 °C and 478.1 °C, respectively. In terms of heat transfer, maximum heat transfer rate on the hot side for hot air inlet temperature of 600 °C and Re number of 16800 is specified as 180.4 W and 205.1 W, respectively, while the maximum heat transfer rate on the cold side is specified as 168.0 W and 192.6 W. The maximum pressure drop occurs as 304.4 Pa for the Re number of 16800. As a result, increasing hot air inlet temperature and Re number yields an increase in the temperature difference, the heat transfer rate on the hot side, and the heat transfer rate on the cold side. Besides, pressure drop increases with increasing Re number.

Keywords: Thermoelectric generator, waste heat, CFD modeling, temperature distribution, heat transfer.

Isı Kuyuları Kullanılarak Bir Termoelektrik Jeneratörün Sıcak ve Soğuk Yüzeyindeki Isı Transferinin Sayısal Olarak İncelenmesi

Öz: Bu çalışmada, sıcak havanın atık ısısını geri kazanmak için ısı kuyuları kullanılarak bir termoelektrik jeneratörün (TEG) iki yüzeyindeki ısı transferinin iyileştirilmesi için yapılan Hesaplamalı Akışkanlar Dinamiği (HAD) analizleri sunulmaktadır. Bu bağlamda, ısı transferinin ve buna bağlı olarak TEG'in çıkış gücünün iyileştirilmesi için TEG'in sıcak ve soğuk yüzeyleri arasındaki sıcaklık farkı, sıcak ve soğuk yüzeyindeki ısı transfer hızı ve sıcak ve soğuk havanın giriş ve çıkışı arasındaki basınç düşüşü değişken sıcak hava giriş sıcaklığı ve Re sayısı için incelenmiştir. Sayısal sonuçlara göre, 600 °C sıcak hava giriş sıcaklığı ve 16800 Re sayısı için maksimum sıcaklık farkı sırasıyla 418,9 °C ve 478,1 °C olarak belirlenmiştir. Isı transferi açısından, 600 °C sıcak hava giriş sıcaklığı ve 16800 Re sayısı için sıcak yüzeydeki maksimum ısı transfer hızı sırasıyla 180,4 W ve 205,1 W olarak belirlenirken soğuk yüzeydeki maksimum ısı transfer hızı 168,0 W ve 192,6 W olarak belirlenmiştir. Maksimum basınç düşüşü, 16800 Re sayısı için 304,4 Pa olarak gerçekleşmiştir. Sonuç olarak, artan sıcak hava giriş sıcaklığı ve Re sayısı, sıcaklık farkı ve sıcak ve soğuk yüzeylerdeki ısı transfer hızlarında artışa neden olmuştur. Ayrıca, basınç düşüşü, artan Re sayısı ile artmıştır.

Anahtar kelimeler: Termoelektrik jeneratör, atık ısı, CFD modelleme, sıcaklık dağılımı, ısı transferi.

Nomenclature

A_{TEG}	Total TE leg cross-sectional area of the TEG	T	Temperature
c_p	Specific heat	T_c	Cold side temperature of the TEG
$C_{1\epsilon}$	Constant	T_{ci}	Cold air inlet temperature
$C_{2\epsilon}$	Constant	T_{co}	Cold air outlet temperature
$C_{3\epsilon}$	Constant	T_h	Hot side temperature of the TEG
G_k	Generation of the turbulence kinetic energy due to mean velocity gradient	T_{hi}	Hot air inlet temperature
G_b	Generation of the turbulence kinetic energy due to buoyancy	T_{ho}	Hot air outlet temperature
k	Thermal conductivity	V	Velocity
k	Turbulence kinetic energy	Y_M	Contribution of the fluctuating dilatation to the overall dissipation
P	Pressure	zT	Figure of merit
		ΔP	Pressure drop

* Corresponding author: eneskilinc@karabuk.edu.tr. ORCID Number of authors: ¹ 0000-0002-9585-998X

\dot{q}_c	Heat transfer rate on the cold side of the TEG	ΔT	Temperature difference
		ε	Dissipation rate
\dot{q}_h	Heat transfer rate on the hot side of the TEG		
P	Output power of the TEG	μ_t	Turbulent viscosity
Re	Reynolds number	ρ	Density
S_k	User defined source term	σ_k	Turbulent Prandtl number for k
S_ε	User defined source term	σ_ε	Turbulent Prandtl number for ε

1. Introduction

Thermoelectric (TE) devices are novel waste heat recovery solutions that convert heat energy directly into electrical energy [1,2]. They have been studied for industrial areas such as space applications, photovoltaic (PV) technology, the automotive industry, and power plants [3]. Applying temperature difference between the hot and cold sides of TE devices yields voltage occurrence and electrical power generation, known as the Seebeck effect [4]. TE devices are advantageous in power generation in terms of having no moving parts, being compact, quiet, environmentally friendly, and maintenance-free [5]. However, reasonably low heat-to-electricity conversion efficiencies of TE devices are the major task in improving waste heat recovery using TEs [6].

For the last decades, many researchers have focused on improving the figure of merit (zT) of TE materials, optimizing the design of thermoelectric generators (TEGs), and improving operating conditions of TEGs in terms of increasing the conversion efficiency of TEGs [7]. Regarding improving operating conditions, TEGs have been modeled and characterized to specify the effects of the crucial parameters on the performance of TEGs [8]. Therefore, heat transfer enhancement on the hot and cold sides of the TE modules is crucial for the performance of TEGs [7]. Within this scope, Li et al. numerically investigated the effects of leg length and heat radiation on the thermal performance of a TEG sandwiched between cold and hot blocks under steady-state and transient conditions [9]. They have found that numerical and experimental performance curves agree, and the radiation heat transfer and the length of TEG's leg are negligible on the thermal performance of the TEG. Miao et al. investigated the effect of the geometric structure of a TE module on power generation [10]. They have stated that the conversion efficiency changes with the change in heat absorption of the TE module. As a result, the conversion efficiency of the TE module decreases when the heat absorption is higher. Nour Eddine et al. investigated the effect of clamping pressure on the performance of two commercial TE modules for marine applications [11]. They have obtained conversion efficiencies in the range of 0.05-0.35% and 0.26-0.4% for the $\text{Si}_{80}\text{Ge}_{20}$ and Bi_2Te_3 TE modules, respectively, for a Diesel engine exhaust temperature of 380 °C. In their other work, Nour Eddine et al. established a model to investigate a TEG for waste heat recovery from the exhaust gas of an automotive engine [12]. They have reached a maximum generated TEG power of 42 W for 671 K of TEG hot side temperature and 354 K of cold side temperature.

Gürbüz et al. designed a three-layer sandwich-type TEG consisting of two cooling heat exchangers placed on both sides of the middle rectangular exhaust heat exchanger coupled to the exhaust path in a propane-fueled spark-ignition (SI) engine. They performed both experimental and computational fluid dynamics analyses to visualize both the cold and hot surface temperatures of the TEMs. According to the results, electrical power of the TEG with propane is higher in the range of 11.5–12.1% compared to the TEG without propane in the 1500–5000 rpm range of the SI engine in a good correlation between the experimental and numerical findings, varying between 3% and 15% with the engine speed [13]. In another study, Topalçı et al. developed a theoretical model with Matlab/Simulink of a thermoelectric generator used for waste heat recovery in a spark ignition (SI) engine. As a result, the DC electrical power production with the Matlab/Simulink model of the TEG changed in the range of 6.36-50.96 W for the engine speed range of 1500-4000 rpm [14]. Kunt et al. designed a waste heat recovery system with a thermoelectric generator for the exhaust system of a motorcycle engine with a cylinder volume of 50 cc [15]. The maximum recovery power has been found as 2.05 W at an engine speed of 6000 r/min and the maximum system efficiency has been found as 2.41% at an engine speed of 4000 r/min. Schwurack et al. considered inner heat losses in a TEG system for high-temperature applications [16]. As a result of the optimization study, total power output has been increased by 0.56%. Akçay et al. performed a numerical analysis of a 3-layer TEG consisting of a middle exhaust heat exchanger and two cooling water heat exchangers placed on both surfaces of the middle exhaust heat exchanger using computational fluid dynamics. As a result, it was found that the temperature difference increased by 32.45% by dividing the internal volume of the hot heat exchanger into two equal parts with a separator plate and the temperature difference increased by an additional 18.79% by adding flow diverter fins on the separator plate surfaces [17]. Ökmen et al. optimized hot-side heat exchangers with different fin numbers and arrangements in terms of surface temperature and temperature distribution in a thermoelectric

generator where electrical energy is generated from the exhaust waste heat energy of a spark ignition engine using the computational fluid dynamics [18]. In addition, Wang et al. constituted a mathematical model for harvesting the heat energy of vehicle exhaust gas through a TEG to investigate the effects of exhaust gas mass flow rate, temperature and mass flow rate of different coolants, and convection heat transfer coefficient [19].

In this study, the effects of Re number and hot air inlet temperature (T_{hi}) on the temperature difference (ΔT) between the hot and cold sides of a TEG, on the heat transfer rate on the hot (\dot{q}_h) and cold sides (\dot{q}_c) of the TEG, and on the pressure drop (ΔP) between the inlet and outlet of the hot and cold air were numerically investigated in terms of heat recovery from hot air. In the literature, there are few studies which focus on the heat transfer analysis of both hot and cold sides of the TEG. Besides, operating temperature of the TEGs are within low temperature range. Within this scope, hot air inlet temperatures ranged between 200-600 °C and Re numbers for the hot and cold air varied between 5600-18600, which point out the originality of the study. Hot air as the hot fluid and cold air as the cold fluid are modeled to flow in a counter-current manner on the hot and cold sides of the TE module, respectively. Temperature distributions in the hot and cold air, \dot{q}_h , \dot{q}_c , ΔP and ΔT were evaluated in terms of improving the operating conditions of TEGs.

2. Methodology

2.1. Physical Configuration

The objective of this study is to utilize heat energy in terms of generating electricity using TEG. In this respect, ΔT , \dot{q}_h , \dot{q}_c , and ΔP of a TEG are investigated in terms of improving the output power of the TEG. The TEG model consists of a TEG, two heat sinks on the hot and cold sides of the TEG, and hot and cold air as the fluids. To increase the output power of the TEG, one side of the TEG is heated by hot air, while the other side is cooled by cold air. Hot and cold air flowing over the hot and cold sides of the TEG are modeled to flow in a counter-current manner to increase the heat transfer. A heat sink with straight fins made of aluminum is used to enhance the heat transfer on both sides. **Figure 1** illustrates the physical model of the study, including hot air, cold air, heat sinks, and the TEG. The TEG used in the model comprises eight pairs of p- and n-type legs made of $\text{Ca}_{2.5}\text{Ag}_{0.3}\text{Eu}_{0.2}\text{Co}_4\text{O}_9$ and $\text{Ca}_{2.96}\text{Dy}_{0.02}\text{Ho}_{0.02}\text{MnO}_3$, respectively. Dimensions of the TEG are 44 mm x 44 mm x 7 mm. Accordingly, the base dimension of the heat sinks is 44 mm x 44 mm, and the height of the heat sink is 48 mm (**Figure 2**). Hot and cold air passes through the heat sinks. Solid and fluid properties used in the model are constant and are given in **Table 1**.

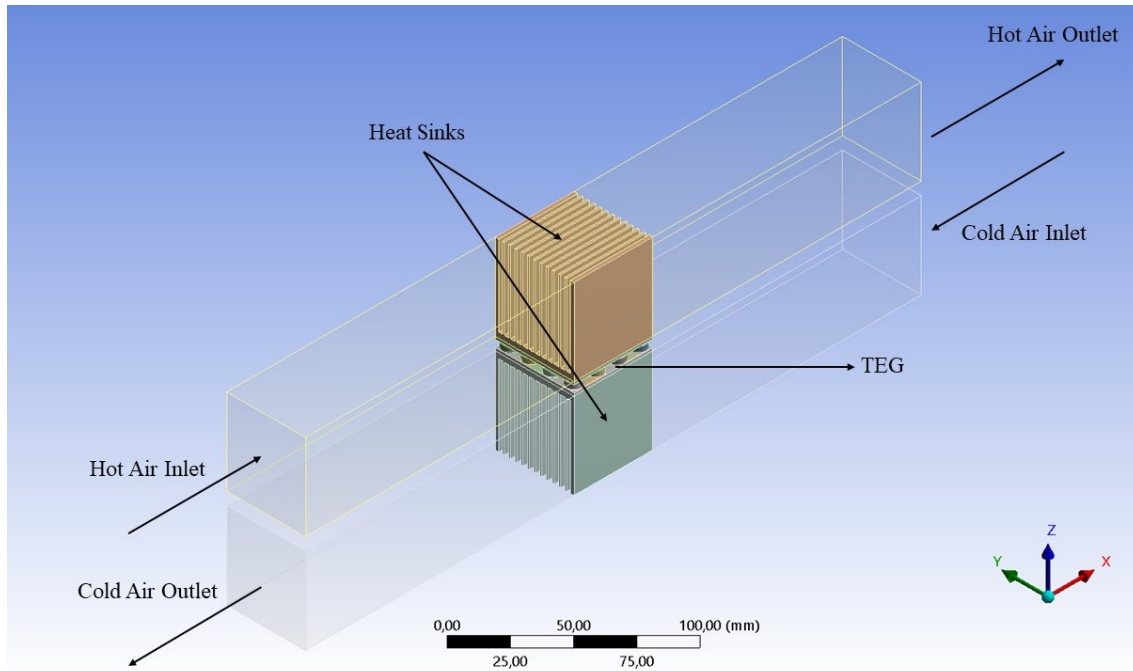


Figure 1. Physical model and boundary conditions of the TEG model.

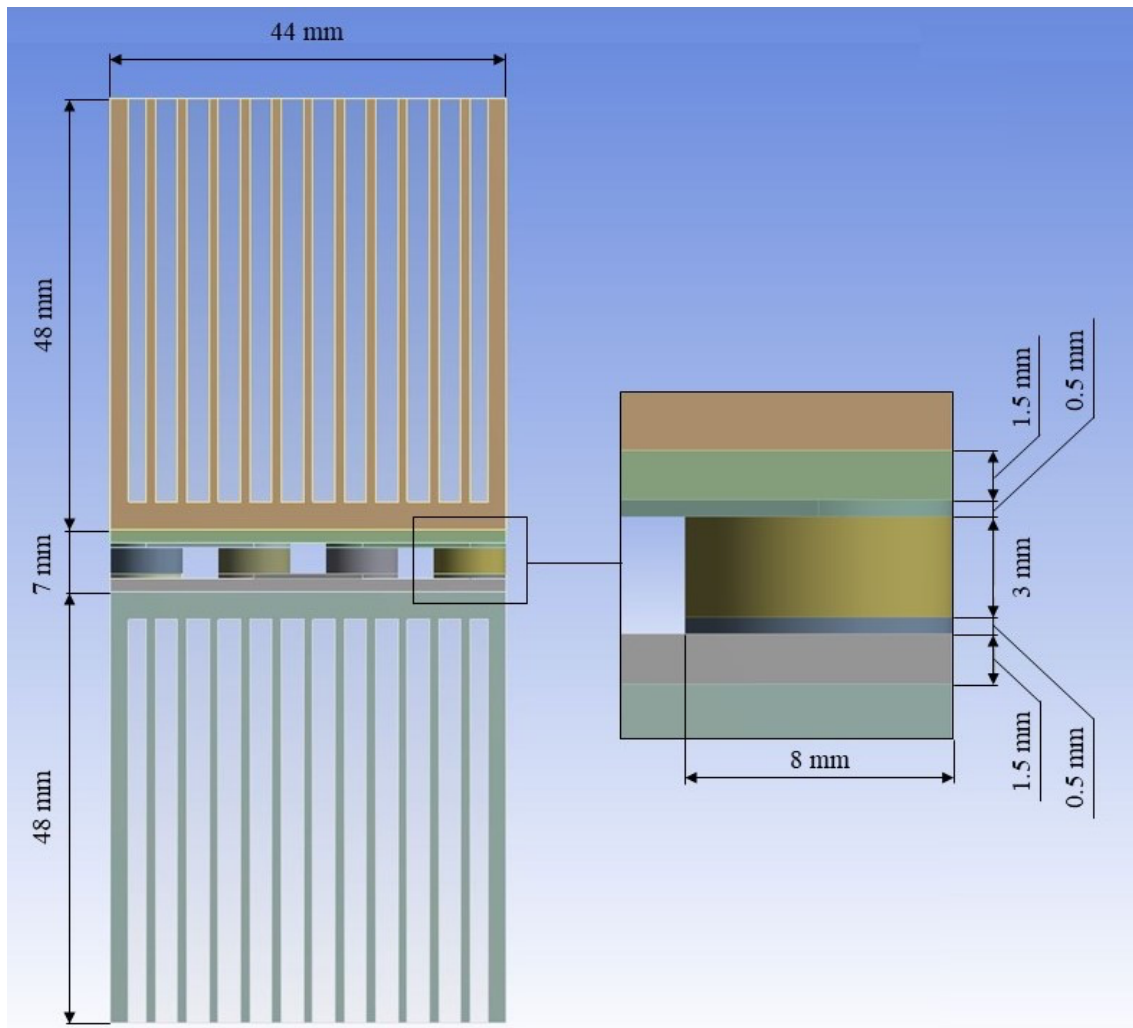


Figure 2. Dimensions of the TEG and the heat sinks in the model.

2.2. Turbulence Model and Boundary Conditions

Hot and cold flows in the model are designed to be three-dimensional, steady, and turbulent. The flow is assumed to be incompressible, and the fluid properties are assumed to be constant. The standard k- ϵ model is applied for the turbulent flow characteristics. The related governing equations and the turbulent kinetic energy are given as follows. Continuity equation is given as

$$\nabla \cdot (\rho \vec{V}) = 0 \quad (1)$$

where ρ is the density and V is the velocity of the fluid. Momentum equation is expressed as

$$\rho \vec{V} \cdot \nabla \vec{V} = -\nabla P + \nabla \cdot [\mu (\nabla \vec{V} + (\nabla \vec{V})^T)] \quad (2)$$

where P is the pressure. Energy equation is given as

Table 1. Material properties used in the TEG model.

Material	Definition	Value
Air	Thermal Conductivity	0.0242 W/m·K
	Specific Heat	1006.43 J/kg·K
	Density	1.225 kg/m ³
	Viscosity	1.7894x10 ⁻⁵ kg/m·s
Heat Sink	Thermal Conductivity	218 W/m·K
	Specific Heat	900 J/kg·K
	Density	2690 kg/m ³
P-type Leg	Thermal Conductivity	2.49 W/m·K
	Specific Heat	735 J/kg·K
	Density	3870 kg/m ³
N-type Leg	Thermal Conductivity	0.73 W/m·K
	Specific Heat	843 J/kg·K
	Density	2470 kg/m ³
Alumina Plate	Thermal Conductivity	25 W/m·K
	Specific Heat	880 J/kg·K
	Density	3720 kg/m ³
Silver Conductor	Thermal Conductivity	429 W/m·K
	Specific Heat	237 J/kg·K
	Density	10497 kg/m ³

$$\nabla \cdot (\vec{V} \rho c_p T) = \nabla \cdot (k \nabla T) + S_g \quad (3)$$

where c_p is the specific heat, k is the thermal conductivity, and T is the temperature of the fluid. Turbulence kinetic energy k is expressed as

$$\frac{\partial}{\partial x_i} (\rho k u_i) = \frac{\partial}{\partial x_j} \left[\left(\mu + \frac{\mu_t}{\sigma_k} \right) \frac{\partial k}{\partial x_j} \right] + G_k + G_b - \rho \varepsilon - Y_M + S_k \quad (4)$$

where Y_M is the contribution of the fluctuating dilatation to the overall dissipation. Dissipation rate ε is given as

$$\frac{\partial}{\partial x_i} (\rho \varepsilon u_i) = \frac{\partial}{\partial x_j} \left[\left(\mu + \frac{\mu_t}{\sigma_\varepsilon} \right) \frac{\partial \varepsilon}{\partial x_j} \right] + C_{1\varepsilon} \frac{\varepsilon}{k} (G_k + C_{3\varepsilon} G_b) - C_{2\varepsilon} \rho \frac{\varepsilon^2}{k} + S_\varepsilon \quad (5)$$

In these equations, G_k and G_b are the generation of the turbulence kinetic energy due to mean velocity gradient and buoyancy. Turbulent viscosity, μ_t is calculated as $\mu_t = \rho C_\mu \frac{k^2}{\varepsilon}$. Constants of $C_{1\varepsilon} = 1.44$, $C_{2\varepsilon} = 1.92$, and $C_{3\varepsilon} = 0.09$, and turbulent Prandtl numbers of $\sigma_k = 1.0$ and $\sigma_\varepsilon = 1.3$ are determined experimentally. S_k and S_ε are user defined source terms [20].

The walls of the hot and cold air and outside surfaces of the heat sinks are modeled as adiabatic, and the heat transfer coefficient of 10 W/m·K is defined on the outside surfaces of the TEG. The no-slip boundary condition is applied on the surfaces of the heat sinks. Heat radiation is neglected in the whole model. Regarding accuracy and minimizing the simulation time, the mesh structure is optimized, and the number of grids for the model is 10,500,000. Body sizing applied to the TEG and the heat sinks are most influential in the number of grids. The TEG model is designed in Ansys DesignModeler, and Ansys Fluent is used to determine the temperature distributions in the hot and cold air, \dot{q}_h , \dot{q}_c , ΔP , and ΔT . Boundary conditions are demonstrated in **Figure 1**.

To improve the \dot{q}_h and ΔT of the TEG, T_{hi} is altered as 200 °C, 300 °C, 400 °C, 500 °C, and 600 °C while the cold air inlet temperature (T_{ci}) and Re number are held constant at 25 °C and 5600, respectively. Re numbers for the hot and cold air are assumed to be the same and varied as 5600, 8400, 11200, 14000, and 16800 after specifying the optimum T_{hi} to enhance \dot{q}_h . During the analyses, T_{hi} and T_{ci} are held constant at 600 °C and 25 °C, respectively. Outlet pressures of the hot and cold air are specified as the atmospheric pressure.

3. Results and Discussion

3.1. Temperature Distribution in the Hot and Cold Air

Temperature distributions in the hot and cold air were obtained as a result of CFD analyses concerning different T_{hi} and Re numbers. **Figure 3** illustrates the temperature distribution in the hot and cold air for T_{hi} . According to the figure, T_{hi} decreases when the hot air flows through the heat sink, while T_{ci} increases when the cold air flows through the heat sink. The reason for the decrease in T_{hi} and the increase in T_{ci} is the heat transfer to the TEG by the heat sink. When **Figure 3a - Figure 3e** are investigated, the difference between T_{hi} and hot air outlet temperature (T_{ho}) increases with increasing T_{hi} as the difference between T_{ci} and cold air outlet temperature (T_{co}), which leads to the increase in the heat transfer between the heat sinks and the TEG. Accordingly, the air temperature decreases on the surfaces of the heat sink fins for the hot air. In contrast, the air temperature increases on the surfaces of the heat sink fins for the cold air due to the convection heat transfer between the air and the heat sink. It can be seen from the figures that the hot air temperature is the lowest at the surfaces of the outside fins of the heat sinks due to the convection boundary condition defined on the outside surfaces of the heat sinks. Similarly, the temperature of the cold air is the highest at the surfaces of the outside fins of the heat sinks due to the convection boundary condition defined on the outside surfaces of the heat sinks. For $T_{hi} = 600$ °C, temperatures of the hot and cold air at the outlet of the heat sinks are obtained as 592 °C and 33 °C, respectively.

When the temperature distribution in the hot and cold air concerning different Re numbers is investigated, it can be seen from **Figure 4** that similar observations are obtained with the effects of the T_{hi} on the temperature distribution. According to **Figure 4a - Figure 4e**, T_{hi} decreases when the hot air flows through the heat sink, while T_{ci} increases when the cold air flows through the heat sink. It can be seen from the figures that an increase in Re number yields a significant increase in T_{ho} while yields a significant decrease in T_{co} . However, this effect reduces the temperature differences between T_{hi} and T_{ho} as the temperature difference between T_{ci} and T_{co} , which leads to a decrease in the heat transfer between the heat sinks and the TEG. As a result, temperature of the hot air at the outlet of the heat sink increased and reached to the value of 598 °C, while temperature of the cold air at the outlet of the heat sink decreased to 27 °C.

3.2. Velocity Distribution in the Hot and Cold Air

Velocity distributions in the hot and cold air are presented in **Figure 5a – Figure 5e** with respect to the Re numbers. Hot and cold air enters the flow channels at velocities of 5 m/s, 7.5 m/s, 10 m/s, 12.5 m/s, and 15 m/s for the Re numbers of 5600, 8400, 11200, 14000, and 16800, respectively. According to the figure, velocities of the hot and cold air are equal to zero due to the no-slip boundary condition on the outer surfaces of the hot and cold air. In addition, velocities of the hot and cold air increase due to the steady flow while passing through the fins of heat sinks since the flow area decreases at these regions. As it can be seen from the figures that maximum velocity is obtained at the flow axis, decreasing towards the outer surfaces of the hot and cold air. Velocities of the hot and cold air increase when the Re number increases and become maximum between the fins of the heat sinks. The velocities of the hot and cold air increase up to 10 m/s, 15 m/s, 20 m/s, 25 m/s, and 30 m/s, for Re numbers of 5600, 8400, 11200, 14000, and 16800, respectively. The increase in the velocity yields an increase in the heat transfer between the heat sinks and the fluids resulting a significant increase in hot air temperature and a significant decrease in cold air temperature. Velocity contours for the hot and cold air shows similar characteristics since the Re numbers, flow geometry, and flow parameters are the same for both fluids. The only variable which has a negligible effect on the velocity is the temperature of the hot and cold fluid.

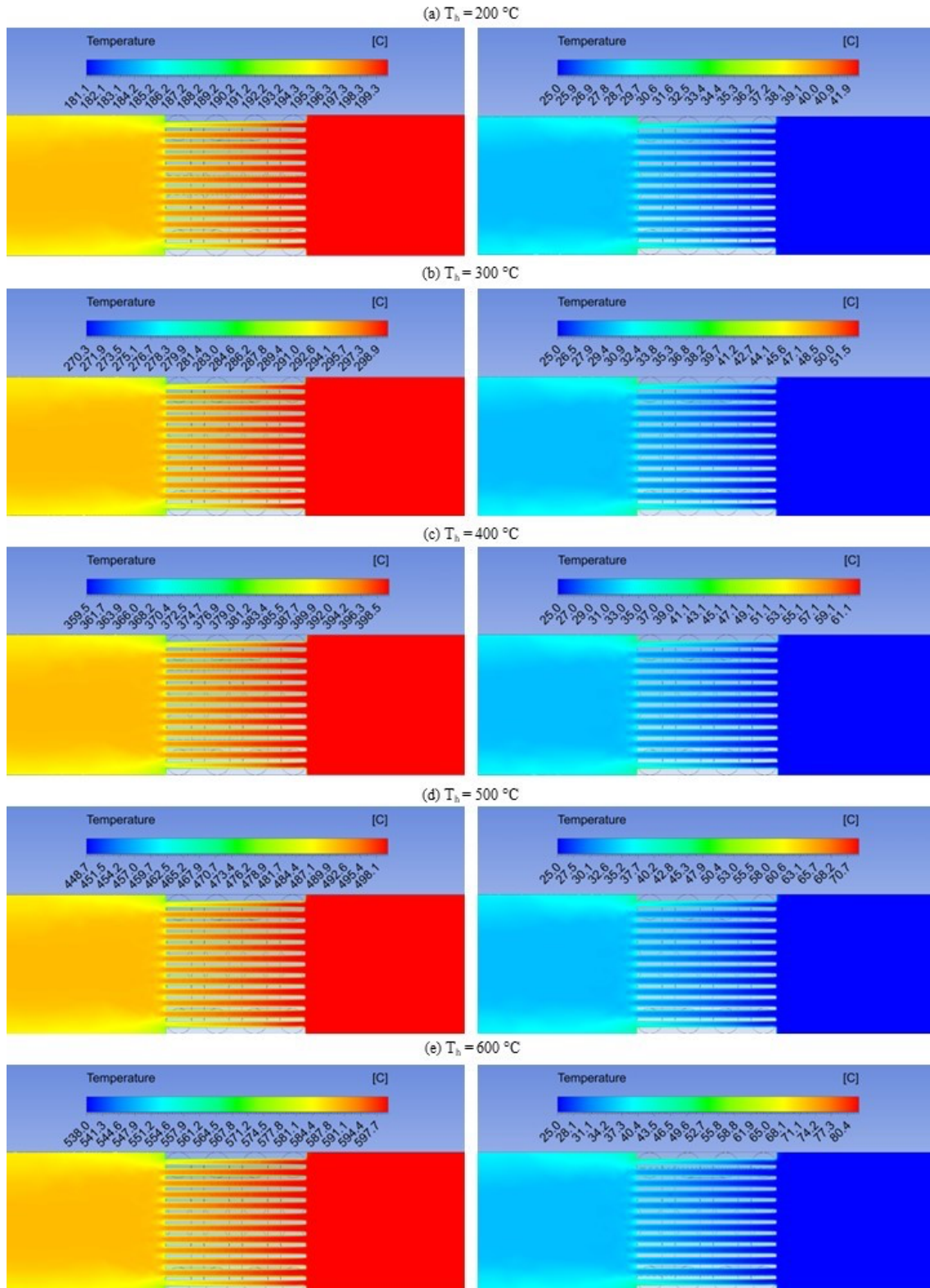


Figure 3. Temperature distribution in the hot and cold air for T_{hi} (a) $T_{hi} = 200 \text{ }^\circ\text{C}$ (b) $T_{hi} = 300 \text{ }^\circ\text{C}$ (c) $T_{hi} = 400 \text{ }^\circ\text{C}$ (d) $T_{hi} = 500 \text{ }^\circ\text{C}$ (e) $T_{hi} = 600 \text{ }^\circ\text{C}$.

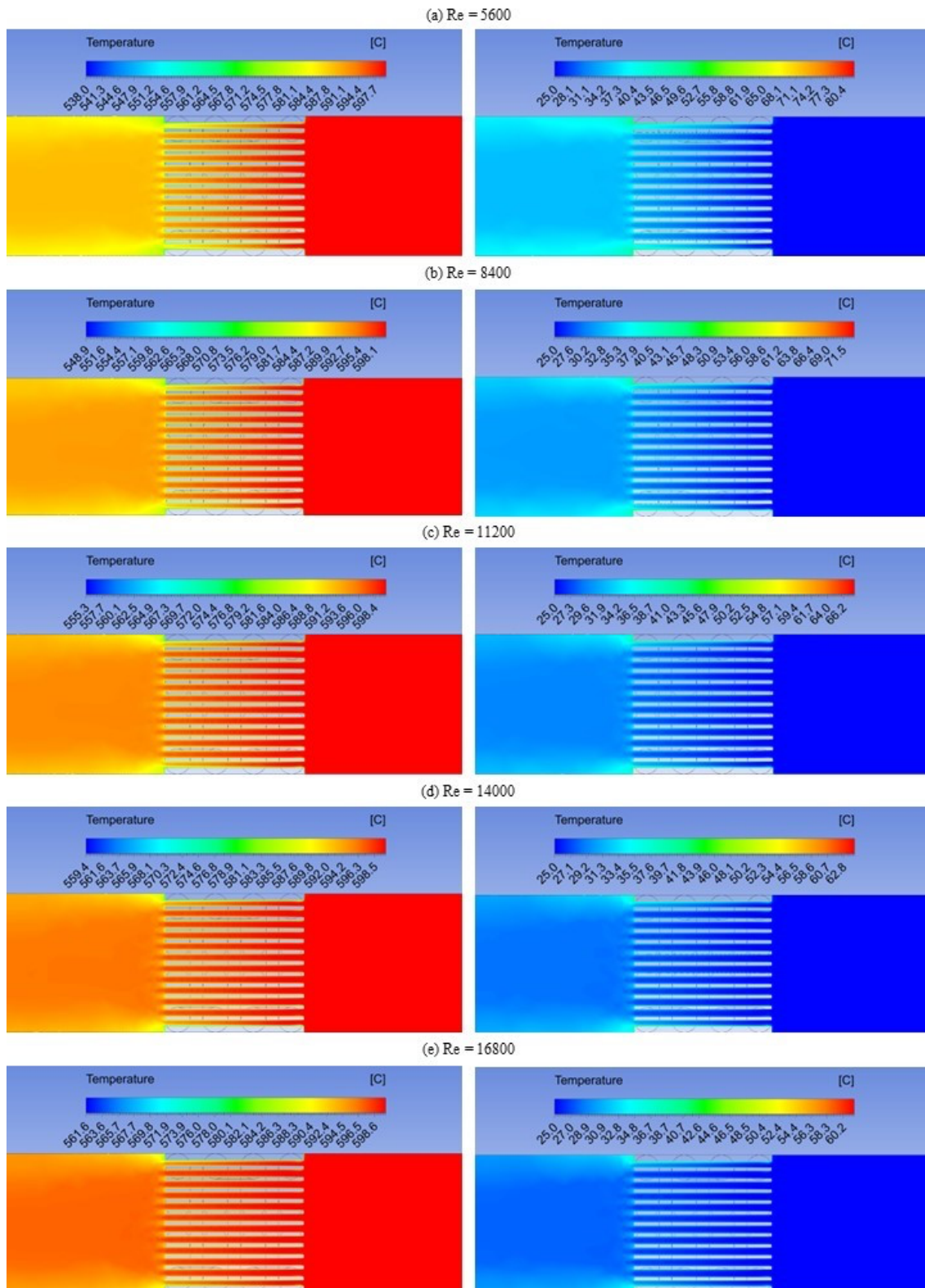


Figure 4. Temperature distribution in the hot and cold air for (a) $Re = 5600$ (b) $Re = 8400$ (c) $Re = 11200$ (d) $Re = 14000$ (e) $Re = 16800$.

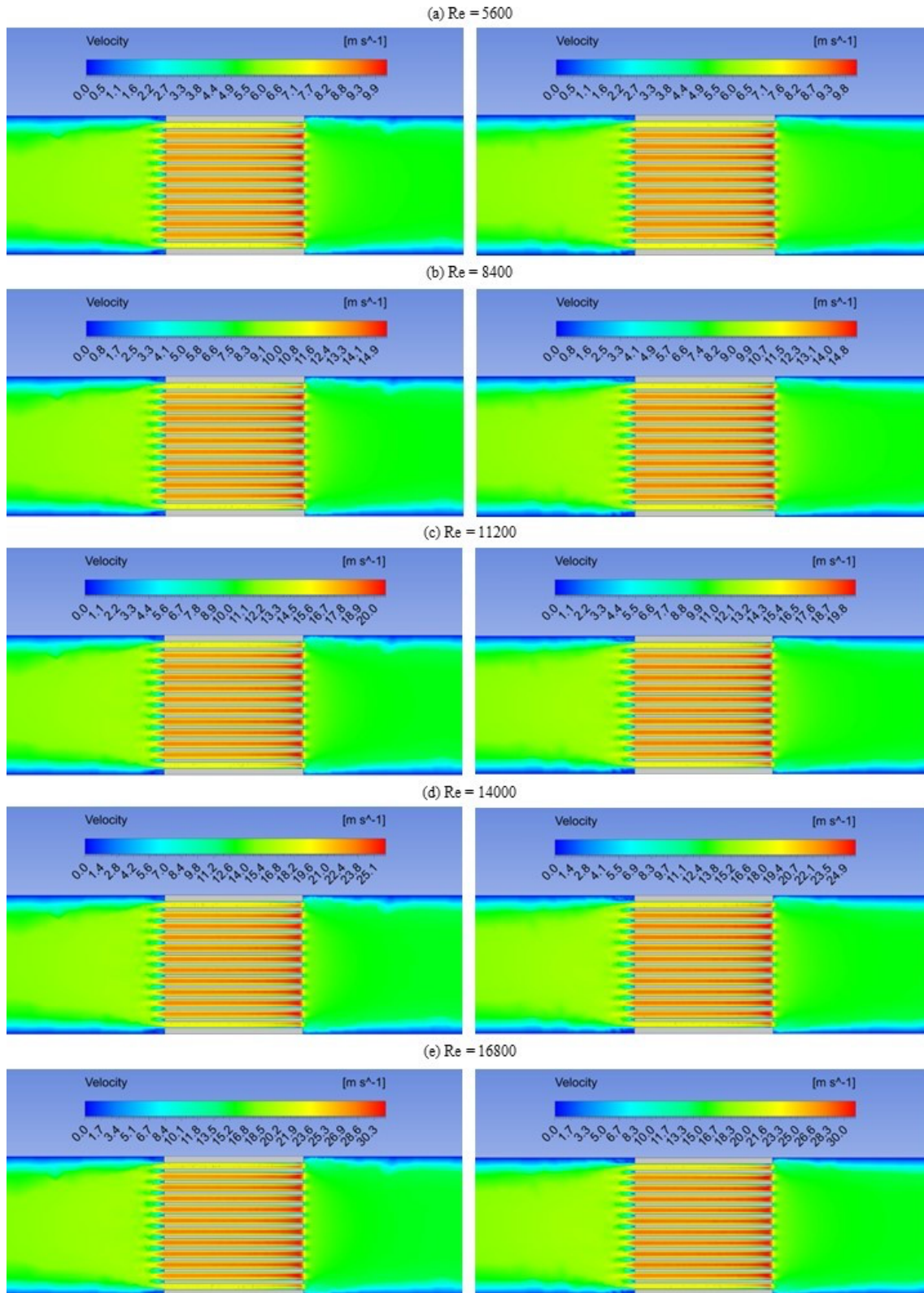


Figure 5. Velocity distribution in the hot (on the left) and cold air (on the right) for (a) $Re = 5600$ (b) $Re = 8400$ (c) $Re = 11200$ (d) $Re = 14000$ (e) $Re = 16800$.

3.3. Temperature Difference Between Hot and Cold Sides of the TEG (ΔT)

The performance of TEGs is directly related to the ΔT . To increase the ΔT , the hot side temperature (T_h) and cold side temperature (T_c) of the TEG are investigated with respect to different T_{hi} and Re number. Since the temperature of the waste heat sources differs in the industry, T_{hi} of 200 °C, 300 °C, 400 °C, 500 °C, and 600 °C are applied in the analyses to obtain the highest ΔT . After obtaining the highest ΔT for T_{hi} , the Re number of the flow is varied as 5600, 8400, 11200, 14000, and 16800 to increase the ΔT further. **Figure 6** and **Figure 7** illustrate the T_h , T_c , and ΔT concerning T_{hi} and Re number, respectively. It can be seen from both figures that T_h increases with increasing T_{hi} and Re numbers. However, T_c increases with increasing T_{hi} while decreases with increasing Re number. The reason for this behavior is the convection heat transfer between hot and cold air and the heat sink. While the temperature increase in T_{hi} directly affects the T_h , the increase in Re number affects the surface temperature indirectly, including other flow parameters. This effect results in the linear variation in T_h , T_c , and ΔT concerning T_{hi} , whereas polynomial variation is confirmed with respect to the Re number.

According to both figures, ΔT increased with increasing T_{hi} and Re numbers. It can be noted that the Re number is effective on the ΔT in addition to T_{hi} to increase the ΔT further. The increase in the Re number yields an increase in the Nu number and the convection heat transfer coefficient. According to the results, T_h values are obtained as 175.4 °C, 261.3 °C, 347.3 °C, 433.2 °C, and 519.2 °C, while ΔT values are obtained as 127.4 °C, 200.3 °C, 273.2 °C, 346.0 °C, and 418.9 °C for T_{hi} of 200 °C, 300 °C, 400 °C, 500 °C, and 600 °C, respectively. Meanwhile, T_c values are obtained as 519.2 °C, 532.6 °C, 540.6 °C, 546.0 °C, and 550.0 °C, while ΔT values are obtained as 418.9 °C, 444.6 °C, 459.9 °C, 470.4 °C, and 478.1 °C for Re number of 5600, 8400, 11200, 14000, and 16800, respectively. As a result, maximum T_h with respect to T_{hi} of 600 °C and Re number of 16800 is specified as 519.2 °C and 550.0 °C, respectively, while maximum ΔT is specified as 418.9 °C and 478.1 °C. According to the results, T_h of 550 °C is higher than the results of Kim et al [21]. In their study, the maximum hot side temperature increased to 229 °C where the number of fin was eight. T_h in this study is higher than the study of Kim et al. since the number of fins, geometrical dimensions and boundary conditions are different.

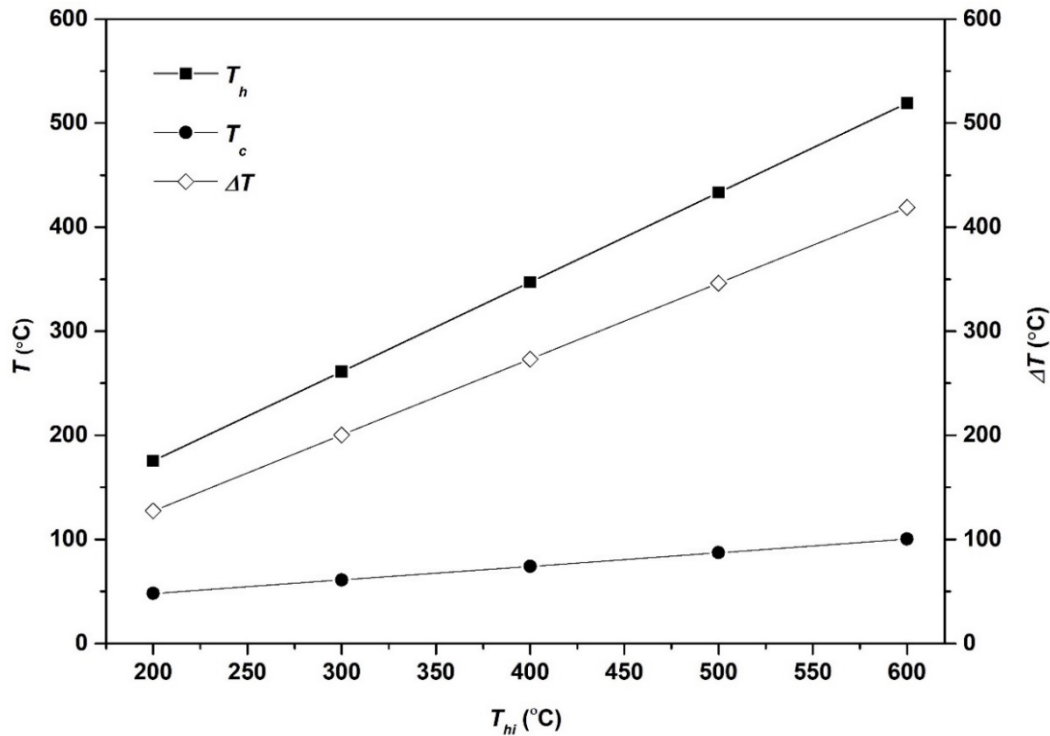


Figure 6. T_h , T_c , and ΔT of the TEG for T_{hi} .

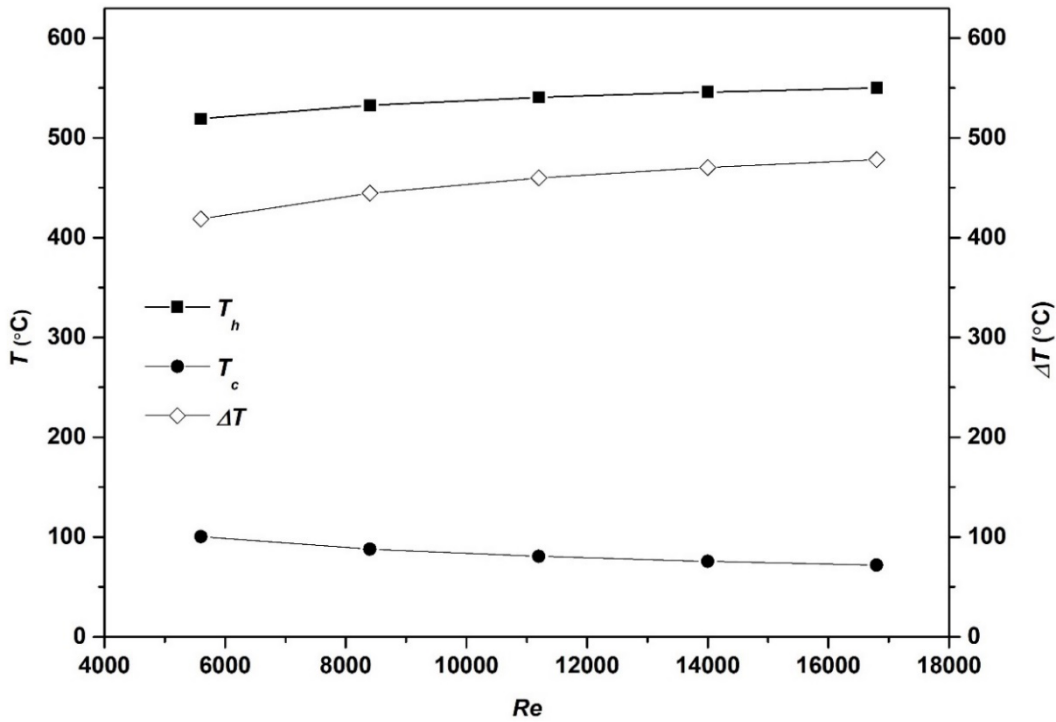


Figure 7. T_h , T_c , and ΔT of the TEG for Re number.

3.4. Heat Transfer Rate and Output Power of the TEG (\dot{q} , P)

Increasing \dot{q}_h and \dot{q}_c for the TEG means better heat transfer rates on two sides of the TEG and yields an increase in ΔT and the power generation performance of TEGs. In this study, \dot{q}_h and \dot{q}_c are investigated concerning different T_{hi} and Re numbers to increase the power generation performance of TEGs. Since the temperature of the waste heat sources differ in the industry, T_{hi} of 200 °C, 300 °C, 400 °C, 500 °C, and 600 °C are applied in the analyses to obtain the highest \dot{q}_h and \dot{q}_c . After varying T_{hi} and obtaining the highest \dot{q}_h and \dot{q}_c for T_{hi} , the Re number of the flow is varied as 5600, 8400, 11200, 14000, and 16800 to increase the \dot{q}_h and \dot{q}_c further. **Figure 8** and **Figure 9** illustrate the \dot{q}_h and \dot{q}_c with respect to T_{hi} and Re number, respectively. It can be seen from both figures that \dot{q}_h and \dot{q}_c increase with increasing T_{hi} and Re numbers. While the temperature increase in T_{hi} directly affects the \dot{q}_h and \dot{q}_c , the increase in Re number affects the \dot{q}_h and \dot{q}_c indirectly including other flow parameters. This effect results in the linear variation in \dot{q}_h and \dot{q}_c for T_{hi} , whereas polynomial variation is confirmed with respect to the Re number.

According to both figures, it can be noted that the Re number is effective on the \dot{q}_h and \dot{q}_c in addition to T_{hi} to further increase the \dot{q}_h and \dot{q}_c . The increase in the Re number yields an increase in the Nu number and the convection heat transfer coefficient. According to the results, \dot{q}_h values are obtained as 54.9 W, 86.2 W, 117.6 W, 149.0 W, and 180.4 W, while \dot{q}_c values are obtained as 51.2 W, 80.4 W, 109.6 W, 138.8 W, and 168.0 W for T_{hi} of 200 °C, 300 °C, 400 °C, 500 °C, and 600 °C, respectively. Meanwhile, \dot{q}_h values are obtained as 180.4 W, 191.1 W, 197.5 W, 201.8 W, and 205.1 W, while \dot{q}_c values are obtained as 168.0 W, 178.7 W, 185.1 W, 189.4 W, and 192.6 W for Re numbers of 5600, 8400, 11200, 14000, and 16800, respectively. As a result, maximum \dot{q}_h with respect to T_{hi} of 600 °C and Re number of 16800 are specified as 180.4 W and 205.1 W, respectively, while the maximum \dot{q}_c is specified as 168.0 W and 192.6 W. In this study, \dot{q}_h reached to the value of 192.6 W which is much higher than the study of Chen et al [20]. In their study, they obtained a lower \dot{q}_h of 85.85 W for the plate fins due to the difference in number of fins, geometrical dimensions, and boundary conditions.

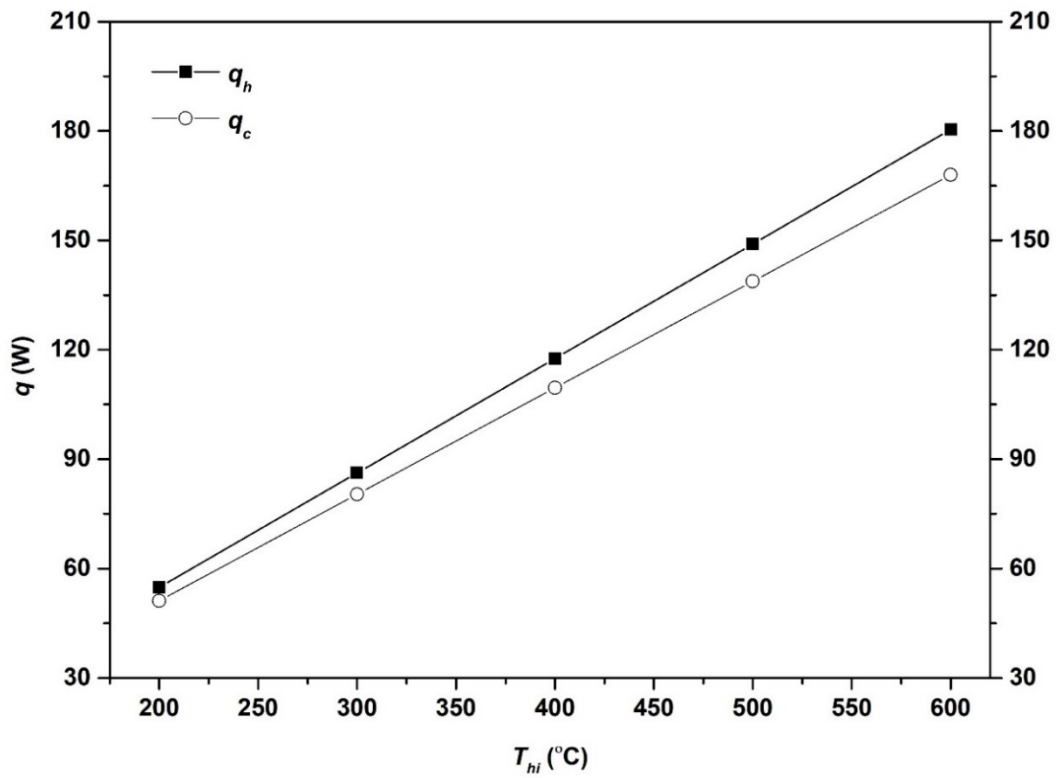


Figure 8. q_h and q_c with respect to T_{hi} .

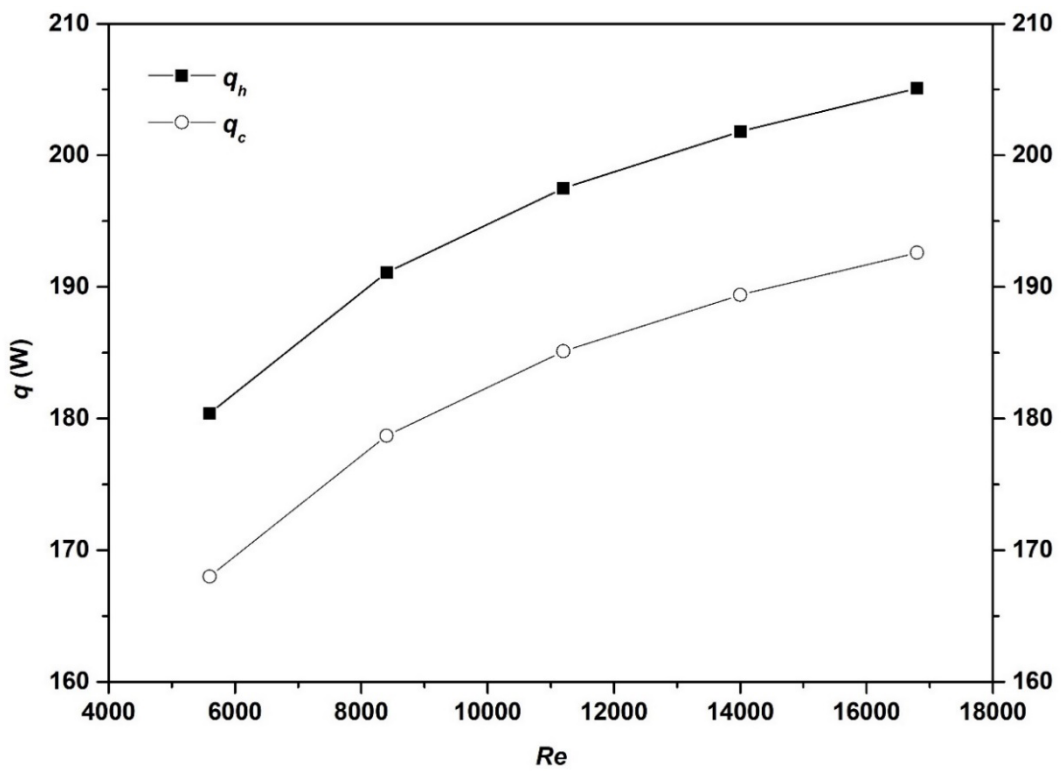


Figure 9. q_h and q_c with respect to the Re number.

Output power of the TEG is calculated using $P = (\dot{q}_h - \dot{q}_c) \chi A_{TEG}$ [20], where A_{TEG} is the total TE leg cross-sectional area of the TEG, and given in **Figure 10**. It can be seen from the figure that P of the TEG increase with increasing T_{hi} . According to the results, P values are obtained as 0.003 W, 0.005 W, 0.006 W, 0.008 W, and 0.010 W for T_{hi} of 200 °C, 300 °C, 400 °C, 500 °C, and 600 °C, respectively. As a result, maximum P with respect to T_{hi} of 600 °C is specified as 0.01 W. Since the A_{TEG} in this study is lower, P values of the TEG is lower. A_{TEG} should be increased by increasing TE leg cross-sectional area or using many pieces of TEGs to increase the output power.

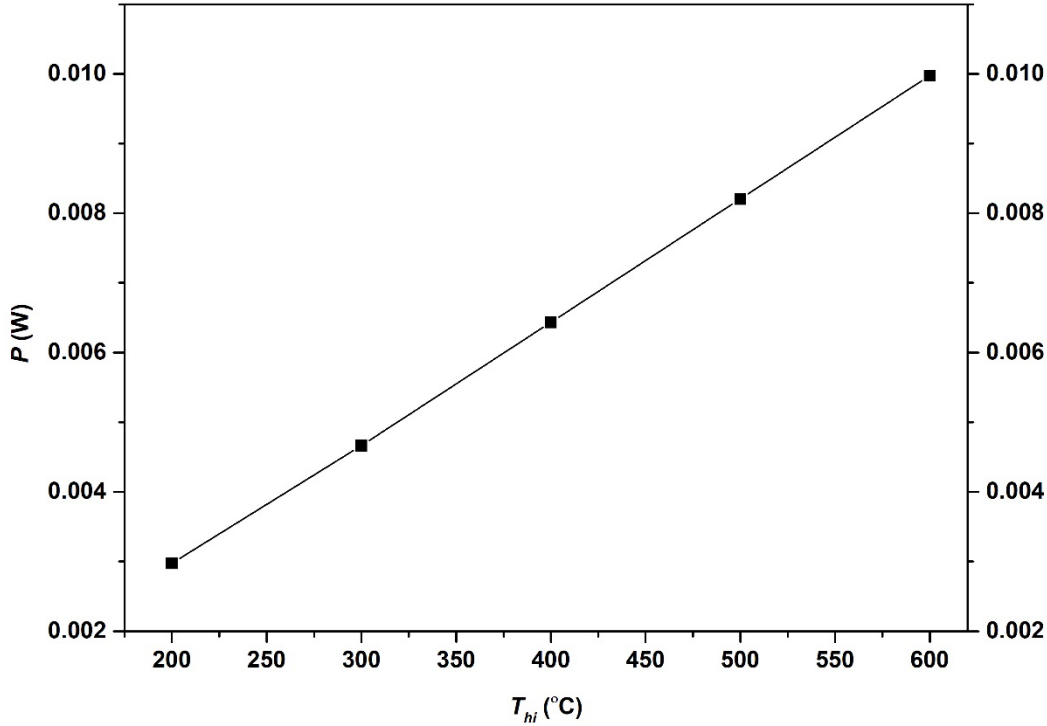


Figure 10. P with respect to T_{hi} .

3.5. Pressure Drop (ΔP)

It is important to calculate the ΔP , which occurs when a fluid flows through a flow system to specify additional power to manage the friction loss between the solid surfaces and the fluid. Increasing ΔP in TEG systems increases the net output power of the TEG systems. Within this respect, the ΔP between the inlet and outlet of the hot air is investigated concerning different Re numbers. In this study, Re numbers are varied as 5600, 8400, 11200, 14000, and 16800 to increase \dot{q}_h and \dot{q}_c and the ΔP results concerning Re numbers are illustrated in **Figure 11**. According to the figure, ΔP increases with increasing Re number in agree with the increase in the Nu number and the convection heat transfer coefficient. The increase in ΔP requires additional pumping power for the hot air. This situation originates from the increasing velocity of the hot air, which causes higher resistance losses. The variation in T_{hi} does not have a significant effect on the ΔP . As a result, the maximum and the minimum ΔP occur as 304.4 Pa and 36.7 Pa for the Re numbers of 5600 and 16800, respectively. When the ΔP is compared to the literature for the plate fin heat sinks, ΔP values are higher than the literature values [20–22]. Since the ΔP is calculated using $\Delta P = f \frac{L \rho V^2}{D 2g}$, the ΔP is directly related to the length (L) of the flow duct. In this study, ΔP values are higher than the literature values due to the length of the flow model. In addition, number of fins of this study is higher than the study of Kim et al. [21], which further increases the ΔP .

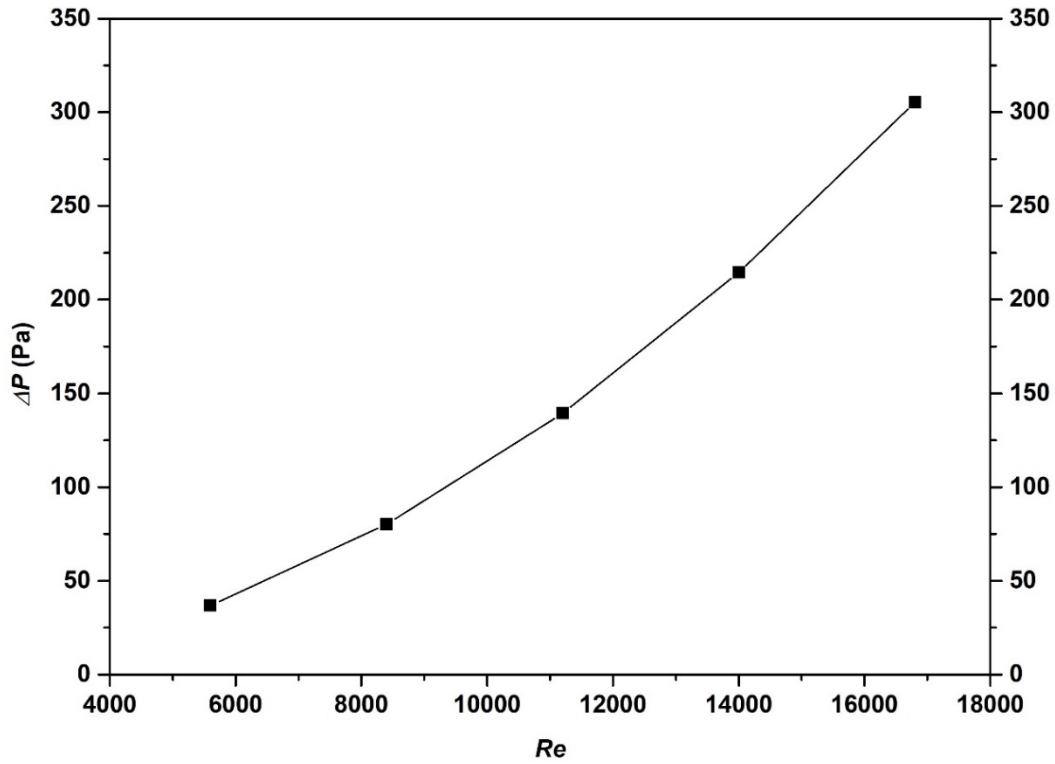


Figure 11. ΔP with respect to Re number.

T_h , T_c , ΔT , \dot{q}_h , \dot{q}_c , and ΔP of a TEG are evaluated as a result of CFD analyses to improve the output power of the TEG. The study's complete results are tabulated in **Table 2** and **Table 3** with respect to T_{hi} and Re number, respectively.

Table 2. T_h , T_c , ΔT , \dot{q}_h , and \dot{q}_c of the TEG with respect to T_{hi} .

T_{hi} [°C]	T_h [°C]	T_c [°C]	ΔT [°C]	\dot{q}_h [W]	\dot{q}_c [W]
200	175.4	48.0	127.4	54.9	51.2
300	261.3	61.0	200.3	86.2	80.4
400	347.3	74.1	273.2	117.6	109.6
500	433.2	87.2	346.0	149.0	138.8
600	519.2	100.3	418.9	180.4	168.0

Table 3. T_h , T_c , ΔT , \dot{q}_h , \dot{q}_c , and ΔP of the TEG with respect to Re .

Re	T_h [°C]	T_c [°C]	ΔT [°C]	\dot{q}_h [W]	\dot{q}_c [W]	ΔP
5600	519.2	100.3	418.9	180.4	168.0	36.8
8400	532.6	88.0	444.6	191.1	178.7	80.1
11200	540.6	80.7	459.9	197.5	185.1	139.4
14000	546.0	75.6	470.4	201.8	189.4	214.5
16800	550.0	71.9	478.1	205.1	192.6	305.3

4. Conclusion

Steady-state numerical heat transfer analyses on both sides of a TEG were conducted using CFD to improve the power generation performance. Effects of T_{hi} and Re numbers are investigated to increase ΔT , \dot{q}_h , \dot{q}_c , and ΔP of the TEG. T_{hi} is altered as 200 °C, 300 °C, 400 °C, 500 °C, and 600 °C, while the Re number for the hot and cold air is varied as 5600, 8400, 11200, 14000, and 16800. The TEG model consists as the TEG will be between two heat sinks through which hot and cold air flows as turbulent to recover the waste heat of the hot air. When the temperature distributions through the hot and cold air are investigated, T_{hi} decreases when the hot air flows through the heat sink, while T_{ci} increases when the cold air flows through the heat sink. As a result, temperature of the hot air at the outlet of the heat sink increased and reached to the value of 598 °C, while temperature of the cold air at the outlet of the heat sink decreased to 27 °C for $T_{hi} = 600$ °C and $Re = 16800$. When the velocity distributions in the hot and cold air are investigated, velocities of the hot and cold air increases when the Re number increases and become maximum between the fins of the heat sinks. The velocities of the hot and cold air increase up to 10 m/s, 15 m/s, 20 m/s, 25 m/s, and 30 m/s, for Re numbers of 5600, 8400, 11200, 14000, and 16800, respectively.

The results show that increasing T_{hi} and Re number yields an increase in ΔT , \dot{q}_h , and \dot{q}_c . Besides, ΔP between the inlet and outlet of the hot air increases with increasing Re number. In terms of investigating ΔT , maximum T_h with respect to T_{hi} of 600 °C and Re number of 16800 is specified as 519.2 °C and 550.0 °C, respectively, while maximum ΔT is specified as 418.9 °C and 478.1 °C. Considering \dot{q}_h , and \dot{q}_c , maximum \dot{q}_h with respect to T_{hi} of 600 °C and Re number of 16800 are specified as 180.4 W and 205.1 W, respectively, while the maximum \dot{q}_c is specified as 168.0 W and 192.6 W. As a result of ΔP analyses, the maximum and the minimum ΔP occur as 304.4 Pa and 36.7 Pa for the Re numbers of 5600 and 16800, respectively. To improve the heat transfer rate on the hot and cold sides of the TEG, future studies could focus on the optimization of the fin geometry and number of fins for the purpose of waste heat recovery applications.

Acknowledgments

E. K., responsible for the entire article (conceptualization, literature investigation, numerical analyses, interpretation of the results, writing, editing).

References

- [1] Erturun U, Erermis K, Mossi K. Influence of leg sizing and spacing on power generation and thermal stresses of thermoelectric devices. *Appl. Energy* 2015; 159: 19–27.
- [2] Ma Q, Fang H, Zhang M. Theoretical analysis and design optimization of thermoelectric generator. *Appl. Therm. Eng.* 2017; 127: 758–764.
- [3] Höglblom O, Andersson R. A simulation framework for prediction of thermoelectric generator system performance. *Appl. Energy* 2016; 180: 472–482.
- [4] Esarte J, Min G, Rowe DM. Modelling heat exchangers for thermoelectric generators. *J. Power Sources* 2001; 93: 72–76.
- [5] Erturun U, Mossi K. Thermoelectric devices with rotated and coaxial leg configurations: Numerical analysis of performance. *Appl. Therm. Eng.* 2015; 85: 304–312.
- [6] Huang K, Li B, Yan Y, Li Y, Twaha S, Zhu J. A comprehensive study on a novel concentric cylindrical thermoelectric power generation system. *Appl. Therm. Eng.* 2017; 117: 501–510.
- [7] Liao M, He Z, Jiang C, Fan X, Li Y, Qi F. A three-dimensional model for thermoelectric generator and the influence of Peltier effect on the performance and heat transfer. *Appl. Therm. Eng.* 2018; 133: 493–500.
- [8] Lee H, Sharp J, Stokes D, Pearson M, Priya S. Modeling and analysis of the effect of thermal losses on thermoelectric generator performance using effective properties. *Appl. Energy* 2018; 211: 987–996.
- [9] Li W, Paul MC, Montecucco A, Siviter J, Knox AR, Sweet T, Gao M, Baig H, et al. Multiphysics simulations of thermoelectric generator modules with cold and hot blocks and effects of some factors. *Case Stud. Therm. Eng.* 2017; 10: 63–72.
- [10] Miao Z, Meng X, Zhou S, Zhu M. Investigation for power generation based on single-vertex movement of thermoelectric module. *Sustainable Cities Soc.* 2020; 53: 101929.
- [11] Nour Eddine A, Chalet D, Faure X, Aixala L, Chessé P. Optimization and characterization of a thermoelectric generator prototype for marine engine application. *Energy* 2018; 143: 682–695.
- [12] Nour Eddine A, Sara H, Chalet D, Faure X, Aixala L, Cormerais M. Modeling and simulation of a thermoelectric generator using bismuth telluride for waste heat recovery in automotive diesel engines. *J. Electron. Mater.* 2019; 48 (4): 2036–2045.
- [13] Gürbüz H, Akçay H, Topalçı Ü. Experimental investigation of a novel thermoelectric generator design for exhaust waste

- heat recovery in a gas-fueled SI engine. *Appl. Therm. Eng.* 2022; 216 (March): 119122.
- [14] Topalçı Ü, Gürbüz H, Akçay H, Demirtürk S. Buji Ateşlemeli Bir Motorda Egzoz Atık Isı Geri Kazanımı İçin Termoelektrik Jeneratör Modelinin Geliştirilmesi. *Mühendislik Bilimleri ve Tasarım Dergisi* 2020; 8 (2): 582–596.
- [15] Kunt MA, Gunes H. An experimental study on design and performance of a waste heat recovery system with a thermoelectric generator to be used in exhaust systems of motorcycle engines. *Proceedings of the Institution of Mechanical Engineers, Part E: J. Process Mech. Eng.* 2021; 236 (3): 779–789.
- [16] Schwurack R, Unz S, Beckmann M. The Importance of considering parasitic heat losses when modeling teg performance for high-temperature applications. *J. Electron. Mater.* 2019; 48 (4): 1917–1925.
- [17] Akçay H, Gürbüz H, Demirtürk S, Topalçı Ü. Tipik Bir Buji Ateşlemeli Motorda Egzoz Atık Isısı Enerjisinin Geri Kazanımı İçin Geliştirilen Termoelektrik Jeneratörün HAD Analizi. *El-Cezeri Fen ve Mühendislik Dergisi* 2020; (3): 1088–1100.
- [18] Ökmen AB, Gürbüz H. CFD analysis of optimum exhaust heat exchanger arrangement in thermoelectric generator designed for exhaust waste heat recovery of spark ignition engine. *El-Cezeri J. Sci. Eng.* 2021; 8 (2): 1060–1080.
- [19] Wang Y, Dai C, Wang S. Theoretical analysis of a thermoelectric generator using exhaust gas of vehicles as heat source. *Appl. Energy* 2013; 112: 1171–1180.
- [20] Chen WH, Wang CM, Huat Saw L, Hoang AT, Bandala AA. Performance evaluation and improvement of thermoelectric generators (TEG): Fin installation and compromise optimization. *Energ. Convers. Manage.* 2021; 250 (October): 114858.
- [21] Kim TY, Lee S, Lee J. Fabrication of thermoelectric modules and heat transfer analysis on internal plate fin structures of a thermoelectric generator. *Energ. Convers. Manage.* 2016; 124: 470–479.
- [22] Zhou F, Catton I. Numerical evaluation of flow and heat transfer in plate-pin fin heat sinks with various pin cross-sections. *Numer. Heat Tr. A-Appl.* 2011; 60 (2): 107–128.

Measurement of Ultraviolet Light Transmittance of Different Contact Lens Types

Ahmet BARLIK¹, Gonca ATEŞ^{2*}

^{1,2} Department of Opticianry, Vocational School of Health Service, Sırnak University, Şırnak, Türkiye

¹ahmet.barlik2@gmail.com.tr, ^{2*}gates@sirnak.edu.tr

(Geliş/Received: 14/06/2023;

Kabul/Accepted: 17/08/2023)

Abstract: Scientific evidence showing the harmful effects of ultraviolet radiation on different ocular tissues has led manufacturers to incorporate UV-blocking monomers into contact lenses. In this study, the spectral and optical properties of contact lenses were analyzed in the ultraviolet and visible light wavelength ranges using the JASCO V-730 UV/Vis spectrophotometer device. The results obtained showed that the light transmittance in the wavelength (550nm) range to which the human eye is most sensitive in the lens samples examined was over 70 % and that B contact lens had a maximum value of 72,98 %. The largest cutting-edge wavelength value was obtained in the A contact lens as 376 nm. At 550 nm, the absorption spectra were found to be below 0.12. In terms of visual quality, visible light transmittance is expected to be high and ultraviolet alight transmittance is expected to be minimal. The degree of damage caused by the amount of ultraviolet light absorption increases. Among the contact lenses with and without ultraviolet-protected monomers, lens A did not transmit the UV-B wavelength region, while lens B transmitted UV-A and UV-B wavelengths. This result showed that the protection of lens A was higher. It is seen that the UV transmittance taken with the phocometer is 45% UV in A lens and 91% UV in B lens. The results obtained by UV/Vis spectrophotometer and phocometer supported each other. The results will contribute to the literature by revealing the importance of UV-protected monomer-containing contact lenses in vision equipment, and by enabling the development and selection of full-protection contact lenses.

Key words: Contact lens, eye health, UV radiation, light transmission.

Farklı Türden Kontak Lenslerin Ultraviyole Işık Geçirgenliğinin Ölçülmesi

Öz: Ultraviyole radyasyonun farklı oküler dokular üzerinde zararlı etkilerini gösteren bilimsel kanıtlar üreticileri UV bloke edici monomerleri kontak lenslere dâhil etmeye yönlendirmiştir. Bu araştırmada, kontak lenslerin spektral ve optik özellikleri ultraviyole ve görünür ışık dalga boyu aralıklarında JASCO V-730 UV/Vis spektrofotometre cihazı kullanılarak analiz edildi. Elde edilen sonuçlar incelenen kontak lens örneklerinde insan gözünün en duyarlı olduğu dalga boyu (550 nm) aralığında ışık geçirgenliğinin %70'nin üzerinde olduğunu ve maksimum değere %72,98 olarak B kontak lensin sahip olduğunu gösterdi. En büyük kesme kenarı dalga boyu değeri A kontak lensinde 376 nm olarak elde edildi. 550 nm'de soğurma spektrumlarının ise 0.12 altında olduğu bulundu. Görme kalitesi açısından görünür ışık geçirgenliğinin yüksek olması, ultraviyole ışık geçirgenliğinin minimum olması beklenir. Ultraviyole korumalı monomer içeren ve içermeyen kontak lenslerden A lensinin UV-B dalga boyu bölgesini geçirmediği, B lensinin ise UV-A ve UV-B dalga boylarını geçirdiği görüldü. Bu sonuç A lensinin korumasının daha yüksek olduğunu gösterdi. Fokometre ile alınan UV geçirgenlikleri A lensinde %45, B lensinde %91 olarak görülmektedir. UV/Vis spektrofotometre ile fokometreden alınan sonuçlar birbirini destekledi. Sonuçlar, görme gereçlerinde UV korumalı monomer içerikli kontak lenslerin önemini ortaya çıkararak, tam korumalı kontak lenslerin geliştirilmesini ve seçilmesini sağlayarak literatüre katkı sağlayacaktır.

Anahtar kelimeler: Kontak lens, göz sağlığı, UV radyasyon, ışık geçirgenliği

1. Introduction

According to TUIK 2021 [1] data, it is stated that the use of glasses or lenses has increased by 2.6% and the number of individuals blind increased by 0.3%. This situation has led manufacturers to increase the number of contact lenses. The development of contact lenses has been researched by scientists for centuries. Silicone hydrogel contact lenses, hard contact lenses, soft hydrogel contact lenses, and today, hydrogel lenses with high oxygen permeability have been used chronologically by adding silicon with high oxygen permeability, methacrylic acid for wettability, and methyl methacrylate for optical properties [2,3]. Contact lenses are basically divided into soft and hard. Soft contact lenses have high water content, high oxygen permeability and can remain stable in the cornea due to their diameter width, have a short adaptation time and do not cause blurred glasses, photophobia and glare. Soft contact lenses are used in the structure of HEMA (2-hydroxyethyl methacrylate), MMA (methacrylate acid), MMA (methyl methacrylate), GMA (glycerin methacrylate). Hard contact lenses, on the other hand, are

* Corresponding author: gates@sirnak.edu.tr. ORCID Number of authors: ¹ 0000-0002-6123-368X, ² 0009-0001-5077-6240

lightweight, durable, transparent, but have a long adaptation time and low water content. It is not preferred because it causes hypoxia [4-6]. Contact lenses affect the structure of the cornea because they create a hypoxic environment. Therefore, it was tried to minimize the hypoxic effect by adding silicone with high oxygen permeability to soft lenses. Therefore, soft contact lenses are largely preferred as visual aids [3-4,7]. Contact lenses are expected to have good parameters such as light transmission and ultraviolet light protection and correction of eye defects. According to the American National Standards Institute, lenses with Ultraviolet (UV) blocking absorb 95% of UVB and 70% of UVA, while lenses without UV blocking transmit 90% of the UV spectrum [8]. Looking at the literature UV-blocking lenses obtained by adding UV-absorbing monomer to soft contact lenses [9] have been shown to reduce the amount of UV light coming into the eye and protect against damage caused by UV in ocular tissues [10-13]. Soft contact lenses provide more protection than hard contact lenses because they completely cover the cornea and conjunctiva [8].

In order to protect the eye against ultraviolet radiation, contact lenses are preferred as well as UV protection glasses. Although UV-blocking glasses provide good protection, UV light is reflected when the sun is overhead, as the eyebrow is blocked by the eyelid, but about 98% of the light is absorbed when the light comes parallel to the eye. Light cannot provide full protection to the eye due to reflection from the back of the lenses due to the temporal and upper parts [14]. UV blocking lenses effectively protect the eye when glasses are insufficient. The phenomenon of vision occurs when light falls on the photoreceptor cone and rod cells located in the macular region of the retina. The wavelength of visible light to which the human eye is sensitive is between 400-700 nm [15]. The light transmission of a good contact lens is expected to be very high in this range, and the maximum vision corresponds to a wavelength of 550 nm. Contact lenses must exhibit maximum light transmittance at these wavelengths [16].

Ultraviolet light makes up 5% of the electromagnetic radiation energy from the sun reaching the earth's surface. Ultraviolet (UV) is an electromagnetic radiation ranging in wavelengths of light (100-400 nm). The UV Radiation spectrum is divided into three bands according to the wavelength. UVA (320-400 nm), UVB (280-320 nm), UVC (100-280 nm) [17]. Although UVC is retained by the ozone layer, recently due to the thinning of the ozone layer, short-wavelength electromagnetic radiation reaching the earth has been increasing [18]. The eye is a complex dioptric system and the light coming into the eye is absorbed or transmitted in the refractive environment of the eye in the cornea, aqueous fluid, lens and vitreous fluid. The cornea is the transparent layer located in the anterior part of the eyeball and is the first barrier to absorb all wavelengths shorter than 295 nm. The second barrier is the crystalline lens, which absorbs all of the UVB and most of the UVA, but wavelengths of 400 nm and above are not absorbed by the cornea and lens. Although the effect of UV on the skin is known by 85% of the population, only 7% of the population is aware of its effect on the eye [19]. The damage caused by UV radiation to the lens of the eye, which is a radiosensitive tissue, determines the intensity of the light and the wavelength received by the ocular tissues [20,30]. Since UV light has more energy than visible light, it acts more on ocular tissues [21]. Long-term exposure to UV causes cataracts, pterygium, photokeratitis in the human eye [22,23] and has been expressed in experimental studies [8,14,24-25]. Our eyes are exposed to UV every day, causing damage to ocular tissues that can accumulate over a lifetime [16] UV blocking contact lenses have increased in importance as the treatment of ocular diseases increases health care costs.

In this study, UV/VIS spectrophotometer and photometer devices were used to measure the UV absorption and transmittance of different types of contact lenses. Measurements were taken and data on the permeation and absorption spectra were plotted using OriginPro-8 software. The data were compared with the standards in the literature and a different perspective was brought to contact lenses for our eye health.

2. Material and Method

Due to its chemical structure, composition, light structure, high water content, short adaptation time and low hypoxic, many types of soft contact lenses widely used in the optical industry are available on the market. The soft contact lenses used in this study belong to different companies and the necessary information for the lenses is given in Table 1. In Table 1, the samples A, B represent two different firms. For the absorption and permeability measurements including the visible region of different soft contact lenses that the user may prefer, the JASCO V-730 UV/Vis Dual Beam Spectrophotometer device, shown in Figure 1 and located in Şırnak University Technology and Research Center Laboratory, was used. The number of photons transmitted from the contact lenses and the absorption of light according to the material properties are explained by the Beer-Lambert law [31]. After the contact lens was removed from the blister pack, it was placed in the lens holder compartment with the convex side facing the scan beam. The spectrum was chosen, which allowed absorption and transmission measurements to be made continuously as the wavelength changed. In this study, the permeability and absorption spectra of soft

contact lenses used in visual aids were measured by UV/Vis spectroscopy. For all the results, relevant graphs were drawn using the OriginPro-8 software.

Table 1. Some parameters for contact lenses used.

Lenses	Materials	Diameter (mm)	UV Protection	Coating Type	Thickness (mm)	Power of Lens (D)
A	Senofilcon A	14.3	Yes	8.5	0.07	-5.00
B	Lotrafilcon B	14.2	No	8.5	0.08	-5.00

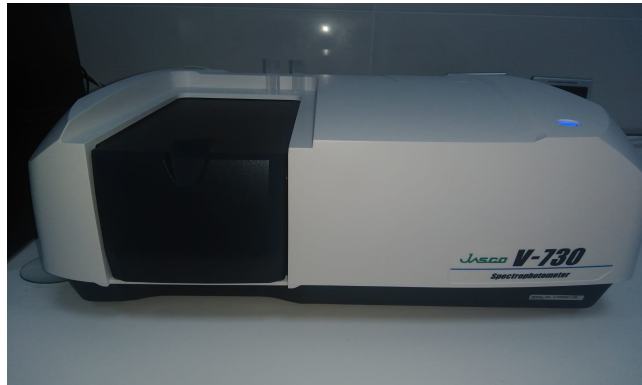


Figure 1. The JASCO V-730 UV/Vis dual beam spectrophotometer device.

The UV transmittance of contact lenses with Table 1 specifications from different companies was also measured with the TUSCONY brand digital phocometer in Şırnak University Optician Laboratory. The phocometer is an optical device used to determine the spherical and cylindrical diopters of spectacle lenses, the axes of cylindrical lenses, the diopters of contact lenses and UV transmittances. By selecting the UV measurement mode of the digital phocometer for the measurement, its display switched to the UV measuring mode. The contact lens was placed on the meter. We based the measurement on two different environments because it was measured in light and dark environments, considering that the light from the surroundings could affect the UV transmittance of the lens. When we look at the values measured in the bright environment with the digital phocometer, the UV transmittance value of the A lens was as 45% and the UV transmittance value of the B lens as 91% in Figure 2. When the same process was measured in a dark environment, the transmittance values for both lenses decreased at %3.

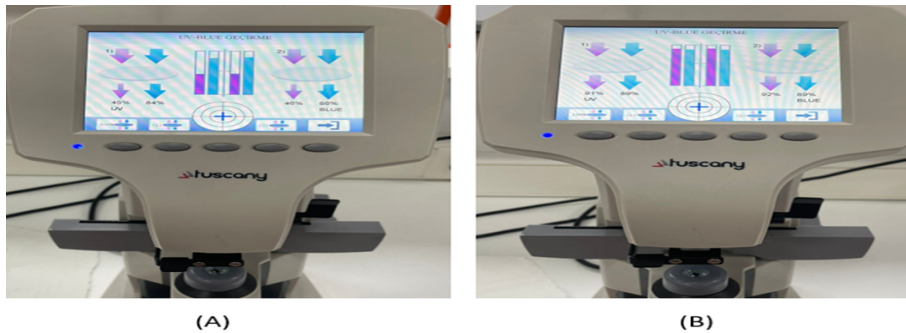


Figure 2. UV Transmittance of TUSCONY brand phocometer and A and B contact lenses.

3. Results and Discussion

Many types of contact lenses offered by optical companies are available on the market. In this study, absorption and transmittance measurements were made using UV/Vis Dual Beam Spectrophotometer device to investigate the optical properties of contact lenses (A, B) whose properties are given in Table 1. When the measurements were made, the wavelength was taken in the range of 200-800 nm.

In a study conducted in 2000, Harris et al measured the transmittance of different types of contact lenses. As a result of the measurement, they found that the UV transmittance of lenses containing UV-protective monomers experimentally decreased [27]. In studies on the effect of other parameters on the UV transmittance of contact lenses, it has been shown that the diopter power and center thickness of the lenses affect the level of UV protection [34]. Faubl and Quinn at study in 2000, stated that contact lenses with thin center thickness absorb less UV radiation than thick contact lenses [35]. In addition, Ateş and Bilici (2022) and K. Mutlu and Ekem (2021) found in their studies on lenses that as the center thickness increases, the absorbance increases and the UV transmittance decreases [17,36]. In the study, when interpreting the UV transmittance of contact lenses, it was not included in the interpretation because the diopter was the same and the center thickness was approximately the same. In addition, the interpretation of the graphics is based on the American National Standards Institute (ANSI Z80.20-2016) [32]. UV transmittance values for ANSI sunglasses are attached to contact lenses. With standard values, it can block 95% of UV-B and 70% of UV-A [28, 29].

UV light and visible light are electromagnetic waves. For the UV protective A contact lens, the graph in Figure 3 shows that it has no transmittance in the UV-B range and has a peak at 260 nm, with 5.66% of it. We see that the amplitude consumed to deplete the UV-A range is low and the transmittance continues to increase from 370 nm. It seems to meet ANSI Z80.20-2016 version. From 370 nm the capture amplitude started to increase and again at 730 nm there was a decrease. The maximum visibility in a good contact lens corresponds to a wavelength of 550 nm, and light expectation is expected to be very high in this range. The light transmittance at 550 nm is 71.87%, with a maximum value of 75.75% in the visible wavelength range.

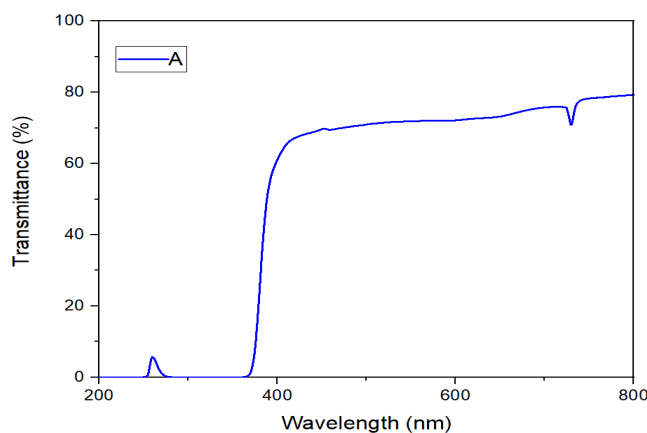


Figure 3. Wavelength versus transmittance plot for lens A.

When the graph in Figure 4 of the B contact lens without UV protection is examined, it is seen that the permeability increases from 241 nm and the permeability is present in the UV-B and UV-A ranges. We see that the UV-B range starts with 40% and ends with 55%, while the UV-A range ends with 62%. There seems to be a reduction of 730 nm, as in the A lens. The wavelength to which the human eye is most sensitive is 72.98% at 550 nm. It is seen that the permeability increases in the visible light region and the maximum transmittance value is 75.05%. B lens is more transparent to visible light.

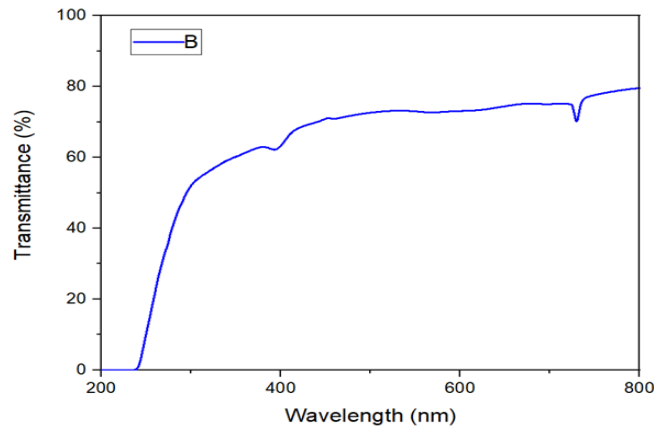


Figure 4. Wavelength versus transmittance plot for lens B.

Since UV light absorption affects the optical and mechanical properties of lens materials, the absorbance value graphs against the wavelength of different lenses A and B are given in Figure 5 and Figure 6. The absorbance of A lens in the UV region range absorbs more than the UV range of B lens than its region. It is seen that B lens passes through UV-A and UV-B wavelengths and the absorbance of both contact lenses in the visible region is very low.

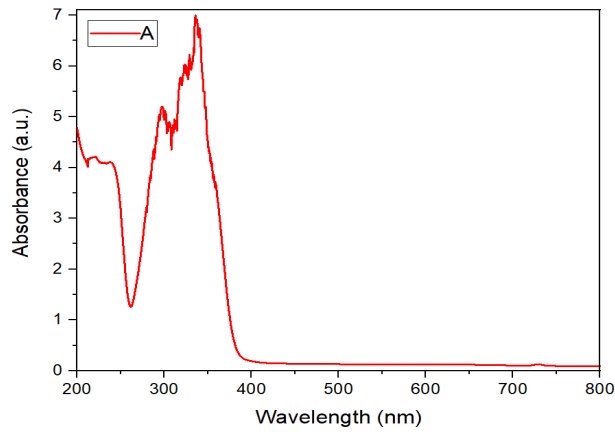


Figure 5. Wavelength versus absorbance plot for lens A.

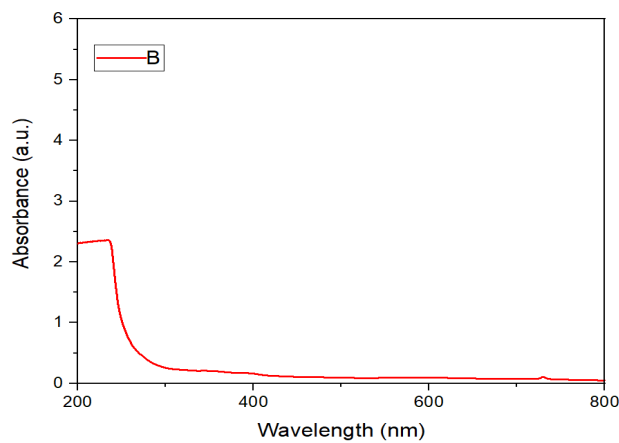


Figure 6. Wavelength versus absorbance plot for lens B.

4. Conclusion

In the electromagnetic spectrum, the wavelength range of UV (100-400 nm) corresponds to the wavelength range of visible light (400-700 nm). The cornea of the human eye shows transparency to light with high permeability and allows light to pass through the ocular tissues and reach the retina. The retina contains sensitive cells that are stimulated by sunlight, and in the retina the optical quality of the image depends on the incoming light. For eye health and quality vision, contact lenses should have low UV transmittance and high visible light transmittance. At the wavelength to which the human eye is most sensitive (550 nm), contact lenses should show maximum light transmission. When we look at the transmittance of two different contact lenses, we see that the A contact lens has no transmittance in the UV-B wavelength range, with a transmittance peak of 5.66% at 260 nm. In B contact lenses, the UV transmittance starts from 241 nm and increases to a maximum of 62% in the UV-A region and a maximum of 55% in the UV-B region. In the visible region (~550 nm), lens A is 71.87%, while lens B is 72.98%. When we look at the UV transmittance values with the phocometer device, the A contact lens passes 45% and the B contact lens passes 91%. Looking at the measurement results taken from different devices, the results supported each other. The absorbance graphs show that the UV wavelength range B contact lens has low absorbance, while A contact lens also has high absorbance. The low absorbance is interpreted as the beginning of light transmission, that is, the transition of the valence electrons of the incident photon to the conduction band [38]. Considering all these results, we can say that A contact lens has less UV transmittance and higher absorbance value than B contact lens, and A lens can provide better protection for our eye health. In addition, lens A had a transmittance of 5.66% in the UV region, and it was stated in the literature that UV transmittance could be seen even if lenses that completely block radiation were worn. Lens A fulfills the requirement for contact lenses specified by International ANSI Z80.20-2016, while lens B does not. The cut-off value in the absorbance plots represents the wavelength at which absorbance ends and transmission begins. The cut-off value of the A lens corresponds to 376 nm, and the cut-off value of the B lens corresponds to 252 nm. The higher the cut-off value, the higher the protection and we can say that the A contact lens provides better protection. Light and dark environments were selected while measuring in the phocometer. The aim was to determine whether the light coming from different angles had an effect on the UV transmittance. Since the lights coming from different angles are blocked in the dark environment, the UV transmittance value of both contact lenses decreased by 3% compared to the bright environment. The results show that the light intensity of the environment affects the UV transmittance. Considering all these data and comments, it is tried to express whether the contact lenses available in the market provide UV protection, and if so, how much they provide and to contribute to the literature.

Acknowledgements

The application numbered 1919B012210596 within the scope of the 2209-A University Students Research Projects Support Program, carried out by the TÜBİTAK Scientist Support Programs Presidency (BİDEB) in the 1st term of 2022, was entitled to receive support. We would like to thank Şırnak University for enabling the use of the Technology and Research Center Laboratory in the spectral analysis of contact lenses with the UV/Vis Spectrophotometer device in the project titled "Measurement of UV Light Transmittance of Different Types of Contact Lenses".

References

- [1] Concepcion-Grande P, González A, Chamorro E, Miguel Cleva J, Alonso J, Gómez-Pedrero JA. Eye movements as a predictor of preference for progressive power lenses. *J Eye Mov Res* 2022; 15(2): 1-14
- [2] Dillehay SM. Does the level of available oxygen impact comfort in contact lens wear? A review of the literature. *Eye Cont Lens* 2007; 33(3):148-155.
- [3] Karadağ AS, Bağdaş M, Bilen A, Önder F. Demographic data of patients using contact lenses. *Acta Med Nicomedia* 2021; 4(1): 1-3.
- [4] Podskochoy A. Protective role of corneal epithelium against ultraviolet radiation damage. *Acta Ophthalmologica Scandinavica* 2004; 82(6): 714-717
- [5] Kanpolat A. Contact Lenses: Past, Present, Future. *Türkiye Klinikleri J Ophthalmol-Special Topics* 2008; 1(1):1-13.
- [6] Efron N, Morgan PB, Nichols JJ, Walsh K, Willcox MD, Wolffsohn JS, Jones LW. All soft contact lenses are not created equal. *Cont Lens Anterior Eye* 2022; 45(2): 1-10
- [7] McCanna DJ, Driot JY, Hartsook R, Ward KW. Rabbit models of contact lens-associated corneal hypoxia: a review of the literature. *Eye Cont Lens* 2008; 34(3): 160-165.

- [8] Bergmanson J, Söderberg P. The significance of ultraviolet radiation for eye diseases: a review with comments on the efficacy of UV-blocking contact lenses. *Ophthalmic Physiol Opt* 1995;15(2): 83-91.
- [9] Quesnel NM, Simonet P. Spectral transmittance of UV-absorbing soft and rigid gas permeable contact lenses. *Optom Vis Sci* 1995; 72(1): 2-10.
- [10] Ringvold A. Corneal epithelium and UV-protection of the eye. *Acta Ophthalmol Scand* 1998; 76(2): 149-153.
- [11] Ayala MN, Michael R, Söderberg PG. Influence of exposure time for UV radiation-induced cataract. *Invest Ophthalmol Vis Sci* 2000; 41(11): 3539-3543.
- [12] Merriam JC, Löfgren S, Michael R, Söderberg P, Dillon J, Zheng L, Ayala M. An action spectrum for UV-B radiation and the rat lens. *Invest Ophthalmol Vis Sci* 2000; 41(9): 2642-2647.
- [13] Bergmanson JP, Pitts DG, Chu LW. Protection against UVR using the Vistakon UV-bloc soft contact lens. *Acta Ophthalmol (Copenk)* 1987; 14(1): 279-286.
- [14] Bergmanson JP, Sheldon TM. Ultraviolet radiation revisited. *Eye Cont Lens* 1997; 23(3): 196-204.
- [15] Coroneo M. Ultraviolet radiation and the anterior eye. *Eye Cont Lens* 2011; 37(4): 214-224.
- [16] Lai CF, Li JS, Fang YT, Chien CJ, Lee CH. UV and blue-light anti-reflective structurally colored contact lenses based on a copolymer hydrogel with amorphous array nanostructures. *RSC advances* 2018; 8(8): 4006-4013.
- [17] Ateş G, Bilici S. Investigation of spectral and optical properties of some organic eyeglass lenses. *Journal of Inonu University Health Services Vocational School* 2023; 11(1): 1042-1053.
- [18] Harris MG, Chin RS, Lee DS, Tam MH, Dobkin CE. Ultraviolet transmittance of the Vistakon disposable contact lenses. *Cont Lens Anterio Eye* 2000; 23(1): 10-15.
- [19] Harris MG, Dang M, Garrod S, Wong W. Ultraviolet transmittance of contact lenses. *Optom Vis Sci* 1994;71(1):1-5.
- [20] Raffé D. The concept of transition system. *J Educ Work* 2008; 21(4): 277-296.
- [21] Rahmani S, Mohammadi Nia M, Akbarzadeh Baghban A, Nazari MR, Ghassemi-Broumand M. Spectral transmittance of UV-blocking soft contact lenses: a comparative study. *Cont Lens Anterior Eye* 2014; 37(6): 451-454
- [22] Rocha FS, Gomes AJ, Lunardi CN, Kaliguine S, Patience GS. Experimental methods in chemical engineering: Ultraviolet visible spectroscopy UV-Vis. *T Can J For Chem Eng* 2018; 96(12): 2512-2517.
- [23] Bergmanson J, Söderberg P. The significance of ultraviolet radiation for eye diseases: a review with comments on the efficacy of UV-blocking contact lenses. *Ophthalmic Physiol Opt* 1995; 15(2): 83-91.
- [24] Wagoner MD. Chemical injuries of the eye: current concepts in pathophysiology and therapy. *Surv Ophthalmol* 1997; 41(4): 275-313.
- [25] Pitts DG, Cullen AP, Hacker PD. Ocular effects of ultraviolet radiation from 295 to 365 nm. *Invest Ophthalmol Vis Sci* 1977;16(10): 932-939.
- [26] Dumbleton KA, Cullen AP, Doughty MJ. Protection from acute exposure to ultraviolet radiation by ultraviolet-absorbing RGP contact lenses. *Ophthalmic Physiol Opt* 1991;11(3): 232-238.
- [27] Walsh JE, Bergmanson JP. Does the eye benefit from wearing ultraviolet-blocking contact lenses? *Eye Cont Lens* 2011; 37(4): 267-272.
- [28] Harris MG, Chamberlain MD. Light Transmission of Hydrogel Contact Lenses. *Am J Optom Physiol Opt* 1978; 55(2): 93-96.
- [29] Bergmanson JP, Sheldon TM. Ultraviolet radiation revisited. *CLAO J* 1997; 23(3): 196-204.
- [30] Genç S, Sands J. Sun and the eye: prevention and detection of light-induced disease. *Clin Dermatol* 1998; 16(4): 477-485.
- [31] Bilici S, Kamislioglu M, Guclu EEA. A Monte Carlo simulation study on the evaluation of radiation protection properties of spectacle lens materials. *Eur Phys J Plus* 2023; 138(1): 1-13.
- [32] Bilici S, Bilici A, Külahcı F. Comparison Photon Exposure and Energy Absorption Buildup Factors of CR-39 and Trivex Optical Lenses. *Turkish Journal of Science and Technology* 2022; 17 (1): 23-35.
- [33] American National Standards Institute (ANSI), American National Standard Requirements for Non- Prescription Sunglasses and Fashion Eyewear, Standart Z80.3-1996, ANSI, New York, 1996
- [34] Rahmani S, Mohammadi Nia M, Akbarzadeh Baghban A, Nazari MR, Ghassemi-Broumand M. Spectral transmittance of UV-blocking soft contact lenses: a comparative study. *Cont Lens Anterior Eye* 2014; 37(6): 451-454.
- [35] Faubl H, Quinn MH. Spectra of UV-absorbing contact lenses: relative performance. *Inte Cont Lens Clinic* 2000; 27(3): 65-74.
- [36] Mutlu HK, Ekem N. Analysis of the Anti-Reflection Coated Eyeglass Used in Turkey. *International Journal of Eastern Anatolia Science Engineering and Desing* 2021;3(1):157-166.
- [37] Moore L, Ferreira JT. Ultraviolet (UV) transmittance characteristics of daily disposable and silicone hydrogel contact lenses. *Cont Lens Anterio Eye* 2006; 29(3):115-122.
- [38] Kalaycı T, Kinaytürk NK, Tunalı B. Experimental and theoretical investigations (FTIR, UV-VIS spectroscopy, HOMO-LUMO, NLO and MEP analysis) of aminothiophenol isomers. *Bull Chem Soc Ethiopia* 2021; 35(3): 601-614.

An Analysis Tool for Cryptographic Designs Based on Chaotic Systems

Yılmaz AYDIN^{1*}, Fatih ÖZKAYNAK²

^{1*} Department of Software Engineering, Faculty of Engineering, Firat University, Elazig, Turkey

² Department of Software Engineering, Faculty of Technology, Firat University, Elazig, Turkey

^{1*} y.aydin@firat.edu.tr , ² ozkaynak@firat.edu.tr

(Geliş/Received: 24/04/2023;

Kabul/Accepted: 18/08/2023)

Abstract: Chaos-based cryptography research is one of the application areas for chaotic systems. Numerous design studies have been put up that take use of the connection between chaos and cryptography. This study has demonstrated how to exploit this relationship to decrypt cryptography designs. It has been looked at if chaos analysis techniques may be used to analyze cryptography protocols. The effectiveness of random number generators has been evaluated using Lyapunov exponents, a chaos analysis technique. The findings of the investigation demonstrated that Lyapunov exponents can be utilized as a standard in assessing random number generators. The paper highlights the issues with the NIST test suite, a popular method of analysis for assessing the statistical characteristics of random number generators. These issues have been seen to not exist with the new test tool that has been suggested. These findings demonstrate that the suggested strategy can be successfully applied in a variety of future applications.

Key words: Chaos, Cryptography, Lyapunov Exponents, Random Numbers.

Kaotik Sistemler Tabanlı Kriptografik Tasarımlar için Bir Analiz Aracı

Öz: Kaos tabanlı kriptografi araştırmaları, kaotik sistemlerin uygulama alanlarından biridir. Kaos ve kriptografi arasındaki bağlantıdan yararlanan çok sayıda tasarım çalışması yapılmıştır. Bu çalışma, kriptografi tasarımlarının şifresini çözmek için bu ilişkinin nasıl kullanılacağını göstermiştir. Kriptografi protokollerini analiz etmek için kaos analiz tekniklerinin kullanılıp kullanılmayacağına bakılmıştır. Rastgele sayı üreteçlerinin etkinliği, bir kaos analizi tekniği olan Lyapunov üstelleri kullanılarak değerlendirilmiştir. Araştırmanın bulguları, Lyapunov üstellerinin rasgele sayı üreteçlerini değerlendirmede bir standart olarak kullanılabilceğini göstermiştir. Makale, rasgele sayı üreteçlerinin istatistiksel özelliklerini değerlendirmek için popüler bir analiz yöntemi olan NIST test takımıyla ilgili sorunları vurgulamaktadır. Önerilen yeni test aracı ile bu sorunların olmadığı görülmüştür. Bu bulgular, önerilen stratejinin gelecekteki çeşitli uygulamalarda başarıyla uygulanabileceğini göstermektedir.

Anahtar kelimeler: Kaos, kriptografi, Lyapunov Üsleri, Rastgele sayılar

1. Introduction

The main purpose of science and engineering studies is to understand real world systems and to use these results for the benefit of mankind. During these studies, chaos theory became increasingly important. Because this phenomenon is needed to understand the logic of real world events. Therefore, chaos theory has started to find its place in many applications [1]. One of the most common practical applications is the design of chaos based encryption systems [2]. In the simplest expression, chaos theory is defined as the randomness of a deterministic system. In other words, despite the fact that real world events are mathematical models, they contain an unpredictable randomness. This exciting relationship is the fundamental phenomenon desired in the cryptographic system design process [3]. A cryptographic protocol is an algorithm. However, this algorithm should provide two basic requirements, called confusion and diffusion. Chaos based cryptography studies have become increasingly popular among researchers over the last two decades, since chaotic systems have both a mathematical model and the randomness properties will provide confusion and diffusion requirements [4].

This close relationship between chaos theory and cryptography science has been used in the design process. In other words, chaotic systems have been used as an entropy source and this entropy source has been transformed into cryptographic primitives such as image encryption schema [2, 5, 6, 7, 8], hash functions [9, 10], s-box designs [11, 12] and key generators with the help of a protocol [13-17]. Again, random numbers and bits have been generated with FPGA using chaos-based maps in studies in the literature [18-20].

* Corresponding author: y.aydin@firat.edu.tr ORCID Number of authors: ¹0000-0001-6057-3693 , ²0000-0003-1292-8490

When the common aspects of these cryptographic primitive studies are examined, it is seen that the hypotheses of the researchers are based on the fact that the complexity of the entropy source contributes to the design of the cryptographic primitive. In other words, it is claimed that there is a strong relationship between the complexity of the chaotic system used as an entropy source and the robustness of the cryptographic protocols [2, 3, 4].

This study approaches this theory from a different angle. It has been looked at if chaos analysis techniques may be used to analyze cryptography protocols. The work tries to prove the notion that chaos analysis methods can be used to evaluate the quality of these cryptographic protocols if the complexity of the chaotic system employed in the protocol design contributes positively to it. This notion was tested in this study using cryptographic random number generators.

Random number generators used in cryptography have been evaluated for quality using Lyapunov exponents, a chaos analysis technique. The findings of the investigation demonstrated that Lyapunov exponents can be utilized as a standard in assessing random number generators. These findings supported the putative idea. It has also demonstrated that it might offer a different way to handle issues when testing the statistical characteristics of applications that require short length sequences, particularly cryptographic key generators.

The remainder of the research is structured as follows. In the second section, it was briefly described how to calculate the Lyapunov exponents for a dataset using chaos analysis methods. The design architecture of the chaos-based random number generator is described in the third section. alternative datasets for three alternative initial circumstances and control parameter values of the chaotic system employed in the generator have been obtained, and they are presented in this section. The system exhibits periodic, chaotic, and optimally chaotic behavior for the chosen initial circumstances and control parameters. Results of the randomness test and Lyapunov analyses for various datasets are presented in the fourth section. The link between the results of the two investigations demonstrates that the purported hypothesis is accurate. The final section includes a summary of the findings and recommendations for additional research.

2. Materials & Methods

2.1. Chaos Analysis with Lyapunov Exponents

Since chaotic behavior is an important characteristic, many researchers want to examine the existence of chaos in their systems [21, 22]. In this process, methods such as phase space portrait, power spectrum, Poincare mapping bifurcation diagram have been some of the most common methods used to determine chaotic behavior. However, the common point of these methods is that they are qualitative approaches. In other words, there is a need for an expert to interpret and evaluate the results. The chaos analysis method known as Lyapunov exponents has become more popular than others because it is a quantitative approach [22].

The idea that fixed (invariant) exponents could be used to determine the stability states of the sets of differential equations of nonlinear dynamic systems was first shown by Sonya Kovalevskaya in 1889. Following the introduction of this hypothesis, it was based on theoretical foundations by Alexandr Mikhailovich Lyapunov. In the Lyapunov study, he explained only the basics of his thoughts about the change of trajectories of a dynamic system (as a function of time) with Lyapunov exponents. The reliance of chaotic systems on their initial circumstances and control settings serves as the foundation for chaos analysis utilizing Lyapunov exponents. Chaos analysis can be done by relocating the orbits away from one another or by allowing them to converge in situations where a chaotic system is formed from two very close neighboring beginning conditions. A mathematical technique that gauges this separation between adjacent orbits is the use of Lyapunov exponents. Lyapunov exponentials are likened to eigenvalues used in linear systems [21, 22].

Lyapunov exponents can be calculated for continuous time system, discrete time systems and time series obtained from experimental or simulation results. Sensitivity to the initial conditions of a dynamic system is measured by Lyapunov exponents. Firstly, two trajectories have been determined with very close initial conditions on an attractor. If the attractor is showing chaotic behavior, the orbits are divided on an exponential rate, characterized by the largest Lyapunov exponent. The detection of a positive Lyapunov exponential is sufficient for the existence of chaos and indicates instability in a particular direction.

The TISEAN 3.0.0 package will be used for the calculation of Lyapunov exponents [23]. There are two different algorithms to make the calculations using the program. These algorithms have been developed by Rosenstein and Kantz. These algorithms are coded as `lyap_r` and `lyap_k` in the program respectively. It has been shown to give similar results in both `lyap_r` and `lyap_k`. It is stated that the small differences that can be neglected in the calculations are due to various calculation parameters such as embedding time, embedding delay, iteration number etc. The calculations in the fourth section are realized by using Kant algorithm (`lyap_k`).

2.2. Chaos Based Random Number Generator

An overview of the chaos-based random number generator that will be employed in the investigation is shown in Figure 1 [24]. The chaotic system has been utilized as an entropy source, as seen in Figure 1. The outputs of a chaotic system are computed for the chosen beginning conditions and control settings. The output values of the calculation are subjected to a threshold value function. Eq. (1) contains the thresholding function's mathematical model. The chaotic system outputs are converted to 0 or 1 values via this function. The resultant bit sequence was broken up into blocks of 8 bits each and transformed into values between 0 and 255.

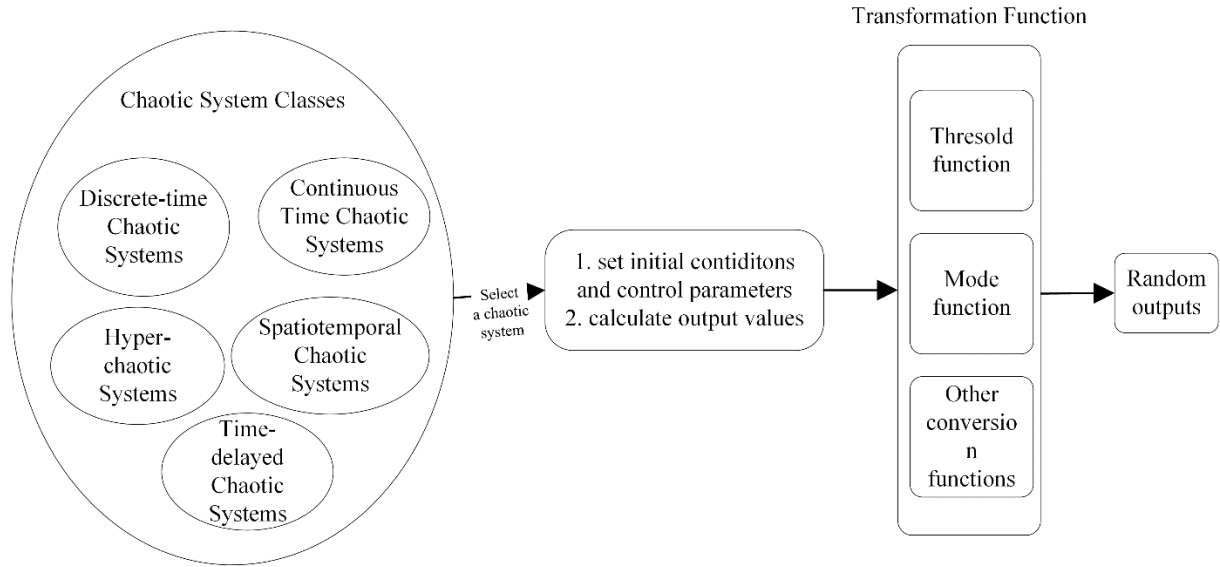


Figure 1. Overview of the chaos based random number generator

$$f_{threshold} = \begin{cases} x < 0.5 \rightarrow 0 \\ x \geq 0.5 \rightarrow 1 \end{cases} \quad (1)$$

The logistic map [22] has been used as the chaotic system in the study. The reason for choosing the logistics map is its simple structure. The simple structure will contribute to the faster operation of the generator. The mathematical model of the logistic map is given in Eq. (2). The map has only one initial condition and one control parameter.

$$x_{n+1} = a \cdot x_n (1 - x_n) \quad (2)$$

The pseudocode is included in Table 1 so that readers can better comprehend how the suggested algorithm functions as a random number generator.

The complexity of the entropy source (the chaotic system) is the fundamental tenet of chaos-based cryptography schemes. In other words, the quality of the random numbers will be higher in more complicated chaotic systems. Twelve different 1,000,00 lengths datasets have been generated using the proposed algorithm in the Table 1. Different initial conditions and control parameters have been used to obtain twelve different datasets.

Figure 2 shows the bifurcation diagram of the logistic map. As can be seen in Figure 2, when the control parameter a is set to between 0 and 3.5, the system shows periodic behavior. That is, when a value is selected in this range, the resulting logistic map outputs cannot be converted to random numbers by the proposed algorithm. Because values are not chaotic. The first six dataset used in the analyzes has been obtained for $a=3.0$, $a=3.1$, $a=3.2$, $a=3.3$, $a=3.4$, $a=3.3$ and $x_0=0.3$.

When a value between 3.5 and 4 is selected, the resulting logistic maps outputs can be converted to random numbers. Because, as can be seen from the bifurcation diagram, the outputs are unpredictable. The five dataset used in the study has been obtained in this direction $a=3.6$, $a=3.7$, $a=3.8$, $a=3.9$ and $a=4.0$ and $x_0=0.3$. When generating these dataset $x_0=0.3$ is selected randomly. The initial value is fixed to be consistent in all datasets.

Table 1. Chaos Based Random Number Generator.

Algorithm	Chaos Based Random Number Generator
Input	x_0 : initial condition of logistic map a : control parameter of logistic map n : length of sequence
Output	n -length sequence values ranging from 0-255
<pre> rng_sequence[1:n] Xold = X 0 for i in 1000 Xnew = a * Xold * (1-Xold) end for j in n value="" for k in 8 Xnew = a * Xold * (1-Xold) value=value+convert_str (fthreshold(Xnew)) end for rng_sequence[j]= convert_decimal (value) end for return rng_sequence </pre>	

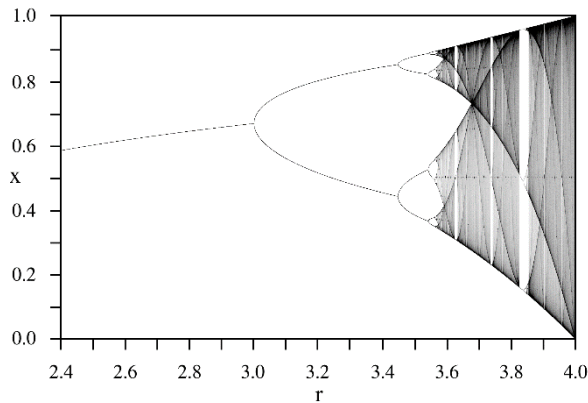


Figure 2. Bifurcation diagram of logistic maps

The final dataset illustrates the connection between chaos and randomness using optimization strategies. The best values for a and x_0 are looked at first. With the assistance of the differential evaluation optimization procedure, a and x_0 values have been established. In this direction, the last dataset has been obtained for $a=4$ and $x_0=0.444369092261707$.

3. Results

Randomness is related to probability, so that the properties of the random sequence can be defined as probabilistic. There are many statistical tests to evaluate the probabilistic properties of random numbers. These tests are used in the process of identifying samples that will ensure that the sequence is random.

Because there are many statistical tests, a generator that passes all tests cannot even say randomly. Because there is a possibility that the generator will fail for a new test. Therefore, the results of statistical tests should be interpreted well.

In order for a value to be defined random, it must be arbitrarily selected from the sequence and the values must be uniformly distributed.

However, when the distribution of a non-random sequence is examined, it does not seem to have a uniform distribution. Therefore, the probability distribution of the sequence is examined to test the randomness.

One of the simplest approaches to assess the randomness of a generator is the chi-square test. This test analyzes whether the data is uniformly distributed. If m random data is generated from the values between 0 and n , then it is expected that each value will be m/n units for the ideal situation. The chi-square values are calculated using Eq. (3).

$$X_c^2 = \sum \frac{(O_i - E_i)^2}{E_i} \tag{3}$$

If the calculated chi-square value is smaller than the confidence values determined for the degree of freedom, the data may be random. 16 different values ranging from 0 to 15 are produced using RNG, therefore the degree of freedom is 16. The confidence values for this degree of freedom are given in Table 2.

Table 2. Confidence values for degree of freedom 16

DF	0.20	0.10	0.05	0.025	0.02	0.01	0.005	0.002	0.001
16	20.465	23.542	26.296	28.845	29.633	32.000	34.267	37.146	39.252

Calculated chi-square values for twelve different random sequences are given in Figure 3. The number of observed data from each value is given in Figure 4.

Name of Dataset	Chi-square Value
a=3 and $x_0=0.3$	3750000.0
a=3.1 and $x_0=0.3$	3750000.0
a=3.2 and $x_0=0.3$	3750000.0
a=3.2 and $x_0=0.3$	3749872.1
a=3.4 and $x_0=0.3$	3749904.1
a=3.5 and $x_0=0.3$	3749872.1
a=3.6 and $x_0=0.3$	1172184.7
a=3.7 and $x_0=0.3$	439080.7
a=3.8 and $x_0=0.3$	298875.8
a=3.9 and $x_0=0.3$	131710.9
a=4 and $x_0=0.3$	16.2
Optimum values	10.6

Figure 3. Chi-Square Values for Random Sequences

Dataset Name	0	1	2	3	4	5	6	7	8	9	10	11	12	13	14	15
a=3 and $x_0=0.3$	0	0	0	0	0	0	0	0	0	0	0	0	0	0	0	250000
a=3.1 and $x_0=0.3$	0	0	0	0	0	0	0	0	0	0	0	0	0	0	0	250000
a=3.2 and $x_0=0.3$	0	0	0	0	0	0	0	0	0	0	0	0	0	0	0	250000
a=3.3 and $x_0=0.3$	0	0	0	0	0	249996	0	0	0	0	0	0	0	0	0	4
a=3.4 and $x_0=0.3$	0	0	0	0	0	0	0	0	0	0	249997	0	0	0	1	2
a=3.5 and $x_0=0.3$	0	0	0	0	0	0	0	0	0	0	3	0	0	0	249996	1
a=3.6 and $x_0=0.3$	0	0	0	0	0	0	0	0	0	0	113757	68262	0	0	67980	1
a=3.7 and $x_0=0.3$	0	0	0	0	0	23841	0	32213	0	0	23532	32108	0	32231	31691	74384
a=3.8 and $x_0=0.3$	0	0	0	0	0	23760	18754	27409	0	0	23358	45952	0	45518	27580	37669
a=3.9 and $x_0=0.3$	0	0	24617	0	14220	38559	15601	14276	0	24849	27916	29805	11052	18870	14217	16018
a=4 and $x_0=0.3$	15695	15373	15680	15455	15696	15458	15523	15649	15665	15656	15521	15729	15905	15672	15685	15638
Optimum values	15682	15723	15466	15454	15527	15536	15725	15578	15774	15717	15600	15523	15759	15723	15602	15611

Figure 4. The Number of Observed Data from Each Value

The most widely used statistical test package is NIST tests [25]. This analysis method, published as a test package, is accepted as the standard in many studies. There are 15 tests in NIST test package. These tests are “Monobit test, Frequency within block test, Runs_test, Longest run ones in a block test, Binary matrix rank test, Dft test, Non overlapping template matching test, Overlapping template matching test, Maurers universal test, Linear complexity test, Serial test, Approximate entropy test, Cumulative sums test, Random excursion test, Random excursion variant test”.

NIST test results for twelve different dataset are given in Figure 5 and Figure 6. The S and F symbols in the figure indicate successful and unsuccessful test results, respectively. P symbol is the calculated probability value of the test. The test results revealed some problems of the NIST test package. The logistic map output values are periodic for control parameter less than 3.5. The periodicity of output of logistic map can be observed both in the bifurcation diagram in Figure 2 and in the distribution of numbers in Figure 4. However, NIST test results for random sequences generated for $a = 3.3$ and $a = 3.4$, are better than the sequences generated for $a = 3.6$, $a=3.7$, $a=3.8$, $a=3.9$. In other words, according to NIST test results, the values produced from periodic data are more random than the values produced from chaotic data. However, it is understood from the data distribution in Figure 4 that this claim is invalid. This indicates that the NIST test package cannot be used for analysis alone.

Nist Test	selected initial conditions and control parameters											
	a=3.0 and x ₀ =0.3		a=3.1 and x ₀ =0.3		a=3.2 and x ₀ =0.3		a=3.3 and x ₀ =0.3		a=3.4 and x ₀ =0.3		a=3.5 and x ₀ =0.3	
	S/F	P-Value	S/F	P-Value	S/F	P-Value	S/F	P-Value	S/F	P-Value	S/F	P-Value
Monobit test	F	0	F	0	F	0	S	0.98723	S	0.99202	F	0
Frequency within block test	F	0	F	0	F	0	S	1	S	1	F	0
Runs test	F	0	F	0	F	0	F	0	F	0	F	0
Longest run ones in a block test	F	2.1e-203	F	2.13e-203'	F	2.7e-203	F	2.1e-159'	F	2.3e-159	F	3.2e-164
Binary matrix rank test	F	0	F	0	F	0	F	0	F	0	F	0
Dft test	F	0	F	0	F	0	F	0	F	0	F	0
Non overlapping template matching test	F	0	F	0	F	0	F	0	F	0	F	0
Overlapping template matching test	S	0.5839	S	0.5839	S	0.5839	S	0.5839	S	0.5839	S	0.5839
Maurers universal test	F	0.002398	F	0.0023989	F	0.0024	S	0.014128	S	0.014128	S	0.06119
Linear complexity test	S	1	S	1	S	1	S	1	S	1	S	1
Serial test	F	0	F	0	F	0	F	0	F	0	F	0
Approximate entropy test	F	0	F	0	F	0	F	0	F	0	F	0
Cumulative sums test	F	0	F	0	F	0	S	1	S	1	F	0
Random excursion test	F	2.7e-12	F	2.772e-12	F	2.7e-12	F	2.77e-12	F	2.7e-12	F	2.77e-12
Random excursion variant test	S	0.4795	S	0.81366	S	0.4795	S	0.4795	S	0.4795	S	0.13559
Total success rate	3/15		3/15		3/15		7/15		7/15		4/15	

Figure 5. Nist Test Results For Twelve Different Dataset Part 1

Nist Test	selected initial conditions and control parameters											
	a=3.6 and x ₀ =0.3		a=3.7 and x ₀ =0.3		a=3.8 and x ₀ =0.3		a=3.9 and x ₀ =0.3		a=4.0 and x ₀ =0.3		Optimum values	
	S/F	P-Value	S/F	P-Value	S/F	P-Value	S/F	P-Value	S/F	P-Value	S/F	P-Value
Monobit test	F	0	F	0	F	0'	F	0	S	0.67887	S	0.68034
Frequency within block test	F	0	F	0	F	0'	F	0	S	0.9832	S	0.79594
Runs test	F	0	F	0	F	0'	F	0	S	0.54995	S	0.94088
Longest run ones in a block test	F	3.2e-164	F	2.e-14	F	8.32e-28	F	0.005723	S	0.88981	S	0.48956
Binary matrix rank test	F	0	S	1	S	1	S	1	S	1	S	1
Dft test	F	0	F	0	F	3.6e-123	F	0	S	0.14708	S	0.08449
Non overlapping template matching test	F	0	F	0	F	0'	F	0	S	0.11967	S	0.68789
Overlapping template matching test	S	0.5839	S	0.5839	S	0.5839'	S	0.5839	S	0.5839	S	0.5839
Maurers universal test	S	0.18923	S	0.34316	S	0.54998'	S	0.89908	S	0.56887	S	0.57023
Linear complexity test	S	1	S	1	S	1'	S	1	S	1	S	1
Serial test	F	0	F	0	F	0 0'	F	0	S	0.76667	S	0.929425
Approximate entropy test	F	0	F	0	F	0'	F	0	S	0.7883	S	0.93674
Cumulative sums test	F	0	F	0	F	0 0'	F	0	S	1	S	1
Random excursion test	F	8.63e-19	F	2.77e-12	F	3.9e-14'	F	2.72e-16	F	0.003005	S	0.840948
Random excursion variant test	S	0.13559	S	0.41422	S	0.83117	S	0.81366	S	0.08453	S	0.739789
Total success rate	4/15		5/15		5/15		5/15		14/15		15/15	

Figure 6. Nist Test Results For Twelve Different Dataset Part 2

Table 3 shows the calculated Lyapunov exponential values for the outputs obtained by converting the chaotic system outputs to random numbers.

Table 3. Lyapunov Exponents For Rng Sequences

Name of Dataset	Lyapunov exponents
a=3 and $x_0=0.3$	does not compute
a=3.1 and $x_0=0.3$	does not compute
a=3.2 and $x_0=0.3$	does not compute
a=3.2 and $x_0=0.3$	does not compute
a=3.4 and $x_0=0.3$	does not compute
a=3.5 and $x_0=0.3$	does not compute
a=3.6 and $x_0=0.3$	0.23337
a=3.7 and $x_0=0.3$	0.23397
a=3.8 and $x_0=0.3$	0.26141
a=3.9 and $x_0=0.3$	0.29167
a=4 and $x_0=0.3$	0.30655
Optimum values	0.37462

The analysis has been shown that the NIST test results and the Lyapunov exponents calculated for both raw chaotic data outputs and random number sequence have been consistent. Another statement that the calculated Lyapunov exponential for a random number sequence is positive can be used as an indicator for the cryptographic quality of the generator.

4. Discussion

In the literature, it is seen that various statistical tests are used in the evaluation of many new chaos based cryptography proposals. The approaches such as histogram analysis, NPCR, UACI, and correlation analysis are used almost as standard in the analysis of image encryption algorithms. However, cryptanalysis studies in the literature have shown that many designs that pass these tests can be easily broken [26-31]. That is, these cryptanalysis have repeatedly shown that statistical analysis are necessary but not sufficient for the evaluation of chaos based designs. Therefore, new testing tools are needed to make more detailed assessments.

An important statistical analysis is known to be the NIST statistical randomness test suite. This analysis is seen as an important criterion in the evaluation of chaos based RNG studies. However, the analysis results in the section 3 showed that random numbers produced from non-chaotic data may show better statistical characteristics than random numbers produced from chaotic data. This is a significant disadvantage of the NIST test. The presence of a similar problem is shown on both monobit and chi-square tests.

Another problem with the NIST test suite is the number of bits required to perform the tests. 1000000 bits are required to evaluate the statistical properties of the generator. This is a very large number for cryptography applications. Because it is often taken into account that the generators are used in the key planning algorithm of cryptographic design, short length bit sequences like 256 bits (AES) or 1024 bits (RSA) are needed.

It has been revealed that these problems can be eliminated by the proposed new analysis method. The analysis results can be interpreted as follows.

- Whether it is produced from periodic or chaotic data, it has been shown to have negative Lyapunov implications if the generated sequence do not meet the randomness requirements.
- The fact that the Lyapunov exponents can be calculated in short-length sequences has eliminated the 1000000-bit requirement problem.
- The simplicity of the calculations increases the applicability of the method.

5. Conclusions

Theoretically, cryptography and chaos have a close link. The two fields' primary traits are similar to one another. The creation of new cryptographic protocols has always taken advantage of this tight link. This study has demonstrated how to exploit this relationship to decrypt chaos-based encryption schemes. The generated data can be used as a key or seed value in similar chaos-based encryption algorithms [32].

To be considered secure, a cryptographic design is assumed to meet the conditions for confusion and dispersion.

According to some, the Lyapunov exponential can be used to measure these criteria. An analytical tool for quantifying chaos is the Lyapunov exponent. Given the connection between chaos and cryptography, it has been proposed that mixing and diffusion requirements can be verified by the presence of chaos.

This study has demonstrated that Lyapunov exponents can be used to examine random number generators. The successful analytical results supported the potential of the suggested approach to serve as a test tool for cryptography design. It has also been demonstrated that a number of issues with the NIST test suite can be fixed.

Acknowledgements

This study is supported by the TUBITAK Project Number 120e444.

References

- [1] Strogatz SH. *Nonlinear Dynamics and Chaos: With Applications to Physics, Biology, Chemistry, and Engineering*. Boca Raton, FL Westview Press, 2014.
- [2] Özkaynak F. Brief review on application of nonlinear dynamics in image encryption. *Nonlinear Dyn.* 2018; 92: 305–313.
- [3] Li C, Zhang Y, Xie EY. When an attacker meets a cipher-image in 2018: A year in review. *Journal of Information Security and Applications* 2019; 48: 102361.
- [4] Özkaynak F. Role of NPCR and UACI tests in security problems of chaos based image encryption algorithms and possible solution proposals. 2017 International Conference on Computer Science and Engineering (UBMK); 2017; Antalya, Turkey. pp. 621-624
- [5] Liu X, Song Y, Jiang G. Hierarchical Bit-Level image encryption based on Chaotic Map and Feistel network. *Int. J. Bifurcation Chaos* 2019; 29: 1950016.
- [6] Shen Q, Liu Y. A novel digital image encryption algorithm based on orbit variation of phase diagram. *Int. J. Bifurcation Chaos* 2017; 27(13): 1750204.
- [7] Yin Q, Wang C. A new chaotic image encryption scheme using Breadth-First search and dynamic diffusion. *Int. J. Bifurcation Chaos* 2018; 28(4): 1850047.
- [8] Ye G, Pan C, Huang X, Zhao Z, He J. A chaotic image encryption algorithm based on information entropy. *Int. J. Bifurcation Chaos* 2018; 28(1): 1850010.
- [9] Chenaghlu MA, Jamali S, Nikzad-Khasmakhi N. A novel keyed parallel hashing scheme based on a new chaotic system. *Chaos, Solitons & Fractals* 2016; 87: 216–25.
- [10] Li Y, Li X. Chaotic hash function based on circular shifts with variable parameters. *Chaos, Solitons & Fractals* 2016; 91: 639–48.
- [11] Solami EA, Ahmad M, Volos C, Doja MN, Beg MMS. A new hyperchaotic System-Based design for efficient bijective Substitution-Boxes. *Entropy* 2018; 20: 525.
- [12] Tanyıldızı E, Özkaynak F. A new chaotic S-Box generation method using parameter optimization of one dimensional chaotic maps. *IEEE Access* 2019; 7: 117829–38.
- [13] Kanso A, Ghebleh M. A fast and efficient chaos-based keyed hash function. *Commun. Nonlinear Sci. Numer. Simul.* 2013; 18: 109–23.
- [14] Lambić D, Nikolić M. Pseudo-random number generator based on discrete-space chaotic map. *Nonlinear Dyn.* 2017; 90: 223–32.
- [15] Sahari ML, Boukemara I. A pseudo-random numbers generator based on a novel 3D chaotic map with an application to color image encryption. *Nonlinear Dyn.* 2018; 94: 723–44.
- [16] Zambrano-Serrano E, Munoz-Pacheco JM, Campos-Cantón E. Chaos generation in fractional-order switched systems and its digital implementation. *AEU Int. J. Electron. Commun. AEU International* 2017; 79: 43–52.
- [17] Avaroğlu E. Pseudorandom number generator based on Arnold cat map and statistical analysis. *Turk. J. Electr. Eng. Comput. Sci.* 2017; 25: 633–43.
- [18] Avaroğlu E, Koyuncu İ, Özer AB, Türk M. Hybrid pseudo-random number generator for cryptographic systems. *Nonlinear Dyn.* 2015; 82: 239–48.
- [19] Türk Ö. FPGA simulation of chaotic tent map-based S-Box design. *Int. J. Circuit Theory Appl.* 2022; 50: 1589–603.
- [20] Koyuncu İ, Özcerit AT, Pehlivan I, Avaroğlu E. Design and implementation of chaos based true random number generator on FPGA. 22nd Signal Processing and Communications Applications Conference; 2014; Trabzon, Turkey. pp. 236-239
- [21] Hilborn RC. *Chaos and Nonlinear Dynamics: An Introduction for Scientists and Engineers*. New York: Oxford Univ. Press, 2000.
- [22] Sprott JC. *Chaos and Time-Series Analysis*. USA : Oxford University Press, 2003.
- [23] Kantz H, Schreiber T. *Nonlinear Time Series Analysis*. *Technometrics* 2005; 47: 381.
- [24] Özkaynak F. Cryptographically secure random number generator with chaotic additional input. *Nonlinear Dyn.* 2014; 78: 2015–20.
- [25] Rukhin AL, Soto J, Nechvatal J, Smid ME, Barker EB. *A Statistical Test Suite for Random and Pseudorandom Number Generators for Cryptographic Applications.*, 2010.
- [26] Arroyo D, Hernández F, Orue AB. Cryptanalysis of a Classical Chaos-Based Cryptosystem with Some Quantum Cryptography Features. *Int. J. Bifurcation Chaos* 2017; 27: 1750004.

- [27] Li C, Lin D, Lu J, Hao F. Cryptanalyzing an image encryption algorithm based on autoblocking and electrocardiography. *IEEE MultiMedia* 2018; 25: 46–56.
- [28] Li C, Lo K-T. Optimal quantitative cryptanalysis of permutation-only multimedia ciphers against plaintext attacks. *Signal Process.* 2011; 91: 949–54.
- [29] Li S, Li C, Chen G, Bourbakis NG, Lo K-T. A general quantitative cryptanalysis of permutation-only multimedia ciphers against plaintext attacks. *Signal Process. Image Commun.* 2008; 23: 212–23.
- [30] Lin Z, Yu S, Feng X-L, Lu J. Cryptanalysis of a chaotic stream cipher and its improved scheme. *Int. J. Bifurcation Chaos* 2018; 28: 1850086.
- [31] Muhammad ZMZ, Özkaynak F. Security problems of chaotic image encryption algorithms based on cryptanalysis driven design technique. *IEEE Access* 2019; 7: 99945–53.
- [32] Ari A. CDIEA: Chaos and DNA based Image Encryption Algorithm. *TJST* 2023; 18: 261–73.

The Effect of TiO₂ Thin Films Produced in Different Thicknesses on Dye-Sensitized Solar Cell Performance

Fehmi ASLAN^{1*}

¹ Department of Motor Vehicles and Transportation Technologies, Yesilyurt Vocational School, Malatya Turgut Ozal University, Malatya, Türkiye
*¹ fehmi.aslan@ozal.edu.tr

(Geliş/Received: 08/05/2023;

Kabul/Accepted: 24/08/2023)

Abstract: Dye-sensitized solar cells (DSSC) are known as 3rd generation solar cells. One of the most important parameters affecting the performance of DSSCs is the thin film thickness that forms the photoanode layer. In this study, we examined how 38, 60 and 76 µm thick TiO₂ thin films change dye-sensitized solar cell performance. The highest efficiency (4.73%) was seen in the solar cell with 38 µm thin film thickness. In addition, the mineralogical and morphological analyses of the produced TiO₂ nanopowders were performed with X-ray diffraction (XRD) and Scanning electron microscopy (SEM). XRD analyses showed that TiO₂ was in the anatase crystal phase. SEM photographs confirmed the formation of microspheres in close contact with each other.

Keywords: DSSC, photoanode, thin film thickness, cell performance.

Farklı Kalınlıklarda Üretilen TiO₂ İnce Filmlerinin Boya Duyarlı Güneş Pili Performansına Etkisi

Öz: Boya duyarlı güneş pilleri (DSSC) 3. nesil güneş pilleri olarak bilinmektedir. DSSC'lerin performansını etkileyen en önemli parametrelerden birisi fotoanot katmanı oluşturan ince film kalınlığıdır. Bu çalışmada 38, 60 ve 76 µm kalınlığındaki TiO₂ ince filmlerinin boya duyarlı güneş pili performansını nasıl değiştirdiğini inceledik. En yüksek verimlilik (%4.73) 38 µm ince film kalınlığına sahip güneş pilinde görüldü. Ayrıca üretilen TiO₂ nanotozlarının mineralojik ve morfolojik analizleri X-ışını difraksiyonu (XRD) ve Taramalı elektron mikroskobu (SEM) ile gerçekleştirildi. XRD analizleri TiO₂'nin anataz kristal fazında olduğunu gösterdi. SEM fotoğrafları ise birbirine yakın temasta mikrokürecik yapıların oluşumunu doğruladı.

Anahtar kelimeler: DSSC, fotoanot, ince film kalınlığı, hücre performansı.

1. Introduction

Today, our lives are getting easier thanks to technological developments that are gaining momentum very quickly. The new inventions that human beings add to our lives play a major role in increasing our quality of life. Every building that provides convenience for our comfort is fed from an energy source [1]. To meet this energy need, exhaustible, renewable and nuclear energy sources are used today [2].

Since the electrical energy produced by solar energy is renewable, environmentally friendly and will continue to exist as long as the world exists, its usage areas are very wide. For this reason, it is thought that solar energy will play a major role in solving the energy problem, which is one of the biggest problems of humanity. Another factor that makes solar energy important is that it is a renewable energy source, does not pose any danger and is environmentally friendly. Since solar energy is an energy source that all human beings need, it requires extensive research in reducing energy dependence [3,4].

Dye-sensitized solar cells (DSSCs), like other solar cells, work with the principle of converting light into electrical energy. A typical DSSC consists of a photoanode, dye, redox electrolyte and counter electrode to catalyze the reaction [5]. They are formed by dipping the semiconductor metal oxide material coated on a conductive glass surface into the dye and then joining it with the counter electrode after pouring the electrolyte solution. The schematic structure of a typical DSSC is given in Fig. 1. More research is needed to increase the commercial use of DSSCs and to transform this technology into a more competitive product in the world market. To increase commercial production, it is necessary to obtain an efficiency of more than 15% from DSSCs [6]. Researchers have worked to increase the power conversion efficiency of DSSCs by producing dyes with high extinction coefficients, metal oxide photoanodes with increased specific surface area, new redox electrolytes and counter electrodes [7,8].

* Corresponding author: fehmi.aslan@ozal.edu.tr. ORCID Number of authors: 0000-0002-5304-0503

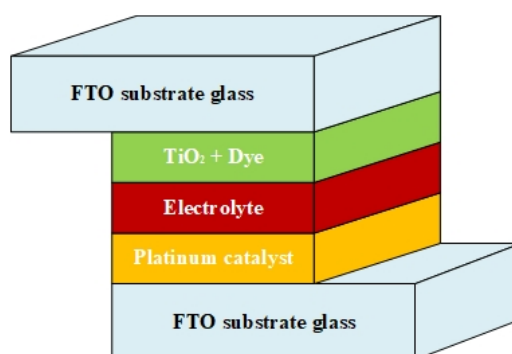


Figure 1. Schematic structure of a typical DSSC [9].

In addition to the morphological and electronic structure of TiO₂, the film thickness also significantly affects cell performance. Most of the cracks and shrinkage in the TiO₂ layer are related to the layer thickness. Cracks seen in the thin film layer slow down electron transport, cause a short circuit and reduce the active surface area [10]. For this reason, the thickness of the TiO₂ layer of DSSC should be optimized. In a study by Kao et al., when TiO₂ thin films of different thicknesses (0.5 μm, 1 μm, 1.5 μm and 2 μm) were examined, an increase of 5% in the short circuit current density and open circuit voltage of DSSC with 1.5 μm thin film thickness was observed [11]. The cell with 10 μm TiO₂ film exhibited the highest light absorption and lowest charge recombination among photoanodes with layers of different thicknesses (6, 10 and 14 μm) [12]. When the layer thickness exceeds 15 μm, photovoltaic parameters such as power conversion efficiency and short-circuit current density decrease [13]. In previous studies, it is known that the performance of DSSCs decreases when the thin film thickness reaches around 15 μm. Especially when the film thickness exceeds 15 μm, it is known that there is a great decrease in productivity. In this study, it was investigated how the photovoltaic parameters were affected by using thicker films.

In this study, the extent to which higher film thicknesses affect the performance of DSSCs was investigated. For this purpose, TiO₂ layers with 38, 60 and 76 μm thickness were produced.

2. Experiments

All chemical materials required for this study were purchased commercially and used without further purification. All experiments were carried out in sterile conditions in a laboratory environment.

2.1 Materials used in the experiment

In this study; Titanium IV isopropoxide (TTIP, ≥97.0%, Sigma-Aldrich), ethyl alcohol (≥99.5%, Sigma-Aldrich), ethyl cellulose (Sigma-Aldrich), alpha-terpinol (Sigma-Aldrich), acetone (99.5%, Sigma-Aldrich), Fluorine doped tin oxide coated glass (FTO, surface resistivity approximately 13 Ω/sq), Electrolyte solution (Iodolyte AN-50, Solaronix) and Platinum (Pt) paste (Solaronix) were used.

2.2 Production of titanium dioxide (TiO₂) nanoparticles

In this study, the hydrothermal system shown in Fig. 2 was used for the production of TiO₂ nanopowders. Initially, 40 ml of deionized water and 1.6 g of urea were mixed for 1 h until a homogeneous solution was formed. While this process was continuing, 3.5 ml of TTIP was added dropwise and mixed for another 30 min. After this mixture was ultrasonically treated for 30 min, it was placed in a Teflon autoclave integrated hydrothermal device at 120 °C for 24 h. After the Teflon autoclave was cooled to room temperature, the collected particles were washed several times with deionized water and alcohol to remove unwanted residues. The precipitate formed was dried in an oven at 50 °C for 12 h and calcined in a muffle furnace at 450 °C. Produced TiO₂ particles were pounded in a mortar and made ready for paste making.

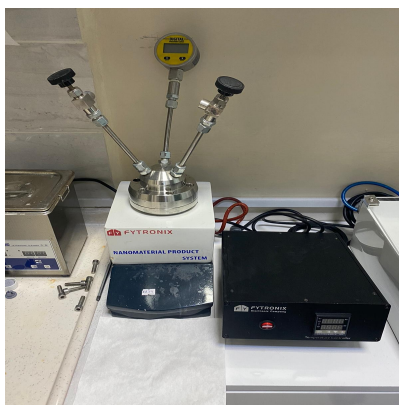


Figure 2. Hydrothermal system used in nanopowder production.

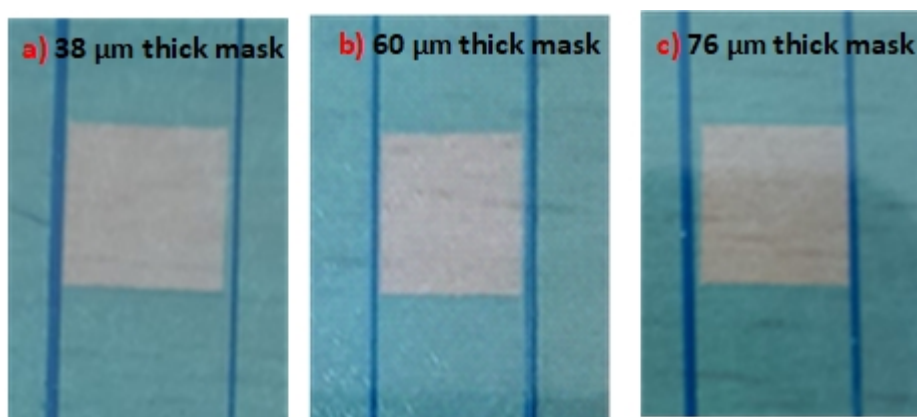


Figure 3. Masks of different thicknesses are pasted on the FTO.

2.3. Preparation of DSSCs

To prepare the paste, 2 g of TiO_2 , 0.9 g of ethyl cellulose and 6 ml of terpinol were mixed in a mortar until the appropriate paste concentration was obtained. Non-marking masking tapes with 38, 60 and 76 μm thickness and $0.6 \text{ cm} \times 0.6 \text{ cm}$ opening adhered to the $2 \text{ cm} \times 2 \text{ cm}$ FTO conductive glass surface. Masks pasted on the FTO are shown in Fig. 3. The pre-prepared TiO_2 paste was coated with a doctor-blade technique on the conductive surface of the FTOs with the help of a glass rod. The produced photoanodes were calcined at $450 \text{ }^\circ\text{C}$ for 45 min with gradual heating. After cooling the photoanodes at room temperature, they were immersed in 0.5 mM Ru dye dissolved in anhydrous alcohol and kept in a dark environment for 24 h. The photoanodes immersed in dye are given in Fig. 4. Photoanodes removed from the dye were washed several times with alcohol to remove non-absorbable residues on the surface and quickly dried. To produce Pt counter electrodes, Pt-based paste was coated on the conductive surface of the FTO with the help of an acrylic brush. FTO coated with Pt paste was sintered at $450 \text{ }^\circ\text{C}$ for 15 min and counter electrodes were prepared. After a few drops of electrolyte solution was dropped on the part where TiO_2 was located on the photoanode layer, it was combined with the Pt counter electrode. After this process, the DSSCs are ready to take measurements. The representative view of the prepared DSSCs is given in Fig. 5.

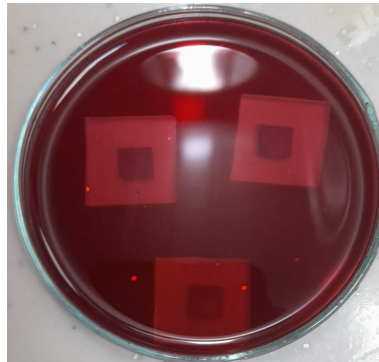


Figure 4. The appearance of photoanodes with different thicknesses in Ru dye.



Figure 5. The representative view of the prepared DSSCs

3. Discussion and results

The XRD patterns of the produced TiO₂ nanopowders are given in Fig. 6. XRD measurements were performed at 2 θ angles from 10° to 80°. XRD analyses (performed by the Rigaku X-ray Diffraction system) confirmed the high-quality crystal structure and anatase phase of TiO₂. In addition, (101), (004), (200), (105), (211), (204), (116), (220), (215) XRD crystal planes overlap the 2 θ angles of anatase TiO₂ [14].

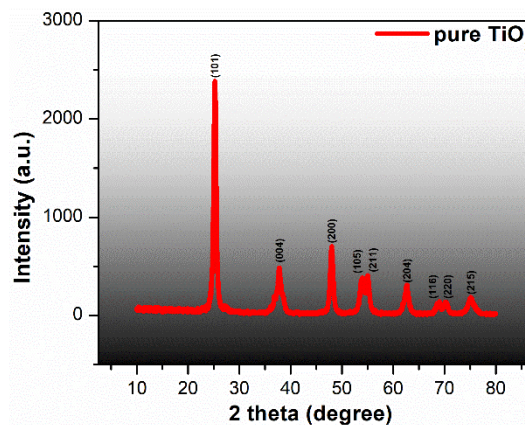


Figure 6. XRD patterns of produced TiO₂ particles.

The surface morphology of TiO₂ powders produced by the hydrothermal method was examined by SEM analysis (performed by ZEISS Sigma-300). The surface morphologies of TiO₂ particles are given in Fig. 7. The particles were composed of tightly packed microspheres, and this tight contact facilitated electron transport.

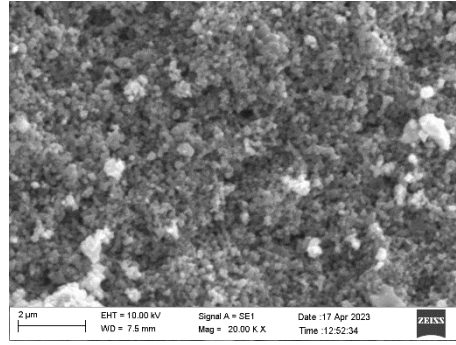


Figure 7. SEM images of the produced TiO₂ particles.

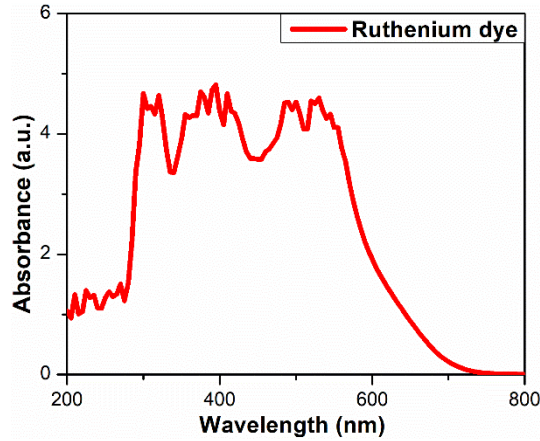


Figure 8. UV-vis spectrum of ruthenium-based dye.

Photoanodes with TiO₂ layers of different thicknesses were immersed in a Ru-based dye solution, which showed the highest cell performance for DSSCs. The UV-vis absorption spectrum lines of the Ru dye are shown in Fig. 8. Thanks to the high absorption of Ru-based dye in the wavelength range of 340-760 nm, DSSCs with 38, 60 and 76 μm TiO₂ layer thicknesses showed photoelectric conversion efficiency (η) of 4.73%, 3.89% and 3.82%, respectively.

Photovoltaic parameters and charge transfer properties of the produced DSSCs were recorded by the Fytronix Solar Simulator LSS 9000 I-V Characterization System under simulated sunlight (AM1.5G, 100 mW/cm² light intensity, 1.0 Sun). Fig. 9 shows the J_{sc}-V (short-circuit current density-voltage) curves of DSSCs with thin films of different thickness under 100 mW/cm² light intensity (AM1.5G). Photoelectric conversion efficiencies (η) and filling factors (FF) of the produced cells are calculated by Eq. 1 and 2, respectively [12]. In these equations, η is the power conversion efficiency; P_{in}, P_{max}, J_{sc}, and V_{oc} represent input power, maximum power, short-circuit current density, and open-circuit voltage, respectively; V_{max} and J_{max} correspond to the maximum voltage and current density, respectively.

$$\eta = \frac{P_{\max}}{P_{in}} = \frac{V_{oc} \times J_{sc} \times FF}{P_{in}} \quad (1)$$

$$FF = \frac{J_{\max} \times V_{\max}}{J_{sc} \times V_{oc}} \times 100 \quad (2)$$

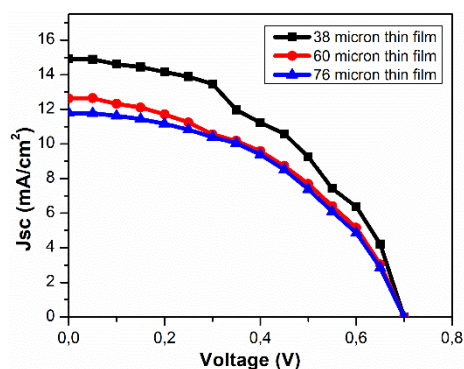


Figure 9. J_{sc}-V curves of DSSCs with different TiO₂ thicknesses.

Table 1. Photovoltaic parameters of DSSCs.

Sample	J _{sc} (mA/cm ²)	V _{oc} (V)	FF	η (%)
DSSC with 38 μm film thickness	14.92	0.64	0.47	4.73
DSSC with 60 μm film thickness	12.63	0.67	0.50	3.89
DSSC with 76 μm film thickness	11.78	0.64	0.49	3.82

When the photovoltaic parameters of the prepared DSSCs given in Table 1 were examined, the highest η (4.73%) and J_{sc} value (14.92 mW/cm²) was seen in the cell with the thinnest layer of 38 μm. In addition, it has been determined that there is a decrease in η and J_{sc} as the TiO₂ film thickness increases. This can be explained by low-charge recombination and high light absorption in cells with thinner layers [15]. Cracks may occur in the film layer, especially when the thin film thickness exceeds the optimized values. These cracks reduce power conversion efficiency and short-circuit current density [16].

4. Conclusions

TiO₂ particles were produced by hydrothermal method and their mineralogical structures were confirmed by XRD. SEM images revealed tightly packed microsphere structures that facilitate electron transport. Terpinol and ethyl cellulose were used as binders in the paste prepared to produce the photoanodes. The doctor blending method was used to create a TiO₂ layer on FTO glasses. Among DSSCs with different thickness of TiO₂ layer, the cell with 38 μm film thickness exhibited the highest power conversion efficiency (4.73%) and short-circuit current density (14.92 mW/cm²). Higher-performance cells can be obtained by producing photoanodes with different layer thicknesses.

Declaration of Competing Interest

The authors declare that they have no known competing financial interests or personal relationships that could have appeared to influence the work reported in this paper.

Credit Authorship Contribution Statement

Fehmi Aslan: Conceptualization, Data curation, Formal analysis, Investigation, Methodology, Validation, Visualization, Writing – original draft, Writing - review & editing.

References

- [1] Bikçe M, Çelik AR, Çakır M. Investigation of solar energy efficiency in education laboratory: Case Study İskenderun. Cukurova University Journal of the Faculty of Engineering. 2016;31: 395–404.
- [2] Özgöçmen A, Electricity generation using solar cells. MSc, Gazi University, Ankara, Turkey, 2007.
- [3] Hernandez RR, Hoffacker CB. Efficient use of land to meet sustainable energy needs. Nat. Clim. Change. 2015;5: 353–358.
- [4] Zatirostami A. A dramatic improvement in the efficiency of TiO₂-based DSSCs by simultaneous incorporation of Cu and Se into its lattice. Opt. Mater. 2021;117: 110-111.
- [5] Chu L, Qin Z, Zhang Q, Chen W, Yeng J, Yang J, Li X. Mesoporous anatase TiO₂ microspheres with interconnected nanoparticles delivering enhanced dye-loading and charge transport for efficient dye-sensitized solar cells. Appl. Surf.

- Sci. 2016;360: 634–640.
- [6] Eden Ç, Characterization and dye-sensitized solar cell performance of TiO₂/ZnO nanocomposite structures synthesized at different temperatures. MSc, Erzincan Binali Yıldırım University, Erzincan, Turkey, 2019.
- [7] Xie Y, Huang N, You S, Liu Y, Sebo B, Liang L, Fang X, Liu W, et al. Improved performance of dye-sensitized solar cells by trace amount Cr-doped TiO₂ photoelectrodes, *J. Power Sources*. 2013;224: 168–173.
- [8] Qi K, Liu S, Chen Y, Xia B, Li GD. A simple post-treatment with urea solution to enhance the photoelectric conversion efficiency for TiO₂ dye-sensitized solar cells. *Sol. Energy Mater. Sol. Cells*. 2018;183: 193–199.
- [9] Supriyanto A, Nurosyid F, Ahliha AH. Carotenoid pigment as sensitizers for applications of the dye-sensitized solar cell (DSSC). *IOP Conf. Ser. Mater. Sci. Eng.* 2018;432: 012060.
- [10] Hossain MK, Rahman MT, Basher MK, Manir MS, Bashir MS. Influence of thickness variation of gamma-irradiated DSSC photoanodic TiO₂ film on structural, morphological and optical properties. *Opt*. 2019;178: 449–460.
- [11] Kao MC, Chen HZ, Young SL, Kung CY, Lin CC. The effects of the thickness of TiO₂ films on the performance of dye-sensitized solar cells. *Thin Solid Films*. 2009;517: 5096–5099.
- [12] Selyanin IO, Steparuk AS, Irgashev RA, Mekhaev AV, Rusinov GL, Vorokh AS. TiO₂ paste for DSSC photoanode: Preparation and optimization of application method. *Chim. Tech. Acta*. 2020;7(4): 140–149.
- [13] Fitra M, Daut I, Irwanto M, Gomes N, Irwan YM. Effect of TiO₂ thickness dye solar cell on charge generation. *Energy Procedia*. 2013;36: 278–286.
- [14] Xu J, Wang G, Fan J, Liu B, Cao S, Yu J. G-C₃N₄ modified TiO₂ nanosheets with enhanced photoelectric conversion efficiency in dye-sensitized solar cells. *J. Power Sources*. 2015; 274: 77–84.
- [15] Baglio V, Girolamo M, Antonucci V, Aricò AS. Influence of TiO₂ film thickness on the electrochemical behavior of dye-sensitized solar cells. *Int. J. Electrochem. Sci*. 2011;6: 3375–3384.
- [16] Kumari J, Sanjeevadarshini N, Dissanayake M, Senadeera G, Thotawatthage C. The effect of TiO₂ photoanode film thickness on photovoltaic properties of dye-sensitized solar cells. *Ceylon J. Sci*. 2016;45: 33.

Second Generation Current Controlled Current Conveyor Based Low Pass Filter Design For The Processing of EEG Signals

Kübra TEKİN^{1*}, Hasan GÜLER²

¹ Elektrik-Elektronik Mühendisliği, Mühendislik Fakültesi, Dicle Üniversitesi, Diyarbakır, Türkiye

² Elektrik-Elektronik Mühendisliği, Mühendislik Fakültesi, Fırat Üniversitesi, Elazığ, Türkiye

*¹ kubra.tekin@dicle.edu.tr, ² hasanguler@firat.edu.tr

(Geliş/Received: 27/01/2023;

Kabul/Accepted: 29/08/2023)

Abstract: EEG signals are noisy signals that allow brain activity to be analyzed. In recent years, it has been seen that current conveyor-based circuits, which have many advantages such as wide bandwidth, high linearity, low power consumption, have been used instead of operational amplifiers in the analysis of these signals. In this study, a second-generation current controlled current conveyor (CCCII+) low pass filter circuit with a cut-off frequency of 100 Hz has been presented for the analysis of EEG signals. The simulation of the circuit was carried out with the Orcad pspice program. In addition, the application circuit of this low-pass filter circuit has been made and oscilloscope images have been obtained for some frequency values. AD844 IC is used as current conveyor in the application circuit. The data of epilepsy patients and normal people taken from the University of Bonn were applied to the CCCII+ low pass filter circuit and the frequency bands of these signals were examined. It has been predicted that if this CCCII+ low pass filter circuit is used in EEG measurements, it will give good results in the diagnosis of neurological diseases such as epilepsy.

Key words: Current conveyor, EEG, Active filter, Pspice.

EEG Sinyallerinin İşlenmesi için İkinci Nesil Akım Kontrollü Akım Taşıyıcı Tabanlı Alçak Geçiren Filtre Tasarımı

Öz: EEG sinyalleri, beyin aktivitesinin analiz edilmesini sağlayan gürültülü sinyallerdir. Son yıllarda, bu sinyallerin analizinde işlemsel yükselteçlerin yerine geniş bant aralığı, yüksek doğruluk, düşük güç tüketimi gibi birçok avantaj sahip olan akım taşıyıcı tabanlı devrelerin kullanıldığı görülmüştür. Bu çalışmada EEG sinyallerinin analizi için 100 Hz kesim frekansına sahip bir ikinci nesil akım kontrollü akım taşıyıcı (CCCII+) alçak geçiren filtre devresi sunulmuştur. Devrenin benzetimi Orcad pspice programı ile gerçekleştirilmiştir. Ayrıca bu alçak geçiren filtre devresinin uygulama devresi yapılmış ve bazı frekans değerleri için osiloskop görüntüleri elde edilmiştir. Uygulama devresinde akım taşıyıcı olarak AD844 IC kullanılmıştır. CCCII+ alçak geçiren filtre devresine, Bonn Üniversitesinden alınan epilepsi hastası ve normal kişilere ait veriler uygulanmış ve bu sinyallerin frekans bantları incelenmiştir. Bu CCCII+ alçak geçiren filtre devresinin EEG ölçümlerinde kullanılması durumunda epilepsi gibi nörolojik hastalıkların tanısında iyi sonuçlar vereceği öngörülmüştür.

Anahtar kelimeler: Akım taşıyıcı, EEG, Aktif filtre, Pspice.

1. Introduction

Electroencephalography is the recording by the EEG device of electrical signals occurring in nerve cells in the brain tissue with the help of electrodes placed on the skull in case of sleep and wakefulness. The study and imaging of bioelectrical signs obtained as a result of the neural activities of the brain are also called Electroencephalogram (EEG) [1,2]. EEG signals are bioelectrical signals with variable amplitude, phase, and frequencies that are not stationary. While EEG signals have a frequency band range of 0.5-100 Hz, clinical and physiological studies are concentrated between 0.5-30 Hz [1,2]. EEG signals are divided into five sub-frequency bands that indicate certain biological activities [3,4]. Delta (δ , 0.5-4 Hz), theta (θ , 4-8 Hz), alpha (α , 8-14 Hz), beta (β , 14-30 Hz) and gamma (γ , > 30 Hz). These frequency bands are small amplitude signals ranging from 1-400 μ V peak to peak.

Analysis of EEG signals has an important place in diagnosing neurological diseases. Various integrated circuits are used for biomedical signals such as EEG signals. These circuits are in many structures, such as OP-AMP based [5], CMOS-based [6], time-frequency based [7], and computer interface based [8]. In this study, a new current-controlled current conveyor (CCCII+) low-pass filter circuit is designed for EEG signals. Current conveyor based circuits have many advantages such as wide bandwidth, wide dynamic range, high linearity, high rate of

* Corresponding author: kubra.tekin@dicle.edu.tr. ORCID Number of authors: ¹ 0000-0002-6050-9760, ² 0000-0002-9917-3619

change, low power consumption [9-11]. For this reason, in recent years, several studies such as CCII with CMOS technology, differential differential current conveyor (DDCC) with low voltage and low power capacity, a new electronically adjustable current mode instrumentation amplifier (CMIA), CMOS and differential voltage second generation current conveyors (DVCCII) have been presented to apply to biomedical signals, and thus the interest in current conveyor-based circuits has increased [10, 12-14].

In this study, it is aimed to design a filter circuit with a current conveyor for the analysis of EEG signals. EEG dataset obtained from the University of Bonn was applied to the CCCII+ based low pass filter circuit designed in this study [15]. In this data set, the data sets of A healthy person with epilepsy seizure and E eyes open were used, each of which contained a 23.6-second recording and corresponded to 4097 data points. A low-pass filter circuit with CCCII+ with a cutting frequency of 100 Hz is designed. The Pspice program has been used to simulate this circuit and the Q2N3904 and Q2N3905 BJTs are preferred. An application study of the designed circuit has been made, and AD844 IC, which can show the current conveyor feature, was used in the study, and oscilloscope results were obtained.

2. Second Generation Current-Controlled Current Conveyor (CCCII+)

It was first introduced by Fabre to provide electronic control of the second generation current conveyors. Io are circuits that can be controlled with low biasing current [16]. The CCCII circuit has a 3-pronged structure, X, Y and Z. If the direction of the current flowing from the Z end is towards the circuit, it is called a positive type second generation current controlled current conveyor (CCCII+), and the simulation of the circuit performed with BJTs in the Pspice program is as shown in Figure 1.

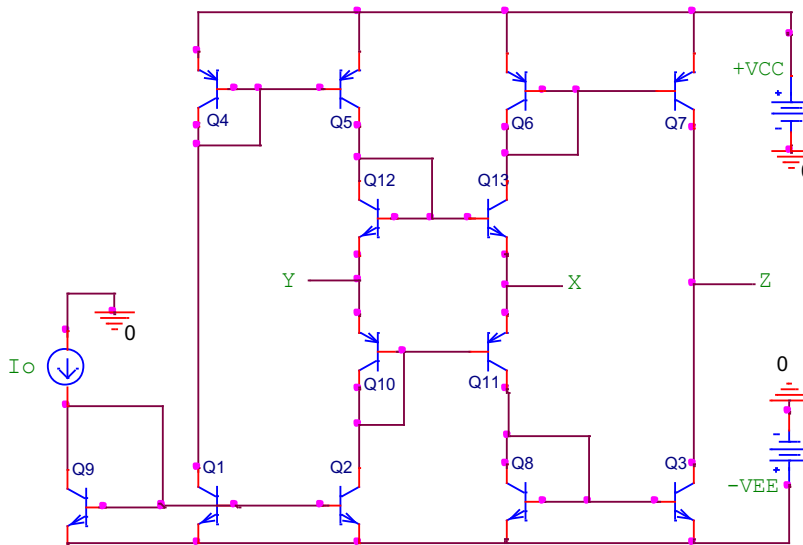


Figure 1. BJT circuit structure of CCCII

The ideal definition relative to the current conveyor circuit in Figure 1 is shown in Equation 1. a, and the equations of the biasing current (I_0) and the (R_X) parasitic resistance, which can be controlled by the polarization current, are shown in the equation 1.b. [17].

$$\begin{bmatrix} I_Y \\ V_X \\ I_Z \end{bmatrix} = \begin{bmatrix} 0 & 0 & 0 \\ 1 & R_X & 0 \\ 0 & \mp 1 & 0 \end{bmatrix} \begin{bmatrix} V_Y \\ I_X \\ V_Z \end{bmatrix} \quad (1. a)$$

$$I_X = 2I_0 \cdot \sinh(V_X/V_T) \quad , \quad V_X \ll V_T \quad , \quad R_X = \frac{V_T}{2I_0} \quad (1. b)$$

The parasitic resistance R_x varies depending on the bias current I_0 and thermal voltage V_T . The approximate value of the thermal voltage V_T at room temperature is considered to be 25.85 mV. In order to avoid inaccuracies in frequency responses, the R_x resistance should be taken into account.

AD844 IC was used as the CCCII+ circuit in the application circuit. The AD844 Integrated Circuit [18] has been put on the market as a circuit that can show a current conveyor property. Thus, a current conveyor-based circuit whose simulation is performed can be put into practice and results can be obtained. The implementation of the CCII+ circuit with AD844 is shown in Figure 2. In addition, the CCCII circuit can be designed with AD844 integrated by replacing the resistance located at the x end of the CCII circuit with a parasitic resistance that can be controlled by bias current.

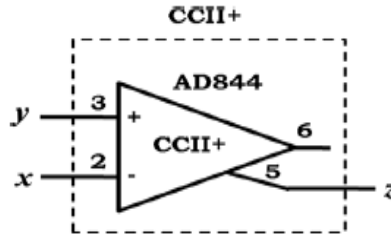


Figure 2. CCII+ implementation using AD844 [19]

3. Simulation Circuit of Low pass filter designed with CCCII+

Low-pass filters are filters that pass signals up to the specified cut-off frequency. The circuit diagram of the voltage mode low-pass filter designed with a second-generation current-controlled current conveyor is given in Figure 3 [20].

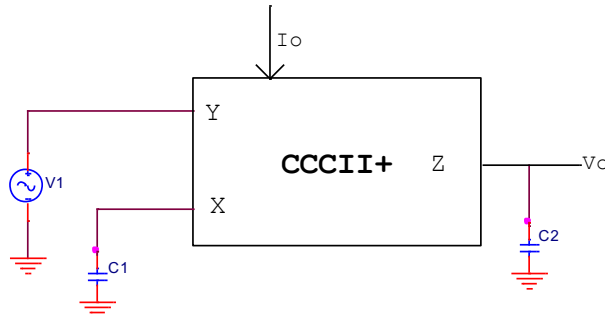


Figure 3. CCCII+ low pass filter circuit diagram

In this circuit diagram, 2 capacitors, one of which is grounded at the X and Z terminals, are used and R_x parasitic resistance is used. The relations between the output and input voltages of the circuit and the cut-off frequency relations of the circuit are given below.

$$\frac{V_{out}(s)}{V_{in}} = \frac{1}{1+sR_xC} \quad (2)$$

$$f_c = \frac{1}{2\pi R_x} \sqrt{\frac{1}{C_1 C_2}} \quad (3)$$

In Figure 4, the simulation circuit of the CCCII+ low-pass filter with a cut-off frequency of 100 Hz, designed with Q2N3904 and Q2N3905 type BJT in the Pspice program, is given.

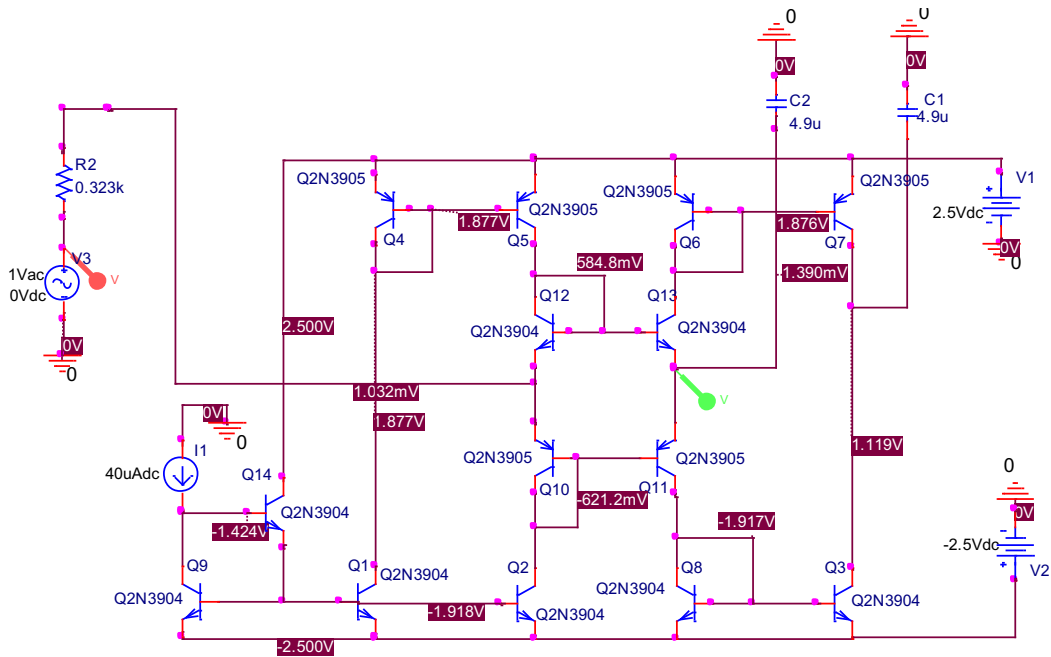


Figure 4. CCCII+ low-pass filter simulation circuit

In the designed circuit, the value of the capacities connected to the X and Z terminals was selected as $4.9\mu\text{F}$. The bias current of the circuit is $40\mu\text{A}$ and accordingly the value of the parasitic resistance is approximately 323Ω . The frequency gain graph of the CCCII+ low-pass filter is given in Figure 5.

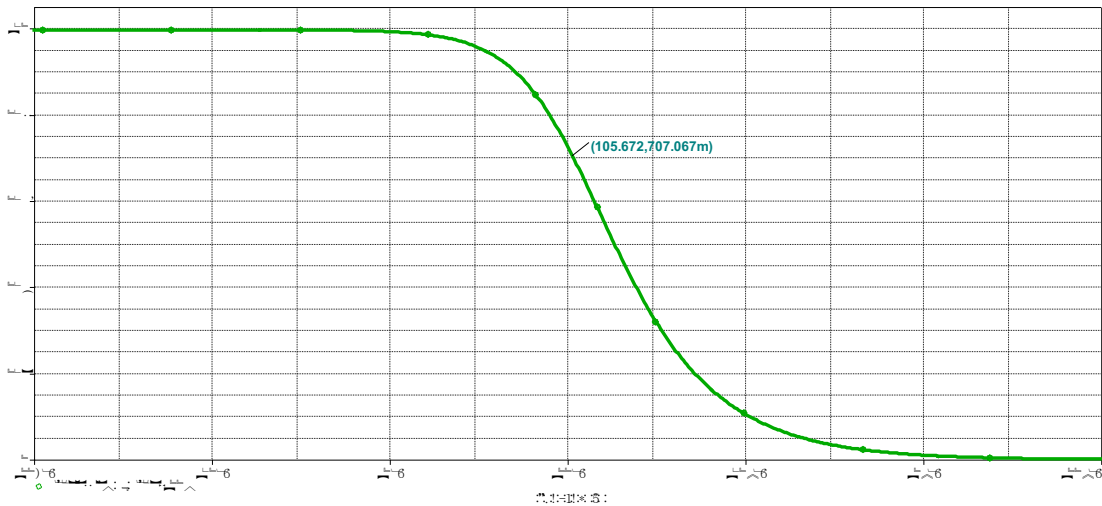


Figure 5. CCCII+ frequency gain graph of low pass filter

While the cut-off frequency of the filter was found to be 100.56 Hz according to the calculations, the cut-off frequency measured according to the frequency gain graph we obtained in Pspice was found to be 105.67 Hz . The maximum frequency gain of the filter is 1.

4. Experimental Results

The CCCII+ low-pass filter circuit simulated in the Pspice program has been applied in the laboratory environment and real-time results have been obtained. A general view of the application study is given in Figure 6.

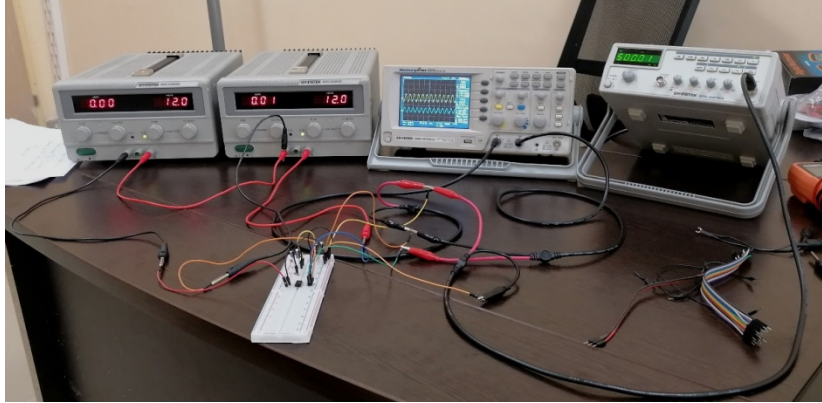


Figure 6. A general view of the application work

In Figure 7, the application circuit of the CCCII+ low-pass filter designed with AD844 integrated into the breadboard is given.

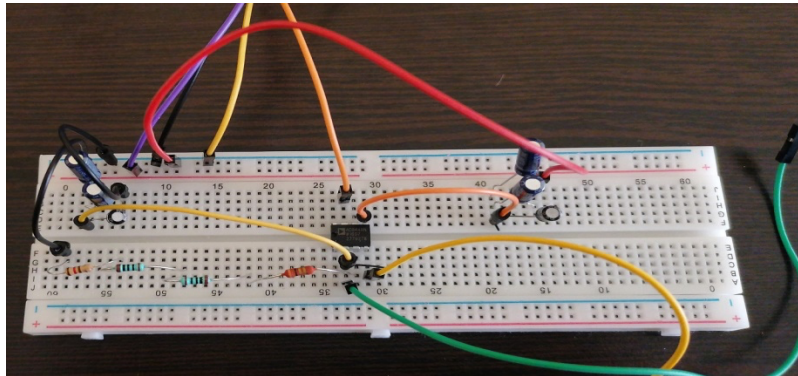


Figure7. Application circuit of the CCCII+ low-pass filter

The oscilloscope images of the low-pass filter designed with CCCII+ are as given in Figures 8, 9, and 10.

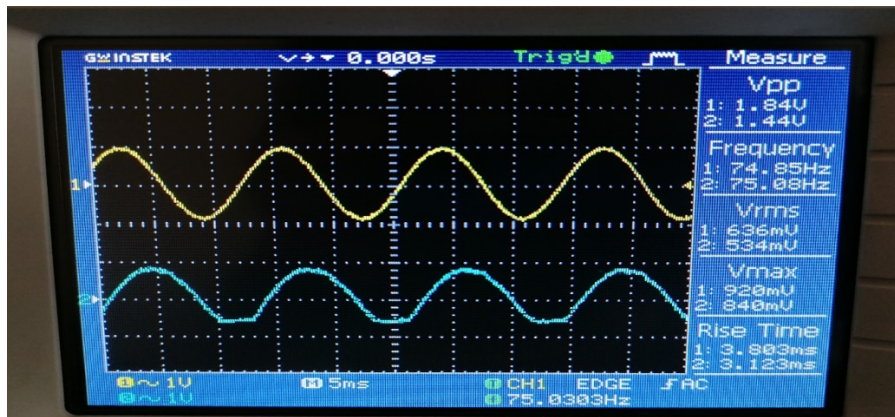


Figure 8. Low-pass filter designed with CCCII+ image at 75 Hz

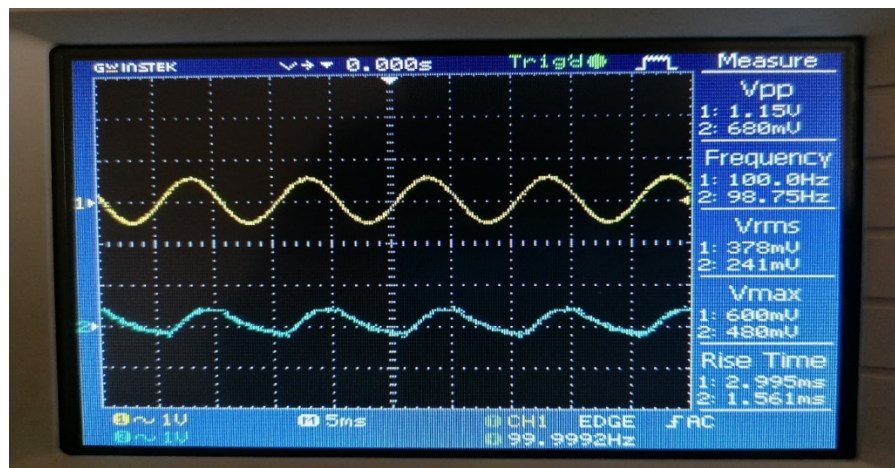


Figure 9. Low-pass filter designed with CCCII+ image at 100 Hz

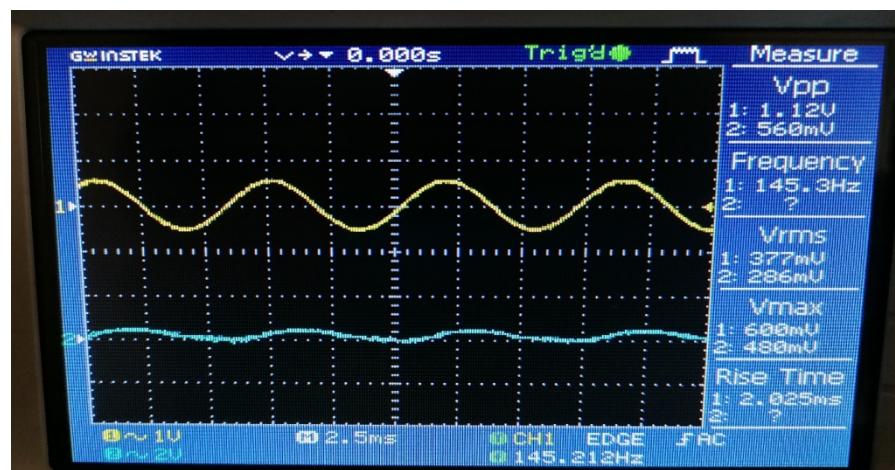


Figure 10. Low-pass filter designed with CCCII+ image at 145 Hz

CCCII+ low-pass filter circuit designed as 100 Hz cut-off frequency is designed with AD844 integrated. The results of the cut-off frequency of the filter circuit at the lower and upper-frequency values were taken and it was seen that the designed filter also cuts off after 98 Hz. It has been determined that the designed filter has good filtering.

5. Conclusion and Discussion

In this study, it is aimed to show the effects of the current conveyor filter circuit for EEG signals by designing a current conveyor (CCCII+) low-pass filter circuit. Here, the low-pass filter is designed for a cut-off frequency of 100 Hz. EEG signals of both epilepsy patients and healthy people were given to the low-pass filter input designed in this study, and the results were examined in a Pspice environment. The input signals of the epilepsy patient and healthy person obtained are as follows (Please see Fig.11, and Fig.12):

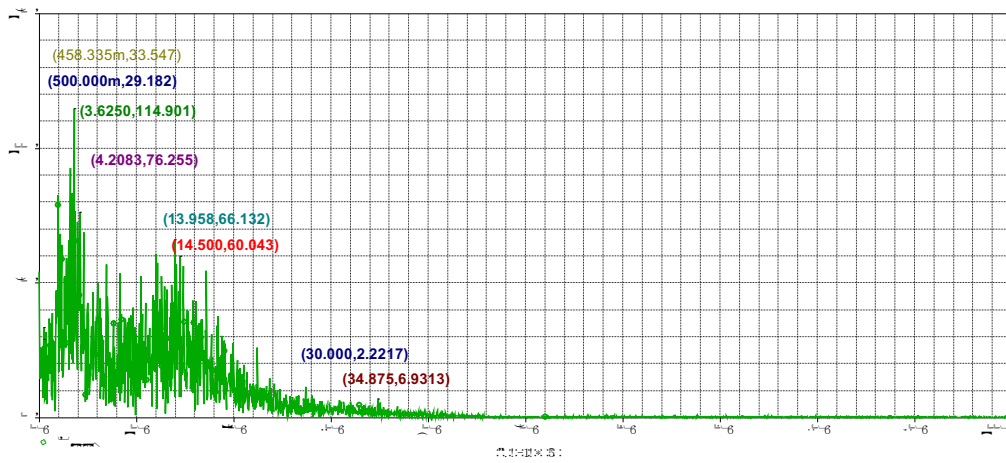


Figure 11. Epilepsy input signal

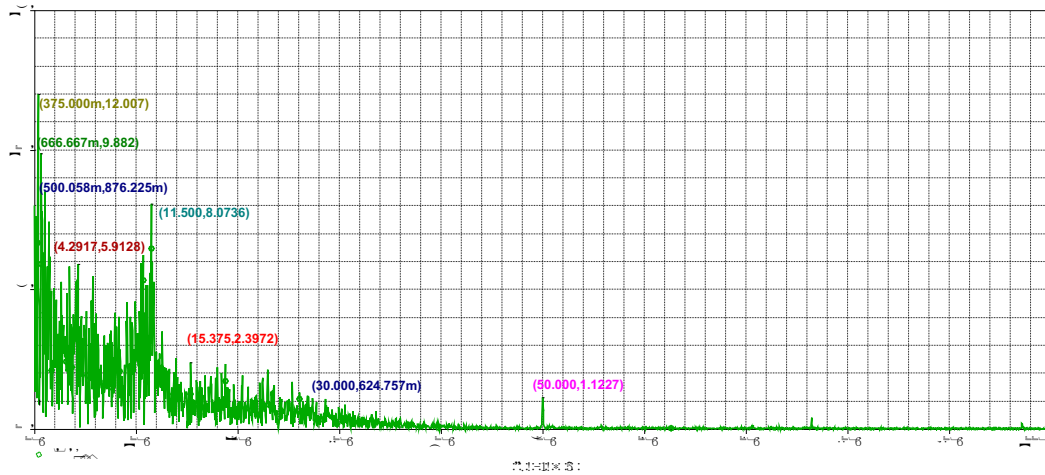


Figure 12. Healthy input signal

The output signal of a healthy person with epilepsy, obtained as a result of Fourier analysis and CCCII+ low-pass filter application, is given below (Please see Fig.13, and Fig.14):

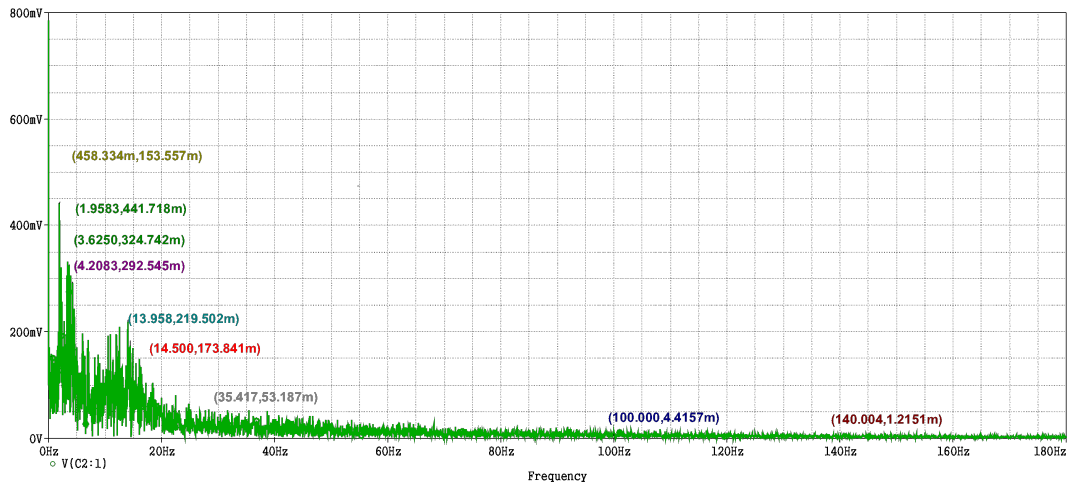


Figure 13. CCCII+ low-pass filter-output signal of an epilepsy patient

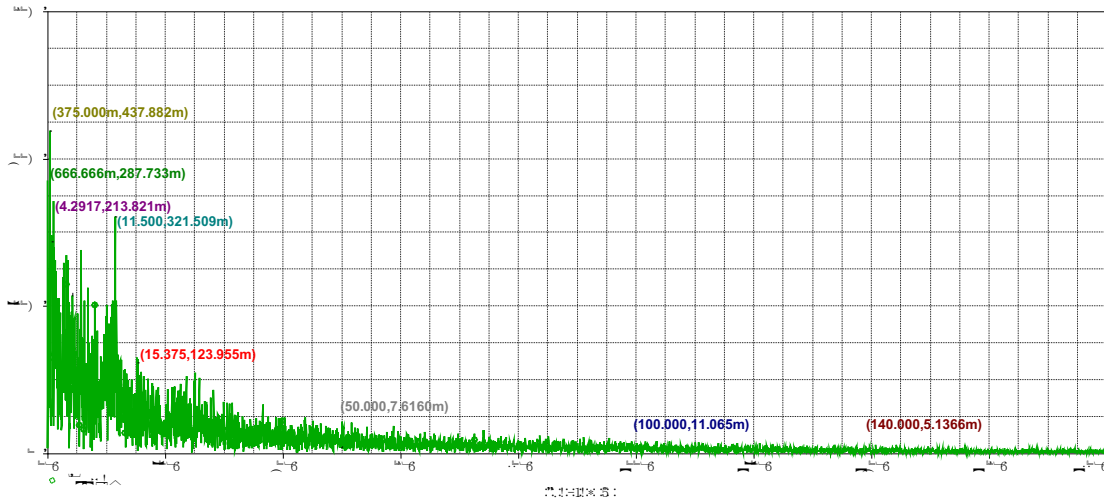


Figure 14. CCCII+ low-pass filter-output signal of a healthy person

Fourier analysis was applied to the signals obtained as a result of the application of the low-pass filter to the epileptic patient and the healthy person, and the changes in the EEG waves were examined. The frequency gain response of current conveyor circuits is very good. In addition, the common-mode signal rejection ratio (CMRR) is important in the high-order common-mode signal rejection process. Since this ratio is quite high in the current conveyor circuit structure, the rejection process can be done easily in the current conveyor circuit.

In this paper aims to see the results of a CCCII+ based low pass filter for a biomedical signal. The results were obtained both with the Pspice program and as an oscilloscope image. When the input signals of the epilepsy patient and the healthy person are examined, it is seen that the amplitude values of the epileptic patient are higher than the healthy person. When a 100 Hz CCCII+ low-pass filter is applied, it is seen that a healthy person with epilepsy filters well when examined for each wave in the EEG signal. The results were obtained according to the oscilloscope images of the CCCII+ low pass filter circuit obtained at different frequencies and by applying the data of epilepsy and healthy people to the simulation circuit. The rate of change in EEG waves, frequency response and the change of output signals were examined. According to the results obtained, we have seen that the CCCII+ circuit performs a better filtering process compared to operational amplifiers. This designed filter circuit will be

used in EEG measurements, and it is predicted that the CCCII+ filter circuit will give better results in the diagnosis of diseases such as epilepsy.

Acknowledgment

This study is a part of Kübra TEKİN's master's thesis.

References

- [1] Yazgan E, Korürek M. Tıp Elektroniği. Ofset Baskı Atölyesi 1996; İstanbul.
- [2] Stern JM, Engel J. Atlas of EEG Patterns. Lippincott Williams & Wilkins 2005; California, USA.
- [3] Sanei S, Chambers JA. EEG signal processing. John Wiley & Sons 2007; London.
- [4] Aydemir Ö, Kayıkçıoğlu T. EEG Tabanlı Beyin Bilgisayar Arayüzleri. Akademik Bilişim'09 - XI. Akademik Bilişim Konferansı Bildirileri 2009; Harran Üniversitesi, Şanlıurfa; 7-13.
- [5] Dimalanta VSM, Hubilla BCR, Marquez JCJS, Quiambao VPT, Tungala KL, Prado SV. Correlation of Emotion to Film Rating Classification Using EEG Signal Analysis. 5th. International Electrical Engineering Congress 2017; Thailand; 1-4.
- [6] Abdallah A, Diab M, Mahmoud S. A Micropower EEG Detection System Applicable for Paralyzed Hand Artificial Control. 40th International Conference on Telecommunications and Signal Processing 2017; Spain; 411-414.
- [7] Lerga J, Saulig N, Lerga R, Stajduhar I. TFD Thresholding in Estimating The Number of EEG Components and The Dominant IF Using The Short-Term Renyi Entropy. International Symposium on Image and Signal Processing and Analysis 2017; Slovenia; 80-85.
- [8] Aydemir Ö. Combining Sub-band Power Features Extracted from Different Time Segments of EEG Trials. 40th International Conference on Telecommunications and Signal Processing 2017; Spain; 383-386.
- [9] Kitiş Ş, Apaydın H, Güntürkün R. Designed Filter with CCII+ and Analysis of EEG for Epilepsy and Alzheimer. Acta Phys. Pol. A 2017; 132(3): 423-426.
- [10] Karami Horestani F, Karami Horastani Z, Björzell N. Band-Pass Instrumentation Amplifier Based on a Differential Voltage Current Conveyor for Biomedical Signal Recording Applications. Electronics 2022; 11(7): 1087.
- [11] Karami Horestani F, Eshghi M, Yazdchi M. An ultra-low power amplifier for wearable and implantable electronic devices. Microelectronic Engineering 2019; 216: 111054.
- [12] Stornelli V, Ferri G. A Single Current Conveyor-based Low Voltage Low Power Bootstrap Circuit for ElectroCardioGraphy and ElectroEncephaloGraphy Acquisition Systems. Analog Integr. Circuits Signal Process., 2014; 79(1): 171-175.
- [13] Kumngern M, Khateb F, Kulej T. Extremely low-voltage low-power differential difference current conveyor using multiple-input bulk-driven technique. AEU Int. J. Electron. Commun 2020; 123: 1-11.
- [14] Psychalinos C, Minaei S, Safari L. Ultra low-power electronically tunable current-mode instrumentation amplifier for biomedical applications. AEU Int. J. Electron. Commun 2020; 117: 153-120.
- [15] Andrzejak RG, Lehnertz K, Rieke C, Mormann F, David P, Elger CE. Indications of nonlinear deterministic and finite-dimensional structures in time series of brain electrical activity: Dependence on recording region and brain state. Phys. Rev. E, 2001; 64: 061907.
- [16] Fabre A, Saaid O, Wiest F, Boucheron C. Current controlled bandpass filter based on translinear conveyors. Electron. Lett. 1995; 31(20): 1727-1728.
- [17] Fabre A, Alami M. Universal current-mode biquad implemented from two second-generation current conveyors. IEEE Trans. Circuits Syst. I: Fund.Theo. and Appl. 1995; 42(7): 383-385.
- [18] Analog Devices AD844. 60 MHz 2000 V/ μ s Monolithic Op Amp. Rev. 2017.
- [19] Paul SK, Choubey CK, Tiwari G. Low power analog comb filter for biomedical applications. Analog Integr. Circuits Signal Process 2018; 97: 371-386.
- [20] Fabre A, Saaid O, Wiest F, Boucheron C. High-frequency application based on a new current controlled conveyor. IEEE Trans. Circuits Syst. I: Fund.Theo. and Appl. 1996; 43(2): 82-91.

The Effect of Using Molybdenum Profile in Columns of Steel Building Models on The Modal Parameters

Furkan GÜNDAY^{1*}

¹ Department of Civil Engineering, Faculty of Engineering, Giresun University, Giresun, Turkey

*¹ furkan.gunday@giresun.edu.tr

(Geliş/Received: 25/02/2023;

Kabul/Accepted: 30/08/2023)

Abstract: From past to present, building designs and materials used are developing. Especially against the destructive effects of ground movements and free vibrations on structures, many structural system designs and composite structure designs have been developed. The purpose of the composite structure design is to choose different types of materials according to the structural load-bearing system stress, in short, to choose the most advantageous material type according to the cross-sectional stresses or to eliminate the negative aspects of one material with the positive aspects of another material. It is a known fact that the dynamic performance of steel structure carrier systems is high under the influence of ground movements and free vibrations. However, in cases where the section geometry cannot be changed due to architectural concerns due to architectural design difficulties, there are cases where the rigidity of the structure is not sufficient. In such cases, profiles made of different materials other than steel can be used in order to increase the rigidity of the structure, especially in the columns, which are a very important component of the structural load-bearing elements. Therefore, in this study, the effect of using molybdenum profile instead of steel profile on modal parameters in model steel structure columns was investigated. In the light of the information obtained, a decrease of approximately 23.72 percent was observed in the period value in the 1st free vibration mode of the steel-molybdenum structure model. Thus, it is understood that the rigidity of the model steel structure system increases. In cases where it is not possible to change the architectural design in steel structures, it is recommended to use column profiles as molybdenum profiles instead of steel profiles in order to provide the necessary rigidity and increase rigidity.

Key words: Molybdenum profile columns, steel structures, modal parameters, finite element method

Çelik Bina Modellerinin Kolonlarında Molibden Profil Kullanımının Modal Parametrelere Etkisi

Öz: Geçmişten günümüze yapı taşıyıcı sistem tasarımları ve kullanılan malzemeler gelişmektedir. Özellikle yer hareketleri ve serbest titreşimlerin yapılar üzerindeki yıkıcı etkisine karşı birçok yapı taşıyıcı sistem tasarımları ve kompozit yapı tasarımı geliştirilmiştir. Kompozit yapı tasarımındaki amaç farklı türde malzemelerin yapı taşıyıcı sistem zorlanması durumuna göre tercih edilmesi kısacası kesit zorlanmalarına göre en avantajlı malzeme türünün seçilmesi veya bir malzemenin olumsuz yönlerinin başka bir malzemenin olumlu yönleri ile giderilmesi işlemidir. Çelik yapı taşıyıcı sistemlerinin yer hareketleri ve serbest titreşimlerin etkisinde dinamik performansın yüksek olduğu bilinen bir gerçektir. Fakat mimari tasarım zorluklarına bağlı olarak mimari kaygılar nedeniyle kesit geometrisinde değişiklik yapılamaması durumlarında yapı rijitliğinin yeterli olmadığı durumlar görülmektedir. Bu gibi durumlarda özellikle yapı taşıyıcı elemanlarının çok önemli bir birleşeni olan kolonlarda yapı rijitliğini artırmak amacıyla çelik dışında farklı malzemeden üretilmiş profiller kullanılabilir. Bu nedenle bu çalışmada model çelik yapı kolonlarında çelik profil yerine molibden profil kullanımının modal parametrelere etkisi araştırılmıştır. Elde edilen bilgiler ışığında oluşturulan çelik-molibden yapı modelinin 1. serbest titreşim modunda periyot değerinde yaklaşık yüzde 23,72 oranında bir azalma gözlemlenmiştir. Böylece model çelik yapı sisteminin rijitliğinin arttığı anlaşılmaktadır. Çelik yapılarda mimari tasarımın değiştirilmesinin mümkün olmadığı durumlarda gerekli rijitliğin sağlanması ve rijitliğin artırılması amacıyla kolon profilleri çelik profil yerine molibden profil olarak kullanılması önerilmektedir.

Anahtar kelimeler: Molibden profil kolonlar, çelik yapılar, modal parametreler, sonlu elemanlar metodu

1. Introduction

In recent years, in the world and our country, the determination of the effect of vibrations on structures and structural behavior has become very important. [1]. Especially, the negative effects of environmental vibrations on structures draw attention. It is known that there is resonance in structures in another important issue. The “resonance” event that occurs in buildings is when the ground dominant period (hence its frequency) and the natural period of the building (hence its frequency) are the same, the addition of two forces in the same direction that cause the building to oscillate, and as a result, the oscillation (amplitude) of the building, hence the acceleration (therefore the acting force) is an increase. As a result of resonance, structures are exposed to great forces and thus

* Corresponding author: furkan.gunday@giresun.edu.tr. ORCID: ¹ 0000-0003-2979-9373

to great damage. [2]. It is a known fact that environmental vibrations can cause structures to resonance. Therefore, free vibration analysis is very important. [3-7]. Building structures have a natural frequency and result in a harmonious movement. Smooth ripple motion occurs in a certain flow pattern along the height and length of the building. Seismic frequencies similar to the natural frequency of the foundation ground and the structure cause the greatest movement or shaking in the structure. Frequencies similar to the natural frequency of the structure increase motion, while frequencies that are dissimilar dampen motion. The natural frequency of low-rise buildings is generally expected to be higher than that of high-rise buildings. Low structures are prone to damage from high-frequency body waves, whereas tall structures are generally damaged by low-frequency surface waves. High-frequency waves (body waves) carry energy farther than low-frequency waves (surface waves). As a result, low structures are more prone to damage if they are located near the epicenter, while tall structures can be damaged even when they are located quite far from the epicenter. The Structure Period is equal to $1/\text{natural frequency}$. Therefore, it is the opposite for the period. Vibration does not only occur as a result of external effects such as wind and earthquake. Structures constantly vibrate within themselves. The period of each structure changes according to the characteristics of the carrier system. The two most important factors that determine the period are the mass of the structure and the rigidity of the structure. Accordingly, the force on the structure depends on the mass of the structure and the acceleration of the structure. The acceleration value can be found depending on the period thanks to the spectrum graphs. The stiffness of the system can be interpreted by looking at the period values. The decrease in the period of the structure is related to the increase in the stiffness. In this case, it is expected that the displacements will decrease in a structure with a decreasing period. [8-14].

The aim of this study is that sometimes the desired rigidity cannot be achieved in steel structures. Section changes may not be possible due to architectural reasons. For such cases, the stiffness of the structure can be changed by changing the material in the structural system elements. For all these reasons, it is aimed to observe the effects of this change on the structural modal parameters and structural rigidity by changing the steel columns, which have critical importance in the structural system elements, and using molybdenum columns.

2. Materials and Methods

Molybdenum is an alloying element that increases hardenability, toughness, wear resistance, corrosion resistance, strength at high temperatures and creep resistance in cast irons, steels, heat resistant alloys and corrosion resistant alloys. It is frequently used in pure form or as a molybdenum-based alloy in parts used at high temperatures, abrasive and corrosive conditions. [15]. Molybdenum is a refractory metal used mainly as an alloying element in cast irons, steels and superalloys to improve some mechanical properties. In particular, molybdenum added to steels as an alloying element increases the tensile strength and yield limit of steels, and reduces the % elongation and section contraction. It also increases the hardenability, toughness, wear and corrosion resistance of steels. These properties that molybdenum gives to alloys; It is of great importance for materials used in high voltage, wide temperature ranges and extremely corrosive environment conditions. [16]. Molybdenum materials are used in many special areas from the nuclear industry to the chemical industry, from the defense industry to the aviation industry. Molybdenum has an excellent resistance to heat. Therefore, it has a special place in the steel and iron industry. It is especially known for giving hardness to steels. Like other refractory metals, molybdenum has a high density and melting point, and is resistant to heat and wear. At $2,623\text{ }^{\circ}\text{C}$ ($4,753\text{ }^{\circ}\text{F}$), molybdenum has one of the highest melting points of all metal elements, while its coefficient of thermal expansion is one of the lowest of any engineering material. Molybdenum also has a low toxicity. The modulus of elasticity of molybdenum has a higher value than metals such as magnesium, aluminum, titanium, cast iron and steel. Molybdenum is a transition metal with atomic number 42, atomic weight 95.95 g/mol , density 10.28 g/cm^3 and in the 6B group of the periodic table. Its modulus of elasticity is 325 GPa , and the poisson's ratio is 0.31 . Also yield strength is 565 MPa , tensile strength is 655 MPa , shear modulus is 126 GPa , bulk modulus is 230 GPa . [17-22].

Finite element method was used method in this study. The SAP2000 package program was used in the modeling and analysis of the steel structure and the newly created structure consisting of molybdenum columns. It is known that the finite element method is widely used in academic studies. With the finite element method, [23-28] studies were used in the modeling and analysis stages. In order to comparatively investigate the effect of molybdenum profile usage on modal parameters, a steel structure model consisting of steel columns and a steel-molybdenum structure model consisting of molybdenum columns were created. In this study, ANSI/AISC 360-16 regulation was used. Modulus of elasticity is 325 GPa , and the poisson's ratio is 0.31 , yield strength is 565 MPa , tensile strength is 655 MPa , shear modulus is 126 GPa , bulk modulus is 230 GPa parameters are used for molybdenum in The SAP2000 package program. The necessary parameters for the steel material were taken according to ASTM A992.

2.1. Steel Structure Model Using Steel Columns

The steel structure model is modeled with 4 spans in X and Y directions. Each span is taken as 4.5 meters. The steel structure model has 8 floors, with a floor height of 3.15 meters. Beams are W30X108 profile, columns are W36X135 profile, slab thickness is 0.02 meters. The total height of the building is 25.20 meters, and the width of the building in both directions is 18 meters. The model is designed symmetrically and simply. The purpose of this is to include fewer variables in the comparison phase. The dimensions of the steel structure model are given in figure 1 and the 3-dimensional view of the steel structure model is given in figure 2.

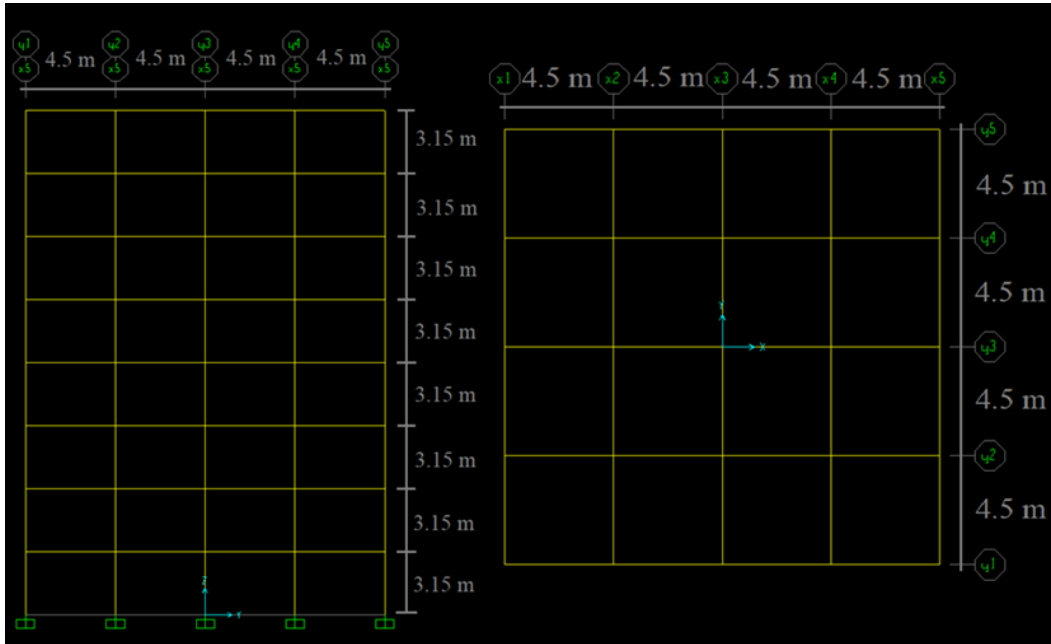


Figure 1. The dimensions of the steel structure model

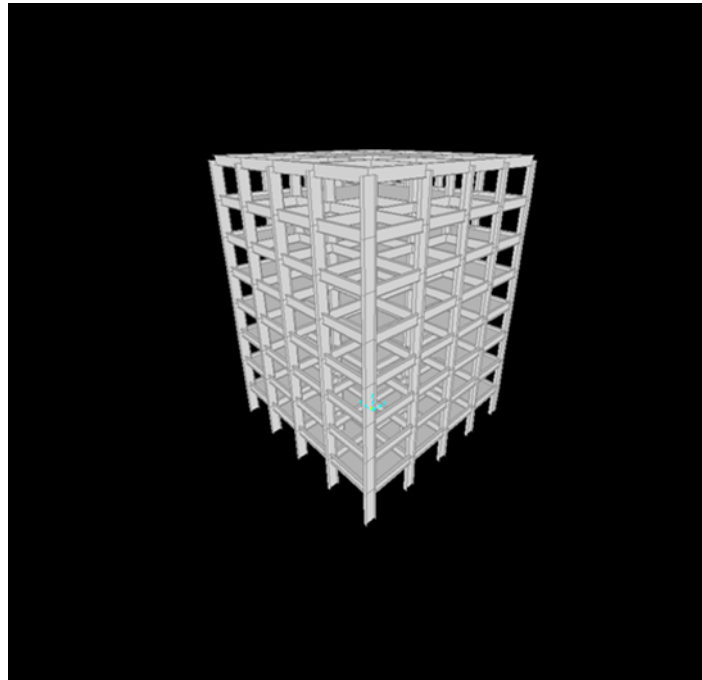


Figure 2. 3D view of the steel structure model with steel columns

2.2. Steel Structure Model Using Molybdenum Columns

In this model, the dimensions of the steel structure model, including the profiles, were fixed, and only the columns of the steel structure model were changed to molybdenum profiles (W30X108, W36X135) and a new model was created. Thus, it is aimed to make the analysis results more reliable and to determine the effect of the use of molybdenum profile on the modal parameters more accurately. The 3D shape of the newly created steel structure model is given in figure 3.

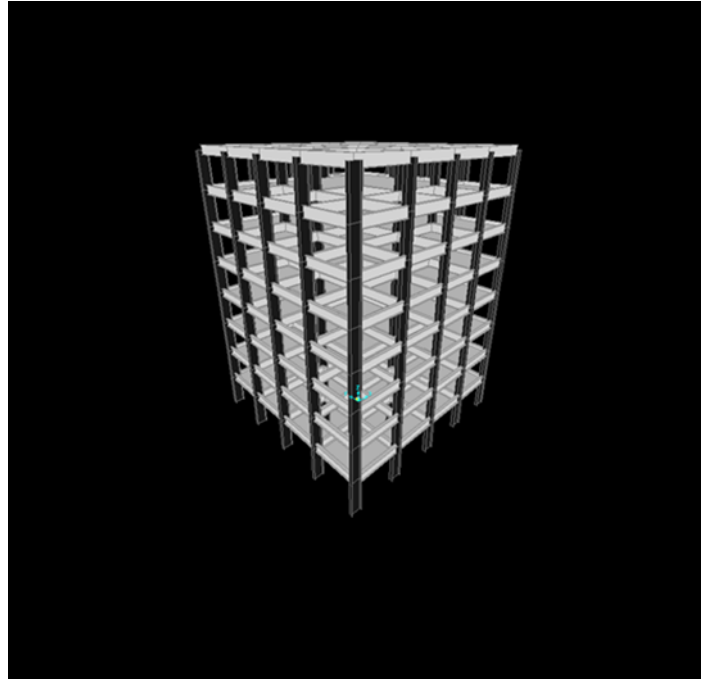


Figure 3. 3D view of the steel structure model with molybdenum columns

3. Findings and Discussion

Both models were analyzed by finite element method, respectively. Modal parameters were obtained with the help of SAP2000 package program. Obtained modal parameters (Mode shapes and period) are presented under separate headings and finally the results are meticulously compared. For comparison, the first 5 mode shapes and period values of each model were taken into account.

3.1. Analysis of Steel Structure Model Using Steel Columns

The mode shapes of the first 5 modes are given together with the period values in figures 4,5,6,7,8 respectively.

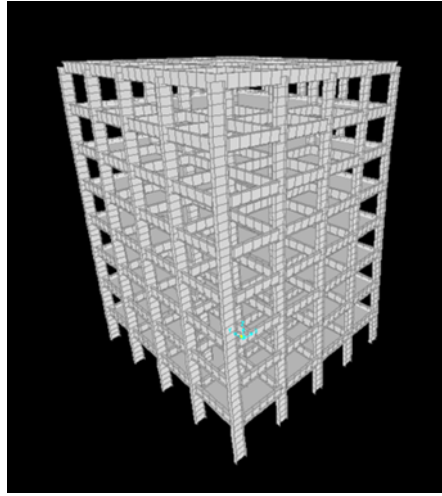


Figure 4. 1. Mode (period value = 0.862881 s)

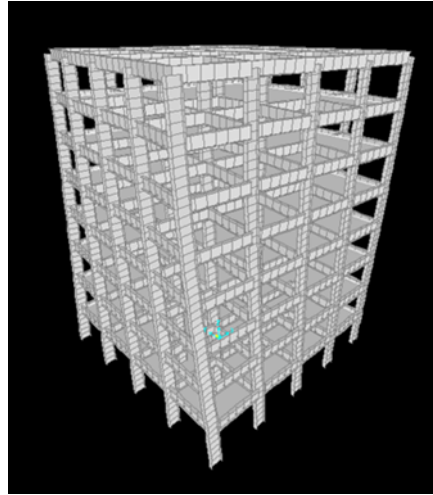


Figure 5. 2. Mode (period value = 0.514943 s)

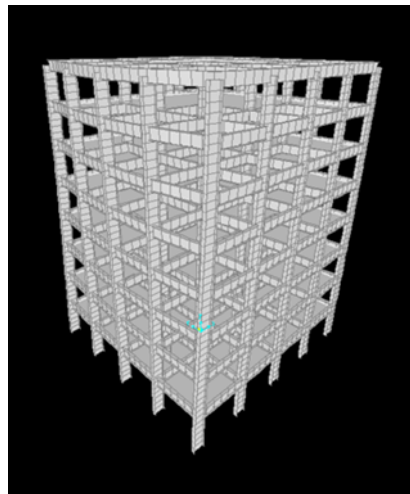


Figure 6. 3. Mode (period value = 0.355794 s)

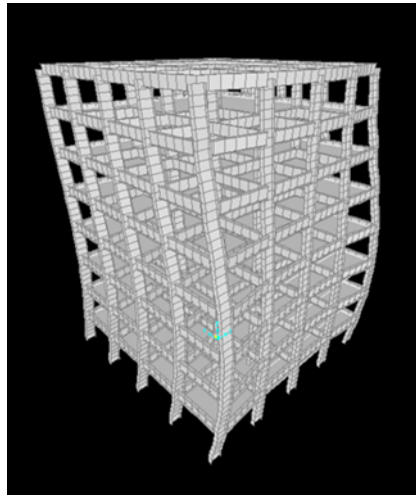


Figure 7. 4. Mode (period value = 0.324945 s)

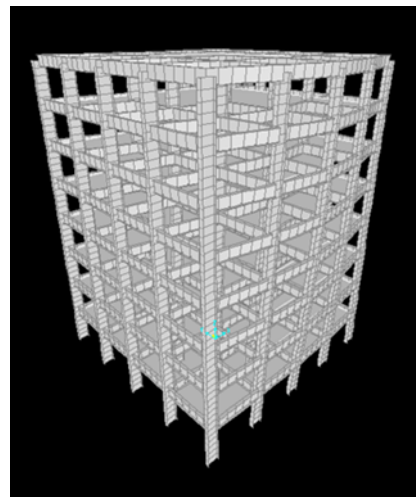


Figure 8. 5. Mode (period value = 0.276291 s)

3.2. Analysis of Steel Structure Model Using Molybdenum Columns

The mode shapes of the first 5 modes are given together with the period values in figures 9,10,11,12, and 13 respectively.

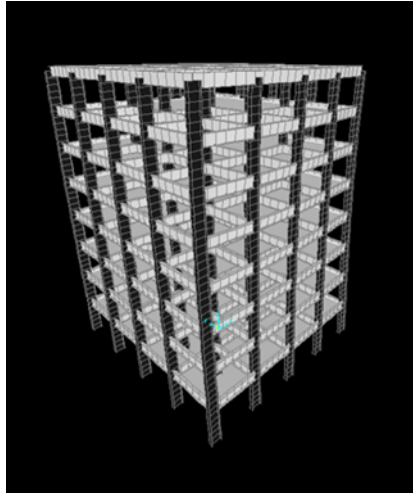


Figure 9. 1. Mode (period value = 0.658191 s)

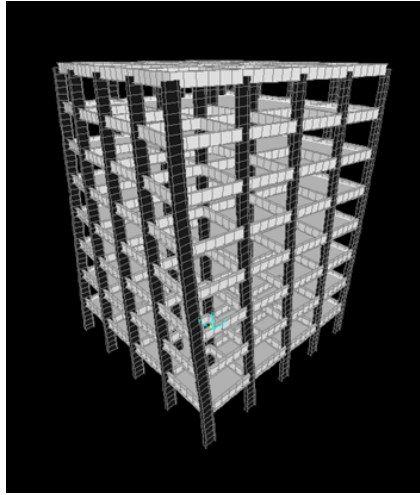


Figure 10. 2. Mode (period value = 0.442845 s)

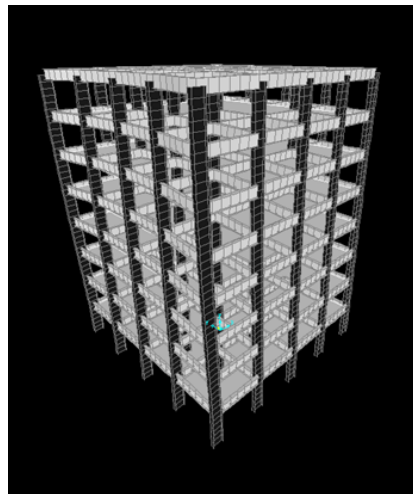


Figure 11. 3. Mode (period value = 0.318558 s)

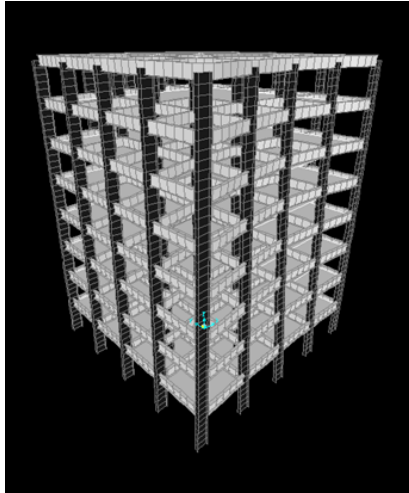


Figure 12. 4. Mode (period value = 0.26628 s)

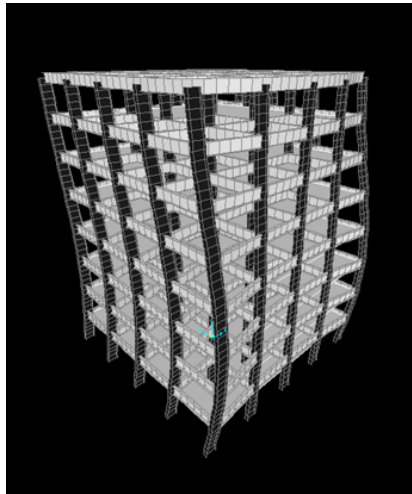


Figure 13. 5. Mode (period value = 0.251915 s)

3.3. Comparison of Analysis Results

The modal analysis results of both models are compared in tables. In Table 1, period values and comparisons of both models are given. Mode shapes are compared in Table 2.

Table 1. Comparison of period values each mode

	1. Mode	2. Mode	3. Mode	4. Mode	5. Mode
Steel Column Model	0.862881	0.514943	0.355794	0.324945	0.276291
Molybdenum Column Model	0.658191	0.442845	0.318558	0.26628	0.251915
Difference (s)	0.20469	0.072098	0.037236	0.058665	0.024376
Difference (%)	23.72	14.00	10.46	18.05	8.82

Table 2. Comparison of mode shapes each mode

	1. Mode	2. Mode	3. Mode	4. Mode	5. Mode
Steel Column Model	Translational (Y)	Torsional	Translational (X)	Translational (Y)	Translational (Y)
Molybdenum Column Model	Translational (Y)	Torsional	Translational (X)	Translational (Y)	Translational (Y)

4. Conclusions

When the 1st mode period values of the steel structure model consisting of steel columns and the steel structure model consisting of molybdenum columns are compared; 0.20469 seconds, 23.72% decrease was observed in percent. When the 1st mode shape of both models is examined, translation in the Y direction is observed in both cases.

When the 2nd mode period values of the steel structure model consisting of steel columns and the steel structure model consisting of molybdenum columns are compared; 0.072098 seconds, 14.00% decrease was observed in percent. When the 2nd mode shape of both models is examined, translation in the torsion is observed in both cases.

When the 3rd mode period values of the steel structure model consisting of steel columns and the steel structure model consisting of molybdenum columns are compared; 0.037236 seconds, 10.46% decrease was observed in percent. When the 3rd mode shape of both models is examined, translation in the X direction is observed in both cases.

When the 4th mode period values of the steel structure model consisting of steel columns and the steel structure model consisting of molybdenum columns are compared; 0.058665 seconds, 18.05% decrease was observed in percent. When the 4th mode shape of both models is examined, translation in the Y direction is observed in both cases.

When the 5th mode period values of the steel structure model consisting of steel columns and the steel structure model consisting of molybdenum columns are compared; 0.024376 seconds, 8.82% decrease was observed in percent. When the 5th mode shape of both models is examined, translation in the Y direction is observed in both cases.

In the light of all this information, it has been determined that the highest decrease in the period value, especially in the 1st mode, is experienced when the columns are used as molybdenum profiles in the steel structure model. Decreases were also observed in the period values in other modes. In this case, it can be easily said that the rigidity of the structure model increases. In addition, the fact that there is no change in mode shapes is interpreted positively. More research should be done on the use of molybdenum profiles in steel structures. According to the results of this study, column profiles can be used as molybdenum profiles instead of steel profiles in cases where the rigidity of the column cross-sections of steel structures needs to be increased without changing their dimensions.

References

- [1] Tuhta S. GFRP retrofitting effect on the dynamic characteristics of model steel structure. *Steel Compos Struct* 2018; 28(2): 223–231.
- [2] Kasınoz AA. *Fundamentals of Structural Dynamics and Applications in Earthquake Engineering*. Ankara, Turkey: Nobel Academic Publishing, 2018.
- [3] Çelebi M. GPS in dynamic monitoring of long-period structures. *Soil Dynam Earthq Eng* 2000; 20(5): 477-483.
- [4] Tuhta S. Optimal Determination of Structural Dynamical Parameters Using Ambient Vibration. *KSU J Eng Sci* 2018; 21(1): 55–65.
- [5] Keçeli A, Cevher M. Soil Dominant Period and Resonance Relation of Building Height. *Journal of Applied Earthsciences* 2018; 17(2): 203-224.
- [6] Kasınoz AA, Tuhta S, Günday F, Aydın H. Obtaining Dynamic Parameters by Using Ambient Vibration Recordings on Model of The Steel Arch Bridge. *Period Polytech Civ Eng* 2021; 65(2): 608-618.
- [7] Kao CY, Hung SL. Detection of structural damage via free vibration responses generated by approximating artificial neural networks. *Comput Struct* 2003; 81(28): 2631-2644.
- [8] Çelep Z, Kumbasar N. *Deprem mühendisliğine giriş ve depreme dayanıklı yapı tasarımı*, İstanbul, Türkiye: İhlas Matbaacılık, 2000.
- [9] Çelep Z. *Yapı dinamiği*, İstanbul, Türkiye: Beta Dağıtım, 2014.

- [10] İncetaş S, Tanrikulu, K. Binaların birinci doğal titreşim periyodunun yaklaşık olarak belirlenmesi 2002.
- [11] Nassani, DA. A simple model for calculating the fundamental period of vibration in steel structures. *APCBEE Procedia* 2014; 9: 393-346.
- [12] Aksoyulu C, Arslan, MH. Çerçeve türü betonarme binaların periyod hesaplarının farklı ampirik bağıntılara göre irdelenmesi. *Bitlis Eren Üniversitesi Fen Bilimleri Dergisi* 2019; 8(2): 569-581.
- [13] Aras F, Akbaş T, Ekşi H, Çeribaşı S. Progressive damage analyses of masonry buildings by dynamic analyses, *Int J Civ Eng* 2020; 18: 903-917.
- [14] Özşahin B. Türkiye Bina Deprem Yönetmeliği 2018’de Bina Doğal Titreşim Periyodunun Belirlenmesi İçin Verilen Ampirik Formülün Donatısız Yığma Binalar İçin İrdelenmesi, *Afyon Kocatepe University Journal of Science and Engineering* 2020; 22(2022): 873-892.
- [15] Benzeşik K. Molibden Konsantrelerinin Değerlendirilmesi. MSc, İstanbul Teknik Üniversitesi, İstanbul, Türkiye. 2016.
- [16] Polyak DE. Molybdenum, U.S. Geological Survey 2012 Minerals Yearbook: Molybdenum (Advance Release), 2012, 50.1-50.13, U.S. Department of the Interior.
- [17] Durkan C, Ilie A, Saifullah MSM, Welland ME. Mechanics of nanosprings: Stiffness and Young’s modulus of molybdenum-based nanocrystals, *Appl Phys Lett* 2002; 80(22).
- [18] Chatterjee, KK. *Uses of Metals and Metallic Minerals*, New Delhi: New Age International (P) Limited Publishers, 2007.
- [19] Joshi, KD, Gupta, SC. On mechanical stability of molybdenum, *High Press Res* 2007; 27(2): 259-268.
- [20] Laribi M, Vannes AB, Treheux D. Study of mechanical behavior of molybdenum coating using sliding wear and impact tests. *Wear*, 2007; 262(11): 1330-1336.
- [21] Nakajima K, Ohno H, Kondo Y, Matsubae K, Takeda O, Miki T, Nakamura S, Nagasaka T. Simultaneous Material Flow Analysis of Nickel, Chromium, and Molybdenum Used in Alloy Steel by Means of Input–Output Analysis. *Environ Sci Technol* 2013; 47(9): 4653-4660.
- [22] Gao S, Cui X, Zhang S. Utilization of Molybdenum Tailings in Concrete Manufacturing: A Review. *Appl Sci* 2020; 10(1):138.
- [23] Kasımcı AA. *Finite Element Method Fundamentals and Applications in Structural Mechanics*, Ankara, Turkey: Nobel Academic Publishing, 2018.
- [24] Kasımcı AA. *Structural Design and Analysis in The Light of Current Regulations with SAP2000 on The Basis of FEM*, Ankara, Turkey: Nobel Academic Publishing, 2021.
- [25] Ziada M, Tuhta S, Gençbay E. H, Günday F, Tammam Y. Analysis of Tunnel Form Building Retrofitted with CFRP using Finite Element Method. *Int J Trend Res Dev* 2019; 3(2): 822–826.
- [26] Tuhta S, Günday F, Alihassan A. The Effect of CFRP Reinforced Concrete Chimney on Modal Parameters Using Finite Element Method. *Int J Innov Eng Technol* 2020; 7(2): 1–6.
- [27] Bakkour F, Tuhta S, Günday F. Determination of Modal Parameters of Reinforced Concrete Box Culvert Retrofitted with GFRP Using Finite Element Method. *Int J Innov Eng Technol* 2022; 9(4): 1–9.
- [28] Hammoud MA, Tuhta S, Günday F. Determination of Modal Parameters of Reinforced Concrete Tunnel Retrofitted with CFRP using Finite Element Method. *Int J Innov Eng Technol* 2022; 9(4): 10–18.

Computer Vision Based AutoML Platform

Burak ŞAHİN¹, Aytuğ BOYACI^{2*}

¹ ATASAREN, Milli Savunma Üniversitesi, İstanbul, Türkiye

² Bilgisayar Mühendisliği Bölümü, Milli Savunma Üniversitesi, Hava Harp Okulu, İstanbul, Türkiye

¹ bsahin215@gmail.com, ^{2*} aboyaci@hho.msu.edu.tr

(Geliş/Received: 16/03/2023;

Kabul/Accepted: 11/08/2023)

Abstract: The rapid increase in data production, thanks to technological developments and scientific research, leads to the development of Machine Learning (ML) and similar new data analysis tools. It was announced that Amazon Web Services (AWS), a cloud service provider, stored 500EB of data in 2021 [1]. ML is an alternative to traditional engineering methods and does not require field knowledge of the problem to obtain a solution. However, the implementation of ML Algorithms can be complex depending on the content of the data set, and expert knowledge is the most important factor to use these algorithms effectively. Various methods have been developed to find a solution to this problem. There are many different areas and problems that machine learning can be applied to. We have limited our research to problems that can be solved using computer vision and AutoML. We have used AutoML and computer vision-based solutions to solve object classification, detection and segmentation problems. Our goal is to develop a platform that will work without the intervention of any expert. Users can load their datasets, choose the method they want, and train their models according to the problem they choose without any other intervention. After the training process is over, they can use their models in real time by transferring them over the platform in real time with their own hardware.

Key words: AutoML, Computer Vision, Deep Learning, Machine Learning, Object Classification, Object Detection.

Bilgisayarlı Görü Tabanlı AutoML Platformu

Öz: Teknolojik gelişmeler ve bilimsel araştırmalarla sayesinde veri üretimindeki hızlı artış, Makine Öğrenimi (ML) vb. yeni veri analiz araçlarının geliştirilmesine neden olmaktadır. Bir bulut servis sağlayıcısı olan Amazon Web Hizmetleri'nin(AWS) sadece 2021 yılında 500EB'lik veri depolandığı açıklandı. ML, geleneksel mühendislik yöntemlerine bir alternatiftir ve çözüm elde etmek için sorunun saha bilgisini gerektirmez. Bununla birlikte, ML Algoritmaları uygulanması veri setinin içeriğine göre kompleks olabilmektedir ve bu algoritmaları etkin bir şekilde kullanmak için uzman bilgisi en önemli etkidir. Bu soruna çözüm bulmak için çeşitli yöntemler geliştirilmiştir. Makine öğreniminin uygulanabileceği birçok farklı alan ve sorun bulunmaktadır. Çalışmada bilgisayarlı görü ve AutoML kullanılarak çözüm elde edilebilmek hedeflenmiştir. Bu anlamda çalışmada obje sınıflandırma, tespit etme ve segmentasyon sorunlarını çözmek için AutoML ve bilgisayarlı görü tabanlı çözümler kullanılmıştır. Hedefimiz, herhangi bir uzmanın müdahalesi olmadan çalışacak bir platform geliştirmektir. Kullanıcılar verisetlerini yükleyip, istedikleri yöntemi seçip ve başka hiçbir müdahale de bulunmadan seçtikleri sorun özelliğinde modellerini eğitebilmektedirler. Eğitim süreci bittikten sonra, kendi donanımlarıyla gerçek zamanlı bir şekilde platform üzerinden aktarım yapıp modellerini gerçek zamanlı bir şekilde kullanabilmektedirler.

Anahtar kelimeler: AutoML, Bilgisayarlı Görü, Derin Öğrenme, Makine Öğrenmesi, Nesne Sınıflandırma, Nesne Tespit Etme

1. Introduction

Today we are observing huge increase in the data generation with the developments of new technologies and the new scientific research [1]. The acceleration that observed on the data generation, leads to new advancement to new data analysis tools, which aim to examine the data and obtain meaningful results form the data. Machine Learning is the one of those tools [2]. Machine Learning is developed as an alternative for conventional engineering methods [3]. The main difference between machine learning and conventional engineering approaches are to obtain solutions to the problem, it doesn't require to field knowledge of the problem. The solution can be reached by using the data set obtained directly from the problem. Although this method more succesful than hand crafted methods, it is not perfect. In Prediction Based Modelling Methods, there is not a direct approach for usage of machine learning algorithms. This situation increases the dependencies on the expert's knowledge about these algorithms. Because there is a wide variety of algorithms and problem types. Development of the machine learning algorithms and applicability to many different fields at the same time brings the need of increasing numbers of experts about these algorithms. The knowledge of experts in these algorithms, significantly affects the success of algorthim. Since experts are not always sufficiently and equally competent, various methods have been developed to automate these algorithms in a way that requires minimum expert intervention.

Machine learning pipeline has consist of six different stages. This phases in respectively; data gathering, data cleaning and feature engineering, choosing a model that suitable with dataset, hyperparameter configuration,

training and evaluation. At each of these stages, there are required various adjustments processes by the expert and because of this adjustments success of the model directly affecting by the knowledge of the expert. Maybe the most important of this stages, hyperparameters adjustments and developing a suitable model for the dataset.

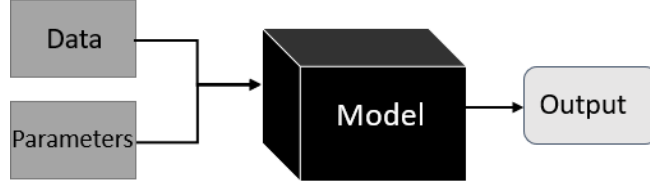


Figure 1. Black Box Model [4].

As seen in **Figure 1**, machine learning models also can be named as Black Box Models. The reason for this “that is as systems that hide their internal logic to the users” [4]. If we need to phrase in different way “Furthermore, the models learn from artificial datasets, often with bias or contaminated discriminating content” [5]. These models are given the dataset for training and the hyper-parameters that will be used during the training of the model for the developed model and cannot be changed by the model during the training. Since each of these stages is a separate subject of expertise, poorly trained models may lead to incorrect results due to the wrong model and hyperparameter selection. It is not always possible to find experts to develop these models and adjust the hyperparameters according to the distribution, quantity, and diversity of the available dataset. This situation leads to birth of a new approaches like Combined Algorithm and Hyper-parameter Selection(CASH). As given in the Equation 1, CASH Approach is aiming to get best model and the hyperparameters for the model with testing different algorithms($A = \{A^1, A^2, A^3\}$) with different hyperparameters($\theta = \{\theta^1, \theta^2, \theta^3\}$) on the same problem.

$$A^*, \theta^* = \operatorname{argmin}_{A \in A, \theta \in \theta} E[L_{\tau}(A_{\theta}(D_{\text{Train}}))] \quad (1)$$

Deep Learning is a subfield of Machine Learning. The major difference between them, in The Deep Learning models build as a iteratively stacked layers of architecture [6]. Before The Deep Learning has proven itself, SIFT was the state of art method used various application such as image matching and object detecting in the computer vision [7]. The work of Alex et al. maybe one of the biggest game changers in the Computer Vision [8]. After this work, researchers have begun to use Deep Learning more frequently in their research. As we mentioned before there are lots of different problems and algorithm variations for this reason in our work we only focused Computer Vision and in this field we choose the focusing object detection, classification and segmentation problems.

2. Related Work

When the AutoML field is examined, there are three generally accepted basic titles. These are Meta Learning, Neural Architecture Search and Hyperparameters Optimizations. Meta-learning is a technique where a machine learning algorithm learns from other algorithms that have been successfully trained and tested and working on the same or similar problem. Meta-learning was first introduced by J.Schmidhuber in 1987 under the title of “method that learns by referencing a group of learning” [9]. Since this date, the increasing amount of data and the increasing training time as a result of growing Deep Learning Algorithm Architectures have had a significant impact on the prominence of meta learning.

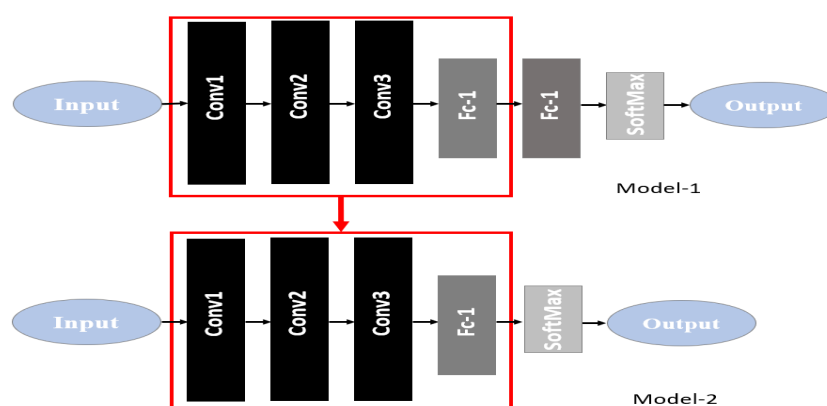


Figure 2. Transfer Learning.

To overcome these and similar problems, a number of new methods such as transfer learning and few-shot learning have been developed. Transfer learning. As can be seen in **Figure 2**, it provides the transfer of information between fields [10]. Instead of training a model from scratch to solve the current problem, we take the weights of another model that was previously trained to solve a similar problem, transfer it to model we want to use and customize it for our own needs. This approach not only shortens the model training time, but also allows us to obtain good results by fine-tuning in cases where the amount of data is low.

In a study in terms of AutoML and computer vision, it was done by Zeng Y. et al. [11]. In this study, thanks to the Google Cloud AutoML platform offered by Google as a service, they were able to train a model to detect breast cancer, which is mostly seen in women, by simply uploading the dataset.

In a study by Daniela M. et al., two separate models, SAI-G and SAI-C, using Google Cloud AutoML and Clarifai platforms; were trained to detect positive and negative emotions, and performance results were compared [12].

The MNIST Database was created by Yan L. et al. to set a standard for comparing the performance of Machine Learning Algorithms [13].

Jiancheng Y. et al. collected a similar dataset for 10 different cancer types and tested various AutoML approaches using AutoKeras, auto-sklearn tools and Google Cloud Vision Platform [14].

Intrusion is an important problem especially for countries with large borders and neighboring many countries. Countries with such geographical disadvantages set up walls and surveillance systems along their borders in order to ensure their border security. Because these systems are connected to a network, they suffer from a number of security vulnerabilities that every networked device suffers from. Intrusion Detection Systems have been developed to overcome these and similar problems. As in many fields, there are various Machine Learning applications in this field. In their study, Abhilash S. et al. developed an AutoML approach to select and train the most suitable machine learning algorithm for the Wireless Sensor Network's features [15]. Four features of the network were selected (the area covered by the network, the sensing distance, the transmission distance and the number of sensors), and a sensors data set was obtained by randomly generating these features within a certain range that can be found in real life. Then, they trained this dataset with the AutoML model they developed and determined the most suitable machine learning algorithm for the sensor at hand. Due to the complex data model space in AutoML techniques, researchers often limit their research to small models and data.

U-NET is a CNN-based image segmentation algorithm developed by Olaf R. et al. [16]. In the method section, the operation of this algorithm will be mentioned. On the other hand, Tonmoy S. et al. have tried to AutoML approach for a larger architecture such as the encoder-decoder architecture U-NET [17].

Up to this point, we have talked about a lot of AutoML studies. When it comes to machine learning, there is no universal AutoML System suitable for every problem that will meet everyone's needs. We have some methods available with a variety of tested successful results. However, even in this case, we need to be able to compare these systems in order to find out which system is the most suitable for the problem at hand. The study by Gijbers et al. provides us with a framework to compare AutoML systems [18]. This tool they developed and has been tested on five different AutoML algorithms and thirty nine different datasets.

Erin et al. developed a distributed architecture platform called H2o [19]. The platform does many steps itself, including data preprocessing. However, H2o is limited to supervised learning only.

Evolutionary algorithms can be defined as "EA aims to find solutions to complex real-world problems using the simulated evolution method." [20]. These algorithms improve the available solution population by mutating the individuals proposed for the solution of the problem and transferring information among themselves during a

certain iteration period. Using Evolutionary Algorithms, Liang et al. have developed an AutoML Framework that allows both to reduce the size of deep neural network architectures and to optimize hyperparameters [21].

Reinforcement learning(RL) “Helps agents communicate efficiently with their environment, enabling sequential decisions to be made” [22]. Agents are trained with the rewards and punishments they receive as feedback from their environment as a result of each decision they make. Mobile devices are widely used today. With the spread of these devices, they have started to apply various machine learning methods in the applications used in these devices. However, these devices, unlike desktop computers, do not have a stable energy source, and they also use smaller and less capable hardware. For this reason, especially deep artificial neural network etc. architectures need to be as compact as possible. Yihui et al., using the rl method in their study; They offer an AutoML Framework that will reduce the size of deep neural networks for mobile devices [23].

Apostolos et al. developed an edge computing-based method for video analysis [24]. The AutoML method they developed adjusts the parameters of both the wireless sensor network and the Artificial Neural Network.

Artificial neural networks are added layer by layer on top of each other, and while the size of the architectures continues to increase, more successful but computationally costly models emerge. This leads to the emergence of various, specialized hardware such as deep learning accelerators that aim to train artificial neural networks faster. A deep learning accelerator can be defined as “Deep learning accelerators are considered as hardware architecture, which are designed and optimized for increasing speed, efficiency and accuracy of computers that are running deep learning algorithms” [25]. In their study, Suyog et al. developed an AutoML approach that adjusts the parameters of the model by returning the loss value, taking into account the computational power of the accelerator [26].

3. Method

Our aim in the study is to enable users to make predictions with their models using their own cameras on the same platform in real time after they have uploaded the data to the platform in a pre-prepared format, selected the model suitable for the purpose they want, and trained their models, without having deep learning knowledge. The aforementioned structure is summarized in **Figure 3**. Before starting to explain our work we should set the limits of current status of our experimental platform design. Designing platform is a complex task. Our platform is limited to working with only image datasets which is structurally stored. In the computer vision there are lots of problem that to waiting for solution or optimization and improvement. As we try to build a complete platform and in order to demonstrate our platform strong sides, we have chosen from some proven solutions such as object classification, detection and segmentation.

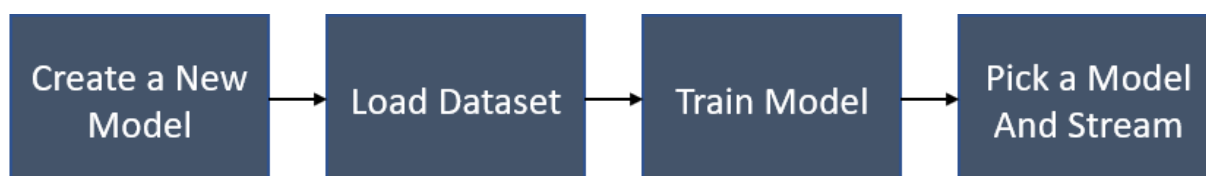


Figure 3. Main Event Loop

Convolutional Neural Networks(CNN) were first introduced by Yann LeCun et al. and it was used to detect single-digit numbers written in handwritten format [27]. Compared to classical Machine Learning methods, we need a large amount of data to train CNN. As the amount of data needed increases, the training time increases. These and similar problems have caused delays in the spread of CNN. A simple CNN Architecture is given in **Figure 4**. We use the same architecture in our own work while classifying objects. There is no feature that makes this architecture special. We chose this architecture because we wanted an architecture that would work fast and suitable for the generalized approach. We used the CIFAR-10 dataset to test our classification model [28]. The CIFAR-10 dataset consists of a total of 60,000 images of 10 different classes.

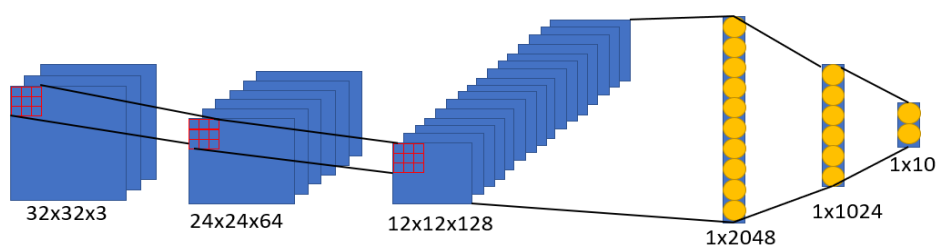


Figure 4. Basic Net

We used the Rectified Linear Unit(ReLU) activation function between the layers in the network we used for classification. ReLU entered the literature for the first time with a study by Fukushima K. [29]. The function is given in Equation 2. The feature that makes this function more successful than other activation functions is that it prevents the Disappearing Gradient Problem. “Disappearing Gradient Problem in back propagation stage, Convolutional Neural Networks calculate gradient using chain rule method. Multiplication of small numbers causes exponential reductions in gradients.” [30].

$$f(x) = \begin{cases} 0, & x < 0 \\ x, & x > 0 \end{cases} \quad (2)$$

Our model consists of 3 convolutions followed by MaxPooling Layers. Convolution process; as seen in the red kernel in **Figure 3**, it is the process of moving a 3x3 kernel over the image and obtaining various feature maps from the image. The MaxPooling method is a process that we apply to reduce the dimensions of the obtained feature maps. The MaxPooling method selects the maximum value in a kernel and you get another feature map with a smaller size than the feature map to which it is applied [31]. Of all the pooling methods, we specifically choose this method because it focuses on the most important points in the feature map. The equation of the MaxPooling method is given in Equation 3.

$$\sum_{k=1}^d \max \{x_k, \dots, x_{k+4}\} \quad (3)$$

We preferred the Yolov3 algorithm for object detection [32]. The Yolo Algorithm was developed by Josep R. et al. [33]. Since Object detection algorithms such as Region Based Convolutional Neural Networks(R-CNN) do not create an artificial Neural Network structure from start to finish, the feature extractor layer in the first layer of the algorithm cannot be trained and improved with more data. Yolo algorithms, on the other hand, give better results as they are trained, as they create an entire Neural Network structure. There are newer versions of the Yolo algorithm that produce better results. However, we chose to use Yolov3 because problems such as hardware and server created a bottleneck for us. Yolo algorithms divide an image into bounding boxes(bboxes) of equal size. Each box is responsible for detecting the object falling into itself in the image. Yolo has a single detection layer of 13x13 in total, while Yolov3 as given in **Figure 5**, has three different sized detection layers, 13x13, 26x26 and 52x52. The reason why this structure is preferred is to facilitate the detection of small-sized objects. We used the COCO dataset to test our model [34]. The COCO dataset consists of 80 different objects and 330 thousand images in total.

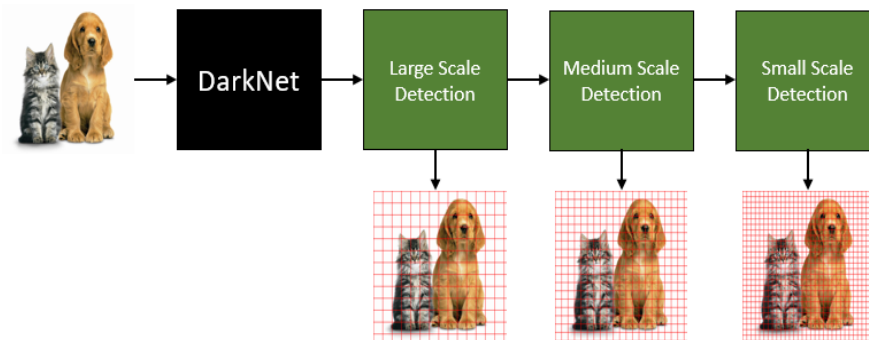


Figure 5. Top Level Yolov3 Algorithm

We need to talk a little bit about the Architecture of the Yolov3 Algorithm and how it works. Yolo algorithms basically consist of object detection layers added to the output of a pre-trained object classification algorithm. In the structure we use, DarkNet-53 is used as an object classifier. This architecture is a powerful architecture consisting of several residual net layers. The biggest innovation in Yolov3 is the addition of multiple object detection layers to the output of the object classifier. In this building, a method similar to the pyramid-shaped architecture made by Lin T. et al. was used [35]. It is the detection of small-scale objects by dividing an image into identical boxes of different sizes at different scales. Three anchor boxes with different geometric shapes are

assigned to each of these boxes. Anchor Boxes are “used as the first estimates of bounding boxes of many modern Deep Learning based object detectors” [36]. Anchor Boxes are predefined and loaded into the model. As a result, the model returns the coordinates, class and confidence score of the detected object, obtained from the boxes in 3 different detection layers. While testing the model we built, we trained 5 epochs and made sure it got the results we wanted. In order to speed up the testing process, we used the weights of the previously trained model by Joseph R. [37]. We mentioned that Yolo Algorithms get better as they are trained. When we say better, we are talking about both the accuracy and working speed of the algorithms. At the end of each iteration, it produces the result given in Equation 4 for three different scales. As given in Equation 4, b_x and b_y are the center of the bounding box, b_w and b_h are the width and length; p_c and c represent the probability of confidence score and the total number of classes.

$$y = (b_x, b_y, b_w, b_h, p_c, c) \quad (4)$$

Based on this result alone, we can see how costly an algorithm Yolo is. While training the Yolo algorithm, the p_c value in the bboxes it estimated over time gives more accurate results. Since the algorithm's metric is p_c , which basically allows us to decide whether there is an object in the predicted bbox, the higher this value, the faster our process of evaluating the remaining bboxes is eliminated. **Figure 6** shows the running state of the Yolov3 model. In order to demonstrate working state of real time detection, we have decided to take totally 10 seconds of a time interval. We have divided this time interval into three parts with five-second time lapses. In frame $t = 0.0$'s our platform makes only one prediction with using trained Yolov3 model for person (green prediction box) on the front of the camera. In frame $t = 5.0$'s our model makes three predictions for person, chair and window in orderly green, purple and pink prediction boxes. In $t = 10.0$'s our model makes only one prediction for chair in the front of the camera. As we can see from the last frame our model is not perfect. Frame $t = 10.0$'s and $t = 5.0$'s are nearly identical but it's not able to detect window as it did in frame $t = 5.0$'s. There are lots of improvements that can be made for this situation for example; using more advanced yolo versions, some data augmentation techniques, more data or spending more time on the training phase.

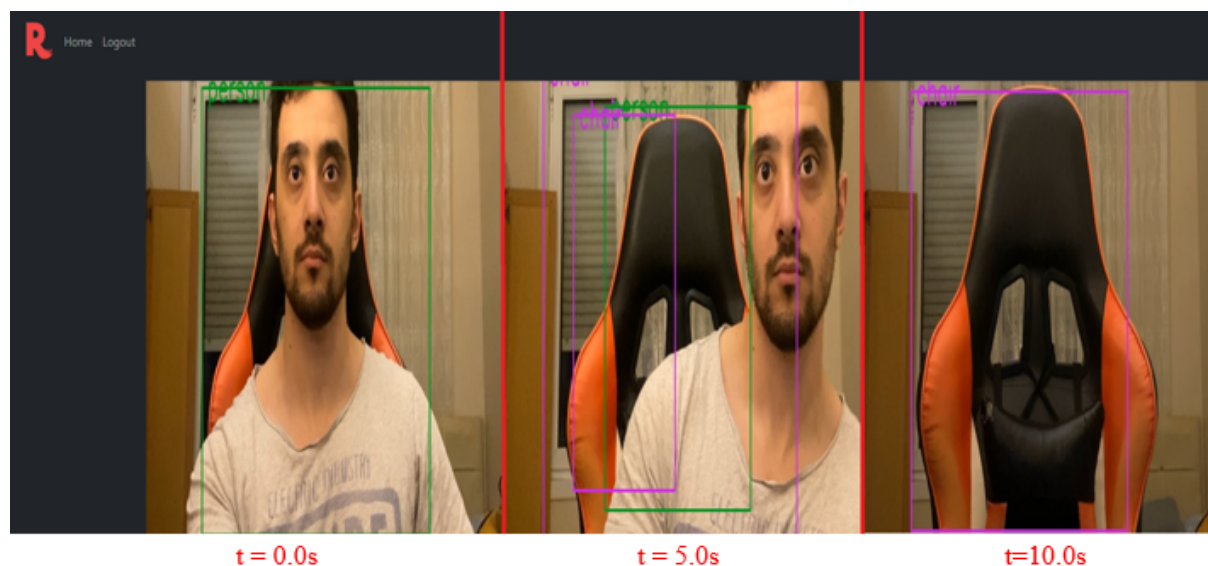


Figure 6. Object Detection On Working

Object Segmentation is mostly used in autonomous vehicles [38,39]. In its simplest form, segmentation is the process of assigning all pixels in an image to a class. What makes segmentation different from detection; While detecting only the relevant objects in the detection process, the segmentation process gives us more information about the structural features of the scene. Depending on the size and variance of the image at hand, the running speed of your algorithm is also affected.

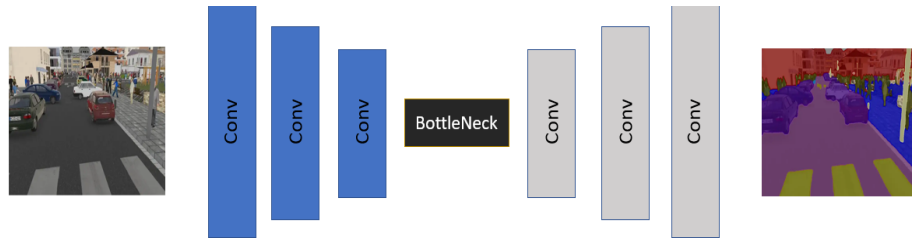


Figure 7. Encoder-Decoder Architecture Top View

There are many different types of architecture and approaches in the literature for Object Segmentation. Yuan et al. also tried a model using Transformers, which gave good results on the cityscapes dataset [40,41]. Yan et al. developed a model that examines the image at different scales, similar to Yolov3 [42]. Another Transformers-based study was done by Choi et al.[43]. Unlike the aforementioned studies, we preferred the previously mentioned U-Net model. These models we mentioned work more regionally. Our purpose in adding Object Segmentation to our platform is to gain more general information about what the scene is about. Therefore, as shown in **Figure 7**, U-Net, an Encoder-Decoder based architecture, was preferred. Encoders are used to compress information. They transfer the information they have compressed to the next layer. As information gets compressed, the size of the available data is getting smaller and smaller. Finally, the layer called BottleNeck is reached. The function of this layer is to keep the most important structural features necessary for us to reconstruct the data. The decoder, on the other hand, allows to regenerate the data based on the information in the BottleNeck layer. While Convolution Layers are used in Encoder Architecture, Convolution Transpose layers are used in Decoder. To define the work done by the Convolution Transpose layer, it “makes a transformation going in the opposite direction of a normal convolution” [44]. These two layers do the opposite of what each other does. While the layers learn the attributes of the data (color, brightness, etc.), the BotteleNeck layer learns the skeleton of the data. We used the Cityscapes dataset to test our segmentation model. This dataset consists of 20,000 images obtained from 50 different cities, with a total of 30 classrooms. We only used 19 classes in our study because we thought some classes were unnecessary. While setting up the models, we made use of another pre-installed ready models [45,46]. We had to make some performance improvements to make our model run faster when running in real time. One of these methods is to make an estimation by converting the image to a smaller size than its original size, and then converting the obtained segmentation map back to its original dimensions. Another method we apply is to convert the image to black and white. All these measures we have taken may not be a problem with better equipment. But we need to take these precautions for our current hardware.

4. Conclusion

We observed that the number of studies combining the field of computer vision with AutoML is very few in the literature. In order the demonstrate, these two fields can merge in a single product for solving object classification, detection and segmentation tasks, in our work we have try to design a platform that can train a ML model and stream the outputs of the model to the user without any expert intervention at all. We must warn the readers in this part, our platform is not production ready and unfortunately, we can't not host it at this stage. This work is an attempt to explore what can be done experimentally rather than a finished product. While we successfully handled the object classification and detection tasks, we had some difficulties with the segmentation task. The reason for this is that we prefer a computationally heavy model and method in order to obtain a generalizable model for segmentation and to obtain general information about the stage without disturbing the integrity of the stage. For object classification task, we have used BasicNet and achieved %77 classification accuracy on Cifar-10 datasets. As we explained in method section, we had to use trained weights sets whis has %55.3 mAP and 35 fps [37]. We did bulk of the computing in server side. This is not useful in delicate usage of real world environment (Traffic, Railway crossing). For the future work several improvements can be made for segmentation task and Edge Computing can be added, as Apostolos et al did.

Acknowledgment

This study was carried out within the scope of the thesis of the National Defence University, Atatürk Institute of Strategic Studies and Graduate Education. The idea stage of this study was carried out by B.Ş. and A.B., implementation phase carried out by B.Ş.

References

- [1] Adadi A. A survey on data-efficient algorithms in big data era. *Journal of Big Data* 2021; 24: 8(1).
- [2] Borgi T, Zoghalmi N, Abed M, Naceur, MS. Big data for operational efficiency of transport and logistics: a review. In 2017 6th IEEE International conference on Advanced Logistics and Transport (ICALT) 2017; pp. 113-120.
- [3] Simeone O. A very brief introduction to machine learning with applications to communication systems. *IEEE Transactions on Cognitive Communications and Networking* 2018; 4(4): 648-664.
- [4] Guidotti R, Monreale A, Ruggieri S, Turini F, Giannotti F, Pedreschi D. A survey of methods for explaining black box models. *ACM computing surveys (CSUR)* 2018; 51(5): 1-42.
- [5] Buhrmester V, Münch D, Arens, M. Analysis of explainers of black box deep neural networks for computer vision: A survey. *Machine Learning and Knowledge Extraction* 2021; 3(4): 966-989.
- [6] Alzubaidi L, Zhang J, Humaidi AJ, Al-Dujaili A, Duan Y, Al-Shamma O, ... & Farhan L. Review of deep learning: Concepts, CNN architectures, challenges, applications, future directions. *Journal of big Data* 2021; 8: 1-74..
- [7] Lowe DG. Object recognition from local scale-invariant features. In *Proceedings of the seventh IEEE international conference on computer vision* 1999; 2: 1150-1157.
- [8] Krizhevsky A, Sutskever I, Hinton GE. ImageNet classification with deep convolutional neural networks. *Communications of the ACM* 2017; 60(6): 84-90.
- [9] Hospedales T, Antoniou A, Micaelli P, Storkey A. Meta-learning in neural networks: A survey. *IEEE transactions on pattern analysis and machine intelligence* 2021; 44(9): 5149-5169.
- [10] Zhuang F, Qi Z, Duan K, Xi D, Zhu Y, Zhu H, ... & He Q. A comprehensive survey on transfer learning. *Proceedings of the IEEE* 2020; 109(1): 43-76.
- [11] Zeng Y, Zhang J. A machine learning model for detecting invasive ductal carcinoma with Google Cloud AutoML Vision. *Computers in biology and medicine* 2020; 122: 103861.
- [12] Marcu D, Mirela D. Sentiment Analysis From Images-Comparative Study of SAI-G and SAI-C Models' Performances Using AutoML Vision Service from Google Cloud and Clarifai Platform. *International Journal of Computer Science & Network Security* 2021; 21(9): 179-184.
- [13] Bottou L, Cortes C, Denker JS, Drucker H, Guyon I, Jackel LD, ... & Vapnik V. Comparison of classifier methods: a case study in handwritten digit recognition. In *Proceedings of the 12th IAPR International Conference on Pattern Recognition, Vol. 3-Conference C: Signal Processing* 1994; 2: 77-82.
- [14] Yang J, Shi R, Ni B. Medmnist classification decathlon: A lightweight automl benchmark for medical image analysis. In 2021 IEEE 18th International Symposium on Biomedical Imaging (ISBI) 2021; pp. 191-195.
- [15] Singh A, Amutha J, Nagar J, Sharma S, Lee CC. AutoML-ID: Automated machine learning model for intrusion detection using wireless sensor network. *Scientific Reports* 2022; 12(1): 9074.
- [16] Ronneberger O, Fischer P, Brox T. U-net: Convolutional networks for biomedical image segmentation. In *Medical Image Computing and Computer-Assisted Intervention–MICCAI 2015: 18th International Conference 2015; Part III* 18: pp. 234-241.
- [17] Saikia T, Marrakchi Y, Zela A, Hutter F, Brox T. Autodispnet: Improving disparity estimation with automl. In *Proceedings of the IEEE/cvf international conference on computer vision* 2019; pp. 1812-1823.
- [18] Gijbbers P, Bueno ML, Coors S, LeDell E, Poirier S, Thomas J, ... & Vanschoren J. Amlb: an automl benchmark. *arXiv preprint* 2022; arXiv:2207.12560.
- [19] LeDell E, Poirier S. H2o automl: Scalable automatic machine learning. In *Proceedings of the AutoML Workshop at ICML* 2020.
- [20] Vikhar PA. Evolutionary algorithms: A critical review and its future prospects. In 2016 International conference on global trends in signal processing, information computing and communication (ICGTSPICC) 2016; pp. 261-265.
- [21] Liang J, Meyerson E, Hodjat B, Fink D, Mutch K, Miikkulainen R. Evolutionary neural automl for deep learning. In *Proceedings of the Genetic and Evolutionary Computation Conference* 2019; pp. 401-409.
- [22] Dridi S. Reinforcement Learning-A Systematic Literature Review 2022.
- [23] He Y, Lin J, Liu Z, Wang H, Li LJ, Han S. Amc: Automl for model compression and acceleration on mobile devices. In *Proceedings of the European conference on computer vision (ECCV)* 2018; pp. 784-800.
- [24] Galanopoulos A, Ayala-Romero JA, Leith DJ, Iosifidis G. AutoML for video analytics with edge computing. In *IEEE INFOCOM 2021-IEEE Conference on Computer Communications* 2021; pp. 1-10.
- [25] Bolhasani H, Jassbi SJ. Deep learning accelerators: a case study with MAESTRO. *Journal of Big Data* 2020; 7, 1-11.
- [26] Gupta S, Akin B. Accelerator-aware neural network design using automl. *arXiv preprint* 2020; arXiv:2003.02838.
- [27] Forsyth DA, Mundy JL, di Gesù V, Cipolla R, LeCun Y, Haffner P, ... & Bengio Y. Object recognition with gradient-based learning. *Shape, contour and grouping in computer vision* 1999: 319-345.
- [28] Krizhevsky A, Hinton G. Learning multiple layers of features from tiny images 2009.
- [29] Fukushima K. Cognitron: A self-organizing multilayered neural network. *Biological cybernetics*, 1975; 20(3-4): 121-136.
- [30] Shah A, Kadam E, Shah H, Shinde S, Shingade S. Deep residual networks with exponential linear unit. In *Proceedings of the third international symposium on computer vision and the internet* 2016; pp. 59-65.
- [31] Gholamalinezhad H, Khosravi H. Pooling methods in deep neural networks, a review. *arXiv preprint* 2022; arXiv:2009.07485.

- [32] Redmon J, Farhadi A. Yolov3: An incremental improvement. arXiv preprint 2018; arXiv:1804.02767.
- [33] Redmon J, Divvala S, Girshick R, Farhadi A. You only look once: Unified, real-time object detection. In Proceedings of the IEEE conference on computer vision and pattern recognition 2016: pp. 779-788.
- [34] Lin TY, Maire M, Belongie S, Hays J, Perona P, Ramanan D, ... & Zitnick CL. Microsoft coco: Common objects in context. In Computer Vision–ECCV 2014: 13th European Conference 2014; 6(12), pp. 740-755.
- [35] Lin TY, Dollár P, Girshick R, He K, Hariharan B, Belongie S. Feature pyramid networks for object detection. In Proceedings of the IEEE conference on computer vision and pattern recognition 2017: pp. 2117-2125.
- [36] Zhong Y, Wang J, Peng J, Zhang L. Anchor box optimization for object detection. In Proceedings of the IEEE/CVF Winter Conference on Applications of Computer Vision 2020: pp. 1286-1294.
- [37] Yolov3 Weights Retrieved January 2, 2023 from <https://pjreddie.com/darknet/yolo/>
- [38] Ma Y, Mosskull A, Xiang A. 3D Semantic Segmentation for Autonomous Cars.
- [39] Zhang Z, Fidler S, Urtasun R. Instance-level segmentation for autonomous driving with deep densely connected mrfs. In Proceedings of the IEEE Conference on Computer Vision and Pattern Recognition 2016: pp. 669-677.
- [40] Cordts M, Omran M, Ramos S, Rehfeld T, Enzweiler M, Benenson R, ... & Schiele B. The cityscapes dataset for semantic urban scene understanding. In Proceedings of the IEEE conference on computer vision and pattern recognition 2016: pp. 3213-3223.
- [41] Yuan Y, Chen X, Wang J. Object-contextual representations for semantic segmentation. In Computer Vision–ECCV 2020: 16th European Conference, 2020; 6(16): pp. 173-190.
- [42] Yan H, Zhang C, Wu M. Lawin transformer: Improving semantic segmentation transformer with multi-scale representations via large window attention 2022; arXiv:2201.01615.
- [43] Choi S, Kim JT, Choo J. Cars can't fly up in the sky: Improving urban-scene segmentation via height-driven attention networks. In Proceedings of the IEEE/CVF conference on computer vision and pattern recognition 2020: pp. 9373-9383.
- [44] Dumoulin V, Visin F. A guide to convolution arithmetic for deep learning 2016; arXiv:1603.07285.
- [45] UNet Model Retrieved February 10, 2023 from: <https://github.com/hamdaan19/UNet-Multiclass>
- [46] Yolov3 Pytorch Implementation Retrieved January 2, 2023: github.GitHub Retrieved from: <https://github.com/eriklindernoren/PyTorch-YOLOv3>

Investigation of Flight Performance of Notched Delta Wing Rockets on Different Types of Nose Cones

Cihan OZEL^{1*}, Cevher Kursat MACIT², Meral OZEL³

^{1,2,3}Department of Mechanical Engineering, Engineering Faculty, Firat University, Elazığ, Türkiye

¹cozel@firat.edu.tr, ²macitkursatcevher@gmail.com, ³mozel@firat.edu.tr

(Geliş/Received:31/01/2023)

Kabul/Accepted:22.08.2023)

Abstract: In this study, four solid fuel model rockets with conical, parabolic, power and haack series nose cones that can carry 4 kg payload at an average altitude of 3 km were designed in the OpenRocket program. Later, the notched delta fin model was mounted on these designed model rockets. The effects of this fin model on the changes in the speed, stability, acceleration, weight and altitude of the rockets were analyzed numerically in the OpenRocket program. As a result of the analysis, it was determined that the conical nose rocket showed the worst flight performance and the Haack series nose cone rocket model showed the best performance. When used with the notched delta fin of the Haack series model, it was determined that the rocket's altitude increased by 7.67%, and its speed increased by 1.83%, but decreased by 1.2% in mach number, 0.6% in weight, 0.3% in acceleration, and 4.5% in stability. As a result, it was seen that it would be beneficial to consider the nose cone and fin together when evaluating the flight performance of the rocket. The results obtained in the study have shown that the notched delta fin model can be used experimentally in defense industry and model rocket applications and the studies can be advanced.

Keywords: OpenRocket program, Nose cones, Notched delta fin, Rocket flight performance

Farklı Tip Burun Konilerinde Çentikli Delta Kanat Roketlerin Uçuş Performansının İncelenmesi

Öz: Bu çalışmada, konik, parabolik, power ve haack serisi burun konilerine sahip ortalama 3 km irtifaya 4 kg yükü taşıyabilen katı yakıtlı dört adet model roket OpenRocket programında tasarlandı. Daha sonra, tasarlanan bu model roketlerin üzerine çentikli delta kanat modeli monte edildi. Bu kanat modelinin roketlerin hızında, stabilitesinde, ivmesinde, ağırlığında ve irtifasındaki değişimlere etkileri OpenRocket programında sayısal olarak analiz edildi. Yapılan analizler sonucunda, en kötü uçuş performansını konik burunlu roketin en iyi performansı ise Haack serisi burun konisine sahip roket modelinin gösterdiği belirlendi. Haack serisi modelin çentikli delta kanat profiliyle birlikte kullanıldığında roketin irtifasında %7,67, hızında %1,83 artışın olduğu ancak mach sayısında %1,2, ağırlığında %0,6, ivmesinde %0,3, stabilitesinde ise %4,5 oranında azalmaların olduğu belirlendi. Sonuç olarak, roketin uçuş performansı değerlendirilirken burun konisi ve kanat profilinin birlikte ele alınmasının faydalı olacağı görüldü. Çalışmada elde edilen sonuçlar çentikli delta kanat modelinin deneysel olarak savunma sanayisi ve model roket uygulamalarında kullanılabileceğini ve çalışmaların ilerletilebileceğini göstermiştir.

Anahtar kelimeler: OpenRocket programı, Burun konileri, Çentikli delta kanat, Roket uçuş performansı

1. Introduction

It includes studies on issues such as aviation design problems, aerodynamics, structural components, propulsion, flight mechanics, control, manufacturing and maintenance [1-3]. Another rocket component to be considered in rocket designs is nose cones. The design of the nose cone, which first encounters the air flow, significantly changes the altitude to be reached by affecting the aerodynamic efficiency [4]. In order to increase flight performance, it is a must to design the nose cone that best suits both the physical characteristics of the rocket and the flight parameters. The nose cone design also helps maintain the rocket's static margin, which is defined as the minimum distance between the rocket's center of gravity and its center of pressure. The undesired sway of the rocket due to the wind can be controlled by nose cones designed for lifting force acting on its surface through the center of pressure [5]. In addition to aerodynamic efficiency in rockets, one of the most important conditions for flight is stability.

The location of the center of gravity and center of pressure is of great importance for a stable flight. Fins have significant effects on the center of pressure and flight stability [6].

* Corresponding author: cozel@firat.edu.tr. ORCID Number of authors: 10000-0002-3227-6875, 1 0000-0003-0466-7788,10000-0002-9516-4715

In recent engineering and academic studies, it is seen that flight analyzes and simulations of model rockets are made by designing them in computer environment. In this context, Niskanen developed the OpenRocket simulation program, which is a model rocket simulation software [7]. Thanks to the simulation programs developed, it has become easier to analyze and interpret the flight performances of rockets numerically. Campbell et al. used model rockets to simulate flight trajectory and examine flight performance [8]. In rocket science, it is known that the fin and nose cone design are the most important parameters that affect the flight performance of rockets. The design of these two parameters has important effects on the aerodynamic efficiency and stability of the rocket and significantly changes the altitude, speed, acceleration and stability of the rocket [9-13]. Choosing an appropriate geometry to reduce friction as much as possible is essential in nose cone design. A nose cone with an aerodynamically competent geometry that will provide the least resistance to flight makes a significant contribution to flight performance. To ensure optimum rocket flight, a wide variety of nose cones have been developed and tested to meet these and other aerodynamic requirements [14]. In rocket designs, the nose cone design is an important parameter for the stable flight of the rocket in atmospheric conditions [13]. Shah et al., in their study, designed the Ogive, VonKarman and Power nose cone models and analyzed the nose profiles in the Ansys Fluent program under certain atmospheric conditions and at different Mach numbers [15].

Varma et al. examined the design features of 4 different nose cone models and their effects on rocket performance [9]. The aerodynamic response of rockets to air resistance under extreme ambient conditions and at high speeds can be largely represented by the response of the nose cone [10]. The aerodynamic behavior of the nose cone is important enough to determine the behavior of all components of the rocket [11]. Optimizing the geometric shape of the rocket nose cone is seen as the first step in the design process. In literature studies, spherically blunted conical, biconical, tangent ogive, secant ogive, elliptical, parabolic and Von Karman nose cone are generally known as the preferred nose cone types [13-18]. Among the literature studies, Ogive nose cone geometry is widely used for model rockets due to the convenience they provide in application and production [14,15]. Yeshwanth and Senthil analyze the effect of nose cone shape on drag in subsonic flow by considering various nose cone shapes [20]. In another study, a new type of fin model called notched delta fin was designed. This airfoil was mounted on a model rocket with a conical nose cone and the flight performances of the rocket were compared with other fin models used in practice. As a result of these comparisons, the new type notched delta fin model showed the best performance [21].

In this study, the notched delta airfoil [21], which was previously presented as a new wing model, was mounted on model rockets with parabolic, conical, power and haack series nose cones, and flight analyzes of these model rockets were made. With these flight analyzes, the different nose cone profiles of the delta wing model and the speed, acceleration, altitude, center of gravity and pressure center parameters were examined in the OpenRocket program under the same flight parameters. As a result of these analyzes, the model rocket and nose cone with the best performance were determined. With the results obtained from this study, it is aimed to make a modeling on the model rocket and defense industry applications.

2. Materials and Method

2.1. The design of the model rocket

In order to analyze the changes in the speed, stability, acceleration, weight and altitude of the model rocket with 4 different nose cones according to the notched fin, the solid model of the model rocket was designed in the OpenRocket program as follows (Figure 1). In order to make flight analyzes for rocket applications, the weight is distributed throughout the rocket and it is important to know how the weight distribution is for solving the problem. The distribution of these weights on the body was determined as in Figure 1, taking into account the literature [21-25].

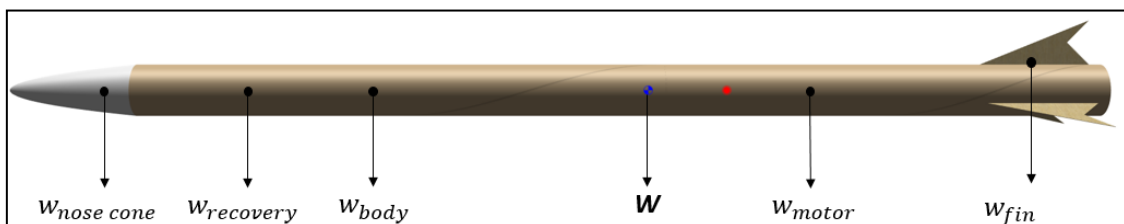


Figure 1. CAD design and weight distribution of the model rocket

The total weight of the model rocket in Figure 1 was calculated using the equation (1) below [21-25].

$$W_{Total} = W_{nose\ cone} + W_{recovery} + W_{body} + W_{motor} + W_{fin} \quad (1)$$

In this numbered equation, the weight of each component is calculated using the formula $W=m.g$. In this formula, m is the mass of the component and g is the gravitational acceleration. It is also important to determine the position of the center of gravity for the rocket trajectory and stability. In this study, the position of the center of gravity was determined according to the mass of the main parts of the rocket (nose, recovery system, fuselage tube, fins, engine, etc.) and the reference point as shown in Figure 2 [21-25].

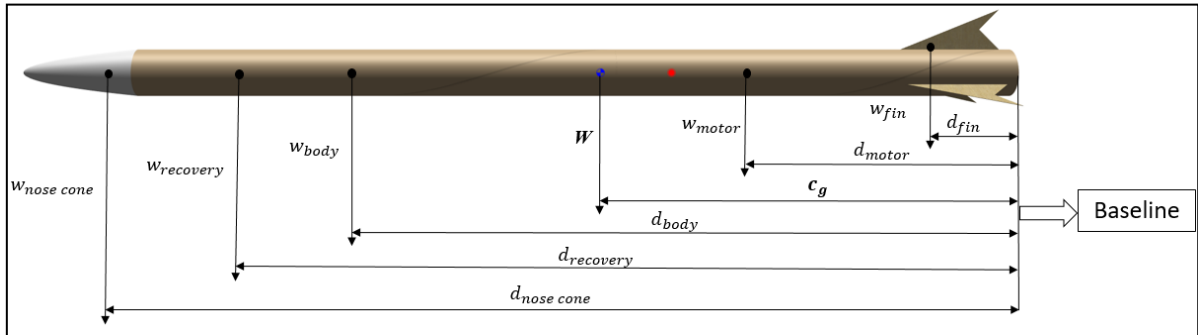


Figure 2. Center of mass of the model rocket

The distance of the center of gravity from the baseline is c_g multiplied by the total weight of the rocket, equal to the sum of the weight of each component times the distance from the baseline. In this case, the center of gravity of the rocket is calculated by equation (2) [21-25].

$$c_g W = d_{nose\ cone} W_{nose\ cone} + d_{recovery} W_{recovery} + d_{body} W_{body} + d_{motor} W_{motor} + d_{fin} W_{fin} \quad (2)$$

In the literature, the center of pressure is accepted as the point where all the forces applied to any object pass but do not create a moment. This center is the point where the forces caused by the air pressure on the rocket are affected. In other words, forces due to the weight of the rocket act on the center of gravity of the rocket, and aerodynamic forces act on the center of pressure. The center of pressure of the rocket was determined as shown in Figure 3 [21-25].

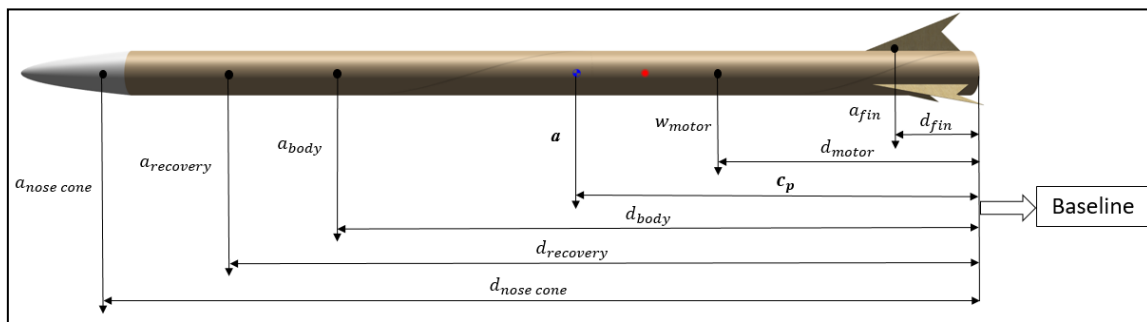


Figure 3. Center of pressure of the model rocket

The distance of the center of pressure from the reference line times the total area (A) of the c_p rocket is equal to the sum of the area of each component multiplied by the distance from the reference line. The center of pressure of the rocket is calculated by equation (3) in the literature [21-25].

$$c_p A = d_{nose\ cone} A_{nose\ cone} + d_{recovery} A_{recovery} + d_{body} A_{body} + d_{motor} A_{motor} + d_{fin} A_{fin} \quad (3)$$

Rocket stability is one of the most important parameters for flight and for the rocket to go on its orbit in a stable manner. The stability of the model rocket is defined in terms of the static margin (SM), the dimensionless

distance between the rocket's center of pressure and its center of gravity. In the literature, rocket stability is defined as in the equation SM, numbered [9]. In the equation, C_p is the center of pressure, C_g is the center of gravity and D is the body diameter of the rocket.

$$SM = \frac{C_p - C_g}{D} \tag{4}$$

While the model rockets were designed in the OpenRocket program, it was taken into account that these rockets could carry a load of 4 kg up to an altitude of approximately 3 km, and the other components and dimensions of these rockets were modeled with the exception of the nose cones (Figure 4).

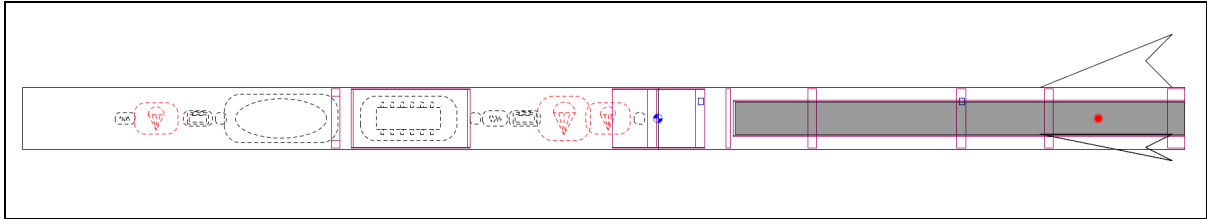
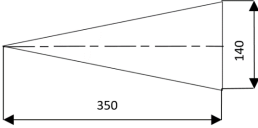
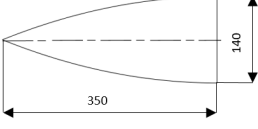
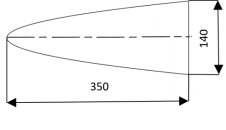
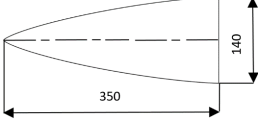


Figure 4. Design of the model rocket

In this study, conical, parabolic, power and haack models used in practice for nose cones mounted on model rockets were taken as reference. The profiles of these nose cones and the sizes on them are as in Table 1 [15,16,18,26].

The geometry and dimensions of the new type of notched fin model used on rockets with different nose cones were taken from the literature (Figure 5) [21].

Table 1. Geometry of nose cones given in the literature [15,16,18,26]

Nose Cone Types	Dimensions of Nose Cones Used in the Study
Conical	
Parabolic	
Power Series	
Haack Series (Von Karman)	

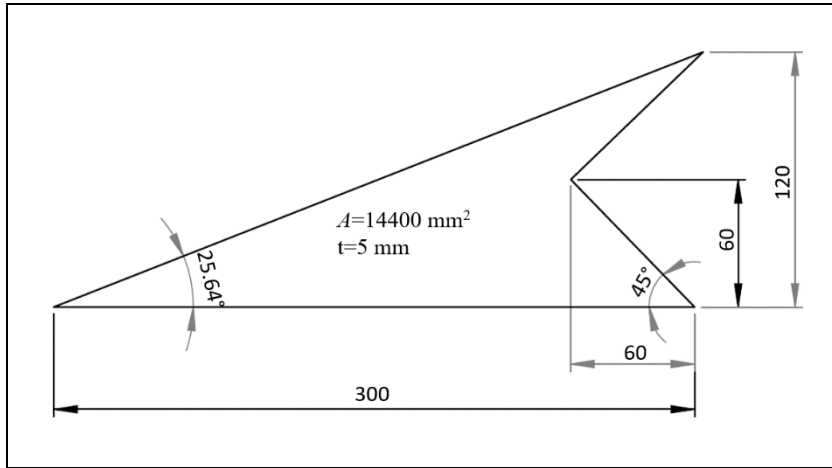


Figure 5. New type notched delta fin [21]

Table 2. Dimensions (mm) and weights (gr) of nose cone models

Nose Cone Model	Conical	Parabolic	Power	Haack
Nose Cone Length (L)	560	560	560	560
Diameter (D)	140	140	140	140
Weight (G)	4653	6251	6571	6251

All components, weights, materials and dimensions of the model rocket used in the study were calculated by considering equations (1, 2 and 3) and baseline (Figures 2 and 3). In Figure 6, the assembled state of all the components of the rocket and the calculated values in Table 1 are given.

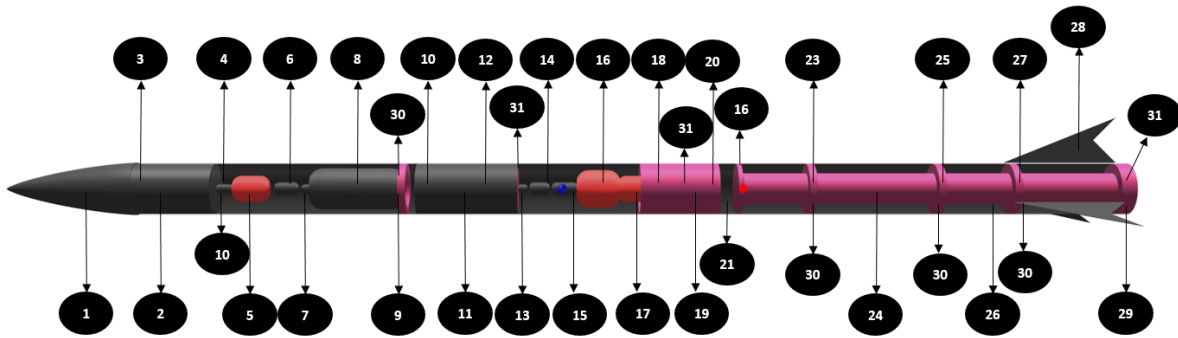


Figure 6. Components of the notched delta fin model rocket

Table 3. Dimensions, weights and materials of all components of the model rocket

Component	Piece	Number	Size (mm)	Material	Weight (gr)
Components of the nose cone					
Nose cone and body	1	1,2	560	Carbon fiber	Table 2
Map	1	3	25	Hammered steel	104
Shock cord	1	4	35	Paracord	2.7
$W_{nose\ cone}$					423.7
Components of the recovery system					
Payload parachute	1	5	100	Ripstop Nylon	131
Launch mechanism	1	7	65	ABS Filament	200
$W_{recovery}$					331
Body components					
Map	1	6	25	Hammered steel	104
Payload	1	8	260	-	4000
Centering ring	1	9	20	Blockboard	21.2
Electronic circuit box	1	10	270	Fiberglass	383
Flight computer	1	11	220	-	1450
Upper body	1	12	Length (1700) diameter (140)	Carbon fiber	3333
Map	1	13	25	Hammered steel	104
Shock cord	1	14	35	Paracord	2.7
Launch mechanism	1	15	65	ABS Flement	200
Big parachute	1	16	150	Ripstop Nylon	874
Small parachute	1	17	100	Ripstop Nylon	132
Body connecting element	1	18	210	Aluminum	700
Bulkhead	1	19	20	Blockboard	90.3
Bulkhead	1	20	20	Blockboard	90.3
Underbody	1	21	Length (1100) diameter (140)	Carbon fiber	2758
Bulkhead	1	22	20	Blockboard	90.3
W_{body}					14332.8
Components of the engine					
Motor centering ring	1	23	51	Blockboard	55.6
Motor stock	1	24	940	Carbon fiber	1262
Motor and fin centering ring	1	25	51	Blockboard	55.6
Motor	1	26	51	-	7878
W_{motor}					9251.2
Components of the fin					
Motor and fin centering ring	1	27	51	Blockboard	55.6
Fin	3	28	30	Carbon fiber	340
Motor centering ring	1	29	40	Blockboard	55.6
W_{fin}					1131.2
M5 screw	27	30	6	Steel	1.21
M8 screw	4	31	10	Steel	5.03
W_{screw}					52.79

2.2. Investigation of rocket flight analysis

The effects on the weight, speed, acceleration, stability, center of gravity and pressure and mach number of the rockets were analyzed in the open-source program, open rocket, for 4 different nose cones designed with the same length and height, at constant engine power, with constant parameters such as wind speed.

3. Results and Discussion

Flight analyzes of each of the model rockets, whose designs are given in Figure 5, were performed in the OpenRocket program. The results obtained from these analyzes are given below in terms of both bar diagrams and time-dependent changes in weight, velocity, acceleration, center of gravity and pressure, stability, Mach number and altitude of each model rocket (Figure 7-13). The nose cone design directly affects the rocket weight and flight performance of the rocket. The lowest weight in the nose cone designs was achieved in the conical nose model rocket design. Rocket weight directly affects all results from rocket flight data. In the literature, it is stated that the changes in the design of the nose cones cause significant changes in the altitude, speed, acceleration, stability and weight of the rockets [3,9-13,27]. As a matter of fact, in this study, it was observed that the flight performances of each rocket model with the same components but different nose cones changed (Figure 7-13). While the flight performance of the conical-nosed model rocket with the lowest rocket weight is expected to give better results than other models, it was seen that the Haack series nose cone rocket gave the best performance as a result of all

flight analyzes (Figures 9 and 10). This result was found to be in agreement with the literature [9,15,28]. The conical-nosed model rocket also showed the lowest performance compared to other models other than the Haack series (Figures 9 and 10).

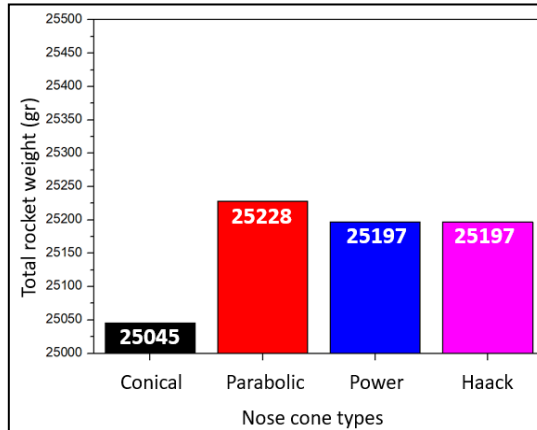


Figure 7. Total weights of model rockets

In previous studies in the literature, it was stated that the Mach number should be greater than 0.8 for a rocket that will fly at subsonic speeds, in the range of 0.8-1.2 in transonic flights, in the range of 1.2-5 in supersonic speeds and 5-10 in hypersonic speeds [29- 31]. In this study, it was seen that the Mach number reached in the model rockets whose flight performance was examined was greater than 0.80 and the rocket was suitable for flight at transonic speeds (Figure 8).

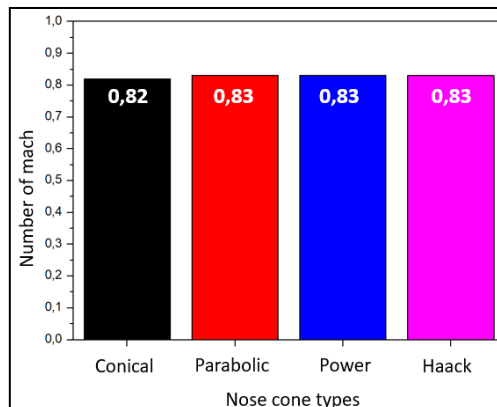
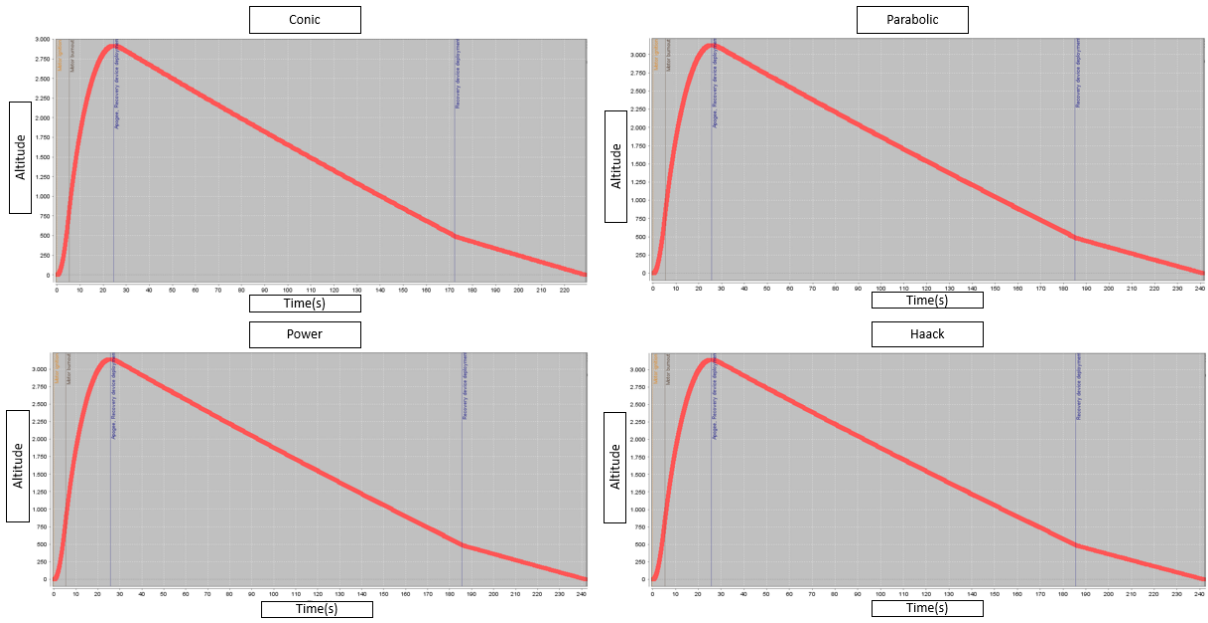
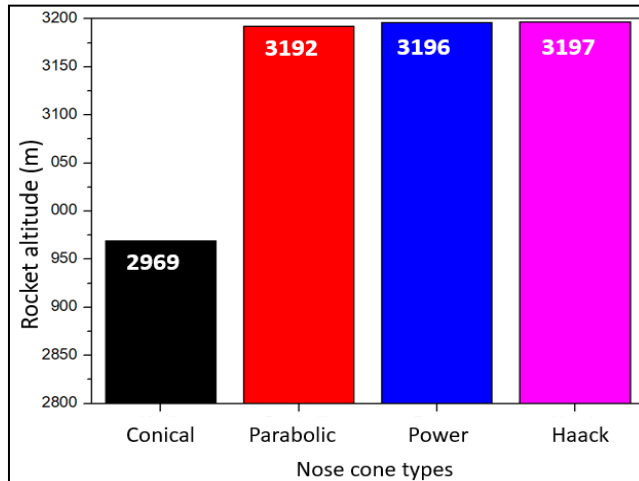


Figure 8. Effect of nose cone on Mach number

In the flight analyzes made depending on time, it was seen that the nose cone had a significant effect on the maximum altitude that the model rocket could reach (Figure 9). In the case of using the notched delta fin model on the Haack nose cone rocket, it was observed that an increase of 128 meters occurred in the altitude of the rocket compared to the cone nose rocket (Figure 9 a and b). The results were also visualized in bar diagrams so that the numerical values of the maximum altitudes reached by the model rockets could be seen much more clearly (Figure 10b).



a) Changes in altitude over time



b) Maximum altitudes

Figure 9. Changes in altitude of rockets

The changes in the stability of model rockets depending on time are shown in Figure 10. The center of gravity and pressure of the model rockets were calculated using the equations (2) and (3) given in the literature, and these values are given in Figures 11a and b. Again, the effects of the centers of gravity and pressure on the stability values of the rockets were calculated using the equation (4) given in the literature [9]. Bar diagrams are presented in Figures 11 a, b, and c to show the changes in all these values more clearly.

Investigation of the Effects of Notched Delta Fin on Flight Performance of Rockets with Different Nose Cone

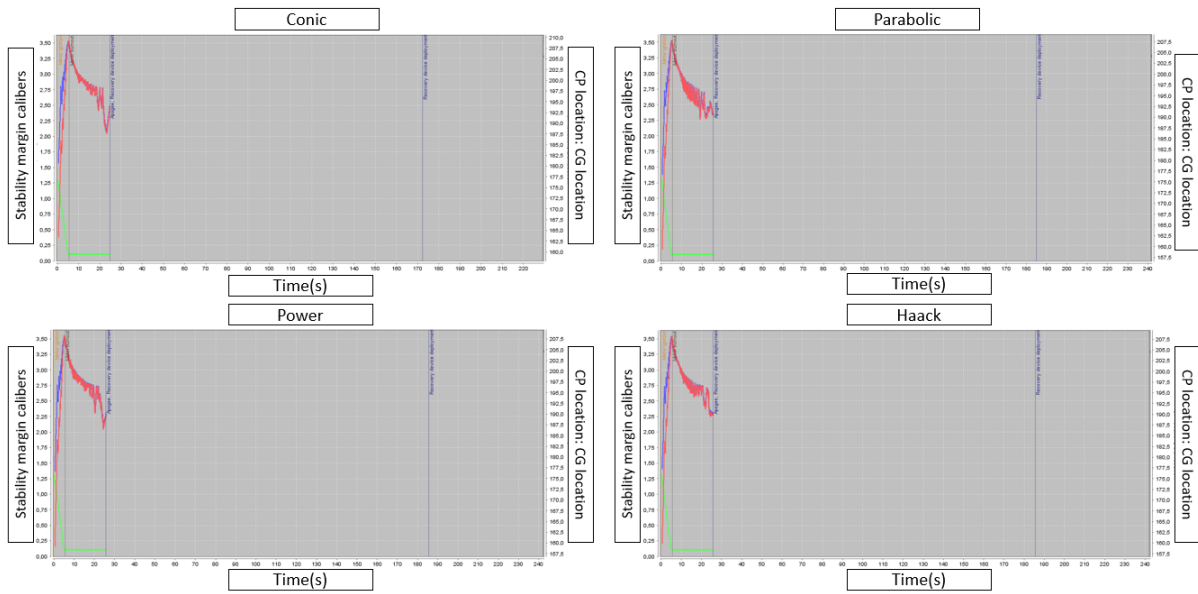
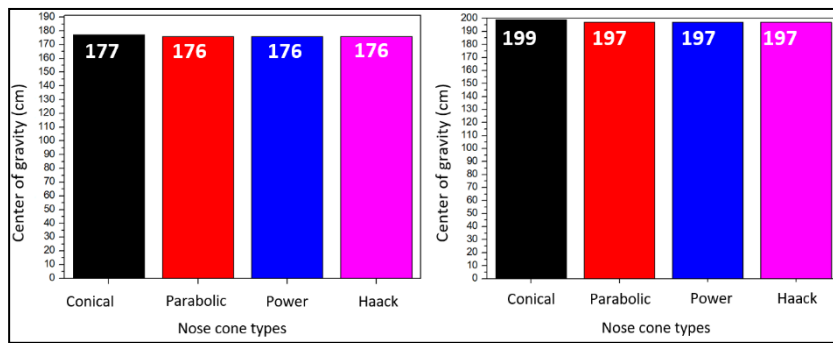
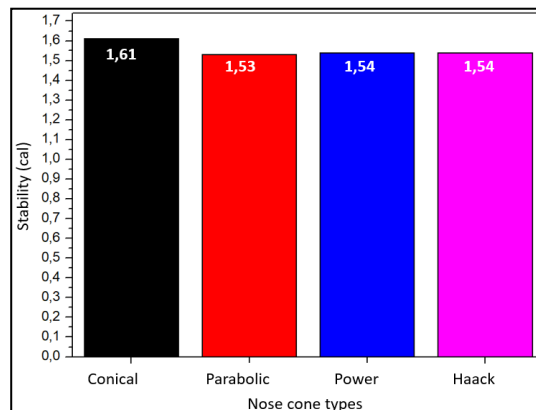


Figure 10. Change in the stability of rockets over time



a) Centers of gravity of rockets

b) Pressure centers of rockets



c) Effects of gravity and pressure centers on the stability of rockets

Figure 11. Effects of changes in nose cones on weight, pressure and stability of rockets

In order for the stability of the rocket to be stable, there must be a distance of at least the diameter of the hull between the center of pressure and the center of gravity. If the center of pressure and the center of gravity are too close to each other, the rocket may be dynamically underdamped [32]. Likewise, if the distance between the

center of pressure and the center of gravity is too far, the rocket becomes overstable, which may cause the rocket to fall. In order for the rocket to make a stable flight, the center of pressure (C_p) must be behind the center of gravity (C_g) [2,33-35]. Considering this literature information, it is seen that all model rockets designed here can perform a stable flight. In the case of using the notched delta fin model by changing the nose cones, the changes in the velocity of the rockets over time are presented below, both graphically and as a bar diagram (Figure 12).

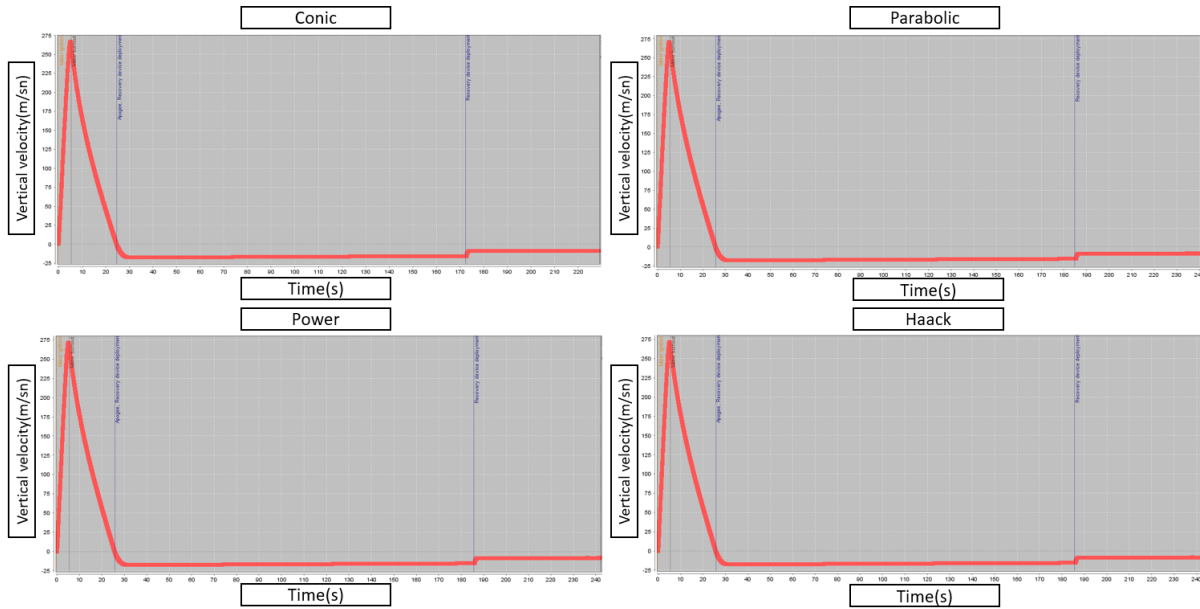
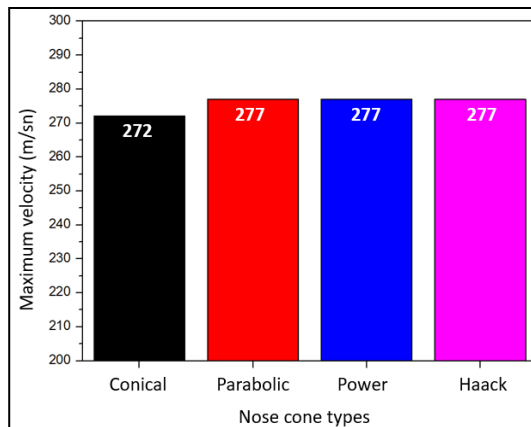


Figure 12. Changes in velocity with time

The maximum values of the maximum velocities reached by the rockets depending on the time given above are shown in the bar diagram below (Figure 13). In this graph, it was seen that the minimum velocity value was reached in the conical-nosed model rocket. The highest velocity values were reached in Parabolic, Power and Haack nose cones, respectively. The same velocity value was obtained for these three nose cones.

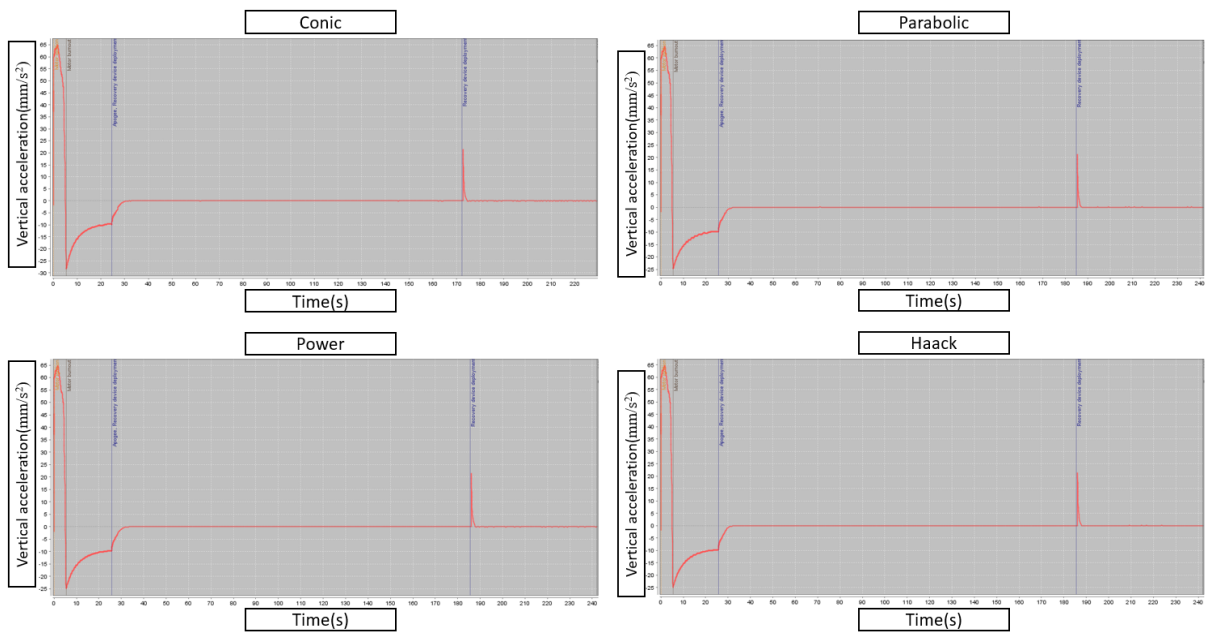


b) Maximum speeds

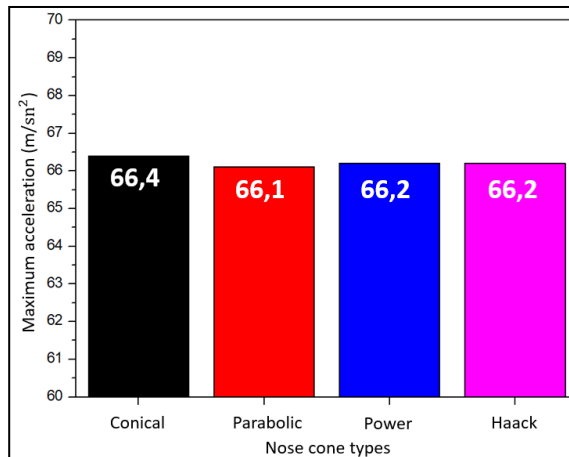
Figure 13. Changes in rockets speeds

The changes in the accelerations of the model rockets according to the changes in the geometry of the nose cones are given below, both in time and as a bar diagram (Figure 14a and b). According to nose cones, the highest acceleration was 66.4 mm/s^2 in the conical nose rocket, the lowest acceleration was 66.1 mm/s^2 in the Parabolic nose rocket, and 66.2 mm/s^2 in the Power and Haack series.

Investigation of the Effects of Notched Delta Fin on Flight Performance of Rockets with Different Nose Cone



a) Changes in acceleration with time



b) Changes in acceleration

Figure 14. Changes in acceleration of rockets

4. Conclusion

In the article, notched delta fin mounted proof is shown in model rockets with Conical, Parabolic, Power and Haack series nose cones, and the changes in velocity, stability, acceleration, weight and altitude of these rockets are numerically analyzed in the OpenRocket open source program. According to the analysis results, while the Haack nose rocket showed the best flight performance, the Conical nose rocket showed the worst performance. Especially in the case of using the notched delta fin model in the Haack nose rocket, it was observed that the rocket's altitude increased by 7.67% and its speed increased by 1.83%. Although the rocket weight is lower in the conical nose rocket model compared to other models, it is thought that it does not provide the expected flight performance and this is due to the flat and sharp edges on the nose cone. In addition, curvature was found to be an important parameter in nose cone designs. Because in this study, it was seen that the flight performances of Parabolic and Power nose model rockets gave better results than Conical nose rockets. It is thought that the studies can be expanded experimentally, and flow analysis of the model rocket produced with the nose cone model and delta wing model, which gives the best results in future studies.

References

- [1] Barbosa AN, Guimarães LNF, Multidisciplinary design optimization of sounding rocket fins shape using a tool called mdo-sonda. *J Aerosp Technol Manag* 2012; 4: 431-442.
- [2] Priyadarshi P, Alam M, Saroha K, Multi-disciplinary multi-objective design optimization of sounding rocket fins. *Int J Adv Eng Sci Appl Math* 2014;6(3): 166-182.
- [3] Baloda Y, Jaiswal A, He X, Datye A. Theoretical and experimental performance evaluation of shark-caved, sounder, and trapezoidal fins. *NCUR Proceedings*, 2020.
- [4] Bilgic HH, Coban S, Yapici A. Designing, Modeling and Simulation of Solid Fuel Rocket ALP-01,2019.
- [5] Rohini D, Sasikumar C, Samiyappan P, Dakshinamurthy B, Koppula N. Design & analysis of solid rocket using open rocket software. *Mater Today Proc* 2022; 64: 425-430.
- [6] Azevedo FS, Knowing the stability of model rockets: A study of learning in interest-based practices, *Cognition and Instruction*, 2013; 31(3): 345-374.
- [7] Niskanen S, Development of an Open Source model rocket simulation software, MSc. Dissertation, Helsinki University of Technology, Faculty of Information and Natural Sciences, 2009.
- [8] Campbell TA, Seufert ST, Reis RC, Brewer JC, Limberger Tomiozzo R., Whelan C. E., Okutsu M. Model rocket projects for aerospace engineering course: Simulation of flight trajectories. In 54th AIAA Aerospace Sciences Meeting 2016; 1577.
- [9] Varma AS, Sathyanarayana GS, Sandeep J. CFD analysis of various nose profiles. *Int. J. Aerosp. Mech. Eng.*,2016; 3(3): 26-29.
- [10] Ledu J, Pollak C. Flight testing results on a hypersonic reentry nose cone. *J. Spacecraft Rockets* 1969; 6 (9): 1044–1047.
- [11] Ericsson RA, Guenther WR, Stake, Olmsted GS. Combined effects of nose bluntness and cone angle on unsteady aerodynamics. *AIAA J* 1974; 12(5): 729–732.
- [12] Mari VA, Maharaj PN, Muthuraman ES. Design and analysis of spherically blunted conic and spherically blunted tangent ogive nose section of the aircrafts using CFD. *Int. J. Adv. Res. Manag. Arch. Tech. Eng.*, 2019; 5(4): 61–70.
- [13] Pandey PK, Rajput B, Narayan A, Narayanan S. Numerical simulation of supersonic flow past a biconic nose cone. *Int. J. Adv. Res. Sci. Eng.*, 2017; 6(3): 604–610.
- [14] Milligan A., “Drag of nose cones,” [apogeerockets.com. https://www.apogeerockets.com/education/downloads/Newsletter346.pdf](https://www.apogeerockets.com/education/downloads/Newsletter346.pdf) (accessed Sep. 22, 2021).
- [15] Chalia S, Bharti MK. Mathematical modeling of ogive forebodies and nose cones. *Int Res J Eng Tech* 2016; 3(3):744–747.
- [16] Parvez D, Chalia S. Investigation on aerodynamic performance of elliptical and secant give nose cones. *Int J Sci Res Eng Tren* 2019; 5(4): 1291–1300.
- [17] Narayan A, Narayanan S, Kumar R, Kumar R. Hypersonic flow past parabolic and elliptic nose cone configurations: a comparative study. *Simulation* 2018; 94(8): 665–680.
- [18] Varma AS, Sathyanarayana GS, Sandeep J. CFD analysis of various nose profiles. *Int J Aerosp Mech Eng* 2016; 3(3):26–29.
- [19] Lim S, Kim SD, Song DJ. The influence of Chine nose shapes on a slender body flight vehicle at high angles of attack. *J Aerosp Eng* 2012; 226(2): 182–196.
- [20] Yeshwanth A, Senthil PV. Nose cone design and analysis of an avion. *Int J Pure Appl Math* 2018; 119(12): 15581– 15589.
- [21] Ozel C, Macit CK, Ozel M. Investigation of the Effects of the New Type Notched Delta Wing Model on the Flight Performance of the Rocket. *Firat University Journal of Engineering Sciences*, 2023; 35(1): 175-193.
- [22] Hernandez RN, Singh H, Messimer SL, Patterson AE. Design and performance of modular 3-D printed solid-propellant rocket airframes. *J Aerosp* 2017; 4(2): 17.
- [23] Rocketschools. Rocket Stability.<http://www.rockets4schools.org/images/Basic.Rocket.Stability.pdf>. Accessed on January 20, 2023.
- [24] Nasa. Determining center of pressure-cp. On 14 Jan 03 Accessed on January 16, 2023. <https://www.grc.nasa.gov/www/k12/VirtualAero/BottleRocket/airplane/rktcp.html>
- [25] Rocketsan model rocketry. https://www.roketsan.com.tr/uploads/docs/1628594512_20.03.2020model-roketcilik-master-dokumanv04.pdf. Published on 20.03. 2020.Accessed on January 18, 2023.
- [26] Crowell GA. (1996). The descriptive geometry of nose cones. URL: <http://www.myweb.cableone.net/cjcrowell/NCEQN2.doc>.

- [27] Datye A. Effects of Shark Caved Fins on Altitude Performance of a High-Powered Rocket. 2019 NCUR, 2019.
- [28] Shah S, Tanwani N, Singh SK, Makwana MM. Drag analysis for sounding rocket nose cone. *Int Res J Eng Technol* 2020; 7(07).
- [29] Fraley ER. Design, Manufacturing, and Integration of Fins for 2017-2018 OSU ESRA 30k Rocket 2018.
- [30] Neutrium. Mach Number, Neutrium, https://neutrium.net/fluid_flow/mach-number/ Published October 2014. Accessed on January 20, 2023.
- [31] Zhang GQ, Ji LC, Xu Y, Schlüter J. Parametric study of different fins for a rocket at supersonic flow. *Proc Inst Mech Eng Part C*, 2015; 229(18): 3392-3404, 2015.
- [32] Negahban S, Design of a Model Rocket Flight Logging System and In-Air Deployable Rover, 2019.
- [33] Bar-Haim B, Seginer A. Aerodynamics of wraparound fins. *J Spacecr Rockets* 1983; 20(4): 339-345.
- [34] Yarce A, Rodríguez JS, Galvez J, Gómez A, García MJ. Simple-1: Development stage of the data transmission system for a solid propellant mid-power rocket model. *J Phys Conf Ser.* 2017; 850(1): 012019
- [35] Nakka, R., Fins for Rocket Stability, Experimental Rocketry Accessed on January 18, 2023.

Development of Unmanned Aerial Vehicle for Detecting the Forest Fires

Baris Mert KADIOGLU¹, Secil KARATAY^{2*}, Yucel CETINCEVIZ³, Faruk ERKEN⁴

¹⁻⁴ Electrical Electronics Engineering, Faculty of Engineering and Architecture, Kastamonu University, Kastamonu, Turkey

¹ barismertkadioglu@gmail.com, ^{2*} skaratay@kastamonu.edu.tr, ³ ycetinceviz@kastamonu.edu.tr, ⁴ ferken@kastamonu.edu.tr,

(Geliş/Received: 24/05/2023;

Kabul/Accepted: 30/08/2023)

Abstract: In recent years, forest fires can be brought under control in line with the information obtained from Unmanned Aerial Vehicles (UAVs), which play an important role in determining the progression of fires, detecting heat points and determining intervention locations. In this study, if the UAV detects the fire by autonomously positioning in the area where the fire is located, the point where the fire reaches the most intense temperature is determined with the help of the thermal camera, and it is ensured that the fireball is dropped to the target with a 100% success rate. The requirements of the UAV, which will be produced in order to realize this task, such as fast, load-carrying and stable flight are also taken into consideration. In addition to being economical and long-lasting of the materials inside, it will be able to fly efficiently in most weather conditions (foggy, dark, etc.). In the construction of the UAV, a domestic Electronic Speed Controller (ESC) with a unique design is produced to meet the sufficient current. With this acquisition, ESC, which will meet the requirements by sending sufficient current to more than one Brushless DC (BLDC) motor, has been tested on our Radio Controlled (RC) aircraft and included in the project.

Key words: Unmanned Aerial Vehicle, Forest Fire, Electronic Speed Controller, Autonomous Flight.

Orman Yangınlarının Tespiti İçin İnsansız Hava Aracı Geliştirilmesi

Öz: Son yıllarda yangınların seyrinin belirlenmesinde, ısı noktalarının tespit edilmesinde ve müdahale yerlerinin belirlenmesinde önemli rol oynayan İnsansız Hava Araçları'ndan (İHA) elde edilen bilgiler doğrultusunda orman yangınları kontrol altına alınabilmektedir. Bu çalışmada İHA'nın, yangının bulunduğu bölgede otonom olarak konumlanarak yangını tespit etmesi durumunda, termal kamera yardımıyla yangının en yoğun sıcaklığa ulaştığı nokta belirlenmekte ve ateş topunun %100 başarı oranı ile hedefe düşürülmesi sağlanmaktadır. Bu görevi gerçekleştirmek üzere üretilecek olan İHA'nın hızlı, yük taşıma ve stabil uçuş gibi gereksinimleri de göz önünde bulundurulmuştur. İçerisindeki malzemelerin ekonomik ve uzun ömürlü olmasının yanı sıra çoğu hava koşulunda (sisli, karanlık vb.) verimli bir şekilde uçabilecektir. İHA yapımında yeterli akımı karşılamak için özgün tasarıma sahip yerli Elektronik Hız Kontrol Cihazı (ESC) üretilmiştir. Bu satın alma ile birlikte birden fazla Fırçasız DC (BLDC) motora yeterli akım göndererek gereksinimleri karşılayacak olan ESC, Radyo Kontrollü (RC) uçagımızda test edilmiş ve projeye dâhil edilmiştir.

Anahtar kelimeler: İnsansız Hava Aracı, Orman Yangını, Elektronik Hız Kontrol Cihazı, Otonom Uçuş.

1. Introduction

In today's world, as a result of the great development in the field of defense industry with Unmanned Aerial Vehicles (UAVs), UAVs can be integrated into other fields and can perform many operations without the need for manpower and without endangering human life [1, 2, 3]. Early detection of forest fires and at the same time the timeliness of the first response is of vital importance. One of the mission objectives of UAVs has been to notify the fire to the ground station by means of target detection and first response with the UAV fixed wing model, and to keep the fire under control, with the aim of preventing the increase in the destruction caused by the delay and inadequate response to forest fires, which have increased in recent years. By making extensive surveillance with UAVs, both the size of the fire can be determined faster and the correct locations can be intervened with the information obtained from these vehicles during extinguishing. Especially at night, monitoring the general course of fires, determining the heat points and determining the intervention places more clearly prevent the spread of flames to wider areas.

Preliminary studies on UAV technologies for remote sensing of forest fires started in the early 2000s. This period is characterized by the use of remotely controlled High Altitude and Long Endurance UAVs (HALE UAVs) utilized by research agencies as a complement to existing satellite tracking systems. HALE UAVs can fly for hours at high altitude and carry significantly heavy payloads, are expensive systems and do not provide

* Corresponding author: skaratay@kastamonu.edu.tr. ORCID Number of authors: ¹ 0009-0001-5194-9158, ² 0000-0002-1942-6728, ³ 0000-0001-6834-9442, ⁴ 0000-0003-2048-1203

more precise data than satellites [4]. In [5], a remote-controlled UAV equipped with a thermal scanner has been designed for forest fire mapping. Images in the study have been transmitted to the ground station via a satellite link and then geo-corrected to produce a fire map in real time. The system has been tested in a controlled burn zone using an ALTUS II UAV in 2001 and produced 5 geo-corrected images with a spatial resolution of 2.5 m during an hour of flight. The architecture of the fire system in this study is probably the first example of a complete wildfire monitoring system, serving as the foundation for more capable ones to come in the years to come.

In [6], a UAV has been designed that can follow a predefined flight plan that can be updated at any time from a ground control station. While performing the mission, the aircraft is able to capture high-resolution images transmitted in real time to the ground station via a satellite link. The raw images can then be forwarded to a Central Data Processing Center for additional processing, which archives all georeferenced images produced and allows end users to refer to the information. [7] suggests a system for cooperative fire detection using a fleet of diverse UAVs. The fire detection algorithm is based on cooperation between UAVs with IR cameras and other UAVs with visible cameras to increase the detection probability. The designed system has been tested in the field and very successful results have been obtained. [8] focuses on developing accurate and reliable forest fire recognition algorithms for UAVs. Experimental results in this study have shown that the structured Forest Fire Detection technique can achieve good execution with significantly increased reliability and accuracy in Forest Fire Detection applications. The purpose of [9] is to provide useful knowledge on various UAV-based wildfire control systems and machine learning algorithms to predict and effectively deal with bushfires in inaccessible locations. In spite of the potential advantages of UAVs for bushfire management, it is decided in this study that there are accuracy issues, and solutions must be optimized for successful bushfire management. In [10], a metal oxide CO₂ detector has been designed using a screen printing approach to detect the CO₂ gas from the sensors to watch and make the appropriate controls in case of a fire in the areas and it has been observed that it may be used in conjunction with fire detectors to improve detection accuracy and shorten alarm duration with current fire detectors. In [11], a novel fire detection dataset has been used to propose a forest fire detection approach based on a Convolutional Neural Network (CNN) architecture. Experimental results in this study demonstrate that the approach can recognize forest fires within photos with a 97.63% accuracy, a 98.00% F1 Score, and an 80% Kappa after being trained on the dataset.

The effectiveness of an effective wildfire and smoke detection solution is suggested by [12], who proposes an architecture that combines the YOLO architecture with two weights with a voting ensemble CNN architecture to tackle two different computer vision tasks in a stage format. The classification model used in the study has an F1 score of 0.95, an accuracy of 0.99, and a sensitivity of 0.98. By reaching a 0.85 mean average precision with a 0.5 threshold score for the smoke detection model and 0.76 mAP for the combined model, the evaluation of the detector model displays strong findings. Strong results are obtained from the evaluation of the detector model, which achieved a 0.85 mean average accuracy with a 0.5 threshold score for the smoke detection model and 0.76 mAP for the combined model. A 0.93 F1-score is also achieved by the smoke detection model. [13] includes a comprehensive explanation of the flame and smoke detection algorithms utilized by each optical remote sensing technology as well as a description of how these technologies are used in early fire warning systems. A number of models attempting to detect fire occurrences with high accuracy in difficult conditions are explored, and three types of systems—terrestrial, airborne, and space borne—are identified in this study. A thorough comparison of the three types of early fire detection systems, using a scale of 0 (low) to 5 (high) for performance (Accuracy), volume of research papers (Volume of works), future potential, minimum fire size that can be detected (Minimum fire size), monitoring area covered by the system (Coverage area), and response time. A summary of the literature on UAVs that use computer vision to detect fire is studied in [14]. In order to document the many types of UAVs, the hardware and software utilized, and the suggested datasets, the research has been done throughout the past ten years. The study revealed that multi-copters were the most popular kind of vehicle and that most applications involved combining an RGB camera with a thermal camera. [15] describes their control design process and indoor testing findings using a small fixed-wing autonomous glider that can perform a forceful high angle-of-attack landing maneuver. They begin by building an incredibly accurate model of the aircraft using unstable flight regimes and actual kinematic flight data collected in a motion-capture environment. A numerical nonlinear (approximate) optimum control approach is then utilized to construct a feedback control strategy for the elevator deflection using the study's model. Finally, they provide the results of their experiments showing how this basic glider may use pressure drag to perform a high-speed perching maneuver. Forest fires in Turkey are detected and intervened with TB2 produced by BAYKAR Technology in 2014. TB2, which can carry 150 kg of payload, has an important position in its field. Instant fire detection, transfer of images to the Fire Management Center in Ankara, Forestry Operations Directorates and Fire Extinguishing Systems is provided by image processing in TB2. In addition, archiving the images, using the tablet with the raven system, transmitting the instructions of

the Fire Management Center to the field teams, monitoring the instant status of the fire fighting vehicles on the map of the General Directorate of Forestry and directing them to the fire area, analysis of meteorological data and instantaneous wind information in the fire area as a result of the progress of the fire can be provided with software that allows calculating the direction and intensity [16].

The purpose of this study is to intervene in increasing forest fires without endangering human life. For this reason, a fixed-wing UAV capable of carrying loads and reaching the fire zone as quickly as possible has been developed. The reason for not using a rotary-wing UAV is that the high temperature in the fire zone could damage a hovering drone, and also due to the lower payload capacity compared to a fixed-wing UAV. First and foremost, the boundaries of the fire will be determined using image processing to prevent the fire from spreading in order to stop the growth of the targeted fire. It is designed to autonomously perform its task by easily reaching the hard-to-reach areas of the fire.

The proposed system sends real-time images to the ground station both during reconnaissance flights and when it arrives at the area in response to a fire alarm. This facilitates knowledge of the size and status of the fire. Its innovative feature is its ability to intervene in the fire and its maneuverability. Thanks to the harmony between the mission mechanism and the flight computer, it has a high accuracy rate.

The UAV, which is initially considered for forest fires and whose design is completed, is capable of performing different types of load-dropping operations by changing the software and/or payload. Completing the mission with an efficient flight, the UAV immediately returns to the command area and becomes ready for a new flight by renewing its charge and loads. This fully national project, designed as a solution to the problem of delaying the detection of forest fires and having difficulties in extinguishing them, has a fixed-wing UAV design as it can carry heavy loads. The design and method of the produced UAV are given in Section 2, and the observations and findings are included in Section 3.

2. Material and Method

In this study, a durable, economical, domestic and national UAV is designed, which is fast, capable of carrying loads, can process the image and detect the fire thanks to its software, and can release the fireball without losing time with its easy activation feature thanks to the task mechanism designed to extinguish the fire. At the same time, it is aimed that the UAV has a large wing surface area and a high lift force, and with the sufficient ability of the control surfaces, it is aimed to provide the desired speed and maneuverability to the flight.

The airfoil structure used in the body strength and mechanical system of the UAV is chosen as NACA 6409, which will provide the required lifting force as a result of the analysis and calculations made. The drag reduction parameter is taken into account in the FoM (Figure of Merit) figure to select the configurations. An ideal chassis design is planned according to the weight measurements determined for electronic equipment by optimizing the chassis weight. With this factor, a body is designed in which electronic and mechanical systems can be placed easily. The UAV's weight with payload is 7800 grams, its length is 1100mm, its wingspan is 2000mm, and its body width is 80mm. According to the Reynolds (Re) number, NACA 6409 is chosen as the airfoil. The wing is made of EPP Foam and reinforced with carbon fiber pipes. The wing analysis of L , CD , CL ALPHA, CD ALPHA are shown in Figure 1. The dimension of the design of the UAV is demonstrated in Figure 2. The UAV is assembled based on the design in Figure 2.

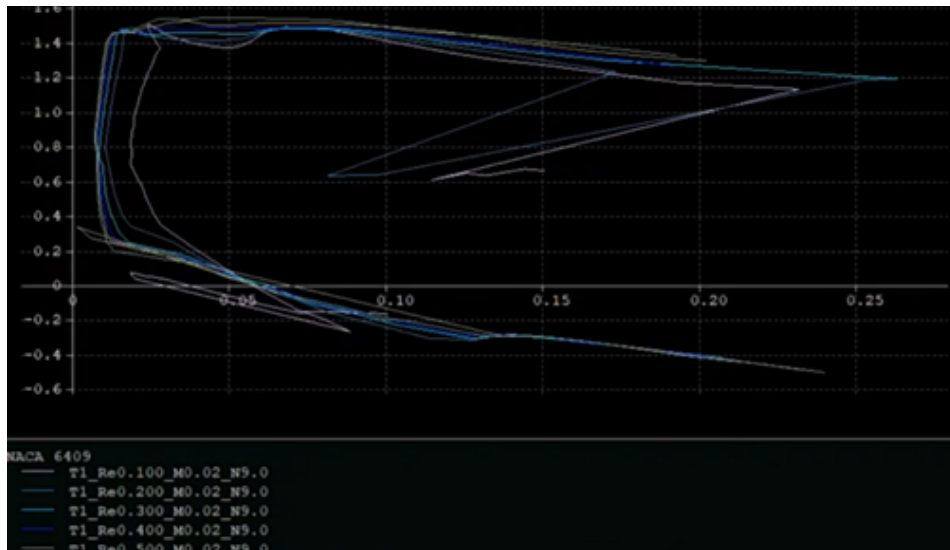


Figure 1. Aerodynamic analysis of CL and CD.

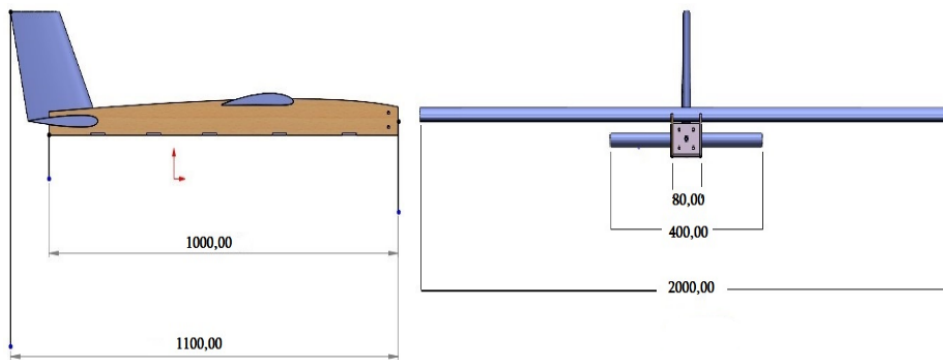


Figure 2. Dimensions of the designed UAV.

The image from the camera is divided into squares, and each of the frames takes certain values with reference to the color shades of white and black. Thus, when the camera captures the desired color and object, the algorithm detects this and activates the task mechanism as shown in Figure 3. With the vertical use of the design, it is aimed to reduce the area covered by the mission mechanism on the aircraft and to prevent the shift in the center of gravity during the release of the six balls, which is the duty of releasing the fireball, so that the flight control device is not affected for a stable flight. In the task mechanism, two crescent caps are controlled by a single servo motor. The first crescent cover has a small surface area and is ready to be pulled in front of the ball with a portion of it that can hold the ball inside the cylinder. If the servomotor is activated, it is pulled from the front of the ball and leaves the first ball. The second crescent cap has a larger surface area than the first crescent cap. In this way, the servomotor pulls the first crescent cap from the front of the ball; the second crescent will return to the starting position of the first crescent and prepare it for the second and final shot.

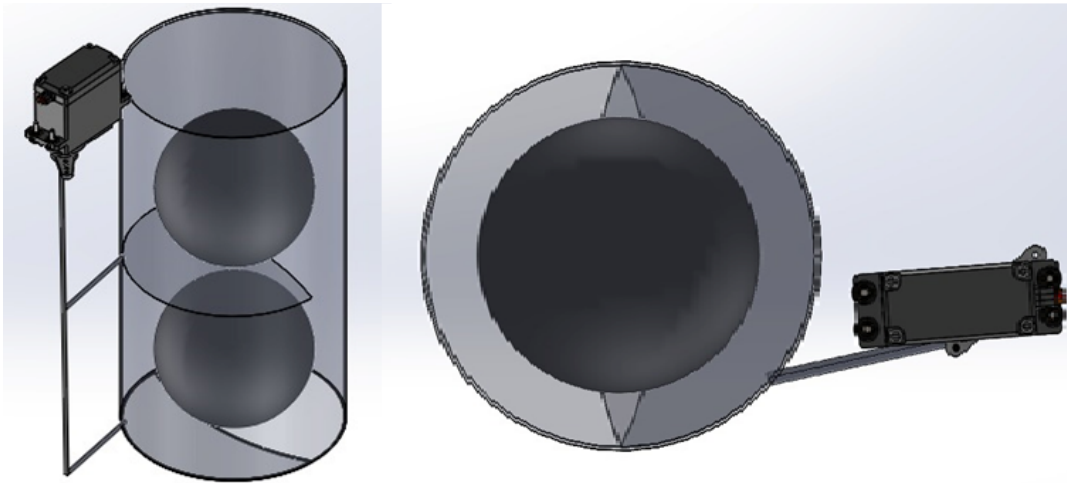


Figure 3. View of the side and top sections of the task mechanism.

X4125-440KV V3 2430W 5-6S brushless RC aircraft motor is used for the motor of the UAV. ESC value, Lipo battery (Lithium Polymer battery) value and propeller dimensions are determined as 100A, 6S 22000mAh 25C and 16x10 APC, respectively. Electronic components and circuit diagram, control card selected for flight control, sensors, RF receiver and transmitter systems, battery systems, power modules, fuse and current breaker, electronic equipment to be used in the mission mechanism system, radio control, ground station software and information about the systems in UAV are given in Table 1. The placement of the UAV on the fuselage and wings and the circuit diagram are given in Figure 4. Figure 4 shows how the direct current (DC) from the LiPo battery follows the servomotors such as S1, S2, S3, S4, S5.

Table 1. Electronic equipment and features of the designed UAV.

Electronic Components	Feature	Model
Motor	X4125 – 440kV Motor	SUNNYSKY X4125-440KV V3 2430W 5-6S Brushless Motor
ESC	Domestic ESC and 90A UBEC electronic speed controller	Designed 90A ESC
LiPo Battery	46.62mA that can provide 21 minutes of stay in the air, feeds the flight controller and image processing computer	Leopard Power 22000 mAh 22,2V 6S 25C
Flight Controller	Flight controller that provides more stable control and autonomous flight with its 32-bit processor for autonomous flights	Pixhawk 2.4.8
Servo Motor	180-degree metal gears to move the aircraft's control surfaces such as aileron, elevator and rudder and to control the mission mechanism.	Emax ES08D II 8.5G Digital Servo
Computer and Camera	High performance and high image resolution in image processing	Nvidia Jetson Nano Computer and Camera
Pitot Tube	Pitot Tube Sensor kit to measure the airspeed of the UAV and to see it at the ground station	Pixhawk PX4 Differential Airspeed Sensor Set
GPS	GPS module that shows the position of the UAV at the ground station with less deviations and enables it to move more sharply to the positions sent in autonomous missions	HERE 3
Ground Station Software and Systems	It has a more understandable interface that facilitates the use of the flight controller	Mission Planner
Telemeter	Transferring information such as the aircraft's motor temperature, battery status, altitude, bank angle to the ground computer	SiK Telemetry Radio V3 433MHz

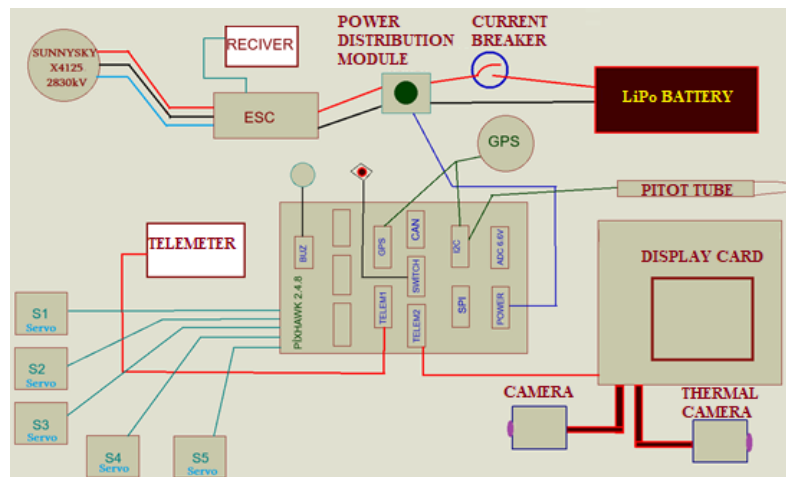


Figure 4. Electronic circuit diagram of the UAV.

As soon as the fire extinguisher is activated, it emits an audible sound (99 decibels) and warns people as an alarm. The approximate weight of the ball is 1.3 kg. It contains dry chemical powder obtained from 90 Mono Ammonium Phosphate or Native BOR powder. Simply throwing the ball into the fire or the area at risk of fire is sufficient. It gives accurate results within 3-5 seconds from the moment the ball comes into contact with Electric activation or fire. Since there is no need to approach the fire, it prevents the user from being harmed by fire or dense smoke. It does not harm the environment at the time of explosion.

In this study, the ESC circuit is designed and implemented to drive the motor. The current drawn by the X4125-440KV V3 2430W 5-6S Brushless RC aircraft motor mounted on the UAV is controlled by the designed ESC. STM32F105RCT microcontroller is used in motor driver (ESC) circuit for BLDC motor speed control, position control and torque control because it has more performance and lower power consumption. Hall Effect sensors are also used to determine the rotor position. A counter is created with the TIMER unit and this counter value signal period is recorded with an algorithm at each rising edge of the signal coming from the feedback element. Speed control and current control algorithms are also developed. "Anti-Windup" algorithm is developed in order to prevent integral clutter. It is aimed to avoid the undesirable effects of the integral term to control the motor speed or position using the "Anti-Windup" algorithm. In this way, it is possible to control the speed or position of the motor more stably and to achieve better performance with less overreactions. The analysis of the time dependent change in the full thrust state of the motor used with the 100 Ampere current passing ESC is given in Figure 5.

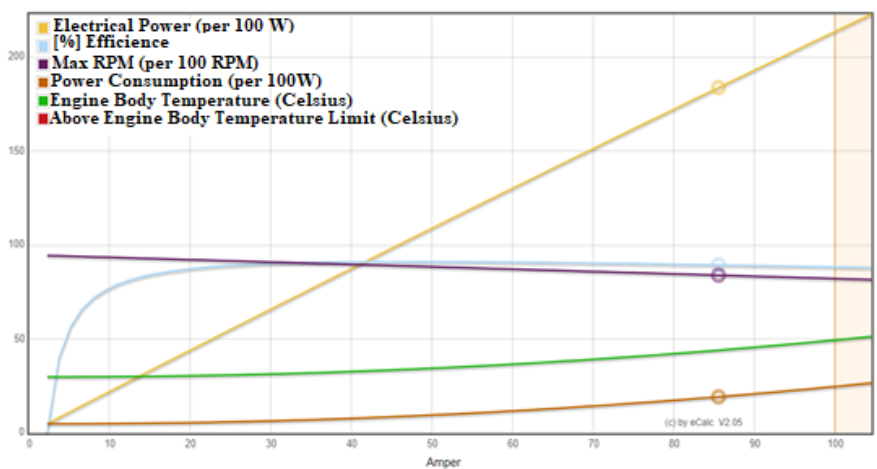


Figure 5. Characteristics of the motor at full thrust.

Electronic materials that have been analyzed together and obtained optimal values: ESC is 100A, LiPo (Lithium Polymer Battery) is 4S 22000mAh 120C and the propeller is 16x10 APC electric type propeller. These optimal values are obtained by examining the gradual partial load of the motor as presented in Table 2. The efficiency, electrical power, voltage, current and thrust (gram) values obtained from the produced ESC, used battery and propeller are as seen in Table 2.

Table 2. Gradual partial load of the motor.

Propeller rpm	Impulse %	Current A	Voltage V	Power W	Efficiency %	Impulse g	Impulse			Pitching Speed		Speed (level)		Engine Run (85%)
							oz	g/W	oz/W	km/h	mph	km/h	mph	
1200	13	0.4	22.2	8.7	56.1	159	5.6	18.2	0.64	18	11	-	-	2841.8
1800	20	1.0	22.2	22.7	72.9	357	12.6	15.7	0.56	27	17	-	-	1094.1
2400	26	2.2	22.2	48.2	81.4	635	22.4	13.2	0.46	37	23	-	-	514.5
3000	33	4.0	22.2	89.3	85.7	992	35.0	11.1	0.39	46	28	-	-	277.3
3600	40	6.8	22.2	150.2	88.1	1428	50.4	9.5	0.34	55	34	-	-	164.7
4200	47	10.7	22.1	235.2	89.4	1944	68.6	8.3	0.29	64	40	-	-	105.0
4800	54	15.9	22.1	348.4	90.1	2539	89.6	7.3	0.26	73	45	-	-	70.7
5400	61	22.6	22.1	494.4	90.4	3214	113.4	6.5	0.23	82	51	61	38	49.7
6000	69	31.0	22.2	677.8	90.4	3968	140.0	5.9	0.21	91	57	92	57	36.2

Autonomous flight parameters are modeled in the ArduPilot algorithm and uploaded to Pixhawk 2.4.8. After completing the autonomous flight plan, PID settings, GPS calibration and ESC calibration in the Mission Planner interface, the UAV is enabled to take to the runway. Autonomous flight software is developed and communication is provided with Nvidia Jetson Nano. The operations to be performed in detecting any target are tested in the simulation environment and stabilized. The unique autonomous flight algorithm is revealed by meticulous attention to each test.

Fail Safe mode is set to full right rudder full right altitude. It is a mode that allows the unmanned aerial vehicle to land with the least risk in case of a possible connection jam and/or any emergency. The development phase has started after the design and production of the UAV. At this new stage, the features and performance of the UAV are tested in many aspects such as wind tunnel, autonomous flight stability, and target detection in the air. The problems that arise during the development of the algorithm are reviewed again. Stability in the route and flight of the UAV is improved in case of more than one target. The improvements made as a result of these tests and the issues that have changed and remained the same are given in observations and findings in Section 3.

3. Results and Discussion

The airfoil of the produced UAV has been first chosen as NACA-6408A, but the NACA-6409 airfoil is chosen considering analysis and carrier. In this way, the UAV autonomously demonstrates a stable flight without disturbing its stability. In the wing structure, the middle wing structure is abandoned and the upper wing structure is preferred in order to achieve a more stable flight and load carrying process.

Comparing the capability and price performance of the flight controller, it is decided that the Pixhawk Orange Cube is not needed. Adequate maneuverability is achieved in stable flight tests. Test flights are recorded and examined in detail. As a result of these examinations, it is observed that it is not far from a desired stable flight, but that it could be improved. Improvements such as weight reduction, landing gear change are applied. After ESC production is completed, measurements are obtained with an oscilloscope. When the desired results (RPM of the motors, feeding the flight controller and flight computer, having sufficient flight time using the battery effectively, maintaining the ESC temperature) are provided, the transition is made from the perforated copper plate to the copper plate. In the first place, the motor driver circuit was produced with Arduino UNO. The X2212 720kV motor was tested as a prototype. However, as a result of the R&D research, it is decided to use the STM32F105RCT microprocessor due to its high power consumption and lower performance than desired. The deformed life of both the battery and the UBEC (Ultimate Battery Eliminating Circuit) is extended with the UBEC in the ESC. Some objectives such as flight time (including landing and take-off), thrust weight ratio, and the ability of the ESC to work effectively with different types of motors have been determined as a result of the R&D work carried out

during the design phase of the UAV. It can be observed that 92% of these targets have been achieved in Table 3 and 4.

Table 3. Motor and battery analysis results.

Battery		Motor@Optimum Efficiency		Motor@Max	
Load:	3.95 C	Current:	47.14 A	Current:	86.84 A
Voltage:	21.68 V	Voltage:	21.78 V	Voltage:	21.42 V
Rated Voltage:	22.20 V	Speed:	8873 rpm	Speed:	8365 rpm
Energy:	488.4 Wh	Electrical Power:	1026.5 W	Electrical Power:	1860.0 W
Total Capacity:	22000 mAh	Mechanical Power:	936.2 W	Mechanical Power:	1662.8 W
Used Capacity:	18700 mAh	Efficiency:	91.2%	Efficiency:	89.4.2%
Min Flight Time:	12.9 min				
Fixed Flight Time:	22.0 min				
Weight:	3252 g			Wattmeter	
	114.7 oz			Current:	86.84 A
				Voltage:	21.68 V
				Power:	1882.7 W

Table 4. Propeller, driver and speed analysis results.

Propeller		Total Drive		Plane	
Static Thrust:	7712 g 272 oz	Driver Weight:	4093 g 144.4 oz	Total Weight:	7000 g 246.9 oz
Speed:	8365 rpm	Power-Weight:	275 W/kg	Wing Load:	175 g/dm ²
Usable Thrust@0 km/h:	7712 g		125 W/lb		57.3 oz/ft ²
Usable Thrust@0 mph:	272 oz	Thrust-Weight:	1.10:1	Cubic Wing Load:	27.7
Pitching Speed:	128 km/h	Current@Max:	86.84 A	Estimated Adhesion Speed:	63 km/h
	80 mph	P(input)@Max:	1927.9 W		39 mph
Type Speed:	641 km/h	P(output)@Max:	1662.8 W	Horizontal Estimated Speed:	130 km/h
	398 mph	Efficiency @Max:	86.2%		39 mph
Thrust:	4.15 g/W	Torque:	1.90 Nm	Vertical Estimated Speed:	15 km/h
	0.15 oz/W		1.4 lbf.ft		9 mph
				Estimated Climb Speed:	13.4 m/s
					2631 ft/min

The maximum weight of the UAV that emerged within the scope of the study, namely BaSe, is compared with the useful loads it carried by examining the previously produced UAVs. The ratios of the payload to the maximum load of the previously produced UAVs and the Peace are comparatively given in Table 5.

Table 5. Ratio of payload to maximum payload in UAVs.

Model	Maximum Weight (g)	Useful Load (C)	Rate
TB2	650	150	0,2307
Akıncı	6000	1500	0,2500
mq9 Reaper	4760	1700	0,3571
BaSe	7750	2700	0,3483

The mission to be performed by the UAV is being tested on the Nvidia Jetson Nano. The first detection of fire is carried out by switching from BGR color space to HSV color space by including the red tone range of the point where the temperature is most intense in the thermal camera into the algorithm. The temperature and, accordingly, the red tone are evaluated according to the area it covers on the screen. Even if the desired color is obtained, when it is below a certain size, the masking process appears in the window and no other operation is performed. However, if it exceeds a certain size, it is determined by taking it into a square. For the normal camera, the top view of the flame and smoke is imported into Nvidia Jetson Nano using the color detection algorithm. This section is completed using ready-made code. After the test process on smoke and fire related videos is completed, the AZURE UAV team, which is prepared for the Teknofest competitions within Kastamonu University, is tested with the LUNA-37 aircraft on the inverter and integrated into BaSe. During the test, the first mission is successfully achieved by lifting two balls on a red tarpaulin. The segmentation of the red target is given in Figure 6.

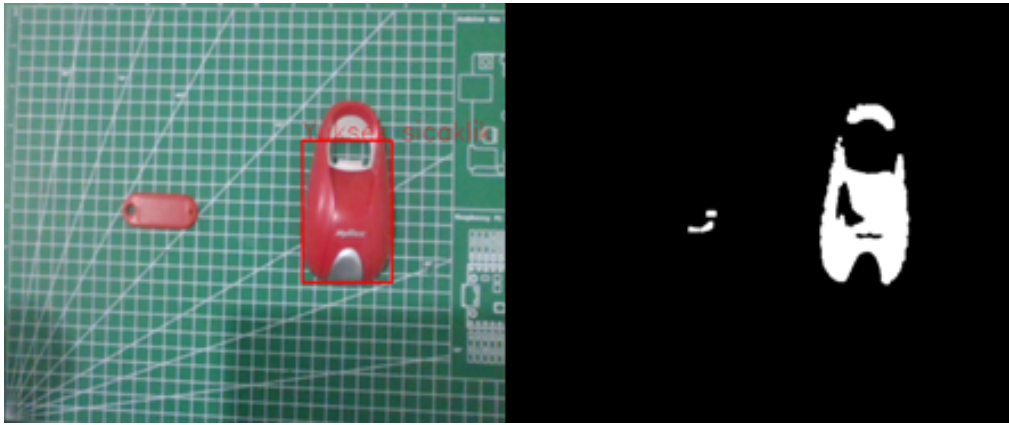


Figure 6. Segmentation of the target.

An ESC was developed using the STM32F401CCU6 microcontroller during the production phase. The desired efficiency is achieved and the operation is carried out with the X4125-440KV brushless motor integrated into the wings and the motor driver placed on the fuselage. Thus, multiple brushless motor control is realized with an ESC. The software part of the ESC is completed by performing the speed and position, trapezoidal commutation switching, development of the control module, and anti-windup algorithm, respectively. The soldering process is completed on the perforated copper plate and production is carried out as a result of the hardware configuration drawn in Proteus. The body is fixed in its proper position, considering that it is not affected by the magnetic field and the calculations of the center of gravity. The fact that the maximum current (I) that the ESC will receive from the LiPo battery chosen as the power source can be changed, enabled the motor driver to be used without the need for a change in case the battery and/or motor change. Thus, it is observed that BaSe can be used in many air, land and sea vehicles with its high compatibility.

4. Conclusion

In this study, an Unmanned Aerial Vehicle (UAV) is designed and produced by determining the purpose first. A fixed-wing model was preferred for rapid and effective response to forest fires. The fireball release process has been carried out with a rotary wing UAV in the literature. However, with this study, the fireball release process is performed for the first time with the fixed wing model. Considering that the high temperature of the fire with the rising of the heated air can negatively affect a rotary wing UAV and damage electronic components such as battery, ESC and motor, it has been planned and realized to minimize these effects with the fixed wing model. The fact that forest fires are more frequent in mountainous and hilly areas creates a disadvantage in the runway requirement of a fixed wing model aircraft. In order to minimize this disadvantage, a UAV that can take off in a short distance and stay in the air for a long time is produced in this study. In this way, it is observed that BaSe can stay in the air for a longer time and take off in a short distance by carrying a higher load compared to the rotary-wing UAV. In addition, a domestic motor driver is also produced in this study. With this motor driver, different motor types can be driven and two motors are connected and tested. In this way, one ESC is sufficient without the need for an extra ESC to be used. The unique value of the produced ESC is highlighted by a unique algorithm and PCB design drawn in Proteus.

Total cost of the UAV including ESC production (excluding fireballs and fireballs) is 26,300.00 TL. It is in a remarkable position in the price-performance balance with its economic cost in this area. BaSe can carry four fireballs weighing approximately 1.3 kg. With image processing methods, it can gradually drop the balls in question to the point where the fire temperature is most intense (the highest shade of red). In this way, convenience is provided in cases where it is difficult to reach the center of the fire by human power. Upon the communication of the computer with the flight controller, the location of the fire is determined by the normal camera and transmitted to Pixhawk 2.4.8. Position is determined autonomously and fireballs are released by passing over the fire. BaSe can perform the intervention by being suspended in the air and minimally affected by high temperature. As a result, BaSe's test missions, target detection, gun release, autonomous take-off and landing, and reporting of fire to the ground station are successfully accomplished. Therefore, it is observed that BaSe has become suitable for use in the area.

Acknowledgement

This work was supported to participate Teknofest in part by TÜBİTAK 2209-A with the research project number 1919B012222889 and by the scientific research project by Kastamonu University. The authors would like to thank TÜBİTAK and Kastamonu University Scientific Research Projects Coordination Unit for their outstanding contribution.

References

- [1] Ucar UU, Isleyen SK. A New Solution Approach for UAV Routing Problem with Moving Target – Heterogeneous Fleet. *J Polytechnic* 2019; 22(4): 999 – 1016.
- [2] Yilmaz T, Ayranci AA, Bacanlı E, İlhan H. UAV-Assisted NOMA-Based Network with Alamouti Space-Time Block Coding. *J Polytechnic* 2022; 25(3): 967 - 973.
- [3] Ozcan O. Performance Evaluation of Bridges Under Scour by UAS Based Measurements. *J Polytechnic* 2019; 22(2): 385 - 391.
- [4] Bailon-Ruiz R, Lacroix S. Wildfire remote sensing with UAVs: A review from the autonomy point of view. In *IEEE 2020 International Conference on Unmanned Aircraft Systems (ICUAS)*; 01-04 September 2020; Athens, Greece. New York, NY, USA: IEEE. pp. 412-420.
- [5] Ambrosia VG, Wegener SS, Sullivan DV, Buechel SW, Dunagan SE, Brass JA, Stoneburner J, S. Schoenun M. Demonstrating UAV-Acquired Real-Time Thermal Data over Fires. *Photogramm Eng Remote Sens* 2003; 69(4) 391-402.
- [6] Lewyckj N, Biesemans J, Everaerts J. OSIRIS: A European Project Using A High Altitude Platform For Forest Fire Monitoring. In: *Safety and Security Engineering II*. Rome: Wessex Institute of Technology Press, 2007. pp. 205-213.
- [7] Merino L, Caballero F, Martinez-de Dios JR, Ollero A. Cooperative Fire Detection using Unmanned Aerial Vehicles. In: *IEEE 2005 IEEE International Conference on Robotics and Automation*; 18-22 April 2005; Barcelona, Spain. New York, NY, USA: IEEE. pp. 1884-1889.
- [8] Sudhakar VVS, Kumar CS, Priya V, Ravi L, Subramaniaswamy V. Unmanned Aerial Vehicle (UAV) based Forest Fire Detection and monitoring for reducing false alarms in forest-fires. *Comput Commun* 2020; 149:1-16.
- [9] Partheepan S, Sanati F, Hassan J. Autonomous Unmanned Aerial Vehicles in Bushfire Management: Challenges and Opportunities. *Drones* 2023; 7(47): 1-34.
- [10] Masat M, Saglam HK, Ertugrul M, Korul H. The use of unmanned aerial vehicles in the detection of forest fires with a gas detection technique. *NanoEra* 2021; 1(1): 14-18.
- [11] Rahman AKZR, Sakif SMN, Sikder N, Masud M, Aljuaid H, Bairagi AK. Unmanned Aerial Vehicle Assisted Forest Fire Detection Using Deep Convolutional Neural Network. *Intell. Autom Soft Comput* 2022; 35(3): 3259-3277.
- [12] Bahhar C, Ksibi A, Ayadi M, Jamjoom MM, Ullah Z, Soufiene BO, Sakli H. Wildfire and Smoke Detection Using Staged YOLO Model and Ensemble CNN. *Electronics* 2013; 12(1): 1-15.

- [13] Barmpoutis P, Papaioannou P, Dimitropoulos K, Grammalidis N. A Review on Early Forest Fire Detection Systems Using Optical Remote Sensing. *Sensors* 2020; 20(22): 1-26.
- [14] Moumgiakmas SS, Samatas GG, Papakostas GA. Computer Vision for Fire Detection on UAVs—From Software to Hardware. *Future Internet* 2021; 13(8): 1-17.
- [15] Cory R, Tedrake R. Experiments in Fixed-Wing UAV Perching. In: *AIAA Guidance, Navigation and Control Conference and Exhibit*; 18-21 August 2008; Honolulu, Hawaii.
- [16] B. Technology, "BAYKAR Technology," [Online]. Available: <https://baykartech.com/tr/orman-yanginlariyla-mucadele>. [Accessed 16 04 2023].

A Hybrid Classification Approach for Fasteners Based on Transfer Learning with Fine-Tuning and Deep Features

Canan TASTIMUR^{1*}, Erhan AKIN²

¹ Department of Computer Engineering, Faculty of Engineering-Architecture, Erzincan Binali Yildirim University, Erzincan, Turkey

² Department of Computer Engineering, Faculty of Engineering, Firat University, Elazig, Turkey

*¹ ctastimur@erzincan.edu.tr, ² eakin@firat.edu.tr

(Geliş/Received: 20/06/2023;

Kabul/Accepted: 28/08/2023)

Abstract: Deep learning, which has seen frequent use in recent studies, has helped solve the problem of classifying objects of many different types and properties. Most studies both create and train a convolutional neural network (CNN) from scratch. The time spent training the network is thus wasted. Transfer learning (TL) is used both to prevent the loss of time due to training the dataset and to more effectively classify small datasets. This study performs classification using a dataset containing eighteen types of fastener. Our study contains three different TL scenarios. Two of them use TL with fine-tuning (FT), while the third does so with feature extraction (FE). The study compares the classification performance of eighteen different pre-trained network models (i.e., one or more versions of EfficientNet, DenseNet, InceptionResNetV2, InceptionV3, MobileNet, ResNet50, Xception, and VGGNet) in detail. When compared to other research in the literature, our first and second scenarios provide excellent implementations of TL-FT, while our third scenario, TL-FE, is hybrid and produces better results than the other two. Furthermore, our findings are superior to those of most previous studies. The models with the best results are DenseNet169 with an accuracy of 0.97 in the TL-FT1 scenario, EfficientNetB0 with 0.96 in TL-FT2, and DenseNet169 with 0.995 in TL-FE.

Key words: Classification, fastener, feature extraction, fine tuning, transfer learning.

Derin Öznitelik ve İnce-Ayar ile Aktarım Öğrenme Tabanlı Bağlantı Elemanlarının Hibrit Sınıflandırma Yaklaşımı

Öz: Son yıllarda yapılan çalışmalarda sıkça kullanılmaya başlanan derin öğrenme, birçok farklı tür ve özellikteki nesnelerin sınıflandırılması sorununun çözülmesine yardımcı olmuştur. Çoğu çalışma, sıfırdan bir evrimsel sinir ağı (CNN) oluşturur ve eğitir. Ağı eğitmek için harcanan zaman böylece boşa harcanır. Transfer öğrenme (TL) hem veri setinin eğitilmesinden kaynaklanan zaman kaybını önlemek hem de küçük veri setlerini daha etkin bir şekilde sınıflandırmak için kullanılmaktadır. Bu çalışma, on sekiz tip bağlantı elemanı içeren bir veri seti kullanarak sınıflandırma yapmaktadır. Çalışmamız üç farklı TL senaryosu içermektedir. Bunlardan ikisi ince ayar (FT) ile TL kullanırken, üçüncüsü özellik çıkarma (FE) ile yapmaktadır. Çalışma, on sekiz farklı önceden eğitilmiş ağ modelinin (yani EfficientNet, DenseNet, InceptionResNetV2, InceptionV3, MobileNet, ResNet50, Xception ve VGGNet) sınıflandırma performansını ayrıntılı olarak karşılaştırmaktadır. Literatürdeki diğer araştırmalarla karşılaştırıldığında, birinci ve ikinci senaryolarımız TL-FT' nin iyi sonuçlarla uygulamalarını sağlarken, üçüncü senaryomuz TL-FE hibrit bir yöntem olup diğer iki senaryodan daha iyi sonuçlar üretmiştir. Ayrıca, bulgularımız literatürdeki çalışmaların çoğundan daha üstün olduğu fark edilmiştir. En iyi sonuçlara sahip modeller TL-FT1 senaryosunda 0,97 doğrulukla DenseNet169, TL-FT2'de 0,96 ile EfficientNetB0 ve TL-FE'de 0,995 ile DenseNet169'dur.

Anahtar kelimeler: Sınıflandırma, bağlantı elemanı, özellik çıkarma, ince ayar, transfer öğrenme.

1. Introduction

Fasteners are critical to the proper operation of industrial machinery. Quality control and fault diagnosis applications must ensure that fasteners on machines are complete and flawless. The detection of problems with fasteners can benefit from the use of computer vision technologies. Potential major problems in industrial machines—fastener failure, breakage, wear and tear, and so on—can be avoided thanks to advanced fault diagnosis using computer vision technologies. Using computer vision techniques to determine the condition of industrial machinery will help ensure the safety of industrial machines by avoiding the unnecessary use of human resources and costly expenses due to failures.

Recently, the deep learning (DL) approach has commonly been used in fault diagnosis, detection, and classification. Fasteners are highly similar to each other, which complicates the identification, detection, and classification of the carrying element. Many studies have used DL for object detection and classification, and the transfer learning (TL) method can help provide more effective results by improving learning capacity. TL is a

* Corresponding author: ctastimur@erzincan.edu.tr. ORCID Number of authors: ¹ 0000-0002-3714-6826, ² O 0000-0001-6476-9255

technique in which models are trained on large datasets, allowing the trained network to be used ready-made from other datasets. In classification studies, a pre-trained network saves time and provides high performance in classifying small datasets. Thanks to the information obtained from a model previously trained on a large-scale TL dataset, classification uses a new, different dataset with the same or a different model. Thus, the information in the pre-trained model is transferred and the performance of the network improves. Since our dataset is small, TL provided better performance than in many other studies in the literature.

Using a fine-tuning-based and feature-inference-based transfer learning method, it is intended to identify data sets with high similarity. This study classified 18 fastener types using TL-based feature extraction and fine-tuning techniques. The proposed method includes three different classification scenarios. The first scenario involves fine-tuning by updating only the number of classes in the classifier layer of the pre-trained model. In the second, after adding two dense layers to the end of the pre-trained model, fine-tuning has been applied with the classifier layer updated. In the last scenario, features were extracted, with the pre-trained network using the feature extractor capability of the pre-trained model. So, the new CNN model takes inputs as local features, leading to more accurate results.

The main contributions of this study are listed below:

- It proposes three different methods to classify TL-based fasteners. Two of them use the fine-tuning (FT) approach, while the third adopts the feature extraction (FE) approach. While studies in the literature classify fasteners using only one of the FT methods, our study compares three different scenarios in detail. From this point of view, it is a very comprehensive and useful TL resource, as compared to the studies in the literature.
- Classification using FE, the third of the proposed classification scenarios, is a hybrid method. Examining the studies in the literature shows this to be an important study. In the third scenario, which combines CNN architecture and a pre-trained TL network, the features extracted by the TL network, rather the raw image, are given as input to the CNN network, thus improving the success of the network.
- Examining the studies in the literature that use FT shows that FT can be performed in two ways. Our study compares performance outputs by applying both FT approaches separately. This led to more successful results than in most studies in the literature.
- Existing studies involving FT use a maximum of 6 pre-trained TL models, whereas our study aims to select the model that gives the best results by applying almost all (specifically, 18) of the TL models used for classification in the literature. This study is thus the most comprehensive TL study in the literature.
- In addition, because the deep CNN network is trained by using TL-FT and TL-FE on a dataset with a low number of images, classification results have very high performance.

2. Related Works

Several studies have used TL to classify objects. In one study on how to detect COVID, a hospital took 4986 chest CT images, and used DenseNet121, DenseNet201, VGG16, VGG19, InceptionResnetV2, and Xception models to test TL [1]. Fine-tuning was accomplished by freezing feature extractor layers on DenseNet201, which produced the best COVID classification results based on these chest images. Fine-tuning hyper-parameters were adjusted with Dropout 0.2, 0.3, and 0.3 after Conv2D (3,3x3), Global Average Pooling, and three fully connected layers with 256,128,64 neurons. After comparing the performance of these TL models, DenseNet201 achieved an accuracy rate of 0.9818. Meanwhile, another COVID detection study [2] used TL with VGG19, ResNet50V2, DenseNet121, and MobileNet. Fine-tuning involved adding Conv2D, Average Pooling, Flatten, and Sigmoid layers to the last layers of the models for a 460-image dataset. The best result was achieved with MobileNet. [3] used the ResNet50 model with fine-tuning for disease classification on 20,639 crop images. This model modified the values of the batch size, epoch, and learning rate hyper-parameters. In addition, the study removed the model's final three layers and added Conv2D, Average Pooling, Fully Connected, and Softmax layers, in that order, to the model. Classifying 15 different disease states with 300 images from each class yielded an accuracy of 99.26.

Kudva et al. applied hybrid TL using VGG16 and AlexNet networks for cervical cancer detection based on 2198 positive and negative images of the cervix [4]. The hybrid TL method built a CNN from scratch using the initial weights of AlexNet and VGG16. Successful results were obtained, with an accuracy rate of 0.9146. Another study is based on the fact that farmers have a hard time identifying insect pests since they seem identical during the growing stages of the crop [5]. This problem was solved with a deep CNN, with three datasets used to classify the insects. There were 40 classes in the first dataset, 24 in the second, and 40 in the third. The study compared the AlexNet, VGGNet, GoogLeNet, and Resnet TL approaches for insect categorization. Hyper-parameter adjustment for pre-trained networks improved classification performance: the accuracy rate was 0.9675 in the first dataset, 0.9747 in the second, and 0.9547 in the third. All pre-trained models were fine-tuned by adding Average Pooling, Fully Connected, and Softmax layers [5]. Talo et al. used the CNN-based ResNet-34 TL model to analyze MRI images in order to detect abnormalities in the brain [6]. They upgraded the model's last layers, the Dense and

Softmax layers, and achieved 100% accuracy with a 5-fold classification on 613 MR images. Another study, to classify brain tumors, only updated the Softmax part of the pre-trained model [7]. The networks used in the study were AlexNet, GoogLeNet, SqueezeNet, ResNet50, and ResNet101. After hyper-parameter adjustment, AlexNet achieved the highest accuracy rate, 0.9904.

Yang et al. classified spare parts into three categories using TL [8]. They used the VGG19, Alexnet, and ResNet50 models, with the VGG19 model yielding the highest success rate at 0.963. Another study classified benign and malignant skin lesions using a deep CNN [9]. This method was compared to AlexNet, VGG16, DenseNet, MobileNet, and ResNet and found to give the best results, with an accuracy of 0.9143. A skin lesion classification study [10] used ResNet152V2, DenseNet201, and Xception, with accuracy rates of 0.874, 0.874, and 0.891. This study added Global Average Pooling, Dense, Dropout, and Softmax layers while fine-tuning the model, and used two different datasets for malware classification. Another study used VGG16, VGG19, ResNet50, and InceptionV3 as both feature extractors and classifiers to classify malware images [11]. It added the last two layers of VGG16 to the new Dense layers, and only updated the Softmax layers of the other pretreated networks. [12] used fine-tuning in the VGG16 model to classify flowers into five categories by updating only the number of classes in the Softmax layer.

A study on the classification of 21 different cat and dog breeds performed fine-tuning with the VGG16 and VGG19 models [13], with two 4096 sized fully connected layers added to the end of its network. VGG16 and VGG19 achieved accuracy levels of 0.9847 and 0.9859, respectively. For plastic waste classification with FT, [14] utilized InceptionResNetV2, VGG19, VGG16, InceptionV3, and MobileNet. This study added Dropout, Flatten, Dense, Dropout, and Softmax layers to the end of the pre-trained model, and ran experiments on the model's hyper-parameters. A model to classify fresh tea leaves achieved a success rate of 0.98 by applying the InceptionV3 model [15]. In another study, chicks, hatching eggs, and unhatched eggs were classified using VGG16 and VGG19 with Flatten and Softmax layers, achieving success rates of 0.90 and 0.92, respectively [16]. Indian food was classified with InceptionV3, VGG16, VGG19, and ResNet [17]. Global Average Pooling and Softmax layers were applied to the pre-trained network, with InceptionV3 attaining the highest accuracy rate. [18] classified nutrients using EfficientNetB0, EfficientNetB4, Dense201, and MobileNetV3. The last of these had the highest accuracy rate, with Global Average Pooling, Dropout, and Softmax layers added to the end of the model.

3. Materials and Method

TL is a technique for storing information obtained while solving one problem and then implementing it to solve another, related problem. That is, it is a machine learning method in which a model trained for one task can be reused for another [19]. Using this method, the training of the network will take less time and computational power. Furthermore, TL can be used when the number of images in a dataset is insufficient for classification. As a result, classifying small datasets with TL can help achieve high performance. The FT technique, which is used in association with the TL approach, is devoted to making layer or parameter changes to a TL model. There are two broad approaches to TL that use FT in this study. The first of the FT methods duplicates the layer weight values of a trained CNN for a model designed for a new dataset [20]. The training is done only at the classification layer level in the first option, whereas in the second option, a specific part is transferred to the new model rather than copying the weights of all the trained model layers.

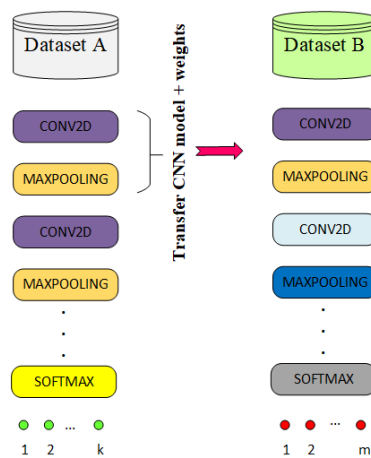


Figure 1. A visual representation of the transfer of some layers and weights from the model trained on Dataset A to the model trained on Dataset B.

Several methods use pre-trained models in applications. The TL technique has improved; as pre-trained networks can now classify new images other than the ImageNet dataset. Performing FT on a pre-trained model changes the hyper-parameters and/or network structure of the model. FT is carried out without changing the weight values of the pre-trained network. There are 3 ways to apply FT to a model.

1. *Extraction of features*: This is the use of the pre-trained network as a feature extractor. After the output layer is deleted from the network, the entire network is used as the new dataset to be classified. Our study used this option and named it the TL-FE scenario.
2. *Use the pre-trained model's architecture*: By assigning the weights of the pre-trained model randomly and retraining the entire network, only the architecture of the network is used.
3. *Fine Tuning*: Another way to use a pre-trained network is to only partially train it and keep initial weight values constant. There are four ways to perform fine-tuning:

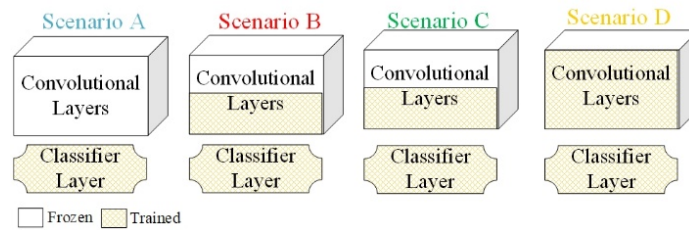


Figure 2. FT framework scenarios from TL.

Scenario A is used when the new dataset is small and very similar to that used by the pre-trained network. In this case, we do not need to train the network from scratch; we simply update the hyper-parameter value in the output layer. The TL-FT1 scenario in our study works according to this logic.

Scenario B applies when the new dataset is small and has little similarity to the ImageNet dataset. The first layers of the pre-trained model are frozen, and the remaining layers are trained. This scenario involves such updates as adding new layers to the network, removing existing layers, and changing the hyper-parameter values of the network. This is how the TL-FT2 scenario in our study works.

Scenario C is utilized when the new dataset is large and highly similar to the ImageNet dataset. In this case, the architecture and initial weights of the pre-trained model remain constant and the model is retrained.

Scenario D is for when the new dataset is large but not very similar to the ImageNet dataset. In this case, the neural network is trained from scratch.

3.1. Pre-Trained Models

Of the pre-trained models used with TL, those examined in this study, briefly explained below, are as follows: VGG16, VGG19, InceptionV3, InceptionResNetV2, Xception, ResNet50, MobileNet, MobileNetV2, DenseNet169, DenseNet201, EfficientNetB0, EfficientNetB1, EfficientNetB2, EfficientNetB3, EfficientNetB4, EfficientNetB5, EfficientNetB6, and EfficientNetB7.

A. The VGGNet Model

The VGG16 model is a CNN-based architecture developed by Simonyan and Zisserman [21]. The VGG16 model consists of 16 layers, of which 13 are convolutions and 3 are fully connected. The filter size in the convolution layers is 3x3 pixels.

The VGG19 model, meanwhile, has 16 convolutions, 5 pooling, and 3 fully connected layers. Since VGG19 has a deep network, the filters used in the convolution layer help reduce the number of parameters. The size of the filter used in the architecture is 3x3 pixels.

B. The Inception Net Model

This is the third version of the DL convolution architecture series developed by Google [22]. It is one of the most advanced architectures used in the field of image classification, and involves a model that combines multiple, differently sized convolutional filters into a new filter, thus reducing both the number of parameters to be trained and the computational complexity [23].

InceptionV3 has a depth of 22 sets of layers and contains 144 layers [23]. The Inception module uses a variety of filters to reduce size. The filter elements in the Inception module are of size 1x1, 3x3, and 5x5. Unlike other DL architectures, this model creates a deep structure rather than a layered one.

InceptionResNetV2 is a variation of InceptionV3, but with a significantly deeper structure. It is a combination of the Inception structure and a residual connection. Multidimensional convolution filters are combined with residual connections [24], which reduces the training time of the network.

C. The MobileNet Model

This is a deep neural network proposed by Google in 2017. It is smaller and faster than other models. Using depthwise separable convolutions, it applies a single filter in each input channel and a 1x1 filter is used in some convolutions [25]. The separable layers are similar to the convolutional layers in terms of depth, but they differ because they carry out the filtering and merging operations by separating them into two layers. There is a total of 28 layers, excluding point convolutions. Except for the fully connected layer that feeds the softmax layer, each layer is followed by batch normalization and relu activation layers [26].

The MobileNetV2 architecture is a development of the MobileNet model, but faster and more efficient. The size of the feature maps is reduced through a 1x1 convolution. In addition, thanks to the skip connection technique used in the ResNet models, the calculation process is faster [27].

D. The DenseNet Model

When training neural networks, feature maps are reduced due to convolution and subsampling operations. There is also a loss of image quality when transitioning between layers. DenseNet has been developed to use image feature information more effectively [28]. In this model, each layer is fed forward to the other layers, so any layer can access feature information from all previous layers [29]. Thus, the propagation rate of the features to the network increases and the number of parameters decreases.

Figure 3 discusses the common and different parameter numbers and values of the layers in the DenseNet169 and DenseNet201 architectures.

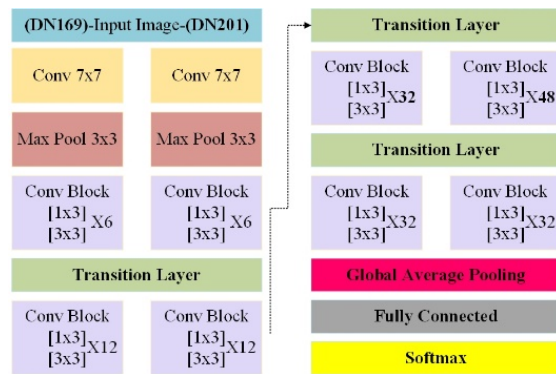


Figure 3. DenseNet169 and DenseNet201 model architectures.

E. The EfficientNet Model

This is a network of eight models. As the number of models increases, the number of parameters calculated remains relatively stable [31]. Unlike other advanced models, EfficientNet produces more efficient results by scaling in terms of depth, width, and resolution while trying to reduce the model. EfficientNet requires the channel size to be a multiple of 8. The network width, depth, and resolution are scaled evenly by a set of fixed scaling factors.

F. The ResNet Model

This is the architecture developed by the Microsoft research team to reduce the difficulty of training neural networks at great depth. Unlike standard CNN architecture, this architecture uses short-path connections [32]. Shortcut links have no extra parameters and do not increase computational complexity [33]. They allow the transfer of important information from the previous layer to the next. This architecture includes global average pooling and fully connected layers at the end of the network. The ResNet50 has 50 weight layers.

G. The Xception Net Model

This is basically an evolving network added atop the InceptionV3 network. It is its convolutional layer that makes it different from other networks. A normal network convolution section creates operations by moving a filter over multidimensional matrices, such as width, height, and depth. Xception, on the other hand, provides two distinct approaches to convolution, namely depth wise convolution and pointwise convolution [34]. Depth wise

convolution reaches the result by processing only one channel. Since this will cause a loss of features, pointwise convolution is then applied to the image obtained by processing over a channel; the result obtained is a classical convolution $1 \times 1 \times \text{channel number}$ [35].

3.2. The Proposed Method

This study proposes three TL-based approaches for the classification of screw, bolt, and nut fasteners. Two of the proposed approaches use FT, and the other uses FE. In scenario 1, only the classifier layer in the pre-trained network model is updated, using TL and FT. Scenario 1 is designated as TL-FT1. Scenario 2 adds TL and FT in the last layers of the model, i.e., it adds new layers to the pre-trained model to obtain a new one. Scenario 2 is designated as TL-FT2. Scenario 3 proposes a new approach: a hybrid structure is created by making use of TL's feature extraction capability and using FE and CNN together. Scenario 3 is designated as TL-FE. Fig. 4 provides an overview of this study.

Given that the datasets to be classified are small, this study uses pre-trained networks because of their high performance and low computation time. Before the implementation of each scenario, the dataset needs to be prepared. In TL-FT1, the classifier layer of the pre-trained network is updated to 18, then the Flatten layer is added to the end of the network. The weight and layer values of the pre-trained network are completely frozen. In TL-FT2, after all the layers and weights of the pre-trained network are frozen, global average pooling, 256 dense, activation relu, 256 dense, and activation relu layers are added to the end of the network, and the number of softmax classifier classes is updated to 18. Network training is completed by training the newly added parts of the network and freezing the previous parts.

In TL-FE, after freezing all the layers and weights of the pre-trained network, the features obtained by training the first network serve as input into the CNN network built from scratch. Unlike other classification studies in the literature, which use images as input to the CNN network, this study uses features as input. Thus, the classification performance of the network significantly improves.

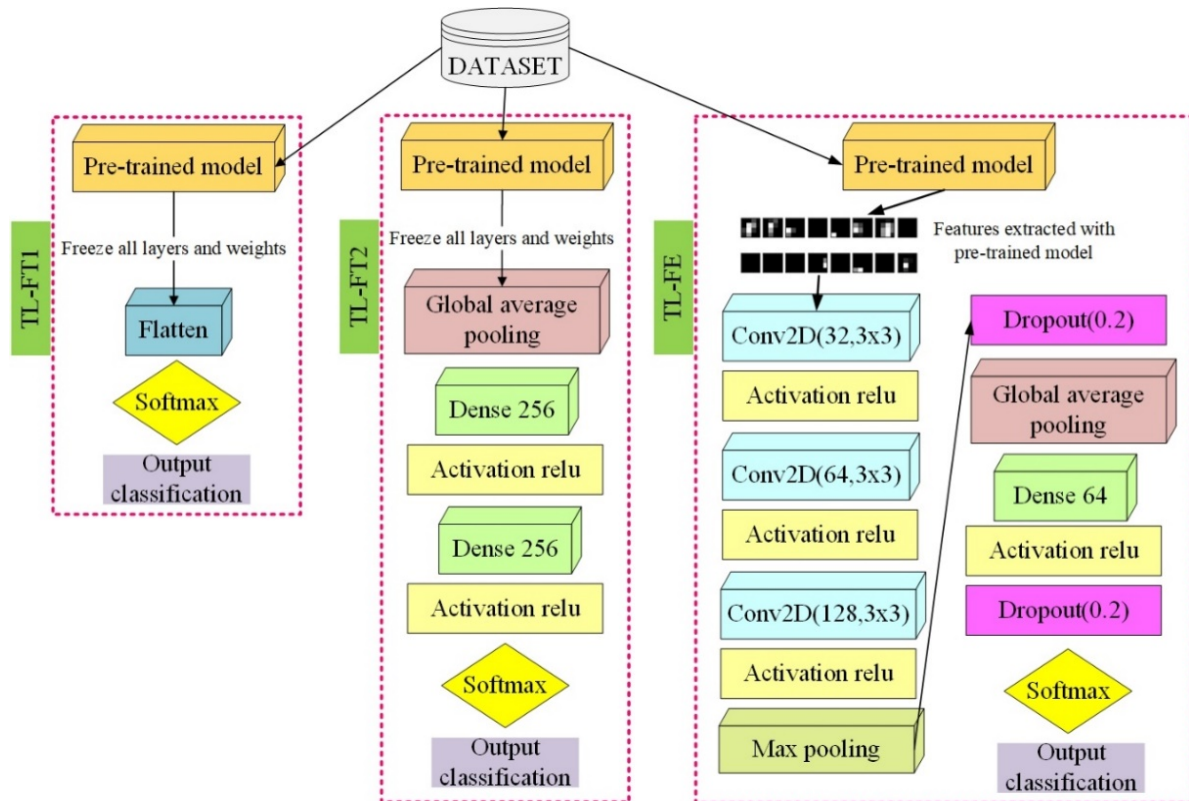


Figure 4. The framework of the proposed approach.

4. Experimental Results

Different scenarios using pre-trained networks have been proposed to classify fasteners. This study examined the performance outputs of each scenario in detail by using 18 different pre-trained networks based on VGGNet, DenseNet, EfficientNet, MobileNet, InceptionNet, ResNet, and Xception. The dataset used for classification includes bolts, screws, and nuts. The performance of each approach proposed in our study was examined in detail, and our study was compared with other studies in the literature. The epoch value in our study is 100, the optimizer algorithm is Adam, the batch size is 32, the learning rate is 0.01, and the image size is 150x150. The hardware features of the computer used in this study are an Intel i7 processor 1.8 GHz CPU, 8GB RAM, and NVIDIA GeForce MX150 GPU.

4.1. Creating Dataset

The dataset contains 150x150 pixel fastener images in RGB format. The fastener images, which contain 18 different classes, include six screw-type, five nut-type, and seven bolt-type classes. The images in the dataset were augmented with data augmentation techniques. For this purpose, each image was shifted by 0.2 on the x axis and by 0.2 on the y axis, as well as being rotated by a 30-degree angle, tilted by 0.2, and magnified by 0.2 percent. In addition, the images were rotated on the horizontal axis. Each class includes approximately 100 images, with 1760 images for the training and 176 images for the testing.



Figure 5. Sample images for the classes in the dataset used in this study.

In Fig. 6, there are some results related to testing different transfer learning models for three different scenarios proposed. When the results of the VGG16 and VGG19 models from the VGGNet architecture were examined, it was observed that the VGG16 achieved higher performance and the best result was 99.43% with the TL-FE scenario. When the results of InceptionV3 and InceptionResNetV2 models from the InceptionNet architecture are examined, it is observed that InceptionResNetV2 achieves higher performance and the best result is 99.2% with the TL-FE scenario. Similarly, when DenseNet and MobileNet architectures are examined, the best performance is in DenseNet169(99.5%) and MobileNet(97.5%) models, respectively. When the XceptionNet and ResNet architectures are examined, the best performance was achieved with TL-FE scenario, Xception(99.1%) and ResNet50(97.2%), respectively.

The Fig.7 and Fig.8 depict the accuracy rates of each of the EfficientNet models over the three scenarios. The highest performance was achieved with the TL-FE scenario on all EfficientNet models. When the success rates of each scenario are examined, EfficientNetB0 93% in TL-FT1, EfficienNetB0 96% in TL-FT2 and EfficientNetB6 99.4% in TL-FE.

The Fig. 9, Fig.10 and Fig.11 shows the success rates of all TL models for TL-FT1, TL-FT2 and TL-FE scenarios, respectively. When the figures are examined, it can be noticed that the TL-FE scenario has a higher performance than the other two scenarios.

A Hybrid Classification Approach for Fasteners Based on Transfer Learning with Fine-Tuning and Deep Features

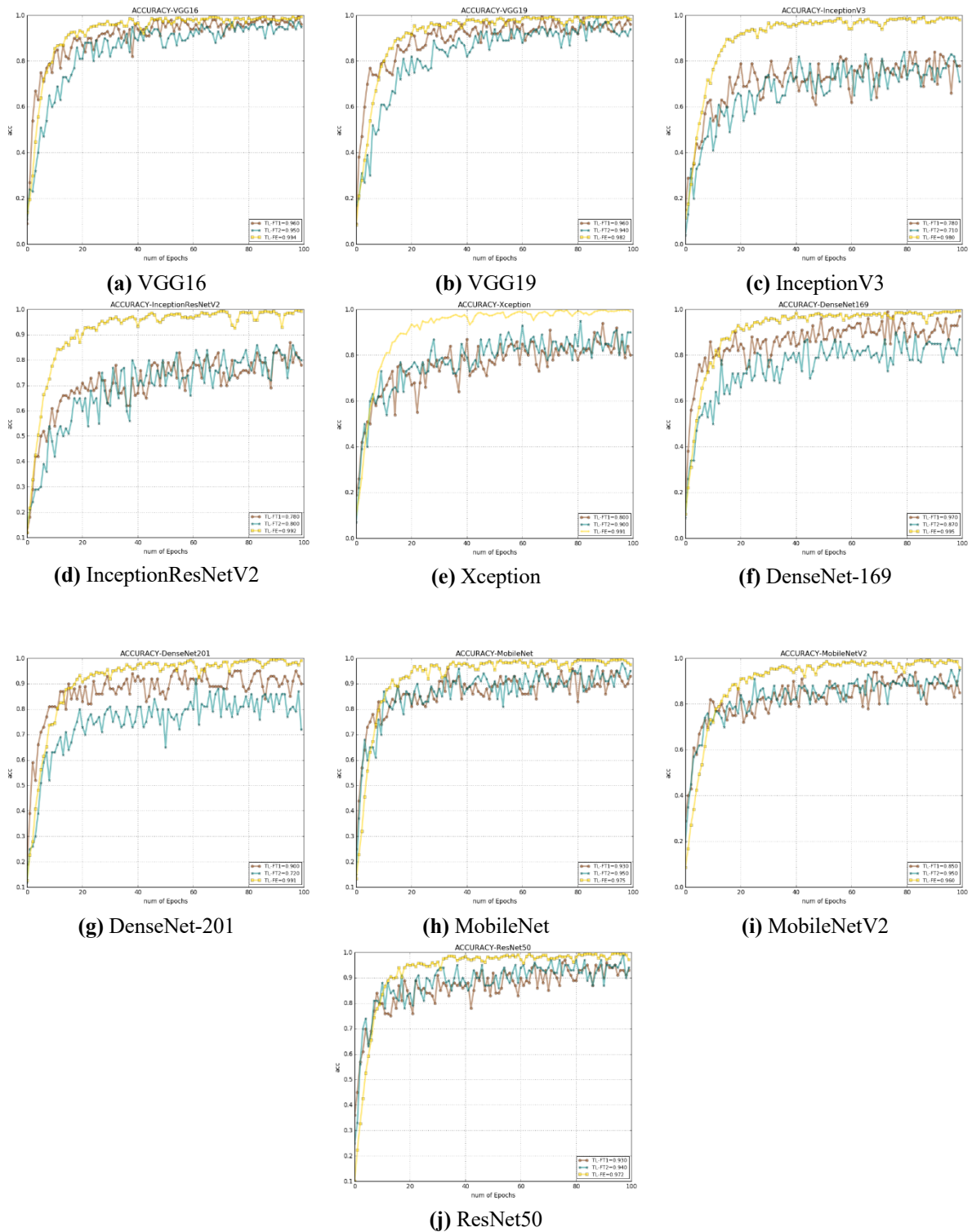


Figure 6. Accuracy distribution of the VGGNets, InceptionNets, XceptionNet, DenseNets, MobileNets and ResNet models according to TL-FT1, TL-FT2, and TL-FE.

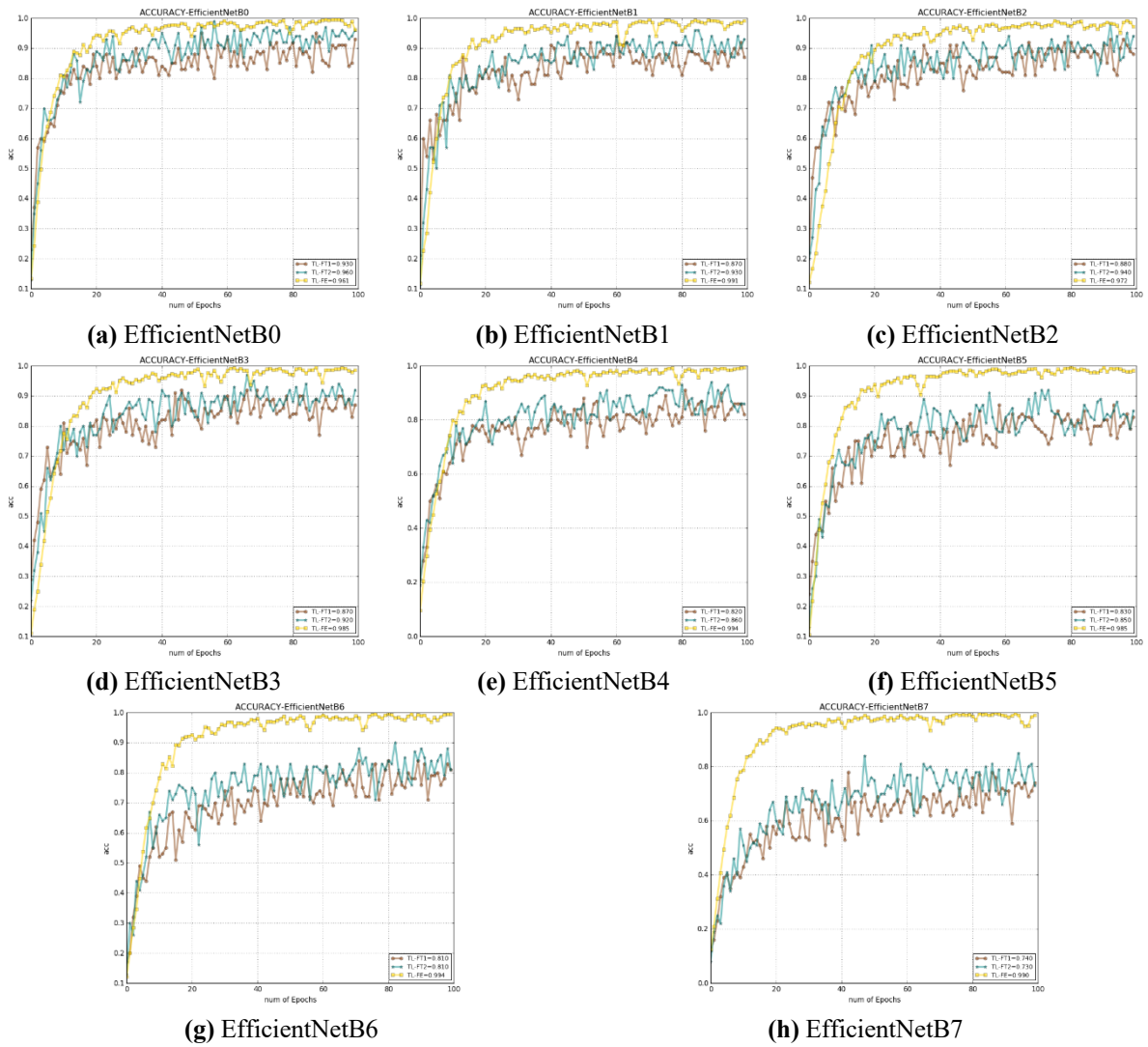


Figure 7. Accuracy distribution of the EfficientNet models according to TL-FT1, TL-FT2, and TL-FE.

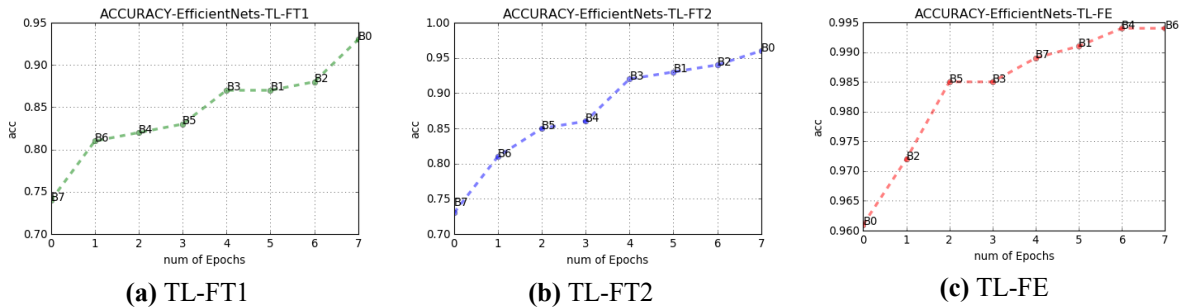


Figure 8. Accuracy rates of EfficientNets according to (a), (b), and (c) scenarios.

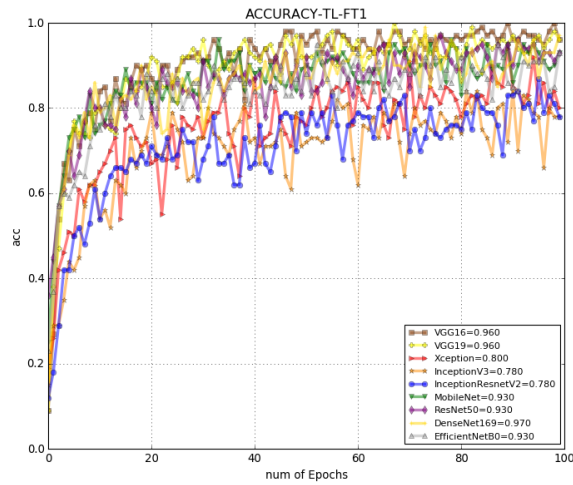


Figure 9. Accuracy rates of all models according to TL-FT1 scenario.

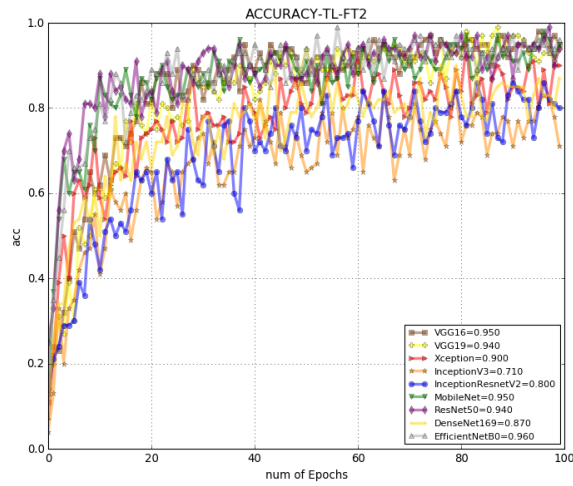


Figure 10. Accuracy rates of all models according to TL-FT2 scenario.

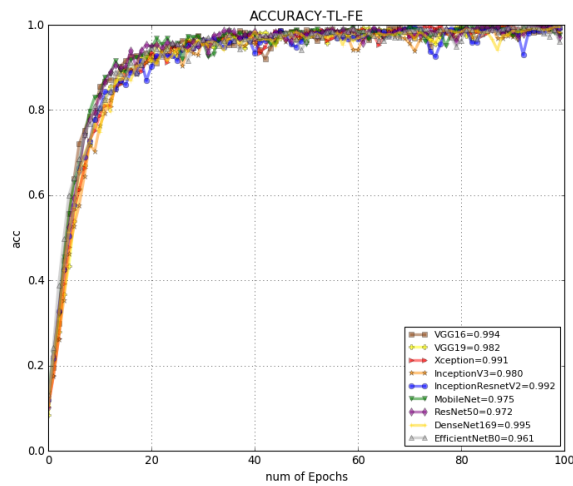


Figure 11. Accuracy rates of all models according to TL-FE scenario.

Table 1. Hyper-parameter values of all scenarios.

Hyper-parameters	Value
Optimizer algorithm	Adam
Iteration	100
Batch size	32
Learning rate	0.001
Input image size	150x150

Table 2. Comparison of the accuracy rates of all scenarios.

Model	TL-FT1	TL-FT2	TL-FE
VGG16	0.960	0.950	0.9943
VGG19	0.960	0.940	0.982
InceptionV3	0.780	0.710	0.980
InceptionResNetV2	0.780	0.800	0.992
Xception	0.800	0.900	0.991
MobileNet	0.930	0.950	0.975
MobileNetV2	0.850	0.950	0.960
ResNet50	0.930	0.940	0.972
DenseNet169	0.970	0.870	0.995
DenseNet201	0.900	0.710	0.991
EfficientNetB0	0.930	0.960	0.961
EfficientNetB1	0.870	0.930	0.991
EfficientNetB2	0.880	0.940	0.972
EfficientNetB3	0.870	0.920	0.985
EfficientNetB4	0.820	0.860	0.994
EfficientNetB5	0.830	0.850	0.985
EfficientNetB6	0.810	0.810	0.994
EfficientNetB7	0.740	0.730	0.989

Table 1 contains the hyper-parameter values of all scenarios. Table 2 shows that the TL-FE scenario gives the best results among all models. This means that the proposed new model is successful. As shown in Table 2, the models with the best results were DenseNet169 with an accuracy of 0.97 in the TL-FT1 scenario, EfficientNetB0 with 0.96 in TL-FT2, and DenseNet169 with 0.995 in TL-FE.

Table 3. Performance evaluation of all models according to TL-FT1.

Model	Accuracy	Validation accuracy	AUC	Validation AUC	Precision	Validation precision	Recall	Validation Recall
VGG16	0.960	0.860	0.964	0.964	0.899	0.899	0.820	0.821
VGG19	0.960	0.880	0.964	0.964	0.897	0.898	0.814	0.814
InceptionV3	0.780	0.510	0.819	0.819	0.563	0.564	0.537	0.537
InceptionResNetV2	0.870	0.270	0.781	0.781	0.494	0.494	0.465	0.465
Xception	0.800	0.480	0.826	0.825	0.605	0.605	0.597	0.597
MobileNet	0.930	0.700	0.896	0.896	0.747	0.747	0.742	0.743
MobileNetV2	0.850	0.510	0.848	0.848	0.659	0.659	0.655	0.655
ResNet50	0.930	0.030	0.741	0.741	0.498	0.498	0.456	0.456
DenseNet169	0.970	0.460	0.995	0.753	0.970	0.460	0.970	0.460
DenseNet201	0.900	0.430	0.979	0.721	0.900	0.430	0.900	0.430
EfficientNetB0	0.930	0.500	0.984	0.792	0.930	0.505	0.930	0.500
EfficientNetB1	0.870	0.420	0.962	0.731	0.870	0.420	0.870	0.420
EfficientNetB2	0.880	0.310	0.962	0.676	0.880	0.310	0.880	0.310
EfficientNetB3	0.870	0.320	0.957	0.671	0.869	0.327	0.860	0.320
EfficientNetB4	0.820	0.370	0.926	0.706	0.820	0.374	0.820	0.320
EfficientNetB5	0.830	0.420	0.951	0.723	0.838	0.420	0.830	0.420
EfficientNetB6	0.810	0.210	0.925	0.595	0.816	0.210	0.800	0.210
EfficientNetB7	0.740	0.240	0.892	0.598	0.740	0.232	0.740	0.230

Table 4. Performance evaluation of all models according to TL-FT2.

Model	Accuracy	Validation accuracy	AUC	Validation AUC	Precision	Validation precision	Recall	Validation Recall
VGG16	0.950	0.860	0.960	0.960	0.890	0.890	0.737	0.738
VGG19	0.940	0.840	0.959	0.959	0.890	0.890	0.713	0.714
InceptionV3	0.710	0.510	0.870	0.870	0.606	0.606	0.487	0.488
InceptionResNetV2	0.800	0.320	0.803	0.803	0.498	0.498	0.400	0.400
Xception	0.900	0.570	0.886	0.886	0.659	0.660	0.563	0.564
MobileNet	0.950	0.660	0.941	0.941	0.783	0.783	0.716	0.716
MobileNetV2	0.950	0.480	0.906	0.906	0.702	0.702	0.626	0.627
ResNet50	0.940	0.070	0.858	0.858	0.897	0.897	0.426	0.426
DenseNet169	0.870	0.420	0.995	0.812	0.884	0.603	0.840	0.350
DenseNet201	0.720	0.410	0.971	0.830	0.758	0.479	0.690	0.230
EfficientNetB0	0.960	0.540	1.000	0.885	0.970	0.587	0.960	0.540
EfficientNetB1	0.930	0.430	0.999	0.851	0.948	0.442	0.920	0.420
EfficientNetB2	0.940	0.460	1.000	0.795	0.959	0.469	0.940	0.380
EfficientNetB3	0.920	0.550	0.993	0.875	0.935	0.538	0.870	0.420
EfficientNetB4	0.860	0.410	0.990	0.814	0.903	0.463	0.840	0.380
EfficientNetB5	0.850	0.300	0.993	0.720	0.878	0.304	0.790	0.280
EfficientNetB6	0.810	0.350	0.991	0.823	0.839	0.491	0.780	0.280
EfficientNetB7	0.730	0.330	0.966	0.840	0.788	0.340	0.670	0.320

Table 5. Performance evaluation of all models according to TL-FE.

Model	Accuracy	Validation accuracy	AUC	Validation AUC	Precision	Validation precision	Recall	Validation Recall
VGG16	0.994	0.972	1.000	0.994	0.995	0.972	0.994	0.972
VGG19	0.982	0.977	0.999	0.997	0.983	0.977	0.980	0.972
InceptionV3	0.980	0.977	0.999	0.994	0.981	0.983	0.978	0.977
InceptionResNetV2	0.992	0.972	1.000	0.994	0.993	0.972	0.992	0.972
Xception	0.991	0.943	0.999	0.988	0.991	0.943	0.991	0.938
MobileNet	0.975	0.943	0.999	0.996	0.977	0.949	0.974	0.943
MobileNetV2	0.960	0.938	0.997	0.990	0.961	0.938	0.959	0.938
ResNet50	0.972	0.909	0.997	0.981	0.973	0.909	0.972	0.909
DenseNet169	0.995	0.989	1.000	1.000	0.995	1.000	0.995	0.989
DenseNet201	0.991	0.989	1.000	0.997	0.992	0.989	0.989	0.989
EfficientNetB0	0.961	0.926	0.998	0.985	0.967	0.931	0.960	0.926
EfficientNetB1	0.991	0.972	1.000	0.994	0.991	0.972	0.989	0.972
EfficientNetB2	0.972	0.966	0.998	0.997	0.973	0.966	0.970	0.966
EfficientNetB3	0.985	0.989	1.000	1.000	0.987	0.989	0.984	0.989
EfficientNetB4	0.994	0.972	1.000	0.997	0.994	0.972	0.993	0.972
EfficientNetB5	0.985	0.926	1.000	0.973	0.987	0.926	0.985	0.926
EfficientNetB6	0.994	0.960	1.000	0.988	0.994	0.960	0.993	0.960
EfficientNetB7	0.990	0.938	1.000	0.985	0.991	0.938	0.990	0.938

Tables 3,4 and 5 show the performance evaluations of TL-FT1, TL-FT2 and TL-FE. The data examined in the table are accuracy, precision, recall and AUC values. When Table 3 is examined, the best results in accuracy, precision, recall and AUC values were 97%, 99.5%, 97% and 97% with DenseNet169, respectively. When Table 4 is examined, the best results in accuracy, precision, recall and AUC values were 96%, 100%, 97% and 96%, respectively, with EfficientNetB0. When Table 5 is examined, the best results in terms of accuracy, precision, recall and AUC values were 99.5% 100%, 99.5% and 99.5% with DenseNet169, respectively.

Table 6. Comparison of the proposed study with the methods in the literature.

Reference	Number of classes	Dataset size	Model	Method	Accuracy ratio	
[1]	2	4986	DenseNet201 DenseNet121 VGG19 VGG16 InceptionResNetV2 Xception	TF-FT2	0.9818 0.9577 0.9637 0.9437 0.9457 0.9195	
[2]	2	460	VGG19 DenseNet121 ResNet50 MobileNet	TF-FT2	0.8511 0.8533 0.8206 0.8642	
[3]	15	20.639	ResNet50	TF-FT2	0.9926	
[4]	2	2198	VGG16	TF-FT2	0.9146	
[5]	2	Dataset1 with 40 classes Dataset2 with 24 classes Dataset3 with 40 classes	AlexNet VGGNet GoogLeNet	TF-FT2	0.9675 0.9747 0.9597	
[6]	2	613	ResNet-34	TF-FT1	1.000	
[8]	4	236	AlexNet VGG19 ResNet50	TF-FT2	0.9153 0.9587 0.8983	
[10]	7	38.000	ResNet150V2 Xception DenseNet201	TF-FT2	0.874 0.874 0.891	
[11]	25	9339	VGG16 VGG19 InceptionV3 ResNet50	TF-FT1	0.9839 0.9871 0.9625 0.9871	
[12]	5	3520	VGG16	TF-FT1	0.9767	
[13]	21	20.574	VGG16 VGG19	TF-FT2	0.9847 0.9859	
[14]	3	1596	Xception VGG16 VGG19 InceptionV3 InceptionResNet2 MobileNet	TF-FT2	0.7830 0.7212 0.7006 0.7430 0.7840 0.7237	
[15]	3	11.862	InceptionV3	TF-FT1	0.9800	
[16]	3	3924	VGG16 VGG19	TF-FT1	0.9000 0.9200	
[17]	20	10.000	VGG16 VGG19 InceptionV3	TF-FT1	0.7890 0.7820 0.8790	
[18]	7	5648	EfficientNetB4 DenseNet201 EfficientNetB0 MobileNetV3	TF-FT1	0.9552 0.9405 0.9298 0.9640	
[36]	4	1908	DenseNet201	TL-FT1	0.7333	
[37]	2	5000	MobileNetV2 VGG16 ResNet152V2 DenseNet201	TL-FT1	0.8880 0.9140 0.8958 0.9089	
Our study	18	1760	VGG16 VGG19 InceptionV3 InceptionResNetV2 Xception MobileNet ResNet50 Dense201	TF-FT1 TF-FT2	TL-FT1 0.960 0.960 0.780 0.780 0.800 0.930 0.930 0.900	TL-FT2 0.950 0.940 0.710 0.800 0.900 0.950 0.940 0.710

The accuracy rate of VGG16 is 0.90 and that of VGG19 is 0.92 in [16], applying the TL-FT1 scenario. That of VGG16 is 0.789 and that of VGG19 is 0.782 in [17], applying the TL-FT1 scenario. In our study, the accuracy of VGG16 is 0.960, and that of VGG19 is 0.960.

In [1], implementing the TL-FT2 scenario, the accuracy of VGG16 is 0.9437 and that of VGG19 is 0.9637. In [2], implementing the TL-FT2 scenario, the accuracy of ResNet is 0.8206, that of MobileNet is 0.8642, and that

of VGG19 0.8511. In [4], implementing the TL-FT2 scenario, the accuracy of VGG16 is 0.9146. In [8], implementing the TL-FT2 scenario, the accuracy of ResNet50 is 0.8983. In [10], implementing the TL-FT2 scenario, the accuracy of Xception is 0.874. In [14], implementing the TL-FT2 scenario, the accuracy of VGG16 is 0.7212, that of VGG19 is 0.7006, that of Xception is 0.783, that of InceptionV3 is 0.743, that of InceptionResNetV2 is 0.784, and that of MobileNet is 0.7237.

In our study, the accuracy of VGG16 is 0.950, that of VGG19 is 0.940, that of MobileNet is 0.950, that of Xception is 0.90, that of InceptionV3 is 0.710, and that of InceptionResNetV2 is 0.80.

5. Conclusions

Deep Learning has recently been used to classify many varieties of objects. Since the classification performance of large datasets is higher than that of small datasets, transfer learning (TL) methods have been developed that can also be used on small datasets. Thanks to TL, high computational power is not required during the training of the network, and a network trained on large datasets can also be used to train small ones. Thus, the use of TL has become widespread. There are three different approaches to implementing TL: feature extractor, training from scratch, and fine tuning using the architecture of the pre-trained network. This study suggests the use of TL to classify fasteners. Three different scenarios have been proposed for TL implementation via fine-tuning and feature extraction approaches. The first is to update only the classifier layer of the network using fine-tuning. The second is to add new layers to the end of the mesh using fine-tuning. The last scenario uses the pre-trained network as a feature extractor. The first and second scenarios have been frequently used in the literature. However, the third scenario involves a new method, used here for the first time. In this scenario, the features obtained as a result of the pre-trained network are given as input to a CNN network built from scratch. Thus, the network is guaranteed highly accurate results. In addition, this study tested 18 different models on each scenario one by one, and compared the performance output in detail with results from similar studies in the literature. Those with the best results are DenseNet169 with 0.97 in TL-FT1, EfficientNetB0 with 0.96 in TL-FT2 and DenseNet169 with 0.995 in TL-FE. Of the three scenarios, TL-FE produced the best performance, with results between 0.960 and 0.995. In addition, this study was comprehensive, including more models than other studies in the literature. This study is also important due to including three different approaches and presenting an entirely new one, namely TL-FE. This study developed 1760 images for the classification of fastener datasets, and the approaches proposed in this study can easily be adapted to other datasets.

References

- [1] Pathak Y, Shukla PK, Tiwari A, Stalin S, & Singh S. Deep transfer learning based classification model for COVID-19 disease. *Pattern Recognit. Lett.* 2020; 152: 122-128.
- [2] Akgun D, Kabakuş AT, Senturk Z.K, Senturk A, & Kucukkulahli E. A transfer learning-based deep learning approach for automated COVID-19 diagnosis with audio data. *Turk. J. Electr. Eng. Comput. Sci.* 2021; 29(SI-1): 2807-2823.
- [3] Sravan V, Swaraj K, Meenakshi K, & Kora P. A deep learning based crop disease classification using transfer learning. *Mater. Today Proc.* 2020.
- [4] Kudva V, Prasad K, & Guruvare S. Hybrid transfer learning for classification of uterine cervix images for cervical cancer screening. *J. Digital Imaging* 2020; 33(3): 619-631.
- [5] Thenmozhi K, & Reddy U.S. Crop pest classification based on deep convolutional neural network and transfer learning. *Comput. Electron. Agric.* 2019; 164.
- [6] Talo M, Baloglu UB, Yildirim O, & Acharya UR. Application of deep transfer learning for automated brain abnormality classification using MR images. *Cogn. Syst. Res.* 2019; 154: 176-188.
- [7] Mehrotra R, Ansari M, Agrawal R, & Anand RS. A transfer learning approach for AI-based classification of brain tumors. *Mach. Learn. Appl.* 2020; 2.
- [8] Yang K, Yang T, Yao Y, & Fan SD. A transfer learning-based convolutional neural network and its novel application in ship spare-parts classification. *Ocean Coastal Manage.* 2021; 215.
- [9] Ali MS, Miah M.S, Haque J, Rahman MM, & Islam MK. An enhanced technique of skin cancer classification using deep convolutional neural network with transfer learning models. *Mach. Learn. Appl.* 2021; 5.
- [10] Rahman Z, & Ami AM. A transfer learning based approach for skin lesion classification from imbalanced data. In: 2020 11th International Conference on Electrical and Computer Engineering (ICECE), 2020; Dhaka, Bangladesh. pp. 65-68.
- [11] Kumar S, & Janet B. DTMIC: Deep transfer learning for malware image classification. *J. Inf. Secur. Appl.* 2022; 64.
- [12] Giraddi S, Seeri S, Hiremath P.S, & Jayalaxmi GN. Flower Classification using Deep Learning models. In: 2020 International Conference on Smart Technologies in Computing, Electrical and Electronics (ICSTCEE), 2020; Karnataka, India. pp. 130-133.
- [13] Wang I. H. Lee KC, & Chang SL. Images Classification of Dogs and Cats using Fine-Tuned VGG Models. In: 2020 IEEE Eurasia Conference on IOT, Communication and Engineering (ECICE), 2020; Yunlin, Taiwan: IEEE. pp. 230-233.

- [14] Lee SW. Novel classification method of plastic wastes with optimal hyper-parameter tuning of Inception_ResnetV2. In: 2021 4th International Conference on Information and Communications Technology (ICOIACT): 2021; IEEE. pp. 274-279.
- [15] Qian Y, Li G, Lin X, Zhang J, Yan J, Xie B, & Qin J. Fresh tea leaves classification using inception-V3. In: 2019 IEEE 2nd International Conference on Information Communication and Signal Processing (ICICSP), 2019; Weihai, China: IEEE. pp. 415-419.
- [16] Junaidi A, Lasama J, Adhinata FD, & Iskandar AR. Image Classification for Egg Incubator using Transfer Learning of VGG16 and VGG19. In: 2021 IEEE International Conference on Communication, Networks and Satellite (COMNETSAT), 2021; Malang: IEEE. pp. 324-328.
- [17] Rajayogi JR, Manjunath G, & Shobha G. Indian food image classification with transfer learning. In: 2019 4th International Conference on Computational Systems and Information Technology for Sustainable Solution (CSITSS9), 2019; Miami, Fla: IEEE. pp. 1-4.
- [18] Espejo-Garcia B, Malounas I, Mylonas N, Kasimati A, & Fountas S. Using EfficientNet and transfer learning for image-based diagnosis of nutrient deficiencies. *Comput. Electron. Agric.* 2022.
- [19] Ribani R, & Marengoni M. A survey of transfer learning for convolutional neural networks. In: 2019 32nd SIBGRAPI Conference on Graphics, Patterns and Images Tutorials (SIBGRAPI-T), 2019; Rio de Janeiro, Brazil: IEEE. pp. 47-57.
- [20] Krishna ST, & Kalluri HK. Deep learning and transfer learning approaches for image classification. *Int J Recent Technol Eng.* 2019; 7(5S4): 427-432.
- [21] Simonyan K, and Zisserman A. Very deep convolutional networks for large-scale image recognition. *arXiv Prepr.* 2014; arXiv1409.1556.
- [22] Szegedy C, Vanhoucke V, Ioffe S, Shlens J, and Wojna Z. Rethinking the inception architecture for computer vision. In: *Proceedings of the IEEE conference on computer vision and pattern recognition*, 2016; Las Vegas, NV, USA: IEEE. pp. 2818–2826.
- [23] Ucar M. Diagnosis of Glaucoma Disease using Convolutional Neural Network Architectures. *Dokuz Eylul Uni. Fac. of Eng. J. of Sci. and Eng.* 2021; 23(68): 521-529.
- [24] Nguyen LD, Lin D, Lin Z, & Cao J. Deep CNNs for microscopic image classification by exploiting transfer learning and feature concatenation. In: 2018 IEEE International Symposium on Circuits and Systems (ISCAS), 2018; Floransa, Italy: IEEE. pp. 1-5.
- [25] Howard AG, Zhu M, Chen B, Kalenichenko D, Wang W, Weyand T, Andreetto M, and Adam H. MobileNets: Efficient Convolutional Neural Networks for Mobile Vision Applications. *arXiv Prepr.* 2017; arXiv/1704.04861.
- [26] Zeren MT. Comparison of ssd and faster r-cnn algorithms to detect the airports with data set which obtained from unmanned aerial vehicles and satellite images. MSc, Beykent University, Istanbul, Turkey, 2020.
- [27] Baydilli YY. Polen Taşıyan Bal Arılarının MobileNetV2 Mimarisi ile Sınıflandırılması. *Eur. J. Eng. Sci. Tech.* 2021; 21: 527-533.
- [28] Huang G, Liu Z, Maaten LVD, & Weinberger KO. Densely Connected Convolutional Networks. In: *IEEE Conference on Computer Vision and Pattern Recognition (CVPR)*, 2017; Hawaii, ABD: IEEE.
- [29] Aktas A. Image processing applications with deep learning methods. MSc, Marmara University, Istanbul, Turkey, 2020.
- [30] Bayram B, Kilic B, Özoğlu F, Erdem F, Bakirman T, Sivri S, & Delen A. A Deep learning integrated mobile application for historic landmark recognition: A case study of Istanbul. *Mersin Photogramm. J.* 2020; 2(2): 38-50.
- [31] Tan M, and Le QV. EfficientNet: Rethinking model scaling for convolutional neural networks. In: *36th Int. Conf. Mach. Learn. ICML*, 2019; pp. 10691–10700.
- [32] Bayram B, Kilic B, Ozoglu F, Erdem F, Sivri S, Delen A, Bayrak OC. A study on object recognition with deep learning. In: *10. Turkiye Ulusal Fotogrametri ve Uzaktan Algılama Birliği Teknik Sempozyumu (TUFUAB 2019)* 2019; Aksaray, Turkey.
- [33] He K, Zhang X, Ren S, Sun J. Deep residual learning for image recognition. In: *Proceedings of the IEEE conference on computer vision and pattern recognition*, 2016; Las Vegas, NV, USA: IEEE. pp. 770-778.
- [34] Dandil E, and Serin Z. Breast Cancer Detection on Histopathological Images Using Deep Neural Networks. *Eur. J. Eng. Sci. Tech.* 2020; Special Issue: 451-463.
- [35] Chollet F. Xception: Deep learning with depthwise separable convolutions. In: *IEEE conference on computer vision and pattern recognition 2017*; Los Alamitos, California: IEEE.
- [36] Sivari E. Güzel M. S. Bostancı E. & Mishra A. A Novel Hybrid Machine Learning Based System to Classify Shoulder Implant Manufacturers. *Healthc. (Basel)* 2022; 10(3), MDPI.
- [37] Kalkan M. Bostancı GE. Güzel MS. Kalkan B. Özsarı Ş. Soysal Ö. & Köse G. Cloudy/clear weather classification using deep learning techniques with cloud images. *Comput. Electr. Eng.* 2022; 102, 108271.

The Solvent Effect on Nanomaterials Composed of Liquid Crystals and Nanoparticles: uv-vis Absorbance and Fluorescence Spectra

Yunus Emre KARA¹, Yadigar GÜLSEVEN SIDIR^{1*}, Sabit HOROZ²

¹ Faculty of Science and Arts, Department of Physics, Bitlis Eren University, Bitlis, Türkiye.

² Faculty of Natural Sciences and Engineering, Engineering Basic Sciences, Sivas Science and Technology University, Sivas, Türkiye.

¹yemrekara1313@gmail.com, ¹ygsidir@beu.edu.tr, ²sabit.horoz@sivas.edu.tr

(Geliş/Received: 29/06/2023;

Kabul/Accepted: 31/08/2023)

Abstract: We have been investigated in different solvent medium to interactions between 4-Ethoxybenzoic acid (4EOBA), 4-Pentylbenzoic acid (4PentBA), and 4-Pentylphenyl 4-Methylbenzoate (4PP4MetB) liquid crystals with CdS, CdSe and ZnS nanoparticles. For this, the new materials composed from LC compound including the solvent and nanoparticle were investigated by use absorbance and fluorescence spectra. Electronic transitions and differences in absorbance and fluorescence spectra were interpreted. The fluorescence of liquid crystals has been defined in the shifts between wavelengths of the fluorescence of nanomaterials. It can be said that it has occurred blue shift at the maximum fluorescence wavelengths of the 4EOBA-CdS-DMSO and 4EOBA-CdSe-DMSO compared to 4EOBA-DMSO. On the other hand, we can say that in the 4EOBA-ZnS-DMSO solution occurs red shift in the fluorescence band, while the peaks seen in the fluorescence band occur in result of interaction of liquid crystals and nanoparticles.

Key words: Fluorescence spectrum, liquid crystals, nanoparticles, solvent effect, nanomaterials.

Sıvı kristaller ve Nanoyapılardan Oluşan Nanomalzemeler Üzerine Çözücü Etkisi: uv-vis Absorbans ve Floresans Spektrumları

Öz: 4-Etoksibenzoik asit (4EOBA), 4-Pentilbenzoik asit (4PentBA) ve 4-Pentilfenil 4-Metilbenzoat (4PP4MetB) sıvı kristaller ve CdS, CdSe ile ZnS nanopartikülleri arasındaki etkileşimleri farklı çözücüler içerisinde incelenmiştir. Bunun için çözücü ve nanopartikül içeren LC bileşiklerden oluşan yeni malzemelerin absorbans ve floresans spektrumları kullanılarak incelenmiştir. Absorbans ve floresans elektronik geçişleri yorumlanır. Sıvı kristallerin floresansı, nanomalzemelerin floresansının dalga boyları arasındaki kaymalarda incelenmiştir. 4EOBA-CdS-DMSO ve 4EOBA-CdSe-DMSO'nun maksimum floresans dalga boylarında 4EOBA-DMSO'ya göre maviye kayma meydana geldiği söylenebilir. Öte yandan, 4EOBA-ZnS-DMSO çözeltisinde, floresan bandında kırmızıya kayma meydana gelirken, floresan bandında görülen tepe noktaları, sıvı kristaller ve nanopartiküllerin etkileşim meydana geldiğini söyleyebiliriz.

Anahtar Kelimeler: Floresans spektrumu, sıvı kristaller, nanoparçacıklar, çözücü etkisi, nanomalzemeler.

1. Introduction

Liquid crystals in the phase diagram appear as an interphase between solid crystals and liquids. These materials are called liquid crystals because they show the properties of both solid crystals and liquids [1]. In that, liquid crystals are interesting due they are fluid and have a long-range order. At this long distance, the position and orientation of the building blocks of liquid crystals are interrelated [2]. Liquid crystalline compounds have a molecular structure with p-conjugates such as fused benzene and cyclopentadiene rings. These liquid crystals result in delocalized p orbitals of conjugates that facilitate charge transfer to gain or lose electrons. With the realization of intermolecular charge transfer, the materials become organic semiconductors and carry the charge [3]. Liquid crystals are divided into lyotropic and thermotropic. They are formed when more than one substance forms a solution in lyotropic liquid crystals. Thermotropic liquid crystals, on the other hand, are the type formed by temperature change [4]. The structures of liquid crystals can change with external stimuli. Temperature change or low voltage electric fields are the factors that cause this change. Liquid crystals that respond easily to external stimuli are used in many display technologies [5]. Depending on the structure and properties of liquid crystal molecules, they can also interact with nanoparticles and cause their fluorescence to change [6]. It has been previously reported in many studies that nanoparticles cause changes on different properties of liquid crystal compounds [7-9]

* Corresponding author: ygsidir@beu.edu.tr , ORCID Number of authors: ¹ 0000-0002-8412-6633, ² 0000-0002-5329-2815, ³0000-0002-3238-8789

The physical properties of materials in bulk can change when materials are reduced to nano-sizes. Studies are showing that when the size of semiconductor nanoparticles is below 5 nm, their electro-optical properties change [10, 11]. The optical and physical properties of materials with nanometer dimensions can vary depending on the size of these materials. The physical and chemical properties of materials occur when the particle size reaches the nanometer level. For a material to be defined as a nanomaterial, it must have a particle size between 1 nm and 100 nm [12, 13]. It has been reported that a wide photonic band gap of CdSe/ZnS nanoparticles doped into cholesteric liquid crystals is formed and these materials are used in optoelectronic applications [14].

The aim of this study is to examine possible interactions with nanostructures and liquid crystal compounds and to determine electronic structure by observing electronic changes and looking at changes in spectra. So, we have been investigated the interactions and electronic transitions between liquid crystals which is including benzoic acid and benzoate structures, and CdS, ZnS and CdSe semiconductor nanoparticles. In addition, we are by examining the absorbance and fluorescence spectra of nanomaterials formed from nanoparticles with liquid crystal; it is aimed to interpret the electronic structures of both nanoparticles and nanomaterials. In addition, solvent effects on nanoparticle have been determined with using electronic absorbance and fluorescence spectrum in different solvent medium.

2. Materials and methods

2.1. Used liquid crystals materials

Liquid crystals of 4-Ethoxybenzoic Acid (4EOBA), 4-Pentylbenzoic Acid (4PentBA), and 4-Pentylphenyl 4-Methylbenzoate (4PP4MetB) used in this study are of high purity. The molecular structures of these liquid crystals are shown in Figure 1. Methanol, Toluene and DMSO solvents are spectroscopic grade. Both the solvents used and the liquid crystal compounds used were taken from Sigma-Aldrich.

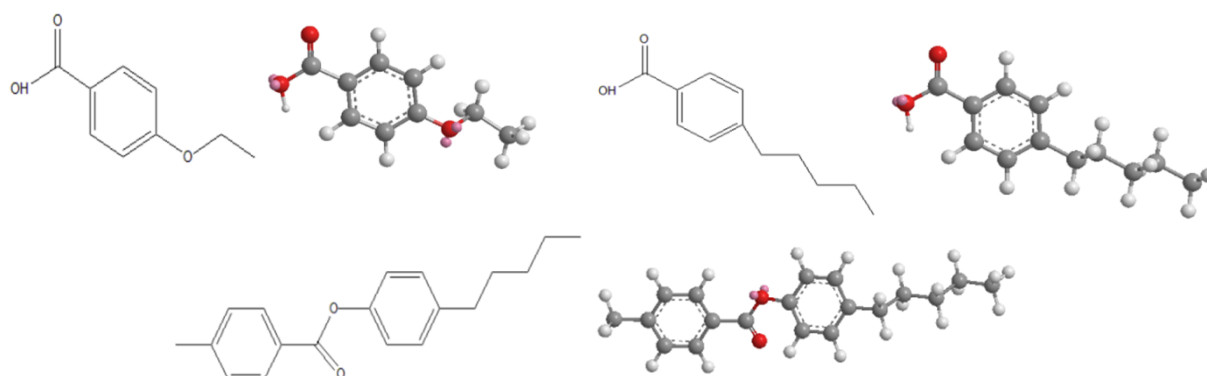


Figure 1. The molecular structure of investigated liquid crystals.

2.2. Syntheses and characterized of nanoparticles

2.2.1. ZnS synthesis and characterize

In a typical process, 100 ml of an aqueous solution containing 0.1 M of $\text{Zn}(\text{CH}_3\text{COO})_2 \cdot \text{H}_2\text{O}$ and Na_2S were put into 250 ml of an ethanol solution containing citric acid (10 ml) and methacrylic acid (5 g). The resultant solution was then cooled to room temperature and refluxed under N_2 for several hours. The resulting powders were separated by centrifuging, and then dried at room temperature in a vacuum. XRD graph of ZnS nanoparticles has been shown in Figure 2.

2.2.2. CdS synthesis and characterize

In a typical process, 100 ml of an aqueous solution containing 0.1 M of $\text{Cd}(\text{CH}_3\text{COO})_2\cdot\text{H}_2\text{O}$ and Na_2S were put into 250 ml of an ethanol solution containing citric acid (10 ml) and methacrylic acid (5 g). The resultant solution was then cooled to room temperature and refluxed under N_2 for several hours. The resulting powders were separated by centrifuging, and then dried at room temperature in a vacuum. The XRD graph of CdS nanoparticles have been shown in Figure 2.

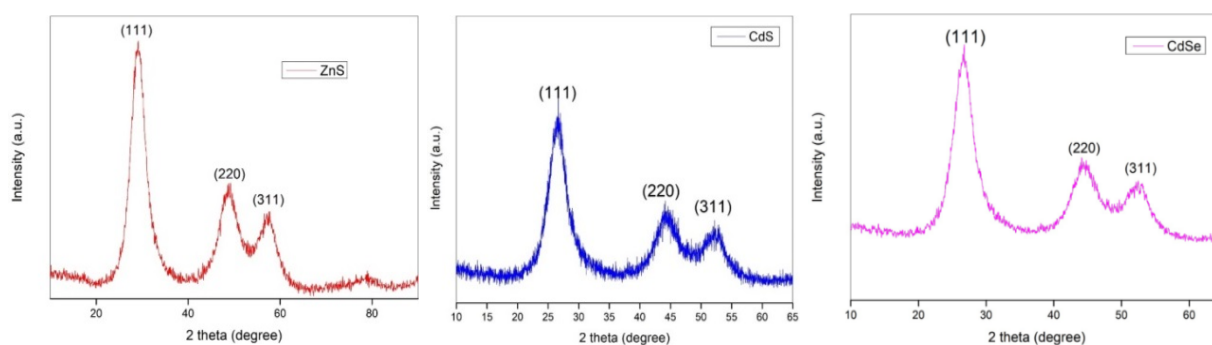


Figure 2. XRD graphs of ZnS, CdS and CdSe nanoparticles

2.2.3. CdSe synthesis and characterize

The cadmium supply was cadmium acetate ($\text{Cd}(\text{CH}_3\text{COO})_2\cdot\text{H}_2\text{O}$), and the selenium source was sodium selenosulfate (Na_2SeSO_3). The pH of the aqueous mixture of mercapto acetic acid (HSCH_2COOH) and cadmium acetate (2 mmol) was adjusted to 10 by adding a 1 M solution of sodium hydroxide. N_2 bubbles were used to dehydrate the solution for 30 minutes. The sodium selenosulfate solution (Na_2SeSO_3) was made by combining the cadmium acetate solution with freshly made Se powder (0.02 mol) and Na_2SO_3 solution (0.2 mol). After that, 2-propanol was added drop by drop while the mixture was being stirred till it turned turbid. To obtain the dry powder, the precipitate was separated using centrifugation. The XRD graph of CdSe nanoparticles has been shown in Figure 2.

2.3. Experimental methods

We have been used in 4-Ethoxybenzoic Acid (4EOBA), 4-Pentylbenzoic Acid (4PentBA), and 4-Pentylphenyl 4-Methoxybenzoate (4PP4MetoxB) liquid crystals. We made the liquid crystals into solutions with 10^{-5} M in methanol, toluene and DMSO solvents. The CdS, CdSe, and ZnS nanoparticles have been used in our study. These nanoparticles have been prepared as about 2×10^{-4} M in DMSO, 1.3×10^{-4} M in Toluene and 1.6×10^{-4} M in methanol solvent. As a result, we have readied liquid crystals and nanoparticles solution, by taking 1 ml of nanoparticle solutions from 9 ml of liquid crystal solutions. The absorbance and fluorescence spectra have measured using the Perkin Elmer Lambda-35 UV-vis spectrophotometer and Perkin Elmer LS-55 fluorescence spectrophotometer.

3. Results and Discussion

3.1. The absorbance spectra of nanoparticles

The absorbance-wavelength and $\alpha h\nu$ -energy graphs of CdS, CdSe, and ZnS nanoparticles are shown in Figure 3-5, respectively. The band gaps of synthesized semiconductor nanoparticles using the Tauc equation given in Equation 1 were calculated as 3.34 eV for CdS, 2.73 eV for CdSe, and 4.30 eV for ZnS, respectively.

$$\alpha h\nu = B \cdot (h\nu - E_g)^p \quad (1)$$

Here, $h\nu$ is the energy of the incident light, E_g is the band gap value, B is a unit less constant expressing the transition probability between energy levels, and p is a unit less constant whose value is 0.5 for direct transitions and 2 for indirect transitions [15-16].

The most important observation obtained as a result of absorbance measurements is that the forbidden energy gaps calculated for the synthesized CdS, CdSe, and ZnS nanoparticles are larger than the bulk forbidden energy gaps of these materials. The bulk forbidden energy range for CdS is 2.42 eV, the bulk forbidden energy range for CdSe is 1.74 eV, and the bulk forbidden energy range for ZnS is 3.56 to 3.76 eV. As the band gap of the synthesized semiconductor quantum dots increases due to the quantum confinement effect, it can be said that the crystallite size of these materials are very small.

3.2. The solvent effect on nanoparticle

The graphs and data of nanoparticles obtained by fluorescence and absorbance spectrum are given in figures 3-5 and tables 1-3, respectively. These solvents which non-polar toluene, polar protic methanol and polar aprotic DMSO solutions are were used in this study to examine the changes between the electronic transitions in nanoparticles.

While taking fluorescence measurements of these nanoparticles, the excitation wavelength values were taken as 370 nm or 380 nm. It has been reported in previous studies that the absorption spectra of synthesized CdS nanoparticles were obtained in DMSO solution with a sharp peak at 327 nm and a shoulder peak at 346 nm [17]. We have been found as 335 nm wavelength in DMSO at room temperature. The have observed two different bands in the fluorescence spectrum of CdS nanoparticle in DMSO solvent are at 388 and 412 nm, while it has been observed fluorescence bands as 420, 440, and 470 nm.

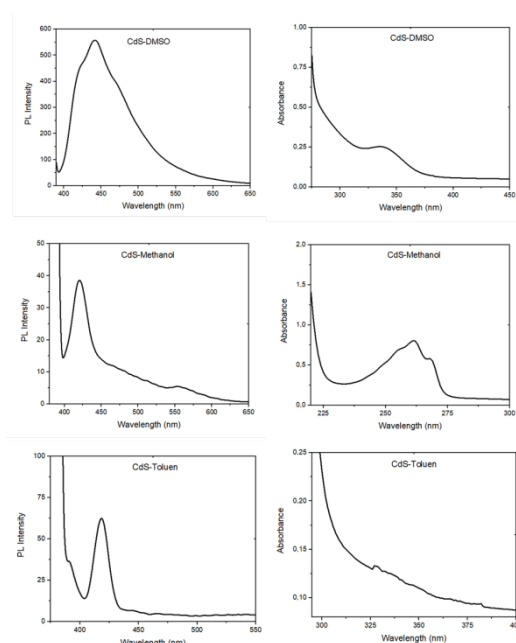


Figure 3. Absorbance and fluorescence spectra of Cadmium Sulfide (CdS) nanoparticle.

Table 1. The absorbance and fluorescence spectra CdS particle.

Solvent	(Excitation Wavelength, 370 nm)	Fluorescence Wavelength	Absorbance Wavelength
DMSO		420-440-470	335
Methanol		420-554	255-261-268
Toluene		391-420	327

As seen in Figure 3, absorbance spectra of CdS nanoparticles dissolved in methanol were observed at 255, 261, and 268 nm, while PL spectra were observed at 420 and 554 nm. In the previous study of CdS nanoparticles [18], the absorbance and fluorescence spectra of CdS in Toluene were found to be approximately 403.7 and 411 nm, and we have observed to 576 nm of CdS nanoparticles in toluene solvent. The UV-vis spectrum generally

decreases with the size of the nanocrystals and the absorption maximum wavelength decreases with the particle size [19]. CdS nanoparticles have unique properties due to their size and shape. It is widely used in fields such as biosensors, bioimaging, nanomedicine, molecular pathology, antimicrobial activities, photovoltaic cells, semiconductors, and drug delivery. It has been reported in the literature that CdS nanoparticles have a strong absorbance band at 420-440 nm in their UV-vis spectra. It is reported that 512 nm (2.42 eV) is the absorption limit for bulk hexagonal CdS [20].

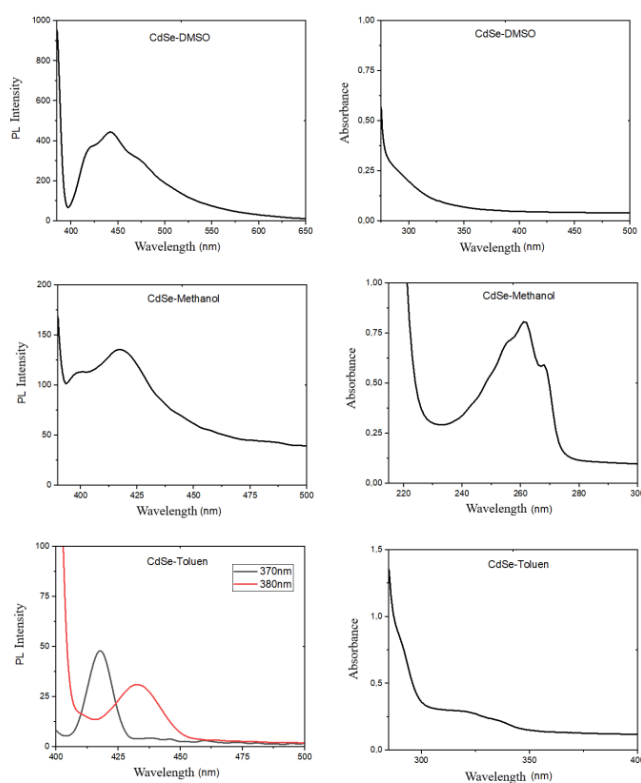


Figure 4. Absorbance and fluorescence spectra of Cadmium Selenide (CdSe) nanoparticle.

Table 2. The absorbance and fluorescence spectra CdSe particle.

Solvent	(Excitation Wavelength, 370 nm)	Fluorescence Wavelength (nm)	Absorbance Wavelength (nm)
DMSO		420-441-470	381
Methanol		400-417	256-261-268
Toluene		417	318-336
Toluene (380 nm)		432	

Electronic absorbance and fluorescence spectra of CdSe nanoparticles in DMSO, methanol, and toluene solvent are shown in Figure 4. Data about these measurements are given in Table 2. Semiconductor CdSe nanoparticles have been widely studied. The absorption spectrum of very small CdSe nanoparticles shifted from 402 nm to 417 nm depending on the size [11]. In our study, it has an absorbance band observed between 256-382 nm. The UV-Vis absorption spectra in previous studies for CdSe were observed in at 360 nm and 385 nm. In this study, an absorption band was observed at 382 nm in DMSO. It is known to have an absorbance band of 385 nm, so it can say as 5.4 nm for CdSe nanoparticle which is smaller than the Bohr radius [21]. Thus, we can say that the CdSe nanoparticle used in this study is around 5 nm. In the study by Ashtoputre [22] et al., a strong peak

at 435 nm and a weak peak at 414 nm were observed when the excitation peak was 362 nm, while a broad peak at 581 nm and a different peak at 437 nm was observed when the excitation peak was 371 nm. Here, a broad band was observed at 420, 441, and 470 nm in DMSO solvent at the excitation wavelength of 370 nm, while a peak was observed at 400 and 417 nm in methanol solvent. In toluene solvent, there are fluorescence bands at both 370 nm and 380 nm excitation values, which we observe in 417 and 418 nm wavelength.

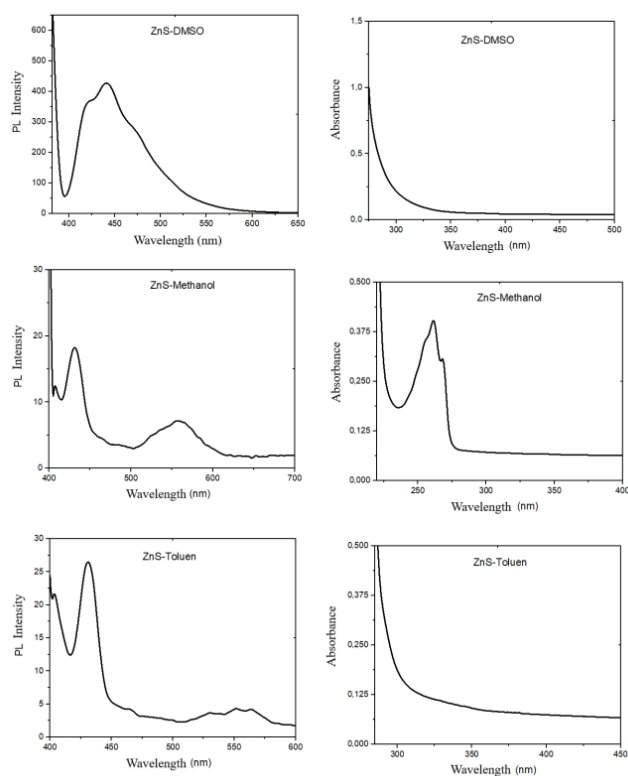


Figure 5. Absorbance and fluorescence spectra of Zinc Sulfide (ZnS) nanoparticle.

Table 3. The absorbance and fluorescence spectra ZnS particle.

Solvent	(Excitation Wavelength, 370 nm)	Fluorescence Wavelength (nm)	Absorbance Wavelength (nm)
DMSO		422-440-468	382
Methanol		431-557	256-261-267
Toluene		403-431-464-530 551-564	382

The absorbance and fluorescence spectra of ZnS nanoparticles in toluene, DMSO, and methanol are given in Figure 5, while the data of these spectra are given in Table 3. The ZnS nanoparticles give good absorption between 220-350 nm [23]. Generally, while ZnS absorbs around 300 nm, a blue shift occurs when bulk ZnS absorbs up to the 345 nm limit. As seen in Table 3, a wide band was observed in the absorbance spectrum for ZnS at 382 nm in DMSO, in addition, electronic absorbance bands in methanol solvent of ZnS nanoparticle have been found as 256, 261 and 267 nm. In toluene, the absorbance spectrum was observed at 382 nm.

Biswas et al. [24], Tamrakar et al. [25], and Chen et al. [26] have been found as about 400 nm in photoluminescence spectra of ZnS nanostructures. Chen et al. have compared the results with that of bulk. In this study, ZnS nanoparticles including methanol solvent have been found as about 422-440 nm as dependent

solvent, which is methanol, DMSO and toluene. Other fluorescence bands are observed to wavelength changed between 468-564 nm.

The reason for the change in absorbance and fluorescence bands of semiconductor nanoparticles due to solvent is that it can cause a change in the semiconductor band of NPs with solvent polarity. Radius lengths of very small nm show a three-dimensional quantum size effect in the electronic structure of semiconductor nanoparticles. The effect of quantum size on band gap absorption energy can be measured by UV-Vis absorbance spectroscopy.

3.3. The interaction between nanoparticle and LC compounds

Here, we have studied spectroscopic properties of doped nanoparticles in LC compounds for investigated possible interactions between nanoparticles with investigated LC compounds, in addition, so, we used liquid crystals and nanoparticles-doped liquid crystals in the same solvent environment. The graphs of fluorescence measurements of the analyzed 4EOBA, 4PentBA and 4PP4MetB LCs and the samples to which CdS, CdSe and ZnS nanoparticles were added are shown in Figures 6, 7 and 8, respectively. We set out to evaluate the fluorescence graphs of a new solution formed by nanoparticles added separately to liquid crystals and the changes in maximum wavelengths based on liquid crystals are listed in Tables 1, 2 and 3.

It is seen in Figure 6 that the maximum wavelengths of 4EOBA-CdS-methanol and 4EOBA-CdSe-methanol solutions consisting of nanoparticles added separately to liquid crystals in solvent media are almost the same.

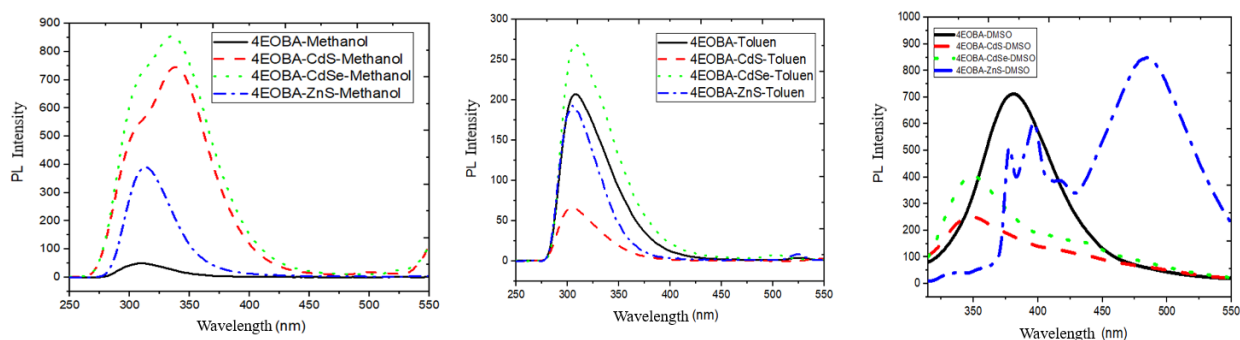


Figure 6. Fluorescence spectra of 4EOBA liquid crystal doped nanoparticles and 4EOBA liquid crystal in solvent environments.

The maximum wavelength of these nanoparticle-doped liquid crystals has a shift of approximately 25 nm compared to that of liquid crystals. In the resulting 4EOBA-ZnS-methanol solution, there is no shift compared to the liquid crystals.

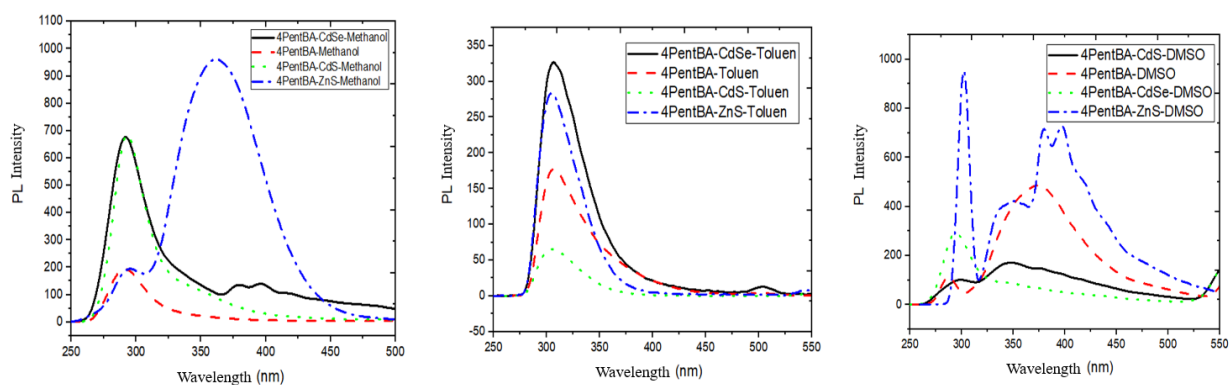


Figure 7. Fluorescence spectra of 4PentBA liquid crystal doped nanoparticles and 4PentBA liquid crystal in solvent environments.

It is seen that the fluorescence graphs of the liquid crystal and nanoparticle-doped liquid crystals are similar when the solvent is toluene in 4EOBA liquid crystal. As can be understood here, it has been observed that there is no interaction between liquid crystals and nanoparticles in toluene solutions.

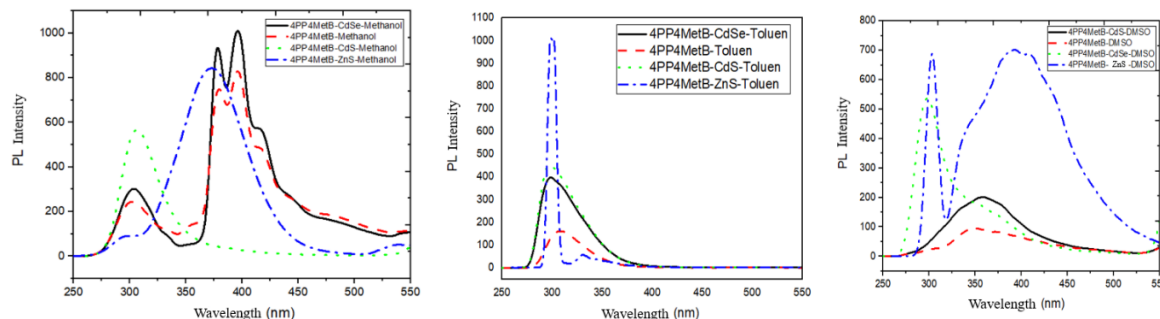


Figure 8. Fluorescence spectra of 4PP4MetB liquid crystal doped nanoparticles and 4PP4MetB liquid crystal in solvent environments.

The fluorescence graphs of the new 4EOBA-CdS-DMSO and 4EOBA-CdSe-DMSO solutions, which are formed by nanoparticles added separately to the 4EOBA-DMSO solution, are similar and their maximum wavelengths are the same. The maximum wavelength of the new 4EOBA-ZnS-DMSO solution formed by the ZnS nanoparticle added to the 4EOBA-DMSO solution has shifted compared to the liquid crystalline solution. Fluorescence graphs and maximum wavelengths of 4PentBA-CdS-methanol and 4PentBA-CdSe-methanol solutions formed by nanoparticles added separately to 4PentBA liquid crystal overlap. However, a shift of about 70 nm occurred in the maximum wavelength of the 4PentBA-ZnS-methanol solution. No significant difference was observed in the fluorescence graphs and maximum wavelengths of the nanoparticles added individually to the 4PentBA-toluene solution. Thus, we can say that 4PentBA liquid crystal and nanoparticles do not interact in the environment where toluene is used as a solvent. Different fluorescence graphs appeared in all new solutions formed with nanoparticles added separately to the 4PentBA-DMSO solution. 4PentBA liquid crystal and nanoparticles interacted in the DMSO solution. The maximum wavelengths are similar to the fluorescence graph of 4PP4MetB-methanol solution and 4PP4MetB-CdSe-methanol which is one of the new solutions formed by nanoparticles added separately to the 4PP4MetB-methanol solution. The maximum wavelength of the 4PP4MetB-ZnS-methanol solution creates a shift of about 43 nm concerning the liquid crystal solution. The new 4PP4MetB-CdS-methanol solution, on the other hand, showed a shift in the maximum wavelength compared to the liquid crystalline solution. It was observed that the fluorescence graphs of 4PP4MetB-CdS-toluene and 4PP4MetB-CdSe-toluene solutions obtained from the new solutions consisting of nanoparticles added separately to the 4PP4MetB-toluene solution were similar to each other. In the fluorescence graph obtained from the 4PP4MetB-ZnS-toluene solution, there was a 22 nm shift in the maximum wavelength compared to that of 4PP4MetB-toluene solution. We have seen that the 4PP4MetB-CdS-DMSO solution, which consists of nanoparticles added separately to the 4PP4MetB-DMSO solution, has a similar fluorescence graph to the liquid crystal solution. Maximum wavelength shift occurred in the 4PP4MetB-CdSe-DMSO solution compared to the 4PP4MetB-DMSO solution. In the 4PP4MetB-ZnS-DMSO solution, a wide peak was observed after the excitation peak. In the environment where methanol is used as a solvent, liquid crystals and solutions with CdS and CdSe nanoparticles interact and the electronic structure of the new solutions formed has changed. The change in the fluorescence graph of the new solutions formed and the difference in the maximum wavelengths are an indication that the charge transfers have taken place. In the environment where toluene was used as a solvent, there was generally no interaction between liquid crystals and nanoparticles. The fluorescence graph and maximum wavelengths of nanoparticle-doped liquid crystals are similar to liquid crystals. From investigated fluorescence spectra has different only in the 4PP4MetB-ZnS-Toluene solution. In the environment where DMSO is used as a solvent, interactions and charge transfers between liquid crystals and nanoparticles are seen from fluorescence graphs. The shifts observed in the maximum wavelengths of nanoparticle-doped liquid crystals compared to liquid crystals indicate that the energy band gaps also change. We can say that liquid crystals and nanoparticles can generally interact in a suitable solvent environment. Among the possible consequences of these interactions is the change of electronic structure with the realization of charge transfers.

Conclusions

In this study, fluorescence and absorbance spectra of nanomaterials consisting of liquid crystals and nanoparticles in solvents were investigated. In general, we observed that nanoparticles and liquid crystals do not interact in the toluene solvent. Solvent polarity may be the reason why the nanoparticle does not interact with liquid crystals in toluene. We can use the dielectric constant to compare the solvent polarity. Therefore, the values of the toluene solvent are 2.38, the values of the methanol solvent are 32.66 and the values of the DMSO solvent are 46.45 [27]. In addition, when looking at the types of solvents used, methanol is polar protic, DMSO is polar aprotic, and toluene is non-polar solvent. However, we observed interaction in the 4PP4MetB-ZnS-Toluene nanomaterial. The electronic structure of newly formed nanomaterials has changed. By changing the electronic structure, new nanomaterials with different optical and electronic properties can be obtained.

Observing the fact that different structure properties of nanoparticles have changed absorbance and fluorescence spectra, we can conclude that the solvent-solute interactions have been effected.

Acknowledgements

The author thanks for support given via Bitlis Eren University Research Foundation (BEBAP-2013.04). YGS; Having an idea, experimental work, interpretation of results; YEK; Conducting experiments; SH; Synthesis and characterization of nanoparticles.

References

- [1] Noël C, Navard P. Liquid crystal polymers. *Prog Poly Sci* 1991; 16: 55–110.
- [2] Lagerwall JPF, Scalia G. A new era for liquid crystal research: Applications of liquid crystals in soft matter nano-, bio- and microtechnology. *Curr App Phy* 2012; 12: 1387–1412.
- [3] Andrienko D. Introduction to liquid crystals. *J Mol Liq* 2018; 267: 520–541.
- [4] Bahadur B. Liquid Crystal Displays. *Mol Crys Liq Crys* 1984; 109: 37–41.
- [5] Smalyukh II. Liquid Crystal Colloids. *Annu Rev Condens Matter Phys* 2018; 9: 207–226.
- [6] Konshina E, Sheherbinin D, Kurochkina M. Comparison of the properties of nematic liquid crystals doped with TiO₂ and CdSe/ZnS nanoparticles. *J Mol Liq* 2018; 267: 308–314.
- [7] Ramazanov MA, Imamaliyev AR, Humbatov SA, Agamaliyev ZA. Effect of barium titanate particles on dielectric and electro-optical properties of a smectic-a liquid crystal. *Russ Phy J* 2018; 60: 1659–1666.
- [8] Teplov GV, Vorozhtsov AB, Vasil'ev SV. Micro and Nanoparticles of Metals and Metal Oxides and Physicochemical Properties of Highenergy Materials Based on Cyclic Nitroamines. *Russ Phy J* 2020; 62: 1813–1821.
- [9] Pandey KK, Tripathi PK, Misra AK, Manohar R. UV response on dielectric properties of nano nematic liquid crystal. *Results Phys*. 2008; 1119–1123.
- [10] Moussaoui M, Saoudi R, Tishchenko AV, Chassagneux, F.: Tunable optical properties of ZnS nanoparticles. *Electromagnetic and Light Scattering XII*. 2010; 178.
- [11] Yang X, Masadeh AS, McBride JR, Božin ES, Rosenthal SJ, Billinge SJL. Confirmation of disordered structure of ultrasmall CdSe nanoparticles from X-ray atomic pair distribution function analysis. *Phy Chem Chem Phys*. 2013; 15: 8480–8486.
- [12] Lakowicz JR, Gryczynski I, Gryczynski Z, Murphy CJ. Luminescence spectral properties of CdS nanoparticles. *J Phy Chem B*. 1999; 103: 7613–7620.
- [13] Mirzaei J, Urbanski M, Yu K, Kitzerow HS, Hegmann T. Nanocomposites of a nematic liquid crystal doped with magic-sized CdSe quantum dots. *J Math Chem* 2011; 21: 12710–12716.
- [14] Bobrovsky A, Mochalov K, Oleinikov V, Sukhanova A, Prudnikau A, Artemyev M, Shibaev, V, Nabiev I. Optically and electrically controlled circularly polarized emission from cholesteric liquid crystal materials doped with semiconductor quantum dots. *Adv Mater*. 2012; 24: 6216–6222.
- [15] Tauc JC. *Semiconductor Amorphous and Liquid*. 1974; 195.
- [16] Tauc J, Mentha A. States in the gap. *J Non-Crys Solids*. 1972; 8–10: 569–585.
- [17] Li Y, Ma L, Zhang X, Joly AG, Liu Z, Chen W. Synthesis and optical properties of sulfide nanoparticles prepared in dimethylsulfoxide. *J Nanosci Nanotechnol* 2008; 8: 5646–5651.

- [18] Rodríguez-mas F, Ferrer JC, Alonso JL, de Ávila SF, Valiente D. Reduced Graphene Oxide Inserted into PEDOT:PSS Layer to Enhance the Electrical Behaviour of Light-Emitting Diodes. *Nanomaterials* 2021; 11: 645.
- [19] Peng WQ, Qu SC, Cong GW, Wang ZG. Concentration effect of Mn²⁺ on the photoluminescence of ZnS:Mn nanocrystals. *J Cryst Growth* 2005; 279: 454–460.
- [20] Maleki, M., Sasani Ghamsari, M., Mirdamadi, S., Ghasemzadeh, R.: A facile route for preparation of CdS nanoparticles. *Semicond Phys Quantum Electron Optoelectron* 2007; 10 (1): 030-032.
- [21] Lihitkar NB, Singh SB, Singh J, Srivastava ON, Naik RH, Kulkarni SK. Optical investigations of interaction between zinc tetra phenyl porphyrin and CdSe nanoparticles. *Chem Phys Let* 2009; 483: 227–232.
- [22] Ashtaputre SS, Deshpande A, Marathe S, Wankhede ME, Chimanpure J, Pasricha R, Urban J, Haram SK, Gosavi SW, Kulkarni SK. Synthesis and analysis of ZnO and CdSe nanoparticles. *Pramana - J Phy.*2005; 65,:615–620.
- [23] Norris D, Bawendi M. Measurement and assignment of the size-dependent optical spectrum in CdSe quantum dots. *Phys Rev B* 1996; 53: 16338.
- [24] Biswas S, Kar S, Chaudhuri S. Synthesis and characterization of zinc sulfide nanostructures. *Synth. React. Inorg. Met.-Org. Chem Nano-Metal Chemistry.* 2006; 36: 33–36.
- [25] Tamrakar R, Ramrakhiani M, Chandra BP. Effect of Capping Agent Concentration on Photophysical Properties of Zinc Sulfide Nanocrystals. *The Open Nano J.* 2008; 2: 12–16.
- [26] Chen L, Zhang J, Luo Y, Lu S, Wang X. Effect of Zn²⁺ and Mn²⁺ introduction on the luminescent properties of colloidal ZnS:Mn²⁺ nanoparticles. *App Phy Let* 2004; 84: 112–114.
- [27] Reichardt C. *Solvents and Solvent Effects in Organic Chemistry.* New York: VCH, 2008.

R&D and Innovation Map of Turkey: Hybrid Model Approach

Muhammed ÇUBUK^{1*},

¹ Fırat Development Agency, Elazığ, Türkiye

*1 muhammedcubuk23@gmail.com

(Geliş/Received: 10/08/2023;

Kabul/Accepted: 28/08/2023)

Abstract: R&D and innovation activities are among the areas of critical importance for a country's national development and pioneering technological developments. R&D and innovation, which is an important field of study in terms of contributing to the evaluation of technical skills and regional specialization, are concepts that aim to achieve goals such as technological development, creation of new products and services, improvement of existing processes and increase in competitiveness. Accordingly, in this study, which focuses on ranking the R&D and innovation potential of provinces in Turkey, DEMATEL, ARAS and COPRAS methods, which are multi-criteria decision-making methods, were used. The weighting of the 12 criteria was done by DEMATEL method and 81 provinces were ranked by ARAS and COPRAS methods using these weight values. Maps were created according to the scores of the provinces from each method. According to the results obtained, most of the 81 provinces in Turkey showed similar results in both methods. A general evaluation was made according to these results and criteria.

Key words: R&D, innovation, DEMATEL, ARAS, COPRAS.

Türkiye Ar-Ge ve İnovasyon Haritası: Hibrit Model Yaklaşımı

Öz: Ar-Ge ve inovasyon faaliyetleri bir ülkenin ulusal kalkınması ve teknolojik gelişmelere öncülük etmesi bakımından kritik öneme sahip alanlar arasındadır. Teknik becerilerin değerlendirilmesine ve bölgesel ihtisaslaşmaya katkı sağlaması açısından önemli bir çalışma alanı olan Ar-Ge ve inovasyon, teknolojik gelişme, yeni ürünler ve hizmetlerin yaratılması, mevcut süreçlerin iyileştirilmesi ve rekabetçilik artışı gibi hedeflere ulaşmayı amaçlayan kavramlardır. Bu doğrultuda, Türkiye'de illerin Ar-Ge ve inovasyon potansiyellerini sıralamaya odaklanan çalışmada çok kriterli karar verme yöntemlerinden DEMATEL, ARAS ve COPRAS yöntemleri kullanılmıştır. Belirlenen 12 kriterin ağırlıklandırılması DEMATEL yöntemiyle yapılmış ve 81 il bu ağırlık değerleri kullanılarak ARAS ve COPRAS yöntemleriyle sıralanmıştır. İllerin her bir yöntemden aldıkları skorlara göre haritalar oluşturulmuştur. Elde edilen sonuçlara göre Türkiye'deki 81 ilin büyük çoğunluğu iki yöntemde de benzer sonuçlar göstermiştir. Bu sonuçlara ve kriterlere göre genel değerlendirme yapılmıştır.

Anahtar kelimeler: Ar-Ge, inovasyon, DEMATEL, ARAS, COPRAS.

1. Introduction

Today, the productivity levels and production structures of countries in the field of economy are of great importance in increasing the welfare levels of societies and ensuring stable economic growth. In this direction, it is seen that countries tend to obtain maximum added value with minimum resources. This situation brings about a significant orientation towards activities and expenditures in the fields of research and development (R&D) and innovation [1].

With the rapid developments in the fields of science and technology, communication has become easier and more accessible, and with globalization, a world of competition based on R&D, innovation, high quality and low price has emerged. In this process of development and change, the scale on which countries and businesses compete has spread all over the world [2]. The emergence of global competitiveness has made it imperative for countries and businesses to take action in the fields of R&D and innovation. In particular, strengthening R&D and innovation ecosystems and improving competitive capabilities in almost all sectors have been among the main policy issues of countries.

R&D and innovation, which have a direct impact on the economic growth of countries, can also affect the competitiveness of regions, the gradation of incentives applied to investments, the training of qualified human resources and regional development. The importance of R&D and innovation in Turkey's growth targets is emphasized in many policy texts. This is also clearly stated in the Eleventh Development Plan: "In order for our country to keep pace with technological transformation, enriching qualified human resources in priority sectors and fields, increasing the diffusion of technology to enterprises, improving the organization and innovation capabilities of firms, and putting effective mechanisms in place for financing research and development (R&D) and innovation stand out as priority issues in the Plan period" [3]. All Five-Year Development Plans prepared in

* Corresponding author: muhammedcubuk23@gmail.com, ORCID Number of author: ¹ ORCID 0000-0002-3655-8036

the planned period include targets for many innovation indicators such as the share of R&D expenditures in GDP, researcher labor force, and private sector R&D share. For example, the Eleventh Development Plan aims to increase the share of the private sector in R&D expenditures and the share of R&D personnel employed in the private sector to 67% [3].

Regional development activities implemented for the realization of the targets set in strategy and policy texts together with the potentials of all regions and the appropriate use of resources provide the opportunity to work in the field of R&D and innovation. Development agencies working for regional development at the scale of NUTS-2 regions also contribute to the development of important components of the technology ecosystem such as R&D, innovation, cooperation culture, resource efficiency and qualified labor force in their regions. In this direction, the development of a culture of partnership between the public sector, universities, civil society and the private sector will ensure the effective and efficient development of the technology ecosystem of regions and provinces.

In this context, this study, which focuses on proposing a new model for the decision-making processes of decision-makers at the policy level, regulatory and implementing agencies involved in the technology ecosystem at the central and local levels, compares the R&D and innovation capabilities of provinces and tries to contribute to the competitiveness of provinces in this field. First of all, the criteria to be used in comparing the R&D and innovation capabilities of 81 provinces were determined by reviewing the relevant literature. DEMATEL (The Decision Making Trial and Evaluation Laboratory) method was used to weight these criteria. With these criteria weights, the R&D and innovation capabilities of 81 provinces were compared with ARAS (Additive Ratio Assessment) and COPRAS (COmplex PROportional ASsessment) methods. Finally, maps were created according to the values of the provinces and evaluations based on the recommendations were given.

In the first part of the study, an introduction to the topic is given. In the second section, a literature review on R&D and innovation fields and the multi-criteria decision making methods used in the study are given. In the third section, the steps to be followed in the application of the methods used in the study are explained and the criteria set is given. In the fourth section, the R&D and innovation capabilities of provinces in Turkey are ranked using multi-criteria decision making methods. The last section presents the results and evaluations obtained in the study.

2. Literature Review

The literature review conducted within the scope of the study has been handled in two dimensions. Firstly, the studies conducted in Turkey and abroad in the field of R&D and innovation, which constitute the subject of the study, were examined. Secondly, previous studies have been grouped and summarized with the methods used.

2.1. R&D and Innovation

When the studies on R&D and innovation are analyzed, it is observed that a wide range of topics such as expenditures, Technology Development Zones (TDZs), economic growth, cooperation, entrepreneurship and regional development are discussed. Accordingly, some studies on R&D and innovation have been compiled.

The study by Demir and Geyik [4] focused on explaining the concept of innovation, evaluating the success of East Asian countries in the field of innovation and examining the development process of innovation in Turkey. As a result of the study, it was concluded that R&D and innovation expenditures in Turkey are not at an adequate level and the number of patent applications and acceptances, which is a reflection of this, remains at very low levels.

Baykul et al. [5] aimed to evaluate the R&D and innovative efficiency of the management companies responsible for the management and operation of Technology Development Zones (TDZs) and the R&D and innovation efficiency of 39 TDZ management companies was evaluated by data envelopment analysis method. Four inputs, namely the number of key personnel, number of firms, stakeholder university score, innovation index score of the province, and two outputs, namely R&D revenues and total number of intellectual property, were used in the efficiency measurement. As a result of the study, 13 TDZs were found efficient according to the CCR (Charnes, Cooper and Rhodes) model and 24 TDZs were found efficient according to the BCC (Banker, Charnes and Cooper) model.

In the study by Kesikoğlu and Saraç [6] titled "The Impact of R&D Expenditures on Growth: Comparative Analysis of NUTS-1 Regions", comparative regional analysis results were obtained by using R&D expenditures and growth data of 12 regions for the period 2010-2014. The study concluded that there is a positive relationship between R&D expenditures and Gross Domestic Product (GDP) in all regions. The highest level of impact is found in the Northeast Anatolia NUTS-1 region.

In the study conducted by Belgin and Avşar [7], it was aimed to measure Turkey's R&D and innovation performance at the level of regions and provinces and Gray Relational Analysis Method, one of the multi-criteria decision-making methods, was used. 29 criteria were used to evaluate the performance levels obtained in the study.

According to the ranking results, the Marmara Region ranked first among the 7 geographical regions in the country with a gray relational degree value of 0.9725, which indicates R&D and Innovation performance. It was concluded that Central Anatolia Region, which ranked 2nd in the overall ranking, scored higher than the regions following it in all sub-components after the Marmara Region.

Dağlı [8] focuses on the determination of innovation efficiency at the regional level in Turkey and the performance ranking of efficient regions. The output-oriented BCC and Super Efficiency Model of data envelopment analysis was used as the methodology. For the analysis, three input (R&D Expenditure, R&D Human Resources, Higher Education Resources) and three output (Advanced Technology Exports, Patent, Trademark) variables for regional innovation measurement were utilized. As a result of the analysis, 10 of the 26 NUTS-2 regions were found to be efficient regions in terms of regional innovation. The performance ranking of these efficient regions according to their super efficiency scores are TR10, TRC1, TR72, TR83, TR41, TR22, TR33, TR63, TRC2 and TRC3 regions.

Sánchez-Sellero and Bataineh [9] examined the link between green innovation and R&D practices inside and outside firms over time. The study concluded that internal and external R&D efforts improve green innovation activities.

Cao et al. [10] investigated the effects of implementing innovation-based development strategies on corporate R&D under political uncertainty. It is concluded that firms' implementation of innovation-based development strategies directly increases R&D investments and the resulting effects are stronger for firms with high growth potential.

2.2. Multi-Criteria Decision Making Methods

The literature on DEMATEL, ARAS, and COPRAS multi-criteria decision making methods used in the study is reviewed and summarized and presented under this heading.

In the study conducted by Çakın and Özdemir [11], the innovation performances of 12 regions in NUTS-1 of the Classification of Territorial Units for Statistics (NUTS) in Turkey in 2010, 2011 and 2012 were evaluated by taking into account basic R&D and innovation indicators. Regression analysis, DEMATEL-based Analytical Network Process (DANP) and TOPSIS methods were used in the study. The regression coefficients obtained through regression analysis were used in DEMATEL method to weight the criteria and TOPSIS method was used to rank the performance of the regions.

In the study conducted by Bulğurcu and Koçak [12], with the help of the fuzzy DEMATEL method, the internal and external risk factors faced by the companies in Adana province that carry out new product development studies in the new product development process and the success factors that affect the project success corresponding to these factors were evaluated and the importance relationship between them was examined.

In the study titled "Analysis of Value-Added Production and Macroeconomic Performance of Turkic World Countries with DEMATEL and COPRAS Methods" by Uludağ and Ümit [13], the macroeconomic and value-added production performances of Azerbaijan, Kazakhstan, Turkmenistan, Uzbekistan and Turkey in the 2008-2016 period were evaluated with DEMATEL and COPRAS methods.

In their study, Yakut and Kuru [14] evaluated the gender equality of the European Union (EU) member countries included in the Global Gender Gap Report (GGDR) prepared annually by the World Economic Forum (WEF-World Economic Forum). Using data from the 2017, 2018 and 2020 reports, a total of 14 criteria were used under 4 main headings, and the rankings of EU member states among themselves were made using Gray Relational Analysis (GRA), ARAS and COPRAS methods.

Çakır and Gök Kısa [15] focused on the internship selection problem for a logistics company with the integrated application of DEMATEL and COPRAS methods and proposed a model for personnel selection processes.

In their study, Goswami et al. [16] proposed hybrid model proposals based on the idea that the use of multi-criteria decision-making techniques alone would not be efficient. In the study, TOPSIS-ARAS and COPRAS-ARAS hybrid methods were applied to the robot selection problem and the results of the hybrid models were compared.

In the study by Özdağoğlu et al. [17], an application was made on the motorcycle selection problem. Six different multi-criteria decision making methods were used to evaluate motorcycle alternatives and the ranking results obtained from these methods were combined with the COPELAND method.

In the study introduced to the literature by Ecer [18], a hybrid model based on SECA, MARCOS, MAIRCA, COCOSO, ARAS and COPRAS methods for the selection of battery electric vehicles was focused on and the results obtained were combined using the Borda Counting Method and COPELAND method.

When the related literature is evaluated, it is seen that the application areas of multi-criteria decision making methods are wide. In recent studies, it is possible to observe that the application of traditional methods alone is

less preferred than hybrid model approaches in which more than one method is used together. It is evaluated that hybrid models created by comparing the results obtained by applying more than one method with each other and including the methods used in combining the results together with the methods tested within themselves will provide more qualified data to decision makers.

On the other hand, it is possible to see that studies in the field of R&D and innovation are handled in a similarly broad framework. In the literature, there are studies comparing provinces and regions at various levels in terms of R&D and innovation. However, it is observed that these studies are mostly addressed using a single method. It is considered that the relevant literature is not sufficient in terms of studies based on a hybrid model that will contribute to the development of competitiveness at the provincial level, to the provision of data that will enable decision-makers at the local or central level to create an efficient R&D ecosystem, and to the forward-looking actions of all stakeholders involved in the R&D/innovation ecosystem.

3. Methodology

In this study, the R&D and innovation capacities of provinces in Turkey were compared and R&D and innovation maps, which are considered to contribute to the competitiveness of provinces according to their index values, were created. Multi-criteria decision-making techniques were used in the comparison of provinces. The criteria used in the comparison of provinces were determined and the DEMATEL method based on expert opinion was used to weight these criteria. With the weight values obtained, 81 provinces were ranked according to ARAS and COPRAS methods. Information on the applications of the methods and the criteria used in the comparison is given below.

3.1. DEMATEL Method

DEMATEL (The Decision Making Trial and Evaluation Laboratory) is a criteria weighting method developed by the Battelle Memorial Institute in Geneva in 1972. The method was introduced by Fontela and Gabus [19]. The DEMATEL method is a comprehensive method that establishes and analyzes the causal relationship between complex factors in a structural model and uses not only raw data, but data obtained based on the opinions of decision makers/expert groups [20]-[21]. The application steps of the method are given below:

Step 1: In the first step of the method, a direct relationship matrix is created. In the creation of this matrix, the pairwise comparison scale consisting of 5 levels shown in Table 1 is used.

Table 1. Pairwise comparison scale

Numerical Values	Linguistic Expression
0	Ineffective
1	Low Impact
2	Medium Impact
3	High Impact
4	Very High Impact

The relationship between the criteria is determined by the expert group using a pairwise comparison scale. A direct relationship matrix is obtained as a result of the comparisons.

Step 2: In this step where the normalized direct relationship matrix is created, the normalized direct relationship matrix (M) is obtained with the smallest value (k) in the row and column using Equation 1 and Equation 2 depending on the direct relationship matrix (A).

$$M = k \times A \quad (1)$$

$$k = \frac{1}{\max_{1 \leq i \leq n} \sum_{j=1}^n a_{ij}}, i, j = 1, 2, \dots, n \quad (2)$$

Step 3: In this step, Equation 3 is used to obtain the total relationship matrix.

$$T = X \cdot (I - X)^{-1} \quad (3)$$

Step 4: In this step, the influencing and influenced criteria groups are identified. The sum of the rows of the total relationship matrix (D_i) expresses the total degree of direct influence of criterion i on the other criteria. The sum of the column sums (R_i) expresses the total degree to which criterion i is influenced by other criteria. ($D_i + R_i$) is the sum of the degrees of influence and impact of criterion i and it is called the central role degree. ($D_i - R_i$) represents the net impact of criterion i . If ($D_i - R_i$) > 0, criterion i is affecting, and if ($D_i - R_i$) < 0, criterion i is affected.

Step 5: Since considering all elements in the total relationship matrix would increase the complexity of the problem, a threshold value (α) is determined to remove the effects that are considered insignificant before drawing the relationship map [22]. The threshold value can be determined by decision makers or it can be obtained with the help of Equation 4.

$$\alpha = \frac{\sum_{i=1}^n \sum_{j=1}^n t_{ij}}{N} \quad (4)$$

If each element of the total relationship matrix is less than this threshold value, they are replaced by zero to prevent them from being taken into account. After this process, the matrix organized according to the threshold value ($T(\alpha)$) is obtained. According to this matrix, the influence diagram is drawn with ($D_i + R_i$) on the horizontal axis and ($D_i - R_i$) on the vertical axis.

Step 6: Calculation of criteria weights using ($D_i + R_i$) and ($D_i - R_i$) values is done with the help of Equation 5 and Equation 6. The w_i values are the final weight values of the criteria.

$$S_i = \sqrt{(D_i + R_i)^2 + (D_i - R_i)^2}, i = 1, 2, \dots, n \quad (5)$$

$$w_i = \frac{S_i}{\sum_{i=1}^n S_i} \quad (6)$$

3.2. ARAS Method

ARAS (Additive Ratio Assessment) method is a multi-criteria decision-making method introduced to the literature by Zavadskas and Turskis [23]. The application steps of the method are as follows [24]:

Step 1: As the first step of the method, the decision matrix is created as shown in Equation 7. In the ARAS method, a row consisting of the optimal values for each criterion is included in the initial decision matrix. Optimum values can be determined using Equation 8 and Equation 9.

$$X = \begin{bmatrix} x_{01} & x_{02} & \dots & x_{0n} \\ x_{11} & x_{12} & \dots & x_{1n} \\ \vdots & \vdots & \dots & \vdots \\ x_{m1} & x_{m2} & \dots & x_{mn} \end{bmatrix} \quad (i = 1, 2, \dots, m) \text{ ve } (j = 1, 2, \dots, n) \quad (7)$$

$$x_{0j} = \max_i x_{ij} \quad \text{utility (maximization)} \quad (8)$$

$$x_{0j} = \min_i x_{ij} \quad \text{cost (minimization)} \quad (9)$$

Step 2: The decision matrix created in the first step is normalized using Equation 10 if the criteria are benefit-oriented and using Equation 11 if they are cost-oriented.

$$\bar{x}_{ij} = \frac{x_{ij}}{\sum_{i=1}^m x_{ij}} \quad (10)$$

$$x^*_{ij} = \frac{1}{x_{ij}} ; \bar{x}_{ij} = \frac{x^*_{ij}}{\sum_{i=0}^m x^*_{ij}} \quad (11)$$

Step 3: In this step, the normalized decision matrix (\bar{X}) is multiplied by the criteria weights w_j in the step to obtain the weighted normalized decision matrix (\hat{X}).

Step 4: Using Equation 12 in the weighted normalized matrix, the optimality value S_i is calculated for each decision value.

$$S_i = \sum_{j=1}^n \hat{x}_{ij} \quad (i = 0,1,2, \dots, m) \text{ and } (j = 1,2, \dots, n) \quad (12)$$

Step 5: The optimality function values S_i of the alternatives are found by using the ratio of their utility values K_i to the best optimal value S_0 using Equation 13. The K_i values obtained for the alternatives are ranked from highest to lowest.

$$K_i = \frac{S_i}{S_0} \quad i = 0,1,2, \dots, m \quad (13)$$

3.3. COPRAS Method

COPRAS (Complex Proportional Assessment) method was developed by Zavadskas and Kaklauskas in 1996 to evaluate qualitative and quantitative factors. It is used to rank and evaluate decision options by considering the positive (benefit) and negative (cost) aspects of the criteria [24]. The application steps of this method are given below:

Step 1: In the first step of the method, the decision matrix is created as shown in Equation 14.

$$X_{ij} = \begin{bmatrix} x_{11} & x_{12} & \dots & x_{1n} \\ x_{21} & x_{22} & \dots & x_{2n} \\ \vdots & \vdots & \dots & \vdots \\ x_{m1} & x_{m2} & \dots & x_{mn} \end{bmatrix} \quad (i = 1,2, \dots, m) \text{ and } (j = 1,2, \dots, n) \quad (14)$$

Step 2: Using Equation 15, the decision matrix is normalized with w_j being the criteria weights.

$$d_{ji} = \frac{x_{ij}w_j}{\sum_{i=1}^m x_{ij}} \quad (i = 1,2, \dots, m) \text{ and } (j = 1,2, \dots, n) \quad (15)$$

Step 3: The weighted normalized indices are summed in this step. In Equation 16, the smaller the s_{-i} calculated according to the cost-side criteria and the higher the s_{+i} calculated according to the benefit-side criteria, the easier it is to achieve the objective.

$$s_{-i} = \sum_{j=1}^n d_{-ji} ; s_{+i} = \sum_{j=1}^n d_{+ji} \quad (i = 1,2, \dots, m) \text{ and } (j = 1,2, \dots, n) \quad (16)$$

Step 4: With the help of Equation 17, the value of Q_j , which indicates the relative importance of the alternatives, is calculated.

$$Q_i = s_{+i} + \frac{s_{-min} \sum_{i=1}^m s_{-i}}{s_{-i} \sum_{i=1}^m \frac{s_{-min}}{s_{-i}}} \quad (i = 1,2, \dots, m) \text{ and } (j = 1,2, \dots, n) \quad (17)$$

Step 5: The degree of utility of the alternatives is determined using Equation 18. The alternative with a utility of 100 becomes the best alternative and the other alternatives are determined according to the best.

$$N_i = \left(\frac{Q_i}{Q_{max}} \right) \times 100 \quad (18)$$

4. Application

In R&D and innovation index calculations, different indicators can be taken into account depending on the purpose or scope of the study. In this context, basic indicators such as innovation environment, innovation subject, knowledge acquisition capacity, knowledge creation capacity, R&D and innovation performance and sub-indicators within these indicators can be determined in determining R&D and innovation capacity at country, regional and/or provincial level (Belgin and Avsar, 2019).

In this study, R&D and innovation performance at the provincial level in Turkey was measured and provinces were mapped. In the performance analysis of the provinces, 12 criteria were used. These criteria values were compiled from the data of Turkish Statistical Institute (TURKSTAT), Small and Medium Enterprises Development Organization (KOSGEB), Scientific and Technological Research Council of Turkey (TÜBİTAK), Turkish Patent and Trademark Office (TURKPATENT) and Ministry of Industry and Technology.

4.1. Criteria Set

In comparing the R&D and innovation capabilities of provinces in Turkey, criteria that are considered to be important indicators in this field have been identified and explanations on each of them are given below.

Table 2. Criteria set

Abbreviation	Criteria	Year	Source	Unit
C1	Number of Design-Patent-Utility Model Applications	2022	TURKPATENT	Number
C2	KOSGEB R&D Innovation Support Amount	2010-2022	KOSGEB	1.000 TL
C3	TÜBİTAK TEYDEB Support Amount	2016-2022	TÜBİTAK	1.000 TL
C4	TÜBİTAK ARDEB Support Amount	2016-2022	TÜBİTAK	1.000 TL
C5	Number of Academic Staff	2022	TURKSTAT	Person
C6	Number of Doctoral Degree Graduates	2022	TURKSTAT	Person
C7	Number of Graduates with Master's Degree	2022	TURKSTAT	Person
C8	Total Number of Technology Development Zones, R&D and Design Centers	2022	Ministry of Industry and Technology	Person
C9	Number of Personnel Employed in R&D and Design Centers	2022	Ministry of Industry and Technology	Person
C10	Socio-Economic Development Index Ranking (SEGE)	2019	Ministry of Industry and Technology	Rank
C11	URAK Interprovincial Competitiveness Index Ranking	2018	URAK	Rank
C12	Brand Skills and Innovation Ranking	2019	FORBES	Rank

Number of Design, Patent, Utility Model Applications (C1): It shows the total number of design, patent and utility model applications for 2022 announced by the Turkish Patent and Trademark Office (TURKPATENT). In the study, the maximum direction (the biggest is the best) is considered.

KOSGEB R&D Innovation Support Amount (C2): It shows the total amount of support in TL given to provinces within the scope of the R&D Innovation Support Program implemented by the Small and Medium Enterprises Development Organization (KOSGEB) between 2010-2022. In the study, the maximum direction (the biggest is the best) is considered.

TÜBİTAK TEYDEB Support Amount (C3): It shows the total amount of support by province for the projects completed between 2016 and 2022 within the scope of 1501-TÜBİTAK Industrial R&D Projects Support Program, 1505-University-Industry Cooperation Support Program, 1507-TÜBİTAK SME R&D Start-up Support Program and 1511-TÜBİTAK Priority Areas Research Technology Development and Innovation Support Program

implemented by the Directorate of Technology and Innovation Support Programs (TEYDEB) within the Scientific and Technological Research Council of Turkey (TÜBİTAK). In the study, the maximum direction (the biggest is the best) is considered.

TÜBİTAK ARDEB Support Amount (C4): It shows the total amount of support given to the projects supported within the scope of ARDEB programs between 2016-2022 within the scope of different support programs carried out by TÜBİTAK Research Support Programs Directorate (ARDEB). In the study, the maximum direction (the largest is the best) was considered.

Number of Academic Staff (C5): In the higher education statistics announced by the Turkish Statistical Institute (TurkStat), it shows the total number of academic staff in all titles working in their own units in higher education institutions. In the study, the maximum direction (the largest is the best) is considered.

Number of Doctoral Degree Graduates (C6): It shows the total number of graduates with doctoral degrees in the province obtained from TurkStat. In the study, the maximum direction (the largest is the best) is considered.

Number of Graduates with Master's Degree (C7): It shows the total number of graduates with master's degree in the province taken from TurkStat. In the study, the maximum direction (the largest is the best) is considered.

Total Number of Technology Development Zones (TDZ), R&D and Design Centers (C8): It refers to the total number of TDZs (including those in the establishment phase), R&D centers and design centers in the province in 2022, taken from the statistics of the Ministry of Industry and Technology (MoIT). In the study, the maximum direction (the largest is the best) is considered.

Number of Personnel Employed in R&D and Design Centers (C9): It refers to the total number of personnel employed in R&D centers and design centers in the province for the year 2022 taken from the data of the General Directorate of R&D Incentives of the Ministry of Industry and Technology. In the study, the maximum direction (the biggest is the best) is considered.

SEGE Ranking (C10): This criterion, which was created using the 2017 Socio-Economic Development Index (SEGE) ranking published by the Ministry of Industry and Technology in 2019, is considered as minimum directional (the lowest is the best) in the study.

URAK Interprovincial Competitiveness Index Ranking (C11): This criterion, which was developed by the International Competitiveness Research Council in 2018 by using 85 different criteria, was included in the study as it is an important indicator on a national scale and was evaluated as minimum directional (the lowest is the best).

Brand Skills and Innovation Ranking (C12): This criterion, which was created using the ranking results of the provinces included in the 2019 FORBES survey, was evaluated as minimum directional (lowest is best) in the study.

4.2. Calculation of Criteria Weights with DEMATEL Method

In this part of the study, the criteria in Table 2 were weighted with the DEMATEL method to be used in ranking the R&D and innovation skills of the provinces according to the determined set of criteria. With the help of the pairwise comparison scale in Table 1, the opinions of an expert team consisting of ten people working in R&D, design centers and Technology Development Zones were taken. The direct relationship matrix in Table 3 was obtained by averaging these expert opinions.

Table 3. Direct relationship matrix

Criteria	C1	C2	C3	C4	C5	C6	C7	C8	C9	C10	C11	C12
C1		2,6	2,7	3	1	1	1,2	1,9	2,1	2,4	2,4	2,7
C2	3		1,9	2	0,8	1	1,1	2	2,4	2,4	2,1	2,3
C3	3	0,9		1,2	1,1	1,3	1,3	1,7	2	2,2	2	2,3
C4	2,9	0,9	1,1		1,2	1,5	1,5	1,3	1,7	2,2	2,1	2,3
C5	2,6	1,5	1,6	1,8		2,4	2,3	1,4	1,4	2	1,8	1,9
C6	2,3	1,7	1,8	1,9	2,1		2,2	1,3	1,7	2,3	2,2	2,3
C7	2	1,5	1,5	1,7	1,7	2,1		1,1	1,7	2,1	2,1	2,1
C8	3	2,5	2,5	2,3	1,4	1,5	1,5		3,4	2,4	2,7	2,9
C9	2,8	2,3	2,2	2	1,1	1,4	1,4	1,5		2,3	2,5	2,8
C10	2,8	2,1	2,1	2,3	2,2	2,3	2	2,5	2,5		2,9	3,1
C11	2,8	2,1	2,2	2,4	2,3	2,3	2,1	2,2	2,4	2,7		2,9
C12	2,8	2,2	2,2	2,4	2,1	2,2	2,2	2,7	2,7	3,1	3,1	

To calculate the normalized direct relationship matrix, Equation 1 and Equation 2 were applied to the direct relationship matrix in Table 3. The normalized direct relationship matrix obtained in this way is given in Table 4.

Table 4. Normalized direct relationship matrix

Criteria	C1	C2	C3	C4	C5	C6	C7	C8	C9	C10	C11	C12
C1		0,094	0,097	0,108	0,036	0,036	0,043	0,069	0,076	0,087	0,087	0,097
C2	0,108		0,069	0,072	0,029	0,036	0,040	0,072	0,087	0,087	0,076	0,083
C3	0,108	0,032		0,043	0,040	0,047	0,047	0,061	0,072	0,079	0,072	0,083
C4	0,105	0,032	0,040		0,043	0,054	0,054	0,047	0,061	0,079	0,076	0,083
C5	0,094	0,054	0,058	0,065		0,087	0,083	0,051	0,051	0,072	0,065	0,069
C6	0,083	0,061	0,065	0,069	0,076		0,079	0,047	0,061	0,083	0,079	0,083
C7	0,072	0,054	0,054	0,061	0,061	0,076		0,040	0,061	0,076	0,076	0,076
C8	0,108	0,090	0,090	0,083	0,051	0,054	0,054		0,123	0,087	0,097	0,105
C9	0,101	0,083	0,079	0,072	0,040	0,051	0,051	0,054		0,083	0,090	0,101
C10	0,101	0,076	0,076	0,083	0,079	0,083	0,072	0,090	0,090		0,105	0,112
C11	0,101	0,076	0,079	0,087	0,083	0,083	0,076	0,079	0,087	0,097		0,105
C12	0,101	0,079	0,079	0,087	0,076	0,079	0,079	0,097	0,097	0,112	0,112	

In the next step, the total relationship matrix was calculated using Equation 3 and is given in Table 5.

Table 5. Total relationship matrix

Criteria	C1	C2	C3	C4	C5	C6	C7	C8	C9	C10	C11	C12
C1	0,443	0,397	0,422	0,449	0,294	0,320	0,324	0,370	0,434	0,471	0,469	0,502
C2	0,509	0,291	0,374	0,394	0,269	0,299	0,300	0,351	0,417	0,443	0,433	0,460
C3	0,473	0,299	0,284	0,341	0,259	0,287	0,285	0,317	0,375	0,405	0,398	0,427
C4	0,463	0,294	0,317	0,294	0,259	0,290	0,288	0,299	0,359	0,400	0,396	0,421
C5	0,481	0,332	0,353	0,376	0,234	0,338	0,332	0,320	0,372	0,418	0,410	0,434
C6	0,494	0,353	0,376	0,397	0,318	0,272	0,343	0,333	0,400	0,447	0,442	0,467
C7	0,446	0,320	0,337	0,360	0,283	0,318	0,245	0,300	0,368	0,406	0,405	0,424
C8	0,598	0,437	0,460	0,474	0,341	0,373	0,370	0,344	0,521	0,522	0,529	0,562
C9	0,524	0,382	0,400	0,411	0,292	0,327	0,324	0,350	0,355	0,459	0,464	0,496
C10	0,603	0,432	0,456	0,483	0,375	0,408	0,395	0,435	0,502	0,452	0,546	0,578
C11	0,593	0,425	0,451	0,479	0,372	0,402	0,393	0,419	0,491	0,533	0,442	0,563
C12	0,618	0,446	0,470	0,498	0,381	0,415	0,411	0,452	0,521	0,567	0,565	0,492

By obtaining the total relationship matrix, affecting and affected criteria groups were identified. The affecting and affected criteria are given in Table 6. The threshold value was determined as 0.272 by averaging the total relationship matrix.

Table 6. $D_i + R_i$ and $D_i - R_i$ values

Criteria	D_i	R_i	$D_i + R_i$	$D_i - R_i$	Impact Group
C1	3,284	4,196	7,480	-0,911	Affected
C2	3,043	2,953	5,996	0,090	Affecting
C3	2,780	3,150	5,931	-0,370	Affected
C4	2,732	3,323	6,055	-0,590	Affected
C5	2,953	2,465	5,418	0,489	Affecting
C6	3,113	2,717	5,831	0,396	Affecting
C7	2,823	2,690	5,513	0,134	Affecting
C8	3,711	2,873	6,584	0,838	Affecting
C9	3,209	3,431	6,640	-0,223	Affected
C10	3,803	3,707	7,510	0,096	Affecting
C11	3,735	3,691	7,426	0,044	Affecting
C12	3,919	3,911	7,830	0,008	Affecting

The Influence Diagram in Figure 1 and the Relationship Diagram in Figure 2 showing the relationship between the criteria were created. The D+R and D-R values in Table 6 are shown in Figure 1 as x-axis and y-axis on the coordinate plane. The criteria above the x-axis (C2, C5, C6, C7, C8, C10, C11, C12) were found to be influencing criteria, while the criteria below the x-axis (C1, C3, C4, C9) were found to be influenced criteria. The relationship between the criteria is visualized in Figure 2.

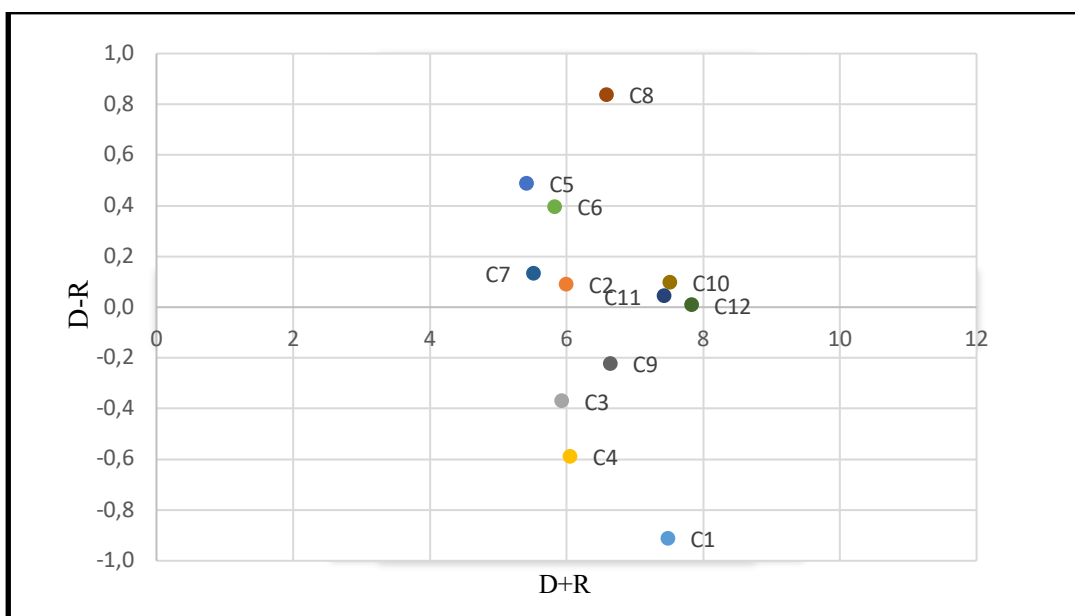


Figure 1. Impact diagram

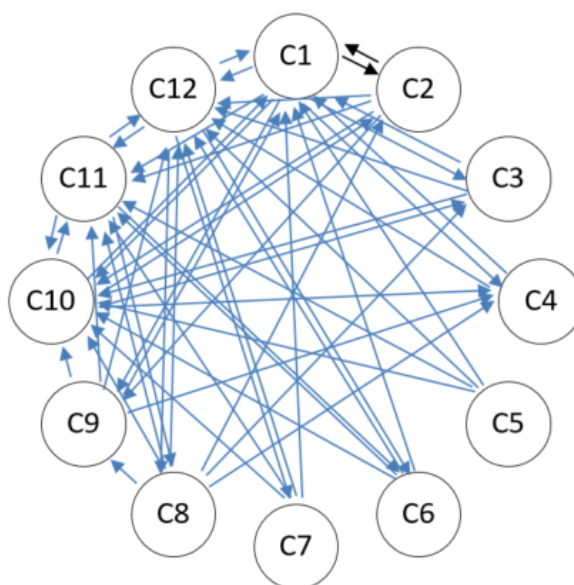


Figure 2. Relationship diagram

In the last step of the DEMATEL method, criteria weights were calculated with the help of Equation 5 and Equation 6 and given in Table 7.

Table 7. Criteria weights

Criteria	w_i	Criteria	w_i	Criteria	w_i	Criteria	w_i
C1	0,096	C4	0,078	C7	0,070	C10	0,096
C2	0,076	C5	0,069	C8	0,085	C11	0,095
C3	0,076	C6	0,075	C9	0,085	C12	0,100

4.3. Calculation of R&D and Innovation Performance of Provinces

Using the criterion weights obtained by DEMATEL method, the R&D and innovation skills of 81 provinces were ranked by ARAS and COPRAS methods. R&D and innovation maps were created according to the results obtained from these methods.

Using the criteria values of 81 provinces and the weights obtained by the DEMATEL method, the process steps of the ARAS method were first applied and the performance ranking of the provinces was made. The performance ranking results obtained are given in Table 8.

Table 8. ARAS method performance ranking

Rank	Province	Score	Rank	Province	Score	Rank	Province	Score
1	İstanbul	0,4431	28	Kahramanmaraş	0,0100	55	Aksaray	0,0044
2	Ankara	0,2678	29	Kütahya	0,0096	56	Nevşehir	0,0042
3	İzmir	0,1044	30	Çanakkale	0,0093	57	Adıyaman	0,0040
4	Kocaeli	0,0904	31	Hatay	0,0090	58	Erzincan	0,0040
5	Bursa	0,0834	32	Edirne	0,0089	59	Yozgat	0,0040
6	Konya	0,0439	33	Düzce	0,0085	60	Osmaniye	0,0040
7	Kayseri	0,0369	34	Elazığ	0,0084	61	Kastamonu	0,0039
8	Eskişehir	0,0359	35	Karabük	0,0081	62	Çankırı	0,0037
9	Antalya	0,0338	36	Şanlıurfa	0,0081	63	Mardin	0,0035
10	Manisa	0,0249	37	Diyarbakır	0,0076	64	Sinop	0,0035
11	Gaziantep	0,0247	38	Zonguldak	0,0073	65	Bartın	0,0030
12	Tekirdağ	0,0244	39	Kırklareli	0,0072	66	Kars	0,0030
13	Sakarya	0,0241	40	Rize	0,0066	67	Artvin	0,0029
14	Adana	0,0214	41	Van	0,0063	68	Tunceli	0,0028
15	Denizli	0,0211	42	Afyonkarahisar	0,0060	69	Batman	0,0028
16	Mersin	0,0202	43	Bilecik	0,0060	70	Gümüşhane	0,0026
17	Trabzon	0,0160	44	Tokat	0,0055	71	Bingöl	0,0026
18	Samsun	0,0159	45	Uşak	0,0055	72	Siirt	0,0025
19	Isparta	0,0141	46	Giresun	0,0054	73	Kilis	0,0024
20	Balıkesir	0,0128	47	Çorum	0,0053	74	Muş	0,0024
21	Muğla	0,0126	48	Burdur	0,0050	75	Şırnak	0,0023
22	Aydın	0,0124	49	Kırıkkale	0,0050	76	Bitlis	0,0023
23	Bolu	0,0108	50	Karaman	0,0049	77	Ağrı	0,0023
24	Yalova	0,0106	51	Niğde	0,0048	78	Iğdır	0,0022
25	Malatya	0,0106	52	Kırşehir	0,0047	79	Bayburt	0,0022
26	Erzurum	0,0104	53	Amasya	0,0046	80	Ardahan	0,0020
27	Sivas	0,0101	54	Ordu	0,0046	81	Hakkâri	0,0019

According to the performance ranking based on the ARAS method, İstanbul ranked first among 81 provinces. Ankara ranked 2nd, İzmir 3rd, Kocaeli 4th and Bursa 5th. Ağrı, Iğdır, Bayburt, Ardahan and Hakkâri were ranked last. The map created according to the scores obtained with the ARAS method is given in Figure 3.

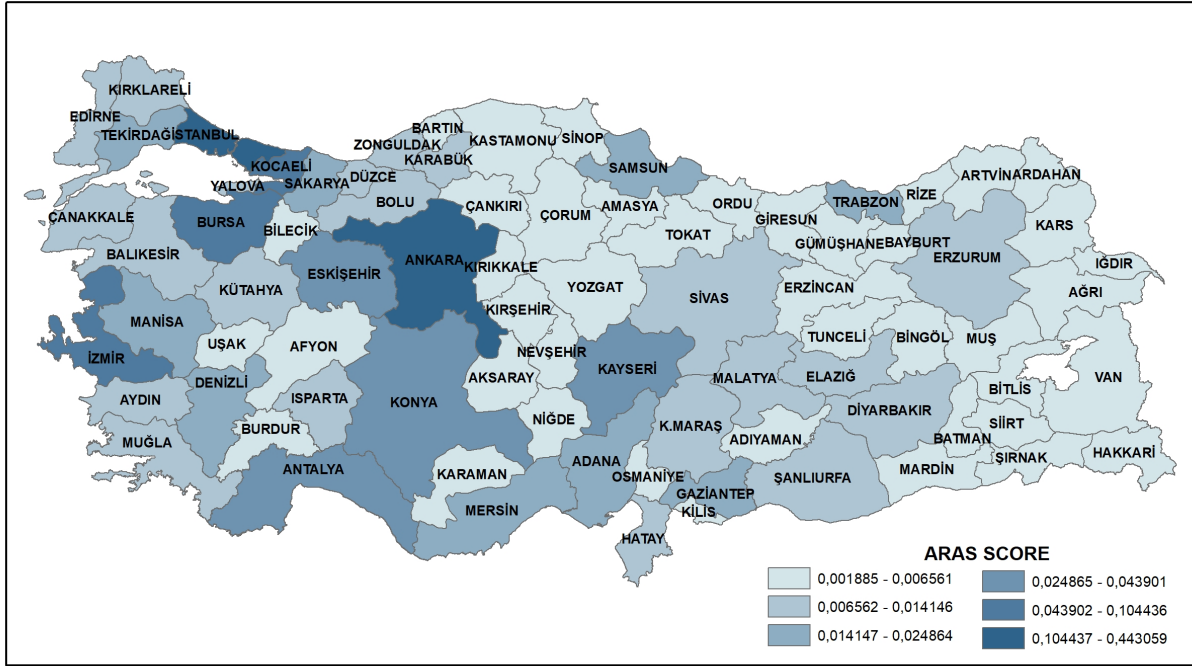


Figure 3. Performance map of provinces according to ARAS results

Similar to the ARAS method, the R&D and innovation performances of 81 provinces were ranked by the COPRAS method using the criteria values of 81 provinces and the criteria weights obtained by the DEMATEL method. The scores and rankings of the provinces from the COPRAS method are shown in Table 9.

The results of the COPRAS method are largely similar to the results of the ARAS method. According to the COPRAS ranking, Istanbul ranked 1st, Ankara 2nd, Izmir 3rd, Kocaeli 4th and Bursa 5th. Şırnak, Iğdır, Bayburt, Ardahan and Hakkâri were ranked last. The R&D innovation map created according to the results of the COPRAS method is shown in Figure 4.

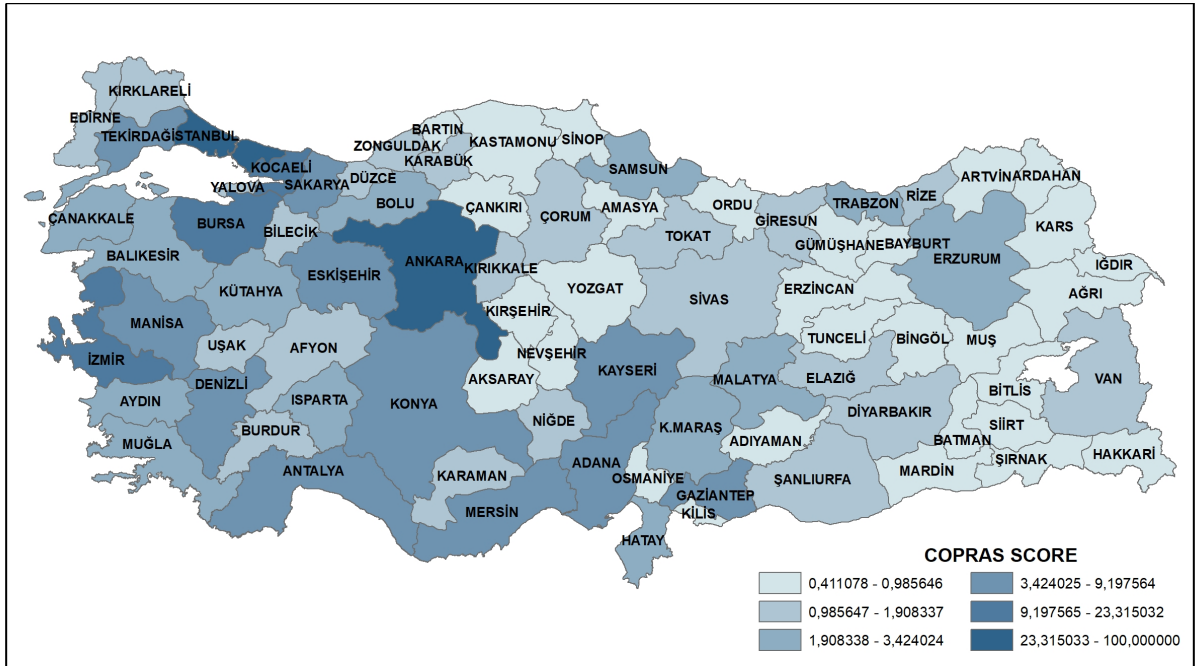


Figure 4. Performance map of provinces according to COPRAS Results

Table 9. COPRAS method performance ranking

Rank	Province	Score	Rank	Province	Score	Rank	Province	Score
1	İstanbul	100,000	28	Çanakkale	2,016	55	Kırşehir	0,912
2	Ankara	60,874	29	Hatay	1,975	56	Nevşehir	0,892
3	İzmir	23,315	30	Sivas	1,908	57	Adıyaman	0,878
4	Kocaeli	20,529	31	Düzce	1,879	58	Osmaniye	0,872
5	Bursa	18,690	32	Elazığ	1,812	59	Yozgat	0,858
6	Konya	9,198	33	Karabük	1,730	60	Erzincan	0,845
7	Kayseri	7,886	34	Yalova	1,710	61	Kastamonu	0,837
8	Eskişehir	7,391	35	Edirne	1,708	62	Çankırı	0,813
9	Antalya	7,241	36	Şanlıurfa	1,661	63	Mardin	0,765
10	Manisa	5,264	37	Diyarbakır	1,641	64	Sinop	0,746
11	Tekirdağ	5,229	38	Zonguldak	1,600	65	Bartın	0,646
12	Gaziantep	5,154	39	Kırklareli	1,444	66	Kars	0,643
13	Sakarya	5,067	40	Rize	1,393	67	Artvin	0,615
14	Adana	4,690	41	Van	1,344	68	Batman	0,610
15	Denizli	4,642	42	Afyonkarahisar	1,288	69	Tunceli	0,567
16	Mersin	4,413	43	Bilecik	1,243	70	Gümüşhane	0,562
17	Samsun	3,424	44	Tokat	1,197	71	Bingöl	0,557
18	Trabzon	3,287	45	Uşak	1,154	72	Siirt	0,541
19	Isparta	2,922	46	Çorum	1,150	73	Kilis	0,531
20	Balıkesir	2,774	47	Giresun	1,090	74	Muş	0,525
21	Aydın	2,668	48	Kırkkale	1,072	75	Bitlis	0,510
22	Bolu	2,305	49	Burdur	1,068	76	Ağrı	0,507
23	Muğla	2,243	50	Niğde	1,063	77	Şırnak	0,507
24	Erzurum	2,171	51	Karaman	1,063	78	Iğdır	0,487
25	Kahramanmaraş	2,155	52	Amasya	0,986	79	Bayburt	0,474
26	Kütahya	2,126	53	Ordu	0,976	80	Ardahan	0,433
27	Malatya	2,053	54	Aksaray	0,970	81	Hakkâri	0,411

4. Results and Discussion

Since high and sustainable productivity growth driven by R&D and innovation is the main factor determining competitiveness, the ability to create and disseminate new ideas and transform them into new and profitable products, processes and services, and hence the development of infrastructure for R&D and innovation, is fundamental to increasing the value added generated. Since technological innovations cause changes in the competition structure, in products and processes as well as in markets, competition for scientific and technological competence has emerged among countries. Therefore, Technology Development Zones and R&D Centers have been established in many countries in order to rapidly put new knowledge into the service of technology by strengthening the cooperation between universities, the public sector and the business world. These centers contribute significantly to the development of countries through their functions such as increasing the productivity and competitiveness of enterprises in the region through R&D-oriented activities, providing high technology and innovation infrastructure, transferring technology, diversifying the economic activities of the region, and providing new job opportunities [7].

In order to achieve rapid progress in the field of R&D and innovation and to ensure a balanced development process in Turkey, not only macroeconomic policies and projections but also projections affecting the geographical spread of development are needed.

Within the scope of this study, DEMATEL, ARAS and COPRAS methods, which are multi-criteria decision-making techniques, were used to reveal Turkey's R&D and innovation potential and to make performance comparisons at provincial level. The model proposed for provinces to create an R&D and innovation performance index is based on the performance components Number of Design-Patent-Utility Model Applications, KOSGEB R&D Innovation Support Amount, TÜBİTAK TEYDEB Support Amount, TÜBİTAK ARDEB Support Amount, Number of Academic Staff, Number of Doctoral Degree Graduates, Number of Graduates with Master's Degree, Total Number of Technology Development Zones, R&D and Design Centers, Number of Personnel Employed in R&D and Design Centers, Socio-Economic Development Index Ranking (SEGE), URAK Interprovincial Competitiveness Index Ranking and Brand Skills and Innovation Ranking. According to the criteria weighting made with the DEMATEL method, the criterion with the highest importance was determined as Brand Skills and Innovation Ranking with 10%. The weights of the other criteria were found to be close to each other.

According to the 81 provincial R&D and innovation performance ranking results, Istanbul ranked first in both ARAS and COPRAS methods. Istanbul is followed by Ankara and Izmir, respectively. In addition to Istanbul, Ankara and Izmir, Kocaeli, Bursa, Konya, Kayseri and Eskişehir also have high performance.

In general, there are no major differences between the other provinces. The provinces of Ağrı, Iğdır, Bayburt and Hakkâri ranked last in both methods. When the distribution of R&D and innovation performance of provinces according to ARAS and COPRAS methods is analyzed, it is found that the provinces ranking first in the performance rankings are similar, and in general, the majority of provinces perform close to each other. It can also be said that provinces such as Manisa, Antalya, Gaziantep and Tekirdağ are developing in terms of R&D and innovation and follow the provinces in the first rankings.

References

- [1] Erkiletlioğlu H. Dünyada ve Türkiye’de Ar-Ge Faaliyetleri. İstanbul: İş Bankası İktisadi Araştırmalar Bölümü, 2013.
- [2] Soylu A. AB 2020 ve Vizyon 2023 stratejilerinde inovasyon hedeflerinin karşılaştırılması. Süleyman Demirel Üniversitesi Sosyal Bilimler Enstitüsü Dergisi. 2011; 14: 105-122.
- [3] T.C. Cumhurbaşkanlığı Strateji ve Bütçe Başkanlığı. On Birinci Kalkınma Planı (2019-2023).
- [4] Demir M, Geyik O. Türkiye’de ar-ge & inovasyon harcamalarının gelişim süreci ve ekonomik etkileri. Journal of Life Economics. 2014; 1(2): 171-190.
- [5] Baykul A, Oruç KO, Dulupçu MA. Teknoloji geliştirme bölgesi yönetici şirketlerinin ar-ge ve yenilikçi etkinliklerinin Veri Zarflama Analizi ile değerlendirilmesi. Bolu Abant İzzet Baysal Üniversitesi Sosyal Bilimler Enstitüsü Dergisi. 2016; 16(2): 51-72.
- [6] Kesikoğlu F, Saraç Ş. Ar-ge harcamalarının büyüme üzerindeki etkisi: İBBS düzey-1 bölgelerinin karşılaştırmalı analizi. Uluslararası Yönetim İktisat ve İşletme Dergisi. 2017; 13(13): 617-626.
- [7] Belgin Ö, Avşar BA. Türkiye’de bölgeler ve iller düzeyinde ar-ge ve yenilik performansının Gri İlişkisel Analiz yöntemi ile ölçülmesi. Verimlilik Dergisi. 2019; (2): 27-48.
- [8] Dağlı I. Türkiye’de bölgesel inovasyon etkinliğinin değerlendirilmesi: düzey-2 bölgelerine yönelik ampirik bir analiz. Erciyes Üniversitesi İktisadi ve İdari Bilimler Fakültesi Dergisi. 2022; (61): 329-352.
- [9] Sánchez-Sellero P, Bataineh MJ. How R&D cooperation, R&D expenditures, public funds and R&D intensity affect green innovation?. Technology Analysis & Strategic Management, 2022; 34(9): 1095-1108.
- [10] Cao Y, Chen Y, Zhang Y. Political uncertainty, innovation-driven strategy, and corporate R&D. Research in International Business and Finance (RIBAF). 2022; 60: 101612.
- [11] Çakın E, Özdemir A. Bölgesel gelişmişlikte ar-ge ve inovasyonun rolü: DEMATEL tabanlı Analitik Ağ Süreci (DANP) ve TOPSIS yöntemleri ile bölgelerarası bir analiz. Dokuz Eylül Üniversitesi İktisadi İdari Bilimler Fakültesi Dergisi. 2015; 30(1): 115-144.
- [12] Bulğurcu B, Koçak FS. Yeni ürün geliştirme projelerinde risk ve başarı faktörlerinin bulanık DEMATEL tekniği ile değerlendirilmesi. İşletme Araştırmaları Dergisi. 2020; 12(1): 732-748.
- [13] Uludağ AS, Ümit AÖ. Türk Dünyası ülkelerinin katma değerli üretim ve makroekonomik performanslarının DEMATEL ve COPRAS yöntemleriyle analizi. Sosyoekonomi. 2020; 28(45): 139-164.
- [14] Yakut E, Kuru Ö. AB ülkelerinin küresel cinsiyet ayrımının kadınlar açısından Gri İlişkisel Analiz, ARAS ve COPRAS yöntemleri ile değerlendirilmesi. OPUS International Journal of Society Researches. 2020; 16(30): 2832-2862.
- [15] Çakır E, Gök Kısa AC. Bütünleşik DEMATEL–COPRAS yöntemi ile stajyer seçimi: bir lojistik firmasında uygulama. Dumlupınar Üniversitesi Sosyal Bilimler Dergisi. 2020; 65: 107-124.
- [16] Goswami SS, Behera DK, Afzal A, Razak Kaladgi A, Khan SA, Rajendran P, Asif M. Analysis of a robot selection problem using two newly developed hybrid MCDM models of TOPSIS-ARAS and COPRAS-ARAS. Symmetry. 2021; 13(8): 1331.
- [17] Özdağoğlu A, Keleş MK, Altınata A, Ulutaş A. Combining different MCDM methods with the COPELAND method: an investigation on motorcycle selection. Journal of process management and new Technologies. 2021; 9(3-4): 13-27.
- [18] Ecer F. A consolidated MCDM framework for performance assessment of battery electric vehicles based on ranking strategies. Renewable Sustainable Energy Rev. 2021; 143, 110916.
- [19] Fontela E, Gabus A. The DEMATEL observer: Battelle Institute, Geneva Research Center, 1976; 56-61.

- [20] Wu WW, Lee YT. Developing global managers' competencies using the fuzzy DEMATEL method. *Expert Syst. Appl.* 2007; 32(2): 499-507.
- [21] Haste H. DEMATEL Yöntemi, Çok Kriterli Karar Verme Problemlerinde Kriter Ağırlıklandırma Yöntemleri, Editör: Bircan H. Ankara: Nobel Akademik Yayıncılık, 2020; 77-96.
- [22] Kashi K. DEMATEL method in practice: finding the causal relations among key competencies. *The 9th international days of statistics and economics*; 2015; Prague. 723-732.
- [23] Zavadskas EK, Turskis Z. A new additive ratio assessment (ARAS) method in multicriteria decision-making. *Technological and Economic Development of Economy.* 2010; 16(2): 159-172.
- [24] Özbek A. Çok Kriterli Karar Verme Yöntemleri. Ankara: Seçkin Akademik ve Mesleki Yayınları, 2021.

Development of a Nanocomposite-Based Electrochemical Sensing of Arsenic in Aqueous Solution

Omer Sadak^{1*}

¹ Department of Electrical and Electronics Engineering, Ardahan University, Ardahan, Türkiye
^{*1} omersadak@ardahan.edu.tr

(Geliş/Received: 11/08/2023;

Kabul/Accepted: 31/08/2023)

Abstract: Contamination of drinking water with heavy metals is a serious threat to the global environment and public health. Currently, approximately 20 countries have been reported for arsenic levels present in drinking water that are higher than the EPA guidelines. Arsenic is highly toxic, widely dispersed and found in the earth's crust. It can be found in inorganic as well as organic compounds in water. Arsenic is released into the environment in a variety of ways, including industrial effluents, pesticides, wood preservative chemicals, combustion of petroleum and coal, and mining operations. Currently, Arsenic is determined using a wide variety of methods that include inductively coupled plasma mass spectrometry (ICPMS), high-performance liquid chromatography (HPLC) with ICPMS and graphite furnace atomic absorption spectrometry (GFAAS). Nevertheless, these methods are slow, expensive and require skilled people to operate. Alternatively, electrochemical sensors have been potentially recognized as a powerful analytical method for the detection of heavy metals at very low concentrations. It also allows on-site and continuous monitoring of heavy metals. A nanocomposite consisting of gold nanoparticles and conducting polymers (polydiallyldimethylammonium chloride (PDDA) and polystyrene sulfonate (PSS)) functionalized graphene was used in this study to detect arsenic, which causes major environmental and health concerns.

Key words: Electrochemical Sensors, Arsenic, Heavy metals.

Sulu Çözüldüde Arseniğin Nanokompozit Tabanlı Elektrokimyasal Algılanmasının Geliştirilmesi

Öz: İçme sularının ağır metallerle kirlenmesi, küresel çevre ve halk sağlığı için ciddi tehdit oluşturmaktadır. Şu anda yaklaşık 20 ülkede içme suyunda bulunan ve EPA yönergelerinden daha yüksek arsenik seviyeleri rapor edilmiştir. Arsenik oldukça zehirlidir, geniş çapta dağılmıştır ve yer kabuğunda bulunur. Suda hem organik hem de inorganik formda bulunur. Arseniğin çevreye salınım kaynakları, endüstriyel atıklar, pestisitler, odun koruyucu maddeler, fosil yakıtların yanması ve madencilik faaliyetleri yoluyla farklı şekillerde ortaya çıkmaktadır. Şu anda Arsenik, endüktif olarak eşleşmiş plazma kütle spektrometrisi (ICPMS), grafit fırınlı atomik absorpsiyon spektrometrisi (GFAAS) ve ICPMS'li yüksek performanslı sıvı kromatografisi (HPLC) dahil olmak üzere çok çeşitli yöntemler kullanılarak belirlenmektedir. Bununla birlikte, bu yöntemler yavaş, pahalıdır ve çalışması için yetenekli insanlar gerektirir. Alternatif olarak, elektrokimyasal sensörler, çok düşük konsantrasyonlarda ağır metallerin tespiti için potansiyel olarak güçlü bir analitik teknik olarak kabul edilmiştir. Ayrıca ağır metallerin yerinde ve sürekli olarak izlenmesine olanak tanır. Bu çalışmada, ciddi çevre ve sağlık sorunlarına neden olan Arsenik'in tespiti için altın nanopartikül ve iletken polimerlerden (polidialildimetilamonyum klorür (PDDA) ve polistiren sülfonat (PSS)) işlevselleştirilmiş grafenden yapılmış bir nanokompozit kullanılmıştır.

Anahtar kelimeler: Elektrokimyasal Sensörler, Arsenik, Ağır metaller.

1. Introduction

Arsenic (As) contamination in drinking water is a worldwide problem. It is poisonous and the long-term exposure may cause serious toxicity and may lead to death [1]–[4]. As pollution in the environment takes place in a number of ways, including industrial effluents, wood preservative compounds, pesticides, burning of petroleum-based products, and mining operations. [5],[6]. Furthermore, the impacts of arsenic poisoning extend beyond human health to the ecosystem, affecting aquatic life and soil quality. Therefore, detection of As is crucial and currently, As³⁺ is determined using a wide variety of methods that include ICPMS, HPLC with ICPMS and GFAAS. However, these instruments are bulky, costly to run and maintain, and in addition, they require well-equipped laboratories and hence are only available for in-field detection of heavy metals [5],[7]–[9].

In contrast, electrochemical method has been potentially recognized as a powerful analytical technique for the detection of heavy metals at their lowest concentration in environmental samples due to its remarkable sensitivity [10]–[12]. There are a variety of electrochemical methods that can be employed for the detection of heavy metals. Among them, differential pulse anodic stripping voltammetry (DPASV) is commonly utilized for the detection of As. It is very robust, sensitive, productive, less expensive and portable for on-site analysis [13],[14]. This DPASV technique for the measurement of As³⁺ consists of electrochemical deposition of arsenic

* Corresponding author: omersadak@ardahan.edu.tr. ORCID Number of authors: ¹ 0000-0001-6717-9672

on an electrode surface for a few seconds, followed by reverse potential scan oxidation of the metal back into solution. As a function of scan potential, the oxidation current, also known as stripping current, is recorded. [15]–[17]. The analytical signal is the resulting from peak-shaped (bell-shaped) voltammogram. DPASV is a two-fold process which first does the deposition of dropped arsenic concentration solution on the working surface before it is stripped [18],[19]. Optimizing DPASV for arsenic detection using a handheld device will reduce cost, allow on-site water analysis, and help initiate a rapid containment response in cases of highly contaminated water sources.

This study focuses on the utilization of a screen-printed carbon electrode (SPE) as the foundation for developing an electrochemical sensor. The working electrode surface of the SPE was modified through a stepwise process involving the incorporation of partially oxidized graphene (po-Gr), followed by the layered assembly of gold nanoparticles (AuNPs), polydiallyldimethylammonium chloride (PDDA), and polystyrene sulfonate (PSS). This tailored modification strategy aimed to enhance the sensor's performance and sensitivity in detecting arsenic ions As^{3+} . Remarkably, the fabricated electrochemical sensor exhibited a linear response in relation to As^{3+} concentration within the detection range of up to 1200 nM. This wide linear range indicates the sensor's capacity to accurately detect and quantify varying levels of As^{3+} ions, showcasing its potential applicability for monitoring arsenic contamination in drinking water sources. The successful integration of graphene, AuNPs, and the polymeric layers onto the SPE platform holds promise for advancing the field of electrochemical sensing, particularly in the context of heavy metal detection and environmental monitoring. The combination of the tailored electrode modification approach and the inherent electrochemical properties of the SPE contributes to the sensor's enhanced sensitivity, selectivity, and reliability, further emphasizing its potential as a cost-effective and efficient solution for the detection of heavy metal contaminants in water samples.

2. Materials and Methods

2.1. Reagents

CH Instruments, Inc. (Bee Cave, TX, USA) supplied the screen printed carbon electrodes (SPE) (TE100). Sigma Aldrich supplied the graphite flakes (150 m). ACROS Organics provided the hydrogen tetrachloroaurate (III) trihydrate ($\text{HAuCl}_4 \cdot 3\text{H}_2\text{O}$), hydrochloric acid (76%), sodium hydroxide, and polydiallyldiammonium chloride (PDDA-20% w/w). The arsenic trioxide (As_2O_3) was obtained from Sigma Aldrich. All other reagents were obtained at the highest grade available from Sigma Aldrich or Fisher Scientific and were used without additional purification. All solutions were made with deionized (DI) water at room temperature with a resistivity of 18.2 M.cm (Ultrapure Water System, Millipore, Billerica, MA, USA).

2.2. Synthesis of AuNPs and po-Gr

Turkevich method was used to synthesize AuNPs [20]. Briefly, 2 mL of 10 mM $\text{HAuCl}_4 \cdot 3\text{H}_2\text{O}$ was mixed with 18 mL DI H_2O . After the solution was boiled, 2mL of 1% sodium citrate was added to the boiling HAuCl_4 solution. The color was turned to dark brown solution and then turned to clear red/purple color.

The po-Gr was prepared as reported in our previous papers with some modification [21],[22]. Briefly, highly pure graphite electrodes were used as anode and cathode using 0.1 M potassium phosphate buffer solution at pH 7 at room temperature as an electrolyte solution. 3 V were applied for 1 h to electrochemically exfoliate graphite electrodes. Then obtained solution was filtered and re-dispersed into DI water. After ultra-sonication for 1h, the solution was collected for further use and concentration of po-Gr was set to 1 mg/ml.

2.3. Functionalization of SPE surface

SPE was functionalized using po-Gr, AuNPs and PDDA-PSS solution as illustrated in Figure 1. First the SPE electrode was immersed in DI water avoiding any air bubbles for 2 minutes and then was allowed to partially dry at room temperature. Firstly, 3 μl of 1 mg/ml of po-Gr was very carefully spiked on the working electrode surface without the pipette tip touching the working surface as it can damage the electrode. Next step was addition of AuNPs prepared by aqueous reduction of HAuCl_4 by sodium citrate, which was then followed by the addition of conductive polymers where, 2 μl of freshly prepared PDDA and PSS mixture (1:1 ratio) was spiked on to the working surface of electrode. Addition of each step is done at room temperature and each step takes approximately 30 min to dry.

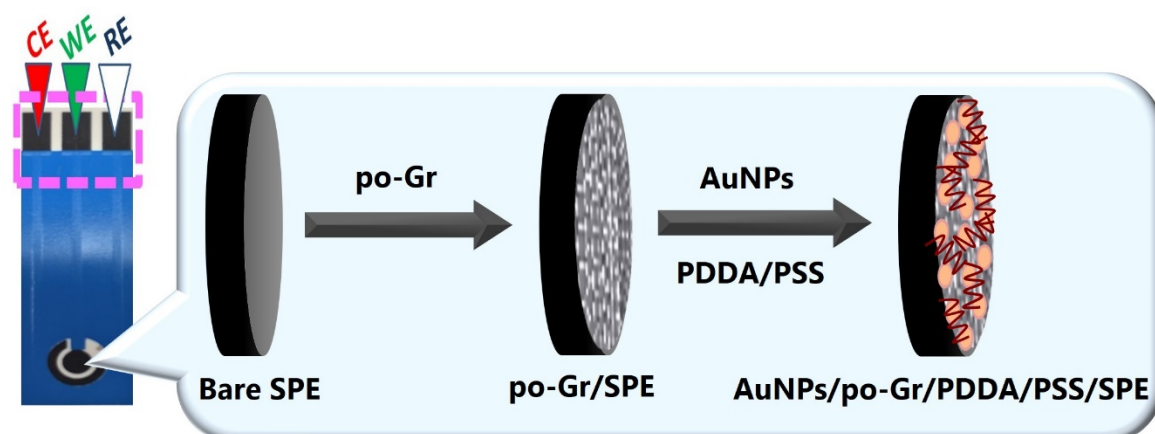


Figure 1. Schematic illustration of SPE preparation.

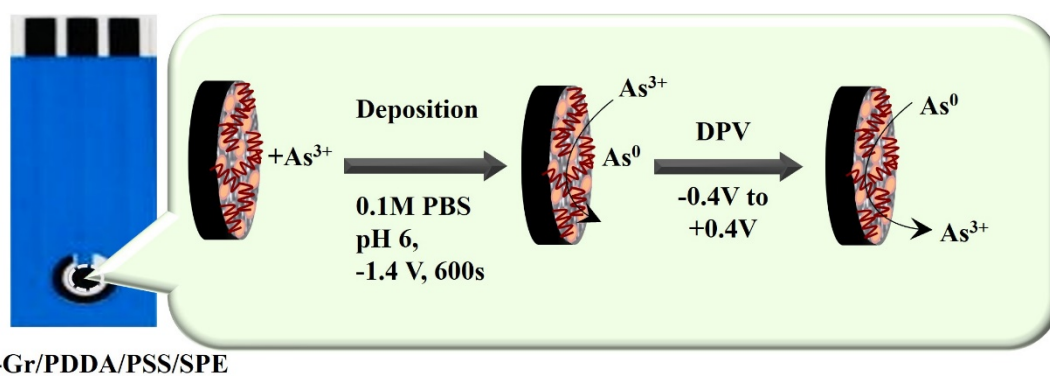
2.4. Electrochemical Measurements

For electrochemical measurements, an electrochemical workstation (660 D, CH Instruments) was employed. The electrochemical measurements consist of 2 steps as shown Figure 2, deposition and stripping. For the deposition step, analyte of interest (arsenic) is spiked onto the electrolyte solution (0.1 M PBS at pH 6). In the deposition step, As^{3+} is electrochemically reduced to As at -1.4V for 600 s. The As is deposited as a thin layer on the working surface of SPE. Next, a differential pulse anodic stripping voltammetry (DPASV) was utilized and As is oxidized to As^{3+} . This reduction and oxidation steps were repeated for various As concentration to obtain a linear fit. The redox reactions taking place during deposition and stripping are summarized below:

Step 1: Deposition



Step 2: Stripping



AuNPs/po-Gr/PDDA/PSS/SPE

Figure 2. Illustration of electrochemical sensing of As^{3+} using functionalized SPE electrode

2.5. Characterization

A scanning electron microscope (FE-SEM) (LEO1530, Carl Zeiss, Germany) was used to study surface morphology and 5 kV working voltage and 4 mm of working distance were used during testing. FEI Tecnai TF30 (Netherlands) were employed to collect transmission electron microscopy (TEM) images. For each sample, one drop of solution was placed on a carbon-coated 400 mesh copper grid, and excess solution was removed with filter paper. The grid was let to dry at ambient temperature before being imaged.

3. Results and Discussions

Figure 3a displays the FT-IR spectra of the synthesized pO-Gr and the pristine graphite sheet. The pristine graphite sheet does not exhibit any significant peaks, while the pO-Gr shows distinct peaks at approximately 3430, 2326, 1725, and 1642 cm^{-1} . These peaks correspond to the stretching vibrations of OH, CO₂, C=O, and C=C bonds, respectively.

In Figure 3b, the Raman spectra of pO-Gr and the pristine graphite sheet are presented. The Raman spectrum of the pristine graphite sheet shows a small D band at 1353 cm^{-1} , indicating structural defects. It also displays a prominent G band at 1593 cm^{-1} , which is associated with the vibration of sp² hybridized carbon atoms in the n-plane, along with a 2D band at 2739 cm^{-1} corresponding to two phonon lattice vibrations. On the other hand, the pO-Gr exhibits significant D, G, and 2D bands at 1343, 1587, and 2687 cm^{-1} , respectively. These observations suggest the presence of localized sp³ defects on the surface of the graphene sheets after exfoliation.

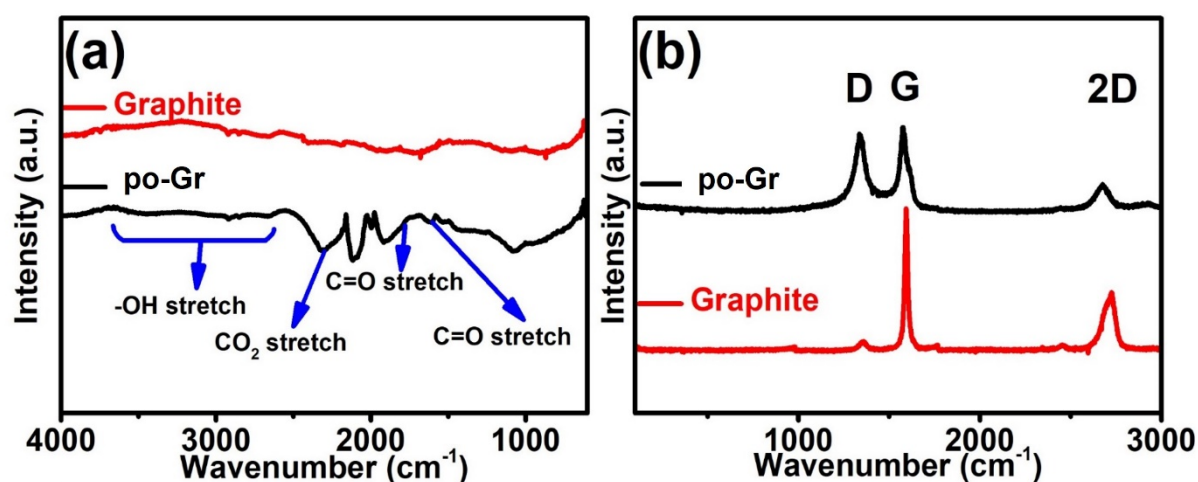


Figure 3. FT-IR and Raman spectra of po-Gr and pristine graphite

After the synthesis of po-Gr, AuNPs were synthesized using the Turkevich method as described above. The determination of both the size and concentration of spherical AuNPs can be achieved directly through analysis of UV-vis spectra. Figure 4 illustrates the UV spectra of AuNPs, demonstrating a pronounced absorption peak at 520 nm, indicating the presence of AuNPs with a particle size ranging from approximately 13 to 15 nm. Additionally, the TEM images of the AuNPs, depicted in Figure 5a, provide further visual confirmation of the formation of AuNPs and their size. Furthermore, particle size analysis of the AuNPs using a particle size analyzer, as shown in the inset of Figure 4, supports the successful formation of ~15 nm AuNPs.

The morphology of po-Gr and AuNPs-decorated po-Gr was analyzed using TEM, as depicted in Figure 5. Examination of po-Gr revealed its characteristic rippled and wrinkled morphology, as shown in Figure 5b. Upon treatment with AuNPs, the po-Gr surface exhibited well-dispersed AuNPs, as illustrated in Figure 5c and 5d. The TEM images clearly demonstrate the presence of AuNPs ranging in size from 10 to 20 nm on the po-Gr surface. This indicates successful deposition and dispersion of AuNPs onto the graphene material [23]. The decorated po-Gr structure with uniformly distributed AuNPs holds significant promise for enhancing the sensing performance and selectivity in the detection of arsenic. The combination of the unique properties of po-Gr and the catalytic activity of AuNPs offers potential advantages in the development of highly efficient electrochemical sensors for heavy metal detection, specifically arsenic, in drinking water. The TEM analyses provide valuable insights into the structural characteristics and morphology of the nanocomposite, validating its potential for effective arsenic detection and suggesting its applicability in addressing environmental and health concerns associated with heavy metal contamination in water sources.

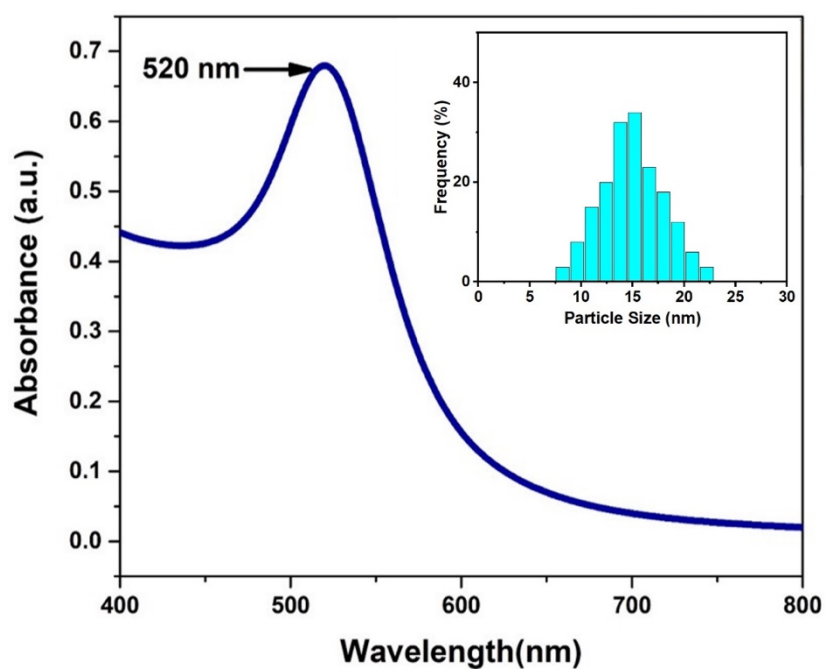


Figure 4. UV spectra of as-synthesized AuNPs. The inset is the particle size distribution of the AuNPs.

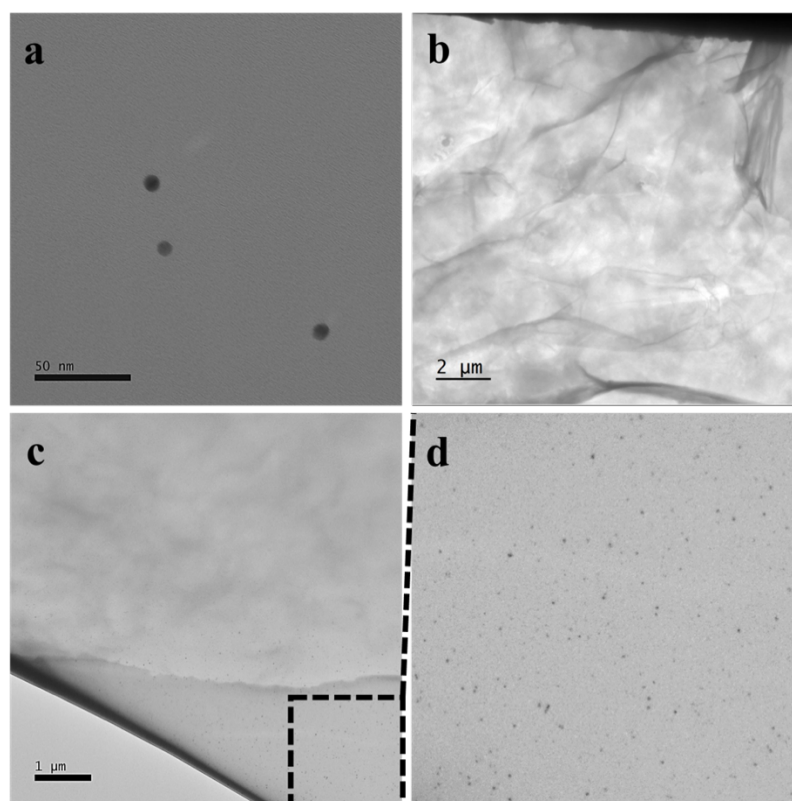


Figure 5. TEM images of (a) AuNPs, (b) po-Gr flake and (c) AuNPs decorated po-Gr flakes. (d) the enlarged view from AuNPs decorated po-Gr flake image.

To examine the surface characteristics of the SPE electrodes, a detailed analysis was performed using FE-SEM. The FE-SEM images provided valuable insights into the morphological features of the electrode surfaces. Figure 6a illustrates the surface morphology of the SPE electrode coated with po-Gr, revealing the distinctive rippled and wrinkled appearance that is characteristic of graphene materials. Subsequently, additional layers were sequentially added onto the po-Gr-coated SPE electrode, including AuNPs, PDDA, and PSS. The FE-SEM image of the AuNPs/po-Gr/PDDA/PSS-coated SPE electrode demonstrated the successful formation of a well-dispersed nanocomposite, as depicted in Figure 6b. The nanocomposite layer exhibited a uniform distribution of AuNPs on the po-Gr surface, further validating the effective fabrication process and the compatibility of the components within the sensor design.

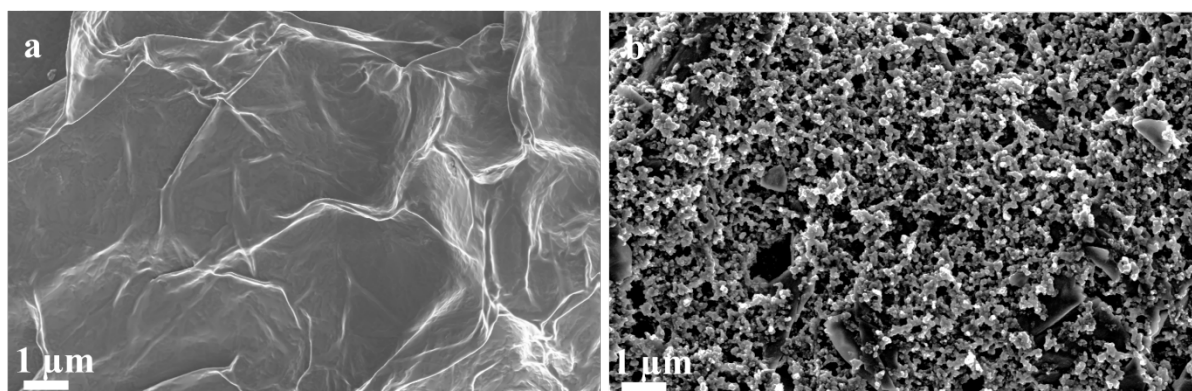


Figure 6. SEM images of (a) po-Gr and (b) AuNPs/po-Gr/PDDA/PSS coated SPE electrode.

Then, the SPE electrode was tested using DPASV method. This analytical technique consists of 2 steps as shown in Figure 2, deposition and stripping. For the deposition step, analyte of interest (arsenic) is spiked on the working surface of the electrode and the supporting electrolyte used is PBS at pH 6 (slightly acidic by addition of HCl). In the deposition step, As^{3+} is electrochemically reduced to As at a sufficiently negative potential (-1.4V) for 600s. The As is deposited as a thin layer on the surface of working electrode. A linearly increasing voltage is provided to the sensor during the electrochemical sensing process, causing As to be oxidized and converted to As^{3+} , resulting in the formation of an anodic current. This current response is recorded for further analysis. To assess the sensitivity and linear range of the sensor, the responses obtained from the DPASV experiments are presented in Figure 7a. The findings indicate that the current peak observed at -0.32 V exhibits an increasing trend as the concentrations of the As^{3+} stock solution is raised.

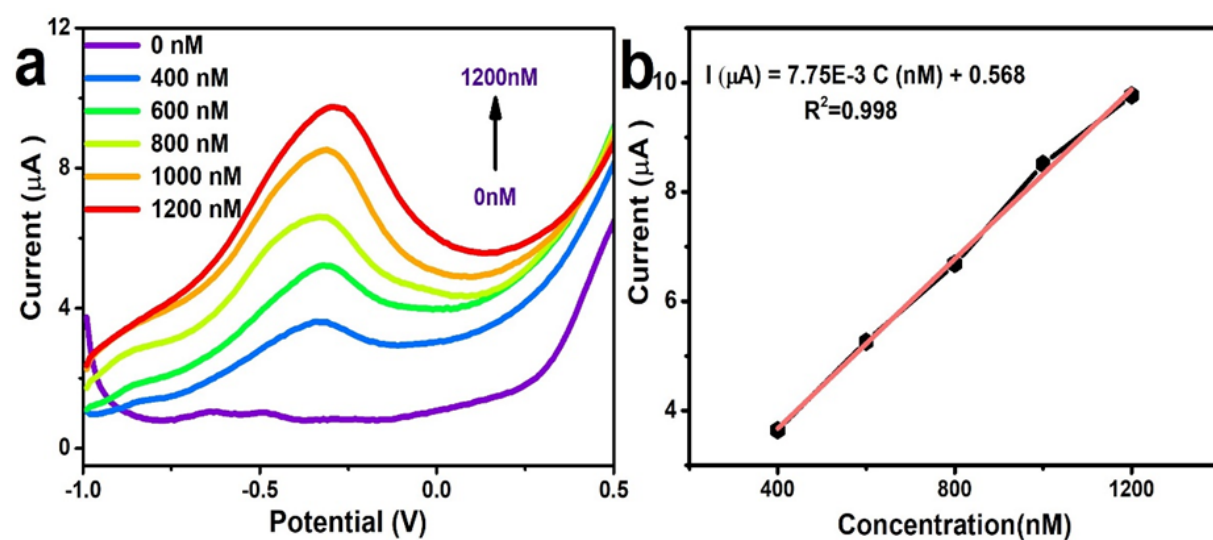


Figure 7. (a) DPASV curves for As^{3+} detection and (b) its linear curve fit

Furthermore, a calibration plot for As^{3+} is constructed by correlating the current peak height with each corresponding concentration. Remarkably, the calibration curve (Figure 7b) exhibits linearity within the

concentration range of 0-1200 nM, as demonstrated by the linear regression equation: $I(\mu\text{A}) = 7.75\text{E-}3 C (\text{nM}) + 0.568$ ($R^2 = 0.998$). This equation signifies a sensitivity of 86.18 $\mu\text{A/nM}$, as depicted in Figure 7b. The results highlight the excellent performance of the sensor in accurately detecting and quantifying varying concentrations of As^{3+} through its electrochemical response.

For the arsenic detection application in this study, the use of a nanocomposite formulation containing conducting polymers (PDDA, and PSS), po-Gr and AuNPs is well-justified. The chosen nanocomposite provides a promising solution to the widespread problem of arsenic contamination in drinking water by utilizing the catalytic properties of AuNPs, the stability and conductivity enhancement of conducting polymers, and the exceptional electrical properties of partially oxidized graphene po-Gr [4],[24]. A screen-printed carbon electrode (SPE) was subjected to a stepwise functionalization process, and the resulting sensor exhibits a broad linear response range for As^{3+} , offering a precise, quick, and affordable solution for addressing arsenic pollution in drinking water sources.

The detection limit attained in this work utilizing the proposed nanocomposite-based electrochemical sensor is relevant and compares favorably to the existing literature on arsenic detection methods. The sensor's sensitivity falls within a range that is appropriate for practical applications, as shown by the linear calibration curve's detection limit of up to 1200 nM. The achieved detection limit of 1200 nM enables the identification of arsenic concentrations that significantly exceed the permissible arsenic concentration levels in drinking water as set by the World Health Organization (WHO) guidelines (10 $\mu\text{g/L}$, equivalent to 133.3 nM) [25]. This suggests that the sensor can detect low quantities of arsenic that could be harmful to human health even when they are present in water sources. An important tool for real-world applications, particularly in areas where exposure to arsenic is a serious concern, is the sensor's ability to detect arsenic at such levels in combination with its portability and on-site monitoring capabilities. As a result, the achieved detection range is not only valuable but also extremely pertinent for real-world environmental and health applications.

4. Conclusions

The SPE electrode was utilized for the fabrication of the sensor by drop-casting the nanocomposite onto its surface employing a layer-by-layer method. Through comprehensive analytical investigations, it was observed that the developed sensor exhibited remarkable detection capability for As^{3+} ions, with a detection limit of up to 1200 nM. This detection limit places the sensor in a highly competitive position when compared to other existing electrochemical sensors. Notably, the proposed sensor offers significant advantages in terms of time and cost efficiency. The utilization of disposable SPEs eliminates concerns regarding surface fouling and electrode saturation, thereby ensuring consistent and reliable performance. Moreover, the unique design and composition of the sensor allow for convenient in situ measurements, enabling real-time monitoring and detection of As^{3+} levels in diverse settings. Overall, the incorporation of the nanocomposite onto the SPE electrode presents a promising approach for the development of a cost-effective, efficient, and portable electrochemical sensor for the detection of heavy metals, particularly As, in drinking water. This advancement holds considerable potential for addressing the pressing environmental and public health challenges associated with heavy metal contamination in water sources worldwide.

Acknowledgments

This study did not receive any specific grant from any funding agencies. Author thanks Prof. Sundaram Gunasekaran and Batul Kachwala for their support during this study.

References

- [1] Chakraborti D, Rahman MM, Mukherjee A, et al. Groundwater arsenic contamination in Bangladesh-21 Years of research. *J Trace Elem Med Biol.* 2015;31:237-248.
- [2] Fisher AT, López-Carrillo L, Gamboa-Loira B, Cebrián ME. Standards for arsenic in drinking water: Implications for policy in Mexico. *J Public Health Policy.* 2017;38(4):395-406.
- [3] Assirelli A, Ieffa S, Bernasconi R, Nobili L, Magagnin L. Graphene Based Materials for Arsenic Sensing and Removal from Contaminated Water. *ECS Meet Abstr.* 2015;MA2015-01(40):2127-2127.
- [4] Udayan APM, Kachwala B, Karthikeyan KG, Gunasekaran S. Ultrathin quasi-hexagonal gold nanostructures for sensing arsenic in tap water. *RSC Adv.* 2020;10(34):20211-20221.
- [5] Colliver TL, Ewing AG. Neurotransmitters, Electrochemical Detection of. *Encycl Anal Chem.* 2000:1-25.
- [6] Wuana RA, Okieimen FE. Heavy Metals in Contaminated Soils: A Review of Sources, Chemistry, Risks and Best Available Strategies for Remediation. *ISRN Ecol.* 2011;2011:1-20.
- [7] Dai X, Nekraseova O, Hyde ME, Compton RG. Anodic stripping voltammetry of arsenic(III) using gold nanoparticle-modified electrodes. *Anal Chem.* 2004;76(19):5924-5929.

- [8] Domínguez-González R, González Varela L, Bermejo-Barrera P. Functionalized gold nanoparticles for the detection of arsenic in water. *Talanta*. 2014;118:262-269.
- [9] Toor SK, Devi P, Bansod BKS. Electrochemical Detection of Trace Amount of Arsenic (III) at Glassy Carbon Electrode Modified with Au/Fe₃O₄ Nanocomposites. *Aquat Procedia*. 2015;4:1107-1113.
- [10] Piech R, Kubiak WW. Determination of trace arsenic with DDTC-Na by cathodic stripping voltammetry in presence of copper ions. *J Electroanal Chem*. 2007;599(1):59-64.
- [11] Profumo A, Merli D, Pesavento M. Voltammetric determination of inorganic As(III) and total inorganic As in natural waters. *Anal Chim Acta*. 2005;539(1-2):245-250.
- [12] Rao Y, Li RH, Zhang DQ. A drug from poison: How the therapeutic effect of arsenic trioxide on acute promyelocytic leukemia was discovered. *Sci China Life Sci*. 2013;56(6):495-502.
- [13] Forsberg G, O'Laughlin JW, Megargle RG, Koirtiyohann SR. Determination of Arsenic by Anodic Stripping Voltammetry and Differential Pulse Anodic Stripping Voltammetry. *Anal Chem*. 1975;47(9):1586-1592.
- [14] Kato D, Kamata T, Kato D, Yanagisawa H, Niwa O. Au Nanoparticle-Embedded Carbon Films for Electrochemical As³⁺ Detection with High Sensitivity and Stability. *Anal Chem*. 2016;88(5):2944-2951.
- [15] Cinti S, Politi S, Moscone D, Paleschi G, Arduini F. Stripping Analysis of As(III) by means of screen-printed electrodes modified with gold nanoparticles and carbon black nanocomposite. *Electroanalysis*. 2014;26(5):931-939.
- [16] Laschi S, Bagni G, Palchetti I, Mascini M. As(III) voltammetric detection by means of disposable screen-printed gold electrochemical sensors. *Anal Lett*. 2007;40(16):3002-3013.
- [17] Niu X, Lan M, Zhao H, Chen C, Li Y, Zhu X. Review: Electrochemical Stripping Analysis of Trace Heavy Metals Using Screen-Printed Electrodes. *Anal Lett*. 2013;46(16):2479-2502.
- [18] Li C. Determination of Arsenic in Water by Potentially Portable Methodology. 2013.
- [19] Mays DE, Hussam A. Voltammetric methods for determination and speciation of inorganic arsenic in the environment-A review. *Anal Chim Acta*. 2009;646(1-2):6-16.
- [20] Nadeau JL. Synthesis of Gold Nanoparticles /. *Introd to Exp Biophys - A Lab Guid*. 2020:154-159.
- [21] Sadak O, Sundramoorthy AK, Gunasekaran S. Highly selective colorimetric and electrochemical sensing of iron (III) using Nile red functionalized graphene film. *Biosens Bioelectron*. 2017;89:430-436.
- [22] Sadak O, Sundramoorthy AK, Gunasekaran S. Facile and green synthesis of highly conductive graphene paper. *Carbon N Y*. 2018;138:108-117.
- [23] Sadak O. One-pot scalable synthesis of rGO/AuNPs nanocomposite and its application in enzymatic glucose biosensor. *Nanocomposites*. 2021;7(1):44-52.
- [24] Sadak O, Wang W, Guan J, Sundramoorthy AK, Gunasekaran S. MnO₂ Nanoflowers Deposited on Graphene Paper as Electrode Materials for Supercapacitors. *ACS Appl Nano Mater*. 2019;2(12):4386-4394.
- [25] Ahn J, Boroje IJ, Ferdosi H, Kramer ZJ, Lamm SH. Prostate cancer incidence in U.S. counties and low levels of arsenic in drinking water. *Int J Environ Res Public Health*. 2020;17(3).

Pretrained Models and the Role of Feature Selection: An Artificial Intelligence-Based Approach in the Diagnosis of Diabetic Retinopathy

Mehmet Kaan KAYA¹, Burak TAŞCI^{2*}

¹ Ophthalmology Clinic, Universal Göz Hospital, Elazığ 23040, Turkey

² Vocational School of Technical Sciences, Firat University, Elazığ 23119, Turkey

¹ opht1980@gmail.com, ^{2*} btasci@firat.edu.tr

(Geliş/Received: 12/08/2023;

Kabul/Accepted: 30/08/2023)

Abstract: Diabetic retinopathy is a significant complication occurring in the retina of the eye as a result of prolonged diabetes. When not detected early, this condition can lead to vision loss. Advanced image processing techniques and artificial intelligence algorithms have enhanced the possibilities of early diagnosis and treatment. This article discusses current advancements in artificial intelligence-based diabetic retinopathy detection and explores future possibilities in this field. In the experimental studies of the article, the Kaggle Aptos 2019 dataset was utilized. This dataset comprises 5 classes and a total of 3662 images. The class distribution is as follows: No DR (No Diabetic Retinopathy): 1805, Mild: 370, Moderate: 999, Severe: 193, Proliferative DR: 295. The study consists of four fundamental stages. These stages are (1) Feature extraction from VGG16 and VGG19 pretrained models, (2) Feature selection using NCA, Relief, and Chi2, (3) Classification with Support Vector Machine classifier, (4) Iterative Majority Voting. Using the proposed method, a high accuracy of 99.18% is achieved. Furthermore, sensitivity of 100% for the No DR class, sensitivity of 100% for the Moderate class, sensitivity of 98.80% for the Severe class, and an F1-Score of 99.89% for the No DR class are obtained. This study demonstrates the effective utilization of machine learning methods in diabetic retinopathy diagnosis. The experimental results underscore the significant contributions of diabetic retinopathy patients' diagnosis and treatment processes.

Key words: VGG16, VGG19, Neighborhood Component Analysis, Relief, Chi2.

Ön Eğitimli Modeller ve Özellik Seçiminin Rolü: Diyabetik Retinopati Tanısında Yapay Zeka Tabanlı Yaklaşım

Öz: Diyabetik retinopati, uzun süreli diyabet hastalığının bir sonucu olarak gözün retinasında meydana gelen ciddi bir komplikasyondur. Erken teşhis edilmediğinde görme kaybına neden olabilen bu durum, gelişmiş görüntü işleme teknikleri ve yapay zeka algoritmalarının kullanımıyla erken teşhis ve tedavi imkanlarını artırmıştır. Bu makalede, yapay zeka tabanlı diyabetik retinopati tespiti alanındaki güncel gelişmeler ve geleceğe yönelik ihtimaller ele alınmıştır. Makalemizin deneysel çalışmalarında, Kaggle Aptos 2019 veri seti kullanılmıştır. Bu verisetinde 5 sınıf bulunmaktadır ve toplamda 3662 görüntü içerir. Sınıf dağılımı şu şekildedir: DR (Diyabet Retinopatisi) yok: 1805, Hafif: 370, Orta: 999, Şiddetli: 193, Proliferatif DR: 295. Çalışma dört temel yapıdan oluşur. Bu aşamalar (1) VGG16 ve VGG19 ön eğitimli modellerinden özellik çıkarma, (2) Nca, relief ve chi2 ile özellik seçimi, (3) destek vektör makinesi sınıflandırıcı ile Sınıflandırma, (4) yinelemeli çoğunluk oylama'dır. Önerilen yöntem kullanılarak %99.18'lik yüksek bir doğruluk elde edilmiştir. Ayrıca, Dr yok sınıfı için %100 hassasiyet, Orta sınıfı için %100 duyarlılık, Şiddetli sınıfı için %98.80 duyarlılık ve Dr yok sınıfı için %99.89 F1-Skoru elde edilmiştir. Bu çalışma, diyabetik retinopati tanısında makine öğrenimi yöntemlerinin kullanılmasının etkili bir yaklaşım olduğunu göstermektedir. Deneysel sonuçları, diyabetik retinopati hastalarının tanı ve tedavi süreçlerine önemli katkılar sağladığını ortaya koymaktadır.

Anahtar kelimeler: VGG16, VGG19, Komşuluk bileşenleri analizi, Relief, Chi2.

1. Introduction

Diabetes is a chronic condition characterized by long-term elevated blood sugar levels due to insufficient or ineffective insulin in the body. This condition leads to disruptions in carbohydrate, protein, and fat metabolism, as well as changes in capillary membranes and progressive atherosclerosis [1]. As of 2019, the global number of individuals with diabetes was estimated at 463 million, projected to rise to 578 million by 2030 [2]. One of the most prevalent microvascular complications of diabetes is called diabetic retinopathy (DR). DR arises due to damage in the blood vessels of the retinal layer. It is considered one of the leading causes of vision loss worldwide [3]. While DR is generally observed in approximately 30% of diabetic individuals, its prevalence increases within the population as diabetes duration lengthens [4], thus elevating the risk of vision impairment. Early diagnosis is crucial to slow down DR progression and prevent vision loss. Consequently, diabetic patients are recommended

* Corresponding author: btasci@firat.edu.tr, ORCID Number of authors: ¹ 0000-0002-3027-9159, ² 0000-0002-4490-0946

to undergo regular retina screenings under the supervision of eye doctors. However, these screenings can be time-consuming and require expertise. To address this challenge and support healthcare professionals, the utilization of rapid and reliable computer-aided automated screening systems is increasingly growing [5].

Artificial Intelligence (AI) is a field of computer science where machines mimic human cognitive processes. It finds extensive applications in the field of health and medicine. AI has been employed in the medical domain since the early 1950s, aiming to enhance diagnostic accuracy through computer-assisted algorithms [6]. Presently, rapid technological advancements in the healthcare sector offer substantial potential for early disease diagnosis and treatment. In this context, the early detection and effective management of chronic conditions like diabetic retinopathy hold paramount importance. Diabetic retinopathy is a severe complication occurring in the retinas of diabetes patients, potentially leading to vision loss. Moreover, due to its suitability for processing complex images, AI has been applied in image-based medical fields such as radiology and ophthalmology [7, 8]. These systems swiftly scan the retinas of diabetic patients, assisting physicians in early problem detection. Therefore, the use of automated screening systems has become an inevitable necessity in contemporary healthcare.

The contributions of the proposed Diabetic Retinopathy detection method based on VGG16, VGG19, and feature selection are provided below. To achieve overall performance, 10-fold cross-validation and extension validation are employed. An SVM classifier was chosen to demonstrate the general success of the proposed VGG16, VGG19, and feature selection-based method. The proposed approach utilizing VGG16, VGG19, and feature selection achieved an exceptional classification rate %99.18 for Diabetic Retinopathy detection using OCT images.

In order to generalize performance and attain a robust model, it is essential to test the model with various datasets. In the future, we are considering exploring the possibility of utilizing the proposed model, using OCT images, to detect different types of diseases. Furthermore, the model we have developed can also serve as a learning model for solving other computer vision problems.

The literature contains numerous studies conducted using deep learning and machine learning techniques [9-11].

Math and Fatima (2021) [12] proposed a segmentation-based approach utilizing deep learning to detect and classify DR and its lesions. Initially, preprocessing was applied to fundus images and factors like normalization. Preprocessed images were employed for image segmentation, adapting a pretrained Convolutional Neural Network (CNN) for obtaining lesion segmentation at the level of DR. Subsequently, all segmentation levels were integrated for fundus image classification. An end-to-end segmentation-based learning approach was used to better identify irregular diabetic retinopathy lesions. The evaluation results of the proposed model yielded values of 96.3% AUC, 96.37% sensitivity, and 96.37% specificity. Mahmoud et al. (2021)[13], proposed a hybrid inductive machine learning-based approach for automated DR diagnosis. The model evaluates color fundus images through four stages: preprocessing, segmentation, feature extraction, and classification. The preprocessing step normalizes retina images to enhance image quality, while the segmentation step involves encoding and decomposition of images. In the feature extraction and classification stages, a multi-instance learning technique was employed. According to experimental results, the suggested hybrid model achieved accuracy of 96.62%, sensitivity of 95.31%, and specificity of 96.88%. Ali et al. (2020) [14], developed an image processing and machine learning-based method for DR diagnosis. The model utilized a total of 2500 retinal images for each DR class. Four different features, including histogram, wavelet transform, co-occurrence matrix, and run-length matrix, were extracted from the images. A hybrid dataset was created using data augmentation to enhance classification accuracy. By applying four different feature selection techniques on 245 hybrid features per image, 13 optimized features were selected. With the proposed model, sequential minimal optimization, logistic regression, Canonical Correlation Analysis (CCA), logistic model tree, and simple logistic machine learning classifiers achieved accuracy of 98.53%, 99%, 99.66%, 99.73%, and 99.73%, respectively. Yildirim et al. [15], conducted DR detection using a dataset comprised of 1365 fundus fluorescein angiography images. In their study, they proposed the utilization of the MobileNetv2 model in conjunction with a nested patch-based image classification approach. Through this methodology, they achieved a classification accuracy of 87.40% on the collected dataset. Kobat et al.[16] proposed a method based on horizontal and vertical patch segmentation for DR classification. With their suggested approach, they achieved accuracy values of 94.06% and 91.55% for three-class classification, respectively. Tang and et al.[17] attempted to automatically detect epiretinal membrane regions using OCT images. They achieved an accuracy of 95.65% at the image level. Pramil et al.[18] classified OCT images of 90 cases of geographic atrophy, 32 cases of intermediate age-related macular degeneration, and 16 healthy controls. They employed a five-fold cross-validation method and data augmentation techniques. Their proposed method demonstrated high repeatability for geographic atrophy area measurements with ICC values of 0.99 and 0.94, along with expansion rates of the geographic atrophy area.

1.1. Motivation

The utilization of technologies such as Artificial Intelligence (AI) and Deep Learning (DL) has sparked a significant revolution in the medical field, particularly in areas like image analysis, pattern recognition, and data mining. In the realm of image-based diagnostics, AI methods hold the potential to mitigate errors made by medical doctors and accelerate the diagnostic process with heightened precision. The incorporation of AI-based techniques in the diagnosis of diabetic retinopathy can enhance patients' quality of life and provide healthcare professionals with a more effective roadmap. The fundamental motivation of this article is to underscore the potential and advantages of AI in diabetic retinopathy diagnosis. The primary focus of this research is to propose a hybrid deep learning model utilizing pretrained VGG16 [19] and VGG19 [19] architectures, thereby highlighting the application of AI in diabetic retinopathy diagnosis.

2. Material and method

2.1. Dataset

In this study, the publicly available APTOS 2019 blindness detection dataset (APTOS 2019) related to the diabetic retinopathy classification competition organized by the Asia Pacific Tele-Ophthalmology Society (APTOS) was employed [20]. The dataset comprises a total of 3662 retinal fundus images collected from multiple clinics using fundus photography by technicians from the Aravind Eye Hospital in India. The image resolutions range from 474×358 pixels to 3388×2588 pixels, and all files are in .png format. Each image has been graded by expert individuals on a scale from 0 to 4 for the detection of diabetic retinopathy. The severity of the disease increases from 0 to 4. The criteria are as follows: criterion 0 for non-DR images, criterion 1 for images with mild NPDR, criterion 2 for images with moderate NPDR, criterion 3 for images with severe NPDR, and criterion 4 for images with PDR. The number of images in each class is presented in Table 1. Sample images from the dataset are provided in Figure 1.

Table 1. Distribution of disease severity levels in the fundus image dataset.

Criterion	DR Condition	Number of Images
0	No DR	1805
1	Mild	370
2	Moderate	999
3	Severe	193
4	Proliferative DR	295

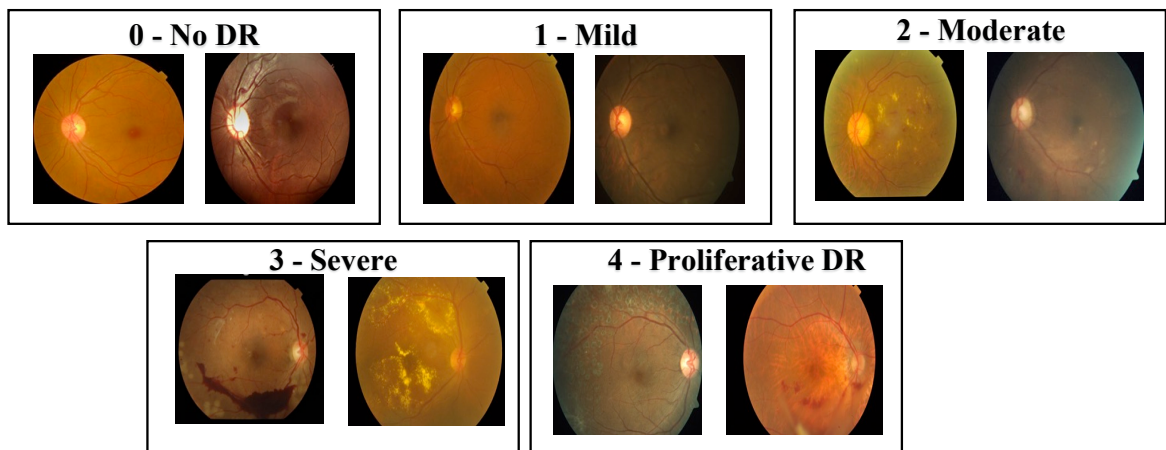


Figure 1. Sample images in APTOS dataset classes.

2.2. The Proposed Model

In this study, DR was classified using the pretrained VGG16 and VGG19 models. The study consists of four stages: (1) Feature extraction, (2) Feature selection, (3) Classification, and (4) Iterative Majority Voting. The proposed method's schematic is illustrated in Figure 2. In the initial stage of feature vector extraction, the fc8 and drop7 layers of the VGG16 and VGG19 pretrained models were utilized (F1: fc8, F2: drop7, F3: fc8, F4: drop7). Subsequently, the extracted feature vectors were selected using the NCA, Relieff, and Chi2 feature selection algorithms. The resulting feature vectors were then classified using an SVM classifier, yielding 12 prediction vectors (P1, P2... P12) after classification. The final outcome was obtained by applying the Iterative Majority Voting algorithm to the obtained prediction vectors. The block diagram of the proposed method is depicted in Figure 2.

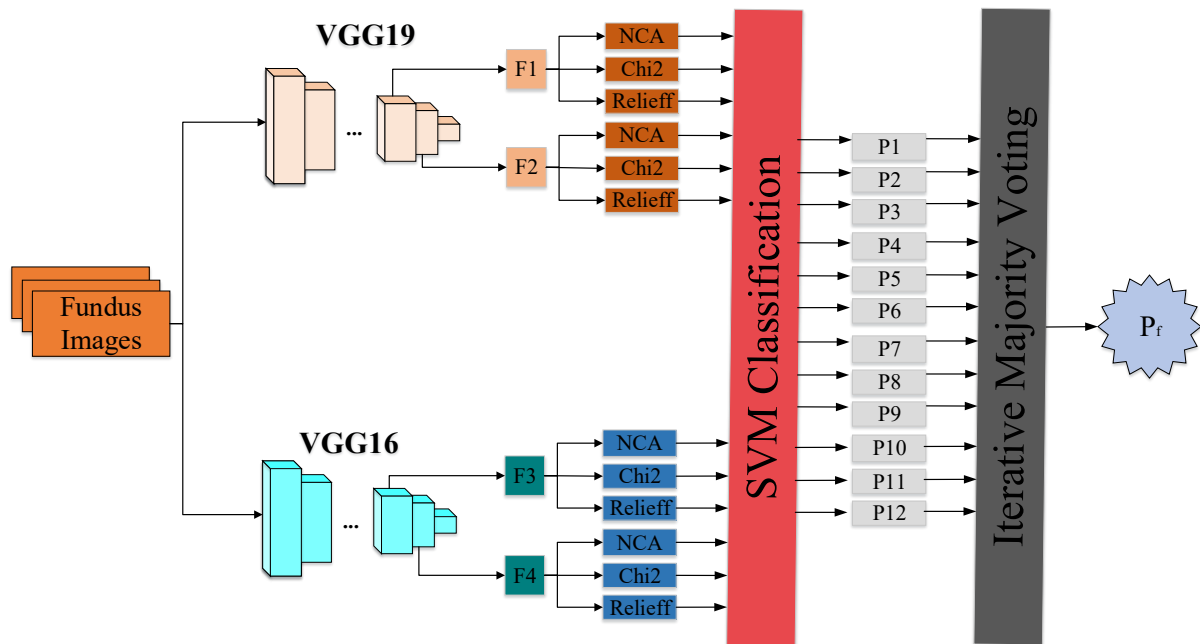


Figure 2. Block diagram of the proposed method

VGGNet: VGGNet, developed by the Visual Geometry Group (VGG) at the University of Oxford, secured the first place in ILSVRC 2014. VGGNet has two widely used variations, namely VGG16 and VGG19, containing 16 and 19 layers, respectively. VGGNet is composed of a stack of 3x3 filters, utilizing 3x3 filters instead of larger ones significantly reduces the number of parameters. In some configurations, 1x1 convolution filters are used with a fixed convolution stride of 1 pixel to ensure a linear transformation of input channels. Padding may be required to maintain resolution after performing convolution operations. VGG16 is a deep learning algorithm consisting of 13 convolutional and 3 fully connected layers. The input layer of the network requires images of dimensions 224 x 224 x 3. The architecture comprises a total of 41 layers, including pooling, fully connected, ReLU, dropout, and classification layers. This deep learning algorithm achieved an accuracy rate of 89% on the ImageNet database [19, 21].

NCA (Neighborhood Component Analysis) [22]: NCA is a feature selection algorithm used in classification problems. Its objective is to enhance the similarity among data points and improve classification performance. NCA calculates a weight matrix for each data point and determines the importance order of features using this matrix. This ensures that more important features contribute more to the classification performance.

Relieff[23]: Relief is an algorithm employed in classification and feature selection problems. Essentially, it computes the proximity of data points to their labels and uses this information to determine the importance order of features. Relief assesses the contribution of features to classification performance and selects the most relevant ones. Additionally, the Relief algorithm performs well on datasets with class imbalance.

Chi2 (Chi-square) [24]: Chi2 is a feature selection algorithm utilized in classification problems. It measures the relationship between features and the target variable using the Chi-square statistical test. The Chi2 test evaluates whether features are independent of the target variable and tests the hypothesis of independence. As a result, it filters out features with weak associations to the target variable and enhances classification performance.

Support Vector Machine (SVM)[25]: SVM is a powerful machine learning algorithm commonly used for data classification and regression problems. Its primary goal is to find a hyperplane or surface that separates data points into two or more classes. The core idea of SVM is to divide data points with the largest margin between classes, aiming to maximize the distance between data points of different classes using a hyperplane or surface.

Iterative Majority Voting[26]: Iterative Majority Voting is a classification method utilized in machine learning and data mining. This technique brings together multiple classifiers to achieve more accurate results. The method employs multiple classifiers to classify each instance in a dataset. These classifiers evaluate data instances in different ways and merge their results through a common voting process. The voting process assigns an instance to a class based on the majority decision made by the classifiers.

3. Experimental results

To obtain the experimental results in this study, Matlab 2023 environment was utilized. The experimental outcomes were obtained using a computer equipped with an Intel Core i9 processor, 128GB RAM, and an NVIDIA graphics card. The study comprises four fundamental stages: (1) Feature extraction, (2) Feature selection, (3) Classification, and (4) Iterative Majority Voting.

The 12 feature vectors' accuracy results, obtained through 10-fold cross-validation and SVM, are presented in Table 2.

Table 2. Classifier results for the 12 feature vectors

No	Generation method			Accuracy	
1	VGG16	fc8	NCA	SVM	96,23%
2		fc8	Chi2	SVM	97,68%
3		fc8	Relieff	SVM	96,26%
4		drop7	NCA	SVM	95,25%
5		drop7	Chi2	SVM	97,27%
6		drop7	Relieff	SVM	95,39%
7	VGG19	fc8	NCA	SVM	96,72%
8		fc8	Chi2	SVM	98,06%
9		fc8	Relieff	SVM	96,37%
10		drop7	NCA	SVM	95,90%
11		drop7	Chi2	SVM	97,30%
12		drop7	Relieff	SVM	95,17%

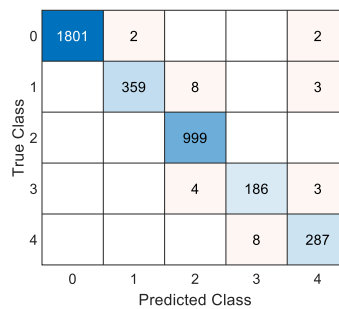


Figure 3. Confusion matrix

The confusion matrix obtained with the proposed method and the APTOS dataset is illustrated in Figure 3. The metrics calculated from the confusion matrix are presented in Table 3.

Table 3. Results of the proposed model.

Classes		Accuracy	Precision	Recall	Sensitivity	F1-score
Proposed Model	No DR	99.18%	100,00%	99,78%	98,73%	99,89%
	Mild		99,45%	97,03%	86,49%	98,22%
	Moderate		98,81%	100,00%	98,80%	99,40%
	Severe		95,88%	96,37%	75,13%	96,12%
	Proliferative DR		97,29%	97,29%	85,08%	97,29%

Based on the results presented in Table 3, the model's ability to recognize five distinct retinal conditions has been examined. The condition of 'No DR,' indicating the absence of Diabetic Retinopathy, stands out as the most successful classification with the highest accuracy, sensitivity, recall, and F1-score. However, there are fluctuations in sensitivity and recall values for other retinal conditions. Particularly, the 'Mild DR' and 'Severe DR' conditions highlight some classification challenges. These results underscore the model's potential to exhibit varying levels of performance for different retinal conditions. This research contributes to our understanding of the strengths and limitations of AI-based classification models in the field of medical imaging.

4. Discussion

In this article, the proposed SVM classifier and the selected CNN-based deep features have been compared with existing systems in the literature, and the results are presented in Table 4

Table 4. Results of studies using the same dataset.

Study	Model	Split:ratio	Dataset	Accuracy (%)
Gangvar et al.[27]	CNN, Inception-ResNet-v2	75:25	APTOS 2019	82.18
Kassani et al.[28]	Xception	70:20:10	APTOS 2019	83.09
Alyoubi et al.[29]	CNN512 and YOLOv3	80:20	APTOS 2019	89.00
Proposed Model	VGG16,VGG19,NCA,Relieff,Chi2,IHMV	10 Fold Cv	APTOS 2019	99.18

Despite using pretrained models and CNN architectures, researchers [27-29] who employed the same dataset in Table 3 achieved lower classification performance compared to our proposed model. With this method, a classification accuracy of 99.18% was achieved.

Our artificial intelligence system aims to complement the practical experience of medical experts, which is its primary purpose. The fundamental objective here is for the recommendations provided by artificial intelligence not to replace the competence and expertise of medical professionals but to play a complementary role. In complex cases, artificial intelligence can assist in delivering more precise and reliable outcomes based on the information gathered from medical professionals.

5. Conclusions

Despite the limitations of traditional diagnostic methods, it is believed that artificial intelligence can support early disease diagnosis using big data analysis, deep learning algorithms, and image processing techniques. Additionally, it has the potential to ease the need for regular patient examinations and monitoring, thus alleviating the burden on healthcare systems. In this study, the proposed method was established using the APTOS 2019 dataset available on the Kaggle platform, consisting of 3662 images. In our suggested model, features were extracted using the drop7 and fc8 layers of pretrained VGG16 and VGG19 models. Extracted features were selected using NCA, Relief, and Chi2. Subsequently, by applying the IHMV algorithm, an accuracy of 99.18% was achieved. In future research, there are plans to explore high-performance network architectures by employing larger datasets with a greater number of images and classes.

References

- [1] Da Rocha Fernandes J, Ogurtsova K, Linnenkamp U, Guariguata L, Seuring T, Zhang P, et al. IDF Diabetes Atlas estimates of 2014 global health expenditures on diabetes. *Diabetes Res. Clin. Pract.* 2016;117:48-54.
- [2] Saeedi P, Petersohn I, Salpea P, Malanda B, Karuranga S, Unwin N, et al. Global and regional diabetes prevalence estimates for 2019 and projections for 2030 and 2045: Results from the International Diabetes Federation Diabetes Atlas. *Diabetes Res. Clin. Pract.* 2019;157:107843.
- [3] Klein R, Klein BE, Moss SE, Davis MD, DeMets DL. The Wisconsin epidemiologic study of diabetic retinopathy: IV. Diabetic macular edema. *Ophthalmology.* 1984;91:1464-74.
- [4] Kobrin Klein BE. Overview of epidemiologic studies of diabetic retinopathy. *Ophthalmic Epidemiol.* 2007;14:179-83.
- [5] Özçelik YB, Altan A. Diyabetik retinopati teşhisi için fundus görüntülerinin derin öğrenme tabanlı sınıflandırılması. *Avr. Bilim Teknol. Derg.* 2021:156-67.
- [6] Secinaro S, Calandra D, Secinaro A, Muthurangu V, Biancone P. The role of artificial intelligence in healthcare: a structured literature review. *BMC Med. Inform. Decis. Mak.* 2021;21:1-23.
- [7] Hosny A, Parmar C, Quackenbush J, Schwartz L. HJ and Aerts. Artificial intelligence in radiology, *Nat. Rev. Cancer.* 2018;18:500-10.
- [8] Hipwell J, Strachan F, Olson J, McHardy K, Sharp P, Forrester J. Automated detection of microaneurysms in digital red-free photographs: a diabetic retinopathy screening tool. *Diabet. Med.* 2000;17:588-94.
- [9] Tasci B, Tasci I. Deep feature extraction based brain image classification model using preprocessed images: PDRNet. *Biomed. Signal Process. Control.* 2022;78:103948.
- [10] Macin G, Tasci B, Tasci I, Faust O, Barua PD, Dogan S, et al. An accurate multiple sclerosis detection model based on exemplar multiple parameters local phase quantization: ExMPLPQ. *Appl. Sci.* 2022;12:4920.
- [11] Kaya D, Gurbuz S, Yildirim IO, Akbal E, Dogan S, Tuncer T. Swin-PHOG-LPQ: An accurate computed tomography images classification model using Swin architecture with handcrafted features. *Biomed. Signal Process. Control.* 2023;86:105183.
- [12] Math L, Fatima R. Adaptive machine learning classification for diabetic retinopathy. *Multimed. Tools Appl.* 2021;80:5173-86.
- [13] Mahmoud MH, Alamery S, Fouad H, Altinawi A, Youssef AE. An automatic detection system of diabetic retinopathy using a hybrid inductive machine learning algorithm. *Pers. Ubiquit. Comput.* 2021:1-15.
- [14] Ali A, Qadri S, Khan Mashwani W, Kumam W, Kumam P, Naem S, et al. Machine learning based automated segmentation and hybrid feature analysis for diabetic retinopathy classification using fundus image. *Entropy.* 2020;22:567.
- [15] Yildirim H, Çeliker Ü, Kobat Sg, Dogan S, Baygin M, Yaman O, et al. An automated diabetic retinopathy disorders detection model based on pretrained MobileNetV2 and nested patch division using fundus images. *J. Health Sci. Med.* 2022;5:1741-6.
- [16] Kobat SG, Baygin N, Yusufoglu E, Baygin M, Barua PD, Dogan S, et al. Automated diabetic retinopathy detection using horizontal and vertical patch division-based pre-trained DenseNET with digital fundus images. *Diagnostics.* 2022;12:1975.
- [17] Tang Y, Gao X, Wang W, Dan Y, Zhou L, Su S, et al. Automated detection of epiretinal membranes in oct images using deep learning. *Ophthalmic Res.* 2023;66:238-46.
- [18] Pramil V, de Sisternes L, Omlor L, Lewis W, Sheikh H, Chu Z, et al. A deep learning model for automated segmentation of geographic atrophy imaged using swept-source OCT. *Ophthalmol. Retina.* 2023;7:127-41.
- [19] Simonyan K, Zisserman A. Very deep convolutional networks for large-scale image recognition. *arXiv preprint arXiv:14091556.* 2014.
- [20] APTOS Dataset. <https://www.kaggle.com/c/aptos2019-blindness-detection/data>.
- [21] Chen L-C, Papandreou G, Kokkinos I, Murphy K, Yuille AL. Deeplab: Semantic image segmentation with deep convolutional nets, atrous convolution, and fully connected crfs. *IEEE Trans. Pattern Anal. Mach. Intell.* 2017;40:834-48.
- [22] Goldberger J, Hinton GE, Roweis S, Salakhutdinov RR. Neighbourhood components analysis. *Adv. Neural Inf. Process. Syst.* 2004;17.
- [23] Robnik-Šikonja M, Kononenko I. Theoretical and empirical analysis of ReliefF and RReliefF. *Mach. Learn.* 2003;53:23-69.
- [24] Liu H, Setiono R. Chi2: Feature selection and discretization of numeric attributes. *Proceedings of 7th IEEE international conference on tools with artificial intelligence: Ieee;* 1995. p. 388-91.
- [25] Noble WS. What is a support vector machine? *Nat. Biotechnol.* 2006;24:1565-7.
- [26] Dogan S, Baygin M, Tasci B, Loh HW, Barua PD, Tuncer T, et al. Primate brain pattern-based automated Alzheimer's disease detection model using EEG signals. *Cogn. Neurodyn.* 2023;17:647-59.
- [27] Gangwar AK, Ravi V. Diabetic retinopathy detection using transfer learning and deep learning. *Evolution in Computational Intelligence: Front. Intell. Comput. Theory Appl. (FICTA 2020)*, Volume 1: Springer; 2021. p. 679-89.
- [28] Kassani SH, Kassani PH, Khazaiezhad R, Wesolowski MJ, Schneider KA, Deters R. Diabetic retinopathy classification using a modified xception architecture. *2019 IEEE international symposium on signal processing and information technology (ISSPIT): IEEE;* 2019. p. 1-6.
- [29] Alyoubi WL, Abulkhair MF, Shalash WM. Diabetic retinopathy fundus image classification and lesions localization system using deep learning. *Sensors.* 2021;21:3704.

Enhancing Strawberry Harvesting Efficiency through Yolo-v7 Object Detection Assessment

Mehmet NERGİZ^{1*}

¹ Bilgisayar Mühendisliği Bölümü, Mühendislik Fakültesi, Dicle Üniversitesi, Diyarbakır, Türkiye

*¹ mnergiz@dicle.edu.tr

(Geliş/Received: 13/08/2023;

Kabul/Accepted: 31/08/2023)

Abstract: Strawberry fruits which are rich in vitamin A and carotenoids offer benefits for maintaining healthy epithelial tissues and promoting maturity and growth. The intensive cultivation and swift maturation of strawberries make them susceptible to premature harvesting, leading to spoilage and financial losses for farmers. This underscores the need for an automated detection method to monitor strawberry development and accurately identify growth phases of fruits. To address this challenge, a dataset called Strawberry-DS, comprising 247 images captured in a greenhouse at the Agricultural Research Center in Giza, Egypt, is utilized in this research. The images of the dataset encompass various viewpoints, including top and angled perspectives, and illustrate six distinct growth phases: "green", "red", "white", "turning", "early-turning" and "late-turning". This study employs the Yolo-v7 approach for object detection, enabling the recognition and classification of strawberries in different growth phases. The achieved mAP@.5 values for the growth phases are as follows: 0.37 for "green," 0.335 for "white," 0.505 for "early-turning," 1.0 for "turning," 0.337 for "late-turning," and 0.804 for "red". The comprehensive performance outcomes across all classes are as follows: precision at 0.792, recall at 0.575, mAP@.5 at 0.558, and mAP@.5:.95 at 0.46. Notably, these results show the efficacy of the proposed research, both in terms of performance evaluation and visual assessment, even when dealing with distracting scenarios involving imbalanced label distributions and unclear labeling of developmental phases of the fruits. This research article yields advantages such as achieving reasonable and reliable identification of strawberries, even when operating in real-time scenarios which also leads to a decrease in expenses associated with human labor.

Key words: Strawberry, Yolo-v7, Object detection, Agriculture, Deep learning.

Yolo-v7 Nesne Tespiti ile Çilek Hasat Verimliliğinin Artırılması

Öz: A vitamini ve karotenoidler açısından zengin olan çilek meyveleri, sağlıklı epitel dokularını korur ve büyümeyi destekleyici faydalar sunar. Çileklerin yoğun ekimi ve hızlı olgunlaşması, bu meyveyi erken hasada duyarlı hale getirerek, çiftçiler için çürük hasat elde etmeye ve mali kayıplara yol açar. Bu durum, çilek gelişimini izlemek ve meyvelerin büyüme aşamalarını doğru bir şekilde belirlemek için otomatik bir algılama yöntemine olan ihtiyacı arttırmaktadır. Bu zorluğun üstesinden gelmek için, bu çalışmada Mısır'ın Giza kentindeki Tarımsal Araştırma Merkezi'ndeki bir serada çekilen 247 görüntüden oluşan Strawberry-DS adlı bir veri seti kullanılmıştır. Veri kümesinin görüntüleri, üstten ve açılı perspektifler dâhil olmak üzere çeşitli bakış açılarını kapsayacak şekilde altı farklı büyüme aşamasını içermektedir: "yeşil", "kırmızı", "beyaz", "dönüşüm", "erken-dönüşüm" ve "geç-dönüşüm". Bu çalışma, farklı büyüme evrelerindeki çileklerin tanınmasını ve sınıflandırılmasını tespit etmek için Yolo-v7 nesne tespiti yöntemini kullanmaktadır. Büyüme aşamaları için elde edilen mAP@.5 değerleri şu şekildedir: "yeşil" için 0,37, "beyaz" için 0,335, "erken-dönüşüm" için 0,505, "dönüşüm" için 1,0, "geç-dönüşüm" için 0,337 ve "kırmızı" için 0,804. Tüm sınıflardaki kapsamlı performans sonuçları ise şu şekildedir: 0,792'de kesinlik, 0,575'te hatırlama, 0,558'de mAP@.5 ve 0,46'da mAP@.5:.95. Özellikle, bu sonuçlar, dengesiz etiket dağılımları ve meyvelerin gelişim evrelerinin etiketlerinin net olmaması gibi etiketleri de içeren bir veri seti ile eğitilip test edilmesine rağmen, hem performans değerlendirmesi hem de görsel değerlendirme açısından önerilen araştırmanın etkinliğini göstermektedir. Bu araştırma makalesi, gerçek zamanlı senaryolarda çalışırken bile çileklerin makul ve güvenilir bir şekilde tespit edilmesi gibi avantajlar sağlamakta ve bu da işçilik maliyetlerinde azalmayı sağlamaktadır.

Anahtar kelimeler: Çilek, Yolo-v7, Nesne tanıma, Tarım, Derin öğrenme.

1. Introduction

The perennial plant, scientifically named *Fragaria x Ananassa*, belongs to the Rosaceae family and is recognized as a herbaceous perennial within the genus strawberry [1]. The wild strawberry has its beginnings in Europe, Asia and America whereas the origin of the contemporary planted strawberry, known for its larger fruits, can be traced back to France [1]. Abundant in carotenoids and vitamin A, strawberries offer advantages for preserving robust epithelial tissues and stimulating growth and maturation [1-2]. The considerable amount of dietary fiber found in strawberries could potentially play a positive role in aiding the digestive process within the gastrointestinal system, as well as in the prevention of both acne and colon cancers [1]. Due to their dense cultivation and rapid maturation, premature harvesting of strawberries can readily result in the spoilage of the fruit, causing financial setbacks for farmers [1]. Currently, the predominant method for gathering strawberries is manual

* Corresponding author: mnergiz@dicle.edu.tr. ORCID Number of authors: ¹ 0000-0002-0867-5518

labor, imposing significant strain on this process due to elevated labor expenses, demanding physical effort, and limited employee productivity [1,3]. Because of these factors, overseeing the development of strawberries proves to be a challenging endeavor, and the manual collection of mature strawberries is a monotonous and time-intensive undertaking [1]. More and more, in recent times, there have been reports of a decline in the number of agricultural laborers due to aging, particularly highlighted during the COVID-19 pandemic, even extending to the cultivation of fruit crops [4-5]. Thus, cultivating strawberries in open fields demands a substantial amount of human workforce, a task that is becoming progressively challenging to enlist manpower for [6].

All these facts about the strawberry cultivation necessitate the creation of an automated detection technique to oversee the progress of strawberries and accomplish precise recognition of matured fruit. Computer vision is a field in which machine learning techniques is commonly applied in medical and agricultural images [7-11]. Presently, this research field functions as a primary instrument for detecting agricultural commodities and has found extensive application in tasks such as identifying maturity levels, remotely monitoring crops, predicting yields, facilitating harvesting robots, and aiding in the selection of suitable plant varieties [1, 12-19]. Nonetheless, the intricate and ever-changing natural surroundings still exert particular impacts on fruit identification. Instances of these include the obscuring caused by leaves, fruit clustering and disturbances from plant arrangement, and fluctuations in lighting. These are prevalent aspects that impact the precision of fruit recognition [1].

There are two primary classifications for object detection model architectures such as one-step and dual-step [1]. One-step object detection algorithms identify targets by capturing features just once, primarily encompassing the SSD technique and the YOLO models [1]. Dual-step object detection algorithms necessitate the initial creation of potential regions before proceeding to employ a convolutional neural network (CNN) for target detection. This category primarily involves the SPPNet and the R-CNN series of algorithms [1]. Historically, in contrast to the dual-step object detection models, the single-step object detection models exhibit superior real-time capabilities while compromising somewhat on accuracy [1]. Nonetheless, due to the ongoing enhancement and advancement of the YOLO algorithm, its precise and effective detection capabilities have garnered substantial attention and practical implementation [1]. The YOLO series algorithms exhibit remarkable versatility and resilience, enabling them to adjust to object detection assignments amid intricate scenarios, encompassing various sizes, orientations, and obstructions. This adaptability is highly valuable for their application in real-world agricultural contexts [1].

1.1. Related works:

Li et al. presented YOLOv5-ASFF, an enhanced real-time deep learning model for detecting strawberries in multiple stages derived from the enhanced YOLOv5 architecture. By integrating the adaptive spatial feature fusion (ASFF) component to the YOLOv5, Li et al. indicated that the model dynamically acquires the combined spatial weights of strawberry activation maps across different scales. This approach targeted to capture comprehensive image feature data related to strawberries more effectively. To validate the capabilities of YOLOv5-ASFF, Li et al. curated an extensive strawberry image dataset that encompasses diverse complex scenarios, including instances of leaf shading, overlapping fruits, and densely clustered fruits [1].

Lemsalu et al. created a real-time application for identifying strawberries and their peduncles using the YOLOv5 model, implemented on an edge device. This system effectively discerned both mature and immature strawberries along with their respective peduncles for automated harvesting purposes. Furthermore, Lemsalu et al. compiled a dataset of strawberries, annotated it, and utilized it to train their model [6].

Zhang et al. introduced YOLOv5s-Straw, a specialized model based on YOLOv5. They adapted the base model by substituting the C3 component in the foundational network with the C2f component, a change that enhanced the flow of feature gradients. Additionally, Zhang et al. integrated the Spatial Pyramid Pooling Fast and the Cross Stage Partial Net into the concluding layer of the YOLOv5s backbone network [4]. This integration aimed to bolster the model's capacity to generalize across the strawberry dataset examined in their research [4].

Lawal introduced YOLOStrawberry, a model version built upon the adapted YOLOv5 structure, and conducted comparisons against other YOLO lightweight variants. In the architecture of YOLOStrawberry, the backbone network incorporates elements like SPPF, Conv_Maxpool, ResNet, Shuffle_Block and SElayer. The neck network employed FPN, while the achievement ratio of strawberry detection was enhanced through the application of the CIoU loss function [20].

Mao et al. presented the RTFD model, an acronym for real-time fruit detection, a slight model tailored for edge CPU gadgets aimed for detecting the fruit and vegetables. Using the PicoDet-S model as a backbone, RTFD refined the architecture, loss and activation functions to elevate the live detection performance specifically for edge CPU gadgets [21].

Mejia et al., introduced an independent rover system designed to identify strawberries and gauge their ripeness within a genuine agricultural field. This was achieved by implementing an image processing pipeline that makes use of visual data from a stereo camera. Additionally, they established a comprehensive strawberry map that

imparts crucial insights to farmers regarding the fruit's development stage, condition, and potential yield. This map was especially valuable for navigating ridge planting environments, characterized by uneven landscapes, confined spaces, and challenging backgrounds [22].

Ren et al., introduced a mobile robotics framework encompassing essential components such as a stereoscopic camera, a robotic manipulator with 6 degrees of freedom and a gripper situated on an independent mobile base. Through the utilization of the Yolo-v4-tiny algorithm, they acquired information concerning the position and maturity level of individual fruits. A software-based open loop algorithm for fruit positioning and manipulation was also developed, enabling the accomplishment of tasks spanning fruit identification, pinpointing, gripping, release and placement [23].

Within this research, the Yolo-v7 approach for object detection is employed to identify strawberries across their various developmental phases and categorize them according to their growth stages. The findings of this proposed research showcase satisfactory outcomes, both from the perspective of performance evaluations and visual assessments, even when confronting intricate circumstances involving infrequent labels and ambiguous developmental phases of the fruits.

Some of the advantageous aspects of this research article on localization and phase classification of strawberries using the YOLO-V7 method are as follows [1]:

- Automated detection and monitoring
- Precise and accurate object detection even in real time
- Adaptability for complex images like obstructions, different orientations, colors and sizes of strawberries
- Reduction of labor costs

2. Material

"Strawberry-DS" dataset which is used in this study is a collection of annotated images featuring strawberries at various phases of development. Renowned for their distinct flavor and nutritional value, strawberries (*Fragaria X Ananassa*) are globally cultivated fruits utilized fresh or processed. With substantial economic importance and export potential, assessing strawberry characteristics during growth stages is pivotal for cultivar selection and yield estimation. Traditionally, growth phase assessment relies on time-intensive visual inspection, prompting the creation of this dataset. Comprising 247 high-resolution RGB images, Strawberry-DS captures strawberries at different developmental stages, annotated by hand through the Roboflow tool. Annotations are provided in YOLO format for reference to the region of interest [24].

Captured using a Sony Xperia Z2 LTE-A D6503 smartphone camera with a 20.7 MP CMOS sensor, the dataset images encompass fully visible strawberries and those partially hidden by foliage or other fruits. Collected from a greenhouse at the Agricultural Research Center in Giza, Egypt, the images span top and various angled views. Strawberry-DS.zip houses 247 .jpg images, depicting six growth phases: "green", "red", "white", "turning", "early-turning" and "late-turning". The general turning phases signify color transitions, with "early-turning" displaying around 10% and 30% red color, "turning" featuring around 30% and 60% red color and "late-turning" showing around 60% and 90% red color [24].

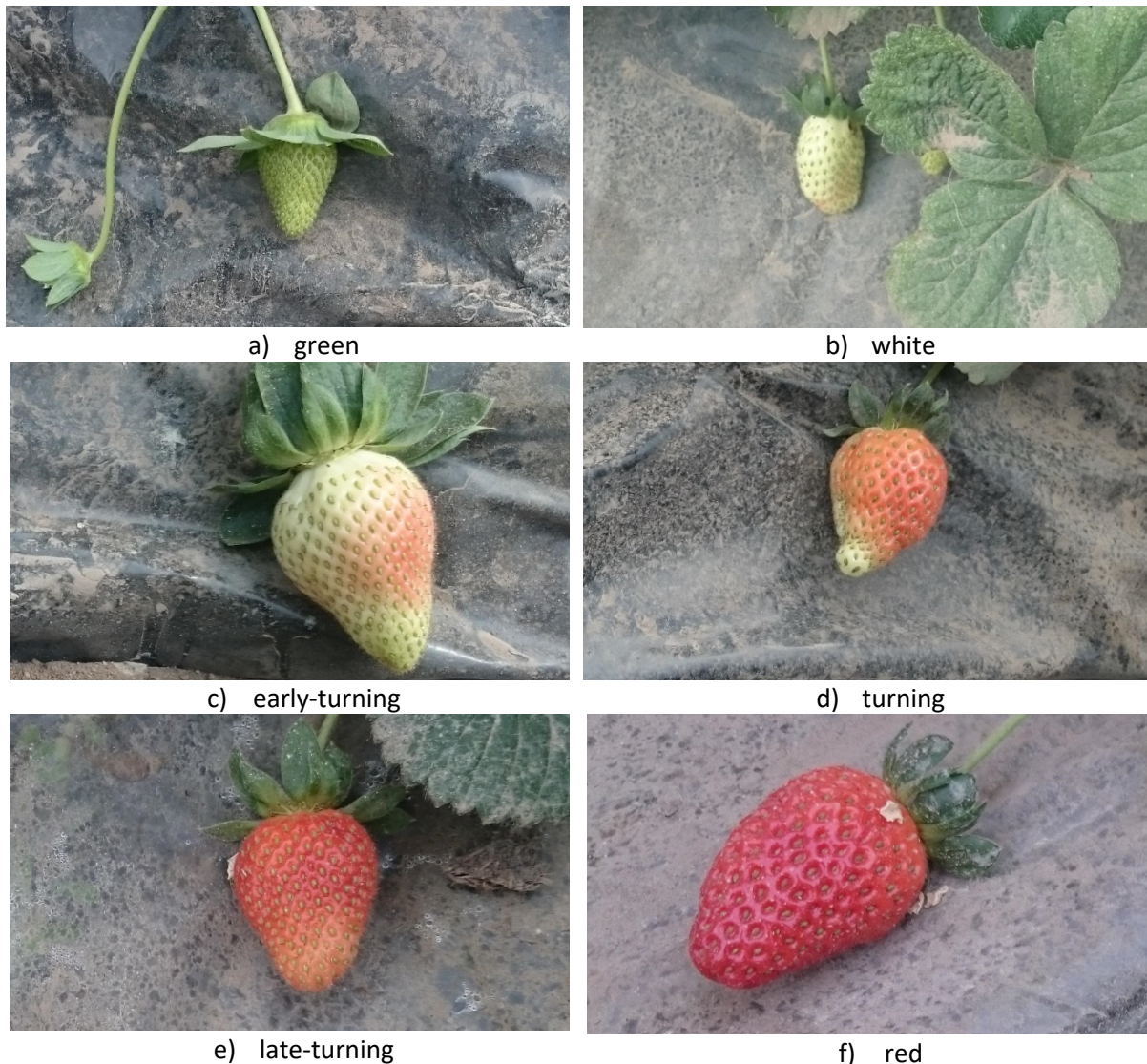
The dataset's significance extends to advanced agriculture automation, offering support for developing robotic harvesting systems that increase yield and reduce production costs. It plays a vital role in constructing robust machine vision models for decision-making in during, before and after harvesting strawberry operations [24]. Furthermore, Strawberry-DS enables smartphone and drone-based monitoring, yield prediction, and accurate evaluation of strawberry harvesting times, providing essential aid to farmers and advancing the agricultural sector. Some sampled images for each class depicting the gradual phase changes of the growth of the strawberries are shared in Figure 1. The image counts and label numbers per class are shared for train, validation and test datasets in Table 1.

3. Methods

The real-time identification of objects has become a pivotal element in a wide array of applications, encompassing diverse domains like self-driving vehicles, robotics, video monitoring, and augmented reality [25].

Table 1. The images numbers and label numbers per class for train, validation and test datasets

Class	Train		Validation		Test		Total	
	Images	Labels	Images	Labels	Images	Labels	Images	Labels
all	172	733	49	225	26	104	247	1062
white	172	168	49	54	26	35	247	257
green	172	308	49	104	26	43	247	455
early-turning	172	19	49	7	26	2	247	28
turning	172	23	49	10	26	2	247	35
late-turning	172	37	49	14	26	3	247	54
red	172	178	49	36	26	19	247	233

**Figure 1.** Sampled images for each class of Strawberry-DS dataset [24]

Amid the numerous algorithms designed for object detection, the YOLO (You Only Look Once) framework has gained prominence due to its exceptional equilibrium between swiftness and precision. This characteristic empowers swift and dependable object recognition within images [25]. Redmon and his colleagues released the initial YOLO paper during the CVPR conference of 2016 [25-26]. For the very first time, it introduced a real-time comprehensive technique for identifying objects. The acronym YOLO signifies its unique ability to perform object detection in just one iteration on the model graph, distinct from earlier methods. Since its introduction, the YOLO

lineage has undergone several iterations, with each iteration improving upon the earlier versions to rectify constraints and elevate efficiency, as illustrated in Figure 2 [25].

The real-time object detection process of YOLO has proven indispensable in self-driving vehicle systems, facilitating swift recognition and monitoring of diverse entities like cars, pedestrians, bicycles, and impediments. Such abilities have found utilization across a multitude of domains, encompassing tasks such as discerning actions within video sequences to facilitate surveillance, analyzing sports activities, and supporting interactions between humans and computers. Within the realm of medicine, YOLO has found application in the identification of cancer, delineating skin areas, and recognizing pills. This application has resulted in heightened precision of diagnoses and streamlined procedures for medical treatment. In the realm of remote sensing, YOLO has been enlisted for the purpose of recognizing and categorizing objects within satellite and aerial images. Yolo has also contributed to tasks such as charting land utilization, urban blueprinting, and overseeing ecological conditions. YOLO models find implementation in the agricultural sector to identify and categorize crops, pests, and diseases. This aids in the adoption of precision agriculture strategies and the automation of farming operations [25].

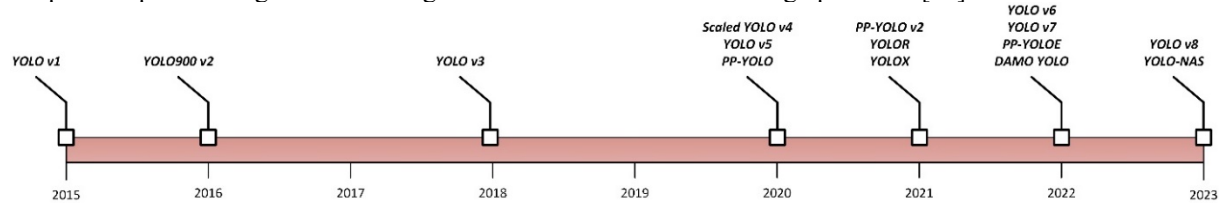


Figure 2. The emergence of lineage of YOLO models throughout the history [25]

The YOLO-v1 model integrates the stages of object detection, enabling the concurrent identification of all bounding boxes at a single scan. To achieve this, YOLO-v1 partitions the image as an S by S rectangles, anticipating B bounding boxes for a particular category and estimating the confidence associated with C distinct classes for each grid segment. YOLO-v1 employs a loss function, also used by the other YOLO models, that comprised sum of three sum-squared error components: one for the accuracy of bounding box coordinates (localization loss), another for object presence or absence confidence (confidence loss), and the third for the precision of category predictions (classification loss) [25].

Since the introduction of the YOLO-v3 model, the structure of YOLO models is delineated into three units: the “backbone”, “neck” and “head”. The “backbone” units are tasked with deriving valuable features from the input image and are generally constituted by a CNN that undergoes training in a comprehensive image classification assignment, like that of ImageNet. The intermediary unit, termed as the “neck,” acts as a bridge connecting the “backbone” with the final unit “head”. Its role involves consolidating and honing the features extracted by the “backbone”, often emphasizing the refinement of spatial and semantic data across varying dimensions. Constituting the concluding unit of an object detection system, the “head” assumes the duty of generating forecasts using the features derived from the “backbone” and “neck” units. Generally, it comprises one or more subnetworks tailored to specific tasks, encompassing localization, classification and in more recent developments, duties such as pose estimation and instance segmentation.

The authors behind YOLO-v4 and YOLOR also introduced YOLO-v7 in July 2022. In YOLO-v7, some sort of alterations are introduced to the architecture along with a range of enhancements aimed at boosting accuracy. These changes are implemented through a collection of beneficial optimizations that improved precision while maintaining the inference speed, albeit impacting solely the duration of the training phase [25,27]. Yolo-v7 proposes new modifications in its architecture known as Extended Efficient Layer Aggregation Network (E-ELAN) and Model Scaling for Concatenation-Based Models.

ELAN serves as a technique that enhances the efficiency of deep models by managing the gradient flow across the shortest and longest pathways, thus facilitating more effective learning and convergence [25,28]. YOLO-v7 introduces the concept of E-ELAN, a mechanism designed to function effectively across models containing an unrestricted number of stacked computational blocks. E-ELAN enhances network learning without disrupting the original gradient trajectory by amalgamating features from various clusters through a process of shuffling and merging cardinality. In YOLO-v7, a novel approach for scaling models based on concatenation is also introduced. This method involves proportionally adjusting both the block's depth and width, ensuring the model's optimal structure is preserved [25,27].

The other proposed changes of Yolo-v7 model are as follows:

- The identity link within reparametrized convolutions (RepConv) is eliminated and referred to as RepConvN [25,27].
- The auxiliary head is set to receive coarse label assignment while the primary head is set to obtain precise label assignment [25,27].

- During the inference phase, the convolutional layer's bias and weight are adjusted to incorporate the mean and variance from batch normalization [25,27].

In this study, the Strawberry-DS image dataset is benchmarked by using the Yolo-v7 technique, employing its standard configuration with the sole exception being the adjustment of the default image dimensions from 640x640 to 960x960. This alteration is implemented to improve the detection potential of the model for smaller strawberries [29]. The training phase entails the execution of 600 epochs, a process executed on a workstation equipped with dual Nvidia RTX A4000 16GB GPUs, an Intel i7-11700F CPU operating at 3.6 GHz and 64 GB of RAM.

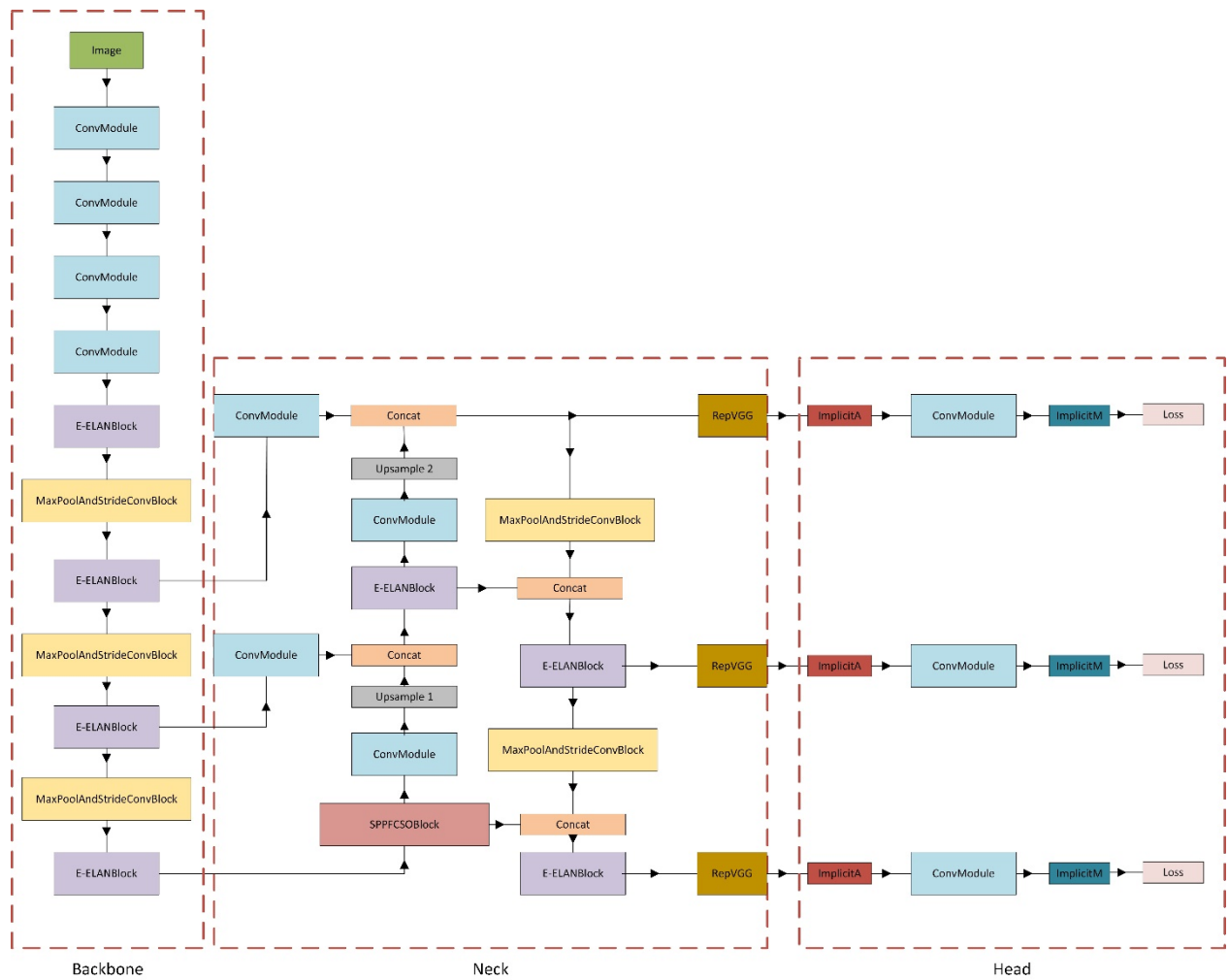


Figure 3. The main architecture of YOLO-v7 model [25,27]

4. Results & Discussion

In this section, the outcomes of the proposed study's training, validation, and testing phases are given. The outcomes of the validation phase, encompassing all categories, are outlined in Table 2. A total of 49 validation images have been examined during training, and 225 labels have been assigned to these images. Among these labels, the "green" class stands as the most prevalent, while the "early-turning" class is the least common. Equations 1, 2, and 3 provide the formulations for intersection over union (IoU), recall and precision metrics respectively. The average precision at an IoU value of 0.5 ($AP@.5$) is computed by calculating the area under the precision x recall curve as illustrated in Figure 5 (d) and equation 4 in which "p(r)" signifies the precision value linked to the indicated recall point on the horizontal axis. The term "mAP@.5" denotes the mean average precision for all classes at an IoU of 0.5. Furthermore, "mAP@.5:.95" signifies the average mean average precision along the IoU range of [0.5, 0.55, 0.6, 0.65, 0.7, 0.75, 0.8, 0.85, 0.9, 0.95]. Higher IoU values tend to reduce false positives and

amplify false negatives, leading to heightened precision and diminished recall. This IoU impact strongly molds the precision x recall curve and governs mAP@IoU values as a secondary effect [30].

$$IoU = \frac{\text{area}(\text{ground truth} \cap \text{prediction})}{\text{area}(\text{ground truth} \cup \text{prediction})} \quad (1)$$

$$\text{Recall} = \frac{\text{True Positive}}{\text{True Positive} + \text{False Negative}} \quad (2)$$

$$\text{Precision} = \frac{\text{True Positive}}{\text{True Positive} + \text{False Positive}} \quad (3)$$

$$AP@IoU = \int_0^1 p(r) dr \quad (4)$$

Table 2 reveals a noteworthy observation: the class "red," despite having fewer labels, attains the highest mAP@.5:.95 metric value. This outcome aligns with expectations, given that red strawberries exhibit a larger, reddish appearance, rendering them distinguishable against the backdrop of greenish leaves. In contrast, the class "late-turning" records the lowest mAP@.5: metric, owing to the lack of labeled ground truths and its resemblance to the "red" class which eventually poses a challenge the model to learn this subtle gradual color change.

In Figure 4, the confusion matrix, representing all validation dataset classes, unveils a distinct pattern. The dark blue diagonal values signify true positives, exposing a noteworthy revelation: the "late-turning" class records the smallest true positive value at 0.38, with 0.54 of all labeled "late-turning" ground truths being erroneously classified as background by the model. In comparison, the model overlooks none of the "early-turning" labels even the least number of labels are provided for this class.

Table 2. Performance results of validation dataset for each class

Class	Images	Labels	Precision	Recall	mAP@.5	mAP@.5:.95
all	49	225	0.689	0.671	0.66	0.526
white	49	54	0.7	0.648	0.583	0.441
green	49	104	0.707	0.719	0.726	0.473
early-turning	49	7	0.738	0.714	0.786	0.67
turning	49	10	0.541	0.6	0.507	0.423
late-turning	49	14	0.606	0.429	0.461	0.394
red	49	36	0.839	0.917	0.896	0.754

Figure 5 illustrates the recall, precision, precision x recall and F1 score curves relating to the validation dataset. Notably, the confidence level represents the model's degree of certainty in its predictions, distinct from the concept of IoU. When predictions coincide with the same ground truth label, the prediction boasting the highest confidence receives the true positive label, while the remaining predictions are classified as false positives. Elevating the confidence threshold results in heightened precision but reduced recall. This pattern is evident in Figure 5 a) and b), where adjustments in precision and recall values align as anticipated along the confidence level axis. In Figure 5 b), while the precision curves for all "red" class converge faster than the rest of the classes. The "late-turning" class's recall curve experiences an earlier decline compared to the delayed reduction in the "red" class's recall curve. The F1 score and precision x recall curves partially mirror the trajectory of the recall curve, as they integrate the precision and recall metrics as multipliers and axes, respectively.

Figure 6 presents a comprehensive view of the loss and performance metrics spanning epochs for both training and validation outcomes. In the leftmost column, there exists the localization loss for the predicted boxes [25]. Moving to the center column, the loss associated with the objectness of these predicted boxes is depicted, often referred to as confidence loss [25]. The third column portrays the classification loss. Notably, across the training and validation sets, all three losses exhibit a consistent decrease over epochs, barring the validation objectness loss, which exhibits a sign of overfitting by a spike around the 200th epoch. As we analyze the trend along the epoch axis, a discernible pattern emerges: the recall, precision, mAP@0.5, and mAP@0.5:0.95 metrics exhibit a steady rise before plateauing. This observation underscores the progressive improvement and eventual stabilization of these metrics over the course of training and validation epochs.

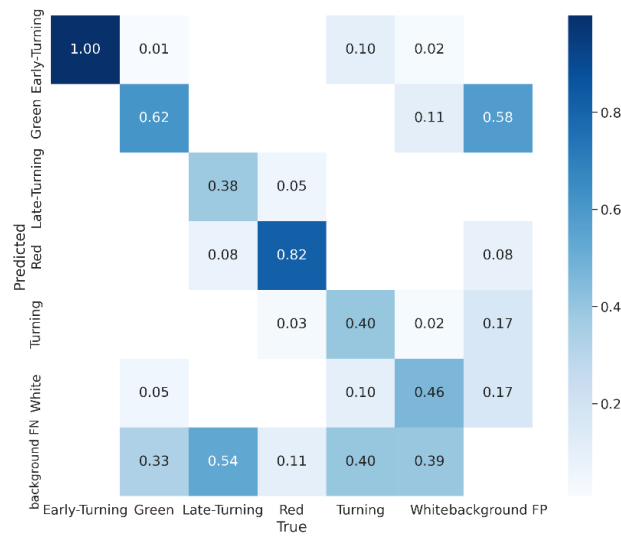


Figure 4. The confusion matrix of validation dataset

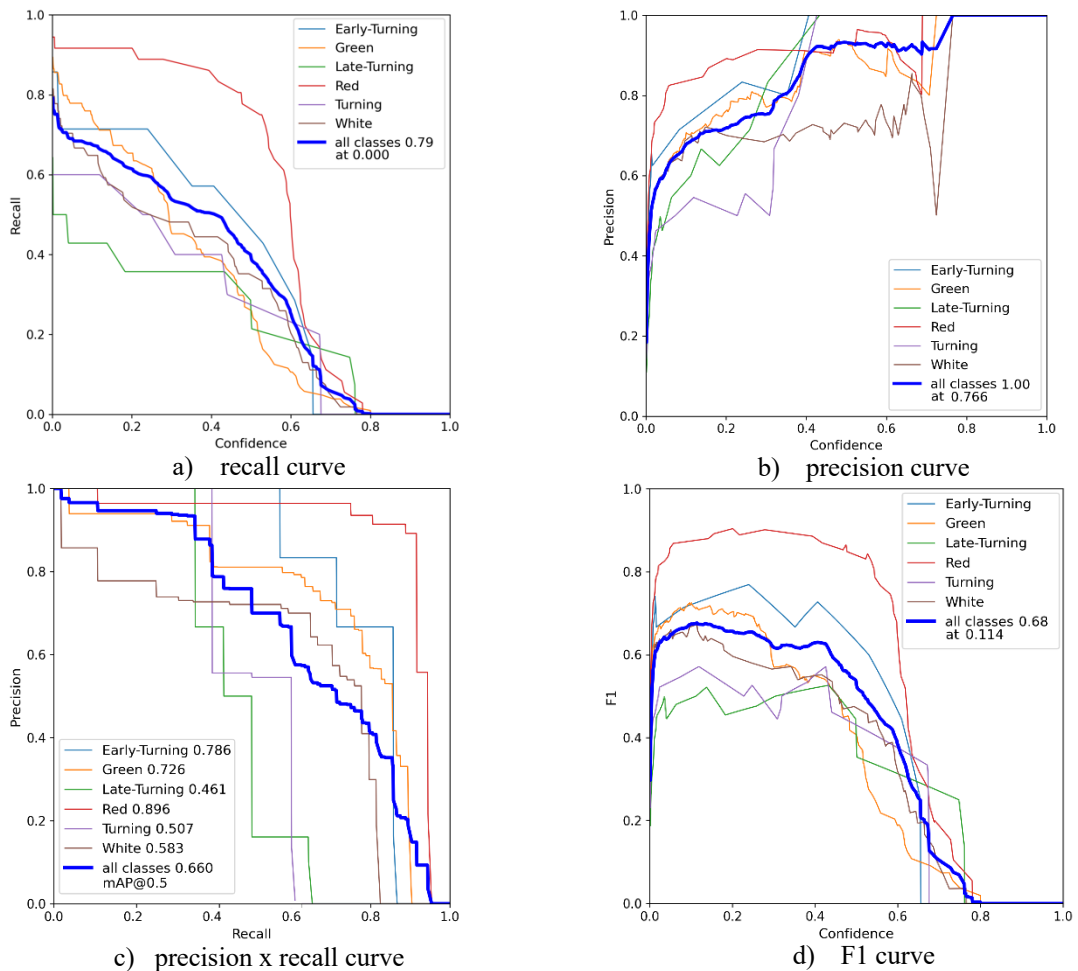


Figure 5. The recall, precision, precision x recall and F1 score curves of validation dataset

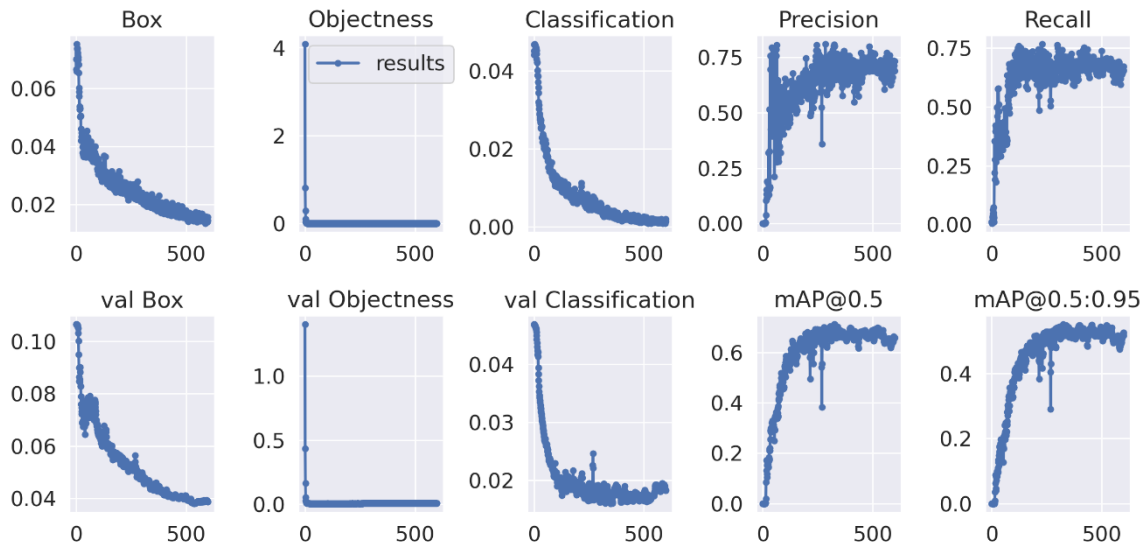


Figure 6. The performance results along the epoch number for training and validation datasets

A comprehensive breakdown of performance metrics across all classes pertaining to the test dataset are shared in Table 3. Notably akin to the validation performance outcomes within Table 2, both the "turning" and "red" categories exhibit the most impressive mAP@0.5 metric values, in contrast to the rest of the classes. The highest performance is obtained by "turning" class because of having only two labels in the test dataset and both of these cases are detected successfully. A higher number of labels of "turning" class would yield a more realistic result. Since the "white" and "green" classes have more than 40 labels and their recall values are not high like "red" and "turning" classes, their mAP@0.5 values are obtained as 0.335 and 0.37 even if their precision values are around seventies. The validation and test results are obtained by a confidence level threshold of 0.25 [29].

The original test dataset have only 2 labels for "early-turning" class and the trained model is observed as not to detect them. In order to get a more balanced result, 2 images having "early-turning" class from the validation dataset is copied to the test data set and thus the total number of the labels are increased to 4. The relative decline of performance of "early-turning" class on the validation dataset with respect to test dataset is because of the noisy structure of the whole dataset especially between the transitional classes like "early-turning", "turning", "late-turning". This sort of noisy datasets are likely to be encountered in the machine learning data ecosystem. The noisy datasets are occasionally handled by the generalization capacity of the state of the art models. However, if some classes are represented only by a few noisy images than this issue should be focused and dataset should be monitored for these classes. Thus, in this study, 2 images from the validation dataset is copied to the test dataset to balance the "early-turning" class performance and obtain a more realistic result.

Another intriguing observation lies in the "turning" class, where the true positive count reaches to 1, and the instances erroneously labeled as background are minimized as 0 derived from the insights emerging from the test dataset's confusion matrix, thoughtfully presented in Figure 7. In tandem, Figure 8 provides a detailed visual representation of recall, precision, precision x recall and F1 score curves corresponding to the test dataset outcomes.

Table 3. Performance results of test dataset for each class

Class	Images	Labels	Precision	Recall	mAP@.5	mAP@.5:.95
all	28	119	0.792	0.575	0.558	0.46
white	28	42	0.631	0.381	0.335	0.27
green	28	47	0.769	0.426	0.37	0.228
early-turning	28	4	1	0.5	0.505	0.455
turning	28	2	1	1	1	0.85
late-turning	28	3	0.5	0.333	0.337	0.303
red	28	21	0.85	0.81	0.804	0.653

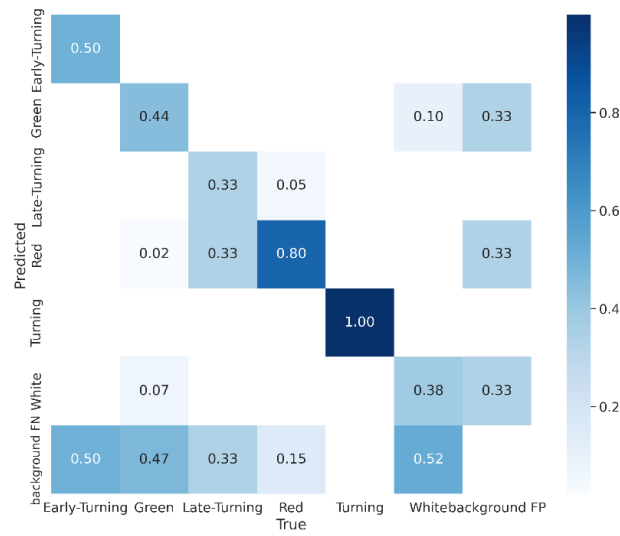


Figure 7. The confusion matrix of test dataset

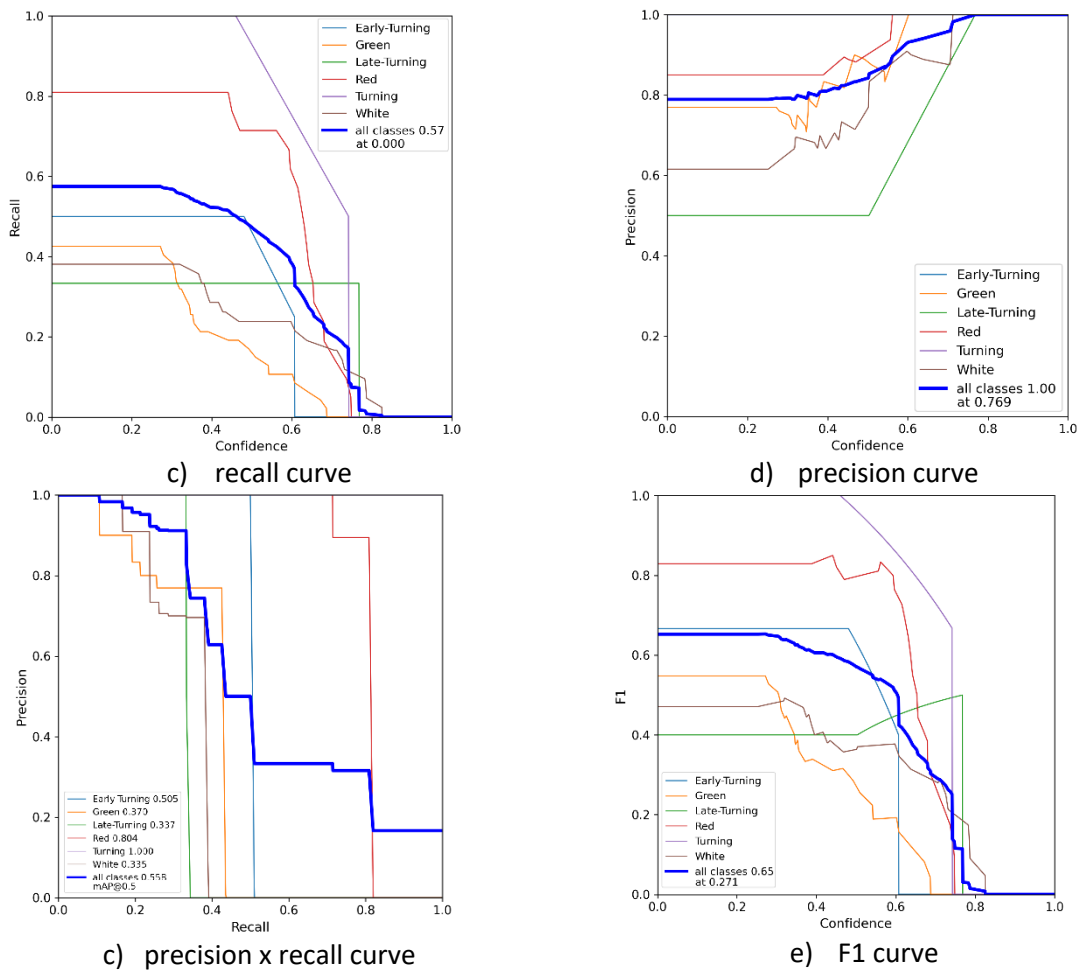


Figure 8. The recall, precision, Precision x Recall and F1 score curves of test dataset

In certain instances, the same images exhibit varying annotations, reflecting the complexities of accurately categorizing strawberries during these intermediary stages. This underscores the need for continual refinement in

both dataset annotation and model development to enhance the robustness and reliability of our detection and classification system. Some instances within the dataset exhibit inconsistent annotations, where identical plants have been labeled differently as shown in Figure 9. This inconsistency introduces challenges to the training and testing processes, as the model must tolerate conflicting labels to establish accurate patterns for classification.

In our study, the sampled images consistently demonstrated impressive detection results for strawberries as shown in Figure 10. For these sampled images, the Yolo-v7 algorithm efficiently identified and localized strawberries within the images, accurately outlining their boundaries with minimal false positives. This level of precision showcases the effectiveness of our approach in robustly identifying and distinguishing strawberries from their background, underscoring its potential for real-world applications in agriculture and food processing.

In our strawberry dataset, it's also important to acknowledge the presence of labeling errors that occasionally affect the accuracy of classification performance and localization boxes. Despite these errors, our model has demonstrated a remarkable ability to still detect many strawberries correctly, often classifying these correctly detected labels as false positives due to the misaligned localization coordinates as shown in Figure 11. Furthermore, the dataset's transitional classes, such as "early-turning," "turning," and "late-turning," present challenges due to ambiguous labels as shown in Figure 11 e) and f).

The impact of extending the training process to 600 epochs in comparison to 100 epochs becomes evident when examining the background false negative values in their respective confusion matrices, as outlined in Table 4. This comparison provides insights into how the model's ability increases to correctly identify the strawberries from the background, particularly those initially missed, evolves as the training duration increases. By analyzing these values, we can gain a deeper understanding of the model's enhanced capacity to distinguish between strawberries and the background, thus highlighting the significance of prolonged training for improved detection accuracy.



a) Ground truth error of validation dataset

b) Ground truth error of validation dataset

Figure 9. Different labeling for identical plants in the Strawberry-DS dataset.

Table 4. Comparison of background false negative values for 100 and 600 epochs training

epochs	early-turning	green	late-turning	red	turning	white
100	1.0	0.9	1.0	0.08	1.0	0.8
600	0.5	0.47	0.33	0.15	0.0	0.52

4.1. Limitations and future work

The potential limitations of this research can be listed as follows:

- Data diversity and generalization capability of model: The trained model by Strawberry-DS dataset might struggle to generalize to entirely new and unforeseen conditions, underrepresented classes and different weather as well as lighting conditions.

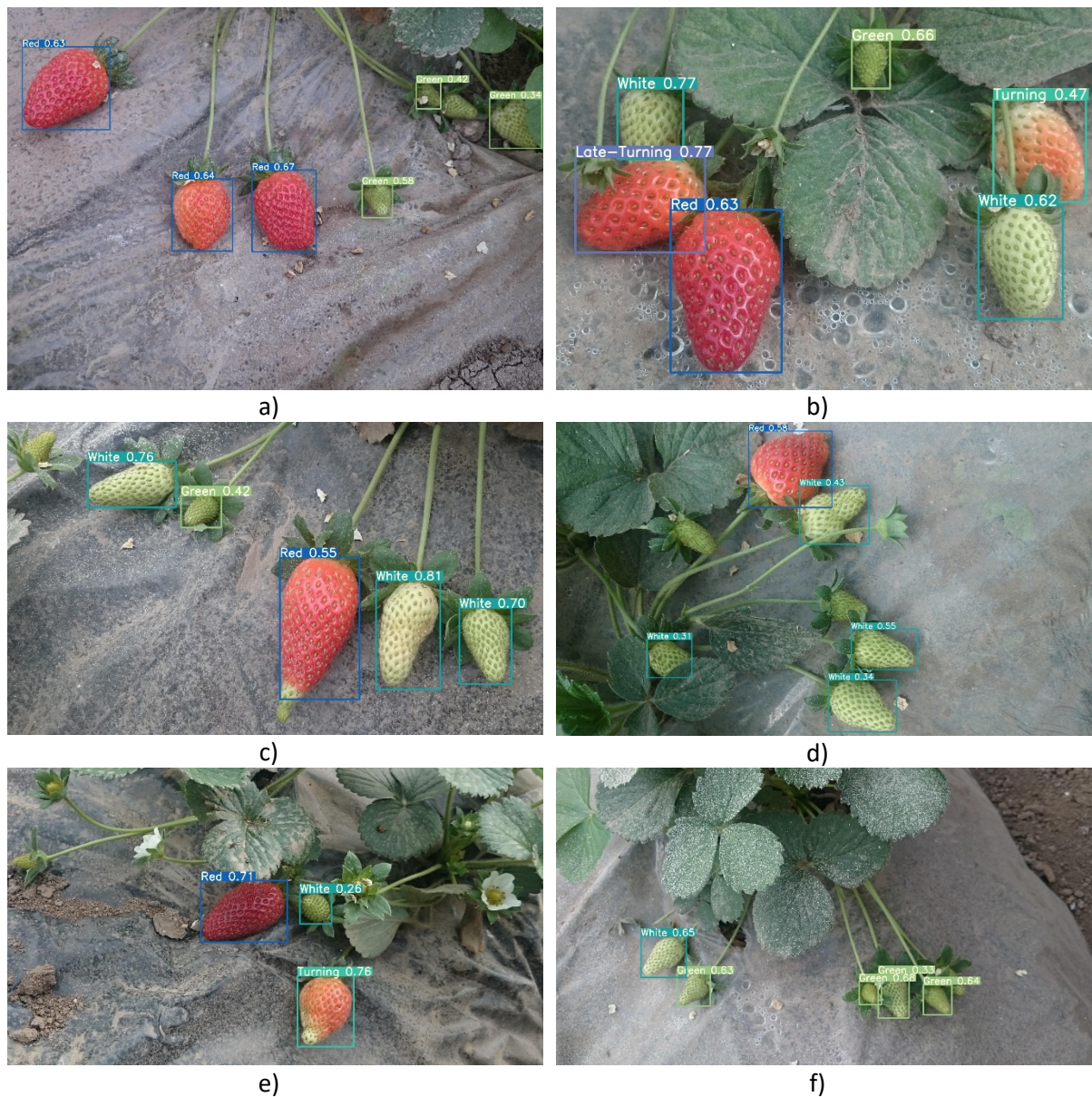


Figure 10. Some sampled images having successful detection results.

- Ambiguity in developmental phases: The performance of the model may be affected when confronted with ambiguous or transitional phases which do not fit neatly into predefined categories.
- Real-time performance and computational resource constraints: In case of deploying the trained model to the environments like edge devices, there may occur some extra limitations in terms of processing power, memory, and energy consumption, which could affect the feasibility of deployment.

The potential improvements of this research can be outlined in the subsequent manner:

- Improved data collection and annotation: Future research can include more other diverse and comprehensive datasets, including extreme scenarios that may not have been previously considered.
- Adapting to the edge devices: The further research direction can focus on optimizing the YOLO-v7 model specifically for edge devices by using techniques like model compression and quantization etc.

- Collaboration of human and AI: In order to tackle the ambiguous phases arises, human input feedback loops and active learning based approaches can be employed to continuously improve model performance.

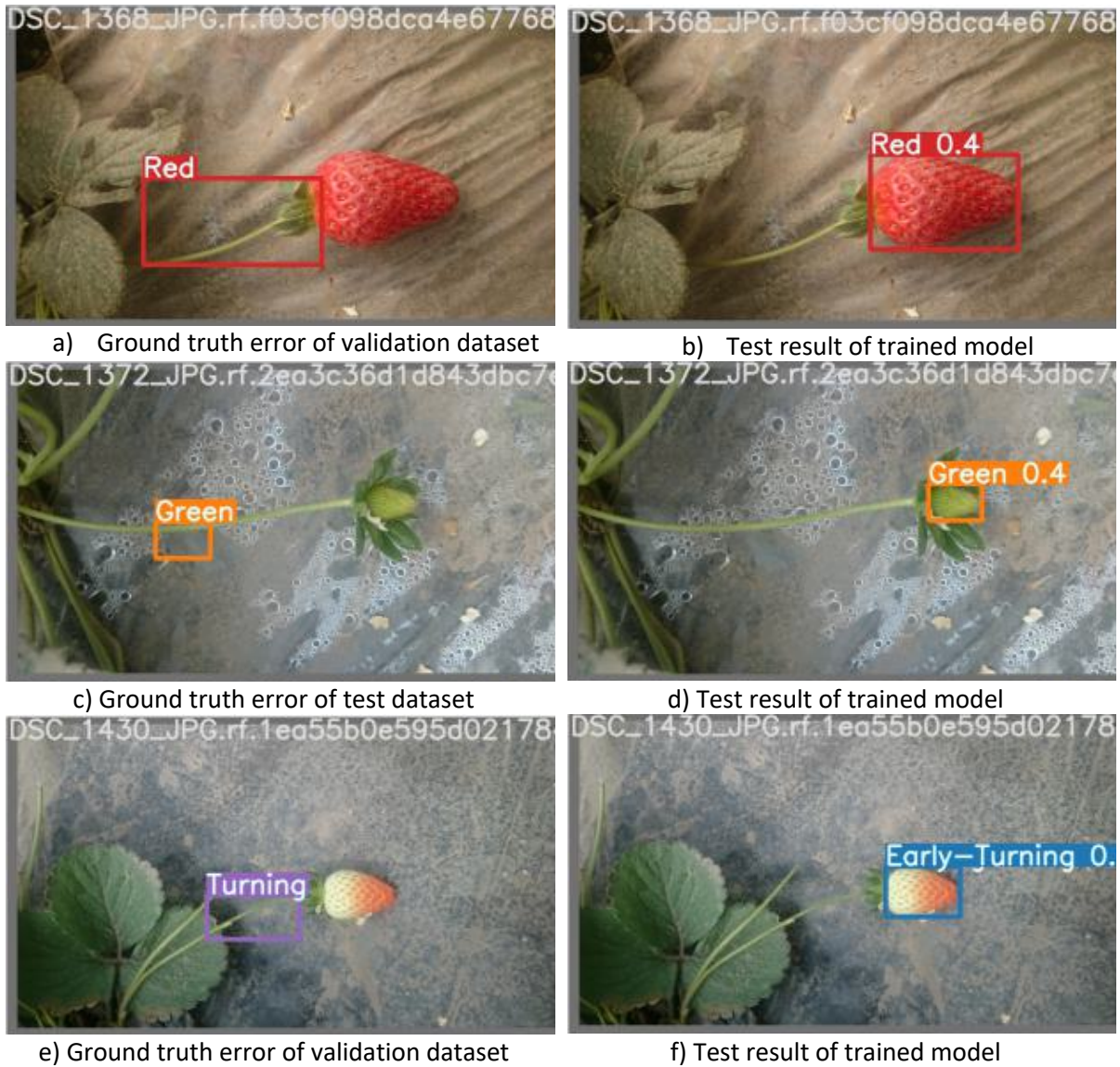


Figure 11. Some sampled localization based labeling errors in the Strawberry-DS dataset.

5. Conclusion

In this proposed study, an automated object detection mechanism is benchmarked to precisely localize and monitor strawberry growth phases. The six classes representing the growth phases of 247 images of Strawberry-DS dataset is localized and classified via the Yolo-v7 model. The classified images are constitute of diverse capturing perspectives and angles as well as imbalanced and noisy labels which stands as an obstacle for an optimal training and testing tasks. The obtained $mAP@.5$ values for the distinct stages of ripeness stand as follows: 0.37, 0.804, 0.335, 1.0, 0.505 and 0.337 respectively for "green", "red", "white", "turning", "early-turning" and "late-turning". The holistic performance metrics across all classes exhibit 0.792, 0.575, 0.558 and 0.46 respectively for precision, recall, $mAP@.5$ and $mAP@.5:.95$. Employing the Yolo-v7 methodology for object detection, the study effectively enables the identification of strawberries across their varying growth phases and the classification of these phases even with a relatively small imaging dataset.

Data Availability

The public Strawberry-DS dataset is publicly available and can be reached from <https://data.mendeley.com/datasets/z6dtfdpzz8/1>

References

- [1] Li Y, Xue J, Zhang M, Yin J, Liu Y, Qiao X, Zheng D, Li Z. YOLOv5-ASFF: A Multistage Strawberry Detection Algorithm Based on Improved YOLOv5. *Agronomy* 2023; 13(7): 1901.
- [2] Baby B, Antony P, Vijayan R. Antioxidant and anticancer properties of berries. *Crit. Rev. Food Sci. Nutr* 2018; 58(15): 2491–2507.
- [3] Zhou C, Hu J, Xu Z, Yue J, Ye H, Yang G. A Novel Greenhouse-Based System for the Detection and Plumpness Assessment of Strawberry Using an Improved Deep Learning Technique. *Front. Plant Sci.* 2020; 11, 559: 1–13.
- [4] He Z, Khana SR, Zhang X, Karkee M, Zhang Q. Real-time Strawberry Detection Based on Improved YOLOv5s Architecture for Robotic Harvesting in open-field environment. *arxiv.org* 2023; [Online]. Available: <http://arxiv.org/abs/2308.03998>.
- [5] Charlton D, Castillo M. Potential Impacts of a Pandemic on the US Farm Labor Market. *Appl. Econ. Perspect. Policy* 2021; 43(1): 39–57
- [6] Lemsalu M, Bloch V, Backman J, Pastell M. Real-Time CNN-based Computer Vision System for Open-Field Strawberry Harvesting Robot. *IFAC-PapersOnLine* 2022; 55(32): 24–29.
- [7] Baygin M, Tuncer T, Dogan S. New pyramidal hybrid textural and deep features based automatic skin cancer classification model: Ensemble DarkNet and textural feature extractor. *arxiv.org* 2022; [Online]. Available: <http://arxiv.org/abs/2203.15090>.
- [8] Yaman O, Tuncer T. Exemplar pyramid deep feature extraction based cervical cancer image classification model using pap-smear images. *Biomed. Signal Process. Control* 2022; 73:103428.
- [9] Baygin M, Yaman O, Barua PD, Dogan S, Tuncer T, Acharya UR. Exemplar Darknet19 feature generation technique for automated kidney stone detection with coronal CT images. *Artif. Intell. Med.* 2022; 127:102274.
- [10] Yaman O, Tuncer T. Bitkilerdeki Yaprak Hastalığı Tespiti için Derin Özellik Çıkarma ve Makine Öğrenmesi Yöntemi. *Fırat Üniversitesi Mühendislik Bilim. Derg.* 2022; 34(1): 123–132.
- [11] Fırat H. Sıkma - Uyarma Artık Ağı kullanılarak Beyaz Kan Hücrelerinin Sınıflandırılması Classification of White Blood Cells using the Squeeze- Excitation Residual Network. *Bilişim Teknolojileri Dergisi* 2023; 16(3):189–205.
- [12] Li S, Zhang S, Xue J, Sun H. Lightweight target detection for the field flat jujube based on improved YOLOv5. *Comput. Electron. Agric.* 2022; 202:107391.
- [13] Qiao Y, Guo Y, He D. Cattle body detection based on YOLOv5-ASFF for precision livestock farming. *Comput. Electron. Agric.* 2022; 204:107579.
- [14] Koirala A, Walsh KB, Wang Z, McCarthy C. Deep learning for real-time fruit detection and orchard fruit load estimation: benchmarking of ‘MangoYOLO. *Precis. Agric.* 2019; 20(6): 1107–1135.
- [15] Ji W, Pan Y, Xu B, Wang J. A Real-Time Apple Targets Detection Method for Picking Robot Based on ShufflenetV2-YOLOX. *Agric.* 2022; 12(6): 1–23.
- [16] Lawal OM. Development of tomato detection model for robotic platform using deep learning. *Multimed. Tools Appl.* 2021; 80(17): 26751–26772.
- [17] Montoya-Cavero LE, Torres RDL, Espinosa AG, Cabello JAE. Vision systems for harvesting robots: Produce detection and localization. *Comput. Electron. Agric.* 2022; 192: 106562.
- [18] Lawal OM. YOLOMuskmelon: Quest for fruit detection speed and accuracy using deep learning. *IEEE Access* 2021; 9:15221–15227.
- [19] Fu X, Li A, Meng Z, Yin X, Zhang C, Zhang W, Qi L. A Dynamic Detection Method for Phenotyping Pods in a Soybean Population Based on an Improved YOLO-v5 Network. *Agronomy* 2022; 12(12): 3209.
- [20] Lawal OM. Study on strawberry fruit detection using lightweight algorithm. *Multimed. Tools Appl.* 2023; [Online]. Available: <https://doi.org/10.1007/s11042-023-16034-0>.
- [21] Mao DH, Sun H, Li XB, Yu XD, Wu JW, Zhang QC. Real-time fruit detection using deep neural networks on CPU (RTFD): An edge AI application. *Comput. Electron. Agric.* 2023; 204:107517.
- [22] Mejia G, Oca AM, Flores G. Strawberry localization in a ridge planting with an autonomous rover. *Eng. Appl. Artif. Intell.* 2022; 119:105810.
- [23] Ren G, Wu T, Lin T, Yang L, Chowdhary G, Ting KC, Ying Y. Mobile robotics platform for strawberry sensing and harvesting within precision indoor farming systems. *J. F. Robot.* 2023; [Online]. Available: <https://doi.org/10.1002/rob.22207>.
- [24] Elhariri E, El-Bendary N, Saleh SM. Strawberry-DS: Dataset of annotated strawberry fruits images with various developmental stages. *Data Br.* 2023; 48:109165.
- [25] Terven J, Cordova-Esparza D. A Comprehensive Review of YOLO: From YOLOv1 to YOLOv8 and Beyond. *arxiv.org* 2023; 1–33. [Online]. Available: <http://arxiv.org/abs/2304.00501>.
- [26] Redmon J, Divvala S, Girshick R, Farhadi A. You Only Look Once: Unified, Real-Time Object Detection. In: *Proc. IEEE Conf. Comput. Vis. Pattern Recognit*; 26 June-1 July 2016; Las Vegas, NV, USA: 779–788.
- [27] Wang CY, Bochkovskiy A, Liao HYM. YOLOv7: Trainable bag-of-freebies sets new state-of-the-art for real-time object detectors. *arxiv.org* 2022; 1–15. [Online]. Available: <http://arxiv.org/abs/2207.02696>.

- [28] Wang CY, Liao HYM, Yeh IH. Designing Network Design Strategies Through Gradient Path Analysis. arxiv.org 2022; [Online]. Available: <http://arxiv.org/abs/2211.04800>.
- [29] “GitHub - WongKinYiu/yolov7: Implementation of paper - YOLOv7: Trainable bag-of-freebies sets new state-of-the-art for real-time object detectors”. [Online]. Available: <https://github.com/WongKinYiu/yolov7> (accessed Aug. 13, 2023).
- [30] Padilla R, Passos WL, Dias TLB, Netto SL, Da Silva EAB. A comparative analysis of object detection metrics with a companion open-source toolkit. *Electron.* 2021; 10(3): 1–28.

Statistical Evaluation of Treatment Compliance In Children With Attention Deficit Hyperactivity Disorder

Duygu MURAT^{1*}, Uğur TEKİN²

¹ Special Child and Adolescent Psychiatry Clinic, İstanbul, Turkey

² Clinic of Child and Adolescent Psychiatry, University of Health Sciences, Bakırköy Dr. Sadi Konuk Training and Research Hospital, İstanbul, Turkey

*¹ duygucalisir44@yahoo.com, ² drutekin@hotmail.com

(Geliş/Received: 16/08/2023;

Kabul/Accepted: 29/08/2023)

Abstract: Attention Deficit Hyperactivity Disorder (ADHD) is a neurodevelopmental disorder. Pharmacological treatment is the first option in the treatment of ADHD. Long-term treatment is required, as the course of the disease often continues throughout life. Long-term adherence to treatment in ADHD is important in terms of reducing the risk of substance use, accidents, and risk-taking behaviours. Medication adherence is very important for the successful outcome of the treatment. In this study, we aimed to evaluate the factors that may affect treatment adherence in the Turkish sample. We found that 39.6% of children with ADHD had high medication adherence accordingly Morisky Medication Adherence Scale. Medication adherence of boys and girls were similar. When the education level of mothers was compared, the education level of mothers with high medication adherence group was higher than those with poor medication adherence group, and this difference was statistically significant ($p=0.013$). We can say that highly educated families who learn that ADHD is a neurodevelopmental disorder and can realize the risks that may arise as a result of being untreated are more careful about drug use.

Key words: Attention Deficit, Hyperactivity, Medication Adherence, Statistical Evaluation.

Dikkat Eksikliği Hiperaktivite Bozukluğu Olan Çocuklarda Tedavi Uyumunun İstatistiksel Değerlendirilmesi

Öz: Dikkat Eksikliği Hiperaktivite Bozukluğu (DEHB) nörogelişimsel bir bozukluktur. DEHB tedavisinde ilk seçenek tedavi farmakolojik tedavidir. Hastalığın seyri çoğu zaman yaşam boyu devam ettiği için uzun süreli tedavi gerekir. DEHB' de tedaviye uzun süreli uyumun olması, madde kullanımı, kaza ve riskli davranışlar riskini azaltabilmektedir. Tedavinin başarılı seyretmesi için ilaç uyumu çok önemlidir. Bu çalışmada tedavi uyumunu etkileyebilecek faktörleri Türkiye örnekleminde değerlendirmeyi amaçladık. Çalışmamızda Morisky İlaç Uyum Ölçeği' ne göre DEHB' li çocukların %39,6'sının ilaç uyumunun yüksek olduğunu saptadık. Kız ve erkek çocukların ilaç uyumu ise benzerdi. Annelerin eğitim durumları karşılaştırıldığında, ilaç uyumu yüksek olan grubun annelerin eğitim düzeyi, ilaç uyumu kötü olan gruba göre daha yüksekti ve bu fark istatistiksel olarak anlamlıydı ($p=0,013$). Sonuç olarak DEHB' nin nörogelişimsel bir bozukluk olduğunu öğrenen ve tedavi edilmediği takdirde ortaya çıkabilecek riskleri fark edebilen eğitim seviyesi yüksek ailelerin ilaç kullanımı konusunda daha dikkatli olduklarını söyleyebiliriz.

Anahtar kelimeler: Dikkat Eksikliği, Hiperaktivite, İlaç Uyumunu, İstatistiksel Değerlendirme.

1. Introduction

Attention Deficit Hyperactivity Disorder (ADHD) is a neurodevelopmental disorder characterized by inattention, hyperactivity and impulsivity. The prevalence of ADHD was found 11% in children and adolescent [1]. In a multi-center study conducted in Turkey included 5830 children, the prevalence of ADHD was found 12.4 % [2]. ADHD symptoms continue in adolescence and adulthood in 40-60% of those diagnosed with ADHD in childhood [3,4]. Pharmacological treatment is the first option in the treatment of ADHD. Stimulants (methylphenidate) and non-stimulants (atomoxetine and guanfacine) are medications with proven effectiveness in the treatment of ADHD. Adding behavioral therapy to drug therapy in ADHD positively affects the course of the disease [5]. Long-term treatment is required, as the course of the disease often continues throughout life.

1.1. Treatment Compliance and Attention Deficit Hyperactivity Disorder

Treatment compliance is defined as the regular and correct use of medication by the patient at the time and amount recommended by the clinician. Factors affecting the treatment compliance may be separated to three factors. The first one is factors related to parents and children, the second one is related to medication type and third one is related to the health system [6]. While the parents who understand that ADHD is a neurobiological

* Corresponding author: duygucalisir44@yahoo.com ORCID Number of authors: ¹ 0000-0001-6372-2930, ² 0000-0001-6720-4292

disease continue the treatment, the others do not even accept the treatment [7]. Parental anxiety about drug side effects makes it difficult to initiate medication for children with ADHD [8]. Therefore, in addition to providing medical treatment to children with ADHD, it is also important to provide psychoeducation to parents. Factors related to children such as older age, comorbid Oppositional Defiant Disorder and reluctant to take medication affects negatively the treatment compliance. Side effects of drugs used in ADHD, such as loss of appetite, insomnia, and increased irritability, also worsen drug compliance [9]. Difficulties in reaching a child and adolescent psychiatrist in Turkey and making appointments to continue the follow-up also complicate treatment compliance. Having information about ADHD, the effects and side effects of drugs, being under the age of 12 and being a girl, easily accessible to the health system increase treatment compliance [10]. In recent years, the use of pharmacotherapy in children and adults with ADHD has been increasing [9,11]. Long-term adherence to treatment in ADHD is important in terms of reducing the risk of substance use, accidents, and risk-taking behaviors [12,13]. Although the effectiveness of drug therapy in ADHD is high, medication non-compliance is common in both young people and adults, with rates varying between 13 and 87% [14]. Poor adherence to treatment may result in persistence of ADHD symptoms. Poor adherence to treatment decreases the child's functionality and the clinician's evaluation of the effectiveness of the treatment, while increasing health expenditures [15]. Medication adherence is very important for the successful outcome of the treatment.

The long or short-acting drug used in ADHD, the duration of treatment and drug side effects affect adherence with treatment [16,17]. The patient's age, gender, and co-morbidities also affect treatment adherence [18,19]. In a study on those who could not continue their ADHD treatment between the ages of 6-45, it was determined that the age with the highest probability of discontinuation treatment was 15-21 [20].

There are many factors that impair treatment compliance in ADHD and it is difficult to evaluate [21]. In this study, we aimed to evaluate the factors that may affect treatment adherence in the Turkish sample. If we can understand the factors that impair medication adherence, it will be possible for us to take the necessary precaution for long-term treatment in ADHD. Children with ADHD will have better long-term academic success, social relationships and quality of life, if treatment continues for a long time. They will not be affected by the negative consequences of ADHD.

2. Material and Method

2.1. Participants

Ethics committee approval of the study was obtained from the ethics committee of Bakırköy Dr. Sadi Konuk Training and Research Hospital. Our study group consisted of 96 children diagnosed with ADHD. Parents and their children who volunteered to participate in the study and those who wanted to continue the treatment at least 6 months were included. Children with Neurological Disease, Autism Spectrum Disorder, Mental Retardation and Participants who refused to use of medications were excluded from the study.

Sociodemographic information form, Morisky Medication Adherence Scale and Conners' Parent Scale Long Form were given to the families participating in the study. In the Sociodemographic data form, the child's age, gender, age of the parents, education and employment status of the mother and father, marital status of the mother and socio-economic level of the family were asked. According to the data of the Morisky Medication Adherence Scale, participants were divided into 2 groups as high medication adherence and poor medication adherence. High adherence group consisted of children with medium and high scores, and the poor adherence group consisted of children with low scores in Morisky Adherence Scale. Using the Clinical Global Impression Scale (CGI), clinicians evaluated disease severity, improvement, and severity of adverse events.

2.2. Measurements

2.2.1. Clinical Global Impression Scale (CGI)

Clinical Global Impression Scale consists of 3 fields, which include the disease severity, improvement and severity of the side effect. The Clinical Global Impression Severity of disease (CGI-S) was developed by the American National Institute of Mental Health and published in 1976. It was developed for the purpose of evaluating the clinical course of psychiatric disorders. CGI-S is a seven-value Likert-type scale. It is evaluated between 1 and 7 points according to the severity of the disease at the time the scale was filled; 1 = Normal, not ill, 2 = Borderline mental illness, 3 = Mildly ill, 4 = Moderately ill, 5 = Significantly ill, 6 = Severely ill, 7 = Severe degree ill. Second part (Clinical Global Impression-Recovery) shows how much the patient has changed since the beginning of treatment. It is useful to evaluate between 1 and 7 points. 1=Healed a lot, 2=Much improved, 3=Minimal recovery, 4= No Change 5=Minimum worsening, 6=Very worsening, 7=It has deteriorated a lot. The third part of the scale is the Clinical Global Impression-Side Effect, it is evaluated over 4 points. These are; 1.

None, 2. Does not significantly affect the functionality of the patient, 3. Significantly affects the functionality of the patient, 4. Influencing at a level that negates the benefits of the therapeutic effect.

2.2.2. Morisky Medication Adherence Scale

It is a self-filled scale measuring drug compliance developed by Donald E. Morisky [22]. The scale consists of four two-choice (yes/no) closed-ended questions. If all questions are answered “no”, medication adherence is considered high, if “yes” is answered for one or two questions, medication adherence is considered medium, if yes to three or four questions, medication adherence is considered low. The validity and reliability study in our country was carried out by Yılmaz to measure adherence to antipsychotic treatment [23].

2.2.3. Conners' Parent Rating Scale Long Form

Conners' Parent Rating Scales are the most used tools for evaluating problem behaviors in children/adolescents, especially ADHD, monitoring the effects of the treatment. The scale developed by Conners consists of seven subscales: Cognitive Problems-Inattention, Oppositional, Hyperactivity, Anxiety-Shyness, Perfectionism, Social Problems, and Psychosomatics [24]. The validity and reliability study in our country was carried out by Kaner [25].

2.3. Statistical Analysis

SPSS version 24 was used to analyze the data of the study. The normal distribution of continuous variables between the two groups was evaluated using the Shapiro Wilk Test. Parametric tests were used for data with normal distribution, and nonparametric tests were used for data with non-normal distribution. The Independent Sample t-test was used to compare the continuous variables with normal distribution with the group, and Mann-Whitney-U test was used to compare quantitative data without parametric distribution. Chi-square test was used to compare the categorical variables in the data. Spearman correlation analysis was used for the evaluation of the relationship between treatment adherence scale scores and disease severity.

3. Results

Total 96 children and adolescents with ADHD between the ages of 8 and 13 were included in the study. The mean age of the children and adolescents participating in the study was 10.4 years. 12.5% of the participants (n: 12) were female and 87.5% (n: 84) were male. We divided 96 children and adolescents with ADHD into 2 groups according to their scores on the Morisky Medication Adherence Scale. The study group consist of 38(39.6%) participant with high medication adherence and 58 (60.4%) participants with poor medication adherence. When we compared mothers and children's age of the high and poor medication adherence groups, there was no statistically significant difference ($p>0.05$). The educational status of the mothers was divided into pre-high school and high school and above. When the education level of mothers in two study group (high and poor medication adherence) was compared, the education level of mothers with high medication adherence group was higher than those with poor medication adherence group, and this difference was statistically significant ($p=0.013$).

Table 1. Comparing medication adherence and maternal education levels.

		High Medication Adherence		Poor Medication Adherence		
		n	%	n	%	p
Mother's Education	Pre-High School	16	43.2	40	69	0.013
	High School and University	21	56.8	18	31	

χ^2 test

As it can be seen in the Figure 1 below, the education level of the mothers of children with high medication adherence was higher than the other.

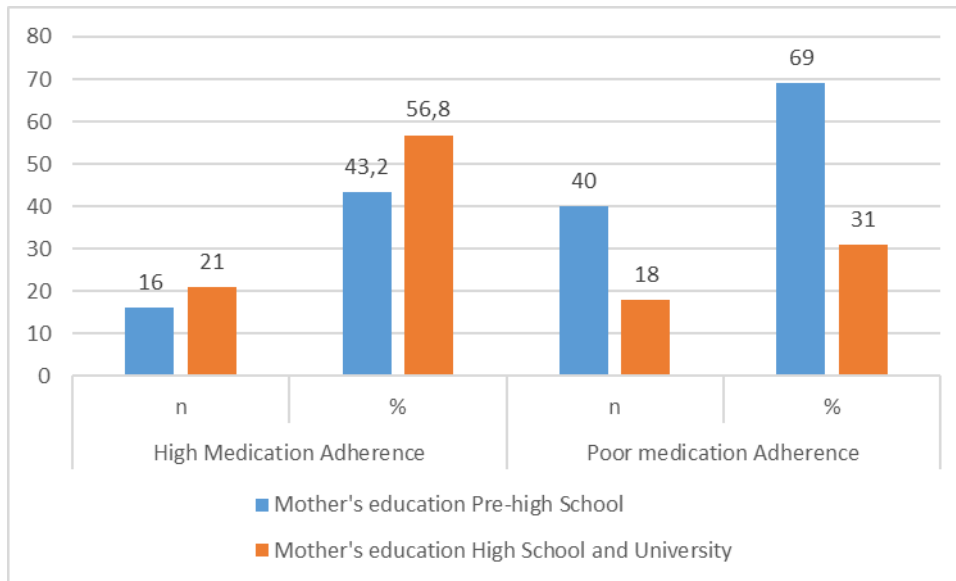


Figure 1. Medication adherence and maternal education levels.

When the father's education levels of those with high and poor medication adherence group compared, no statistically significant difference was found between the education levels of the fathers ($p=0.557$). When the working status of the mothers and fathers of the groups with high and poor drug compliance were compared separately, no statistically significant difference was found between the working status of the mothers and fathers ($p>0.05$).

When the groups (high and poor medication adherence) were compared in terms of marital status of the mother, income of the family, and gender of the child, there was no statistical significant difference between the groups ($p>0.05$).

The mean score value of the subtests of the Conners' Parent Rating Scale was as seen in the Figure 2 below. Those with high medication compliance are shown in blue column, and those with poor medication compliance are shown in red column. Medication compliance was similar according to Conners' subtest scores.

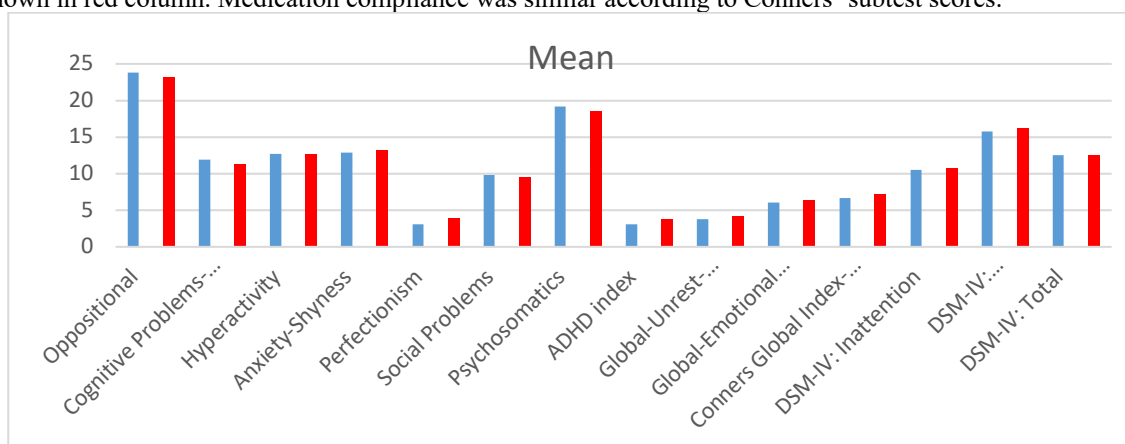


Figure 2. Conners' Parent Rating Scale scores and Medication Adherence.

There was no statistically significant difference between the Conners' Parent Rating Subscales scores of participants with high medication adherence and poor adherence groups.

Table 2. Conners' Parent Rating Scale scores and Medication Adherence.

Conners' Parent Rating Scale	Medication Adherence	n	Mean	Std. Deviation	Std. Error Mean	p values
Oppositional	High	38	23.79	10.81	1.753	0.775
	Poor	58	23.16	10.5	1.379	
Cognitive Problems-Inattention	High	38	11.89	6.5	1.055	0.683
	Poor	58	11.34	6.37	0.837	
Hyperactivity	High	38	12.71	6.42	1.042	0.944
	Poor	58	12.62	5.82	0.764	
Anxiety-Shyness	High	38	12.84	5.2	0.844	0.723
	Poor	58	13.24	5.5	0.722	
Perfectionism	High	38	3.11	2.19	0.355	0.121
	Poor	58	3.88	2.48	0.325	
Social Problems	High	38	9.84	4.91	0.796	0.733
	Poor	58	9.52	4.31	0.565	
Psychosomatics	High	38	19.21	7.25	1.176	0.683
	Poor	58	18.57	7.68	1.009	
ADHD index	High	38	3.05	2.67	0.433	0.273
	Poor	58	3.79	3.52	0.463	
Global-Unrest-Impulsivity	High	38	3.82	2.92	0.474	0.588
	Poor	58	4.19	3.52	0.462	
Global-Emotional Variation	High	38	6.03	3.8	0.616	0.713
	Poor	58	6.31	3.61	0.474	
Conners' Global Index-Total	High	38	6.68	3.86	0.626	0.561
	Poor	58	7.21	4.56	0.599	
DSM-IV: Inattention	High	38	10.55	6.34	1.029	0.892
	Poor	58	10.72	5.87	0.771	
DSM-IV: Hyperactivity-Impulsivity	High	38	15.79	8.08	1.31	0.816
	Poor	58	16.19	8.28	1.087	
DSM-IV: Total	High	38	12.53	6.34	1.029	0.986
	Poor	58	12.55	6.9	0.906	

Independent Sample T test

In our study, there was no statistically meaningful difference between severity of side effects and medication adherence.

Table 3. Side Effect Severity and Medication Adherence.

			Medication Adherence		Total	P value
			High	Poor		
Side Effect Severity	none at all	n	16	22	38	0.718
		% within medication adherence	47.1%	38.6%	41.8%	
	not affect	n	14	28	42	
		% within medication adherence	41.2%	49.1%	46.2%	
	effect	n	4	7	11	
		% within medication adherence	11.8%	12.3%	12.1%	

χ^2 test

As it can be seen in the Figure 3 below, medication compliance was poor in all 3 groups, regardless of the severity of drug side effects.

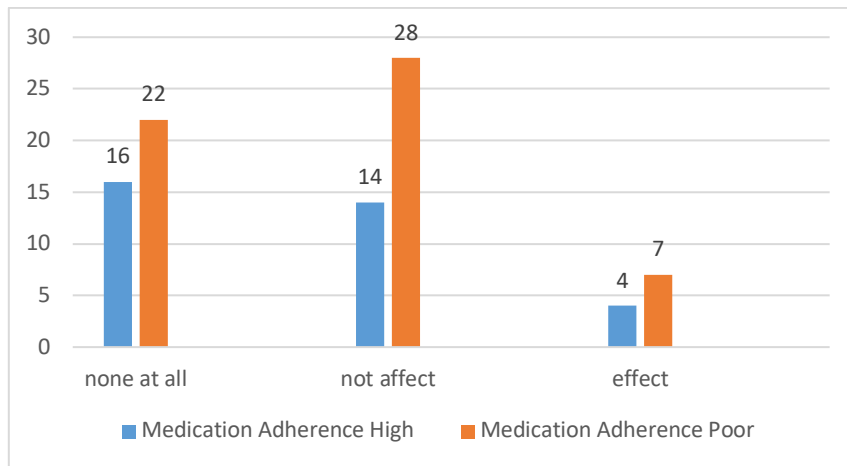


Figure 3. Side Effect Severity and Medication Adherence.

When we examined whether there is a relationship between the scores in the Morisky Medication Adherence Scale and the parameters in the Clinical Global Impression Scale, with Spearman's rho correlation analysis; there was no statistical significant correlation.

Table 4. Correlation analysis of Morisky Medication Adherence Scale and Clinical Global Impression Scale.

		CGI-Side Effect	CGI-Severity	CGI-Recovery
Medication Adherence Scores	r	-0.064	-0.133	-0.203
	p	0.544	0.207	0.055
	n	91	92	90

Spearman's rho correlation analysis

* Correlation is significant at the 0.01 level (2-tailed).

There was no correlation between the Conners' Parent Scale subtest and Morisky Medication Adherence scores.

4. Discussion

In our study, we found that 39.6% of children with ADHD had high medication adherence accordingly Morisky Medication Adherence Scale. In two different studies on drug adherence in ADHD, drug compliance was found in 21% and 45.6% of cases, respectively [26,27]. In our study, medication adherence of boys and girls was similar. In a study conducted in Korea, medication adherence of girls and boys was found to be similar [19]. The fact that our study did not have an effect of gender on medication adherence is compatible with the Korean study. In our study, the ages of children with high medication adherence and poor adherence were similar. In the literature, some of the studies indicated that small aged children had high medication adherence [28,29], and also showed that older aged adolescent had poor medication adherence [30]. In most of the studies, it was found that medication adherence decreased with increasing age. The reason why we did not find similar results in our study may be due to the close age ranges of the children. In the transition from childhood to adolescence as autonomy is gained, medication compliance decreases. The education level of mothers of children with high medication adherence was higher. We can say that highly educated families who learn that ADHD is a neurodevelopmental disorder and can realize the risks that may arise as a result of being untreated are more careful about drug use. Zheng at al. showed that in the training program about ADHD to parents and teachers, learning that ADHD is neurobiological disease and that medication therapy is the first choice increased treatment compliance [31]. We found that there is no correlation between the scores of Conners' Parent Scale subtest, Clinical Global Impression Scale and drug compliance separately. Navak at al. showed that drug adherence was found to be better in patients with low ADHD severity [32]. The inconsistency of the results of our study with the literature may be due to the methodological differences of the studies. Important limitations of our study were that we did not evaluate medication adherence according to the type of drug (stimulant and non-stimulant), the presence of psychopathology in the family and comorbidity of children.

In conclusion, adherence to treatment is an important factor in the treatment of ADHD, as in many medical and psychiatric conditions. In this multifaceted issue, our study indicates that high maternal education has a positive effect on the treatment of ADHD in children. Based on this finding, it can be speculated that mothers with higher education have better understanding of the nature and consequence of ADHD and how it can be managed.

However, given the vitality of treatment compliance in ADHD, more research is needed on our understanding of this issue and possible ways to cope with non-adherence.

References

- [1] Kemper A.R, Maslow G.R, Hill S, Namdari B, N.M AL, Goode AP, Sanders GD. Attention deficit hyperactivity disorder: diagnosis and treatment in children and adolescents Durham: Europe PMC, 2018.
- [2] Ercan E.S, Unsel-Bolat G, Tufan A.E, Karakoc Demirkaya S, Bilac O, Celik G, ... & Ünal F. Effect of impairment on the prevalence and comorbidities of attention deficit hyperactivity disorder in a national survey: nation-wide prevalence and comorbidities of ADHD. *Journal of Attention Disorders* 2022; 26(5): 674-684.
- [3] Klein R.G, Mannuzza S, Olazagasti M.A.R, Roizen E, Hutchison J. A, Lashua E. C, & Castellanos F. X. Clinical and functional outcome of childhood attention-deficit/hyperactivity disorder 33 years later. *Arch. Gen. Psychiatry* 2012; 69(12): 1295-1303.
- [4] Brown T.E. ADHD comorbidities: Handbook for ADHD complications in children and adults. Arlington: American Psychiatric Pub, 2009.
- [5] Barnard-Brak L, Roberts B, Valenzuela E. Examining breaks and resistance in medication adherence among adolescents with ADHD as associated with school outcomes. *Journal of Attention Disorders* 2020; 24(8): 1148-1155.
- [6] Kamimura-Nishimura K. I, Brinkman W. B, & Froehlich T. E. Strategies for improving ADHD medication adherence. *Current psychiatry* 2019; 18(8): 25.
- [7] Charach A, Fernandez R. Enhancing ADHD medication adherence: challenges and opportunities. *Current psychiatry reports* 2013; 15: 1-8.
- [8] Khan M. U, & Aslani P. Exploring factors influencing medication adherence from initiation to discontinuation in parents and adolescents with attention deficit hyperactivity disorder. *Clinical pediatrics* 2020; 59(3): 285-296.
- [9] Raman S. R, Man K. K, Bahmanyar S, Berard A, Bilder S, Boukhris T, ... & Wong I. C. Trends in attention-deficit hyperactivity disorder medication use: a retrospective observational study using population-based databases. *The Lancet Psychiatry* 2018; 5(10): 824-835.
- [10] Soutullo C. A, Are F, & Schield-Grant S. Factors associated with adherence to pharmacological treatment of attention deficit hyperactivity disorder (ADHD): preliminary review. *Medicina* 2023; 83: 27-31.
- [11] Dopheide J. A. The role of pharmacotherapy and managed care pharmacy interventions in the treatment of ADHD. *Am J Manag Care* 2009; 15(5 Suppl): S141-50.
- [12] Mannuzza S, Klein R. G, Bessler A, Malloy P, & LaPadula M. Adult outcome of hyperactive boys: Educational achievement, occupational rank, and psychiatric status. *Arch. Gen. Psychiatry* 1993; 50(7): 565-576.

- [13] Shaw M, Hodgkins P, Caci H, Young S, Kahle J, Woods A. G, & Arnold L. E. A systematic review and analysis of long-term outcomes in attention deficit hyperactivity disorder: effects of treatment and non-treatment. *BMC medicine* 2012; 10: 1-15.
- [14] Rao K, Carpenter D. M, & Campbell C. I. Attention-deficit/hyperactivity disorder medication adherence in the transition to adulthood: associated adverse outcomes for females and other disparities. *Journal of Adolescent Health* 2021; 69(5): 806-814.
- [15] Ahmed R, Aslani P. Attention-deficit/hyperactivity disorder: an update on medication adherence and persistence in children, adolescents and adults. *Expert Rev. Pharmacoeconomics Outcomes Res* 2013; 13(6): 791-815.
- [16] Lachaine J, Beauchemin C, Sasane R, & Hodgkins P. S. Treatment patterns, adherence, and persistence in ADHD: a Canadian perspective. *Postgraduate medicine* 2012; 124(3): 139-148.
- [17] Wehmeier P. M, Dittmann R. W, & Banaschewski T. Treatment compliance or medication adherence in children and adolescents on ADHD medication in clinical practice: results from the COMPLY observational study. *ADHD Attention Deficit and Hyperactivity Disorders* 2015; 7: 165-174.
- [18] Barner J. C, Khoza S, & Oladapo A. ADHD medication use, adherence, persistence and cost among Texas Medicaid children. *Curr. Med. Res. Opin.* 2011; 27(sup2): 13-22.
- [19] Bhang S. Y, Kwack Y. S, Joung Y. S, Lee S. I, Kim B, Sohn S. H, Hwang J. W. Factors that affect the adherence to ADHD medications during a treatment continuation period in children and adolescents: a nationwide retrospective cohort study using Korean Health Insurance data from 2007 to 2011. *Psychiatry Investigation* 2017; 14(2): 158.
- [20] Zetterqvist J, Asherson P, Halldner L, Långström N, Larsson H. Stimulant and non-stimulant attention deficit/hyperactivity disorder drug use: total population study of trends and discontinuation patterns 2006–2009. *Acta Physiol. Scand* 2013; 128(1): 70-77.
- [21] Adler L.D, Nierenberg A. A. Review of medication adherence in children and adults with ADHD. *Postgraduate medicine* 2010; 122(1): 184-191.
- [22] Morisky D.E, Green L.W, Levine D.M. (Concurrent and predictive validity of a self-reported measure of medication adherence. *Medical care* 1986; 1: 67-74.
- [23] Yılmaz S. *Psikiyatri Hastalarında İlaç Yan Etkileri ve İlaç Uyumu. Yüksek Lisans Tezi, İstanbul Üniversitesi, Sağlık Bilimleri Enstitüsü, 2004.*
- [24] Conners C.K, Sitarenios G, Parker J. D, Epstein J. N. The revised Conners' Parent Rating Scale (CPRS-R): factor structure, reliability, and criterion validity. *Journal of abnormal child psychology* 1998; 26: 257-268.
- [25] Kaner S, Büyükoztürk Ş, İşeri E, Ak A, Özaydın L. Conners. Anababa Dereceleme Ölçeği Yenilenmiş Uzun Formu: Faktör Yapısı, Geçerlik Ve Güvenirlik Çalışması. *Çocuk ve Gençlik Ruh Sağlığı Dergisi* 2011; 18(1):45-58
- [26] Safavi P, Saberzadeh M, Tehrani A. M. Factors associated with treatment adherence in children with attention deficit hyperactivity disorder. *Indian J. Psychol. Med.* 2019; 41(3): 252-257.
- [27] Emilsson M, Gustafsson P.A, Öhnström G, Marteinsdottir I. Beliefs regarding medication and side effects influence treatment adherence in adolescents with attention deficit hyperactivity disorder. *European child & adolescent psychiatry* 2017; 26: 559-571.
- [28] Thiruchelvam D, Charach A, Schachar R.J. Moderators and mediators of long-term adherence to stimulant treatment in children with ADHD. *Journal of the American Academy of Child & Adolescent Psychiatry* 2001; 40(8): 922-928.
- [29] Gau S.S.F, Chen S.J, Chou W.J, Cheng H, Tang C.S, Chang H.L, Huang Y. S. National survey of adherence, efficacy, and side effects of methylphenidate in children with attention-deficit/hyperactivity disorder in Taiwan. *Journal of Clinical Psychiatry* 2008; 69(1):131.
- [30] Atzori P, Usala T, Carucci S, Danjou F, Zuddas A. Predictive factors for persistent use and compliance of immediate-release methylphenidate: a 36-month naturalistic study. *J. Child Adolesc. Psychopharmacol.* 2009; 19(6): 673-681.
- [31] Zheng X, Shen L, Jiang L, Shen X, Xu Y, Yu G, & Wang Y. Parent and teacher training increases medication adherence for primary school children with attention-deficit/hyperactivity disorder. *Front. Pediatr.* 2020; 8: 486353.
- [32] Nayak A.S, Nachane H.B, Keshari P, Parkar S.R, Saurabh K.H, & Arora M. Prescription patterns and medication adherence in preadolescent children with attention deficit hyperactivity disorder. *Indian Journal of Psychiatry* 2021; 63(3): 274.

MVSR Normalization Algorithm Method for Improving Vehicle License Plate Recognition

Sertaç YAMAN¹, Yavuz EROL^{2*}

¹ Department of Electrical and Electronics Engineering, Faculty of Engineering, Hakkari University, Hakkari, Türkiye

² Department of Electrical and Electronics Engineering, Faculty of Engineering, Firat University, Elazığ, Türkiye

*¹ sertacyaman@hakkari.edu.tr, ² yerol@firat.edu.tr

(Geliş/Received: 26/08/2023;

Kabul/Accepted: 01/09/2023)

Abstract: Image processing and embedded systems are used in many applications such as object recognition, robotic applications, autonomous and remote control systems developed for the defense industry, medical applications, face recognition, and vehicle license plate recognition. Many vehicle license number plate detection methods are not effective under vehicle license plate images have a degree of rotation or low resolution images. Thus, we used MVSR normalization algorithm to detect vehicle license plate recognition for better accuracy and lower computational cost. The MVSR normalization algorithm, Mean-Variance-Softmax-Rescale processes respectively is applied for high-accuracy real-time vehicle license plate detection.

Key words: MVSR algorithm, vehicle license plate recognition, normalization, artificial neural network.

Araç Plaka Tespitinin İyileştirilmesine Yönelik MVSR Normalleştirme Algoritması Yöntemi

Öz: Görüntü işleme ve gömülü sistemler; nesne tanıma, robotik uygulamalar, savunma sanayi için geliştirilen otonom ve uzaktan kontrol sistemleri, medikal uygulamalar, yüz tanıma, araç plaka tanıma gibi birçok uygulamada kullanılmaktadır. Dönme derecesine sahip veya düşük çözünürlüklü görüntülere sahip araç plaka görüntüleri altında birçok araç plakası tespit yöntemi etkili değildir. Bu nedenle, daha iyi doğruluk ve daha düşük hesaplama maliyeti için araç plakası tanımayı tespit etmek amacıyla MVSR normalleştirme algoritmasını kullandık. Yüksek doğruluklu, gerçek zamanlı araç plakası tespiti için sırasıyla MVSR normalleştirme algoritması, Ortalama-Varyans-Softmax-Yeniden Ölçeklendirme işlemleri uygulanmıştır.

Anahtar kelimeler: MVSR algoritması, araç plaka tespiti, normalizasyon, yapay sinir ağı.

1. Introduction

Vehicle license plate recognition systems are the feature extraction in the image processing applications. It is also both software and hardware-based applications designed to extract vehicle license plate characters from an image or a group of images (video). Therefore, the efficient application of license plate recognition systems has an important place.

In the literature, the study of Nagare [1], they used two different artificial neural networks to determine license plate numbers. After the image is obtained from the camera, some pre-processes (graying, morphological operations, etc.) are applied, and the license plate region is obtained. If the pixels in the same column in the plate region obtained after this step are white, the image cutting process is performed. In this way, pictures with only one license plate character are obtained. After this stage, classification of plate characters is carried out with the proposed LVQ (Learning Vector Quantization) neural network model. Car number plate characters were detected with an accuracy rate of 66.67% in the backward propagation learning model and 94.44% in the LVQ model proposed.

In the study carried out by Zhai and his working group [2], the detection of the plate region in the image was performed using the FPGA embedded system platform. The algorithm proposed in this study was first implemented in the MATLAB environment and then implemented on the RC240 FPGA development board. As a first step, the three-dimensional color image was converted to a grayscale image, then a vertical 3x3 Sobel filter was applied to this image. After this stage, they applied morphological closing with 3x22 structural elements and then morphological opening using 3x5 structural elements. They detected each plate region in the image with an accuracy rate of 99.1% and an average of 3.8 ms.

Indravadanbhai and his working group [3] performed plate reading applications used the OCR method. The disadvantages of this method are that the characters are close to each other, parts of the image with text are in the shade, and some characters are similar, for example, characters such as B and 8, O and zero, I and 1, A and 4, K and X, C and G, D and O. affect the reading accuracy. They carried out studies on image preprocessing (filtering, image enhancement, morphological operations, etc.) and character separation stages to reduce these effects.

* Corresponding author: yerol@firat.edu.tr. ORCID Number of authors: ¹ 0000-0002-0208-8320, ² 0000-0001-6953-0630

Car number plate standards are vary by sizes, colors, and languages used (latin, arabic, chinese characters, etc.). In the studies carried out by Du, Massaud and their study group [4, 5], the recognition of plate characters consisting of Egyptian Arabic letters was carried out. For the detection of the plate region,

- Obtaining the image through the camera
- Converting a color image to a grayscale image
- Implementation of Sobel edge detection algorithm
- Realization of morphological opening and closing operations
- Filling the closed areas in the image
- Applying the 5x5 Median filter to the image

Detection of the plate region by eliminating the closed regions that do not fit the standard plate dimensions.

After the plate region was determined, morphological dilation was applied to increase the distances between the characters in order to distinguish the plate characters appropriately. After the plate characters were separated, the image of each character was converted to the specified standard dimensions. By using the template matching technique, the obtained character images were identified using the statistical correlation (correlation) method. They were defined by the normalized cross-correlation technique between pairs of images representing two separate images, which respectively specify the image to be searched and the template. This system is designed using GUI and UDP under MATLAB software. The proposed system was implemented with 100 image sets with 91% accuracy.

Zhang and his work group [6] used the Support Vector Machine (SVM: Support Vector Machine). This model separates classes from each other by vector space-based classification. After detecting the plate area using the SVM model, the characters were separated from each other using the projection technique and the plate numbers were determined. Convolutional neural network and two classifiers supporting vector machine for multi-channel processing are designed to recognize Chinese characters, numbers and alphabet letters respectively. The images obtained from the camera, and later the plate region was extracted using image processing algorithms. The separation of the characters was carried out using the projection technique. Numerical and alphabetic characters were classified using the CNN model and the Chinese and SVM model. In this study, classification of license plate characters was performed with an accuracy of 99.2%.

Zhai and Bensaali [7] improved the parsing process of the characters after obtaining the license plate region in the image in order to read the license plate faster and more accurately. They used an advanced character parsing algorithm based on pixel projection and morphological operations. In this proposed system, with the application of image processing algorithms, the detection of the plate region, and the separation of the characters with the projection technique were performed with different data sets. After the character separation process, the characters in the plate region were determined by using the OCR technique.

Fan et al. [8], advanced Driver Assistance Systems (ADAS) were developed for road lane detection, automatic parking and detected unmanned vehicles. In this study, image processing algorithms are embedded on TMS320C6678 SoC and they work on lane detection and ADAS systems. The proposed linear strip detection system consists of two main parts; image pre-processing applications and Hough transform are used. In the pre-processing stage, the Gaussian filter is used to reduce small details by blurring the image, removing noise. Then, edge detection operations were carried out by applying the Sobel filter. Algorithm, SoC DSP TMS320C6678 multi-core processor, 1242×375 image resolution, 81 fps speed and 94.1% accuracy rate of tol lane lines were detected. In the study carried out by Calderon and his working group [9], they performed the plate determination process using a computer and FPGA card. It was realized by recognizing the yellow color of the plate region in the HSV plane using a special algorithm for Colombian plates.

In the study by Promrit and Wannarat [10], Real time road lane was determined using FPGA (Zybo board) embedded system platform. In this study, HT and Hyperbola, Bézier Curve, Dot plot, Dot plot and Hyperbola algorithms were compared and lane detection was performed. It has been determined which algorithm is more suitable in real-time applications. Four algorithms are experimentally compared to find the appropriate algorithm for real-time stripe detection on images acquired at 1920×1080 pixel resolution and 60 fps on FPGA Zybo card. Dot graph and Hyperbola technique yielded better results than the other two algorithms. Using these two techniques, the road lane was detected with 0% error rate. They showed that Point graph and Hyperbola algorithms are better for real-time lane detection in applications to be implemented on the FPGA platform.

In the study performed by Li and his study group [11], two sequential CNN models were used to determine the plate region and characterization. The advantage of this method is that after the license plate region (plate present/no license plate) is detected, missing character recognition will be eliminated due to errors that may occur in the character parsing process. A stepwise classification process was performed using two different CNN models. The location of the characters on the image with the first CNN model and the parts without the plate region with the second CNN model were eliminated and the plate region was determined. In this study, classification operations were performed on NVIDIA Tesla K40c GPU with 6GB memory using MatConvNet.

However, this method is not suitable for real-time detection of license plate characters due to its data processing speed. The training database used in this study is divided into three different subgroups for detection and recognition:

- AC: The camera is fixed and the vehicle in the image is at a constant or slow speed
- LE: The vehicle in the image was taken due to a traffic violation
- RP: The vehicle in the image was taken with a motion camera

Xie and his work group [12], problems such as remote acquisition of vehicle images or the plate area not perpendicular to the camera were suggested by CNN-based YOLO (You Only Look Ones) ANN model, after determining the angle of the license plate area relative to the camera and bringing it to a vertical position, the license plate area was determined by character separation method. The characters in the region were tried to be determined. In the original YOLO model, it only estimates the center coordinate, height, and width of each object. In this study, the proposed method is used to determine the angle information and the rotation angle of a given license plate image. Classification processes were performed with accuracy rates of 99.51%-99.43% and 99.46%, respectively, in three different data sets used for license plate tests.

In the study carried out by Hendry and Chen [13], vehicle license plate characters were tried to be determined by using the YOLO-darknet learning model. A six-character Taiwan license plate reading was performed. The characters are determined sequentially by scrolling on the image with the sliding window method. The results of three different image datasets are compared using the proposed model, and the best results were obtained in the AC dataset. The data processing rate for each plate was 800ms-1s, and the system detected an average of 98.22% accuracy in plate detection and 78% of plate characters in recognition of plate characters.

Viju [14], the vehicle license plate recognition system was realized by using K-Means (KM) clustering algorithm and Optical Character Recognition (OCR) technique. After detecting the plate region using basic image processing algorithms such as the median filter and KM, they determined the plate characters with the OCR technique. Yousif et al. [15] proposed a new method for plate recognition in image processing algorithms and an optimized neutronic set (NS) based on genetic algorithm (GA). Using the NS set, they were able to better identify the plate images. They applied a k-means clustering algorithm to segment the characters in the plate region and a correlated component labeling analysis (CCLA) algorithm by grouping the appropriate pixels to extract each character effectively. After the plate characters were separated, all the pictures were converted to the specified size, and then the characters were matched and the plate was determined by using the statistical cross correlation method. Plate characters were determined with an accuracy rate of 96.67% in high resolution images and 94.27% in low resolution images.

Zhang and his work group [16], plate identification was performed using CycleGAN (Generative adversarial networks) model and LSTM (Long short-term memory) based array decoder. With this model, the characters were tried to be determined by using the image similarity feature in the images where the plate region could not be determined exactly. The stages of the proposed model;

- Detection of the plate region by applying the trained YOLOv2 model to the input image
- Detected license plate regions, feature matrices are obtained with a thirty-layer Xception network
- An intermediate feature map with the Xception model for detecting license plate characters is removed
- An LSTM model is used to detect license plate characters with these two feature matrices.

In the study carried out by Agbeyangi and his working group [17], license plate characters were determined using the Optical Character Recognition (OCR) technique using Open Computer Vision (OpenCV) open source libraries using Raspberry Pi. In the study performed by Fernandes and his working group [18], they used Tiny YOLOV3 to detect the plate region and OCR technique to determine the characters in the plate region. Using Jetson TX2 development board for two different data sets, plate characters were detected with 96.87% and 90.56% accuracy rates. In the study carried out by Izidio and his working group [19], they developed a license plate recognition system for Brazil using the CNN model. Tiny YOLOV3 and a second CNN model with an accuracy of 98.43% of the plate characters were used to determine the license plate region.

Castro and his work group [20], they used OpenVINO, an image processing-based artificial intelligence platform developed by Intel, to perform license plate recognition. They performed the separation and recognition of license plate characters by using the single shot detector (SSD) for their own work by extracting the features in the image with the convolutional neural network. With this method, faster plate characters can be determined by using fewer parameters. The results of license plate recognition and character separation of the proposed model are given. Plate characters were detected in 14 ms using a twelve-core Intel Xeon CPU (2.60 GHz) computer and OpenVINO, and 66ms using a Raspberry Pi.

In the study carried out by Weihong and Jiayang [21], the camera used, uneven lighting, unfixed shooting angle, different weather conditions (fog, rain, snow, etc.), the time the image was acquired (night, day), motion blur, and the pollution rate of the license plate area. In this study, suggestions and studies were compared in the

realization of license plate reading in pictures obtained in bad conditions. Ma and Zhang [22], the vehicle logo was determined by using the CNN structure in order to eliminate the errors that may occur while determining the places that may be the license plate area. Thus, they focused on the plate area and analyzed the plate numbers.

Table 1. Applications in the literature of vehicle license plate recognition systems

Recognition of plate area	Character separation	Character Recognition	Platforms	Accuracy	Study
Color conversion, morphological operations	projection technique	NN, LVQ NN	-	66%, 94.44%	[1]
Color conversion, edge detection, morphological operations	Connected Component Analysis (CCA)	OCR	MATLAB, FPGA	99%	[2]
Color conversion, edge detection, morphology operations	Morphology, projection technique	Template matching	MATLAB	91%	[4, 5]
Basic image processing techniques	projection technique	CNN, SVM	-	99.2%	[6]
Color conversion, morphological operations	projection technique	OCR	MATLAB, FPGA	96.2%, 97.7%	[7]
CNN	projection technique	CNN	NVIDIA Tesla K40c	97.75%	[11]
R-CNN	-	-	MATLAB	100%	[23]
YOLO-darknet	-	-	GPU K40	99.5%, 99.43%, 99.46%	[12]
YOLO-darknet	-	-	Nvidia GTX970 GPU	98.2%	[13]
K-Means	projection technique	OCR			[14]
Basic image processing techniques, Morphological operations	Neutrosophic set, K-means,	character matching	MATLAB	96.67%, 94.27%	[15]
YOLO	Xception	LSTM	-	97.3%, 98.3%, 91.9%	[16]
YOLO	-	OCR	Jetson TX2	96.87%, 90.56%	[17, 18, 19]

In Table 1, the methods used in the literature for license plate recognition are compared. It is observed that license plate identification rates are higher when using the open source libraries and embedded system platforms with GPU structure. Performing the determination of the plate region with deep learning models (YOLO, R-CNN, CNN, etc.) increases the accuracy rate.

2. Material and Method

Normalization is one of the commonly used techniques in image processing. These techniques are generally used as an image pre-processing step in applications such as improving the image, reducing the noise on the image and changing the colour distribution and making it occupy less space in the memory [23].

2.1. MVSR normalization technique

In the normalization techniques used in general, the normalized pixel values of the image can have positive or negative pixel values, and negative pixel values are eliminated in some cases (uint8 transformation, etc.). In order not to eliminate the effect of negative pixels as a result of the normalization process, the MVSR normalization technique is recommended. All detail about this technique is given reference [24].

$$\mu_{MVSR} = \frac{1}{M} \sum_{i=1}^M x_i \quad (1)$$

$$\sigma_{MVSR}^2 = \frac{1}{M} \sum_{i=1}^M (x_i - \mu_{MVSR})^2 \quad (2)$$

$$x_i = \frac{x_i - \mu_{MVSR}}{\sqrt{\sigma_{MVSR}^2 + \delta}} \quad (3)$$

$$S(x)_i = \frac{e^{x_i}}{\sum_j e^{x_j}} \quad (4)$$

$$r_i = \frac{S(x)_i}{\max(S(x)_i)} * 255 \quad (5)$$

MVSR Normalization processes are shown in equation 1-5. After the inversion process is applied to the images, new pixel values are obtained by using the mean value of the pixels in equation 1, variance calculation in equation 2, and mean and variance values in equation 3. In order not to eliminate negative value pixels in the new pixels obtained, it is aimed to associate all pixel values with each other by using the softmax activation function given in equation 4. The values obtained after applying Softmax range from 0-1 to 0-255, and the pixel values for the new image were obtained by using equation 5.

2.2. License plate detection and character separation with standard image processing techniques

Considering the disadvantages of license plate recognition applications and the related systems (hardware and software) that should be used for license plate recognition, they are quite costly systems. As the distance between the license plate and the camera decreases in the images obtained by the camera, the cost of the license plate recognition systems decreases.

In license plate recognition systems, license plate identification processes begin when vehicles enter the reading area. The process of determining the license plate consists of three basic processes. The correct detection of the license plate depends on the successful execution of these processes.

- Detection of the plate area
- Separation of characters in the license plate region
- Recognition of license plate characters

The vehicle license plate area was determined by applying image processing techniques on the images that are at different angles to the camera and obtained at a right angle to the camera. With the use of standard image processing techniques, accurate determinations can be made depending on the distance and angle information between the camera and the plate area in the detection of the license plate.

It was performed using standard image processing techniques on the image obtained from different angles. However, it is not sufficient to use basic image processing techniques in detecting the license plate region. Therefore, it is recommended to use different techniques (deep learning-based).

2.3 Detection of vehicle plate region and separation of characters with MVSR technique

It should be considered that the disadvantages of license plate recognition applications and the structures (hardware and software) that should be used for license plate recognition are quite costly systems. As the distance between the license plate and the camera decreases in the images obtained by the camera, the cost of the license plate recognition systems decreases.

Detection of the license plate area on vehicle images obtained from different angles and obtained from Microsoft Research Cambridge Object Recognition Image Database [25] and its stages are shown in Figure 2. Stages of detecting the plate region;

- Converting the original image to a grayscale image
- Application of MVSR normalization technique to grayscale image
- Obtaining the black-and-white image with the threshold value application
- Inclusion of the parts that can be the candidate license plate area in the rectangular regions
- Detection of candidate plate regions by plate aspect ratio

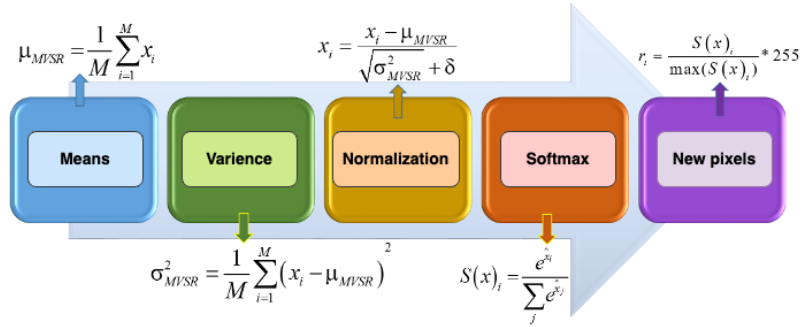


Figure 1. MVSR normalization technique

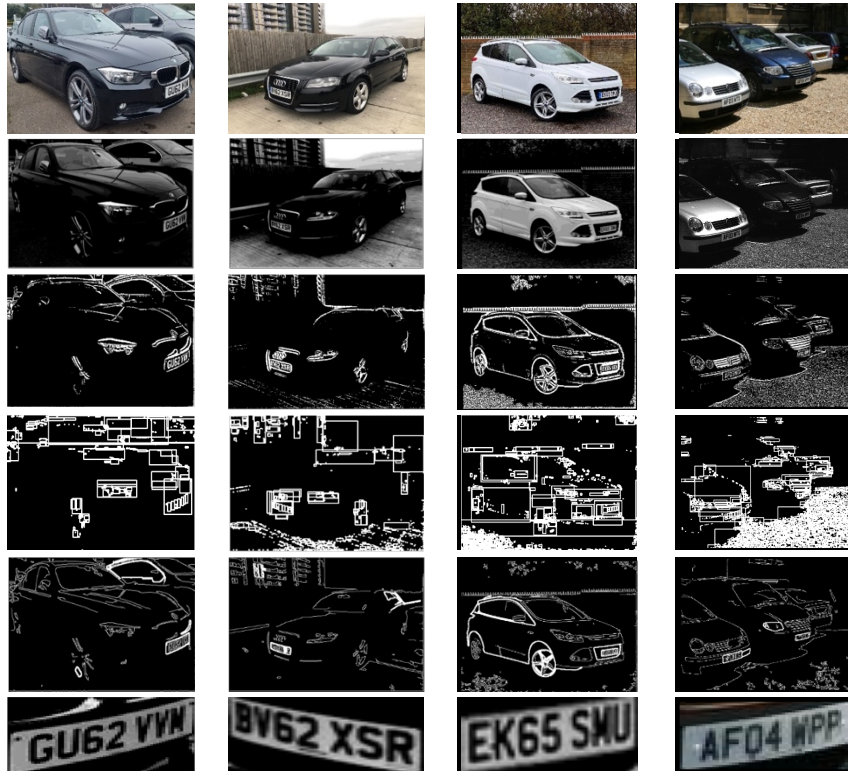


Figure 2. Detection of license plates with different angles by MVSR normalization

The operations of removing the plate region from the image were performed. When the license plate area detection processes were performed without applying the MVSR normalization technique, which is the 2nd step, in the vehicle license plate determination process shown with the step above, the detection of the license plate region could not be performed. However, after applying MVSR normalization, detection of license plate regions can be performed in vehicle images taken from different angles. The determination of the plaque region in the images obtained from different angles was achieved at a rate of 95%.

After the candidate plate regions are determined in Figure 2, at this stage, the sizes of the obtained candidate plate regions are equalized. After applying the adaptive herbaceous algorithm, whose threshold value changes

according to the image, to the candidate regions, an image consisting of black and white pixels will be formed and thus blurring will be eliminated. By applying the morphological opening process to these regions, the distances between the objects in the image are increased (connections are broken), and then the white pixels that do not separate from each other in the row and column are enclosed in a rectangle. Images containing more or less rectangles than the maximum number of characters (seven) found in Turkey's private license plates [26] will be eliminated and the plate region will be determined or image(s) with shapes that cannot be plate region will be obtained.

Table 2. Comparison of detection of license plate area with different image processing techniques

Detection of plate area	Seperation the characters	Accuracy	Studies
Color conversion, morphological operations	projection technique	66%	[1]
Color conversion, edge detection, morphological operations	Connected Component Analysis (CCA)	99%	[2]
Color conversion, edge detection, morphology operations	Morphology, projection technique	91%	[4, 5]
Basic image processing techniques	projection technique	99.2%	[6]
Color conversion, morphological operations	projection technique	96.2%	[7]
MVSR	projection technique	95%	Present study

In Table 2, a comparison of different image processing techniques and applications of detecting license plate area in the literature is given. By using standard image processing techniques in the detection of the plate region, the detection of the plate region was carried out at lower regions. In applications where high percentages of candidate plate regions are realized, there is very little distance between the camera and the plate region and there is no background noise.

In applications carried out using deep learning models (YOLO, R-CNN and CNN etc.), the detection of the license plate area can be achieved at very high rates. In this respect, it is seen that the efficiency of the proposed technique is higher when compared to the applications in the literature performed with only the image normalization technique and the detection of the plate region using the proposed MVSR normalization technique. In the process of detecting the license plate area, the license plate areas that could not be detected in standard methods were determined by the proposed method.

2.4. Classification of license plate characters using CNN model

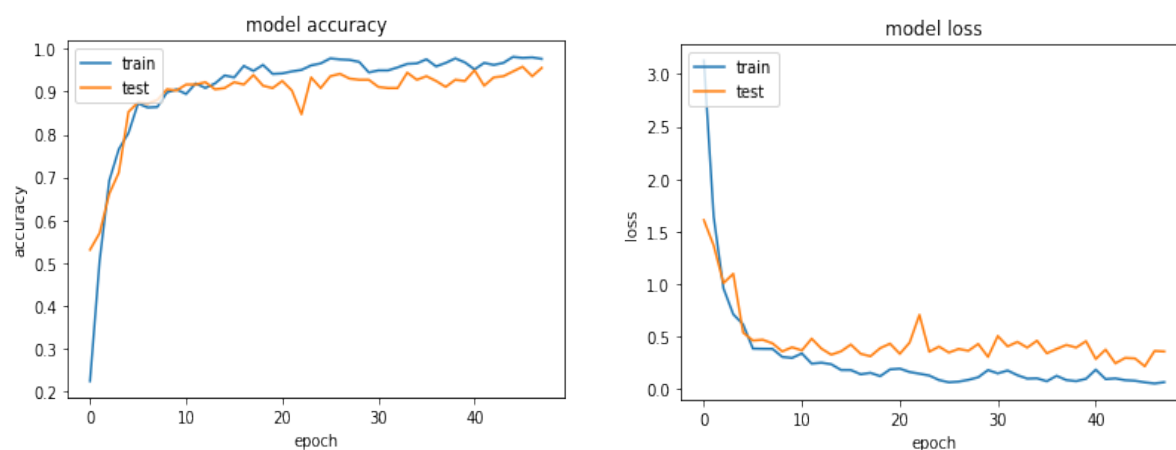
In the license plate recognition system, a convolutional neural network (CNN) model was used to find the license plate region and to determine the characters in the plate region after the characters were separated. Images for this model tutorial are taken from vehicle images. The dimensions of each image obtained were rearranged as 32x32x3.

The structure of the CNN model used in the training of thirty-three different characters (ten numbers and 23 letters) that can be found in the license plate area is shown in Table 3. Batch-Norm technique and ReLU activation function are used after convolution process in convolution layers (Conv1...). The classification process in the output layer is performed using the softmax activation function. The mean square error is used in the calculation of the error function.

At the separation of the vehicle license plate character process, each character will be passed through the model one by one and the detection process will be carried out. The accuracy of the generated CNN model will also determine the result of the license plate recognition system. Therefore, the model training result should be high. CNN model, 1240 images of 32x32 pixels, consisting of letters and numbers, were classified with 48 cycles (Epoch). Figure 3 show the accuracy and loss graphs of the license plate characters, depending on the number of model cycles. As a result of the training, the model accuracy rate was 98.54% and the loss was 0.074.

Table 3. Design of the CNN model created for plate characters

Layers	Layer Configurations			
	S	N	W	H
Input	-	-	32	32
Conv1	3x3	32	32	32
Conv2	3x3	32	32	32
Conv3	3x3	64	32	32
Max-pool.	2x2	-	16	16
Conv3	3x3	128	16	16
Max- pool.	2x2	-	8	8
Conv4	3x3	64	8	8
Max- pool.	2x2	-	4	4
Flattening.1	1024			
Flattening.2	512			
Flattening.3	256			
Output	33			


Figure 3. CNN model accuracy and loss

3. Conclusions

In the realization of the detection the license plate area, in the applications performed using standard image processing techniques, in some cases, it is not possible to perform the license plate detection operations under difficult conditions.

The MVSR normalization technique was used instead of the gaussian and bilateral filtering techniques used in determining the license plate region. By using this method, the number of candidate regions without license plate regions has been considerably reduced. Thus, the processing load to be performed has been reduced and less energy consumption and faster detection of the license plate area has been achieved. In addition, in difficult conditions (the camera sees the license plate area at different angles), the rate of obtaining the license plate area has been increased.

During the filtering (gaussian, bilateral, etc.) phase of the determination of the license plate area, some license plate areas that could not be determined before were successfully detected with the application of the MVSR normalization technique. Thus, after applying the proposed MVSR normalization, the detection of the plate region was achieved with 95% accuracy in some images that could not be determined by negative effects such as the distance and angle of the plate region relative to the camera. The results obtained with the application

of MVSR normalization. When compared with the other applications in the literature, better results were obtained than the applications performed with only standard image processing techniques.

The use of basic image processing algorithms is not recommended in detecting the license plate region. As the distance between the camera and the license plate increases, the number of regions that can be plate regions will increase, so it will be difficult to detect the actual plate region and cannot be found. The MVSR normalization technique was used instead of gaussian and bilateral filtering techniques in determining the license plate region. By using the studied method, the number of candidate regions without license plate regions has been considerably reduced. Thus, the processing load to be performed has been reduced and faster vehicle plate area detection processes have been carried out with less energy consumption. After applying the proposed MVSR normalization, the detection of the license plate region was achieved with 95% accuracy in images that could not be determined by standard image processing techniques with negative effects such as the distance and angle of the plate region relative to the camera. However, it is recommended to detect plate region determination processes using deep learning models (R-CNN, CNN, etc.).

Acknowledgement

This study was produced from the PhD thesis of Sertaç Yaman.

References

- [1] Nagare AP. License plate character recognition system using neural network. *International Journal of Computer Applications* 2011; 25(10): 36-39
- [2] Zhai X, Bensaali F, Ramalingam S. Real-time license plate localisation on FPGA. *IEEE Comput. Soc. Conf. Comput. Vis. Pattern Recognit. Work., IEEE Computer Society* 2011; 14–19.
- [3] Patel C, Patel A, Patel D. Optical character recognition by open source OCR tool tesseract: A case study. *International Journal of Computer Applications* 2012; 55(10): 50-56.
- [4] Du S, Ibrahim M, Shehata M, Badawy W. Automatic license plate recognition (ALPR): A state-of-the-art review. *IEEE Trans. Circuits Syst. Video Technol.* 2013; 23: 311–325.
- [5] Massoud MA, Sabee M, Gergais M, Bakhit R. Automated new license plate recognition in Egypt. *Alexandria Eng. J.* 2013; 52(3): 319–326.
- [6] Zang D, Chai Z, Zhang J, Zhang D, Cheng J. Vehicle license plate recognition using visual attention model and deep learning. *Journal of Electronic Imaging* 2015; 24(3): 033001.
- [7] Zhai X, Bensaali F. Improved number plate character segmentation algorithm and its efficient FPGA implementation. *J. Real-Time Image Process* 2015; 10: 91–103.
- [8] Fan R, Prokhorov V, Dahnoun N. Faster-than-real-time linear lane detection implementation using SoC DSP TMS320C6678. *IST 2016 IEEE Int. Conf. Imaging Syst. Tech. Proc.*; 2016; pp. 306–311.
- [9] Calderon JAF, Vargas JS, Pérez-Ruiz A. License plate recognition for Colombian private vehicles based on an embedded system using the ZedBoard. *2016 IEEE Colombian Conference on Robotics and Automation (CCRA)*; 2016; Bogota, Colombia. pp. 1-6.
- [10] Promrit P, Suntiamorntut W. Design and development of lane detection based on FPGA. *2017 14th International Joint Conference on Computer Science and Software Engineering (JCSSE)*; 2017; NakhonSiThammarat, Thailand. pp. 1-4.
- [11] Li H, Wang P, You M, Shen C. Reading car license plates using deep neural networks. *Image Vis. Comput.* 2018; 72: 14–23.
- [12] Xie L, Ahmad T, Jin L, Liu Y, Zhang S. A new CNN-based method for multi-directional car license plate detection. *IEEE Trans. Intell. Transp. Syst.* 2018; 19: 507– 517.
- [13] Hendry, Chen RC. Automatic License plate recognition via sliding-window darknet-YOLO deep learning. *Image Vis. Comput.* 2019; 87: 47–56.
- [14] Viju VR, Radha. License plate recognition based on K-means clustering algorithm. *Intell. Syst. Ref. Libr. Springer* 2019; pp. 23–29.
- [15] Yousif BB, Ata MM, Fawzy N, Obaya M. Toward an optimized neutrosophic k-means with genetic algorithm for automatic vehicle license plate recognition. *IEEE Access.* 2020; 8: 49285–49312.
- [16] Zhang L, Wang P, Li H, Li Z, Shen C, Zhang Y. A Robust attentional framework for license plate recognition in the wild. *IEEE Transactions on Intelligent Transportation Systems*, 2020; 22(11): 6967-6976
- [17] Agbeyangi AO, Alashiri OA, Otunuga AE. Automatic identification of vehicle plate number using Raspberry Pi. *Int. Conf. Math. Comput. Eng. Comput. Sci. (ICMCECS)*; 2020; Institute of Electrical and Electronics Engineers Inc. pp. 1-4.
- [18] Fernandes LS, Silva FHS, Ohata EF, Medeiros A, Neto AVL, Nogueira YLB, Rego PAL, Filho PPR. A Robust

- automatic license plate recognition system for embedded devices. *Lect. Notes Comput. Sci. (Including Subser. Lect. Notes Artif. Intell. Lect. Notes Bioinformatics)*. Springer Science and Business Media Deutschland GmbH 2020; 226-239.
- [19] Izidio DMF, Ferreira AP, Medeiros HR, Da EN, Barros S. An embedded automatic license plate recognition system using deep learning. *Des. Autom. Embed. Syst.* 2020; 24: 23–43.
 - [20] Castro-Zunti RD, Yépez J, Ko SB. License plate segmentation and recognition system using deep learning and OpenVINO. *IET Intell. Transp. Syst.* 2020; 14: 119–126.
 - [21] Weihong W, Jiaoyang T. Research on license plate recognition algorithms based on deep learning in complex environment. *IEEE Access.* 2020; 8: 91661–91675.
 - [22] Ma L, Zhang Y. Research on vehicle license plate recognition technology based on deep convolutional neural networks. *Microprocessors and Microsystem* 2021; 82: 103932.
 - [23] Rafique AM, Pedrycz W, Jeon M. Vehicle license plate detection using region-based convolutional neural networks. *Soft Computing* 2018; 22: 6429-6440.
 - [24] Yaman S, Karakaya B, Erol Y. A novel normalization algorithm to facilitate pre-assessment of Covid-19 disease by improving accuracy of CNN and its FPGA implementation. *Evolving Systems*. Springer Berlin Heidelberg 2023; 8(14): 581-591.
 - [25] Microsoft. Microsoft Research Cambridge Object Recognition Image Database, 2021. [Online].
 - [26] Bengio Y. Practical recommendations for gradient-based training of deep architectures, *Lecture notes in computer Science*. Berlin, Heidelberg: Springer, 2012.

COPYRIGHT RELEASE FORM

TURKISH JOURNAL OF SCIENCE AND TECHNOLOGY (TJST) Published by Firat University

Firat University, Fen Bilimleri Enstitüsü Müdürlüğü
Turkish Journal of Science & Technology Editörlüğü
Elazığ-TURKEY,
Manuscript title:

Full names of all authors (in order to appear on manuscript):

Name, address etc. of corresponding author:

ID Number: Telephone:

E-mail: Mobile phone:

The author(s) warrant(s) that:

- a) the manuscript submitted is his/her/their own original work;
- b) all authors participated in the work in a substantive way and are prepared to take public responsibility for the work;
- c) all authors have seen and approved the manuscript as submitted;
- d) the manuscript has not been published and is not being submitted or considered for publication elsewhere;
- e) the text, illustrations, and any other materials included in the manuscript do not infringe upon any existing copyright or other rights of anyone. Notwithstanding the above, the Contributor(s) or, if applicable the Contributor's Employer, retain(s) all proprietary rights other than copyright, such as

- a) patent rights;
- b) to use, free of charge, all parts of this article for the author's future works in books, lectures, classroom teaching or oral presentations;
- c) the right to reproduce the article for their own purposes provided the copies are not offered for sale.

However, reproduction, posting, transmission or other distribution or use of the article or any material contained therein, in any medium as permitted hereunder, requires a citation to the Journal and appropriate credit to Firat University as publisher, suitable in form and content as follows:

Title of article, author(s), journal title and volume/issue, Copyright© year.

All materials related to manuscripts, accepted or rejected, including photographs, original figures etc., will be kept by Turkish Journal of Science and Technology editority for one year following the editor's decision. These materials will then be destroyed. I/We indemnify Firat University and the Editors of the Journals, and hold them harmless from any loss, expense or damage occasioned by a claim or suit by a third party for copyright infringement, or any suit arising out of any breach of the foregoing warranties as a result of publication of my/our article. I/We also warrant that the article contains no libelous or unlawful statements and does not contain material or instructions that might cause harm or injury.

This copyright form must be signed by all authors. Separate copies of the form (completed in full) may be submitted by authors located at different institutions; however, all signatures must be original.

ID number: ID number:

Full name (block letters) Full name (block letters)

Signature Date Signature Date

ID number: ID number:

Full name (block letters) Full name (block letters)

Signature Date Signature Date

ID number: ID number:

Turkish authors must supply their ID card number; foreign authors must supply their passport number (if possible)